Assemblies in solution of polymers, ions and gold nanoparticles : assembly mechanism, characterization and applications

Marjorie Yon

Université Fédérale
Toulouse Midi-Pyrénées

THÈSE

En vue de l'obtention du
DOCTORAT DE L'UNIVERSITÉ DE TOULOUSE

Délivré par l'Université Toulouse 3 - Paul Sabatier

Présentée et soutenue par

Marjorie YON

Le 9 décembre 2022

assemblages en solution de polymères, d'ions et de nanoparticules d'or: mécanisme de formation, caractérisation et applications

---

Ecole doctorale : **SDM - SCIENCES DE LA MATIERE - Toulouse**

Spécialité : **Chimie-Biologie-Santé**

Unité de recherche :
IMRCP - Laboratoire des Interactions Moléculaires et Réactivité Chimique et Photochimique

Thèse dirigée par
Jean-Daniel MARTY et Eliza-Diana CIUCULESCU-PRADINES

Jury

Mme Mona TRéGUER-DELAPIERRE, Rapporteure
Mme Nathalie MARCOTTE, Rapporteure
M. Nicolas SANSON, Examinateur
M. Jean-Daniel MARTY, Directeur de thèse
Mme Diana CIUCULESCU-PRADINES, Co-directrice de thèse
M. Fabien DELPECH, Président

Remerciements

Je souhaiterais tout d'abord remercier les 4 membres du jury qui ont accepté de bien vouloir évaluer mon travail de thèse : Pr. Mona Tréguer-Delapierre, Dr. Nathalie Marcotte, Dr. Nicolas Sanson et Pr. Fabien Delpech. Merci pour ces échanges scientifiques qui m'ont permis d'avoir un regard critique et mature sur ce projet de thèse.

Je remercie également les deux autres membres du jury qui ont supervisé ce projet de thèse et qui ont été mes encadrants pendant ces 3 années : Jean-Daniel et Diana. Je vous remercie de m'avoir faite confiance sur ce projet et de m'avoir initiée à la recherche à travers cette thèse. C'était pour moi une expérience enrichissante et je vous remercie de m'avoir accompagnée jusqu'au bout. Jean-Daniel, merci également de m'avoir accueillie dans ce laboratoire et de m'avoir toujours poussée à aller plus loin.

La thèse est un projet scientifique, mais également une expérience humaine très particulière, qu'il n'est pas toujours facile d'apprécier. Je souhaiterais dans ce cadre remercier mon parrain de thèse, qui est également le directeur de mon école doctorale, Eric Benoist, qui m'a aidée tout au long de ce projet autant du point de vue professionnel que du point de vue personnel, à surmonter les différentes étapes qui m'ont conduite jusqu'ici. Merci Eric pour votre temps, votre écoute, vos conseils, vos actions, votre bienveillance et votre soutien.

Je suis fière et heureuse d'avoir eu l'opportunité de travailler sur ce projet avec plusieurs membres de mon équipe Ideas. Merci à Stéphane Gineste, avec qui je pouvais faire des analyses DLS comme des soirées jeux et qui m'a faite rencontrer un appareil indispensable à mon projet de thèse : le pH-mètre. Merci Barbara de m'avoir initiée aux techniques SAXS, de m'avoir emmenée au Synchrotron et pour ton temps pour traiter ces innombrables données. Merci également à Laure, la biologiste de l'équipe, de m'avoir initiée à la culture cellulaire et de m'avoir permise d'évaluer le potentiel de mes échantillons en biologie. Merci à toi Charles-Louis pour tes formations, ton temps, ton aide lorsque les analyses fluo n'émettaient aucune lumière dans mon cerveau.., mais merci aussi pour ta bienveillance au quotidien et tes attentes tardives avant la fermeture du labo. Merci également à Patricia pour tes idées, ton accompagnement et tes encouragements.

Enfin un remerciement spécial pour notre cher directeur du laboratoire : Monsieur Christophe Mingotaud que je vais m'obstiner à vouvoyer même dans ces remerciements. Merci très sincèrement de votre accompagnement dans ce projet scientifique, mais également de votre soutien moral. Merci de votre confiance pour le projet des Olympiades. Merci également de votre écoute, votre temps et vos conseils précieux.

Je souhaiterais remercier les autres membres de cette équipe qui ont suivi régulièrement en surface ce projet de thèse. Nos conversations au sein de nos réunions d'équipe m'ont beaucoup aidée, ainsi que votre temps pour répondre à certaines de mes questions ponctuelles. Merci à Clément pour tes réponses à mes questions parfois tirées par les cheveux, merci également pour ton aide dans les TP, et enfin.. merci pour le Run&bike ! Merci Christophe Coudret pour ces longues heures de remise en question de la science, mais qui furent enrichissantes et très bénéfiques, surtout ponctuées de bonnes blagues et d'anecdotes culturelles. Merci à toi Véronique de ton soutien et de ton aide pour l'enseignement. Merci également à Jean-Claude et Juliette pour votre aide sur le projet lors des réunions d'équipe. Enfin, je souhaiterais remercier Anne-Françoise et Nancy qui m'ont également aidée ponctuellement sur le projet, mais qui m'ont surtout soutenue dans ma démarche de recrutement au sein du laboratoire.

J'ai également eu le plaisir de collaborer avec une autre équipe du laboratoire : P3R, les experts des polymères ! Merci à Mathias et Olivier de m'avoir initiée à la synthèse RAFT et de m'avoir accompagnée dans cette période intensive au laboratoire. Merci pour votre temps et vos réponses à mes questions naïves de physico-chimiste ! Je souhaiterais également remercier Marc, pour tes explications scientifiques, ton aide au laboratoire et également ces conversations diverses qui m'ont également aidée moralement !

Merci à toi Alexandre W. pour ton aide technique sur la synthèse des polymères. C'était un plaisir de collaborer avec toi. Merci également pour ton investissement sans égal dans l'organisation des Olympiades. Je souhaite remercier également les deux stagiaires M1 que j'ai pu encadrées : Mélanie et Camélia, qui ont contribué au travail expérimental de ce projet. Enfin, merci à Céline et Sandrine de votre aide du point de vue administratif.

Je souhaiterais à présent remercier les personnes qui m'ont aidée dans ce projet mais qui ne sont pas membres du laboratoire. Concernant les services de l'ICT, un remerciement spécial adressé à Pascale, qui m'a beaucoup aidée dans la caractérisation de polymères, notamment l'utilisation de la GPC, et certains processus au laboratoire. Merci à Corinne Routaboul et Caroline Toppan pour leur formation sur l'ATR-FTIR et la RMN respectivement, et leur aide précieuse dans l'interprétation des données.

Un remerciement spécial pour le CMEAB dans lequel j'ai peut-être passé le quart de ma 3ème année de thèse… Merci à toi Dominique pour la préparation de mes centaines d'échantillons et de ton aide dans l'utilisation de la microscopie. Merci également à Bruno, Isabelle et Florence, de votre aide dans la réalisation des images de microscopie et de votre patience lors du transfert VOLUMINEUX de ces images.

Merci à Laurent Weingarten et Stéphane Le Blond Du Plouy pour votre aide dans la réalisation d'images en HAADF-STEM et en MEB au centre Raimond Castaing.

Merci à Franck Desmoulins, Carine Pestouri et Joao Piraquive pour les essais in vivo réalisés au CREFRE.

Merci à Yannick Coppel et Christian Bijani pour la réalisation des spectres RMN au LCC.

Merci à Frédéric Gessin pour l'accès à la QCM-D au sein de l'AIME.

Merci à Childérick Séverac pour la formation sur la QCM-D et son aide précieuse sur l'interprétation des données.

Merci à Nofel Merbahi de m'avoir initiée à la technologie du plasma et de m'avoir accompagnée dans des essais exploratoires pas toujours reproductibles mais néanmoins fascinants.

Merci à Kévin Roger de m'avoir initiée à la microfluidique et pour les essais réalisés sur son installation à l'ENSIACET. Merci également pour les pistes d'étude et l'aide dans l'interprétation des données DLS.

Merci à Pénélope Viana de l'IPBS pour les mesures réalisées en cytométrie en flux.

Merci à Chantal Galaup du SPCMIB pour son accompagnement dans les mesures en phosphorescence et son aide dans l'interprétation des données.

Je passe à présent aux remerciements destinés aux personnes désignées comme « non-permanentes » que j'ai pu croiser durant ces 4 ans au laboratoire des IMRCP.

Je voudrais tout d'abord remercier ces personnes avec qui j'ai partagé ce bureau 3034. Merci à toi Magali, même si tu n'es restée que 2 mois dans ce bureau et que tu m'as quittée pour aller 6 bureaux plus loin et avoir deux écrans ! Merci pour ton soutien et nos conversations entre 7h45 et 8h30 du matin !! Merci également à Faniri et Liming qui ont dû me supporter dans ma période intense de rédaction, mais grâce à qui j'ai tenu sur la fin. Merci également aux anciens doctorants et post-doctorants qui ont fréquenté ce bureau et qui m'ont également soutenue moralement dans ce projet : merci à Fang, Baptiste, Qilin, Raphaëlle et Guillaume. Merci enfin aux stagiaires coup de cœur de cette année : Amin, ma secrétaire à temps plein pour organiser ma rédaction et gérer ma salle d'attente, et qui sera mon futur ingénieur (qui sait…) et merci à Nadia, pour ta bonne humeur et ton soutien durant cette période du mois d'août vidée de tous ses membres du laboratoire.

Je voudrais à présent remercier ces personnes que la porte du bureau n'a pas arrêtées. On commence par les anciens. Un merci spécial à mes amies proches Camille, Sara et Judith sans qui cette expérience n'aurait peut-être pas abouti sans encombres et qui ont su apporter du bonheur et du soutien dans mes longues journées (et soirées..). Merci également à Nadiia et Hélène, qui m'ont également beaucoup remontée le moral et soutenue tout au long de ce projet. Merci également à Aline, Vivien, Maxime Demazeau, Mathieu Mestivier et Barbara Farias d'avoir partagé des moments conviviaux au sein de ce laboratoire et en dehors, qui sont malgré tout essentiels à une bonne poursuite de thèse.

Place aux jeunes, je voudrais remercier tout particulièrement cette fille blonde, palotte, à l'allure de miss, qui chante et danse sans arrêt et qui a été une agréable surprise en termes de rencontre au sein de ce laboratoire. Merci à toi Orélia, pour tellement de choses, mais essentiellement pour ton écoute, ton soutien, tes conseils, qui m'ont aidée à surmonter ces deux dernières années autant du point de vue professionnel que personnel. Merci également à Solène, Maxime, Luan et Vincent de votre aide au laboratoire mais surtout de votre amitié, qui m'a beaucoup aidée. Merci à toi Asli de ton écoute, tes conseils et ta bonne humeur contagieuse. Merci à Nicolas pour ton aide dans le projet des Olympiades et également d'avoir fait équipe avec moi pour le comité d'animation ! Merci également à Sasha, Maksym, Bruna, Emmanuelle, Bérénice, Louisa, Alexandre, Tiffany, Geoffrey, Mickael, Joséphine avec qui les moments partagés n'étaient pas assez nombreux, mais néanmoins riches en bonne humeur.

Une petite ligne spéciale pour toi Alexis, qui est parti (trop loin) et sans qui les parties de tarot et les soirées n'ont pas la même saveur. Je suis contente que tu aies pu finalement partir au Japon, merci pour ton amitié et ton soutien durant ces années. A ton retour, karaoké obligé !

Merci à toi Lucie de ton amitié précieuse et de ton soutien tout au long de ces années. Ta bonne humeur légendaire est un rayon de soleil dans ce laboratoire, et je te remercie de m'avoir faite positiver à chaque doute, chaque obstacle.

Je souhaiterais remercier ces personnes qui m'ont aidée dans l'organisation des Olympiades des IMRCP : Fanny, Nicolas, Alexandre, Lucie et Vincent. Ce fut une expérience très riche.

On s'éloigne à présent du laboratoire pour remercier toutes ces personnes qui m'ont également soutenue de près ou de loin dans ce projet. Merci à la team Mulhouse : Johanna, Emilie, Mégane, Christelle, Beverly, Antoine, Yan, John, Stéphane et Emilie P. Merci également à toi Denis, qui depuis le Jura a su me soutenir depuis ces dernières années.

Même sans même sang, on s'aimera. Merci à toi ma Flo, pour ton soutien constant et ton amitié exceptionnelle, qui se renforce d'années en années. Merci à ta famille, à Alexis. Et enfin, merci à toi qui n'est pas sur cette Terre depuis bien longtemps, mais qui a su me ramener aux choses essentielles et fabuleuses offertes par la vie. Un jour tu liras ces lignes, ma petite Ella, qui sont écrites par ta marraine qui t'aime fort.

Merci à vous mes grands-parents, qui me soutiennent depuis toujours et qui ont su trouver les bons mots pour m'aider à avancer et croire en moi. Je vous aime et j'espère vous rendre fiers.

Maman, Papa, quelques lignes ne suffisent évidemment pas.. mais pour résumer, merci pour tout. Merci d'avoir toujours été là. Dans les bons comme les mauvais moments. Merci de votre amour, de votre soutien, de votre écoute, de vos conseils, de vos opinions, de vos critiques, de vos félicitations, de vos encouragements… merci d'avoir cru en moi et de m'avoir poussée à obtenir ce que je souhaitais. J'espère vous rendre aussi fiers de moi que je le suis de vous. Je vous aime de tout mon cœur.

Parce que la vie n'avait pas grand intérêt avant que tu n'y fasses ton entrée, merci d'en faire partie depuis bientôt 26 ans et d'avoir toujours été un pilier essentiel. Mon petit frère adoré, notre complicité est une des choses les plus précieuses que je connaisse (et pourtant j'ai travaillé sur des nanoparticules d'or..) et je suis heureuse de partager avec toi tellement de choses dont cette passion pour la science (et pour les études interminables…). Merci également de ton écoute et de ces discussions sources de motivation. Bientôt ton tour pour devenir docteur, j'espère être en mesure de t'aider autant que tu l'as fait pour moi dans ce projet de thèse. Je t'aime fort.

Enfin, merci à toi, qui a réussi à te faire une place dans cette troisième année de thèse (malgré mon emploi du temps extrêmement chargé..) et grâce à qui cette année si difficile en apparence, s'est finalement vue grandement facilitée. Merci à toi Léo, pour la lumière que tu as apportée à ma vie. Merci pour ton soutien constant durant cette dernière année, tes écoutes tardives, tes remotivations, ta patience, ton attention, ton amour et ton sourire contagieux.

Pour finir, je souhaiterais sincèrement remercier mon cher partenaire de laboratoire : le pH-mètre, sans qui tout ce projet n'aurait pas été réalisable autant d'un point de vue pratique que d'un point de vue… non ben non en fait juste d'un point de vue pratique. A nos journées entières passées ensemble, en hiver comme en été, à attendre que tu veuilles bien te décider à me donner cette valeur précieuse si désirée : le pH.

Table of contents

Abbreviations

3D	Three-dimensional
Abs	Absorbance
AsF4	Asymetrical Flow Field-Flow Fractionation
AFM	Atomic Force Microscopy
ANOVA	Statistical method based on the variance's analysis
ATR-FTIR	Attenuated Total Reflectance- Fourier Transformed Infra Red
ATRP	Atom Transfer Radical Polymerization
BCPs	Block Copolymers
BIC	Block Ionomer Complex
C3M	Complex Coacervation Core Micelle
CAs	Contrast Agents
CCC	Critical Coagulation Concentration
CMC	Critical Micelle Concentration
CTA	Chain Transfert Agent
CV	Coefficient of Variation
DHBCs	Double hydrophilic Block Copolymers
DLS	Dynamic Light Scattering
DLVO	Derjaguin, Landau, Verwey, and Overbeek theory about aggregation regimes
$DP(_n)$	Degree of Polymerization
EDX	Energy Dispersive X-ray
EELS	Electron Energy Loss Spectroscopy
ESI-MS	ElectroSpray Ionization Mass Spectroscopy
ET	Electron Tomography
F4	Flow Field-Flow Fractionation
FDA	Food and Drug Administration
FP	Flocculation Parameter
HAADF-STEM	High Angle Annular Dark-Field detector Scanning Electron Microscopy
HPICs	Hybrid PolyIonic Complexes
HPLC	High Performance Liquid Chromatography
ICP-AES	Inductively Coupled Plasma Atomic Emission Spectroscopy
ICP-OES	Inductively Coupled Plasma Optical Emission Spectroscopy

ICP-MS	Inductively Coupled Plasma Mass Spectrometry
LCST	Lower Critical Solution Temperature
LDH	Layered Double Hydroxide
LLS	Laser Light Scattering
MADIX	Macromolecular Design via the Interchange of Xanthates
MALS	Multi-Angle Light Scattering
MEKC	Micellar ElectroKinetic Chromatography
MRI	Magnetic Resonance Imaging
MWCO	Molecular Weight Cut Off
NMR	Nuclear Magnetic Resonance
NNLS	Non-Negative Least-Squares
NPs	Nanoparticles
NSET	Nanometal Surface Energy Transfer
PIC	PolyIon Complex
PISA	Polymerization Induced Self Assembly
QCM-D	Quartz Crystal Microbalance – Dissipation monitoring
RAFT	Reversible Addition-Fragmentation chain Transfer
RDRP	Reversible Deactivation Radical Polymerization
RI	Refractive Index
ROI	Region Of Interest
SANS	Small Angle Neutron Scattering
SAXS	Small Angle X-Ray Scattering
SCMF	Self-Consistent Mean Field
SD	Standard Deviation
SdFFF	Sedimentation Field-Flow Fractionation
SEC	Size Exclusion Chromatography
SEM	Scanning Electron Microscopy
SERS	Surface Enhanced Raman Spectroscopy
SLD	Scattered Length Density
SLS	Static Light Scattering
SPR	Surface Plasmon Resonance
STEM	Scanning Transmission Electron Microscopy

TEM	Transmission Electron Microscopy
TBP	Triblock polymer
UCST	Upper Critical Solution Temperature
UV-vis	Ultra Violet - Visible

Molecules/ Chemicals / Biologicals

AA	Acrylic Acid
AgNPs	Silver nanoparticles
AIBN	Azobisisobutyronitrile
Ar	Argon
AuNPs	Gold Nanoparticles
AuNP@BSPP	BSPP-functionalized gold nanoparticle
AuNP@citrate	Citrate-functionalized gold nanoparticle
BA	Butyl Acrylate
BDMa	2,4-methacryloyl benzaldehyde oxime
BMA	Bis-methylamide
BSPP	Bis(p-sulfonatophenyl)phenylphosphine
$CaCl_2$	Calcium chloride
$Ca(NO_3)$	Nitrate calcium
CCM	Complete Cell culture Medium
$CDCl_3$	Deuterated Chloroform
$(CF_3SO_2)_2N^-$	bis(trifluoromethane)sulfonimide (Bistriflimide)
ClO_4^-	Chloride anions
CO_2	Carbon dioxide
DMF	Dimethylformamide
DOTA	Acide 1,4,7,10-tétraazacyclododécane-1,4,7,10-tétraacétique
DOX	Doxorucibin
DPS	3-(*N*,*N*-Dimethyldodecyl ammoniopropane sulfonate)
DT	Dodecanethiol
DTPA	Diethylenetriaminepentacetatic acid
EDTMP	Ethylenediamine tetra(methylene phosphonic acid)
EtOH	Ethanol

$Eu(NO_3)$	Nitrate europium
FA	Folic Acid
FBS	Fetal Bovine Serum
Fe_2O_3	Iron oxide
$Gd(NO_3)$	Nitrate gadolinium
GSH	Glutathione
H_2O_2	Hydrogen peroxide
$HAuCl_4.3H_2O$	Tetrachloroauric acid trihydrate
HCl	Chlorhydric Acid
HCT-116	Human Colorectal Tumor cells
HPS	3-(*N*,*N*-dimethylhexadecyl ammoniopropane sulfonate)
KOH	Potassium hydroxide
LiBr	Lithium bromide
Ln	Lanthanide
MA	Methyl Acrylate
MMA	Methyl Methacrylate
MUL	Mercaptoundecanol
NaCl	Sodium Chloride
NaOH	Sodium hydroxide
NO_3^-	Nitrate anions
NVP	N-Vinylpyrrolidone
PEGA	Poly(ethylene glycol) methyl ether acrylate monomer
Rh6GEMA	Rhodamine 6G methyl acrylic acid
SfCM	Serum-free Cell culture medium
t-BA	tert- Butyl Acrylate
TADA	1,2,3-triazole-4,5-dicarboxylic acid
THF	Tetrahydrofuran
TPS	3-(*N*,*N*-dimethyltetradecyl ammoniopropane sulfonate)
TTC	2-(dodecylthiocarbonothioylthio)-2-methylpropionic acid
V-70	2,2'-Azobis(4-methoxy-2,4-dimethylvaleronitrile
XA_1	*O*-ethyl-*S*-(1-methoxycarbonyl) ethyldithiocarbonate (Xanthate)
ZrO_2^+	Zirconyl ions

Polymers

P2VP	Poly(2-vinylpyridine)
P4VP	Poly(4-vinylpyridine)
PAA	Poly(acrylic acid)
P(AAm-*co*-AN)	Poly(acrylamide-*co*-acrylonitrile)
P(AzoMA-co-PEGMA)	poly[4'-[[(2-Methacryloyloxy)ethyl]ethylainino]azobenzene-co-poly (ethylene glycol) methyl ether methacrylate]
PAGA	Poly(2-acrylamido glycolic acid)
PAM	Poly(Acrylamide)
PATC	Poly[(3-acrylamidopropyl) trimethyl ammonium chloride]
PBLG	Poly(γ-benzyl-l-glutamate)
PnBA	Poly(n-butyl acrylate)
PNBA	Poly(*o*-nitrobenzene acrylate)
PBO	Poly(butylene oxide)
PCL	Poly(ε-caprolactone)
PDEAEMA	Poly(*N*,*N*-diethylamino ethyl methacrylate)
PDEGMA	Poly(di(ethylene glycol) methacrylate)
PDMA	Poly(*N*,*N*-dimethylacrylamide)
	Poly[2-(dimethylamino)ethyl methacrylate]
P(DBA-co-DTM)	Poly(2-(dibutylamino) ethyl methacrylate-*co*-dithiomaleimide)
P(DPA-co-DTM)	Poly(2-(diisopropylamino) ethyl methacrylate-*co*-dithiomaleimide)
PEG	Poly(ethylene glycol)
PEGMA	Poly(ethylene glycol) grafted Poly(methacrylate)
PEO	Poly(ethylene oxide)
PGA	Poly(l-glutamic acid)
PHPMA	Poly(2-hydroxypropyl methacrylate)
PiProx	Poly(2-*iso*-propyl-2-oxazoline)
PLGA	Poly(lactide-glycolide)
PMA	Poly(methyl acrylate)
PMAA	Poly(methylacrylic acid)
PMAEFc	Poly(2-methacryloyloxyethyl ferrocenecarboxylate)

P(MET/PBC)	Poly(methionine/ phenylboronic ester carbamate)
PMETAC	Poly(2-(methacryloyloxy)ethyl trimethylammonium chloride)
PMMA	Poly(methyl methacrylate)
PMMPImB	Poly[1-methyl-3-(2-methacryloyloxy propylimidazolium bromine)]
PMPC	Poly[2-(methacryloyloxy)ethyl phosphorylcholine]
PNAM	Poly(4-acryloylmorpholine)
PNBG	Poly(*o*-nitrobenzyl-l-glutamate)
PNBOC	Poly(2-((((2-nitrobenzyl)oxy)carbonyl) amino)ethyl methacrylate)
PNIPAm	Poly(N-isopropylacrylamide)
PNPEDMA	Poly(N-phenylethylenediamine methacrylamide)
PNVCL	Poly(N-vinylcaprolactam)
P(N)VP	Poly(N-vinylpyrrolidone)
PPG	Poly(propylene glycol)
PPO	Poly(propylene oxide)
PPS	Poly[(propylenesulfide)
PS	Poly(styrene)
PSBMA	Poly(sulfobetaine methacrylate)
PSMT	Poly(styrene-*alt*-maleic anhydride) thiol-functionalized
PSPA	Poly(carbamate-containing spiropyran monomer)
P(tBA)	Poly(tert butyl acrylate)
P(TAHB)	Poly(2-(2,2,2-trifluoroethylcarbamoyl)ethylthio)-2-(acrylamido)-*N*-(2-hydroxyethyl)butanamide)
PTPMA	Poly(2,2,6,6-tetramethyl-4-piperidyl methacrylate)
PVAm	Poly(vinyl amine)
PVBA	Poly(3-vinylbenzaldehyde)

Data symbols

D	Diameter (measured in TEM)
D_{core}	Core Diameter
D_H	Hydrodynamic Diameter
Đ	Dispersity Index
λ_{em}	Emission Wavelength

λ_{ex}	Excitation Wavelength
M_n	Molecular weight (number)
M_w	Molecular weight (weight)
PDI	Polydispersity index
q	water molecules number in inner sphere of lanthanides
R	Charges ratio
r_1,r_2	Relaxation rates
R_C	Core Radius
R_g	Gyration Radius
R_H	Hydrodynamic Radius
σ	Error range onto diameter from HAADF-STEM
T_1	Longitudinal relaxation time
T_2	Transveral relaxation time
τ_{D2O}	Luminescence lifetime in D_2O
τ_{H2O}	Luminescence lifetime in H_2O
τ_M	Water residence time
τ_R	Rotational tumbling time
ξ	Zeta potential

Introduction

Nature has always inspired scientific research. Among natural phenomenon, some assembly processes occur to obtain precise nanostructures which size, morphology or architecture are fixed according to equilibrium laws or adaptation to the environment. These assembly mechanisms represent models that nanotechnology tries to mimic by using either compounds from biological environment such as DNA or derivatives, or synthetic building blocks like surfactants or block copolymers (BCPs). Assembly concept can answer numerous problematics, such as to protect a molecule via encapsulation method, to increase properties through collective effect, or act like a detector for some molecular interactions. Latter problematics concerns several fields of applications, like biology, energy, or environment, which require precise architectures and properties.

The investigations into molecular assemblies request then compounds with tunable characteristics to optimize as much as possible the final nanostructures' design and properties. In this context, block copolymers (BCPs) represent a suitable category, as the recent advances in synthetic chemistry now allow to manage in a facile way both size, composition and architecture of the final polymer. BCPs are then largely involved into assemblies at a nanoscale level and more recently into the design of so-called hybrid assemblies, which are composed of both organic and inorganic matter. The main advantage of this hybrid behavior lies into the acquirement of both stability and performance, which are two essential criteria for every application field.

The present manuscript fits in with these problematics related to hybrid assemblies and particularly the understanding of their formation mechanism, with the aim to better control the final nanostructures characteristics and properties. This work focuses on the assembly mechanisms involving three main compounds: block copolymers (BCPs), ions and gold nanoparticles (AuNPs). The manuscript is divided into four major parts dealing with this topic.

First and foremost, it is essential to understand the role of block copolymers into assembly mechanisms and their interactions with inorganic matter to form hybrid assemblies. For that purpose, a review in **chapter I** begins with a quick description of the various possible architectures of the block copolymers found in the literature and rapidly focuses on the linear block copolymers. Self-assembly of the BCPs in solution is explored in details with examples describing the numerous manageable parameters used to control the assembly mechanism. The review examines then the hybrid assemblies made of interactions between ions and BCPs and then between gold nanoparticles and BCPs. Inorganic species can interfere through many ways into assembly mechanism of the BCPs in solution and sometimes are able to bring remarkable properties for further applications. The next point deals with the main characterization techniques of these hybrid assemblies and the particular association of scattering techniques and microscopy is outlined. Finally, the possible applications using these hybrid assemblies with a list

of recent examples are enounced. The project objectives are stated at the end of this chapter to do the transition with the next chapters dealing with the work realized for this project.

The **chapter II** starts with the choice of a suitable block copolymer for the project. In analogy to previous works realized in the team, the double hydrophilic block copolymer (DHBC) PAA-*b*-PVP is synthesized and characterized. The investigation of this BCP into hybrid assemblies in solution with several metal ions is then described. Obtained nanostructures are named Hybrid Polyionic Complexes (HPICs) and are characterized with the usual techniques described in chapter I. The use of gadolinium ions is particularly explored and leads to assays in MRI.

In **chapter III**, the set up of a colorimetric test based on assembly of AuNPs is described. The need for a quick bench titration test of gadolinium ions in the preparation of contrast agents for MRI, is the starting point of this investigation. The AuNPs' optical properties serve then here to inform about the presence of gadolinium ions.

This work ends with the study of the pH-responsiveness of the PAA-*b*-PVP BCP and its ability to self-assemble under pH variation. The **chapter IV** regards on the final polymeric nanostructures obtained and the study is enlarged by introducing inorganic species like AuNPs or gadolinium ions, to obtain pH-responsive hybrid assemblies. The variations of numerous parameters involved in the assembly mechanism are investigated, to fulfill the objective of understanding the process to better control it.

Chapter I

Literature review and project objectives

I Introduction

Molecular assemblies are ubiquitous into nature, e.g. phospholipids' self-assembly aims at forming cell membranes and they are essential for the function of the single molecular entity. Therefore, the synthetic design of organized nanostructures has raised much attention since decades and several strategies to control the assembly mechanism and thus target specific morphologies, have been explored[1–3]. Through the understanding of assembly molecular processes and its impact onto the resulting assembled system's properties, the final architecture of the nanostructure can be easily managed. Therefore, many assembled systems are now used in various fields of applications because of their precise construction and their tunable properties. The most widely used molecules into these molecular assembly processes are surfactants, considered as small molecules, and polymers, more particularly block copolymers (BCPs). This category of polymers is of great interest into the design of assembled systems, as BCPs contain two or more chemically distinct polymer chains that are covalently joined via their respective end groups, the resulting package can lead to compartmental architectures like surfactants assemblies. BCPs' assemblies find many application fields such as energy, biology, environment[4,5], but can either be used as organic templates for molecules incorporation. However, a precisely designed BCP configuration is a key prerequisite for controlling the assembly process leading to highly ordered multimolecular architecture. Progress in polymer science has given rise to a wide range of polymerization methods able to produce a variety of polymers with controlled architecture.

In this chapter, the BCPs' self-assembly mechanisms will be detailed from a theoretical point of view, and then some examples will illustrate the influence of some parameters onto this self-assembly process. A quick focus will be made regarding the use of Double Hydrophilic Block Copolymers (DHBCs) molecules, which represent a sub-category of BCPs, containing two hydrophilic polymers chains and representing suitable strategy to design water-solvated assemblies. The second part of this chapter will then expose several strategies to design hybrid nanostructures through assembly process between block copolymers and the inorganic matter of interest for this project, i.e.: ions and gold nanoparticles. To control the architecture of the obtained assembled system, it is essential to use techniques able to give information about the size and the morphology of the nanostructures present in solution. Finally, the main characterization methods of these polymer-based assemblies will be detailed and examples will illustrate their use in typical studies following the size and morphology evolution during assembly process or during transition morphology mechanisms.

II Block copolymers

II.1 Architectures and functionalities

Copolymers are polymers that contain two or more types of monomer and these monomers can be distributed in many different ways along the polymer chain. Their synthesis is nowadays highly controlled due to the achieved progresses in synthetic chemistry giving rise to a wide range of polymerization techniques. Control over the molecular weight, configuration and architecture, led to linear and branched copolymers as depicted in **Figure 1**. Among linear copolymers, three main configurations can be obtained by adjusting the polymerization process, resulting in original repartition of the monomers along the chain: block, gradient or statistic, and therefore different properties of the polymer could be obtained.

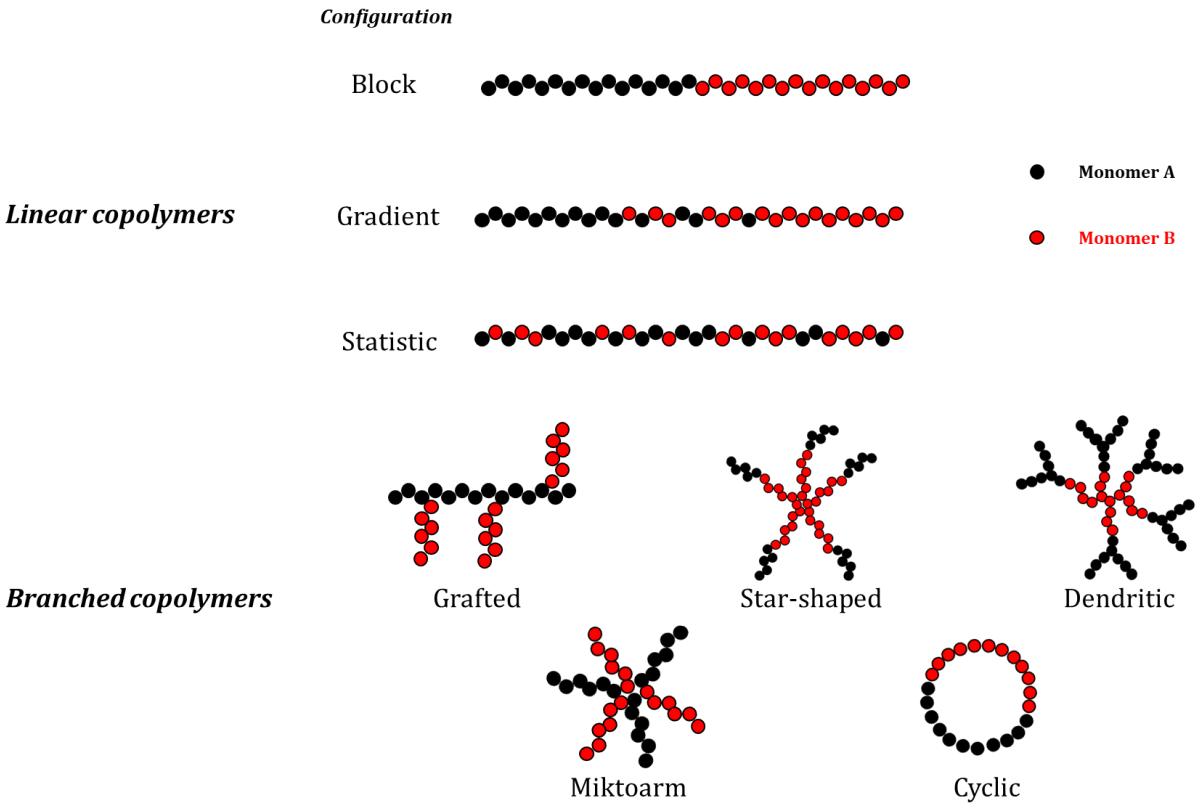

Figure 1. Configurations of linear copolymers (block, gradient, statistic) and architectures of branched copolymers (grafted, star-shaped, dendritic, miktoarm and cyclic)

Among all these configurations, linear block copolymers (BCPs) represent the most studied category in the literature. The combination of two polymers into one macromolecular compound opens many possibilities regarding the hydrophilicity of each block, its length and its chemical function. These choices are made in agreement with the targeted application of the block copolymer. The work is here mainly focused on the use of linear block copolymers in water solvent with potential applications in biological field, comprising thus at least one hydrophilic block

polymer. If the second polymer block is hydrophobic, the copolymer is amphiphilic and if it is hydrophilic, this is double hydrophilic block copolymer (DHBC). Double hydrophobic block copolymers exist as well, but will not be described in this work. Lengths of each block can be managed via controlled polymerization process like Atom Transfer Radical Polymerization (ATRP)[6] or reversible addition-fragmentation chain transfer (RAFT) polymerization.[7] Finally, the choice of the chemical functions depends on the targeted interactions with other chemical compounds or biological entities.

Once all these parameters fixed, the block copolymer can be designed and studied in different environments. The main interest described in the literature concerns the assembly of the block copolymers. Indeed, the segments of the block copolymers control the assembly process, the arrangement of the polymers and the cargo, and the stability of the assemblies, as well as the performances in biological environments. It is therefore interesting to understand how these intrinsic parameters influence the assembly mechanism. In addition, external parameters and the use of stimuli can also be used to design specific assembled structures.

II.2 Assemblies of block copolymers

The main strategies to assemble the BCPs are in bulk and in solution. Other strategies are also employed like assemblies in thin film, zone casting and electro spray[8]. The assembly in bulk is rapidly described here to introduce the notion of microphase separation. Then the assembly in solution will be largely described to better understand the context of the following work.

II.2.1 Block copolymers assembly in bulk[9,10]

The interest in block copolymers lies in their self-assembly at different states (solid, molten, in solution) and at different scales. According to their length, the structuration leads to microphases, mesophases or nanophases. These phase separations are driven by the incompatibility between the two blocks of the copolymer and depends on i) the volume fraction of the A and B blocks (f_A and f_B, with $f_A + f_B = 1$), ii) the total degree of polymerization ($N = N_A + N_B$) and iii) the Flory-Huggins parameter χ_{AB} [9], with specifies the degree of incompatibility between the A and B blocks. This parameter is defined by the following relation:

$$\chi_{AB} = (Z/k_BT).[\varepsilon_{AB} - (1/2).(\varepsilon_{AA} + \varepsilon_{BB})$$

Where χ_{AB} is the free-energy cost per monomer (in units of the thermal energy $k_B.T$) of contacts between A and B monomers; Z is the number of nearest neighbors per repeat unit in the polymer, and ε_{AB}, ε_{AA}, ε_{BB} are the interaction energies per repeat unit of A-A, A-B and B-B respectively. When χ_{AB} is positive there is a net repulsion between A and B blocks whereas when it is negative, the free-energy aims at the mixing of the two blocks.

In order to construct the theoretical phase diagram, several theories have been developed dealing with the phase behavior of diblock copolymers in bulk, such as the self-consistent mean-field (SCMF) theory. By increasing the fraction of monomer A, which is defined as $f_A = N_A/N$, with N_A the number of monomer A units in a macromolecular chain and N the total number of monomer units, several equilibrium morphologies of AB diblock copolymers in bulk can be obtained (**Figure 2**) as described by F.S. Bates and G.H. Fredrickson.[10]

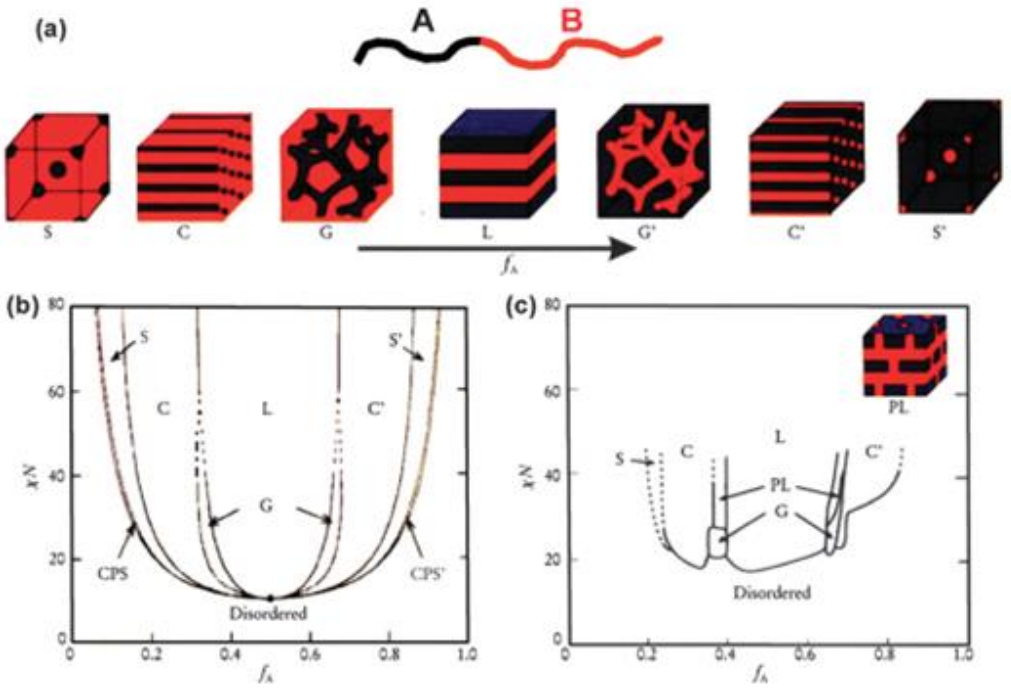

Figure 2. (a) Equilibrium morphologies of AB diblock copolymers in bulk: S and S' body-centered-cubic spheres, C and C0 = hexagonally packed cylinders, G and G0 = bicontinuous gyroids, and L = lamellae. (b) Theoretical phase diagram of AB diblocks predicted by the self-consistent mean-field theory, depending on volume fraction (f) of the blocks and the segregation parameter, χN, where χ is the Flory–Huggins segment–segment interaction energy and N is the degree of polymerization; CPS and CPS0 = closely packed spheres. (c) Experimental phase portrait of polyisoprene-block-polystyrene copolymers, in which f_A represents the volume fraction of polyisoprene, PL = perforated lamellae. (reproduced with permission from ref. [10])

No need to go further into this bulk assemblies' description for the present manuscript, as the work is mainly focused on the assemblies of block copolymers in solution. This short introduction allows anyway to understand the influence of the intrinsic parameters of the block copolymer on its behavior in melt and solid states.

II.2.2 Block copolymers assembly in solution

Previous assembly mechanisms of block copolymers in bulk lead to several nanostructures according to the fraction of one of the monomers to the other. However, the introduction of a solvent makes the system more complex as the solvent can impact the interactions of the block polymers between each other and with their environment. The study of the assembly of block copolymers in solution was largely reported, particularly in water.

The obtained nanostructure could be used as a carrier system for drug delivery or pharmaceutical use[11]. The assembly of block copolymers in solution can be either influenced by "internal" parameters like copolymer concentration or miscibility of the polymers blocks in water, or by "external" parameters such as physical or chemical stimuli[12–14]. The self-assembly behavior of amphiphilic block copolymers in water can be well described from a thermodynamic standpoint. The amphiphilic block copolymers assemble with each other to decrease the interfacial area of the insoluble blocks for lowering the interfacial free energy. The interactions between blocks, and between block and solvent, are governed by intrinsic parameters of the block copolymer such as the relative volume fraction (*f*), the solvophobicity, and the degree of polymerization of each block. These three characteristic parameters are related to another one, named packing parameter, *ρ*, investigated by Israelachvili, Mitchell and Ninham.[15] Indeed, this packing parameter is used to predict the morphology resulting from the self-assembly mechanism of surfactants and can be defined as follow:

$$\rho = (v/a_0.l_c)$$

where v is the volume of the hydrophobic chain, a_0 is the area of the head group at equilibrium and l_c is the length of the hydrophobic tail. The model has been applied to describe the BCP self-assembly and how their volume fraction could influence the final morphology through their own curvature, as illustrated in **Figure 3**.

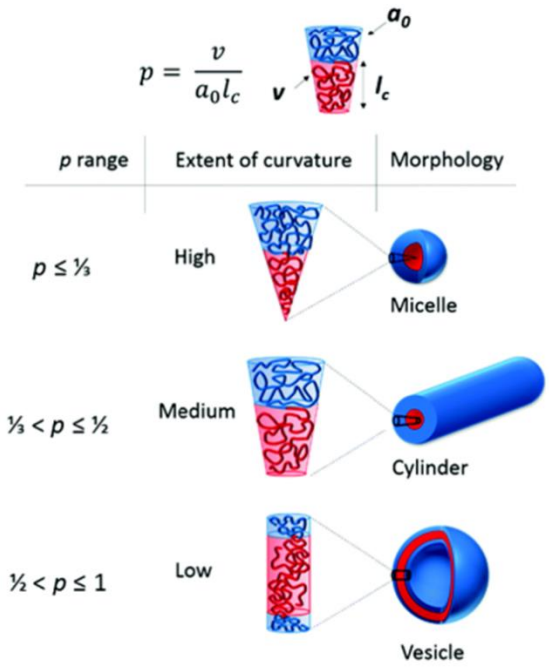

Figure 3. The different morphologies obtained by targeting different packing parameters ρ. [16] Published by the Royal Society of Chemistry

Contrary to surfactants, polymeric assemblies are generally more stable thanks to the greater interfacial free energy derived from the larger insoluble segments. The exchange between free BCP chains and those in micelles is very slow compared to the assembly process, making sometimes the thermodynamically state difficult to achieve. Indeed, block copolymers are able to adopt morphologies which are out of or near equilibrium state, considered as intermediate morphologies. This opens a wider range of accessible morphologies, which are either thermodynamically or kinetically controlled [17–19].

The formation of thermodynamically preferred structures depends on three contributions to the free energy of the system: i) the degree of stretching of the core-forming blocks, ii) the interfacial tension between the micelle core and the solvent outside the core, and iii) the repulsive interactions among corona-forming chains. Numerous factors affect one or several of these three contributions like copolymer composition and concentration, water content in the solution, nature of the common solvent or the addition of compounds like ions or other polymers. **Table 1** sums up the different studies made about latter factors' influence on the final morphology of the assembled BCP.[17,20–25] The general method of preparation of the BCP assembly consists first in the solubilization of the amphiphilic polymer in a common solvent for both blocks and then a solvent which is selective for only one of the two blocks, like water, is introduced to induce assembly mechanism. This method is known as emulsion solvent evaporation-induced self-assembly.[26] The nature of the solvents[20] and their proportion, the configuration of the polymer[27] and the addition of surfactants or other polymers.[28] can have a real impact on the final morphology.

Table 1. Studies about parameters influence onto the final assembly morphology of block copolymers

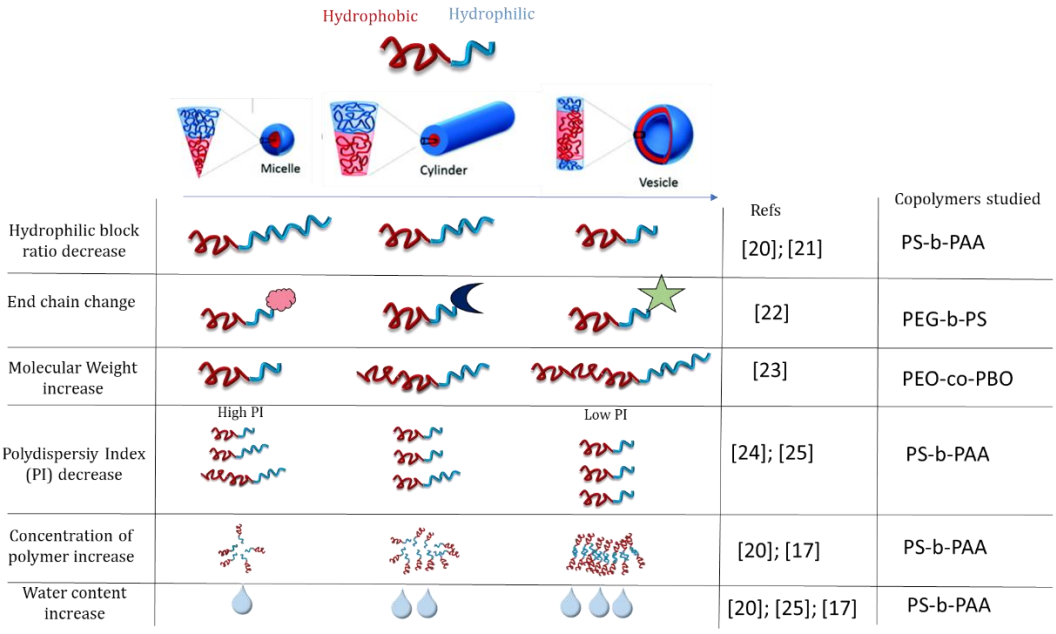

	Refs	Copolymers studied
Hydrophilic block ratio decrease	[20]; [21]	PS-b-PAA
End chain change	[22]	PEG-b-PS
Molecular Weight increase	[23]	PEO-co-PBO
Polydispersiy Index (PI) decrease	[24]; [25]	PS-b-PAA
Concentration of polymer increase	[20]; [17]	PS-b-PAA
Water content increase	[20]; [25]; [17]	PS-b-PAA

II.2.2.1 Influence of external parameters

Stimuli-responsive polymers are macromolecules which undergo phase transitions in response to a change in its near environment, induced by an external factor named stimuli. Three main categories of stimuli are reported; physical, chemical and biological.

BCP responsive to physical stimuli

Some polymers possess chemical functions making them sensitive to physical parameters such as temperature or light. The variation of these physical parameters induce molecular changes in solution and the structure of the polymer can be affected, impacting its final assembled morphology. Physical stimuli are then a strategy to control self-assembly mechanisms of some block copolymers in solution.

Temperature is one of the most studied physical parameters inducing reversible transitions. Thermoresponsive polymers go through phase transitions when temperature is increasing or decreasing. According to their temperature range of solubility, the thermoresponsive polymers exhibit a lower critical solution temperature (LCST) or an upper critical solution temperature (UCST). Over LCST and under UCST, thermoresponsive polymers are getting more and more insoluble in their present solvent, and will tend to aggregate in solution.

The main thermoresponsive polymers displaying a LCST are Poly(N-isopropylacrylamide) (PNIPAm), poly(N-vinylcaprolactam) (PVCL) and poloxamers which are combination of two polymers: Poly(ethylene oxide) (PEO) and Poly(propylene glycol) (PPG).[29] The progressive increase in temperature make the existing hydrogen bonding between the polymer and the water weaker and the dehydration of the polymer starts until aggregation. Regarding polymers displaying UCST, they are generally zwitterionic and are implied in supramolecular bondings, which are weakened when temperature is getting low, leading to phase separation and aggregation.[30]

Block copolymer structures can contain either two thermoresponsive blocks, or one thermoresponsive combined with an inert polymer block which would help for stability. The advantage of having a double thermoresponsive block copolymer is that if transition temperatures are different, the possible structures are multiple. [31,32] The copolymer composition can affect the transition temperatures and the final morphologies as well, as illustrated on **Figure 4**. [32,33]

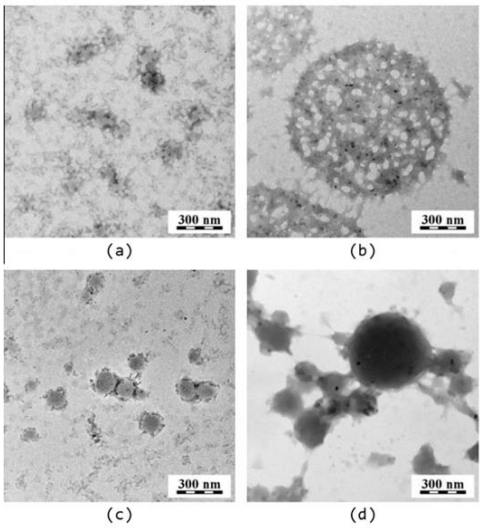

Figure 4. Transmission electron micrographs of PNIPAm-*b*-PnBA aggregates obtained by drying the 1mg/mL solutions at room temperature (a and b) and at 318K (c and d): (a and c) $PNIPAm_{100}$-*b*-$PnBA_{32}$ (b and d) $PNIPAm_{360}$-b-$PnBA_{32}$. Both PNIPAm and PnBA are thermoresponsive polymers. (reproduced with permission from [33])

Light is another physical stimulus which is widely used to induce the self-assembly of block copolymers. Photoresponsive chromophors, such as azobenzene, are introduced into the structure of the block copolymer to better control the assembly mechanisms in solution due to the local change of conformation of azobenzene under light exposure. Some examples are presenting how the light parameters such as irradiation time and wavelengths influence the self-assembly mechanisms of triblock copolymers and the resulting assembled systems.[34,35] (**Figure 5**).

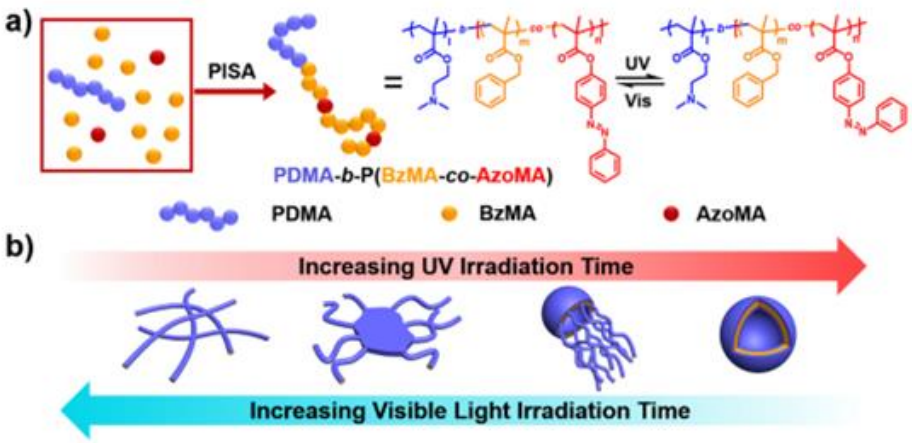

Figure 5. Preparation and isomerization of photoresponsive copolymers (a); Mechanism insights of the photoinduced reversible worm-to-vesicle transformation. The polymer of interest was synthetised by Polymerization-Induced Self-assembly (PISA). (reproduced with permission from [34])

BCP responsive to chemical stimuli

Chemical stimuli, like protonation or deprotonation of an ionizable polymer through pH change, can induce local structural modifications of the BCP leading to an assembly of the BCP. Similarly, the addition of ions without changing pH, or even other polymer compounds can act as chemical stimuli.

pH stimulus represents one of the most used chemical stimuli to induce polymer assemblies as it is easy to modify and it can be related to biological applications like release based on acidity change. As like for the temperature, one critical pH value delimits the two domains into which the polymer is either free or aggregated. The critical pH value is named pK_A value and depends on the nature of the polymer. The composition of pH-sensitive BCP generally contains at least one polymer with an ionizable chemical function, able to be protonated or deprotonated. In the work of N.S. Lee and al.[36], both blocks are pH-responsive, but their pK_A value differs. Under pH variation, several micelles' sizes can then be obtained. Moreover, by changing the configuration of the BCP, block, gradient or statistic, it is possible to influence the pH-responsiveness and thus obtain different morphologies.[37] The emulsion solvent evaporation induced self-assembly method has been widely investigated to obtain attractive polymers-made structures.[38–40] This method consists in first dissolving the polymer into organic solvent and then add surfactants to induce the formation of an emulsion droplets. After evaporation of the organic solvent, polymer-based nanostructures are finally obtained. One example using this emulsion droplet method, shows that pH variation can affect the interfacial properties of the emulsion through the modification of the solubility of the BCP and cause then a change in the final configuration of the assembly.[41] As mentioned before, the pH-responsive assemblies can be investigated into drug release strategies by playing progressively on the disassembly process.[42] Sometimes pH-induced assembly of block copolymers can lead to gelation processes providing different morphologies at each pH value.[43] Finally, the pH can be applied onto existing micelles obtained by a RAFT polymerization-induced self- assembly process (RAFT-PISA)[44], in order to change the global size of the micelle for further applications like using these micelles as reactors to synthesize emulsions.[45] Some morphological transitions can be triggered by adding other kind of ions, small molecules such as surfactants[46] or polymers[21], gases, biological species such as amino acids or through redox reactions.

The addition of ions in micromolar ($CaCl_2$) or millimolar (NaCl) concentrations can change the morphology of "crew-cut" aggregates of amphiphilic block copolymers in dilute solutions[47], forming rodlike, and univesicular or lamellar aggregates. This is explained by a change into the repulsion and steric interactions present into the hydrophilic corona.

Sphere-to-wormlike particles, sphere-to-vesicle, and sphere-to-precipitate transitions were also observed after ion exchange of I^-, SCN^- and PF_6^- for Br^-, morphological transitions being controlled by a competition of solvation and size effects of the newly introduced counter ions.[48] Playing on the ions' concentration can help targeting some specific morphologies when the BCP is coordinating the respective ion[49]. Moreover, this study stresses on the specificity of the coordination process, as the change of the morphology only happens for Pb^{2+} ions and not for Na^+ ones, which could be useful for further sensing applications. Finally, playing on both ion and solvent nature can help changing the final morphology[50] and sometimes another stimuli can be applied, like UV irradiation, on ion-induced assemblies to adjust again the final structure.[51]

A last focus on the addition of chemicals to design assemblies of BCP describes the use of carbon dioxide (CO_2). The bubbling of this gas into water induces change of electroconductivity and pH variation and thus is indirectly the cause of morphological changes of BCP and their self-assembly, like in the work of E. Yoshida.[52] Indeed, the presence of carbonic acid leads to the protonation of the amine functions of the poly(2,2,6,6-tetramethyl-4-piperidyl methacrylate) (PTPMA)-based triblock copolymer forming the initial vesicles, which then change their morphology to micelles. This process is reversible by adding an inert gas like argon (Ar) or N_2. Recent work was investigated onto the influence of CO_2 on assemblies issued from RAFT-PISA process comprising the DMAEMA monomer, which is CO_2-sensitive through its amine functions. This study was realized in methanol, where the resulting assemblies remained spherical with time, whereas in water, the morphologies go from spheres to "jellyfish" and vesicles.[53]

Combined stimuli

A lot of studies report on the combination of the stimuli described above in order to obtain multi-responsive systems and thus multiplying the possible morphologies. Generally, physical stimuli are combined with chemical ones to change both the environment with external sources (temperature or light) and the internal composition of the solution by introducing other chemicals (ions, gas). **Table 2** sums up some recent examples of works[54–62] dealing with multi-responsive block copolymers implied in self-assembly mechanisms resulting in several kind of morphologies.

Table 2. Recent works dealing with multi stimuli-responsive block copolymers and their resulting assemblies

Physical/Chemical stimulus References	Polymer	Temperature	Light	pH	Ions	CO_2	Redox
[54]: C. Nadal et al. (2022)	$PVAm_m$-*b*-$PNIPAM_n$	x		x			
[55]: Y. Cao et al. (2020)	PAA-b-P (AzoMA-co-PEGMA)		x	x			x
[56]: S. Ji et al. (2019)	PEG-*b*-PNBG		x		x		
[57]: S. Lin et al. (2017)	PEG-*b*-P(AAm-*co*-AN)-*b*-PDEAEMA	x				x	
[58]: A. Nabiyan et al. (2020)	P*i*PrOx-*b*-PAGA	x			x		
[59]: Y-J. Sun et al. (2022)	Triblock copolymer	x	x			x	
[60]: X. Zhao et al. (2018)	P(TAHB-*co*-NIPAM)-PCL-PAA (A_2BC_2)	x		x			x
[61]: F. Gao et al. (2017)	PAA-*b*-PAzoMA-*b*-PNIPAM	x	x	x			
[62]: A.E. Smith et al. (2009)	$PDMAEMA_x$-*b*-$PNIPAM_y$	x		x	x		

II.2.2.2 Specific case of Double Hydrophilic Block Copolymers (DHBCs)

DHBCs contained two or more water-soluble blocks of different chemical nature [63–65]. Therefore, one block only promotes solubilization and sometimes stabilization in water, whereas the other block is responsive to an external stimulus or capable of interacting with another polymer, substrate or chemical specie. As previously described, the use of physical or chemical stimuli, such as temperature[66–68], pH[67,69] or ionic strength[70] can induce a change in the hydrophilicity of one of the blocks thus introducing an amphiphilic behavior, which potentially affect the self-assembly of the DHBC. These stimuli and the design of the DHBC remain the only options to induce assembly process, as there is no need to use organic solvent to organize the blocks according to their solubility. H. Sohn et al. tested both variations by increasing progressively the length of PAA block into a PAA-*b*-PEG DHBC and in parallel increasing the concentration of a platinum complex which induces assembly of the block copolymer either by complexation with the PAA block or by both complexation and additionally hydrogen bonding interaction with the second PEG block. This variation between the block length and the concentration of the Pt complexes results in different morphologies of the assemblies. (**Figure 6**)[71].

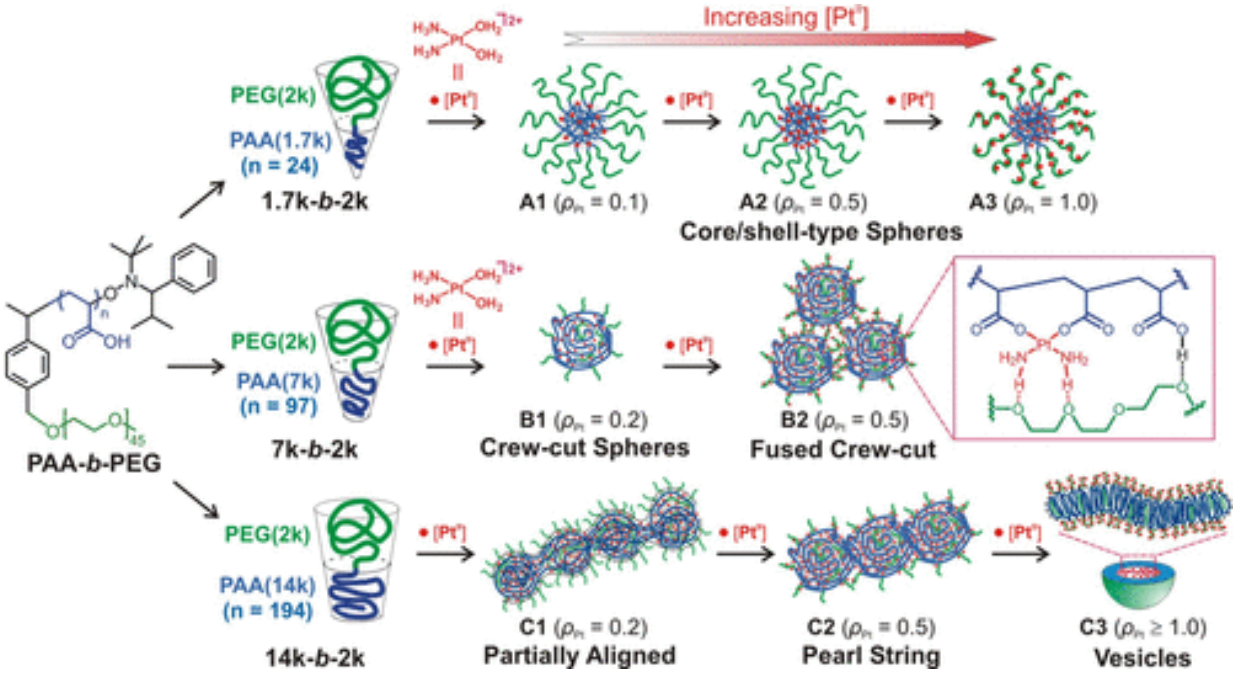

Figure 6. Schematic Illustration Showing the Morphology Transition of Pt^{II}-Incorporated Nanostructures, depending on the Length of Chelating PAA Blocks and Pt^{II} Feeding Ratio (ρ_{Pt}). (reproduced with permission from[71])

Recent development regarding DHBCs deals with block copolymers combining neutral and charged segments, and which form self-assemblies when they are mixed with oppositely charged compounds. Resulting structures are either polyion complex (PIC)[72], either block ionomer complex (BIC)[73] or complex coacervation core micelles (C3M).[74,75] and their formation is mainly driven by the release of counterions triggered by ion-pairing formation. These called polyelectrolytes systems are used to manage assembly process as they are responsive to pH variation and ionic strength and can easily interact with other charged species to perform chemical or biological associations.[76,77] J.Warnant et al.[78] explored the influence of the nature of polyamine onto the core density of the resulting PIC micelle formed between this weak base and a weak acid represented by the DHBC PAA-*b*-PAMPEO. These ionic interactions were used to entrap a fluorescent specie, auramine O, and the core density tenability enabled to vary the resulting fluorescence properties of the polymer-based micelle. The association mechanism remains complex anyway and has been deeply studied by S. Gineste et al. regarding PIC micelles formed from electrostatic interaction between PAA-*b*-PEO as DHBC and dendrigraft poly(L-lysine). The stoichiometry of the PICs has been proved to influence the resulting formed structures.[79]

III Hybrid assemblies based on block copolymers and ions

In this section we will focus on assemblies driven by the interactions of polymer comprising ionizable or complexing groups with inorganic ions such as iron, zinc or copper. The assembly is generally composed of a segregated core and a stabilizing corona. Strengthening the cohesive forces in the core leads to more stable micellar systems with low CAC (critical association concentration). Some examples were previously described mentioning the influence of this type of interaction on the morphology of the assembly (**section II.2.2**). Metallic ions concentration, nature and the polymers intrinsic characteristics like molecular weight or composition can be tuned in order to control the assembly process.

Amphiphilic BPCs in interaction with ions

As a first example, the interaction of two amphiphilic block copolymers (PS-*b*-PAA and PS-*b*-P4VP) with europium ions was investigated in DMF.[80,81]. Final morphology and the resulting luminescence properties are influenced by the ratio between europium ions and the polymer. Indeed, the fluorescence spectra showed a first increase of the intensity of both excitation (λ=300-350nm) and emission peaks (I_{max} at λ=613 nm) when the ratio NVP:Eu is increased. Whatever the hydrophilic block nature (PAA or PVP), the complexation with the Eu^{3+} ions results in an enhancement of the luminescence of Eu^{3+} ions, showing potential interest for fluorescence applications. Further, the evaporation of the solvent solubilizing the amphiphilic BCP can lead to the formation of films or membranes with specific luminescent properties.[81] Another recent example used PS-*b*-PAA BCP combined with metallic ions, Ag^{+}, Zn^{2+} and Cu^{2+}, to make antibacterial membranes and proved that the evaporation time influences the porous shape and size of the obtained membrane.[82]

As described previously, the intrinsic characteristics of the polymer represent a key parameter in the design of polymeric assemblies. In the work of S. Dong et al.[83], the co-assembly of Cu^{2+} ions with amphiphilic block copolymers PEG_{45}-*b*-P(MET/PBC)$_n$ bearing pendant phenylboronic ester carbamate (PBC) and thioether moieties type methionine (MET) in the hydrophobic block, resulted in hybrid polymersomes with Cu^{2+} cross-linked membrane. In the presence of glutathione (GSH) (or sodium ascorbate) and H_2O_2, Cu^{+} ions were in situ produced via the reduction of the entrapped Cu^{2+} ions and subsequently initiated a Fenton-like reaction to generate hydroxyl radicals.

DHBCs interactions with ions

The use of DHBCs in water was largely investigated to obtain hybrid structures based on polymer-metallic ion interactions[84]. As explained before, the interaction between ionized DHBCs and oppositely charged metallic species triggers the block copolymer assembly.

First investigations about the formation of hybrid polyionic complexes (HPICs) by N. Sanson et al., dealt with the understanding of the structural organization of the block copolymer driven by the addition of metallic ions onto DHBCs solution. Indeed, the triggered assembly is composed by a core formed by a water-insoluble complex between ionized block and metallic ions[85]. The second block of the DHBC forms the corona and helps the stabilization of the hybrid structure into water solvent (

Figure *7*). Further studies were focused on the structural characterization[86] and the variation of some parameters such as the nature of ions or the molecular weight of the polymer and their respective influences on the final size of the structure.[87,88] These latter studies allow a better comprehension of the key parameters involved in the assembly process. The purpose is now to use the different properties of these metallic ions to find potential applications for these hybrid structures.

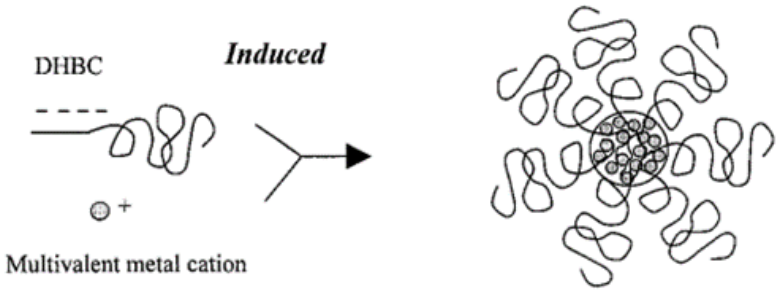

Figure 7. Schematic representation of the hybrid polyion complex micelles (reproduced with permission from [85])

PAAs represent an attractive core forming segment for constructing polymeric micelles from metal complexation. As an example, cis-platine can spontaneously self-assemble in water through polymer-metal complexation with the carboxylate moieties in the PAA segments of the block copolymer. When these micelles are exposed to physiological concentration of chloride ions, the carboxylate platinum complex can be dissociated, showing a sustained drug release and slow disassembly of the micelles. However, when cis-platine loaded micelles of block copolymers in which the PAA block was replaced by L- glutamic acid, a much slower dissociated rate was observed. This stability enhancement were related to the order arrangement of poly(L-glutamic acid-cisplatin) block into alfa helical bundle structures in their core[89].

Based on the same association mechanism between DHBCs and metallic ions, C. Frangville et al. synthetized HPICs nanostructures based on the complexation of gadolinium (Gd^{3+}) or europium (Eu^{3+}) ions with PAA-*b*-PEG.[90] Gadolinium ions are well-known for their paramagnetic properties and are currently incorporated in Magnetic Resonance Imaging (MRI) contrast agents (CAs).[91] Promising results were obtained regarding *in vivo* assays, combining both non-cytotoxicity and high contrast enhancement with an increase of 57% compared to the usually Gd-DOTA contrast agent. In order to strengthen the colloidal stability of these structures, the interactions within PAA core comprising Gd^{3+} ions can be enhanced through the addition of various amounts of zirconyl ions (ZrO^{2-}).[92] This led not only to a reinforced structure, but also to an improvement of relaxivity properties through a favored water exchange mechanism.

Regarding CAs for MRI, the manganese ions (Mn^{2+}) are as well very used as paramagnetic specie to enhance the relaxivity properties. Recent work explains how these cations were incorporated in polymeric nanoparticles resulting from the assembly of PEG-*b*-PAA DHBC holding a pyrene end-chain forming the hydrophobic core.[93] The addition of cisplatin complex onto these Mn (II)-filled polymeric nanoparticles, leads to the formation of polydisperse aggregate based on the substantial interparticle crosslinking. The inside structure of Mn^{2+} complex is close to a nanogel and allows a high water-exchange, which is again related to the relaxation rate property and this assembled system can be then considered as a highly efficient CA for MRI. The same nanostructures containing cisplatin, instead of Mn^{2+} ions, showed higher loading efficiency of ionic species and the inside structure was then different in terms of size and properties.

HPICs structures were used in the photo-Fenton reaction too, by incorporating Cu^{2+} ions into micelles of PAA-*b*-PEG DHBC[94]. The degradation kinetics of a model pollutant demonstrated the efficiency of the HPICs system as catalyst in photo-Fenton-like reaction with 38% of remaining pollutant after 5h. This Cu-HPICs system provides both advantages of simple synthesis compared to classic nanomaterials used in catalysis and sample recovery through dialysis of the HPICs solution after the catalytic reaction.

The two next examples will deal with the impact of electrostatic interactions between polymers and metallic ions, onto the thermoresponsive behavior of the polymers. The first study reports about the electrostatic interaction of PNIPAAm-*b*-PDMAEMA holding a terpyridine end-chain, with either nickel (Ni^{2+}), cobalt (Co^{2+}) or zinc (Zn^{2+}) ions.[95] The formation of metal-terpyridine bis-complexes provides efficient bridges between hydrophilic chains (PDMAEMA) and induces a first assembly step of the DHBC. A second step consists in varying the temperature until seeing the self-assembly of PNIPAAm polymer blocks into micellar cores. It appears that the nature of the metal ion leads to different kind of charged metal-ligand complexes, which will be responsible for a hydrophobic behavior more or less pronounced.

These metal-ligand complexes have some salting effects on the polymer, which involves a modification in its thermoresponsive behavior. The formation of supramolecular gels can then be managed through ions incorporation in the polymeric network and external parameters such as temperature and pH allowed a variety of morphologies, as well as factors related to polymer like concentration and block lengths.

A second example is related the effect of adding ion complexes on the LCST and UCST values of a double thermoreponsive copolymer P(DMAEMA-DEGMA).[96] The UCST-type cloud temperature values increase with increasing concentration of added metallic ions until reaching a plateau. The higher the atomic number of the added ion, the lower the UCST-type cloud temperature. This is explained by a lower electrostatic interaction between protonated amines and metal hexacyano anions with increasing ion radius of the counterions, resulting then in a lower charge density. As the electrostatic interactions are affected by the adding of ion, the variation of the pH will impact as well the thermoresponsive behavior of the polymer solution.

Finally, adding ions into polymeric systems can sometimes initiate some chemical reactions inside the resulting hybrid nanostructure. By this way, some nanoparticles can be created and bring some interesting properties to the assembled system. These last presented hybrid assemblies represent a template to obtain a new chemical system with potential new properties. K. Tarasov et al. did use a HPICs structure composed of PAA-*b*-PAM block copolymer and zinc ions (Zn^{2+}).[97] By adding sulfur ions (S^{2-}) onto the HPICs structure, the formation of ZnS quantum dots took place (**Figure 8**). By varying some polymer characteristics such as molecular weight and block ratios, the size of the structure can be adjusted. However, resulting photoluminescence property is the same whatever the polymer block length or ratio.

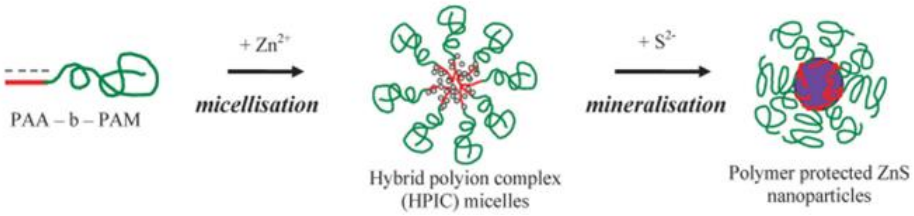

Figure 8. Scheme showing the formation of ZnS nanoparticles with the use of a copolymer PAA-b-PAM (reproduced with permission from [97])

The same block copolymer was used to interact with Al^{3+} and Mg^{2+} cations to form HPICs nanostructures again, but this time the mineralization step consists in adding sodium hydroxide (NaOH) to form hydroxide species by interacting with the cations inside the nanostructure.[98] A layered double hydroxide (LDH) phase is then formed and its characteristics highly depend on the ratio between cations and negatively charged DHBC. This colloid system mixing DHBC and LDH layers can be further used as cargo for drug delivery applications, as they proved high stability upon time and saline solutions.

Polymer assemblies have proved until now that they could present different morphologies by playing on numerous parameters relative either to the polymer characteristics itself or to its environment through stimuli or interactions with other chemical compounds. The design of these assemblies is highly investigated as potential cargo systems for many biological applications. As seen previously the use of ions can help obtaining interesting hybrid structures, whose properties are useful for imaging field for example. Among inorganic chemicals, nanoparticles are able to interact with organic matter and particularly polymers to induce other kind of assemblies and final hybrid morphologies.

IV Assemblies of inorganic nanoparticles and block copolymers

The assembly of inorganic nanoparticles is of great importance in realizing their enormous potentials for broad applications due to the advanced collective properties of nanoparticle ensembles. The literature available on this topic is very large, our interest will be particularly focused onto the gold nanoparticles type.

Gold nanoparticles' assembly is a highly reported topic in the literature because the gold nanoparticles (AuNPs) are easy to synthesize and to functionalize, and they hold interesting properties for biomedical applications.[99] Indeed, their size and shape are easily tunable through well-established synthesis process.[100] Their functionalization can be easily managed and realized with several kind of biological or chemical species. They present no cytotoxicity behavior and are stable against oxidation. Their biocompatibility and their electronic properties make them suitable agents for biomedical applications such as imaging field.[101] As AuNPs have optical properties related to the Surface Plasmon Resonance (SPR) absorbance band[102], their assembly can be visually observed through a color change of the solution containing initially dispersed AuNPs. Thanks to this absorbance variation, the assembly of AuNPs is used as a sensing method for chemical or biological compounds.[103] Other interests of assembling AuNPS concerns the formation of systems with enhanced properties. Indeed, the collective effect brought by this assembly process, allows an amplification of each singular property of the AuNPs. Assembling AuNPS could then allow a minimization of the quantity of nanoparticles by keeping highly performant systems for further biological applications. Numerous strategies are employed to assemble AuNPs, as they are easily functionalized as previously explained. As detailed previously in this work, the use of stimuli represents an assembly method leading to various nanostructures. The study of the different stimuli applied on nanoparticles to induce assembly was made by M. Grzelczak et al.[104]

In this chapter, we will focus on the use of polymers to help both stabilizing AuNPs and assembling them to obtain further hybrid assemblies. In the following section, the functionalization of AuNPs with polymers and particularly block copolymers will be detailed. Then, several examples were selected to illustrate hybrid BCPs and AuNPs assemblies, their assembly mechanism and the resulting properties.

IV.1 Functionalization of gold nanoparticles by polymers

The functionalization of AuNPs by polymers has several advantages as the polymer coating can confer stability against aggregation[105,106], enhance plasmonic properties[107], bring responsiveness behavior at external stimuli[108], prolong blood circulation time and bring targeting ability[109] to the final Au@polymer system. To achieve this goal, three methods are available (**Figure 9**). The first one, named *in situ functionalization,* consists in achieving functionalization of AuNPs during their formation. To do so, the polymer is introduced in the reaction mixture at the beginning of the reaction together with the gold precursors. The second one, named *ex situ or* "grafting to", consists in functionalizing pre-formed AuNPs through ligand exchange. Finally, the third one is based on the polymerization of a monomer onto the AuNPs surface to obtain polymer-functionalized AuNPs and is named "grafting from".

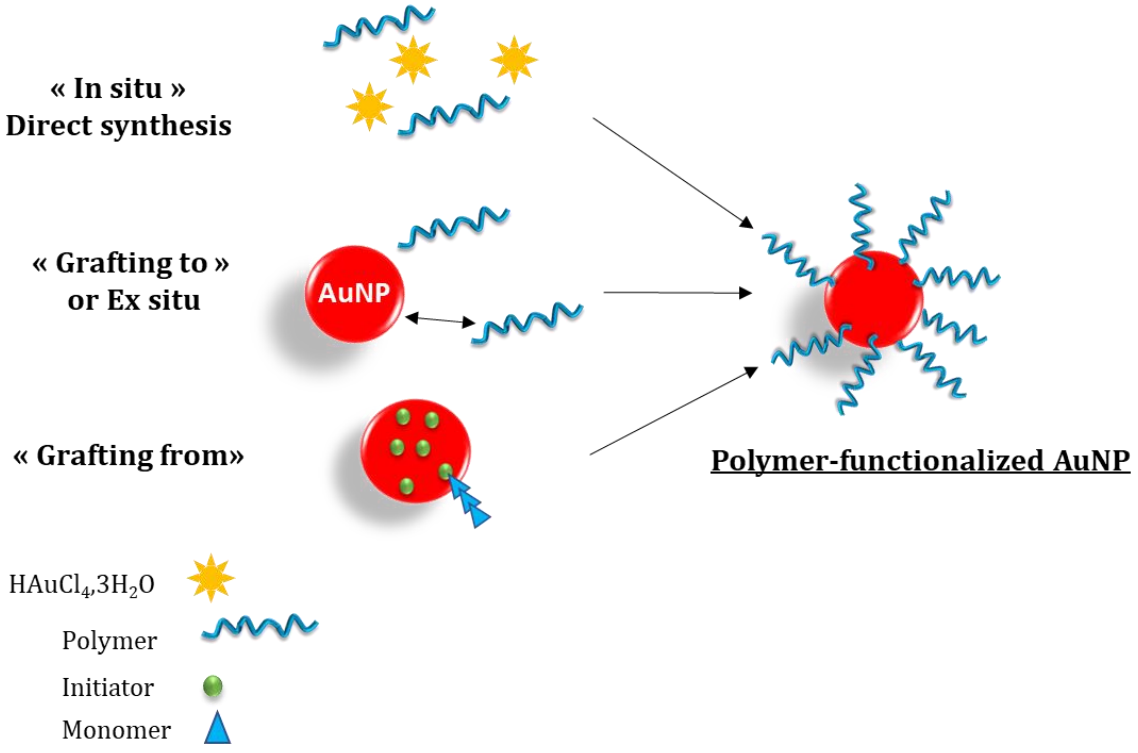

Figure 9. Common approaches to prepare polymer functionalized gold nanoparticles (AuNPs)

IV.1.1 *In situ* method

This first method relies to the formation of AuNPs in the presence of the polymer. The interaction with the polymer can be actually made during the reduction step, by mixing the gold salt, the reductant and the polymer. Many studies have reported this *in situ* synthesis of polymer-functionalized AuNPs and pointed out that the characteristics of the polymer can influence the final size and shape of the AuNPs. For example, S. Sistach et al.[110] demonstrated that increasing polymer's concentration leads to smaller AuNPs with low polydispersity In another study using poly(*N*-isopropylacrylamide) (PNIPAM) polymers[111], the effects of the molecular weight (from 3 700 to 10 000 $g.mol^{-1}$) and of the nature of the end-group (xanthate, thiol or hydrogen) of the polymer onto the final AuNPs were as well investigated. Quartz crystal microbalance adsorption/desorption experiments demonstrated that the polymer termini have a strong impact on the mechanism of polymer adsorption on flat gold surfaces. These differences in polymer structure have in return a strong influence on the colloidal stability and growth mechanism of nanoparticles when directly synthesized in polymer solution. For those properties, the effect of xanthate group compared very favorably to the conventional thiol moiety. Interestingly, the properties of nanohybrids were poorly affected by the molecular weight of the polymer.

Nevertheless, not only small molecules can be used to reduce gold salt, some chemical functions such as amines and amine-boranes represent efficient reductants[112] and can be easily incorporated into polymeric structure.[113] The use of polymer as reducing agent of gold salt into metallic nanoparticles has been largely described and has been particularly studied from a mechanistic point of view to explain the different steps of the reduction process.[114] As proposed by T. Sakai and P. Alexandridis regarding the reaction between a triblock copolymer PEO-PPO-PEO and chloroauric acid ($HAuCl_4$), the mechanism of reduction of gold salt and the formation of the gold nanoparticles is divided into 3 main steps: (1) initial reduction of metal ions facilitated by block copolymer in solution to form gold clusters, (2) absorption of block copolymer on gold clusters and further reduction of metal ions on the surface of these gold clusters, and (3) growth of metal particles stabilized by block copolymers (**Figure 10**). The reduction of $AuCl_4^-$ ions proceeds via oxidation of the oxyethylene groups from PEO block polymers by metal centers as described by L. Longenberger and G. Mills.[115] PEO polymer is then generally used to help forming metallic nanoparticles, gold[116] or silver[117], and by this way functionalize and stabilize them into aqueous solutions.

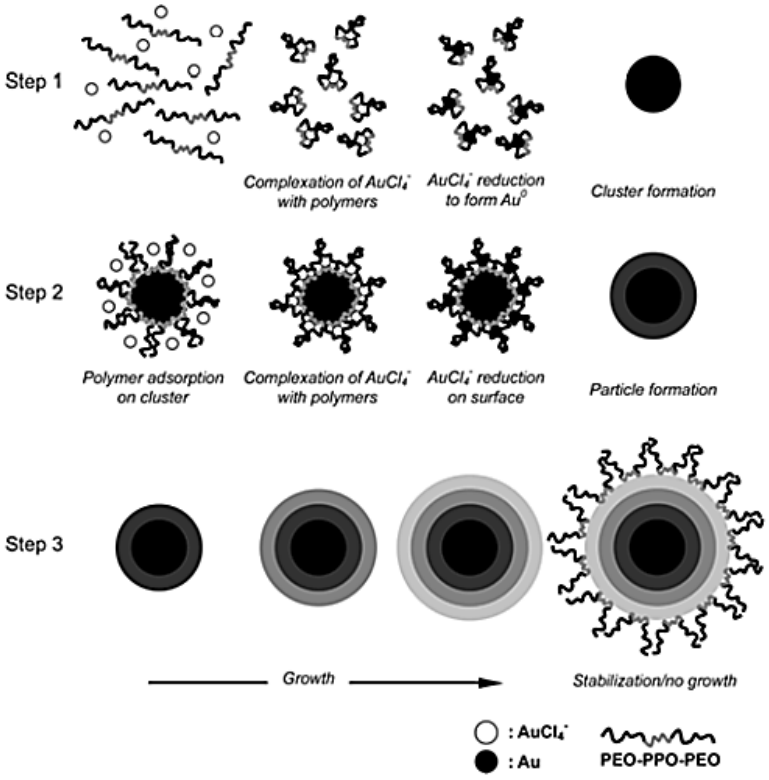

Figure 10. Scheme of the mechanism of gold nanoparticle formation mediated by PEO-PPO-PEO block copolymers (reproduced with permission from[114])

Another example of polymer highly used to induce the reduction of gold salt, it is the Poly(vinylpyrrolidone) (PVP) polymer. Indeed, PVP seems to interact with gold ions, but the mechanism still being unclear.[118] Nevertheless, without any other reducing agent, by mixing PVP with gold salt, AuNPs are obtained and their size and shape can be managed by playing on the ratio between PVP and gold salt. Indeed, the PVP seems to influence both nucleation and growth mechanisms.[119] A recent work[120] did prove the PVP effect onto the formation of gold nanoshells around silica nanoparticles. L. Lermusiaux et al. concluded that PVP seems to slow down the growth process and avoid the coalescence of the gold seeds, enabling then the formation of a thinner and more homogeneous gold nanoshell.

Polymers are then able to induce AuNPs formation through specific chemical functions. Once again, diblock copolymers seem advantageous as they can combine a reducing function with a stabilizing one like PMPC-*b*-PDMA.[121] The use of DHBCs is interesting too as it can provide specific structuration like micelles by playing on ionic interactions between initial gold salt and ionized polymer, like PAA-*b*-PEO.[122] Finally, a structuration before reduction can be realized as well by using a self-assembled polymer. For example, a triblock copolymer PCL-PEO-PCL is first organized in solution by playing on solvent incorporation, then interaction with the metal salt occurs and reduction leads to an assembled polymer decorated with AuNPs.[123] These kind of interactions leading to hybrid assemblies will be detailed later (**IV.2.2**).

IV.1.2 *Ex situ* method

The *ex situ* method for preparing polymer-functionalized gold nanoparticles, is based on the use of preformed AuNPs. The functionalization with a polymer proceeds via ligand exchange at the surface of AuNPs. Usually small molecules, borohydride, citrate and ascorbic acid, are bound to gold surface only via weak bondings, the new bound must be stronger to operate the ligand exchange.

Generally the polymers are functionalized with a thiol function to improve the attachment onto the gold surface through covalent bound.[124–127] Nevertheless, steric stabilization can be achieved as well with polymers bearing functions suitable like C=O and C-N groups for interacting with gold surface like the previous used PEO and PVP polymers. Same PEO-PPO-PEO triblock copolymer was investigated in presence of citrate-capped AuNPs and the influence of each block, either hydrophilic or hydrophobic, on the stabilization of the AuNPs in solution was studied.[128] Electrostatic interactions between AuNPs and charged polymers allows another way of functionalization. Despite the weakness of the interaction, Au@PAA NPs have proved to be more stable in presence of sodium chloride salt, compared to Au@citrate NPs, which can make them suitable probes for biological applications.[129] Moreover, the use of polyelectrolytes as shell around AuNPs can bring responsiveness to pH and temperature and allows adjustment regarding Au@polymer NPs' hydrodynamic size.

IV.1.3 "Grafting from" method

This last method for functionalizing AuNPs with polymer, consists first in functionalizing the AuNPs with ligands able to initiate or help initiating polymerization process of attached monomer and then induce the polymerization process to achieve the polymer functionalization. The anchoring of initiator molecules often implies the use of organic solvent to solubilize the AuNPs before adding polymers. Some of the following examples will then report on both organic or water solubilized functionalized AuNPs. Two polymerization process will be discussed: Atom Transfer Radical Polymerization (ATRP) and Reversible Addition-Fragmentation Transfer (RAFT) polymerization.

ATRP method for polymerization process was firstly reported by J.S. Wang and K. Matyjaszewski in 1995, which describe an efficient reaction to provide well-controlled polymer chains.[6] As ATRP enables precise control over macromolecular structure, order and functionality, many polymer-based nanomaterials for biomedical applications are prepared through this polymerization method.[130] To initiate ATRP polymerization process onto the surface of AuNPs, the initial stabilizing ligand must be composed of transition-metal species which are necessary to induce the redox reactions.

For example, copper salt is complexed by the initiator ligand stabilizing AuNPs, to further drives the polymerization of methyl methacrylate monomer onto the surface.[131] Stimuli-responsive AuNPs can thus be obtained by making the ATRP polymerization of stimuli-responsive polymers onto the gold surface.[132–134]

RAFT polymerization process was developed by Rhodia[7,135] and Dupont de Nemours[136,137] and is based on the use of dithioester or xanthates- based chain transfer agents (CTA). The use of CTA enables to limit the end-chain reactions and thus a better control onto the final macromolecular structure. As previously enounced, some resulting polymers from this RAFT polymerization process bears functions containing sulfur atoms, enabling further *ex situ* functionalization of preformed AuNPs or preferential adsorption onto gold precursors. S. Pereira et al. have then decided to compare the three previous methods used to functionalize AuNPs with polymers.[138] (**Figure 11**)

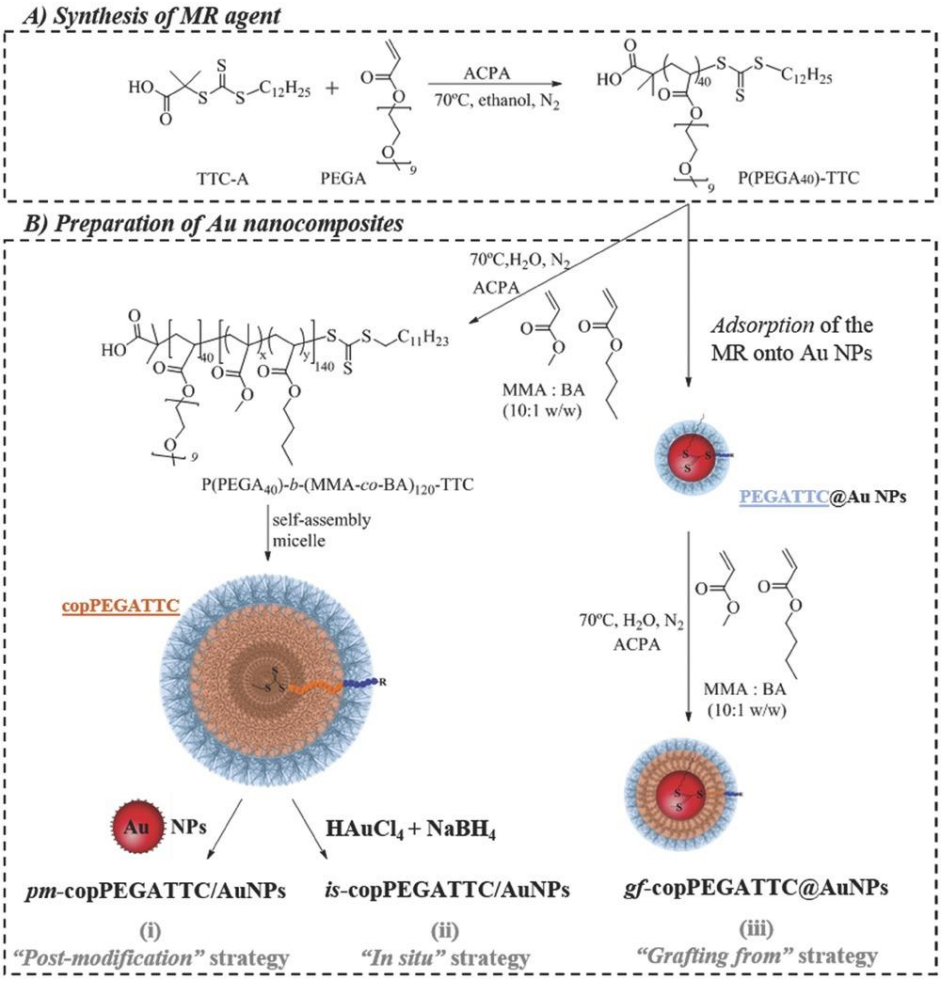

Figure 11. Strategies to functionalize AuNPs using RAFT polymerization (reproduced with permission from[138])

In this particular case, the « grafting from » method seems to be the best adapted as it leads to well-defined shell@core nanostructures. On the contrary, the "grafting to" method onto preformed AuNPs did not succeed, as the AuNPs preferentially interact with the hydrophilic shell of the polymer micelles instead of the hydrophobic core. The *in situ* strategy demands many parameters adjustment to obtain functionalized AuNPs like pH, amount of copolymer or Au/polymer ratio. Following the same idea as for ATRP, this "grafting from" method based on RAFT polymerization can be used to obtain stimuli-responsive AuNPs like the Au@PNIPA poly(*N*-isopropylacrylamide) which are thermosensitive.[139]

IV.2 Assembly mechanisms of AuNPs and polymers

Decorating AuNPs with polymer can help them stabilized but can also play a role into their aggregation process. The strategies to assemble polymer and gold nanoparticles into hybrid structures will be divided into three categories. First ones are based on a functionalization of the AuNPs with stimuli-responsive polymers. The acquired responsiveness of the polymer functionalized AuNPs drives their assembly into hybrid structures. The second way is to first assemble the polymeric system and then add the AuNPs (**Figure 12**). Finally, some studies will stress on the use of polymers to ensure a precise localization of AuNPs in resulting hybrid nanostructures and the influence of this spatial distribution onto resulting properties.

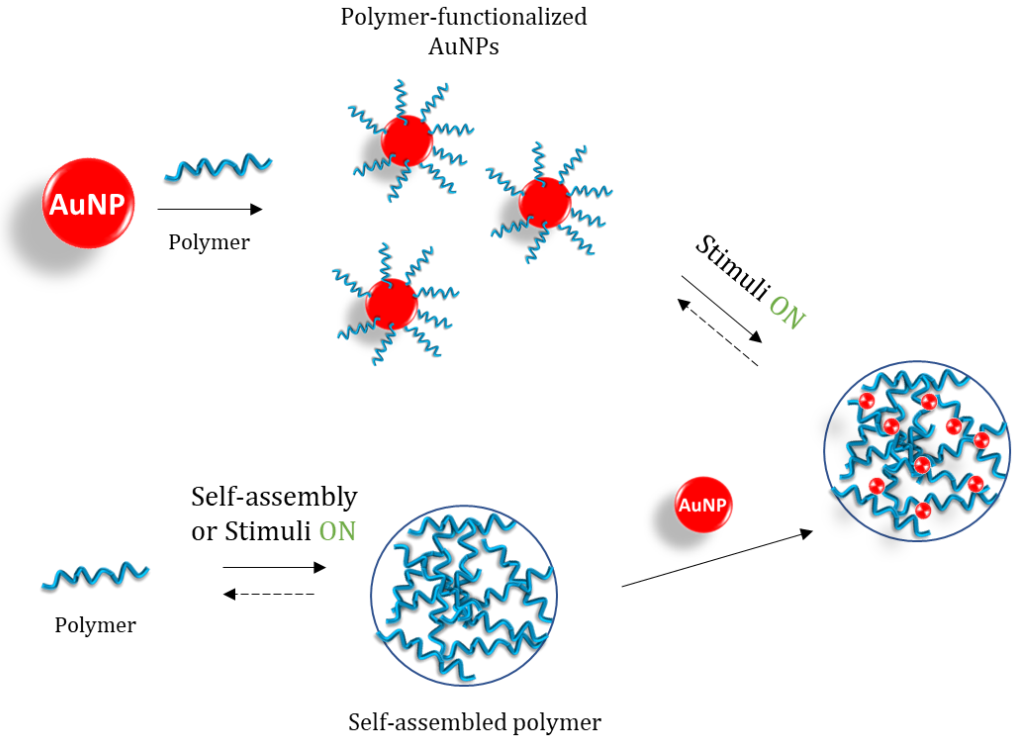

Figure 12. Strategies to assemble polymer and gold nanoparticles into hybrid assemblies

IV.2.1 Starting from polymer-functionalized AuNPs

By functionalizing the AuNPs with these sensitive polymers, the nanoparticles become sensitive to the same stimuli. The AuNPs acquire then new characteristics, for example, the transition temperatures of thermo-sensitive AuNPs are studied in function of the polymer's chain length and molecular weight.[140] The stimuli is then applied to induce assembly of these functionalized AuNPs to form hybrid structures with collective properties.

In this objective, many examples reports the use of a homopolymer for different kind of stimuli such as temperature[141], light[142], pH[143,144] or solvent use[145]. The use of the diblock morphology allows in some cases to combine different stimuli and then multiply the possibilities regarding final architectures. Hence, AuNPs functionalized with PMMPImB-*b*-PNIPAAm block copolymer combines polyelectrolyte and thermosensitive polymer.[146] This double responsiveness gives access to two different hybrid morphologies whether the temperature or the adding of $(CF_3SO_2)_2N^-$ anions, is applied on the initial functionalized AuNPs. Obtained morphologies differ from each other regarding the localization of the AuNPs which are grafted to the thermosensitive part and will then be either in the core when temperature is varying or in the surrounding shell when ionic interactions form the core with PMMPImB polymer and anions. (**Figure 13**)

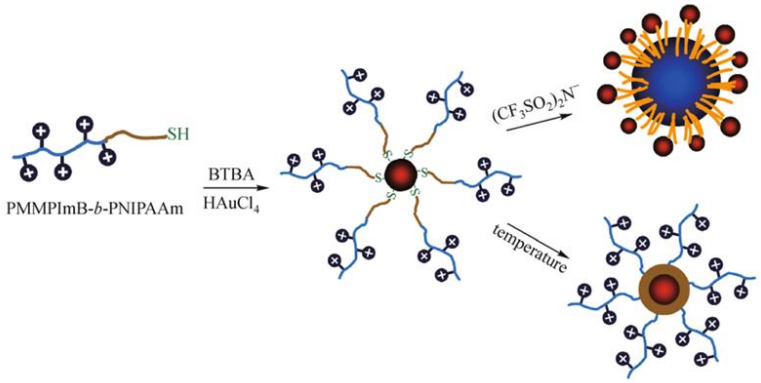

Figure 13. Schematic representation of preparing PMMPImB-*b*-PNIPAAm-Au NPS and its temperature and anion responsive self-assembly (reproduced with permission from [146])

J. Li et al.[147] functionalized AuNPs with PNIPAM-*b*-PMAA block copolymer which is both temperature and pH-responsive. Both Au@PMAA-*b*-PNIPAM and Au@PNIPAM-*b*-PMAA nanoparticles are studied for the two stimuli. For both polymer-functionalized AuNPs, decreasing the pH leads to a progressive aggregation of the AuNPs, detected with the shift of the SPR band onto UV-visible spectra. Nevertheless, the aggregation of the Au@PMAA-*b*-PNIPAM NPs is less pronounced and explained by the protective behavior of the PNIPAM corona, confirmed by TEM images. Temperature increase has a stronger effect on AuNPs having PNIPAM polymer as the corona of the system. The hydrophobic behavior acquired by PNIPAM leads to larger AuNPs and their self-aggregation, whereas Au@PNIPAM-PMAA NPs still be dispersed.

The self-assembly of Au@PS-PEG solubilized in THF can be induced by the addition of water.[148] Both PS molecular weight and AuNPs' initial size are studied regarding their influence onto the final obtained morphologies which can be either micelles, clusters or vesicles. (**Figure 14**)

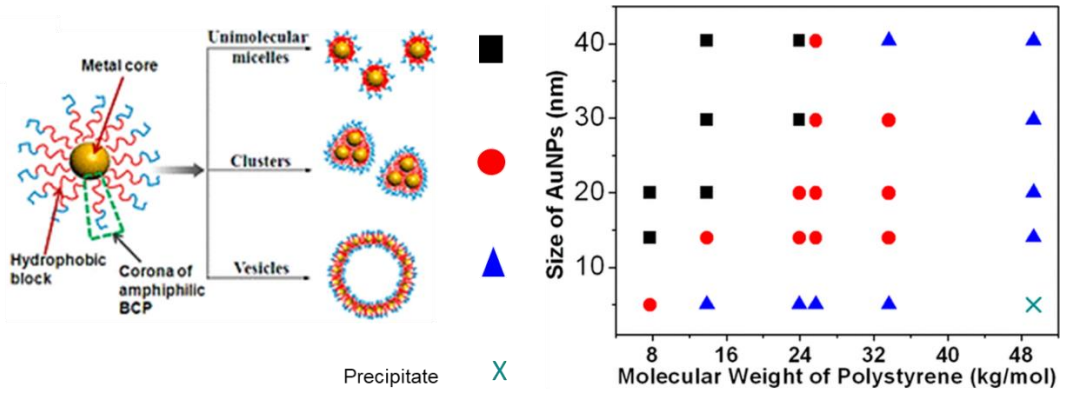

Figure 14. Schematic representations of resulting hybrid assemblies comprising Au@PS-*b*-PEG nanoparticles and the phase diagram of these assemblies with different Molecular weight of BCPs and sizes of initial AuNPs (reproduced with permission from [148])

Finally, light-responsive block copolymer PS-*b*-PNBA-SH containing nitrobenzene function was grafted covalently to AuNPs to bring UV-responsiveness for further assembly process.[149] (**Figure 15**).

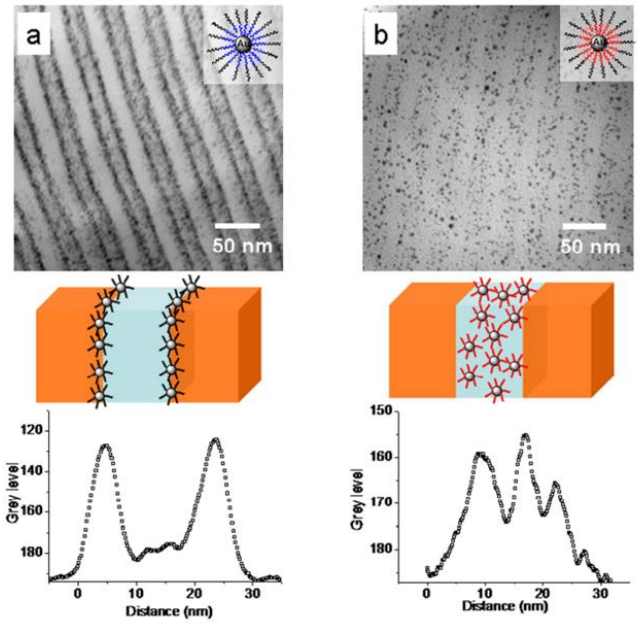

Figure 15. (a) TEM image together with the image analysis of the composites consisting of PS-bP2VP block copolymer (199 kg/mol, fp2vp ~ 0.48) and 20 wt.% of GNPs (PS23-b-PNBA9S-Au). (b) The GNPs were exposed to UV (365 nm) light before mixing with the PS-b-P2VP block copolymer (reproduced with permission from [149])

In this work, the stimuli won't be the factor inducing the aggregation, but will only chemically modify the polymer ligand to further achieve assembly process through hydrogen bonding. By irradiating the Au@SPNBA-*b*-PS NPs with UV light (λ = 365 nm), nitroarene function were eliminated leading to gold nanoparticles functionalized by surface acrylate functions. Both irradiated and non-irradiated AuNPs were incorporated into lamellae of PS-*b*-P2VP diblock copolymer. The non-irradiated AuNPs were localized along the interface between PS and P2VP, whereas irradiated ones interact with pyridine functions through hydrogen bonding with acrylate functions. The light stimulus helps here to have different localization of the AuNPs into polymeric structures, which can be essential for some applications, as explained later in this manuscript. This last example naturally guides us towards new strategies to obtain hybrid assemblies made of polymers and gold nanoparticles, which are mainly based on the incorporation of these AuNPs onto self-assembled polymeric architectures.

IV.2.2 Adding gold onto polymeric nanostructures

Hybrid assembly can be obtained through the interaction of AuNPs or gold salt with self-assembled polymeric structure. Indeed, as seen before, block copolymers are able to self-assemble into organized nanostructures in two main cases: 1) when the BCP needs to minimize free energy between the two blocks or between the blocks and the solvent through thermodynamical equilibrium, 2) when a stimulus is applied onto the BCP solution and induces its assembly. Following examples will deal with these polymeric architectures able to interact either with gold salt (in situ functionalization) or with preformed AuNPs (grafting to or ex situ).

The latest strategy based on preformed AuNPs has been the most commonly used. Hence, AuNPs functionalized with PS with different molecular weight can be incorporated in onion-like vesicles made of PS-*b*-P4VP block copolymer. Solvent evaporative emulsion process aims at forming different morphologies according to the Mn of PS onto AuNPs' surface. The assembly mechanism has been proved to be due to entropic phenomenon. Preformed gold nanoparticles prepared in organic solvent are further incorporated and are localized in the hydrophobic part of this assembled polymeric nanostructure. Lastly, the simple addition of AuNPs onto polymeric nanostructures can induce morphological changes like in the work of Cai et al.[150]

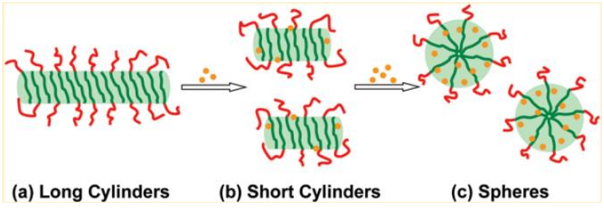

Figure 16. Morphologies of polymer assemblies in solution according to the gold nanoparticles incorporation (reproduced with permission from [150])

The combination of experimental and simulation methods lead to understand that AuNPs induce by their presence a breakage into the packing of the PBLG rod and will be localized at the interface between the core and the shell for intermediate short cylinder morphology and in the micelle core for the final micelle structure.[151] It has to be noted that such polymeric assemblies can also be formed from two homopolymers interacting with each other to form block copolymer complex like it is the case for Pluronic species. By playing on the hydrophilic/hydrophobic balance, several morphologies can be obtained.[152]

Several systems are also based on the use of gold salt and stimuli-responsive systems. Hence J-G Zhang et al. used a micellar structure obtained from a PNIPAM based block copolymer to selectively obtain hybrid assemblies.[153] Poly(2-methacryloyloxyethyl ferrocenecarboxylate)(PMAEFc)-b-PNIPAM block copolymers terminated with a thiol function were synthesized via RAFT polymerization and micellar structures formed in water. Gold salt and reductant were then added to the micelle's solution of BCP and then, AuNPs were synthesized and grafted to the corona of the micelle through covalent S-Au bond. Different block lengths were experimented to study the influence onto CMC and LCST properties of the block copolymer micelles with and without AuNPs. The thermoresponsiveness of PNIPAM is sometimes used to induce morphological changes of the initial hybrid assembly. Starting from a micellar structure with a PNIPAM corona and an amine functionalized core based on Poly(N-phenylethylenediamine methacrylamide) (PNPEDMA) able to interact with a gold salt, AuNPs were obtained from the reduction by the amine functions.[154] These functionalized AuNPs are further able to reversibly assemble under temperature variation in water solvent. A multi-responsive system was described by P. Zheng et al. that synthesized a triblock copolymer poly(ethylene glycol)-*b*-poly(4-vinylpyridine)-*b*-poly(*N*-isopropylacrylamide) (PEG-*b*-P4VP-*b*-PNIPAM) able to respond to pH in addition to temperature.[155] (**Figure 17**).

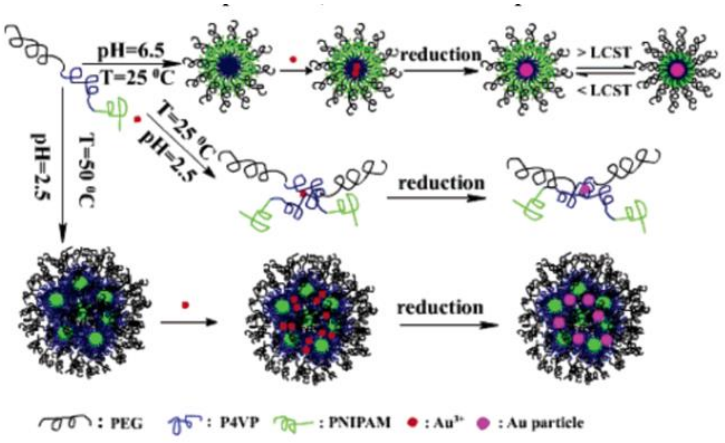

Figure 17. Thermoresponsive and pH-Responsive Micellization of PEG_{110}-b-$P4VP_{35}$-b-$PNIPAM_{22}$ and Synthesis of the Discrete Gold Nanoparticles, Gold@Polymer Core-Shell Nanoparticles, and Gold Nanoparticle Clusters (reproduced with permission from [155])

This dual pH-thermoresponsive triblock BCP can self-assemble into three main configurations according to pH and temperature settings. The three obtained architectures are able to further interact with gold salt to form different morphological hybrid assemblies.

Initial polymeric nanostructures can also be enriched with additional molecules such as surfactants to diversify assembly morphologies. P. Khullar and coworkers did use classic PEO_5–PPO_{68}–PEO_5 triblock copolymer to form initial micelle systems and then added different surfactants to generate mixed micelles.[156] The triblock copolymer creates ether oxygen cavities able to reduce gold salt and obtain micelles enriched with AuNPs located in these cavities. By varying the hydrophobicity of the surfactant and mole fraction, a phase diagram has been established showing the different obtained micelle morphologies (**Figure 18**).

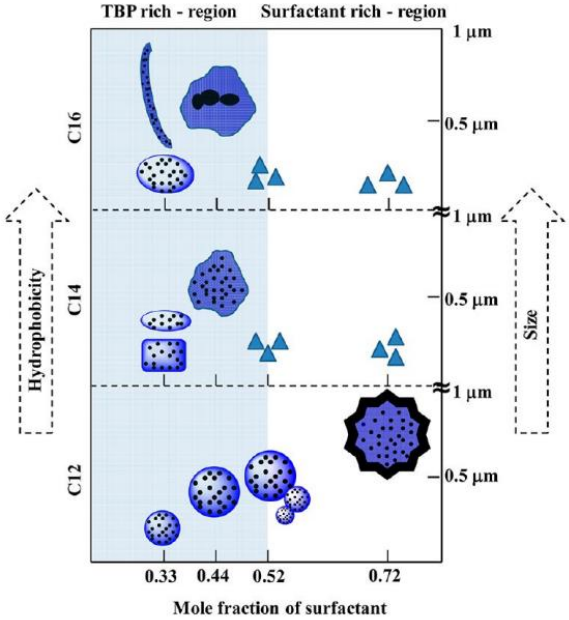

Figure 18. Proposed phase diagram showing the relationship among hydrophobicity, size of the micelles and NPs, and mole fraction of different surfactants. C12, C14, and C16 represent 3-(N,N-Dimethyldodecyl ammoniopropane sulfonate) (DPS), 3-(N,N-dimethyltetradecyl ammoniopropane sulfonate) (TPS), and 3-(N,N-dimethylhexadecyl ammoniopropane sulfonate) (HPS), respectively. Phase diagram has been divided into TBP-rich and surfactant-rich regions (reproduced with permission from [156])

Precise localization of AuNPs into the polymeric nanostructure can be an objective to obtain well-defined hybrid assemblies with specific properties suitable for biological applications. For example, gold salt ($HAuCl_4$) was precisely reduced into the vesicle made of block copolymer containing a fluorescent dye in its structure. The interest is here to obtain a plasmonic structure based on the combination of the AuNPs and the fluorescent dye for further use of Nanometal Surface Energy Transfer (NSET), in sensing, photonics or biological applications. The pH-responsiveness of the BCP helps in modifying the morphologies between vesicles and micelles and thus the final properties of the hybrid structure, which can be used as a cargo delivery system as well.[157]

Finally, two last examples deal with the incorporation of AuNPs onto polymeric nanostructures, which are this time formed onto solid templated surfaces and not in solution. Nanotubes of PS-*b*-P2VP were fabricated through template-assisted assembly by using alumina membranes which are then dissolved, and represent the polymeric nanostructure. Gold salt is introduced to interact with the P2VP polymer and resulting AuNPs are then incorporated into the nanotube. Thanks to pH-responsiveness of P2VP, different rearrangements of the AuNPs into the nanotubes are observed, enabling the hybrid nanomaterial to keep the AuNPs.[158] In the field of Surface Enhanced Raman Spectroscopy (SERS) applications, endoscopy technique needs AuNPs to improve the sensitivity of the nanosensors. To deposit AuNPs, block copolymer PS-*b*-P4VP is dip-coated onto a glass fiber and, according to its curvature, the polymeric surface will be different.[159] Adding AuNPs onto these polymeric surfaces, will either lead to clusters for high curvature or well-dispersed AuNPs for low curvature. By playing on the BCP configuration, block, random or homopolymer of P4VP and on the AuNPs diameter, various covering of AuNPs are obtained (**Figure 19**)

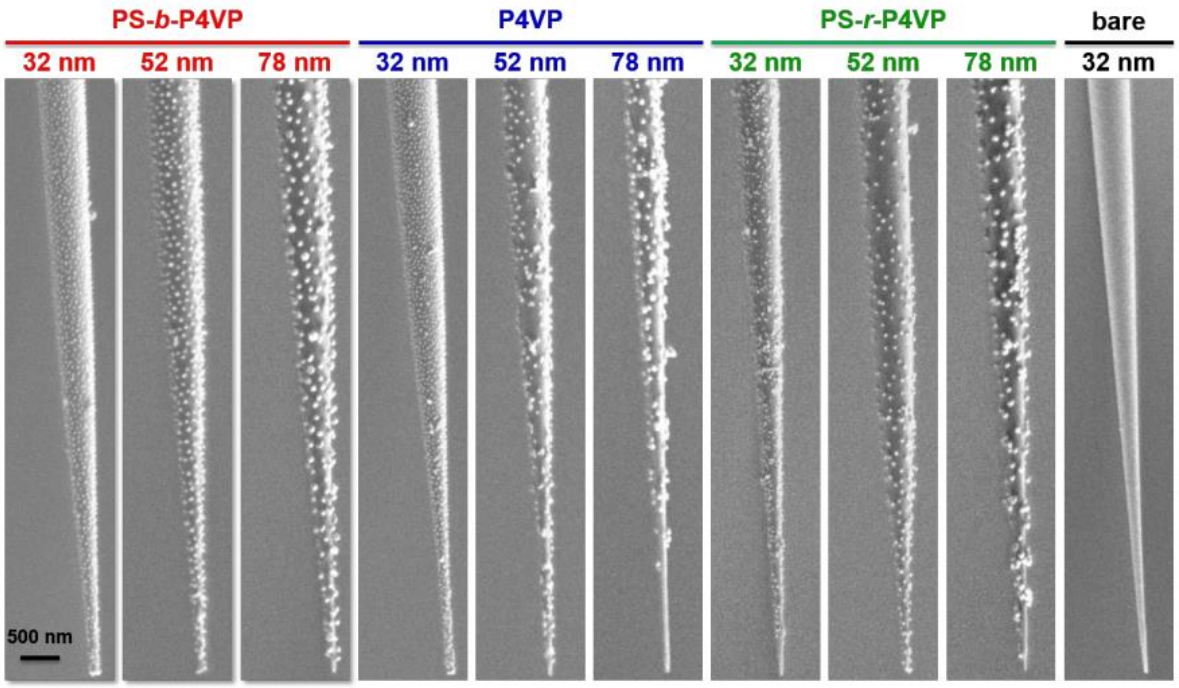

Figure 19. SEM images (scale bar at left valid for all images) of nanofiber tips after the deposition of AuNPs of the diameters indicated using a PS41-*b*-P4VP20 brush-layer template, a P4VP homopolymer template and a PS-r-P4VP random copolymer template, where the templates were obtained by dip-coating from 0.05 mg/mL solutions (THF for the copolymers, THF/EtOH for P4VP), as well as an uncoated nanofiber exposed to 32 nm AuNPs (reproduced with permission from [159])

As seen previously in some examples, the precise localization of gold nanoparticles can be obtained by playing on some parameters such as polymer's functionalities[149], polymer molecular weight[148] or AuNPs' size. This control of localization is important to obtain specific hybrid nanostructures suitable for particular applications.[160]

IV.2.3 Precise modulation of spatially distributed inorganic nanoparticles

In some cases, AuNPs' assemblies must lead to well-defined nanostructures with precise size and configuration, to obtain specific properties. For that purpose, like previously, polymers can be used as templates with controlled morphology for further hybrid systems. In this field, the synthesis of silica-polystyrene clusters in the submicron range was explored in the group of E. Duguet[161] and pertinent parameters such as silica seeds' size, seed-to-latex ration and monomer surface density were varied to obtain multiple morphologies. Once those templates formed, gold nanoparticles can be precisely positioned by functionalizing the polymer with specific functions like amines[162] or DNA[163,164].

Last methods allow the design of well-defined structures through the precise localization of polymer functions able to interact with AuNPs. Another way to have controlled organization into hybrid assemblies consists in playing onto the polymeric shell surrounding AuNPs before incorporate them into polymer network.[165] Not only the nature, but the polymer chain density onto the AuNPs represents a key parameter to localize precisely the AuNPs into polymeric nanostructure.[166] Indeed, Au@PS NPs are incorporated into a PS-*b*-P2VP block copolymer nanostructure and according to the PS areal chain density, the localization of Au@PS NPs will be near the center in the PS region or along the interface between the two blocks. Finally, polymers can help into AuNPs assemblies without functionalizing them, but only interacting with the ligands on their surface. Like in the work of Q. Luo et al.[167], the AuNPs' surface is composed of two surfactants dodecanethiol (DT) and 11-mercapto-1-undecanol (MUL) (**Figure 20**).

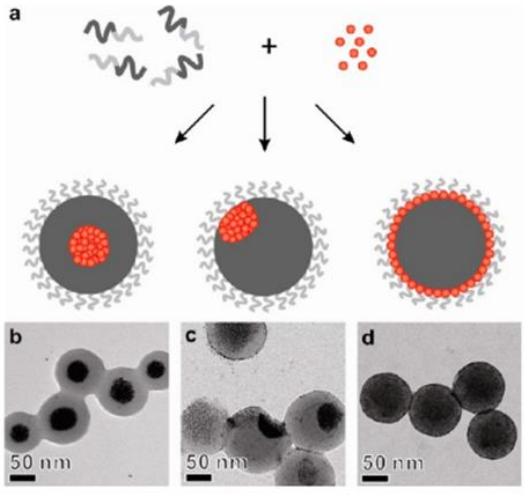

Figure 20. (a) Pictorial description of the self-assembly of PS_{250}-b-PAA_{14} and AuNPs with varying surface ligands. Light gray lines, dark gray lines, and red spheres represent PAA, PS, and AuNP, respectively. (b) A TEM image of coassemblies prepared with AuNPs modified with 100% DT. (c) A TEM image of coassemblies prepared with AuNPs modified with 75% DT and 25% MUL. (d) A TEM image of coassemblies prepared with AuNPs modified with 20% DT and 80% MUL. Note that the PAA layer is not visible in TEM images (reproduced with permission from [167])

By playing on the ratio of these two surfactants, the resulting interfacial properties of the AuNPs can be tuned and lead to different morphologies when they are embedded into the PS-*b*-PAA block copolymer solution. Increasing MUL quantity tends to induce a preferred localization of the AuNPs at the interface between the two polymer blocks, whereas a 100% of DT leads to structures containing AuNPs into the hydrophobic PS core. After investigations about the wetting properties of the functionalized AuNPs, which depend on the composition of the surfactant shell, predictions were elaborated regarding the interfacial properties between the NPs and the block copolymer PS-*b*-PAA. In a second time, the work was then focused onto the incorporation of functionalized AuNPs into polymeric assemblies, resulting from PS-b-PAA self-assembly. A final study was realized by mixing iron oxide and gold nanoparticles to form multicomponent assemblies. The design of the surfactant shell of each kind of nanoparticle enables to localize the two NPs at different places into the hybrid assembly.

A last method deals with the co-assembly of BCPs and AuNPs via emulsion droplet system and by using solvent evaporation. Deeply based on entropy and enthalpy effects into solutions of BCPs and nanoparticles, the work of N. Yan et al. shows interesting resulting hybrid nanostructures with precise alignment of the AuNPs into the polymeric network.[168] Playing on the volume fraction of preformed AuNPs into the emulsion droplet system made of PS-*b*-PVP block copolymer into the chloroform, will affect the interfacial energies of both block copolymer molecules and AuNPs, inducing an attractive interaction between the PS block and the AuNPs. Several morphologies are obtained with the different AuNPs ratio. (**Figure 21**)

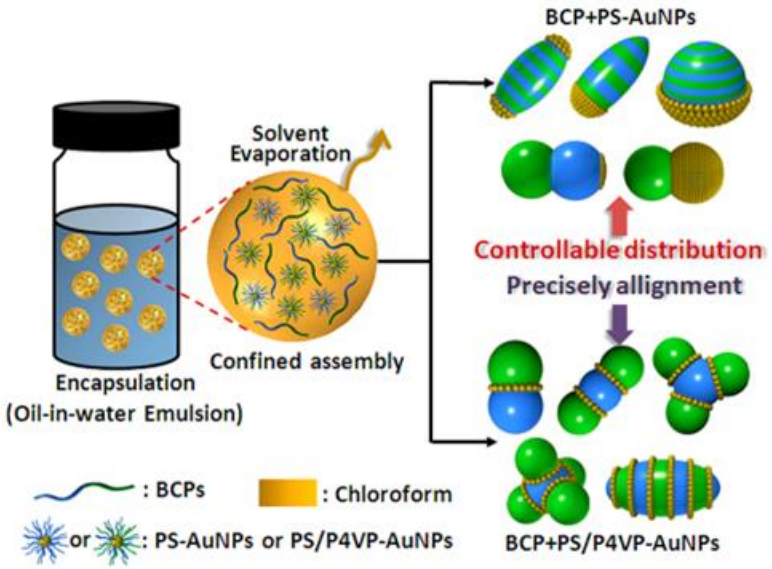

Figure 21. Schematic Showing the Unique Hybrid Nanoparticles from the Co-Assembly of BCPs and AuNPs Confined in the Emulsion Droplets (reproduced with permission from [168])

V Characterization techniques for hybrid assemblies

The following paragraph is dedicated to the characterization of the polymer or hybrid assemblies. This section shows the available techniques giving information about the structure of these assemblies and their acquired properties. Most common techniques are categorized between scattering techniques and microscopy techniques (**Figure 22**). Scattering techniques enable to give statistically relevant results and limit the required preparation step before analysis. However, in most cases the analysis of obtained results necessitates complex fitting processes depending on the nanostructures studied. For that purpose, scattering techniques are generally completed by additional characterization techniques using microscopy technology, providing images of the samples. However, only partial observations can be made on the entire solution, and the results cannot then represent the general trend observed in the sample. Moreover, preparation steps required by some microscopy techniques can induce in some cases artefacts not representative of the colloidal solution. That is the reason why, scattering and microscopy techniques must be combined to give more precise information about the assembled systems detected in solution.

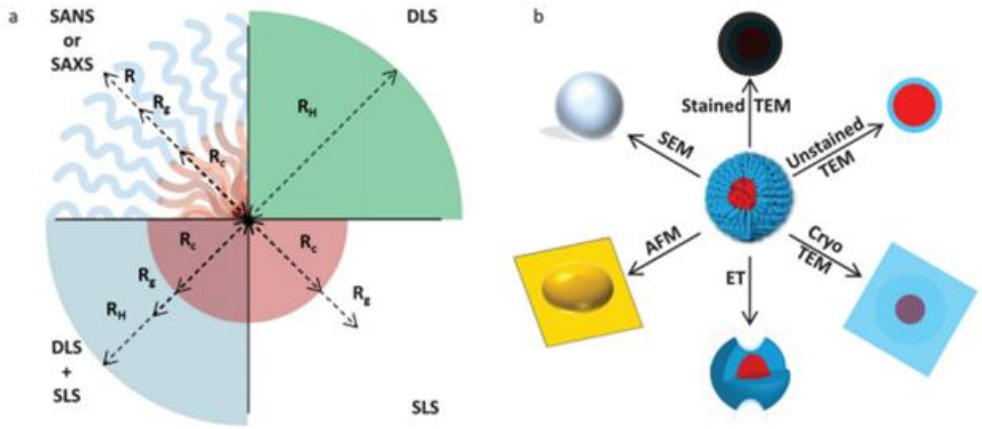

Figure 22. A schematic showing (**a**) the types of information which is obtainable by different scattering techniques and (**b**) the different types of images formed by different microscopy techniques for a spherical polymer micelle (reproduced with permission from [169])

V.1 Scattering techniques

Regarding soft matter structures, the most used scattering techniques are sum up in **Figure 22**: Static or Dynamic Light Scattering (SLS or DLS), Small Angle Neutron Scattering (SANS) and Small Angle X-Ray Scattering (SAXS) methods. They are all based on the irradiation at a known wavelength of the sample in solution and the analysis of the resulting scattered intensity is made at a given angle of detection, in respect with the incident radiation. These scattering techniques differ from each other regarding the wavelength of the incident radiation and the contrast resulting from the interaction between this radiation and the structures.

Measurements give information about the size, the shape of the structures in solution and the intrinsic interactions. Length scales for probing are inversely proportional to the scattering wave vector ***q*** related to the wavelength of the incident radiation ***λ*** and observation angle ***θ*** through the **Equation 1**:

Equation 1. Scattering wave vector ***q*** for a probe irradiated at a wavelength ***λ*** and observed for detection at an angle ***θ*** in a solvent with a characteristic refractive index ***n*** for light scattering (n=1 for SANS and SAXS)

$$q = \frac{4\pi n}{2\lambda} * \sin\left(\frac{\theta}{2}\right)$$

Laser light based scattering methods, DLS and SLS, give information about the diameter of the nanostructures, which is composed of three different values as reported on **Figure 22**: core radius (R_c), gyration radius (R_g) and hydrodynamic radius (R_h). To have access to all these radius values, SLS and DLS must be combined. DLS technique aims at measuring the R_h of a structure considered as a perfect hard sphere. Indeed, measurements are based on the Brownian motion of the particles in a specific solvent at a certain temperature. This motion is associated to a diffusion coefficient D which is closely related to the R_h value through the Stokes-Einstein equation:

Equation 2. Stokes-Einstein equation giving the hydrodynamic radius R_H in function of k_B is Boltzmann's constant, T the absolute temperature and η the viscosity of the solvent

$$R_H = \frac{k_B.T}{6\pi.\eta.D}$$

The resulting R_H value is the theoretical radius of a hard sphere which would move with the same translational diffusion coefficient D as the nanostructures diffusing in the present sample. If structures are hard spheres, then R_H corresponds to the exact radius of the particles, otherwise, if the structures are soft spheres, for example made of polymers, the estimated radius corresponds to the size of the solvated structures. For spherical micelles, the hydrodynamic radius both depends on the maximum chain length of the block copolymer (L_{max}) and the degree of polymer chain stretching (ω) (**Equation 4**). The maximum chain length of the BCP (L_{max}) can be determined from the degree of polymerization of both blocks ($N_{core+corona}$) and the monomer length (L_M) (**Equation 3**). By definition, ω value cannot be over 1, because no R_H can be longer than the maximum chain length of the polymer.

Equation 3. Maximum chain length of the block copolymer implied in the micelle related to the degree of polymerization of both blocks $N_{core+corona}$ and the monomer length L_M

Equation 4. Degree of polymer chain stretching ω related to the maximum chain length (L_{max}) and the hydrodynamic radius (R_H)

$$L_{max} = N_{core+corona} * L_M \qquad \textbf{(Eq. 3)}$$

$$\omega = \frac{R_H}{L_{max}} \qquad \textbf{(Eq. 4)}$$

Static Light Scattering (SLS) measurements are made over time scales on the sample by recording the scattered light intensity and taking the average value. Generally, multiple angles and concentrations are tested to detect all the nanostructures whatever their size range and to know their proportion in the sample according to scattered intensity record. From this technique, the gyration radius (R_g) can be extracted by using Zimm equation (**Equation 7**)

Equation 5. Rayleigh ratio R_θ related to average scattered intensity of the sample (I_{sample}), the solvent ($I_{solvent}$) and the standard ($I_{standard}$), and the Rayleigh ratio associated to the standard.

$$R_\theta = \frac{I_{sample} - I_{solvent}}{I_{standard}} * R_{\theta,standard} \qquad \text{(Eq.5)}$$

Equation 6. K value for a certain laser wavelength (λ), related to the refractive index of the standard ($n_{standard}$)the refractive index increment of the sample (dn/dc) and the Avogadro's number N_A

$$K = \frac{4\pi^2 n_{standard}^2 * \left(\frac{dn}{dc}\right)}{N_A.\lambda^4} \qquad \text{(Eq. 6)}$$

Equation 7. Zimm equation relating K and R_θ to the gyration radius (R_g) of the considered particles and to M_w which is the averaged weight molecular weight of the scatterers.

$$\frac{K.c}{R_\theta} = \frac{q^2.R_g^2}{3M_w} + \frac{1}{M_w} + 2A_2.c \qquad \text{(Eq. 7)}$$

From linear regression of $K.c/R_\theta$ vs. q^2, the radius of gyration can be extracted using the slope. R_g corresponds to the mean distance of one scattering center within the particle, from the center of the particle as a whole. The slope must be sufficiently large to provide accurate value for R_g. Combination of SLS and DLS gives the possibility to calculate the R_g/R_H ratio which is closely related to the morphology model of the studied nanostructure (**Figure 23**).

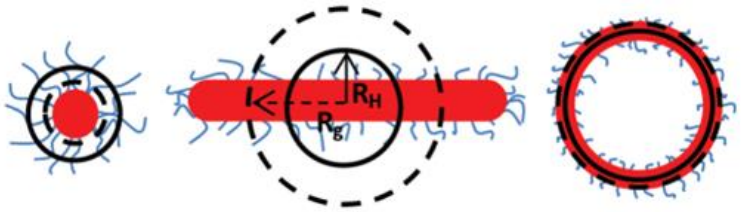

Figure 23. Schematic depicting how different morphologies would display a different R_g/R_H ratio where R_g is the radius indicated by the dashed black line and R_H is the radius indicated by the solid black line

DLS and SLS represent useful techniques to determine the size of the nanostructures by using models and fitting methods. However, these techniques can be advantageously completed with scattering techniques like SANS et SAXS using a different wavelength and origin of contrast. Nevertheless, the use of SANS and SAXS require imposing and expensive equipment, which limit then their use. As the wavelengths of neutrons and X-rays are much smaller (0.1nm) compared to laser light, SANS and SAXS can easily be used to study smaller length scales and provide information about the local structure of the assemblies. Indeed, for the whole structure, small q values are preferred and by increasing this q value (smaller length scale), the interior of the nanostructure can be studied as well, giving more information about the particular shape and organization of the solvophobic and solvophilic blocks within the structure.

SANS analysis is based on neutrons' scattering by the nucleus and the resulting scattered intensity highly depends on the nuclear scattered length density (SLD), generally determined thanks to the chemical formula and the density of the material. Typical SANS model for spherical micelle is shown in **Figure 24**.

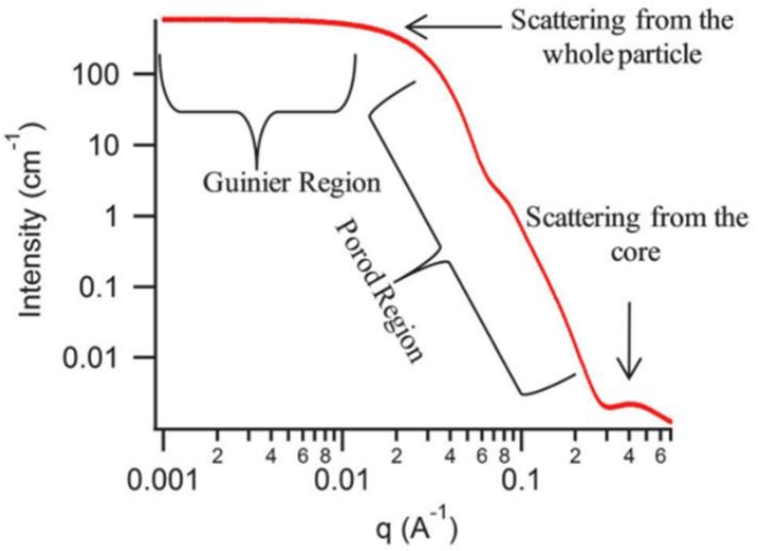

Figure 24. Model taken from V. Degiorgio and M. Corti, Physics of Amphiphiles: Micelles, Vesicles and Microemulsions: Proceedings of the International School of Physics, Elsevier Science Ltd, 1985

Two regions are distinguished onto the plot, bringing each information about different aspects of the nanostructure. The Guinier region is related to the scattering of the nanostructure from a global point of view, whereas the Porod region separates this previous Guinier region from the one dealing with the scattering of the supposed core of the nanostructure. Plotting ln(I) vs. q^2 leads to R_g value using a linear fit onto the Guinier region. Regarding the Porod region, plotting log(I) vs. log(q) helps understanding the morphology adopted by the assembled system, using the gradient study.

All these scattering techniques aim at giving average values regarding sizes of the nanostructures and help understanding the kind of morphologies adopted in solution by the polymer assemblies or hybrid systems. However, all these results require some setting parameters issued from models established for specific morphologies. The interpretation of these results has to be made with caution, because despite a correct fitting, the reality can be totally different from what the scattering techniques can conclude. For this reason, these characterization techniques have to be combined to visual techniques such as microscopy-based ones, to bring more information about the structuration observed.

V.2 Microscopy techniques

It has to be reminded that contrary to scattering techniques, the characterization of the nanostructures in solution through microscopy technology, requires the modification of the initial sample, affecting more or less the internal organization of the chemicals. Moreover, only a part of the sample is analyzed, the results cannot be taken as global estimation of the sample but only a partial overview. Scattering techniques help here to know about the homogeneity of the sample and thus to differentiate what morphologies really reflect the sample.

Microscopy techniques can be divided into three categories: optical, electron and scanning probe. By projecting a beam of radiation, light or electrons, directly onto the sample containing the nanostructures, optical and electron microscopy allow the obtention of an image more or less contrasted whether the sample has been deposited with stained chemical or already contains elements sensitive to electron beams, like gold. Most common corresponding techniques are Transmission Electron Microscopy (TEM) which exist with different versions according to the state of the sample for observation, i.e. dry state for Cryo-TEM, or stained state for stained TEM. Regarding scanning microscopy, the nanostructures are scanned by a probe and the resulting image is built step by step. Common associated techniques are Scanning Electron Microscopy (SEM), Scanning Transmission Electron Microscopy (STEM) and Atomic Force Microscopy (AFM).

Some of the microscopy techniques require to deposit a drop of the sample in solution onto a grid to observe after drying the resulting deposited nanostructures. This is the case of the classic TEM technique, which allows to see high contrasted images of immobilized nanostructures. As explained previously, the observation of nanostructures in TEM needs the sample to scatter more electrons than the support. For that purpose, additional contrasting agent can be added in some cases onto the dried sample grid, like uranyl acetate. For hybrid assemblies containing chemical elements with high Z number, the scattering of the electrons allows to have sufficiently contrasted images with TEM. Once these grids prepared, there is a possibility to use Electron Tomography (ET) technique which consists in tilting the prepared grids at different angles to obtain a 3-dimensional (3D) image of the observed nanostructures and better understand the organization into the assembled system.[170] However, as many images have to be acquired to build the 3D image, a large dose of electrons must be applied to the specimen, leading generally to important modifications of the sample or the support. An additional technique can be combined to the TEM to have further information about the chemical organization into the assembled system. This technique is named Energy Dispersive X-ray (EDX) and is able to give an elemental map of an image of TEM, which is essential to distinguish for example the two blocks of the copolymer or the ions or nanoparticles from the polymer. Scanning TEM (STEM) consists in a using a raster scan based on a small beam of electrons, providing then a higher resolution of the built image. STEM is often combined to analytical tools like EDX or Electron Energy Loss Spectroscopy (EELS) to have chemical information about the structure and understand better the structuration.

Nevertheless, the previous techniques require the sample to be dried and this protocol could unfortunately damage the nanostructures present in the sample. Resulting images are then possibly showing organized systems which are maybe not present in solution, but forms because of the drying process. To avoid this issue, some advanced techniques analyzed the sample in its solvated state by applying cryogenic protocol. The Cryo-TEM technique uses this sample preparation to conserve the hydration of the nanostructures and thus the obtained morphology in solution. The preparation process is illustrated in **Figure 25**.[171] First, the sample is applied onto a perforated carbon film supported on a TEM copper grid and then a solvent-absorbent filter paper is blotting the grid. Finally, the grid is plunged into a cryogen reservoir to do the vitrification process. Once vitrified, the sample is conserved in a liquid nitrogen reservoir to be transferred until the apparatus. The quality of the vitrification process will determine the conservation of the nanostructures.

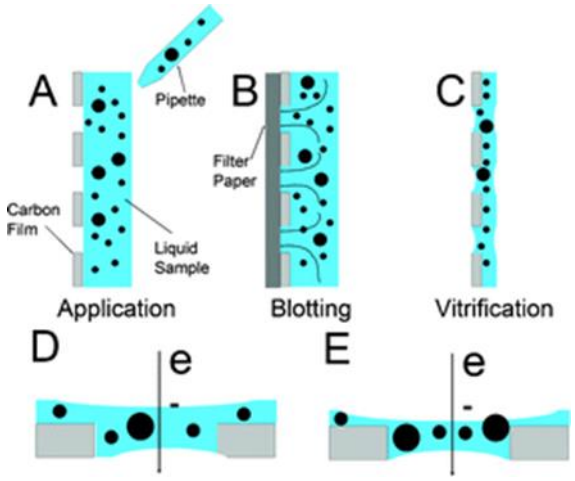

Figure 25. Schematic of cryo-TEM sample preparation: (**A**) Side view of a liquid containing particles (●) being applied to a perforated carbon TEM grid; (**B**) removal of excess solution by blotting grid with filter paper; (**C**) formation of vitrified thin film after rapidly plunging into a suitable cryogen; (**D**) expanded side view of vitrified grid showing the path of the electron beam when viewed in a TEM column; (**E**) size segregation may occur during sample preparation, with larger particles at the edges of the holes and smaller particles at the center of the thin film. Large particles may also protrude from the film. (reproduced with permission from [171])

TEM techniques generally provide 2-dimensional images of 3D structures. Electron Tomography applied on TEM samples was previously presented as a possibility to obtain 3D images, but still represents an expensive and rare scientific protocol. Alternative microscopy techniques can be used to obtain 3D images: Scanning Electron Microscopy (SEM) and Atomic Force Microscopy (AFM). Similar to STEM technique, SEM uses a small beam of electrons, however these electrons are generally less energetic than for STEM and the resulting images will then have poor resolution. However, as the electrons are collected in a back scatter contrary to transmission techniques, SEM images are able to give information about the surface or near surface of the structures, completing then the information about the internal structuration provided by TEM and STEM techniques. Nevertheless, the sample preparation requires the same drying process as for TEM and the same structure modification's problems are met again.

Concerning AFM, it is mainly used to have surface topologies by dragging or tapping a sharp tip across the surface of the sample. AFM resolution is particularly high for the z direction of the deposited sample, giving information about the height of the sample and its surface morphology. As the drying of the sample is required here too, there is an alternative liquid AFM allowing then an observation of a conserved hydrated sample.

V.3 Examples of characterization studies on polymeric assemblies and supplementary techniques for specific structures

As explained in the previous paragraph, the best way to fully characterize assembled systems is to combine the techniques, which bring different kind of information. For example, the self-assembly process of a block copolymer and magnetic particles, iron oxides, leads to different morphologies and repartition of the iron oxides into the polymeric structure.[172] By playing on the solvent nature and the percentage of incorporated nanoparticles, varying nanostructures were obtained and present further different relaxation properties. The several magneto core-shell structures were observed in TEM microscopy, which differentiates the polymer from the nanoparticles through contrast variation (**Figure 26**). The repartition of the nanoparticles can then be guessed and is further confirmed by additional iron intensity signal recording. Dynamic Light Scattering (DLS) technique brings here information about the size variation induced by the solvent change or nanoparticles percentage. In the case of dioxane/THF (96.8%) solvent, the combination of TEM and DLS was particularly efficient as two different morphologies were observed in this sample: magneto core-shell polymersomes (408±46nm) and micelles (166±18nm). TEM helps then in the visualization of these two different structures and DLS brings information about their respective quantitative distribution from a size point of view.

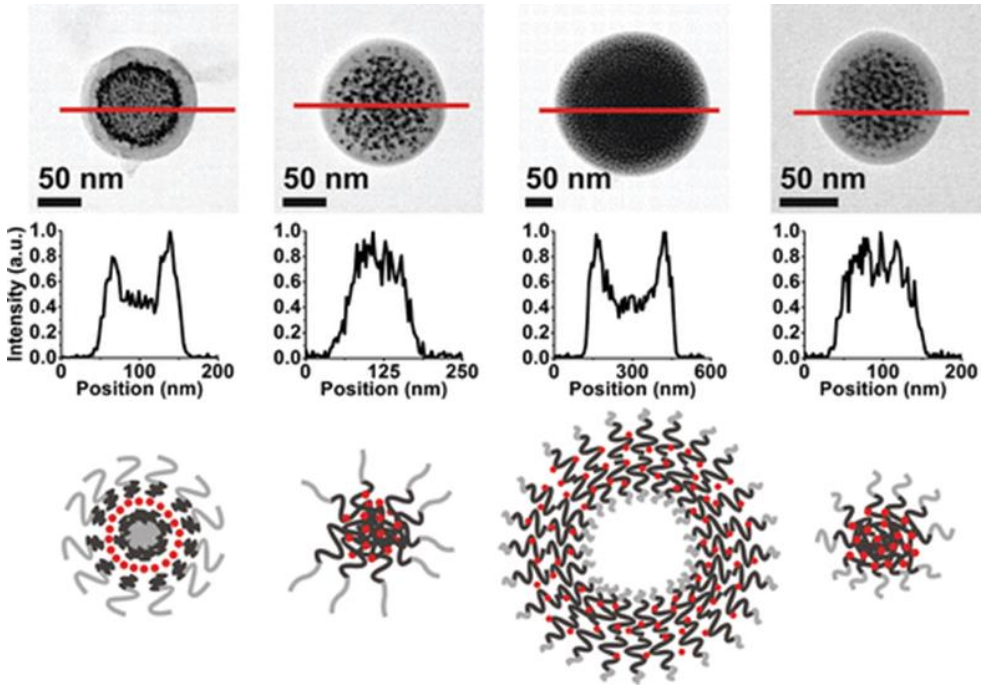

Figure 26. Structural characterization of three different self-assembly structures. STEM images and Fe intensity line scans for (**a**) magneto-core shell assemblies formed in DMF/THF (96.8% DMF), (**b**) magneto-micelles formed in THF, (**c**) magneto-polymersomes formed in dioxane/THF (96.8% dioxane), and (d) magneto-micelles formed in dioxane/THF (96.8% dioxane). The assemblies were prepared with PAA_{38}-b-PS_{189} at the polymer concentration of 0.04 wt % and a nanoparticle mass percent of 27.1%. The self-assembled structures are pictorially described below the EDS data, where light gray lines, dark gray lines, and red dots represent PAA, PS, and nanoparticles, respectively. (reproduced with permission from [172])

Stimuli-responsive polymer assembly mechanisms can then be followed step by step thanks to microscopy techniques such as Cryo-TEM, which captures the acquired morphology under certain parameters such as pH.[173] In this work, DLS technique is used to complete the images with size evaluation. G. Battaglia and A.J. Ryan did a study onto amphiphilic block copolymers' assemblies in bulk, which combines scattering methods, DLS and SAXS, with microscopy techniques such as TEM and Cryo-TEM.[174] DLS was performed just after preparation and after 4 months, and revealed two different sizes, both over 30 nm which confirmed the vesicle morphology, contrary to micelles one generally associated to lower sizes. To have more insights into the geometry and the morphology of the vesicles, TEM pictures were realized by preparing the sample with 3 different ways, to minimize the effect of artifacts. TEM confirmed the vesicle morphology and high magnification enabled to see the core-shell repartition. Membranes' thickness was easily measured on TEM and cryo-TEM pictures. Finally, SAXS analysis allowed to have a third membrane thickness value, by examining the structure factor and the pair distance distribution function.

The multi-technique approach is applied as well onto hybrid systems composed of block copolymer and gold nanoparticles.[175] Pluronic polymers are used here to functionalize in situ synthesized gold nanoparticles. As explained in previous part, UV-visible spectroscopy is highly used in the AuNPs' characterization, due to their SPR property. The progressive synthesis of the AuNPs can then be followed by UV-vis spectroscopy and confirm their stability. TEM confirms the formation of AuNPs and show the different morphologies issued from the variation of gold salt concentration. As gold absorbs X-rays, SAXS technique is particularly well adapted to study the influence of the gold salt concentration onto the resulting morphology from a size point of view. Indeed, by increasing gold salt concentration, the nanoparticles are larger and the polydispersity increases as well, according to SAXS curves. These tendencies are confirming TEM observation and the coexistence of morphologies is evidenced through DLS analysis. Additional SANS measurements help understanding the polymeric structuration, by doing the analysis into D_2O solvent to enhance contrast for hydrogenous compound such as polymers. Three different morphologies were then deduced from the interpretation of SANS analysis evidencing the coexistence of polymer-functionalized AuNPs, micelles and unimers of polymers, with their associated sizes and proportion in solution, according to the gold salt concentration.

Finally, some specific examples are given to enrich the characterization techniques for polymeric assemblies. First, a TEM technique is applied to liquid state and named in situ TEM.[176] The main advantage is to have motion of the observed nanostructures, which can be essential in the understanding of assembly mechanisms.

Regarding instantaneous techniques, Stopped Flow scattering represents a major method to follow precisely the formation of a nanostructure by recording optical properties of the sample like scattering light. The micelle formation based on the pH-responsiveness of the triblock copolymer composing the micelle structure, is thus studied by Stopped Flow Scattering to identify the different phases of the assembly process.[177] Both scattering intensity and hydrodynamic diameter records allowed to describe the following pH-dependent behavior of the sample. In acidic conditions, only unimers constitute the solution and by increasing pH, micelles population appear step by step until being the only morphology detected over pH=7. Regarding ions' influence onto polymer self-assembly, the addition of some ions onto polymer solution can induce rheological changes and then impact the assembly process, and the final morphology as well.[178] By measuring viscosity with time, it is possible to relate the rheological behavior of the sample to the morphology of the polymer assembly contained in this sample. Finally, Flow Field-Flow Fractionation (F4) based techniques are now widely applied for the analysis of nanoparticles or nanoassemblies.[179] The aim of these analysis method is to sort out the different nanostructures composing the sample according to their diffusion coefficient. By this way, the resulting fractions can be further analyzed through other characterization techniques to have precise information about the nanostructures. Comparison of one of this F4 method, AsF4 (asymmetrical) is made with other classical techniques regarding the characterization of polymersomes systems.[180] Recently, thermal version of the F4 technique was used to sort out micelle structures according to their corona composition.[181]

VI Conclusions and project objectives

The design of polymer-based assemblies has been described in detail regarding the self-assembly of block copolymers. This literature review gives an overview of the multiple parameters involved into molecular assembly mechanisms: polymer's configuration, concentration, molecular weight, etc. We particularly focused onto the assembly strategies involving block copolymers and inorganic matter such as ions and gold nanoparticles, to obtain further hybrid colloidal nanostructures in solution. The resulting properties of these hybrid assemblies can be tuned through morphological changes and thus be designed for catalysis or applications in biological medium.

The PhD project related to this work deal with the study of these polymer-based assemblies and particularly the hybrid systems involving block copolymers (BCPs), gold nanoparticles (AuNPs) and metallic ions. As illustrated on the **Scheme 1**, several assembled systems can be obtained from these three chemicals, either by studying each one separated or by mixing two or three of them. The main objectives of this work were to understand the assembly mechanisms implied into the formation of these hybrid systems and to manage the involved parameters in

order to design precise nanostructures with optimal properties for further biological applications. To achieve this goal, the work will be decomposed into three main studies sum up here into three experimental chapters.

The **chapter II** deals with the study of the hybrid systems based on the interactions between DHBCs and metallic ions. First and foremost, the choice of the block copolymer, configuration and functionalities, is primordial to control some of the interactions implied in the assembly mechanism and the final structure as well, as described in this **chapter I**. The assembly mechanism is studied when BCPs and different kind of metallic ions are mixed together and the resulting assembled systems are characterized and tested in some biological applications.

The **chapter III** concerns the study of the assembly of AuNPs in presence of several kind of metallic ions. The aggregation mechanism of the AuNPs is studied with different characterization methods and its understanding allows to assess a sensing method of the concerned metallic ions.

The **chapter IV** finally focuses on the last combination for hybrid systems, i.e. mixing gold nanoparticles with block copolymers. As detailed in this chapter I, several methods exist to induce interaction between polymer and AuNPs, and some of them are explored in this chapter. A focus on the self-assembly of the block copolymer is made to better understand and then control the mechanism for hybrid assembly with AuNPs. Finally, some preliminary tests are made regarding the assembly of the three chemicals: BCPs, AuNPs and metallic ions.

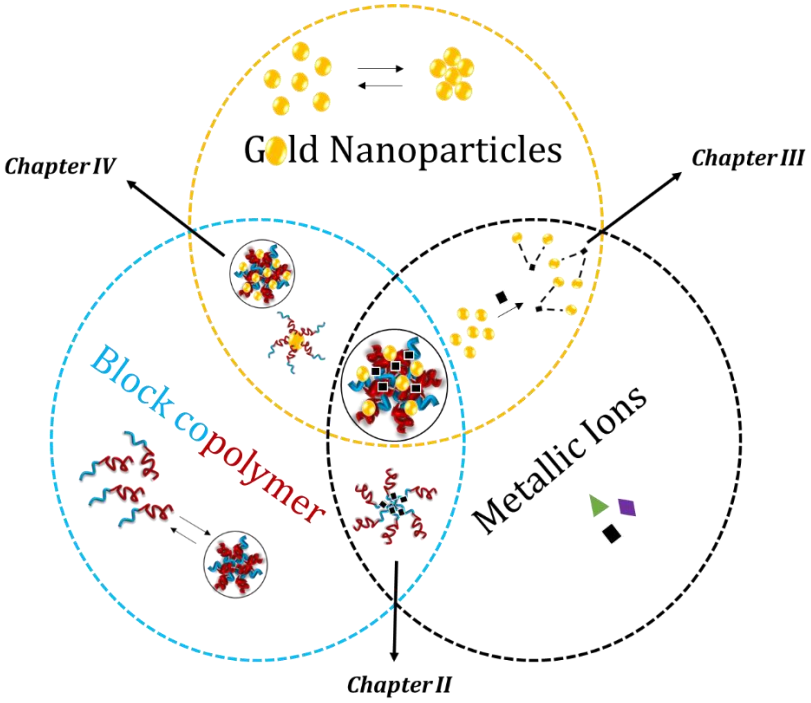

Scheme 1. Potential assembly systems obtained from self-assembly of block copolymers, self-assembly of gold nanoparticles or from hybrid assemblies based on interactions between block copolymers and gold nanoparticles and/or ions.

VII References

(1) Qin, B.; Yin, Z.; Tang, X.; Zhang, S.; Wu, Y.; Xu, J.-F.; Zhang, X. Supramolecular Polymer Chemistry: From Structural Control to Functional Assembly. *Progress in Polymer Science* **2020**, *100*, 101167. https://doi.org/10.1016/j.progpolymsci.2019.101167.

(2) Cheng, M.; Shi, F. Precise Macroscopic Supramolecular Assemblies: Strategies and Applications. *Chemistry – A European Journal* **2020**, *26* (68), 15763–15778. https://doi.org/10.1002/chem.202001881.

(3) Lu, Y.; Lin, J.; Wang, L.; Zhang, L.; Cai, C. Self-Assembly of Copolymer Micelles: Higher-Level Assembly for Constructing Hierarchical Structure. *Chem. Rev.* **2020**, *120* (9), 4111–4140. https://doi.org/10.1021/acs.chemrev.9b00774.

(4) Cummins, C.; Lundy, R.; Walsh, J. J.; Ponsinet, V.; Fleury, G.; Morris, M. A. Enabling Future Nanomanufacturing through Block Copolymer Self-Assembly: A Review. *Nano Today* **2020**, *35*, 100936. https://doi.org/10.1016/j.nantod.2020.100936.

(5) Karayianni, M.; Pispas, S. Block Copolymer Solution Self-Assembly: Recent Advances, Emerging Trends, and Applications. *Journal of Polymer Science* **2021**, *59* (17), 1874–1898. https://doi.org/10.1002/pol.20210430.

(6) Wang, J.-S.; Matyjaszewski, K. Controlled/"living" Radical Polymerization. Atom Transfer Radical Polymerization in the Presence of Transition-Metal Complexes. *J. Am. Chem. Soc.* **1995**, *117* (20), 5614–5615. https://doi.org/10.1021/ja00125a035.

(7) Corpart, P.; Charmot, D.; Biadatti, T.; Zard, S.; Michelet, D.; Rhodia Chimie. Method for Block Polymer Synthesis by Controlled Radical Polymerization. WO1998058974A1.

(8) Hu, H.; Gopinadhan, M.; Osuji, C. O. Directed Self-Assembly of Block Copolymers: A Tutorial Review of Strategies for Enabling Nanotechnology with Soft Matter. *Soft Matter* **2014**, *10* (22), 3867–3889. https://doi.org/10.1039/C3SM52607K.

(9) Flory, P. J. *Principles of Polymer Chemistry*, Cornell University Press.; 1953.

(10) Bates, F. S.; Fredrickson, G. H. Block Copolymers—Designer Soft Materials. *Physics Today* **1999**, *52* (2), 32–38. https://doi.org/10.1063/1.882522.

(11) Blanazs, A.; Armes, S. P.; Ryan, A. J. Self-Assembled Block Copolymer Aggregates: From Micelles to Vesicles and Their Biological Applications. *Macromolecular Rapid Communications* **2009**, *30* (4–5), 267–277. https://doi.org/10.1002/marc.200800713.

(12) Kelley, E. G.; Albert, J. N. L.; Sullivan, M. O.; Epps, III, T. H. Stimuli-Responsive Copolymer Solution and Surface Assemblies for Biomedical Applications. *Chem. Soc. Rev.* **2013**, *42* (17), 7057–7071. https://doi.org/10.1039/C3CS35512H.

(13) Tritschler, U.; Pearce, S.; Gwyther, J.; Whittell, G. R.; Manners, I. 50th Anniversary Perspective: Functional Nanoparticles from the Solution Self-Assembly of Block Copolymers. *Macromolecules* **2017**, *50* (9), 3439–3463. https://doi.org/10.1021/acs.macromol.6b02767.

(14) Deng, Z.; Liu, S. Emerging Trends in Solution Self-Assembly of Block Copolymers. *Polymer* **2020**, *207*, 122914. https://doi.org/10.1016/j.polymer.2020.122914.

(15) Israelachvili, J. N.; Mitchell, D. J.; Ninham, B. W. Theory of Self-Assembly of Lipid Bilayers and Vesicles. *Biochimica et Biophysica Acta (BBA) - Biomembranes* **1977**, *470* (2), 185–201. https://doi.org/10.1016/0005-2736(77)90099-2.

(16) Doncom, K. E. B.; Blackman, L. D.; Wright, D. B.; Gibson, M. I.; O'Reilly, R. K. Dispersity Effects in Polymer Self-Assemblies: A Matter of Hierarchical Control. *Chem. Soc. Rev.* **2017**, *46* (14), 4119–4134. https://doi.org/10.1039/C6CS00818F.

(17) Zhang, L.; Eisenberg, A. Thermodynamic vs Kinetic Aspects in the Formation and Morphological Transitions of Crew-Cut Aggregates Produced by Self-Assembly of Polystyrene-b-Poly(Acrylic Acid) Block Copolymers in Dilute Solution. *Macromolecules* **1999**, *32* (7), 2239–2249. https://doi.org/10.1021/ma981039f.

(18) Tan, Z.; Lan, W.; Liu, Q.; Wang, K.; Hussain, M.; Ren, M.; Geng, Z.; Zhang, L.; Luo, X.; Zhang, L.; Zhu, J. Kinetically Controlled Self-Assembly of Block Copolymers into Segmented Wormlike Micelles in Microfluidic Chips. *Langmuir* **2019**, *35* (1), 141–149. https://doi.org/10.1021/acs.langmuir.8b03028.

(19) Landazuri, G.; Fernandez, V. V. A.; Soltero, J. F. A.; Rharbi, Y. Length of the Core Forming Block Effect on Fusion and Fission Dynamics at Equilibrium in PEO–PPO–PEO Triblock Copolymer Micelles in the Spherical Regime. *Macromolecules* **2021**, *54* (5), 2494–2505. https://doi.org/10.1021/acs.macromol.0c01520.

(20) Yu, Y.; Zhang, L.; Eisenberg, A. Morphogenic Effect of Solvent on Crew-Cut Aggregates of Apmphiphilic Diblock Copolymers. *Macromolecules* **1998**, *31* (4), 1144–1154. https://doi.org/10.1021/ma971254g.

(21) Zhang, L.; Eisenberg, A. Multiple Morphologies and Characteristics of "Crew-Cut" Micelle-like Aggregates of Polystyrene-b-Poly(Acrylic Acid) Diblock Copolymers in Aqueous Solutions. *J. Am. Chem. Soc.* **1996**, *118* (13), 3168–3181. https://doi.org/10.1021/ja953709s.

(22) Ha, S.; Kim, K. T. Effect of Hydrophilic Block End Groups and Block Junction on Block Copolymer Self-Assembly in Solution. *RSC Adv.* **2022**, *12* (12), 7446–7452. https://doi.org/10.1039/D2RA00493C.

(23) Battaglia, G.; Ryan, A. J. Effect of Amphiphile Size on the Transformation from a Lyotropic Gel to a Vesicular Dispersion. *Macromolecules* **2006**, *39* (2), 798–805. https://doi.org/10.1021/ma052108a.

(24) Li, X.; Tang, P.; Qiu, F.; Zhang, H.; Yang, Y. Aggregates in Solution of Binary Mixtures of Amphiphilic Diblock Copolymers with Different Chain Length. *J. Phys. Chem. B* **2006**, *110* (5), 2024–2030. https://doi.org/10.1021/jp055951j.

(25) Terreau, O.; Bartels, C.; Eisenberg, A. Effect of Poly(Acrylic Acid) Block Length Distribution on Polystyrene-b-Poly(Acrylic Acid) Block Copolymer Aggregates in Solution. 2. A Partial Phase Diagram. *Langmuir* **2004**, *20* (3), 637–645. https://doi.org/10.1021/la035557h.

(26) Zhu, J.; Hayward, R. C. Hierarchically Structured Microparticles Formed by Interfacial Instabilities of Emulsion Droplets Containing Amphiphilic Block Copolymers. *Angewandte Chemie International Edition* **2008**, *47* (11), 2113–2116. https://doi.org/10.1002/anie.200704863.

(27) Man, Y.; Li, X.; Li, S.; Yang, Z.; Lee, Y.-I.; Liu, H.-G. Effects of Hydrophobic/Hydrophilic Blocks Ratio on PS-b-PAA Self-Assembly in Solutions, in Emulsions, and at the Interfaces. *Colloids and Surfaces A: Physicochemical and Engineering Aspects* **2019**, *580*, 123684. https://doi-org-s.docadis.univ-tlse3.fr/10.1016/j.colsurfa.2019.123684.

(28) Jeon, S.-J.; Yi, G.-R.; Koo, C. M.; Yang, S.-M. Nanostructures Inside Colloidal Particles of Block Copolymer/Homopolymer Blends. *Macromolecules* **2007**, *40* (23), 8430–8439. https://doi.org/10.1021/ma0712302.

(29) Doberenz, F.; Zeng, K.; Willems, C.; Zhang, K.; Groth, T. Thermoresponsive Polymers and Their Biomedical Application in Tissue Engineering – a Review. *J. Mater. Chem. B* **2020**, *8* (4), 607–628. https://doi.org/10.1039/C9TB02052G.

(30) Seuring, J.; Agarwal, S. Polymers with Upper Critical Solution Temperature in Aqueous Solution. *Macromolecular Rapid Communications* **2012**, *33* (22), 1898–1920. https://doi.org/10.1002/marc.201200433.

(31) Pietsch, C.; Mansfeld, U.; Guerrero-Sanchez, C.; Hoeppener, S.; Vollrath, A.; Wagner, M.; Hoogenboom, R.; Saubern, S.; Thang, S. H.; Becer, C. R.; Chiefari, J.; Schubert, U. S. Thermo-Induced Self-Assembly of Responsive Poly(DMAEMA-b-DEGMA) Block Copolymers into Multi- and Unilamellar Vesicles. *Macromolecules* **2012**, *45* (23), 9292–9302. https://doi.org/10.1021/ma301867h.

(32) Kotsuchibashi, Y.; Yamamoto, K.; Aoyagi, T. Assembly Behavior of Double Thermo-Responsive Block Copolymers with Controlled Response Temperature in Aqueous Solution. *Journal of Colloid and Interface Science* **2009**, *336* (1), 67–72. https://doi.org/10.1016/j.jcis.2009.03.093.

(33) Škvarla, J.; Zedník, J.; Šlouf, M.; Pispas, S.; Štěpánek, M. Poly(N-Isopropyl Acrylamide)-Block-Poly(n-Butyl Acrylate) Thermoresponsive Amphiphilic Copolymers: Synthesis, Characterization and Self-Assembly Behavior in Aqueous Solutions. *European Polymer*

Journal **2014**, *61*, 124–132. https://doi-org-s.docadis.univ-tlse3.fr/10.1016/j.eurpolymj.2014.10.002.

(34) Ye, Q.; Huo, M.; Zeng, M.; Liu, L.; Peng, L.; Wang, X.; Yuan, J. Photoinduced Reversible Worm-to-Vesicle Transformation of Azo-Containing Block Copolymer Assemblies Prepared by Polymerization-Induced Self-Assembly. *Macromolecules* **2018**, *51* (9), 3308–3314. https://doi.org/10.1021/acs.macromol.8b00340.

(35) Dong, S.; Sun, W.; Wang, D.; Zhao, H.; Zu, G.; Zheng, Y. Light-Switching Azo-Copolymers Self-Assembly in Multi-Stationary States. *Macromolecular Rapid Communications* **2019**, *40* (9), 1900058. https://doi.org/10.1002/marc.201900058.

(36) Lee, N. S.; Li, Y.; Ruda, C. M.; Wooley, K. L. Aqueous-Only, PH-Induced Nanoassembly of Dual PKa-Driven Contraphilic Block Copolymers. *Chem. Commun.* **2008**, No. 42, 5339–5341. https://doi.org/10.1039/B810934F.

(37) Zhang, J.; Farias-Mancilla, B.; Kulai, I.; Hoeppener, S.; Lonetti, B.; Prévost, S.; Ulbrich, J.; Destarac, M.; Colombani, O.; Schubert, U. S.; Guerrero-Sanchez, C.; Harrisson, S. Effect of Hydrophilic Monomer Distribution on Self-Assembly of a PH-Responsive Copolymer: Spheres, Worms and Vesicles from a Single Copolymer Composition. *Angewandte Chemie International Edition* **2021**, *60* (9), 4925–4930. https://doi.org/10.1002/anie.202010501.

(38) Wang, Z.; Cao, Y.; Zhang, X.; Wang, D.; Liu, M.; Xie, Z.; Wang, Y. Rapid Self-Assembly of Block Copolymers for Flower-Like Particles with High Throughput. *Langmuir* **2016**, *32* (50), 13517–13524. https://doi.org/10.1021/acs.langmuir.6b03940.

(39) Jeon, S.-J.; Yi, G.-R.; Yang, S.-M. Cooperative Assembly of Block Copolymers with Deformable Interfaces: Toward Nanostructured Particles. *Advanced Materials* **2008**, *20* (21), 4103–4108. https://doi.org/10.1002/adma.200801377.

(40) Higuchi, T.; Tajima, A.; Motoyoshi, K.; Yabu, H.; Shimomura, M. Frustrated Phases of Block Copolymers in Nanoparticles. *Angewandte Chemie International Edition* **2008**, *47* (42), 8044–8046. https://doi.org/10.1002/anie.200803003.

(41) Wu, Y.; Wang, K.; Tan, H.; Xu, J.; Zhu, J. Emulsion Solvent Evaporation-Induced Self-Assembly of Block Copolymers Containing PH-Sensitive Block. *Langmuir* **2017**, *33* (38), 9889–9896. https://doi.org/10.1021/acs.langmuir.7b02330.

(42) Du, J.; Tang, Y.; Lewis, A. L.; Armes, S. P. PH-Sensitive Vesicles Based on a Biocompatible Zwitterionic Diblock Copolymer. *J. Am. Chem. Soc.* **2005**, *127* (51), 17982–17983. https://doi.org/10.1021/ja056514l.

(43) Lovett, J. R.; Warren, N. J.; Ratcliffe, L. P. D.; Kocik, M. K.; Armes, S. P. PH-Responsive Non-Ionic Diblock Copolymers: Ionization of Carboxylic Acid End-Groups Induces an Order–Order Morphological Transition. *Angewandte Chemie International Edition* **2015**, *54* (4), 1279–1283. https://doi.org/10.1002/anie.201409799.

(44) Canning, S. L.; Smith, G. N.; Armes, S. P. A Critical Appraisal of RAFT-Mediated Polymerization-Induced Self-Assembly. *Macromolecules* **2016**, *49* (6), 1985–2001. https://doi.org/10.1021/acs.macromol.5b02602.

(45) Zhou, J.; Wang, L.; Zha, X.; Wang, H. Synthesis of PH-Responsive Block Copolymer Micelles via RAFT Polymerization Induced Self-Assembly and Its Application in Emulsifier-Free Emulsion Polymerization. *Phosphorus, Sulfur, and Silicon and the Related Elements* **2020**, *195* (2), 131–141. https://doi.org/10.1080/10426507.2019.1655419.

(46) Klinger, D.; Wang, C. X.; Connal, L. A.; Audus, D. J.; Jang, S. G.; Kraemer, S.; Killops, K. L.; Fredrickson, G. H.; Kramer, E. J.; Hawker, C. J. A Facile Synthesis of Dynamic, Shape-Changing Polymer Particles. *Angewandte Chemie International Edition* **2014**, *53* (27), 7018–7022. https://doi.org/10.1002/anie.201400183.

(47) Zhang, L.; Yu, K.; Eisenberg, A. Ion-Induced Morphological Changes in “Crew-Cut” Aggregates of Amphiphilic Block Copolymers. *Science* **1996**, *272* (5269), 1777–1779. https://doi.org/10.1126/science.272.5269.1777.

(48) Luo, H.; Tang, Q.; Zhong, J.; Lei, Z.; Zhou, J.; Tong, Z. Interplay of Solvation and Size Effects Induced by the Counterions in Ionic Block Copolymers on the Basis of Hofmeister Series.

Macromolecular Chemistry and Physics **2019**, *220* (4), 1800508. https://doi.org/10.1002/macp.201800508.

(49) Wu, Y.; Tan, H.; Yang, Y.; Li, Y.; Xu, J.; Zhang, L.; Zhu, J. Regulating Block Copolymer Assembly Structures in Emulsion Droplets through Metal Ion Coordination. *Langmuir* **2018**, *34* (38), 11495–11502. https://doi.org/10.1021/acs.langmuir.8b02135.

(50) Zhu, M.-Q.; Li, A. D. Q. Zinc Ion Induced Polymorphism in Macromolecular Self-Assembly of Diblock Copolymers. *Talanta* **2005**, *67* (3), 525–531. https://doi-org-s.docadis.univ-tlse3.fr/10.1016/j.talanta.2005.06.026.

(51) Zhang, J.; Zhang, Y.; Chen, F.; Zhang, W.; Zhao, H. Self-Assembly of Photoswitchable Diblock Copolymers: Salt-Induced Micellization and the Influence of UV Irradiation. *Phys. Chem. Chem. Phys.* **2015**, *17* (18), 12215–12221. https://doi.org/10.1039/C5CP01560J.

(52) Yoshida, E. CO2-Responsive Behavior of Polymer Giant Vesicles Supporting Hindered Amine. *Colloid and Polymer Science* **2019**, *297* (4), 661–666. https://doi.org/10.1007/s00396-019-04484-8.

(53) Qiu, L.; Zhang, H.; Wang, B.; Zhan, Y.; Xing, C.; Pan, C.-Y. CO2-Responsive Nano-Objects with Assembly-Related Aggregation-Induced Emission and Tunable Morphologies. *ACS Appl. Mater. Interfaces* **2020**, *12* (1), 1348–1358. https://doi.org/10.1021/acsami.9b18792.

(54) Nadal, C.; Gineste, S.; Coutelier, O.; Tourrette, A.; Marty, J.-D.; Destarac, M. A Deeper Insight into the Dual Temperature- and PH-Responsiveness of Poly(Vinylamine)-b-Poly(N-Isopropylacrylamide) Double Hydrophilic Block Copolymers. *Colloids and Surfaces A: Physicochemical and Engineering Aspects* **2022**, *641*, 128502. https://doi-org-s.docadis.univ-tlse3.fr/10.1016/j.colsurfa.2022.128502.

(55) Cao, Y.; Cao, J.; Zhang, J.; Zhang, D.; Li, M.; Xu, Y.; He, K.; Chen, G.; Yuan, C.; Dai, L. The Research on Multi-Responsive Azobenzene Block Copolymer and Its Self-Assembly Behavior. *Polymers for Advanced Technologies* **2020**, *31* (4), 759–771. https://doi.org/10.1002/pat.4812.

(56) Ji, S.; Xu, L.; Fu, X.; Sun, J.; Li, Z. Light- and Metal Ion-Induced Self-Assembly and Reassembly Based on Block Copolymers Containing a Photoresponsive Polypeptide Segment. *Macromolecules* **2019**, *52* (12), 4686–4693. https://doi.org/10.1021/acs.macromol.9b00475.

(57) Lin, S.; Shang, J.; Theato, P. CO2-Triggered UCST Transition of Amphiphilic Triblock Copolymers and Their Self-Assemblies. *Polym. Chem.* **2017**, *8* (17), 2619–2629. https://doi.org/10.1039/C7PY00186J.

(58) Nabiyan, A.; Biehl, P.; Schacher, F. H. Crystallization vs Metal Chelation: Solution Self-Assembly of Dual Responsive Block Copolymers. *Macromolecules* **2020**, *53* (13), 5056–5067. https://doi.org/10.1021/acs.macromol.0c00792.

(59) Sun, Y.-J.; Cheng, X.-X.; Miao, T.-F.; Ma, H.-T.; Zhang, W.; Zhu, X.-L. Reversible CO2-, Photo- and Thermo- Triple Responsive Supramolecular Chirality of Azo-Containing Block Copolymer Assemblies Prepared by Polymerization-Induced Chiral Self-Assembly. *Chinese Journal of Polymer Science* **2022**, *40* (1), 56–66. https://doi.org/10.1007/s10118-021-2647-3.

(60) Zhao, X.; Wu, W.; Zhang, J.; Dai, W.; Zhao, Y. Thermoresponse and Self-Assembly of an ABC Star Quarterpolymer with O2 and Redox Dual-Responsive Y Junctions. *Polym. Chem.* **2018**, *9* (9), 1095–1108. https://doi.org/10.1039/C8PY00085A.

(61) Gao, F.; Xing, Y.; Yao, Y.; Sun, L.; Sun, Y.; He, X.; Lin, S. Self-Assembly and Multi-Stimuli Responsive Behavior of PAA-b-PAzoMA-b-PNIPAM Triblock Copolymers. *Polym. Chem.* **2017**, *8* (48), 7529–7536. https://doi.org/10.1039/C7PY01591G.

(62) Smith, A. E.; Xu, X.; Abell, T. U.; Kirkland, S. E.; Hensarling, R. M.; McCormick, C. L. Tuning Nanostructure Morphology and Gold Nanoparticle "Locking" of Multi-Responsive Amphiphilic Diblock Copolymers † Paper No. 138 in a Series on Water Soluble Polymers. *Macromolecules* **2009**, *42* (8), 2958–2964. https://doi.org/10.1021/ma802827p.

(63) Jundi, A. E.; Buwalda, S. J.; Bakkour, Y.; Garric, X.; Nottelet, B. Double Hydrophilic Block Copolymers Self-Assemblies in Biomedical Applications. *Advances in Colloid and Interface Science* **2020**, *283*, 102213. https://doi.org/10.1016/j.cis.2020.102213.
(64) Cölfen, H. Double-Hydrophilic Block Copolymers: Synthesis and Application as Novel Surfactants and Crystal Growth Modifiers. *Macromolecular Rapid Communications* **2001**, *22* (4), 219–252. https://doi.org/10.1002/1521-3927(20010201)22:4<219::AID-MARC219>3.0.CO;2-G.
(65) Nabiyan, A.; Max, J. B.; Schacher, F. H. Double Hydrophilic Copolymers – Synthetic Approaches, Architectural Variety, and Current Application Fields. *Chem. Soc. Rev.* **2022**, *51* (3), 995–1044. https://doi.org/10.1039/D1CS00086A.
(66) Pramanik, P.; Ghosh, S. Thermoresponsive Polymersome from a Double Hydrophilic Block Copolymer. *Journal of Polymer Science Part A: Polymer Chemistry* **2015**, *53* (21), 2444–2451. https://doi.org/10.1002/pola.27735.
(67) Ji-Ping ZHANG, J.-F. D., Shuo-Zhen CHENG, Xue-Feng LI. PH- and Temperature-Induced Micellization of the Dual Hydrophilic Block Copolymer Poly(Methacrylate Acid)-*b*-Poly(*N*-(2-Methacryloylxyethyl) Pyrrolidone) in Aqueous Solution. *Acta Physico-Chimica Sinica* **2016**, *32* (8), 2018. https://doi.org/10.3866/PKU.WHXB201605271.
(68) Zhao, J.; Zhang, G.; Pispas, S. Morphological Transitions in Aggregates of Thermosensitive Poly(Ethylene Oxide)-b-Poly(N-Isopropylacrylamide) Block Copolymers Prepared via RAFT Polymerization. *Journal of Polymer Science Part A: Polymer Chemistry* **2009**, *47* (16), 4099–4110. https://doi.org/10.1002/pola.23470.
(69) Shin, S. H. R.; McAninch, P. T.; Henderson, I. M.; Gomez, A.; Greene, A. C.; Carnes, E. C.; Paxton, W. F. Self-Assembly/Disassembly of Giant Double-Hydrophilic Polymersomes at Biologically-Relevant PH. *Chem. Commun.* **2018**, *54* (65), 9043–9046. https://doi.org/10.1039/C8CC05155K.
(70) Layrac, G.; Gérardin, C.; Tichit, D.; Harrisson, S.; Destarac, M. Hybrid Polyion Complex Micelles from Poly(Vinylphosphonic Acid)-Based Double Hydrophilic Block Copolymers and Divalent Transition Metal Ions. *Polymer* **2015**, *72*, 292–300. https://doi.org/10.1016/j.polymer.2015.04.031.
(71) Sohn, H.; Shin, H.-W.; Lee, S.-M. Metal-Mediated Morphology Regulation of Self-Assembled Double-Hydrophilic Block Copolymers. *ACS Macro Lett.* **2020**, *9* (4), 600–605. https://doi.org/10.1021/acsmacrolett.0c00120.
(72) Insua, I.; Wilkinson, A.; Fernandez-Trillo, F. Polyion Complex (PIC) Particles: Preparation and Biomedical Applications. *European Polymer Journal* **2016**, *81*, 198–215. https://doi.org/10.1016/j.eurpolymj.2016.06.003.
(73) Abolmaali, S. S.; Tamaddon, A. M.; Salmanpour, M.; Mohammadi, S.; Dinarvand, R. Block Ionomer Micellar Nanoparticles from Double Hydrophilic Copolymers, Classifications and Promises for Delivery of Cancer Chemotherapeutics. *European Journal of Pharmaceutical Sciences* **2017**, *104*, 393–405. https://doi.org/10.1016/j.ejps.2017.04.009.
(74) van der Kooij, H. M.; Spruijt, E.; Voets, I. K.; Fokkink, R.; Cohen Stuart, M. A.; van der Gucht, J. On the Stability and Morphology of Complex Coacervate Core Micelles: From Spherical to Wormlike Micelles. *Langmuir* **2012**, *28* (40), 14180–14191. https://doi.org/10.1021/la303211b.
(75) Es Sayed, J.; Brummer, H.; Stuart, M. C. A.; Sanson, N.; Perrin, P.; Kamperman, M. Responsive Pickering Emulsions Stabilized by Frozen Complex Coacervate Core Micelles. *ACS Macro Lett.* **2022**, *11* (1), 20–25. https://doi.org/10.1021/acsmacrolett.1c00647.
(76) Ramasamy, T.; Poudel, B. K.; Ruttala, H.; Choi, J. Y.; Hieu, T. D.; Umadevi, K.; Youn, Y. S.; Choi, H.-G.; Yong, C. S.; Kim, J. O. Cationic Drug-Based Self-Assembled Polyelectrolyte Complex Micelles: Physicochemical, Pharmacokinetic, and Anticancer Activity Analysis. *Colloids and Surfaces B: Biointerfaces* **2016**, *146*, 152–160. https://doi.org/10.1016/j.colsurfb.2016.06.004.
(77) Reboul, J.; Nugay, T.; Anik, N.; Cottet, H.; Ponsinet, V.; In, M.; Lacroix-Desmazes, P.; Gérardin, C. Synthesis of Double Hydrophilic Block Copolymers and Induced Assembly

with Oligochitosan for the Preparation of Polyion Complex Micelles. *Soft Matter* **2011**, *7* (12), 5836–5846. https://doi.org/10.1039/C1SM05230F.

(78) Warnant, J.; Marcotte, N.; Reboul, J.; Layrac, G.; Abdelhafid, A.; Jérôme, C.; Lerner, D.; Gerardin, C. Physicochemical Properties of PH-Controlled Polyion Complex (PIC) Micelles of Poly(Acrylic Acid)-Based Double Hydrophilic Block Copolymers and Various Polyamines. *Analytical and bioanalytical chemistry* **2012**, *403*, 1395–1404. https://doi.org/10.1007/s00216-012-5947-1.

(79) Gineste, S.; Di Cola, E.; Amouroux, B.; Till, U.; Marty, J.-D.; Mingotaud, A.-F.; Mingotaud, C.; Violleau, F.; Berti, D.; Parigi, G.; Luchinat, C.; Balor, S.; Sztucki, M.; Lonetti, B. Mechanistic Insights into Polyion Complex Associations. *Macromolecules* **2018**, *51* (4), 1427–1440. https://doi.org/10.1021/acs.macromol.7b02391.

(80) Xu, Q.; Tang, J.; Wang, Y.; Liu, J.; Wang, X.; Huang, Z.; Huang, L.; Wang, Y.; Shen, W.; Belfiore, L. A. Eu3+-Induced Aggregates of Diblock Copolymers and Their Photoluminescent Property. *Journal of Colloid and Interface Science* **2013**, *394*, 630–638. https://doi-org-s.docadis.univ-tlse3.fr/10.1016/j.jcis.2012.12.062.

(81) Wang, X.; Tang, J.; Xu, Q.; Shen, W.; Wang, Y.; Liu, J.; Wang, Y.; Huang, L.; Jiao, J.; Wang, D.; Song, Y.; Belfiore, L. A. Fluorescent Polymeric Aggregates Induced by Eu3+ Ions and Their Surface Morphologies. *Optical Materials* **2015**, *46*, 28–33. https://doi-org-s.docadis.univ-tlse3.fr/10.1016/j.optmat.2015.03.050.

(82) Cheng, J.; Xu, M.; Cheng, P.; Zhang, W.; Li, N.; Wang, Y.; Yang, J.; Liang, K.; Li, P.; Yu, H.; Qiu, X. Metal Ions 'Sewing' Isoporous Membranes with Polystyrene-Block-Poly (Acrylic Acid) Block Copolymer. *Journal of Membrane Science* **2019**, *587*, 117086. https://doi-org-s.docadis.univ-tlse3.fr/10.1016/j.memsci.2019.05.011.

(83) Dong, S.; Liu, L.; Zhao, H. Copper-Coordination Induced Fabrication of Stimuli-Responsive Polymersomes from Amphiphilic Block Copolymer Containing Pendant Thioethers. *Polym. Chem.* **2021**, *12* (21), 3105–3115. https://doi.org/10.1039/D1PY00371B.

(84) Gineste, S.; Mingotaud, C. Double-Hydrophilic Block Copolymer–Metal Ion Associations: Structures, Properties and Applications. *Advances in Colloid and Interface Science* **2023**, *311*, 102808. https://doi.org/10.1016/j.cis.2022.102808.

(85) Sanson, N.; Bouyer, F.; Gérardin, C.; In, M. Nanoassemblies Formed from Hydrophilic Block Copolymers and Multivalent Ions. *Phys. Chem. Chem. Phys.* **2004**, *6* (7), 1463–1466. https://doi.org/10.1039/B314521M.

(86) Sanson, N.; Putaux, J.-L.; Destarac, M.; Gérardin, C.; Fajula, F. Hybrid Organic-Inorganic Colloids with a Core-Corona Structure: A Transmission Electron Microscopy Investigation. *Macromolecular Symposia* **2005**, *226* (1), 279–288. https://doi.org/10.1002/masy.200550825.

(87) Sanson, N.; Bouyer, F.; Destarac, M.; In, M.; Gérardin, C. Hybrid Polyion Complex Micelles Formed from Double Hydrophilic Block Copolymers and Multivalent Metal Ions: Size Control and Nanostructure. *Langmuir* **2012**, *28* (8), 3773–3782. https://doi.org/10.1021/la204562t.

(88) Volkmann, L.; Köhler, M.; Sobotta, F. H.; Enke, M. T.; Brendel, J. C.; Schacher, F. H. Poly(2-Acrylamidoglycolic Acid) (PAGA): Controlled Polymerization Using RAFT and Chelation of Metal Cations. *Macromolecules* **2018**, *51* (18), 7284–7294. https://doi.org/10.1021/acs.macromol.8b01260.

(89) Mochida, Y.; Cabral, H.; Miura, Y.; Albertini, F.; Fukushima, S.; Osada, K.; Nishiyama, N.; Kataoka, K. Bundled Assembly of Helical Nanostructures in Polymeric Micelles Loaded with Platinum Drugs Enhancing Therapeutic Efficiency against Pancreatic Tumor. *ACS Nano* **2014**, *8* (7), 6724–6738. https://doi.org/10.1021/nn500498t.

(90) Frangville, C.; Li, Y.; Billotey, C.; Talham, D. R.; Taleb, J.; Roux, P.; Marty, J.-D.; Mingotaud, C. Assembly of Double-Hydrophilic Block Copolymers Triggered by Gadolinium Ions: New Colloidal MRI Contrast Agents. *Nano Lett.* **2016**, *16* (7), 4069–4073. https://doi.org/10.1021/acs.nanolett.6b00664.

(91) Yon, M. Gadolinium-Based Contrast Agents_ From Gadolinium Complexes to Colloidal Systems. *International Journal of Pharmaceutics* **2019**, 10.
(92) Yon, M.; Gineste, S.; Parigi, G.; Lonetti, B.; Gibot, L.; Talham, D.; Marty, J.-D.; Mingotaud, C. Hybrid Polymeric Nanostructures Stabilized by Zirconium and Gadolinium Ions for Use as Magnetic Resonance Imaging Contrast Agents. *ACS Applied Nano Materials* **2021**, *4*. https://doi.org/10.1021/acsanm.1c00495.
(93) Shin, H.-W.; Sohn, H.; Jeong, Y.-H.; Lee, S.-M. Construction of Paramagnetic Manganese-Chelated Polymeric Nanoparticles Using Pyrene-End-Modified Double-Hydrophilic Block Copolymers for Enhanced Magnetic Resonance Relaxivity: A Comparative Study with Cisplatin Pharmacophore. *Langmuir* **2019**, *35* (19), 6421–6428. https://doi.org/10.1021/acs.langmuir.9b00406.
(94) Mestivier, M.; Li, J. R.; Camy, A.; Frangville, C.; Mingotaud, C.; Benoît-Marquié, F.; Marty, J.-D. Copper-Based Hybrid Polyion Complexes for Fenton-Like Reactions. *Chemistry – A European Journal* **2020**, *26* (62), 14152–14158. https://doi.org/10.1002/chem.202002362.
(95) Brassinne, J.; Fustin, C.-A.; Gohy, J.-F. Control over the Assembly and Rheology of Supramolecular Networks via Multi-Responsive Double Hydrophilic Copolymers. *Polym. Chem.* **2017**, *8* (9), 1527–1539. https://doi.org/10.1039/C6PY02143C.
(96) Zhang, Q.; Tosi, F.; Üğdüler, S.; Maji, S.; Hoogenboom, R. Tuning the LCST and UCST Thermoresponsive Behavior of Poly(N,N-Dimethylaminoethyl Methacrylate) by Electrostatic Interactions with Trivalent Metal Hexacyano Anions and Copolymerization. *Macromolecular Rapid Communications* **2015**, *36* (7), 633–639. https://doi.org/10.1002/marc.201400550.
(97) Tarasov, K.; Houssein, D.; Destarac, M.; Marcotte, N.; Gérardin, C.; Tichit, D. Stable Aqueous Colloids of ZnS Quantum Dots Prepared Using Double Hydrophilic Block Copolymers. *New J. Chem.* **2013**, *37* (2), 508–514. https://doi.org/10.1039/C2NJ40738H.
(98) Layrac, G.; Destarac, M.; Gérardin, C.; Tichit, D. Highly Stable Layered Double Hydroxide Colloids: A Direct Aqueous Synthesis Route from Hybrid Polyion Complex Micelles. *Langmuir* **2014**, *30* (32), 9663–9671. https://doi.org/10.1021/la502159x.
(99) Nejati, K.; Dadashpour, M.; Gharibi, T.; Mellatyar, H.; Akbarzadeh, A. Biomedical Applications of Functionalized Gold Nanoparticles: A Review. *Journal of Cluster Science* **2022**, *33* (1), 1–16. https://doi.org/10.1007/s10876-020-01955-9.
(100) Elahi, N.; Kamali, M.; Baghersad, M. H. Recent Biomedical Applications of Gold Nanoparticles: A Review. *Talanta* **2018**, *184*, 537–556. https://doi.org/10.1016/j.talanta.2018.02.088.
(101) Bouché, M.; Hsu, J. C.; Dong, Y. C.; Kim, J.; Taing, K.; Cormode, D. P. Recent Advances in Molecular Imaging with Gold Nanoparticles. *Bioconjugate Chemistry* **2020**, *31* (2), 303–314. https://doi.org/10.1021/acs.bioconjchem.9b00669.
(102) Amendola, V.; Pilot, R.; Frasconi, M.; Maragò, O. M.; Iatì, M. A. Surface Plasmon Resonance in Gold Nanoparticles: A Review. *Journal of Physics: Condensed Matter* **2017**, *29* (20), 203002. https://doi.org/10.1088/1361-648x/aa60f3.
(103) Saha, K.; Agasti, S. S.; Kim, C.; Li, X.; Rotello, V. M. Gold Nanoparticles in Chemical and Biological Sensing. *Chem. Rev.* **2012**, *112* (5), 2739–2779. https://doi.org/10.1021/cr2001178.
(104) Grzelczak, M.; Liz-Marzán, L. M.; Klajn, R. Stimuli-Responsive Self-Assembly of Nanoparticles. *Chem. Soc. Rev.* **2019**, *48* (5), 1342–1361. https://doi.org/10.1039/C8CS00787J.
(105) Muddineti, O. S.; Ghosh, B.; Biswas, S. Current Trends in Using Polymer Coated Gold Nanoparticles for Cancer Therapy. *International Journal of Pharmaceutics* **2015**, *484* (1), 252–267. https://doi.org/10.1016/j.ijpharm.2015.02.038.
(106) Dai, Y.; Zhang, X. Recent Advances in Amphiphilic Polymers as the Stabilizers of Colloidal Gold Nanoparticles. *Macromolecular Materials and Engineering* **2018**, *303* (6), 1800105. https://doi.org/10.1002/mame.201800105.

(107) Lu, M.; Zhu, H.; Bazuin, C. G.; Peng, W.; Masson, J.-F. Polymer-Templated Gold Nanoparticles on Optical Fibers for Enhanced-Sensitivity Localized Surface Plasmon Resonance Biosensors. *ACS Sens.* **2019**, *4* (3), 613–622. https://doi.org/10.1021/acssensors.8b01372.
(108) Boyer, C.; Whittaker, M. R.; Luzon, M.; Davis, T. P. Design and Synthesis of Dual Thermoresponsive and Antifouling Hybrid Polymer/Gold Nanoparticles. *Macromolecules* **2009**, *42* (18), 6917–6926. https://doi.org/10.1021/ma9013127.
(109) Yang, H. Y.; Li, Y.; Lee, D. S. Recent Advances of PH-Induced Charge-Convertible Polymer-Mediated Inorganic Nanoparticles for Biomedical Applications. *Macromolecular Rapid Communications* **2020**, *41* (21), 2000106. https://doi.org/10.1002/marc.202000106.
(110) Sistach, S.; Beija, M.; Rahal, V.; Brûlet, A.; Marty, J.-D.; Destarac, M.; Mingotaud, C. Thermoresponsive Amphiphilic Diblock Copolymers Synthesized by MADIX/RAFT: Properties in Aqueous Solutions and Use for the Preparation and Stabilization of Gold Nanoparticles. *Chem. Mater.* **2010**, *22* (12), 3712–3724. https://doi.org/10.1021/cm100674p.
(111) Glaria, A.; Beija, M.; Bordes, R.; Destarac, M.; Marty, J.-D. Understanding the Role of ω-End Groups and Molecular Weight in the Interaction of PNIPAM with Gold Surfaces. *Chem. Mater.* **2013**, *25* (9), 1868–1876. https://doi.org/10.1021/cm400480p.
(112) Yon, A. M.; Marty, B. J.-D.; Ciuculescu-Pradines, C. D. CHAPTER 6 Amines and Amine-Boranes. In *Reducing Agents in Colloidal Nanoparticle Synthesis*; The Royal Society of Chemistry, 2021; pp 130–156. https://doi.org/10.1039/9781839163623-00130.
(113) Sardar, R.; Park, J.-W.; Shumaker-Parry, J. S. Polymer-Induced Synthesis of Stable Gold and Silver Nanoparticles and Subsequent Ligand Exchange in Water. *Langmuir* **2007**, *23* (23), 11883–11889. https://doi.org/10.1021/la702359g.
(114) Sakai, T.; Alexandridis, P. Mechanism of Gold Metal Ion Reduction, Nanoparticle Growth and Size Control in Aqueous Amphiphilic Block Copolymer Solutions at Ambient Conditions. *J. Phys. Chem. B* **2005**, *109* (16), 7766–7777. https://doi.org/10.1021/jp046221z.
(115) Longenberger, L.; Mills, G. Formation of Metal Particles in Aqueous Solutions by Reactions of Metal Complexes with Polymers. *J. Phys. Chem.* **1995**, *99* (2), 475–478. https://doi.org/10.1021/j100002a001.
(116) Stiufiuc, R.; Iacovita, C.; Nicoara, R.; Stiufiuc, G.; Florea, A.; Achim, M.; Lucaciu, C. M. One-Step Synthesis of PEGylated Gold Nanoparticles with Tunable Surface Charge. *Journal of Nanomaterials* **2013**, *2013*, 146031. https://doi.org/10.1155/2013/146031.
(117) Luo, C.; Zhang, Y.; Zeng, X.; Zeng, Y.; Wang, Y. The Role of Poly(Ethylene Glycol) in the Formation of Silver Nanoparticles. *Journal of Colloid and Interface Science* **2005**, *288* (2), 444–448. https://doi.org/10.1016/j.jcis.2005.03.005.
(118) Hoppe, C. E.; Lazzari, M.; Pardiñas-Blanco, I.; López-Quintela, M. A. One-Step Synthesis of Gold and Silver Hydrosols Using Poly(N-Vinyl-2-Pyrrolidone) as a Reducing Agent. *Langmuir* **2006**, *22* (16), 7027–7034. https://doi.org/10.1021/la060885d.
(119) Lim, B.; Camargo, P. H. C.; Xia, Y. Mechanistic Study of the Synthesis of Au Nanotadpoles, Nanokites, and Microplates by Reducing Aqueous HAuCl4 with Poly(Vinyl Pyrrolidone). *Langmuir* **2008**, *24* (18), 10437–10442. https://doi.org/10.1021/la801803z.
(120) Lermusiaux, L.; Plissonneau, M.; Bertry, L.; Drisko, G. L.; Buissette, V.; Le Mercier, T.; Duguet, E.; Tréguer-Delapierre, M. Seeded Growth of Ultrathin Gold Nanoshells Using Polymer Additives and Microwave Radiation. *Scientific Reports* **2021**, *11* (1), 17831. https://doi.org/10.1038/s41598-021-97171-0.
(121) Yuan, J.-J.; Schmid, A.; Armes, S. P.; Lewis, A. L. Facile Synthesis of Highly Biocompatible Poly(2-(Methacryloyloxy)Ethyl Phosphorylcholine)-Coated Gold Nanoparticles in Aqueous Solution. *Langmuir* **2006**, *22* (26), 11022–11027. https://doi.org/10.1021/la0616350.
(122) Seo, E.; Lee, S.-H.; Lee, S.; Choi, S.-H.; Hawker, C. J.; Kim, B.-S. Highly Stable Au Nanoparticles with Double Hydrophilic Block Copolymer Templates: Correlation

between Structure and Stability. *Polym. Chem.* **2017**, *8* (31), 4528–4537. https://doi.org/10.1039/C7PY00773F.

(123) Leiva, A.; Fuentes, I.; Bossel, E.; Urzúa, M.; Méndez, M.; Pino, M.; Radić, D.; Márquez, V.; González-Nilo, Fernando. D. Block Copolymers in the Synthesis of Gold Nanoparticles. Two New Approaches: Copolymer Aggregates as Reductants and Stabilizers and Simultaneous Formation of Copolymer Aggregates and Gold Nanoparticles. *Journal of Polymer Science Part A: Polymer Chemistry* **2014**, *52* (21), 3069–3079. https://doi.org/10.1002/pola.27354.

(124) Xie, M.; Ding, L.; You, Z.; Gao, D.; Yang, G.; Han, H. Robust Hybrid Nanostructures Comprising Gold and Thiol-Functionalized Polymer Nanoparticles: Facile Preparation, Diverse Morphologies and Unique Properties. *J. Mater. Chem.* **2012**, *22* (28), 14108–14118. https://doi.org/10.1039/C2JM31228J.

(125) Aryal, S.; K.C, R. B.; Bhattarai, N.; Lee, B. M.; Kim, H. Y. Stabilization of Gold Nanoparticles by Thiol Functionalized Poly(ε-Caprolactone) for the Labeling of PCL Biocarrier. *Materials Chemistry and Physics* **2006**, *98* (2), 463–469. https://doi.org/10.1016/j.matchemphys.2005.09.082.

(126) Liu, X.; Huang, N.; Wang, H.; Li, H.; Jin, Q.; Ji, J. The Effect of Ligand Composition on the in Vivo Fate of Multidentate Poly(Ethylene Glycol) Modified Gold Nanoparticles. *Biomaterials* **2013**, *34* (33), 8370–8381. https://doi-org-s.docadis.univ-tlse3.fr/10.1016/j.biomaterials.2013.07.059.

(127) Durand-Gasselin, C.; Koerin, R.; Rieger, J.; Lequeux, N.; Sanson, N. Colloidal Stability of Zwitterionic Polymer-Grafted Gold Nanoparticles in Water. *Journal of Colloid and Interface Science* **2014**, *434*, 188–194. https://doi.org/10.1016/j.jcis.2014.07.048.

(128) Rahme, K.; Gauffre, F.; Marty, J.-D.; Payré, B.; Mingotaud, C. A Systematic Study of the Stabilization in Water of Gold Nanoparticles by Poly(Ethylene Oxide)−Poly(Propylene Oxide)−Poly(Ethylene Oxide) Triblock Copolymers. *J. Phys. Chem. C* **2007**, *111* (20), 7273–7279. https://doi.org/10.1021/jp070274+.

(129) Jans, H.; Jans, K.; Lagae, L.; Borghs, G.; Maes, G.; Huo, Q. Poly(Acrylic Acid)-Stabilized Colloidal Gold Nanoparticles: Synthesis and Properties. *Nanotechnology* **2010**, *21* (45), 455702. https://doi.org/10.1088/0957-4484/21/45/455702.

(130) Siegwart, D. J.; Oh, J. K.; Matyjaszewski, K. ATRP in the Design of Functional Materials for Biomedical Applications. *Progress in Polymer Science* **2012**, *37* (1), 18–37. https://doi.org/10.1016/j.progpolymsci.2011.08.001.

(131) Ohno, K.; Koh, K.; Tsujii, Y.; Fukuda, T. Synthesis of Gold Nanoparticles Coated with Well-Defined, High-Density Polymer Brushes by Surface-Initiated Living Radical Polymerization. *Macromolecules* **2002**, *35* (24), 8989–8993. https://doi.org/10.1021/ma0209491.

(132) Kim, D. J.; Kang, S. M.; Kong, B.; Kim, W.-J.; Paik, H.; Choi, H.; Choi, I. S. Formation of Thermoresponsive Gold Nanoparticle/PNIPAAm Hybrids by Surface-Initiated, Atom Transfer Radical Polymerization in Aqueous Media. *Macromolecular Chemistry and Physics* **2005**, *206* (19), 1941–1946. https://doi.org/10.1002/macp.200500268.

(133) Li, D.; He, Q.; Cui, Y.; Wang, K.; Zhang, X.; Li, J. Thermosensitive Copolymer Networks Modify Gold Nanoparticles for Nanocomposite Entrapment. *Chemistry – A European Journal* **2007**, *13* (8), 2224–2229. https://doi.org/10.1002/chem.200600839.

(134) Li, D.; He, Q.; Cui, Y.; Li, J. Fabrication of PH-Responsive Nanocomposites of Gold Nanoparticles/Poly(4-Vinylpyridine). *Chem. Mater.* **2007**, *19* (3), 412–417. https://doi.org/10.1021/cm062290+.

(135) Chiefari, J.; Chong, Y. K. (Bill); Ercole, F.; Krstina, J.; Jeffery, J.; Le, T. P. T.; Mayadunne, R. T. A.; Meijs, G. F.; Moad, C. L.; Moad, G.; Rizzardo, E.; Thang, S. H. Living Free-Radical Polymerization by Reversible Addition−Fragmentation Chain Transfer: The RAFT Process. *Macromolecules* **1998**, *31* (16), 5559–5562. https://doi.org/10.1021/ma9804951.

(136) Phuong Le, T.; Moad, G.; Rizzardo, E.; Thang, S. H. Polymerization with Living Characteristics. WO1998001478A1.

(137) Charmot, D.; Corpart, P.; Adam, H.; Zard, S. Z.; Biadatti, T.; Bouhadir, G. Controlled Radical Polymerization in Dispersed Media. *Macromolecular Symposia* **2000**, *150* (1), 23–32. https://doi.org/10.1002/1521-3900(200002)150:1<23::AID-MASY23>3.0.CO;2-E.
(138) Pereira, S. O.; Barros-Timmons, A.; Trindade, T. A Comparative Study of Chemical Routes for Coating Gold Nanoparticles via Controlled RAFT Emulsion Polymerization. *Particle & Particle Systems Characterization* **2017**, *34* (2), 1600202. https://doi.org/10.1002/ppsc.201600202.
(139) Raula, J.; Shan, J.; Nuopponen, M.; Niskanen, A.; Jiang, H.; Kauppinen, E. I.; Tenhu, H. Synthesis of Gold Nanoparticles Grafted with a Thermoresponsive Polymer by Surface-Induced Reversible-Addition-Fragmentation Chain-Transfer Polymerization. *Langmuir* **2003**, *19* (8), 3499–3504. https://doi.org/10.1021/la026872r.
(140) Beija, M.; Marty, J.-D.; Destarac, M. Thermoresponsive Poly(N-Vinyl Caprolactam)-Coated Gold Nanoparticles: Sharp Reversible Response and Easy Tunability. *Chem. Commun.* **2011**, *47* (10), 2826. https://doi.org/10.1039/c0cc05184e.
(141) Jones, S. T.; Walsh-Korb, Z.; Barrow, S. J.; Henderson, S. L.; del Barrio, J.; Scherman, O. A. The Importance of Excess Poly(N-Isopropylacrylamide) for the Aggregation of Poly(N-Isopropylacrylamide)-Coated Gold Nanoparticles. *ACS Nano* **2016**, *10* (3), 3158–3165. https://doi.org/10.1021/acsnano.5b04083.
(142) Huebner, D.; Rossner, C.; Vana, P. Light-Induced Self-Assembly of Gold Nanoparticles with a Photoresponsive Polymer Shell. *Polymer* **2016**, *107*, 503–508. https://doi-org-s.docadis.univ-tlse3.fr/10.1016/j.polymer.2016.05.073.
(143) Sardar, R.; Bjorge, N. S.; Shumaker-Parry, J. S. PH-Controlled Assemblies of Polymeric Amine-Stabilized Gold Nanoparticles. *Macromolecules* **2008**, *41* (12), 4347–4352. https://doi.org/10.1021/ma800407s.
(144) Li, D.; He, Q.; Yang, Y.; Möhwald, H.; Li, J. Two-Stage PH Response of Poly(4-Vinylpyridine) Grafted Gold Nanoparticles. *Macromolecules* **2008**, *41* (19), 7254–7256. https://doi.org/10.1021/ma800894c.
(145) Wei, Z.; Liu, C.-H.; Duan, H.; Luo, Q.; Huang, M.; Thanneeru, S.; Nieh, M.-P.; He, J. Self-Assembly of Gold Nanoparticles Grafted with Amphiphilic Supramolecular Block Copolymers. *Giant* **2022**, *10*, 100102. https://doi-org-s.docadis.univ-tlse3.fr/10.1016/j.giant.2022.100102.
(146) Li, J.; Zhao, J.; Wu, W.; Liang, J.; Guo, J.; Zhou, H.; Liang, L. Temperature and Anion Responsive Self-Assembly of Ionic Liquid Block Copolymers Coating Gold Nanoparticles. *Frontiers of Materials Science* **2016**, *10* (2), 178–186. https://doi.org/10.1007/s11706-016-0334-z.
(147) Li, J.; Wu, W.; Han, C.; Zhang, S.; Zhou, H.; Guo, J. Aggregation Behavior of PH- and Thermo-Responsive Block Copolymer Protected Gold Nanoparticles. *Colloid and Polymer Science* **2014**, *292* (7), 1657–1664. https://doi.org/10.1007/s00396-014-3225-9.
(148) He, J.; Huang, X.; Li, Y.-C.; Liu, Y.; Babu, T.; Aronova, M. A.; Wang, S.; Lu, Z.; Chen, X.; Nie, Z. Self-Assembly of Amphiphilic Plasmonic Micelle-Like Nanoparticles in Selective Solvents. *J. Am. Chem. Soc.* **2013**, *135* (21), 7974–7984. https://doi.org/10.1021/ja402015s.
(149) Song, D.-P.; Wang, X.; Lin, Y.; Watkins, J. J. Synthesis and Controlled Self-Assembly of UV-Responsive Gold Nanoparticles in Block Copolymer Templates. *J. Phys. Chem. B* **2014**, *118* (44), 12788–12795. https://doi.org/10.1021/jp508212f.
(150) Cai, C.; Wang, L.; Lin, J.; Zhang, X. Morphology Transformation of Hybrid Micelles Self-Assembled from Rod–Coil Block Copolymer and Nanoparticles. *Langmuir* **2012**, *28* (9), 4515–4524. https://doi.org/10.1021/la204941w.
(151) Xu, J.; Han, Y.; Cui, J.; Jiang, W. Size Selective Incorporation of Gold Nanoparticles in Diblock Copolymer Vesicle Wall. *Langmuir* **2013**, *29* (33), 10383–10392. https://doi.org/10.1021/la402132x.
(152) Jang, J. D.; Jeon, S.-W.; Yoon, Y.-J.; Bang, J.; Han, Y. S.; Kim, T.-H. Self-Assembly of Gold Nanoparticles in a Block Copolymer Aggregate Template Driven by Hydrophobic Interactions. *Polym. Chem.* **2019**, *10* (46), 6269–6277. https://doi.org/10.1039/C9PY01266D.

(153) Zhang, J.-G.; Zhang, X.-Y.; Yu, H.; Luo, Y.-L.; Xu, F.; Chen, Y.-S. Preparation, Self-Assembly and Performance Modulation of Gold Nanoparticles Decorated Ferrocene-Containing Hybrid Block Copolymer Multifunctional Materials. *Journal of Industrial and Engineering Chemistry* **2018**, *65*, 224–235. https://doi.org/10.1016/j.jiec.2018.04.033.
(154) He, Z.; Zhong, A.; Zhang, H.; Xiong, L.; Xu, Y.; Wang, T.; Zhou, M.; Huang, K. In Situ Formation of Dual-Phase Thermosensitive Ultrasmall Gold Nanoparticles. *Chemistry : a European journal.* **2015**, *21* (28), 10220–10225.
(155) Zheng, P.; Jiang, X.; Zhang, X.; Zhang, W.; Shi, L. Formation of Gold@Polymer Core–Shell Particles and Gold Particle Clusters on a Template of Thermoresponsive and PH-Responsive Coordination Triblock Copolymer. *Langmuir* **2006**, *22* (22), 9393–9396. https://doi.org/10.1021/la0609064.
(156) Khullar, P.; Singh, V.; Mahal, A.; Kumar, H.; Kaur, G.; Bakshi, M. S. Block Copolymer Micelles as Nanoreactors for Self-Assembled Morphologies of Gold Nanoparticles. *J. Phys. Chem. B* **2013**, *117* (10), 3028–3039. https://doi.org/10.1021/jp310507m.
(157) Maiti, C.; Banerjee, R.; Maiti, S.; Dhara, D. PH-Induced Vesicle-to-Micelle Transition in Amphiphilic Diblock Copolymer: Investigation by Energy Transfer between in Situ Formed Polymer Embedded Gold Nanoparticles and Fluorescent Dye. *Langmuir* **2015**, *31* (1), 32–41. https://doi.org/10.1021/la504165e.
(158) Chang, S.; Singamaneni, S.; Kharlampieva, E.; Young, S. L.; Tsukruk, V. V. Responsive Hybrid Nanotubes Composed of Block Copolymer and Gold Nanoparticles. *Macromolecules* **2009**, *42* (15), 5781–5785. https://doi.org/10.1021/ma900767s.
(159) Zhu, H.; Masson, J.-F.; Bazuin, C. G. Templating Gold Nanoparticles on Nanofibers Coated with a Block Copolymer Brush for Nanosensor Applications. *ACS Appl. Nano Mater.* **2020**, *3* (1), 516–529. https://doi.org/10.1021/acsanm.9b02081.
(160) Nie, X.-B.; Yu, C.-Y.; Wei, H. Precise Modulation of Spatially Distributed Inorganic Nanoparticles in Block Copolymers-Based Self-Assemblies with Diverse Morphologies. *Materials Today Chemistry* **2021**, *22*, 100616. https://doi.org/10.1016/j.mtchem.2021.100616.
(161) Nguyen, D.; Ravaine, S.; Bourgeat-Lami, E.; Duguet, E. About the Suitability of the Seeded-Dispersion Polymerization Technique for Preparing Micron-Sized Silica-Polystyrene Clusters. *J. Mater. Chem.* **2010**, *20* (42), 9392–9400. https://doi.org/10.1039/B926438H.
(162) Chomette, C.; Tréguer-Delapierre, M.; Schade, N. B.; Manoharan, V. N.; Lambert, O.; Taveau, J.-C.; Ravaine, S.; Duguet, E. Colloidal Alchemy: Conversion of Polystyrene Nanoclusters into Gold. *ChemNanoMat* **2017**, *3* (3), 160–163. https://doi.org/10.1002/cnma.201600315.
(163) Xu, X.; Rosi, N. L.; Wang, Y.; Huo, F.; Mirkin, C. A. Asymmetric Functionalization of Gold Nanoparticles with Oligonucleotides. *J. Am. Chem. Soc.* **2006**, *128* (29), 9286–9287. https://doi.org/10.1021/ja061980b.
(164) Mucic, R. C.; Storhoff, J. J.; Mirkin, C. A.; Letsinger, R. L. DNA-Directed Synthesis of Binary Nanoparticle Network Materials. *J. Am. Chem. Soc.* **1998**, *120* (48), 12674–12675. https://doi.org/10.1021/ja982721s.
(165) Chiu, J. J.; Kim, B. J.; Kramer, E. J.; Pine, D. J. Control of Nanoparticle Location in Block Copolymers. *J. Am. Chem. Soc.* **2005**, *127* (14), 5036–5037. https://doi.org/10.1021/ja050376i.
(166) Kim, B. J.; Bang, J.; Hawker, C. J.; Kramer, E. J. Effect of Areal Chain Density on the Location of Polymer-Modified Gold Nanoparticles in a Block Copolymer Template. *Macromolecules* **2006**, *39* (12), 4108–4114. https://doi.org/10.1021/ma060308w.
(167) Luo, Q.; Hickey, R. J.; Park, S.-J. Controlling the Location of Nanoparticles in Colloidal Assemblies of Amphiphilic Polymers by Tuning Nanoparticle Surface Chemistry. *ACS Macro Lett.* **2013**, *2* (2), 107–111. https://doi.org/10.1021/mz3006044.
(168) Yan, N.; Zhang, Y.; He, Y.; Zhu, Y.; Jiang, W. Controllable Location of Inorganic Nanoparticles on Block Copolymer Self-Assembled Scaffolds by Tailoring the Entropy and Enthalpy Contributions. *Macromolecules* **2017**, *50* (17), 6771–6778. https://doi.org/10.1021/acs.macromol.7b01076.

(169) Patterson, J. P.; Robin, M. P.; Chassenieux, C.; Colombani, O.; O'Reilly, R. K. The Analysis of Solution Self-Assembled Polymeric Nanomaterials. *Chem. Soc. Rev.* **2014**, *43* (8), 2412–2425. https://doi.org/10.1039/C3CS60454C.

(170) Bals, S.; Goris, B.; Liz-Marzán, L. M.; Van Tendeloo, G. Three-Dimensional Characterization of Noble-Metal Nanoparticles and Their Assemblies by Electron Tomography. *Angewandte Chemie International Edition* **2014**, *53* (40), 10600–10610. https://doi.org/10.1002/anie.201401059.

(171) Cui, H.; Hodgdon, T. K.; Kaler, E. W.; Abezgauz, L.; Danino, D.; Lubovsky, M.; Talmon, Y.; Pochan, D. J. Elucidating the Assembled Structure of Amphiphiles in Solution via Cryogenic Transmission Electron Microscopy. *Soft Matter* **2007**, *3* (8), 945–955. https://doi.org/10.1039/B704194B.

(172) Hickey, R. J.; Haynes, A. S.; Kikkawa, J. M.; Park, S.-J. Controlling the Self-Assembly Structure of Magnetic Nanoparticles and Amphiphilic Block-Copolymers: From Micelles to Vesicles. *J. Am. Chem. Soc.* **2011**, *133* (5), 1517–1525. https://doi.org/10.1021/ja1090113.

(173) Tang, R.; Ji, W.; Wang, C. Amphiphilic Block Copolymers Bearing Ortho Ester Side-Chains: PH-Dependent Hydrolysis and Self-Assembly in Water. *Macromolecular Bioscience* **2010**, *10* (2), 192–201. https://doi.org/10.1002/mabi.200900229.

(174) Battaglia, G.; Ryan, A. J. Bilayers and Interdigitation in Block Copolymer Vesicles. *J. Am. Chem. Soc.* **2005**, *127* (24), 8757–8764. https://doi.org/10.1021/ja050742y.

(175) Ray, D.; Aswal, V. Multi-Technique Approach for the Study of Block Copolymer-Mediated Gold Nanoparticles. *Nanoscience & Nanotechnology Letters* **2011**, *3*. https://doi.org/10.1166/nnl.2011.1230.

(176) Proetto, M. T.; Rush, A. M.; Chien, M.-P.; Abellan Baeza, P.; Patterson, J. P.; Thompson, M. P.; Olson, N. H.; Moore, C. E.; Rheingold, A. L.; Andolina, C.; Millstone, J.; Howell, S. B.; Browning, N. D.; Evans, J. E.; Gianneschi, N. C. Dynamics of Soft Nanomaterials Captured by Transmission Electron Microscopy in Liquid Water. *J. Am. Chem. Soc.* **2014**, *136* (4), 1162–1165. https://doi.org/10.1021/ja408513m.

(177) Zhu, Z.; Armes, S. P.; Liu, S. PH-Induced Micellization Kinetics of ABC Triblock Copolymers Measured by Stopped-Flow Light Scattering. *Macromolecules* **2005**, *38* (23), 9803–9812. https://doi.org/10.1021/ma051808c.

(178) Sheng, Y.; Yan, N.; Zhu, Y.; Jiang, W. Online Rheological Investigation on Ion-Induced Micelle Transition for Amphiphilic Polystyrene-Block-Poly(Acrylic Acid) Diblock Copolymer in Dilute Solution. *Langmuir* **2014**, *30* (51), 15392–15399. https://doi.org/10.1021/la503835u.

(179) Zattoni, A.; Roda, B.; Borghi, F.; Marassi, V.; Reschiglian, P. Flow Field-Flow Fractionation for the Analysis of Nanoparticles Used in Drug Delivery. *Journal of Pharmaceutical and Biomedical Analysis* **2014**, *87*, 53–61. https://doi.org/10.1016/j.jpba.2013.08.018.

(180) Till, U.; Gaucher-Delmas, M.; Saint-Aguet, P.; Hamon, G.; Marty, J.-D.; Chassenieux, C.; Payré, B.; Goudounèche, D.; Mingotaud, A.-F.; Violleau, F. Asymmetrical Flow Field-Flow Fractionation with Multi-Angle Light Scattering and Quasi-Elastic Light Scattering for Characterization of Polymersomes: Comparison with Classical Techniques. *Analytical and Bioanalytical Chemistry* **2014**, *406* (30), 7841–7853. https://doi.org/10.1007/s00216-014-7891-8.

(181) Greyling, G.; Pasch, H. Characterization of Charged Polymer Self-Assemblies by Multidetector Thermal Field-Flow Fractionation in Aqueous Mobile Phases. *Journal of Chromatography A* **2018**, *1532*, 175–181. https://doi.org/10.1016/j.chroma.2017.12.008.

Chapter II

Hybrid assemblies based on interactions between block copolymer and lanthanides ions for imaging applications

I Introduction

Hybrid assemblies between inorganic and organic compounds, represent a category of materials, with interesting multiple functions and collective properties emerging from successful combinations of individual compounds. These attractive properties provide materials with potential applications in many fields ranging from catalysis to biomedical applications. Hence, hybrid materials incorporating gadolinium (Gd^{3+}) ions are extensively studied as positive contrast agents (CAs) in Magnetic Resonance Imaging (MRI).[1,2] Indeed, gadolinium, a lanthanide metal ion with seven unpaired electrons, has demonstrated its efficiency in enhancing proton relaxation because of its high magnetic moment, paramagnetic properties and its ability to coordinate water molecules efficiently. However, the toxicity of Gd^{3+} ions related to their substitution or antagonist activity of calcium in a variety of cellular reactions[3] or in the occurrence of nephrogenic systemic fibrosis[4], prevents its direct administration. Therefore, to limit the cytotoxicity of Gd^{3+} ions in commercially available CAs, Gd^{3+} ions are chelated by specific interacting structures, each of them showing pros and cons regarding synthesis and properties.[5] Current clinically approved CAs are mostly made of macrocyclic Gd-based CAs like DOTAREM®. These CAs have no targeting properties and are rapidly extravasated from the bloodstream into the interstitial tissue, extracellular spaces and are rapidly eliminated from the systemic circulation via filtration through the kidneys, for example the half-time of DOTAREM® is about 1.4 +/- 0.2 hr. Nevertheless, these molecular complexes possess limitations, such as residual toxicity[6–9] and reduced efficiency at the higher magnetic fields of modern MRI instruments. This compels the main regulatory health agency in 2017 to control more carefully the use of this kind of CAs and European medicine agency suspended the authorization of the intravenous linear Gd-based CAs.

Current challenge is therefore to develop new Gd-based CAs that avoid the release of the free Gd^{3+} ions to prevent further complications. At the same time there is still a need of Gd-based CAs with enhanced relaxation properties, related to high contrast performance, to decrease the amount of injected compound. As illustrated in **Figure 27**, to reach such a goal, it is possible to play on three main factors which are responsible for the relaxation properties : q, the number of water molecules in the inner coordination sphere of gadolinium ions, τ_M, the residence lifetime of these water-molecules from the inner sphere and τ_R, the rotational correlation time of the molecule.

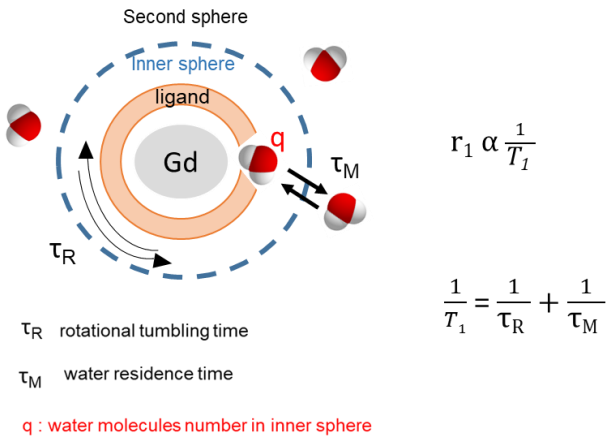

Figure 27. Characteristic times and parameters implied in the definition of the longitudinal relaxation time T_1, represented here in the case of gadolinium specie surrounded by a ligand with potential water molecules in the inner sphere. The formula relating the two times τ_M and τ_R to T_1 is expressed.

In that context, colloidal CAs are of special interest. Indeed, the use of Gd-based colloidal structures in the 10 to 100 nm size range enables to increase the relaxivity of obtained CAs. This effect is related to a much slower tumbling effect compared to molecular gadolinium complexes induced by a huge increase in the molecular weight of the gadolinium species (and of hydrodynamic radius). Slowing tumbling induces higher relaxivity. Gd^{3+} ions located within the colloidal species will rotate at the same (and very low) rate than the whole NPs, increasing the observed relaxivity. Therefore, lower injected levels are permitted. Moreover, colloidal structures present some additional features concerning their stability that make them candidate of choice for new families of CAS. As illustrated on the **Figure 28,** different families of such colloidal Gd-based CAs have been described in literature: 1) gadolinium complexes grafted or in interaction onto colloidal structures, 2) inorganic nanoparticles of controlled shape and properly functionalized.

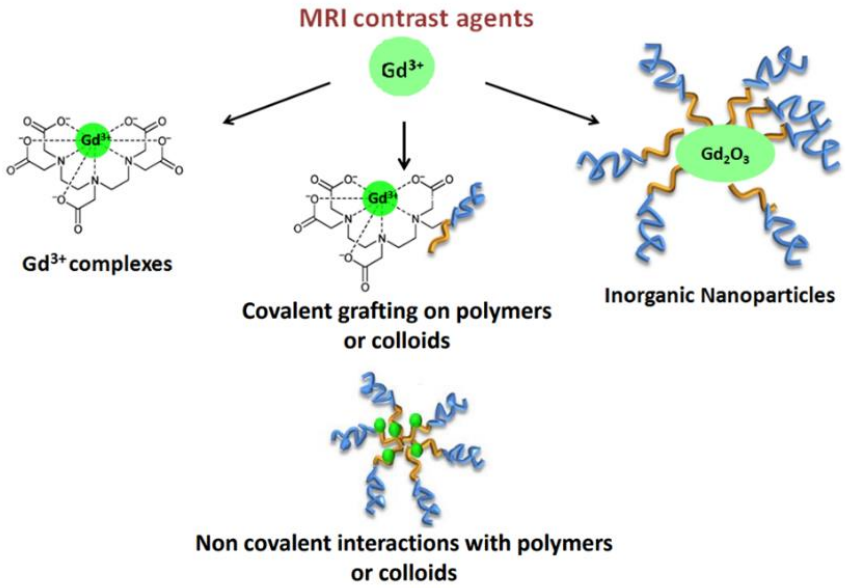

Figure 28. Gadolinium-based structures split into 4 main categories

Among those structures, the ones based on the use of polymers are of specific interest. Indeed, polymers play a key role in controlling the performances of the contrast agent: i) regarding the relation with the captive lanthanide ion, ligands should be capable of strong and multiple interactions allowing one to reach suitable and efficient concentrations for an optimized signal, to prevent them from leaching and to tune the parameters which influence the desired properties; ii) regarding the ligand/biological interface, ligands should act as a shield, keeping the toxic lanthanide ions out of contact with the biological media and ensure biocompatibility and the transport of the payload with long blood-circulation time and possibly specific recognition.

Double hydrophilic block copolymers (DHBCs)[10–13] type ligands have unique advantages for the design of vectors incorporating lanthanide ions.[1,14,15] Typically, one of the blocks which is ionizable can interact with polyvalent metal ions, spontaneously inducing self-assembly of the copolymer into micelles and encapsulation of metal ions into the core, through multiple electrostatic interactions, while the second non-ionizable block forms the shell of micelles in contact with the exterior medium. The negatively ionizable groups of poly(acrylic acid) (PAA), in combination with the obvious advantages of poly(ethylene glycol) (PEG) such as hydrophilicity, biocompatibility, Food and Drug Administration (FDA) approval, reduced immunogenicity and opsonization, etc. make PAA-*b*-PEG block copolymers of choice for loading polyvalent metallic ions.[1,2,14–20] These copolymers can be synthesized by reversible deactivation radical polymerization (RDRP) from functional PEG. This requires first the modification of one of the end groups of PEG in one or two synthetic steps.[21] These modified PEGs then serve either as macro-chain transfer agents for the copolymerization of acrylic acid (AA) by reversible addition-fragmentation chain transfer (RAFT) polymerization[22] or as macroinitiators for the copolymerization of acrylic esters by atom transfer radical polymerization (ATRP) followed by ester cleavage.[23] However, PEG synthesis requires specific conditions because the ethylene oxide monomer is a highly toxic gas under normal conditions, which explains why most authors use commercially available functional PEG, thus limiting the possibility of having access to PAA-*b*-PEG copolymers with a broad range of well-controlled composition and molar mass. Moreover, the different polymerization processes of PEG and PAA do not allow access to specific copolymer structures such as random or gradient. Another drawback related to the use of PAA-*b*-PEG is the difficulty of functionalizing the second extremity of PEG chain with a probe bearing specific properties (fluorescence, targeting….). Lastly, colloids based on the association of PEG-based polymers have limitations related to possible aggregation of PEG-coated NPs during lyophilization.[24]

For all the aforementioned reasons, the substitution of the PEG block with another block offering new perspectives for the preparation of original hybrid polyion complexes (HPICs) represents a challenge of great interest. These tunable DHBCs would provide new opportunities

to enrich the knowledge related to their micellization in the presence of polyvalent metallic ions and to the functionalities of the resulting objects in regard to biomedical applications. In this context, the choice of poly(N-vinyl-2-pyrrolidone), PVP, seems especially relevant: PVP is a highly water soluble, biocompatible polymer, with an ability to prevent nanoparticles opsonization.[25–27] It has been used as a plasma expander[28] and it is used as carrier of iodine (Inadine, Aerodine, Betadine) for antiseptic usage.[29] In addition, contrary to the polymerization of PEG, the polymerization of PVP can be controlled by RDRP methods.[30,31] Lastly, the use of hydrophilic PVP in colloid formulations has led to colloids with improved stability thanks to the cryoprotective properties of PVP that prevent aggregation during lyophilization.[32] In association with PAA, PVP has been mainly used in the composition of interpolymer complexes, based of cooperative hydrogen bonds.[33–39]

Surprisingly, there are only few examples describing the synthesis of PAA-*b*-PVP diblock copolymers: one by consecutive Cu-mediated ATRP[40] of NVP and *t*-butyl acrylate followed by *t*-butyl ester cleavage, and one by direct aqueous RAFT polymerization of AA and NVP.[41] To our knowledge, only one example has reported the use of PAA-*b*-PVP block copolymer for encapsulation of zinc phthalocyanine and doxorubicine into supramolecular assemblies to achieve chemo-photodynamic therapy but no attempt to assemble them in the presence of polyvalent metallic ions has been reported so far.[40]

Objectives

The following work mainly focuses on the synthesis of the PAA-*b*-PVP block copolymer with controlled composition and molar mass. The interaction of PAA-*b*-PVP with different cations (Gd^{3+}, Eu^{3+}, Y^{3+}) is investigated through the characterization of the obtained ionic assemblies named HPICs with scattering techniques, NMR and ATR-FTIR spectroscopy, and fluorescence experiments. The stability of the ionic assemblies is evaluated through pH and ionic strength variations. Some experiments are made with cell culture medium to observe the behavior or the HPICs into biological medium and their resulting properties regarding fluorescence and relaxivity. *In vitro* and *in vivo* tests are performed onto these HPICs structures as potential MRI contrast agents. PVP polymer represents here an alternative stabilizing block to the PEG concerning DHBCs used for hybrid assemblies. A permanent comparison of the obtained structures and their resulting properties will be made between PVP and PEG.

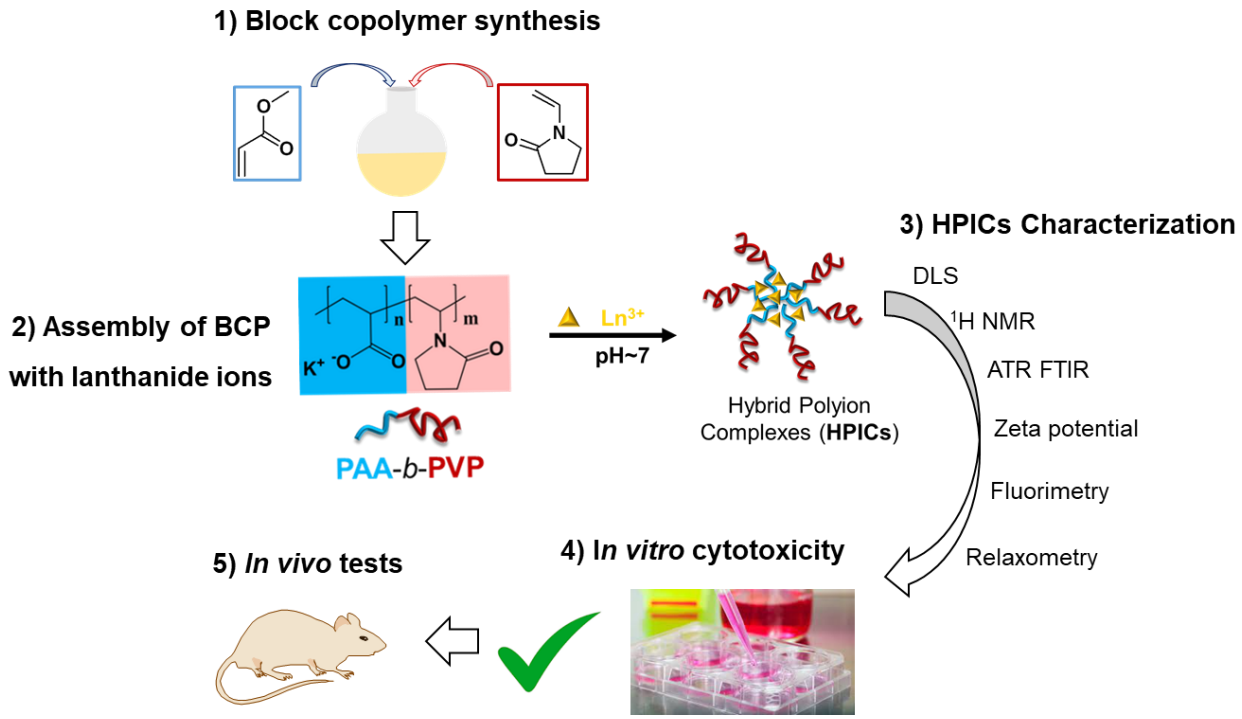

Scheme 2. Objectives of the chapter regarding the synthesis of PAA-*b*-PVP block copolymer and the resulting hybrid polyionic complexes (HPICs) nanostructures obtained after interaction with lanthanide ions.

II Synthesis and characterization of Poly(acrylic acid)-block-Poly(vinylpyrrolidone) (PAA-b-PVP) block copolymer

II.1. General considerations

The synthesis of the block copolymer PAA-*b*-PVP was performed through a RAFT process in collaboration with M. Destarac team (P3R team, IMRCP).

Since almost 20 years, RAFT polymerization is one of the most used reversible-deactivation radical polymerization (RDRP) process. RAFT polymerization is based on the use of transfer agents with a general structure as follows:

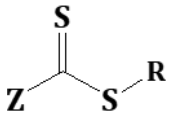

Scheme 3. General structure of a RAFT agent

The RAFT/MADIX (Macromolecular Design via the Interchange of Xanthates) technology was developed by Rhodia[42,43] and Dupont de Nemours[44,45] and is based on the use of Xanthates compounds (Z = OR') as transfer agents (**Scheme 3**). The use of these xanthates-based transfer agents enables to limit the end-chain reactions. More precisely, they allow, by their structure, reversible transfer steps according to an addition-fragmentation process. Consequently, less

irreversible transfer reactions occur and the polymerization reaction can go on and leads to more controlled chains. The complete RAFT mechanism is detailed on **Scheme 4:**

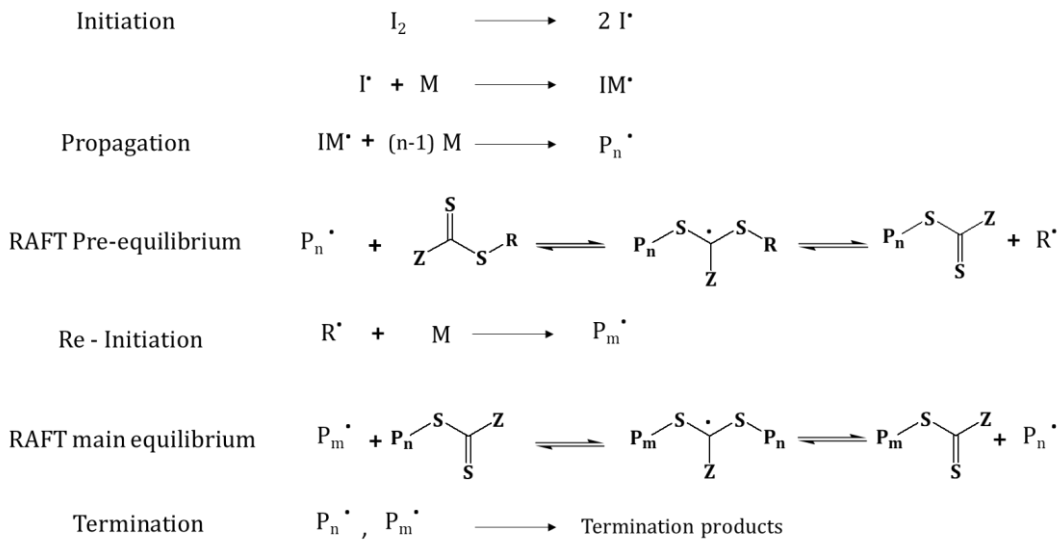

Scheme 4. RAFT polymerization mechanism

As in all the classic polymerization mechanisms, there are three main steps: initiation, propagation and termination, but here the RAFT process brings two more steps of transfer. The RAFT pre-equilibrium phase is driven by the molecular structure of the RAFT agent, which mainly depends on the nature of th Z and R groups. Indeed, Z group should bring enough stability to allow the addition of the first oligoradical from propagation step on the C=S bond. The R group is important as well, as it is supposed to be a suitable leaving group and an effective initiator for the re-initiation step. The RAFT main equilibrium phase finally allows the alternative growth of two polymer chains, revealing the role of the RAFT agent to limit termination reactions. At the end of the RAFT polymerization, the final polymer holds a functional end-chain, which can be further used to start a new polymerization step. This functional polymer would then be considered as the transfer agent for this new RAFT polymerization, leading to a block copolymer structure for example.

Previous work in the laboratory concerning the synthesis of this PAA-*b*-PVP block copolymer by RAFT polymerization was performed in aqueous solvent.[41] In this protocol, the acid form of the PAA is obtained, but leads to chain-end degradation and further side reactions. For these reasons, this protocol was not further considered. To obtain the targeted molecular weight and composition, the synthesis in an organic solvent medium, dioxane, was chosen. In RAFT polymerization process regarding diblock copolymers, the first monomer to polymerize must be the one which will represent the most stable propagating radical for the second polymerization step.[46]

In our case, the radical AMe· is a much more stable radical than NVP· one, so the AA block was synthesized as the first block. However, difficulties were encountered regarding the solubility during the copolymerization step due to the hydrogen bondings formed in dioxane between the two blocks leading to a milky mixture, which was difficult to manipulate and precipitate. To avoid this phenomenon, it was decided to do the copolymerization on an ester derivative polymer of PAA. *Tert*-butyl acrylate (*t*-BA) is a frequently used monomer which can be used to obtain an ester derivative polymer of PAA by RAFT polymerization process. However, the subsequent copolymerization of the N-VP monomer on the Poly(*tert*-butyl acrylate) P*t*BA polymer led to a copolymer which was difficult to isolate from the reaction mixture. Thus, the Poly(methyl acrylate) (PMA) was chosen as the ester derivative polymer of PAA, by using methyl acrylate as a monomer. The subsequent co-polymerization of N-VP on the PMA led this time to the desired co-polymer. To finally obtain a water-soluble polymer, a final hydrolysis step was performed. The targeted molar masses of each block of the polymer was chosen to be close to the ones of commercial PAA_{44}-*b*-PEG_{80} copolymer which was previously used in our team for the formation of hybrid assemblies with Gd^{3+} ions and which will represent our point of comparison.

The PAA-*b*-PVP block copolymer will be then used for the formation of hybrid assemblies with lanthanide ions. Ionic interactions are expected between the PAA block and the positively charged lanthanide ions, leading to structures able to be applied in biological applications such as imaging field.

II.2. Synthesis of Poly(methyl acrylate)-Xanthate polymer (PMA-XA_1)

In a first step, RAFT polymerization of methyl acrylate (MA) monomer was initiated by azobisisobutyronitrile (AIBN) in the presence of *O*-ethyl-*S*-(1-methoxycarbonyl) ethyldithiocarbonate (xanthate XA_1) (**Scheme 3**). This step was performed at 70°C in dioxane for 6h until complete monomer conversion as determined by ^1H NMR in $CDCl_3$ (**Figure 29**). The final mixture is put under pressure to evaporate as much dioxane as possible and obtain the final PMA-XA_1 polymer.

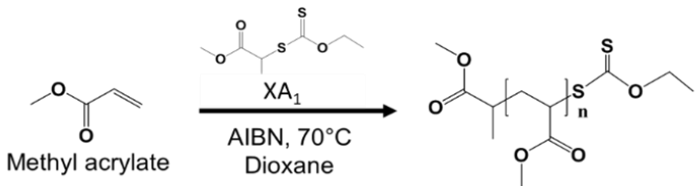

Scheme 5. Polymerization step of the methyl acrylate (MA) monomer through RAFT polymerization using Xanthate RAFT agent to obtain Poly(methyl acrylate)-xanthate terminated block polymer (PMA-XA_1)

Two methods were employed to determine the degree of polymerization (DP_n) of the MA after 6 hours of reaction. The first one is based on the use of trioxane as a standard compound, supposed to be inert in the polymerization process.

By taking the integration of its signal as a reference, it is possible to know the conversion of the monomer by comparing this reference to the monomer's protons signal before and after polymerization. A conversion of 99% was found for this first step of polymerization. By multiplying this conversion with the targeted DP_n, it is further possible to know the effective DP_n: $DP_n = 0.99 * 32 = 32$. This DP value corresponds to a molecular weight of the PMA of: $Mn_{PMA} = 32 * 86 = 2\ 752\ g.mol^{-1}$.

The second method is based on the comparison of the integration of the characteristic protons' signals of the monomer to the ones belonging to the end group. As detailed on **Figure 29**, the protons named ***h*** (4.72-4.6 ppm), integrate for 2 protons as they belong to the xanthate end group of the polymeric chain. The signals of the protons ***g*** (4.47 – 4.33 ppm) and ***e*** (2.49 – 2.25 ppm) were used to determine the DP value by using **Equation 8**:

Equation 8. Degree of polymerization (DP_n) calculation by using ^1H NMR integration values for the PMA

$$DP_n = \frac{2 * (e + g)}{h} \quad \textbf{(Eq 1)}$$

Through this method, a DP_n value of 32 was found, corresponding to a Mn of 2 752 $g.mol^{-1}$, which is in good agreement with the values issued from the first method.

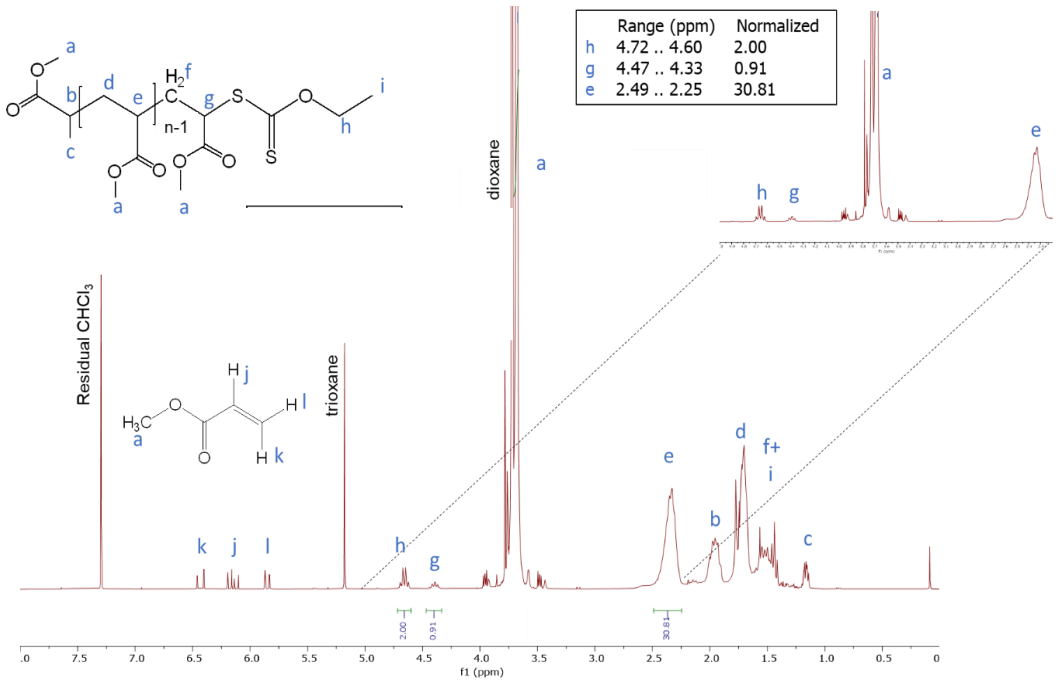

Figure 29. ^1H NMR Spectra ($CDCl_3$) of Poly(methyl acrylate) homopolymer (PMA_{32}-XA_1). Degree of Polymerization (DP_n) was evaluated from the integration of the signals noted as e (^1H, -C<u>H</u>-COOMe – 2.33 ppm) and g (^1H, –CH_2-C<u>**H**</u>(CO_2CH_3)-S(C=S)-OCH_2CH_3 – 4.4 ppm) relative to the one of h (2H, -C<u>H_2</u>-O-CS – 4.66 ppm arbitrary fixed at 2), as followed: DP = (2*(e + g))/h and was estimated around 32.

Size Exclusion Chromatography (SEC) analysis of the PMA, with DMF LiBr as solvent showed a monomodal molar mass distribution, with $M_{n,SEC}$ = 2 530 g.mol^{-1} which agrees with the expected M_n and a corresponding number-average degree of polymerization (DP_n) equal to 32. A dispersity (Đ) equal to 1.4 was also determined, which is in excellent agreement with the chain transfer constant to XA_1 ($2<C_{tr,XA1}<3$) for acrylate monomers.[47] The Mn value of 2 752 g.mol^{-1} issued from ^{1}H NMR results was used for the calculations regarding the second polymerization step of the N-VP monomer.

II.3. Synthesis of the PMA-*block*-PVP block copolymer

The second step of this block copolymerization protocol is the RAFT polymerization of the N-vinylpyrrolidone monomer (N-VP) mediated by the poly(methyl acrylate)- xanthate terminated block polymer (PMA-XA_1) obtained during the previous first step (**Scheme 6**). The polymerization process was realized in dioxane at 35°C by using a more reactive initiator 2,2'-Azobis(4-methoxy-2,4-dimethylvaleronitrile) (V-70). A DP_n value of 50 is targeted for this second block polymerization step.

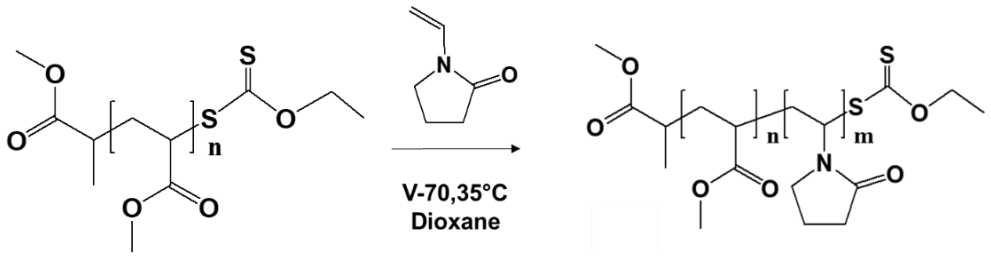

Scheme 6. Polymerization step of the N-vinylpyrrolidone (N-VP) monomer through RAFT polymerization using Xanthate-terminated Poly(methyl acrylate) (PMA-XA_1) as RAFT agent to obtain Poly(methyl acrylate)-*block*-Poly(vinylpyrrolidone) block copolymer (PMA-*b*-PVP)

As for the first PMA polymer block, the proton signals' integrations (**Figure 30**) in the ^{1}H NMR spectra were used to determine the experimental DP_{PVP} value obtained for this second polymer block PVP, using the **Equation 9**:

Equation 9. Degree of polymerization (DP_{PVP}) calculation by using ^{1}H NMR integration values for the PVP

$$DP_{PVP} = \frac{DP_{PMA} * q}{(r + d - q)} \quad \textbf{(Eq 2)}$$

Through this method, a DP_{PVP} value of 59 was found for the PVP block polymer, which is not so far from the targeted DP_n of 50, leading to a molecular weight of 6 550 g.mol^{-1} for the PVP block, and thus around 9 300 g.mol^{-1} for the entire block copolymer PMA-*b*-PVP.

As previously described for PMA, the method based on the internal standard trioxane was also applied and leads to a conversion percentage of 98%, so a M_n of 5 550 g.mol^{-1} for the PVP block and thus around 8 300 g.mol^{-1}, so 1 000 g.mol^{-1} of difference between the two methods.

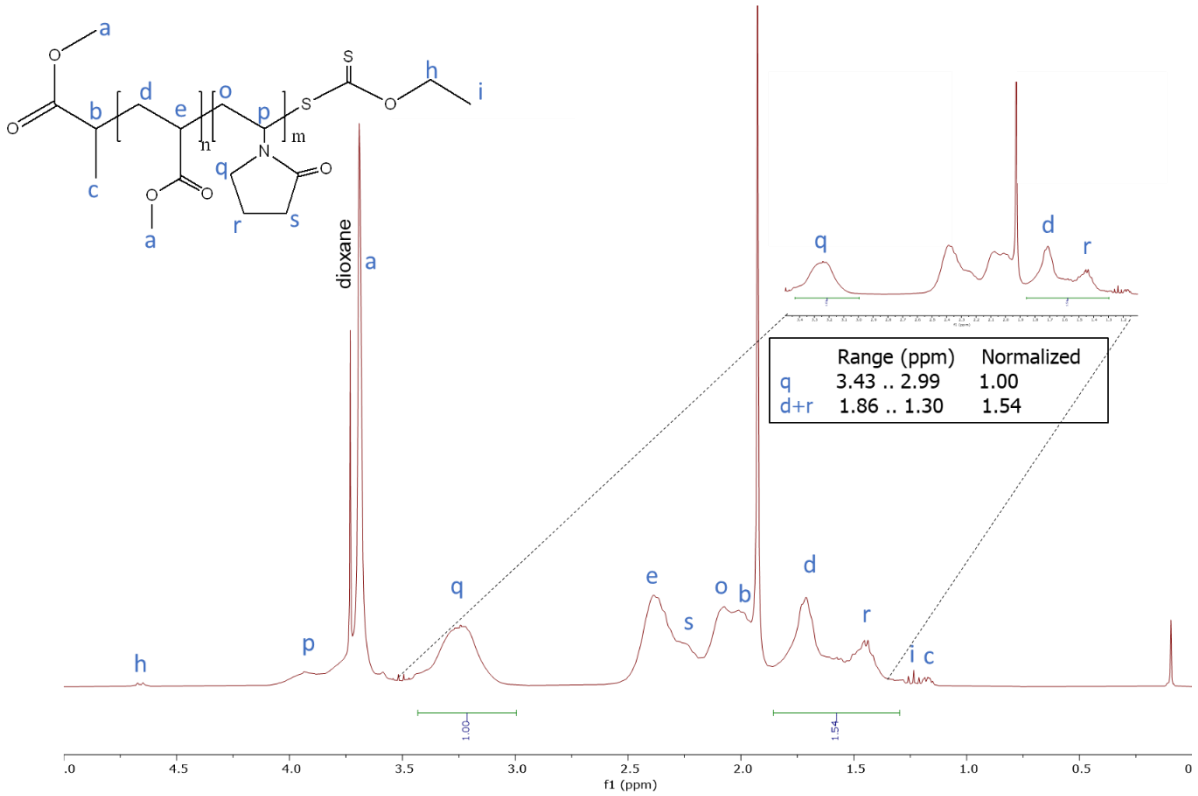

Figure 30. ^{1}H NMR Spectra ($CDCl_3$) of the synthesized Poly(Methyl Acrylate)-block-Poly(vinylpyrrolidone) copolymer (PMA_{32}-*b*-PVP_{59}). Degree of polymerization of N-VP (DP = 59) can be evaluated by directly comparing the ratio of the integrals of signals of PVP (q signal) to the one of PVP plus PMA (r and d signals) assuming a degree of polymerization of PMA block of 32, using the following equation: $DP_{PVP} = (DP_{PMA} * q) / (r + d - q)$

Size Exclusion Chromatography (SEC) was used to provide additional values of M_n regarding the block copolymer, by using the same conditions than for the first block (DMF LiBr as solvent for elution). The chromatograms of the PMA-XA_1 polymer and the PMA-*b*-PVP are shown in **Figure 31**. It could be observed a shift between the dRi signal of the PMA-XA_1 and the PMA-*b*-PVP. This confirms the formation of a block copolymer as its elution time is shorter than the PMA-XA_1. Moreover, these chromatograms show a lower polydispersity for the block copolymer (Đ=1.1).

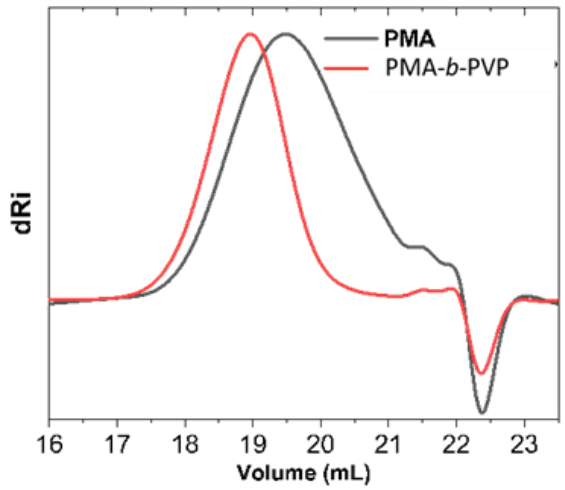

Figure 31. Size exclusion chromatograms (RI traces) in DMF/LiBr 10mM of PMA_{32}-*b*-PVP_{59} (red line) and PMA_{32} (black line)

To have access to the exact Mn of the polymers by using SEC data, it is necessary to know the dn/dc value for each block polymer. Measurements were made with PMA-XA_1 regarding dn/dc value. A value of 0.0558 was found. To obtain the dn/dc value for the block copolymer, a previously measured dn/dc value for PVP polymerwas used and combined to the one of PMA-XA_1. The calculation is as following: (32/ (32+59))*0.0558 + (59/(32+59))*0.093 = 0.0799. Estimated Mn are thus found thank to dn/dc values and all the Mn from all the calculations techniques are sum up in **Table 3**.

Table 3. SEC and ^{1}H NMR analysis of the synthesized polymers

Polymer	$M_{n,th}$ (g·mol^{-1})	$M_{n,NMR}$ (g·mol^{-1})[a]	$M_{n,SEC}$ (g·mol^{-1})[b] (***Đ***)	$DP_{n\ PVP}$ / $DP_{n\ PMA}$ (theoretical. value)[c]
PMA	2750	2750	2530 (1.4)	0/32 (0/32)
PMA-*b*-PVP	8300	9300	8630 (1.1)	59/32 (50/30)

[a] Calculated from ^{1}H NMR (see details in **Figure 29**)

[b] Determined by SEC-RI-MALS in DMF/ LiBr (10 mM); Đ: polydispersity index

[c] Calculated from ^{1}H NMR (see **Figure 29 & Figure 30)**

II.4. Hydrolysis process to obtain PAA-*block*-PVP block copolymer

PAA_{32}-*b*-PVP_{59} was obtained through the hydrolysis of PMA_{32}-*b*-PVP_{59} copolymer. This hydrolysis step is essential to obtain a water-soluble block copolymer containing the PAA block polymer, able to further interact with ionic species in water media.

The hydrolysis protocol was taken from the work of M. Talu and H.B. Özgün.[48] Strong basic conditions (KOH in EtOH) will cleave the ester functions to obtain carboxylate groups. This protocol leads as well to the elimination of the xanthate end-chain group (**Scheme 7**).

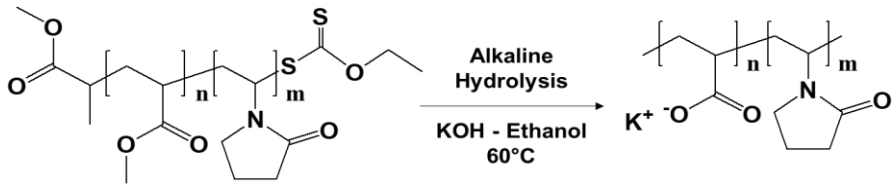

Scheme 7. Final hydrolysis step of the block copolymer synthesis protocol realized in ethanol with a concentration of potassium hydroxide (KOH) salt of 3.4 M and at 60°C to perform the ester cleavage and remove xanthate end-chain.

At the end of the alkaline hydrolysis step, the polymer was purified by dialysis and analyzed by ^{1}H NMR (**Figure 32)** and IR spectroscopy (**Figure 33) .**

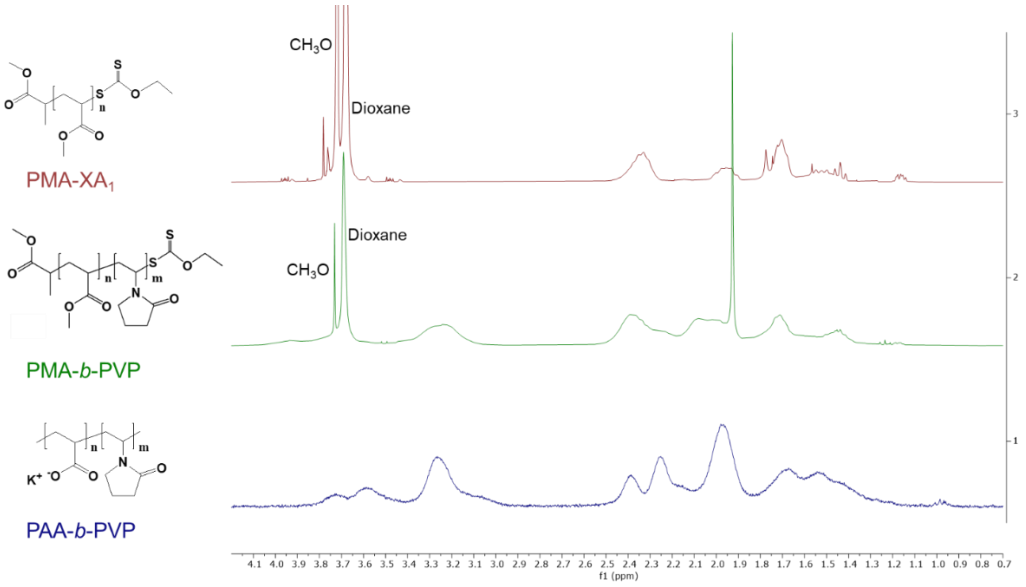

Figure 32. ^{1}H NMR spectra of the polymers obtained after each protocol step: PMA_{32}-XA_1 (red), PMA_{32}-*b*-PVP_{59} (green) and PAA_{32}-*b*-PVP_{59} (blue). On the spectra of the PAA_{32}-*b*-PVP_{59} polymer it could be observed the absence of the -OCH_3 group at 3.73 ppm as results of the hydrolysis step.

ATR-FTIR spectroscopy technique was used to confirm the hydrolysis step of the block copolymer by comparing the absorptions' signals before and after the alkaline hydrolysis (**Figure 33**). ATR-FTIR spectra evidence the disappearance of the carbonyl stretching band of the ester group at 1736 cm^{-1} and the appearance of the carboxylate (OCO) asymmetric and symmetric stretching modes at 1564 cm^{-1} and 1402 cm^{-1}, respectively.

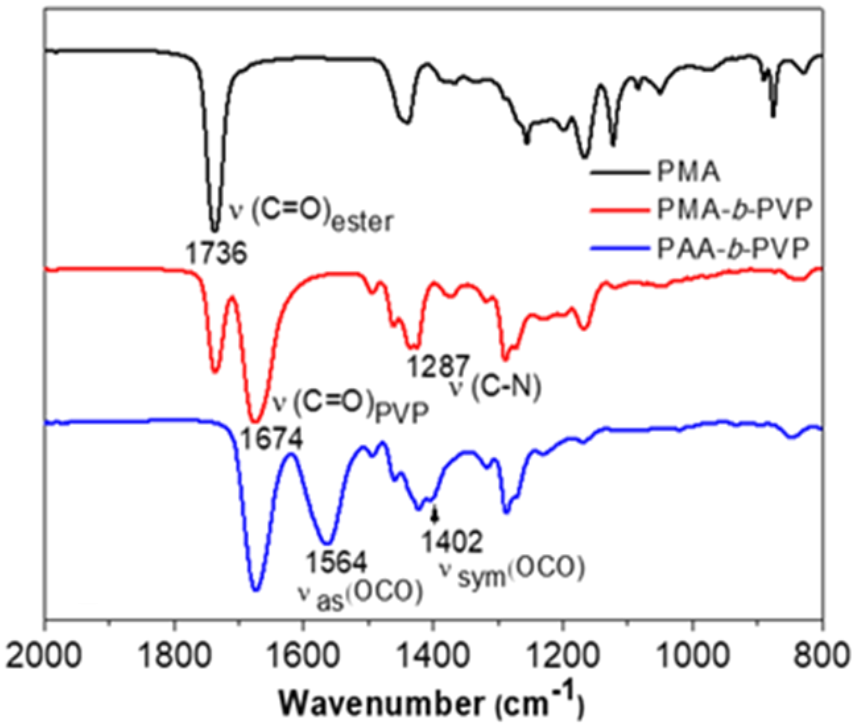

Figure 33. ATR-FTIR spectra of PMA_{32} (black line), PMA_{32}-*b*-PVP_{59} (red line) and PAA_{32}-*b*-PVP_{59} (blue line)

In **Figure 34**, ^1H NMR spectra of the PAA_{32}-*b*-PVP_{59} copolymer shows large peaks for the protons of the two blocks, which superpose in the region from 1 to 2.5 ppm. Due to this, the protons were integrated throughout this region, as a whole, denoted ***u*** on the spectra, corresponding to 6mH for the PVP and 3nH for the PAA.

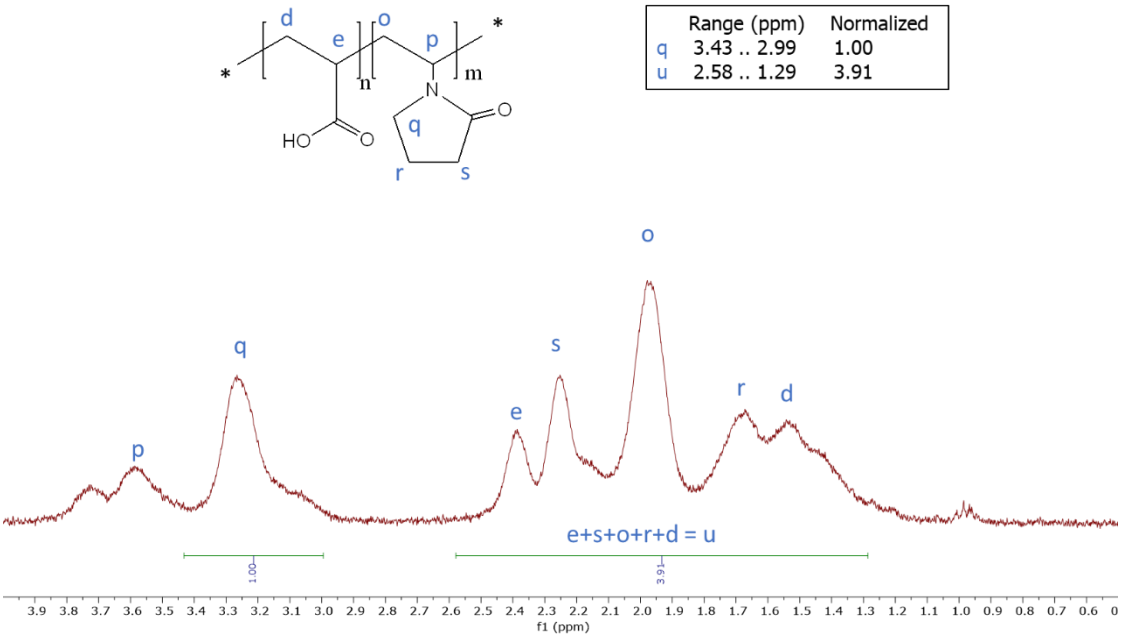

Figure 34. ^1H NMR Spectra of the Poly(acrylic acid)-*block*-poly(vinylpyrrolidone) copolymer (PAA_{32}-*b*-PVP_{59}). Integrated signals used to determine the ratio between acrylic acid and N-vinyl pyrrolidone unities.

The contribution of the PVP block from the ***u*** signal was eliminated by using the ***q*** (3.43 – 2.99 ppm) signal which corresponds strictly to protons of the PVP and integrate for 2mH. Using **Equation 10** and the DP_n of PMA previously determined (DP_{PMA} = 32), a DP_{PVP} value for the PVP block equal to 52 was found, which is close to the targeted DP_n of 50 and the value of 59 obtained by SEC. In the following, the value of 59 obtained by SEC was selected.

Equation 10. Formula used to calculate the degree of polymerization (DP) of PVP by using ^{1}H NMR spectra of the PAA-*b*-PVP copolymer.

$$DP_{PVP} = \frac{3 * DP_{PMA}}{2 * (u - 3q)} \quad \textbf{(Eq 3)}$$

In conclusion, a PAA_{32}-*b*-PVP_{59} block copolymer with a number-average molar mass (M_n) of 8 700 g.mol^{-1} was successfully synthesized by RAFT polymerization.

Additionally, block copolymers with different M_n and/or composition were synthesized (**Table 4**). These modifications include: 1) modification of the PVP block length while keeping constant the PAA length, 2) modification of the ratio between the PAA and the PVP blocks while keeping constant the value of Mn. This enables to study the influence of these parameters on the assemblies obtained either with lanthanide ions or with gold NPs (see chapter IV).

Table 4. ^{1}H NMR and SEC analysis of the synthesized block copolymers PMA-*b*-PVP

	PMA			**PMA-*b*-PVP**			**PAA-*b*-PVP**
Copolymer targeted composition (targetet M_n)	M_n (g.mol^{-1}) [1]: by ^{1}H NMR [2]: by SEC	M_w (g.mol^{-1}) (by SEC)	Đ	M_n (g.mol^{-1}) [1]: by ^{1}H NMR [2]: by SEC	M_w (g.mol^{-1}) (by SEC)	Đ	Copolymer obtained composition (obtained M_n from DP calculated with ^{1}H NMR)
PAA_{32}-*b*-PVP_{50} (7 850 g.mol^{-1})	2 752 [1] 3 788 [2]	4 707	1.24	9 300 [1] 9 300 [2]	10 003	1.08	PAA_{32}-*b*-PVP_{59} (8 853 g.mol^{-1})
PAA_{32}-*b*-PVP_{30} (5 634 g.mol^{-1})	2 752 [1] 3 788 [2]	4 707	1.24	4 528 [1] 7 143 [2]	7 828	1.10	PAA_{32}-*b*-PVP_{16} (4 080 g.mol^{-1})
PAA_{32}-*b*-PVP_{25} (5 079 g.mol^{-1})	2 752 [1] 3 788 [2]	4 707	1.24	4 084 [1] 4 500[2]	4 873	1.08	PAA_{32}-*b*-PVP_{12} (3 686 g.mol^{-1})
PAA_{32}-*b*-PVP_{17} (4 191 g.mol^{-1})	2 752 [1] 3 788 [2]	4 707	1.24	3 307 [1] 4 870 [2]	5 440	1.11	PAA_{32}-*b*-PVP_5 (2 859 g.mol^{-1})
PAA_{48}-*b*-PVP_{48} (8 784 g.mol^{-1})	4 214 [1] 4 349 [2]	5 328	1.22	11 318 [1] 11 040 [2]	11 890	1.08	PAA_{49}-*b*-PVP_{64} (10 299 g.mol^{-1})
PAA_{59}-*b*-PVP_{32} (7 800 g.mol^{-1})	5 246 [1] 5 955 [2]	7 425	1.25	9 353 [1] 10 400 [2]	11 250	1.08	PAA_{61}-*b*-PVP_{37} (8 499 g.mol^{-1})

III Formation and characterization of the Hybrid Polyionic complexes (HPICs) based on interactions between PAA-*block*-PVP and Gd^{3+}, Eu^{3+}, Y^{3+} trivalent ions

Hybrid Polyionic Complexes (HPICs) structures, presented in **Chapter I**, have been firstly studied some years ago in the team by mixing PAA-*b*-PEG block copolymer and lanthanide ions such as gadolinium[14] or metal ions like copper[49] for Fenton-like reactions. Supplementary studies were recently conducted regarding these HPICs structures by examining the behavior of zirconium[15] and gallium ions[50] with this PAA-*b*-PEG block copolymer. The formation mechanism was established to be based on ionic interactions between the positively charged metallic ions and the negatively charged carboxylate groups belonging to PAA block polymer. We propose to evaluate this time the influence of the modifications on the structure of the block copolymer, i.e. the replacement of the PEG block by a PVP one, on the formation of the HPICs with Y^{3+} and lanthanide ions (Gd^{3+} and Eu^{3+}) by evaluating their structural characteristics and their properties.

III.1. Formation and characterization of the PAA-*b*-PVP-based HPICs

HPICs were obtained by the addition of trivalent cations (Gd^{3+}, Eu^{3+}, Y^{3+}) to aqueous solutions of the PAA_{32}-*b*-PVP_{59} copolymer followed by the adjustment of pH to 7. The reaction between the lanthanide ions and the carboxylic acid group can be written as follows:

$$Ln^{3+} + 3\ AA^- = Ln(AA)_3$$

It is thus possible to define the ratio R, between the positive charge arising from the trivalent Gd^{3+} ions and the potentially available negative charges from the ionized or ionizable acrylic acid monomer units (AA) of the polymers as:

$$R = 3 \cdot \frac{[Ln^{3+}]}{[AA]}$$

The electroneutrality between the lanthanide ions and the fully ionized polymers should then correspond to R equal unity.

III.1.1 Size determination and zeta potential measurements

The effect of the addition of increasing amounts of trivalent cations in the formation of the HPICs was first monitored, by mono-angle dynamic light scattering (DLS) measurements (**Figure 35**).

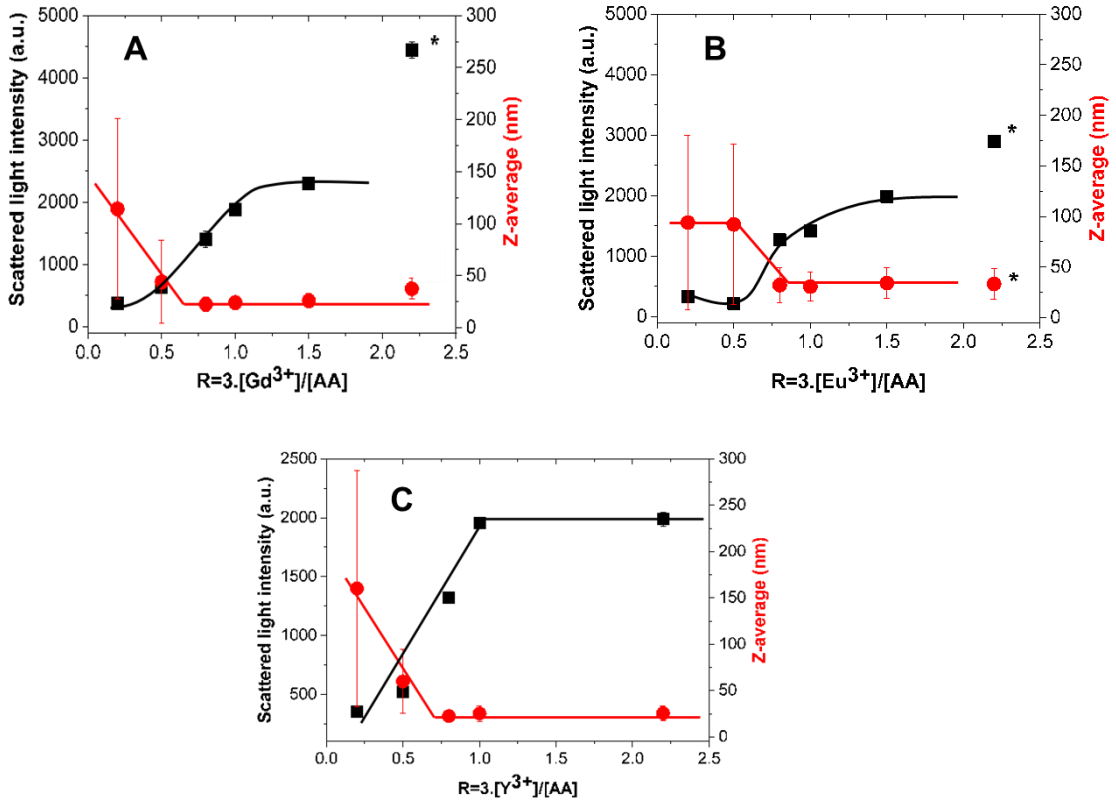

Figure 35. Typical evolutions of the scattered light intensity (black squares) and Z-average diameter (red dots), measured by a mono-angle DLS instrument for Gd^{3+} (**A**), Eu^{3+} (**B**), Y^{3+} (**C**) added to PAA_{32}-*b*-PVP_{59} as a function of the ratio R. The lines are just guide for the eyes. [PAA-*b*-PVP] = 0.1%wt; pH =7

It could be observed, for R values lower than 0.8, that the measured light scattering intensity was low. Consequently, the precision and the significance of Z-average values obtained from the correlograms are poor and not significant of the presence of colloidal objects. Below R=1, the number of negative charges is higher than the positive charges' one. Consequently, there are free polymer chains, able to self-assemble and this could explain the presence of bigger nano-objects. For R larger than 0.8 and up to 1, an increase of scattered intensity was measured, associated with a decrease of Z-average size. This behavior was also observed when HPICs structures were obtained in the presence of PAA-*b*-PEG and lanthanide ions.[14] Around R=1, these colloids exhibit a diameter of ca. 25 nm (in term of Z-average) with a low polydispersity index (PDI = 0.27). A non-negative least-squares (NNLS) analysis (**Figure 36**) confirmed the presence of larger objects (diameter larger than 100 nm) but at a very low concentration (estimated less than 10^{-2} %). Further multi-angle DLS analysis (**Figure 37**) confirmed that the solution contains mainly Brownian colloids with a radius of 12.1 ± 1.3 nm. Similar sizes were obtained with Y^{3+} and Eu^{3+} ions (respectively 14.3 ± 1.5 nm and 12.2 ± 1.4 nm, (**Figure 37**). These values are comparable to the 11.5 ± 1.2 nm radius obtained for HPICs formed by Gd^{3+} ions and PAA-*b*-PEG copolymer.[14]

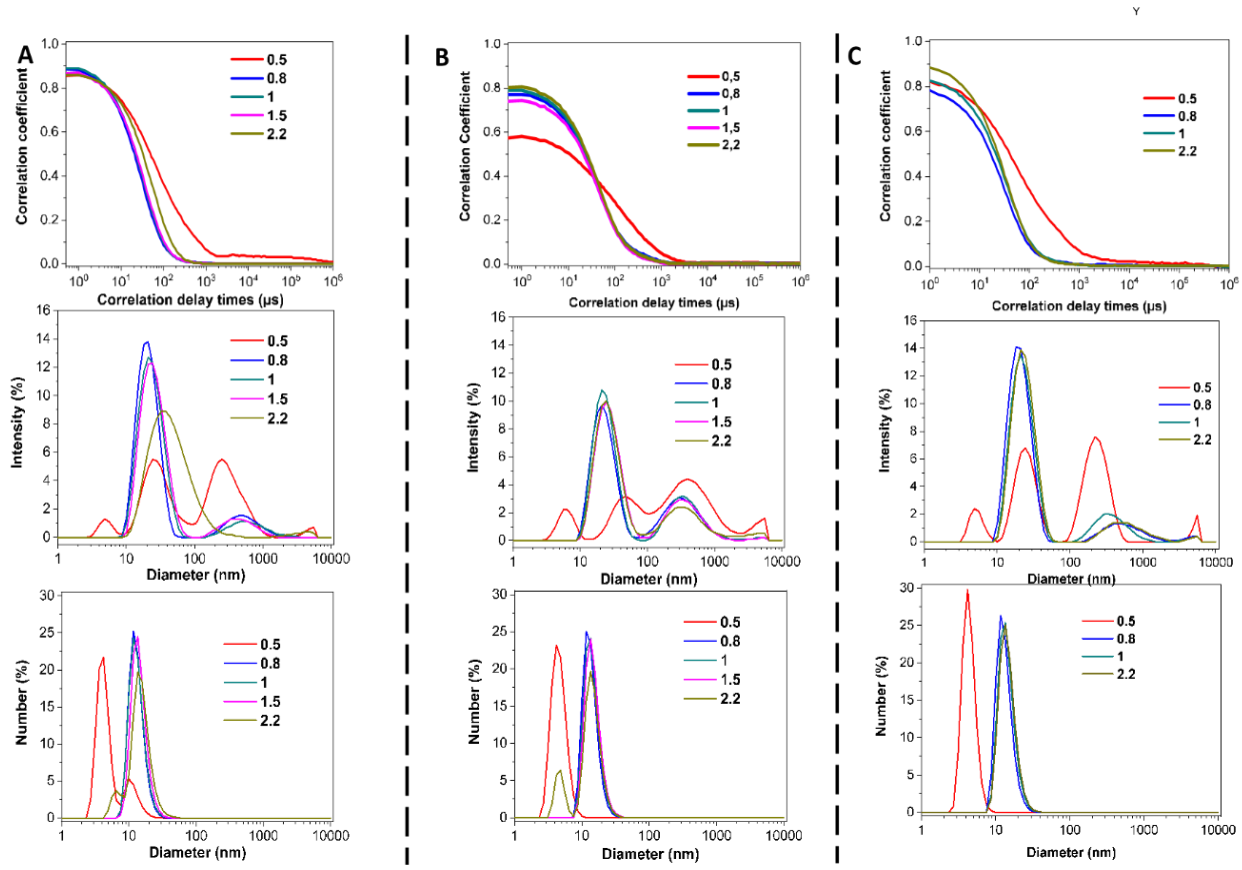

Figure 36. Correlation functions and corresponding distribution average size in intensity and number fitted using the NNLS method for the assemblies formed in the presence of three different cations: (**A**) Gd^{3+}, (**B**) Eu^{3+} and (**C**) $Y^{3+}$and for different R ratio. [PAA-*b*-PVP] = 0.1%wt; pH = 7.

Above R=1, the scattered light intensity becomes stable (**Figure 36**). At the highest ratio (R=2.2) the formation of big aggregates probably made of hydroxide species is suspected, so corresponding values of Z-average size and the scattered light intensity do not correspond solely to HPICs formation.

Zeta potential measurements were performed for samples at different R values in order to evaluate the surrounding electric potential of the colloidal objects formed in the solution between PAA_{32}-*b*-PVP_{59} copolymer and Gd^{3+} ions (**Figure 38**).

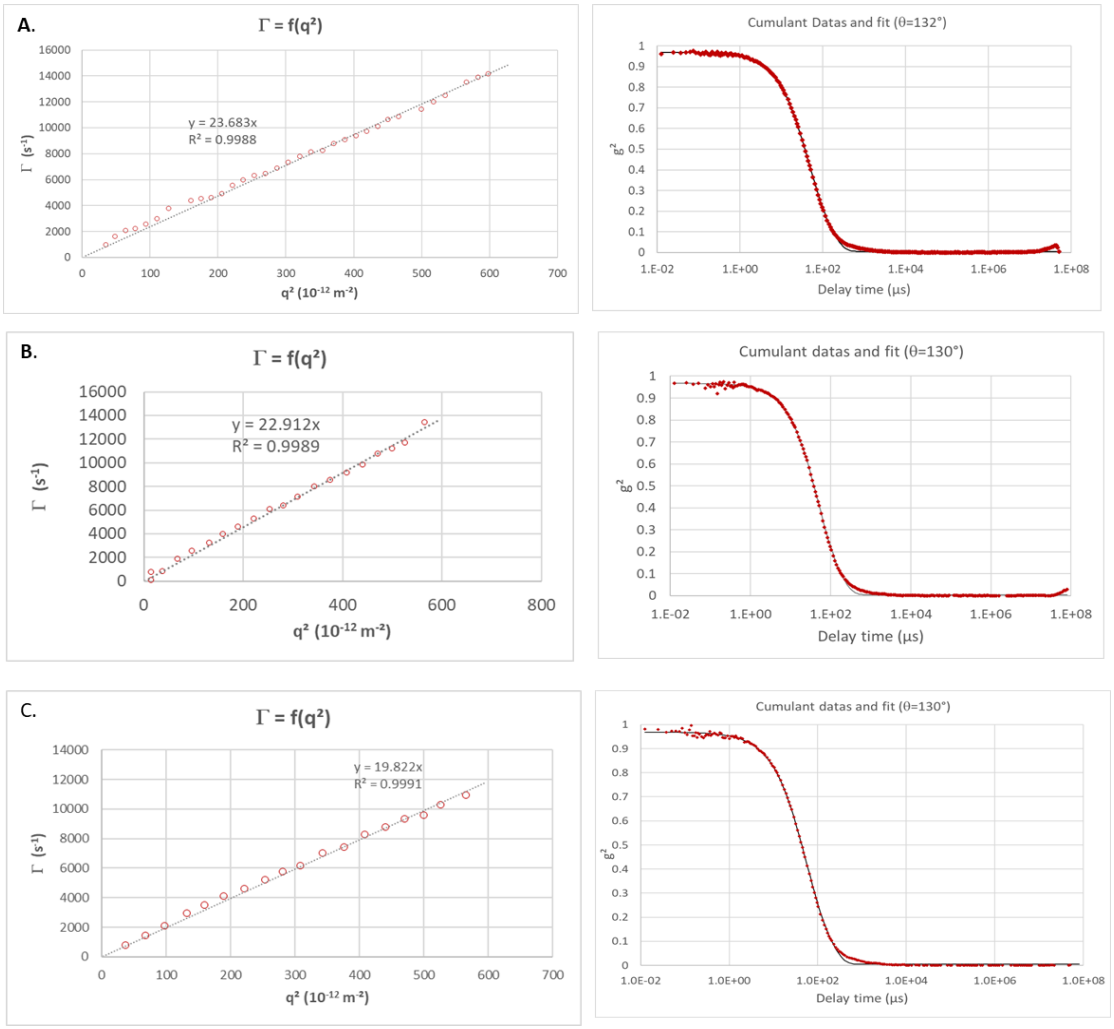

Figure 37. Multi-angle DLS of (**A**) Gd^{3+}/ PAA_{32}-*b*-PVP_{59}, (**B**) Eu^{3+}/ PAA_{32}-*b*-PVP_{59} and (**C**) Y^{3+}/ PAA_{32}-*b*-PVP_{59} HPICs (R=1). Left: Decay rate Γ versus the scattering vector q obtained with cumulant method (second order) Right: Typical g^2 correlogram (red circles) obtained for a defined angle. In black, best fit using the NNLS with the M-STORMS software

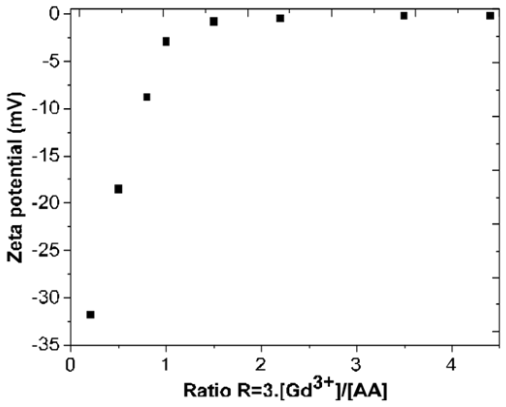

Figure 38. Evolution of zeta potential of colloidal solutions of Gd^{3+}/ PAA_{32}-*b*-PVP_{59} assemblies versus ratio R.

It could be observed that, at very low R values, electric potential is clearly negative, because of the copolymer excess. A zeta potential value of around ζ = -32 ± 2 mV at pH 7 is found for R = 0.2. By increasing R value, positive charges were added inducing the increasing of zeta potential until reaching values near zero. The plateau value of ζ = 0 mV was obtained when for R = 1. Above R = 1, zeta potential remains near zero.

A ratio R = 1 could be a suitable ratio for biological applications, as it does not contain theoretically any excess of free Gd^{3+} ions. To confirm the absence of free Gd^{3+} ions, a quantification of these ions after a filtration process was conducted as followed: solutions of HPICs with different R ratios, 0.95, 2, 5.4 and 8.8, were placed into a centrifugal tube Amicon Ultra 30k to be centrifuged during 90 minutes at 3,000xg and 21°C. Filtrates were kept and analyzed by Inductively Coupled Plasma Mass Spectrometry (ICP-MS) technique. Gadolinium titration was made on the filtrates and allowed to determine the free Gd^{3+} ions' concentration in the solutions containing HPICs colloids. The results show no significant quantity of free Gd^{3+} ions for the ratio of 0.95 and the other values agreed with theoretical free gadolinium concentrations. This confirms that a maximum of Gd^{3+} ions is chelated by carboxylate groups for a charges' ratio near 1 and the corresponding HPICs structures can then be interesting for biological applications.

III.1.2 TEM analysis

Transmission Electron Microscopy (TEM) was used to determine the morphology of these HPICs structures. A low contrast was observed due to the relatively low density of the Gd^{3+} ions in the polymer matrix sample (very roughly estimated from the PAA density around a few gadolinium per nm^3) and of the small size of the nanoparticles. Despite this, a mean diameter of 11.5 nm with a standard deviation σ = 1.5 nm, obtained by a Gaussian fit could be calculated (**Figure 39**).

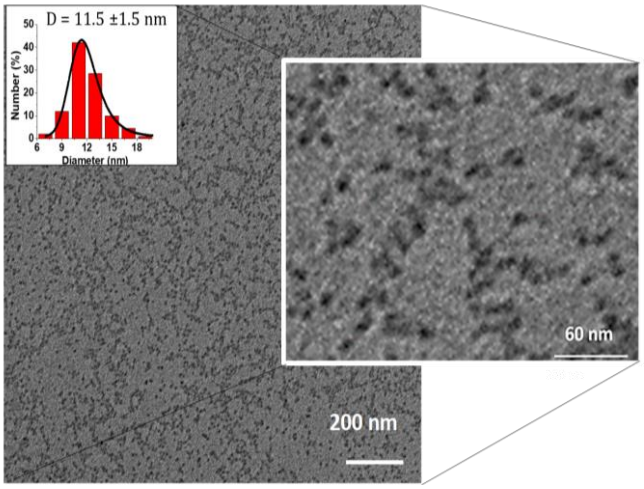

Figure 39. Conventional TEM images of the Gd^{3+}/PAA_{32}-*b*-PVP_{59} HPICs and the corresponding size histogram (R=1).

Additionally, the sample was mapped by scanning transmission electron microscopy using high angle annular dark-field detector (HAADF-STEM) in order to obtain image only from incoherently scattered electrons (Rutherford scattering from the nucleus of the atoms) and thus to observe a better contrast due to variations in atomic number Z of the elements in the sample. [51,52] In **Figure 40,** the regions containing Gd^{3+} ions appear white in contrast to the polymer. The diameter of the white dots is 6.4 nm (σ = 0.8 nm), slightly smaller than the one observed in conventional TEM in agreement with the encapsulation of the Gd^{3+} ions in the polymer objects.

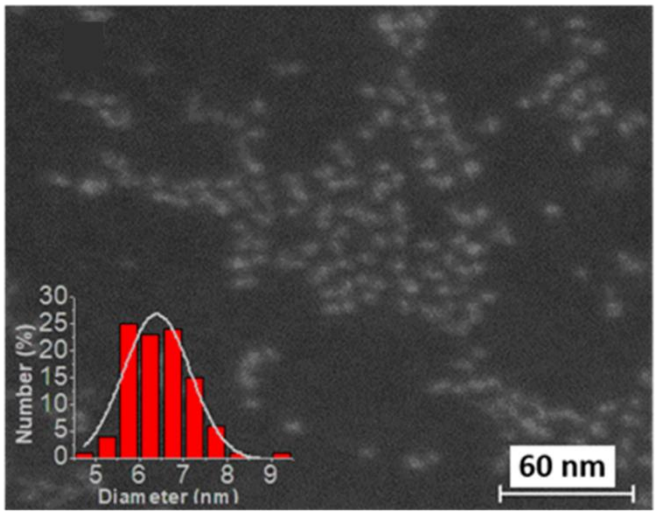

Figure 40. Scanning transmission electron microscopy images using high-angle annular dark-field detector (HAADF-STEM) and inset: the respective size distribution histogram.

III.1.3 Conclusion on HPICs morphology

To conclude on the structure of obtained nanoobjects, whatever the nature of ions (Eu^{3+}, Gd^{3+}, Y^{3+}) is, the addition of these ions and PAA leads to the formation of HPICs nano-objects as evidenced by diffusion and TEM experiments and as previously depicted for PEG-based copolymer with similar composition[14]. From ICP-MS experiments it was demonstrated that while keeping the ratio R below 1, all ions remained within the nanostructure.

To get further insights into the nature of interactions within these nanostructures, ATR-FTIR and ^{1}H NMR experiments will be performed and described in the next section. Then the study of luminescent properties of Eu^{3+}-based HPICs will be described. This will enable to obtain some information about the number of water molecules and their dynamic around lanthanide ions, playing both a key role in MRI properties.

III.2. Characterization of molecular interaction within HPICs

III.2.1. ATR-FTIR of HPICs formation

ATR-FTIR spectra of the PAA_{32}-*b*-PVP_{59} copolymer alone and the separate homopolymers were recorded to identify the characteristic bands of the carboxylate and carbonyl groups of each block (**Figure 41**). The samples were measured as powder solids obtained by lyophilization of the solutions. We can now identify the bands by comparing homopolymers' spectra to block copolymer's one.

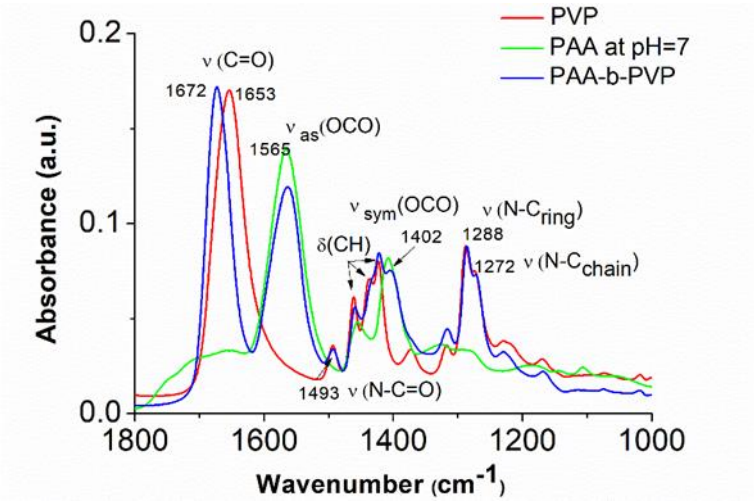

Figure 41. Comparison of the ATR-FTIR spectra of PVP_{72}, PAA_{25} and PAA_{32}-*b*-PVP_{59}, respectively. The pH of PAA_{25} and PAA_{32}-*b*-PVP_{59} was adjusted to 7.

The C=O amide stretching band at 1672 cm^{-1} is attributed to the pyrrolidone ring of the PVP polymer. As the initial pH of the block copolymer in solution is around 9, because of the final alkaline hydrolysis step, the PAA polymer solution is adjusted to a pH of 7 to obtain the spectra for the carboxylate version of the polymer and compare to the block copolymer. It is then possible to identify the bands corresponding to the carboxylate functions (OCO) represented by the asymmetric and symmetric stretching modes appearing at 1565 cm^{-1} (ν_{as}) and 1402 cm^{-1} (ν_{sym}), respectively.

The ATR-FTIR spectra of Gd^{3+}/PAA_{32}-*b*-PVP_{59} HPICs, at different R ratios are shown in **Figure 42**. For a better visualization, all spectra were normalized to the absorbance of C=O amide stretching band (at 1665 cm^{-1}). Addition of Gd^{3+} ions shifts the wavenumbers of the two carboxylate ν_{as} and ν_{sym} bands at 1555 cm^{-1} and 1363 cm^{-1}, respectively. It is especially noteworthy the progressive increase in intensity of these two bands with increasing the amount of Gd^{3+} ions until R=1. This behavior is consistent with the progressive neutralization of the negatively charged carboxylates groups of the polymer by the Gd^{3+} ions until R=1.

The difference (noted Δ) between the wavenumbers of carboxylate symmetric and asymmetric peaks is frequently used to determine the type of coordination with the metal center.[53,54] For a monodentate bonding, Δ increases compared to the free carboxylate anion; for bidentate chelating coordination Δ decreases and for bidentate bridging, Δ remains similar to the free anion.[53] The higher value of Δ=190 cm^{-1} in the presence of Gd^{3+} ions and for all R ratios, compared to the one of the free carboxylate, Δ=161 cm^{-1} suggests a monodentate mode coordination of carboxylates of the polymer to the Gd^{3+} ions. This type of coordination is consistent with the hard acid character of the Gd^{3+} ions, favoring electrostatic interactions with lack of strong directionality in binding donor groups, in the gadolinium first coordination sphere.[55]

The complexation between the Gd^{3+} ions and the carboxylate groups of the PAA block until R=1, is also evidenced by the progressive shift to lower wavenumber, of the characteristic stretching band of the amide C=O group of the pyrrolidone ring initially at 1665 cm^{-1} up to 1658 cm^{-1}. This complexation releases the NVP units of the PVP block from the self-association with the AA units of the PAA block, and thus the characteristic stretching band of the amide C=O group shifts to lower wavenumber, characteristic of a NVP environment in pure PVP, as observed by comparing the ATR-FTIR spectra of the PAA_{32}-*b*-PVP_{59} copolymer and the PVP_{72} homopolymer (**Figure 41**).

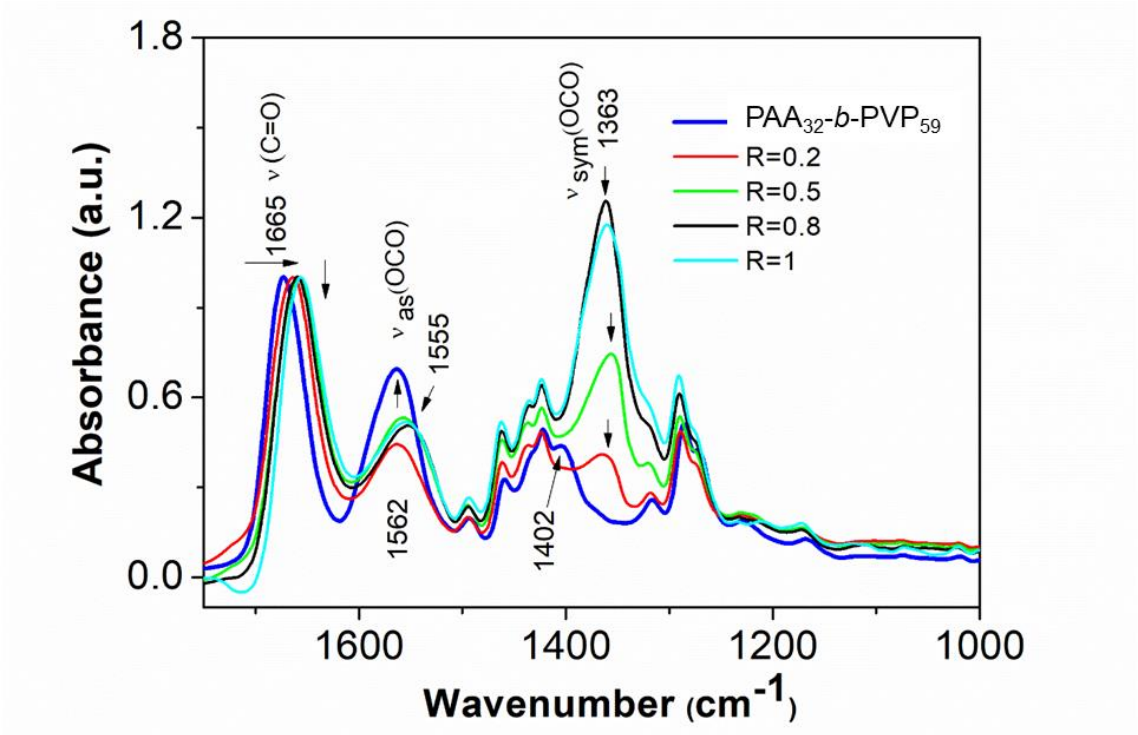

Figure 42. ATR-FTIR spectra of PAA_{32}-*b*-PVP_{59} (blue line) and of Gd^{3+}/PAA_{32}-*b*-PVP_{59} HPICs for different R ratios.

Higher R ratios were analyzed through ATR-FTIR to know about the evolution of the characteristic bands in the presence of an excess of Gd^{3+} ions (**Figure 43**). For R exceeding the neutralization ratio (R>1), no additional interactions with carboxylate functions were formed and the intensities of the carboxylate groups bands remain constant.

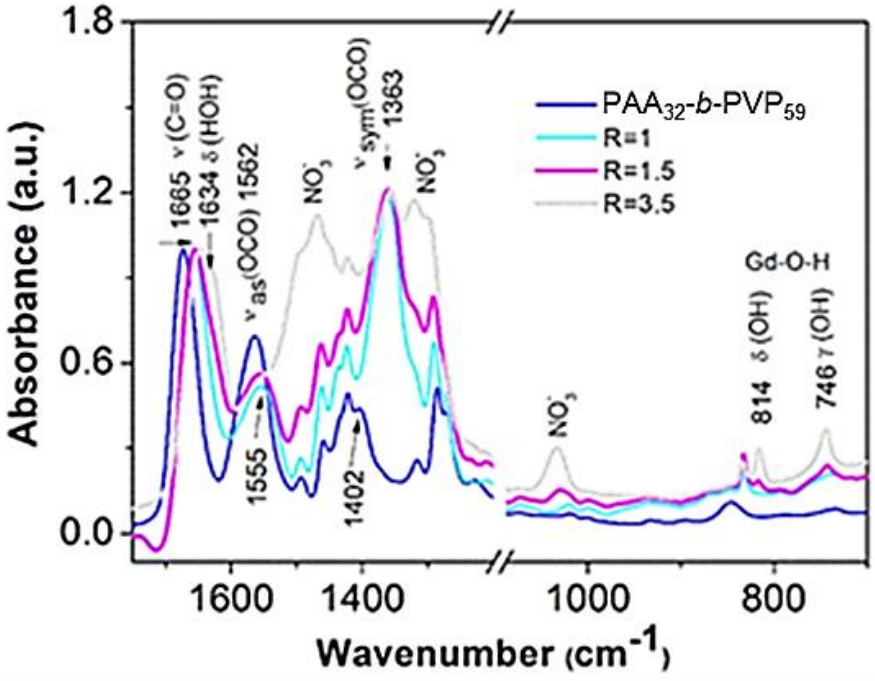

Figure 43. ATR-FTIR spectra of PAA_{32}-*b*-PVP_{59} and the respective Gd^{3+}/PAA_{32}-*b*-PVP_{59} HPICs for ratio R≥1

Additional bands can be observed at 814 cm^{-1} and 746 cm^{-1}, characteristic of the bending vibrations of Gd-O-H (ΔOH and ΓOH, respectively)[56–59] showing clear evidence of the appearance of gadolinium hydroxides. These bands are observed again on **Figure 44** representing the ATR-FTIR spectra of the solution containing gadolinium salt at pH = 7. At pH= 7 in water, the hydroxides species of gadolinium are able to be formed (742 and 813 cm^{-1})

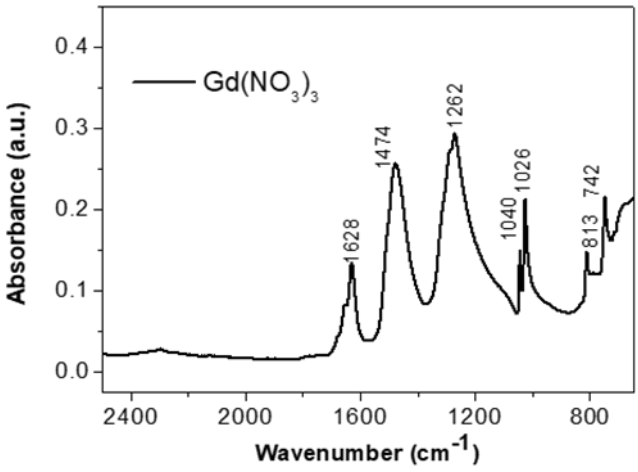

Figure 44. ATR FTIR spectra of $Gd(NO_3)_3$ salt

III.2.2. Characterization by ^{1}H NMR

To get more information on the formation of HPICs, ^{1}H NMR experiments were performed using Y^{3+} ions. Indeed, yttrium presents coordination chemistry similar to the one of lanthanide ions and it is not paramagnetic[60]. The longitudinal relaxation time (T_1) of the protons which can be associated with the mobility of molecular chains was measured (**Figure 45**). The decreasing of the mobility of the PAA chain of the copolymer, due to complexation with the Gd^{3+} ions was evidenced by the increasing of the relaxation time (T_1) of the corresponding protons.

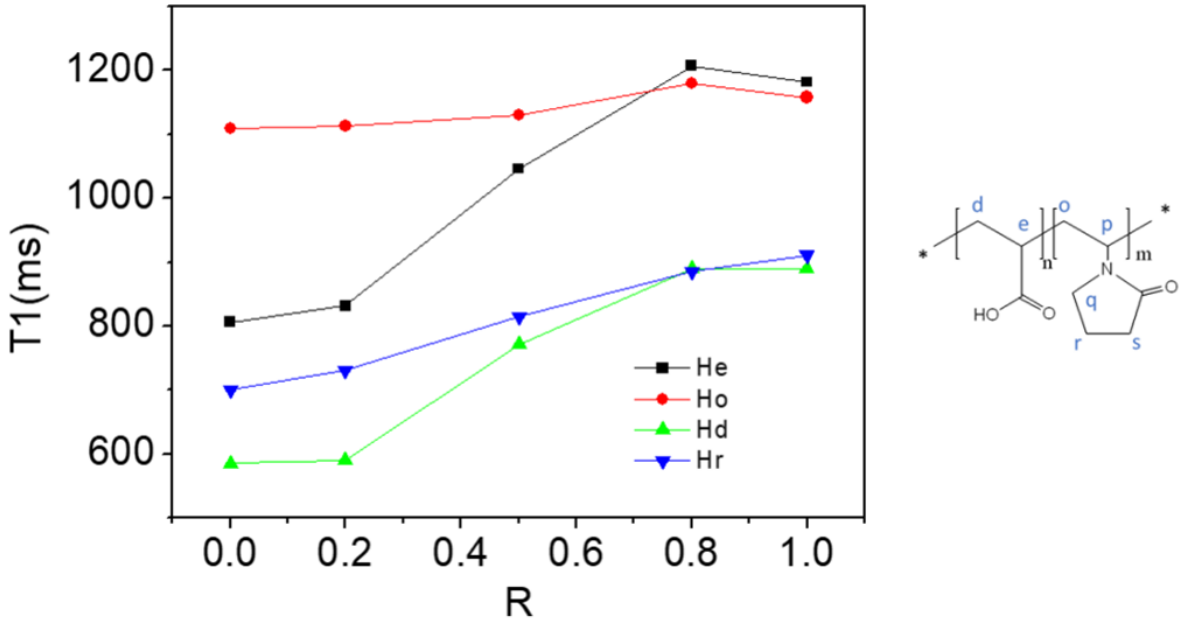

Figure 45. Longitudinal relaxation time (T_1) registered for the protons corresponding to the (PAA) block (Hd and He) and to the (PVP) block respectively (Ho and Hr) as a function of R ratio. [PAA_{32}-*b*-PVP_{59}] = 0.1%wt at pH 7. [Y^{3+}] = 1.3 mM. (in 10% vol. D_2O and 90% vol. H_2O 298 K).

These T_1 values are further considered to acquire ^{1}H NMR spectra in quantitative conditions and to determine the evolution of the integral ratio of the protons associated to the carboxylate block, to the ones of PVP block. As can be seen on **Figure 46**, while the peaks related to PVP block around 3.22, 2.36, 2.22, 1.94 and 1.63 ppm remains roughly constant, the ones associated to the carboxylate block at 1.5 and 2.1 ppm (respectively due to the hydrogen in β and α of the carboxylate function) progressively disappeared when R increased.

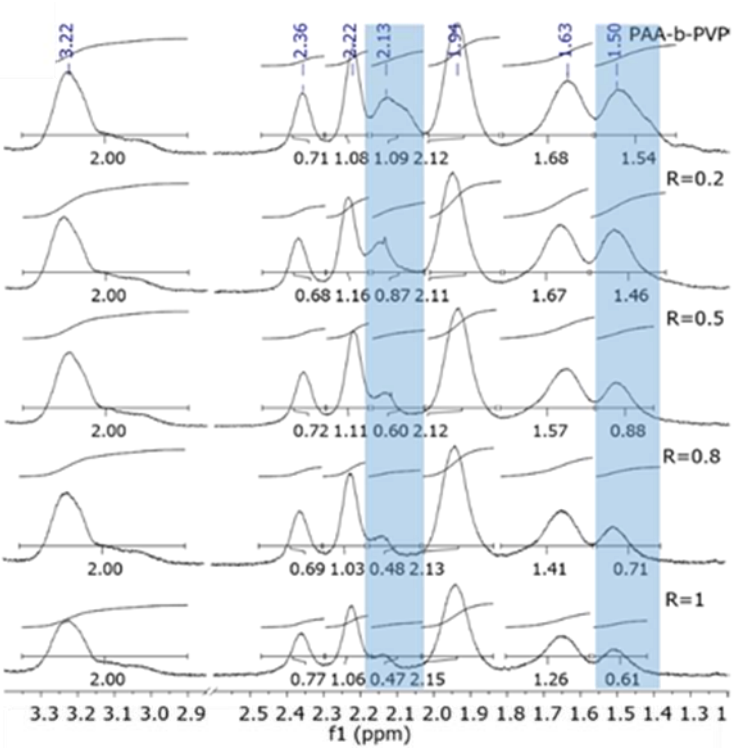

Figure 46. ^{1}H NMR spectra of Y^{3+}/ PAA_{32}-*b*-PVP_{59} HPICs at different R ratios. [PAA_{32}-*b*-PVP_{59}] = 0.1%wt; blue areas correspond to carboxylate function signals α and β at 2.1 and 1.5 ppm, respectively.

Using trioxane as a reference, it was evidenced that both PVP and PAA signals decreased with increasing R ratio (**Figure 47**). However, the protons relative to PAA block were more impacted than the ones of the PVP block.

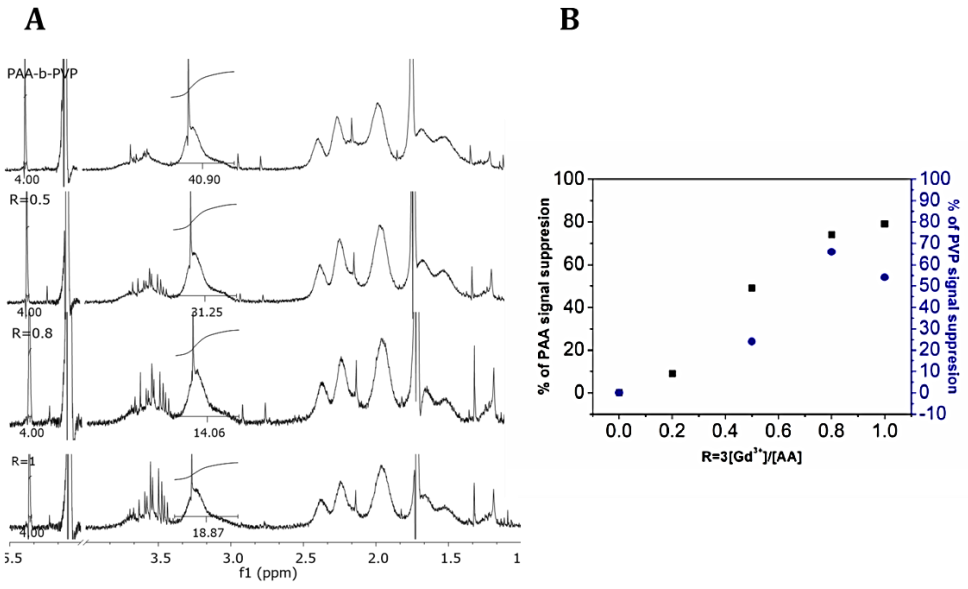

Figure 47. **A**. ^{1}H-NMR (300MHz) spectra (in 10% vol. D_2O and 90% vol. H_2O 298 K) of Y^{3+}/PAA_{32}-*b*-PVP_{59} HPICs for R=0, 0.5, 0.8 and 1 ([polymer]=0.1% wt.) evidencing the decrease of the signal intensity of the PVP block compared to that of the trioxane as internal standard (5.4 ppm). The trioxane was present in a constant concentration in $CDCl_3$ in a capillary introduced in the NMR tube. Additional residual solvent peaks were present at 1.7, 2.1 and 3.5 ppm. **B.** Percentage of the PAA and PVP block signal suppression as a function of R ratio.

The selective suppression of these peaks suggests the preferential Y^{3+} ion binding on PAA residues as expected from the intrinsic chelating capability of acrylates and the way the PAA block is more rigid. It confirms the results issued from ATR-FTIR. This might be ascribed to the formation of HPICs with a core-shell structure with a Y^{3+}/PAA core surrounded by a PVP shell. As expected, Eu-based HPICs present similar ^{1}H-NMR spectra. (**Figure 48**)

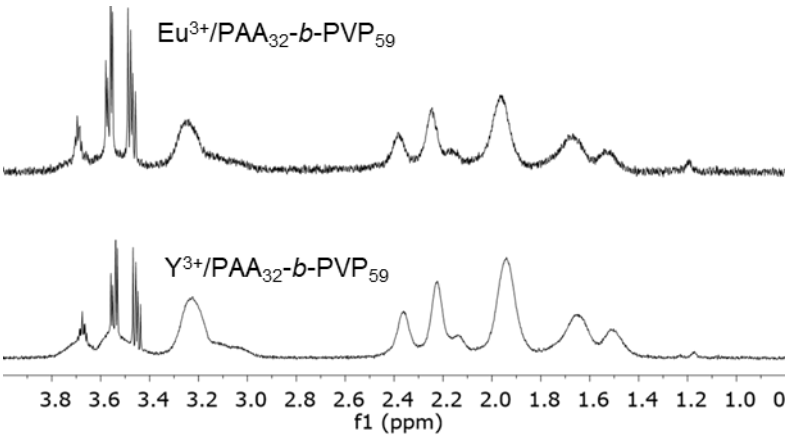

Figure 48. ^{1}H NMR spectra ((in 10% vol. D_2O and 90% vol. H_2O 298 K)) of Eu^{3+}/PAA_{32}-*b*-PVP_{59} and Y^{3+}/PAA_{32}-*b*-PVP_{59} HPICs for R= 1 ([polymer]=0.1% wt.)

III.2.3. HPICs morphology:

The structure of the HPICs is represented in **Scheme 8** and consists in a core-shell type organization containing PAA block polymer with trivalent ions in the core and a stabilizing shell ensured by the PVP block polymer. This core-shell organization has already been proposed for the previous HPICs nanostructures containing PAA-*b*-PEG block copolymer.[14,15,50]

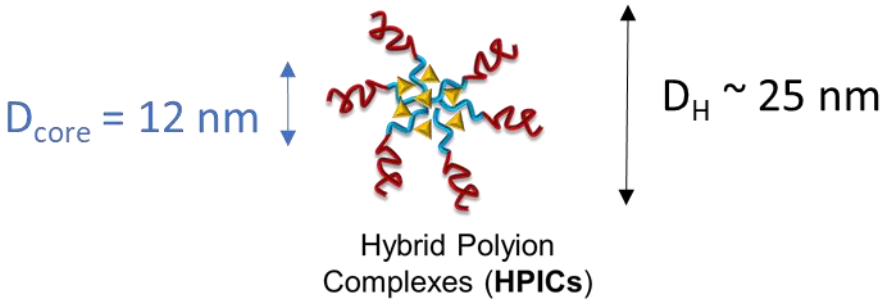

Scheme 8. Schematization of the formation of hybrid polyion complexes (HPICs). Trivalent cations were either Gd^{3+}, Eu^{3+} or Y^{3+} (yellow triangles).

III.3. Study of the luminescent properties of the HPICs

III.3.1 Generalities on the luminescence properties of Europium

Europium is a lanthanide which is currently used for its luminescent properties.[61] Latter properties can be acquired through two different ways: phosphorescence and fluorescence. As explained on **Figure 49**, representing the Perrin-Jablonski diagram, two radiative ways are available from excited states (singlet ones S_1, S_2 ,..,S_n or triplet ones T_1,T_2,..,T_n) to fundamental one (S_0).

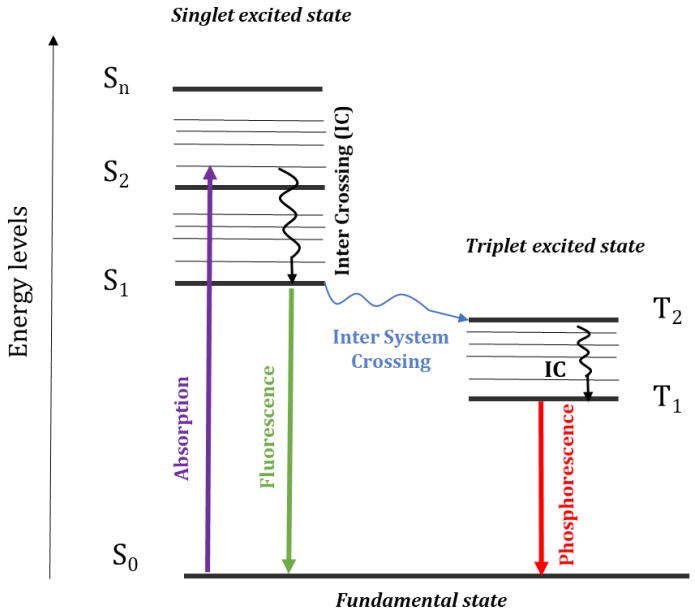

Figure 49. Perrin-Jablonski diagram representing the different radiative ways for Europium to return to its fundamental state after being excited at singlet or triplet states.

After absorption of a specific wavelength, singlet excited state at a certain level of energy (S_1, S_2,,, S_n) were reached. To come back to its fundamental state, it can go through internal conversion (IC) ways until attaining the lowest excited singlet state and then two radiative ways are possible. The first one allows a direct return from S_1 state to fundamental state S_0, this is the fluorescence phenomenon. The second way occurs when europium changes its excited state, it goes from singlet to triplet state, this is an inter system crossing. Then the deexcitation occurs inside the triplet state and the radiative return to fundamental state is named phosphorescence.

Europium lanthanide ions show fluorescence or phosphorescence properties when they are surrounded by both water molecules and counterions such as nitrate (NO_3) or chloride (ClO_4).[62] Water molecules deeply impact the luminescence properties of europium ions as they absorb a part of the electronic energy through O-H oscillators. The more water molecules are surrounding europium lanthanide the less intense the fluorescence and phosphorescence are.[63]

To enhance these luminescent properties, one possibility is to chelate the europium ion with ligands that will replace the water molecules and then limit these energy transfers to O-H oscillators. Another way to increase the intensity of the radiation, is to chelate the lanthanide ion with a ligand able to absorb energy and transfer it to the lanthanide. This is named the antenna effect, but this won't be studied here.[63]

III.3.2 HPICs' luminescence properties as a function of ratio R

To evaluate the luminescent properties of the Eu^{3+}/PAA_{32}-*b*-PVP_{59} nanostructures, several samples with different R ratios were analyzed in fluorimetry. The three main characteristic emission peaks of europium ion are the following transitions: $^5D_0$ – $^7F_1$ at 591 nm, $^5D_0$ – $^7F_2$ at 615 nm and $^5D_0$ – $^7F_4$ at 697 nm.[64] The comparison of the two first transitions bring information about the environment of the Eu^{3+} ions. Indeed, when the intensity of the $^5D_0$ – $^7F_1$ transition is higher than the $^5D_0$ – $^7F_2$ one, it means that Eu^{3+} ions are mainly surrounded by water molecules and are not chelated. On the contrary, when the intensity of the transition $^5D_0$ – $^7F_2$ is higher, it means that the Eu^{3+} ions are chelated by a ligand, that has replaced some of the surrounding water molecules.

Firstly, an excitation spectrum is recorded for the Eu^{3+}/PAA_{32}-*b*-PVP_{59} HPICs with varying R ratios at a fixed emission wavelength of λ_{em} = 615 nm and in the range between 200 nm and 500 nm (**Figure 50**). On this spectrum, the maximal intensity will indicate at which wavelength the samples have to be excited to obtain the most intense emission bands.

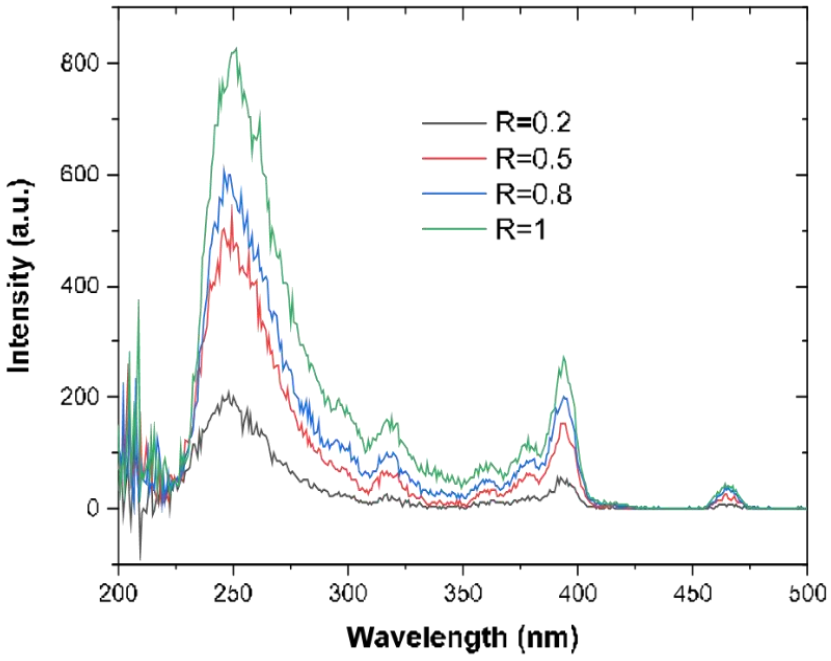

Figure 50. Excitation spectra (λ_{em} = 615 nm) of Eu^{3+}/PAA_{32}-*b*-PVP_{59} HPICs samples with 4 different charges' ratios values: R=0.2 (black), 0.5 (red), 0.8 (blue), 1 (green); [PAA_{32}-*b*-PVP_{59}] = 0.1%wt in water solvent

As expected, for a fixed polymer concentration, the increase of the ratio R (i.e the increase of Eu^{3+}) led to an increase of intensity of measured peaks. For R<1, all free Eu^{3+} ions introduced should be chelated by the excessive number of carboxylate groups. The expected emission spectra for samples with R<1 should present the three main characteristic emission peaks with the $^5D_0 - {}^7F_2$ transition as the most intense one. The suitable excitation wavelength is determined by taking the maximum of intensity on the excitation spectrum (**Figure 50**), i.e λ_{ex} = 256 nm.

The aim now is to obtain the corresponding emission spectra for the different samples with varying ratio R, by using this excitation wavelength of λ_{ex} = 256 nm. As explained before, there are two radiative ways for Eu^{3+} ions to go from excited state to fundamental state: fluorescence and phosphorescence. Those two ways can be set through the apparatus' software to have the possibility to focus on one way or another. The difference between fluorescence and phosphorescence lies in the lifetimes range. Indeed, the lifetime of fluorescent species is very short and requires an instantaneous record of the spectra. Whereas phosphorescent species are characterized by longer lifetimes. There is thus the possibility to record the spectra after a delay time and to definitely make the difference between fluorescent and phosphorescent species.

The tests were performed with the copolymer PAA_{32}-*b*-PVP_{59} alone, the Eu^{3+}/PAA_{32}-b-PVP_{59} HPICs at R=1 and the Eu^{3+} ion alone at the same concentration of Eu^{3+} ions to see the difference between fluorescence and phosphorescence modes (**Figure 51**). The spectra recorded with a fluorescence mode (**Figure 51.A,B**) show the three main characteristic peaks of Eu^{3+} ion and confirmed that this one is chelated as the intensity is much higher than the one corresponding to the lanthanide ion alone (red curve) and besides, the peak at 615 nm is more intense than the one at 591 nm.

An additional large peak is observed at lower wavelengths and appears for the samples containing the copolymer alone (black curve) and the Eu^{3+}/PAA_{32}-b-PVP_{59} HPICs (blue curve). To know if this was attributed to the PAA or PVP or both, homopolymers' solutions are analyzed as well with the same parameters (**Figure 52**). According to these analyses, both homopolymers PVP and PAA led to fluorescence. Indeed, the autofluorescence of PVP polymer is well described in the literature, whatever the polymer is commercial or synthesized in laboratory.[65] The large peak observed in the emission spectra recorded in the fluorescence mode is superposed with the emission peaks of the Eu^{3+} ion and thus could modify the ratio of the intensities of the first and the second transitions, which gives information about the Eu^{3+} ion environment. To avoid the presence of this large absorbance band, the analysis will be performed in the further section in a phosphorescence mode.

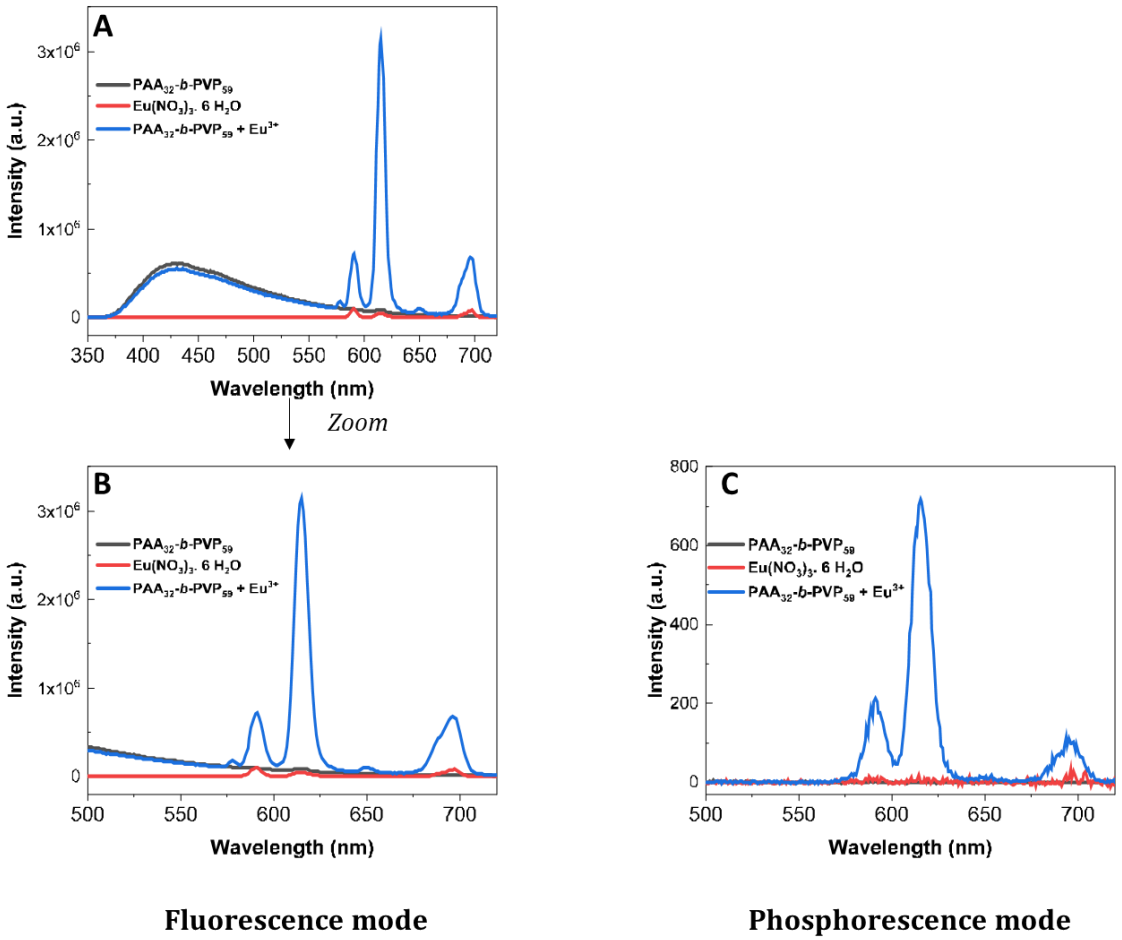

Figure 51. Emission spectra (λ_{ex} = 256 nm.) of 3 samples: PAA_{32}-*b*-PVP_{59} copolymer alone (black), Europium ion alone (red) and Eu^{3+}/PAA_{32}-*b*-PVP_{59} HPICs at R=1 (blue), recorded with two different modes: fluorescence (**A** & **B**) and phosphorescence (**C**). A zoom is made on the fluorescence to have the same wavelength range. [PAA_{32}-*b*-PVP_{59}] = 0.1%wt in water solvent.

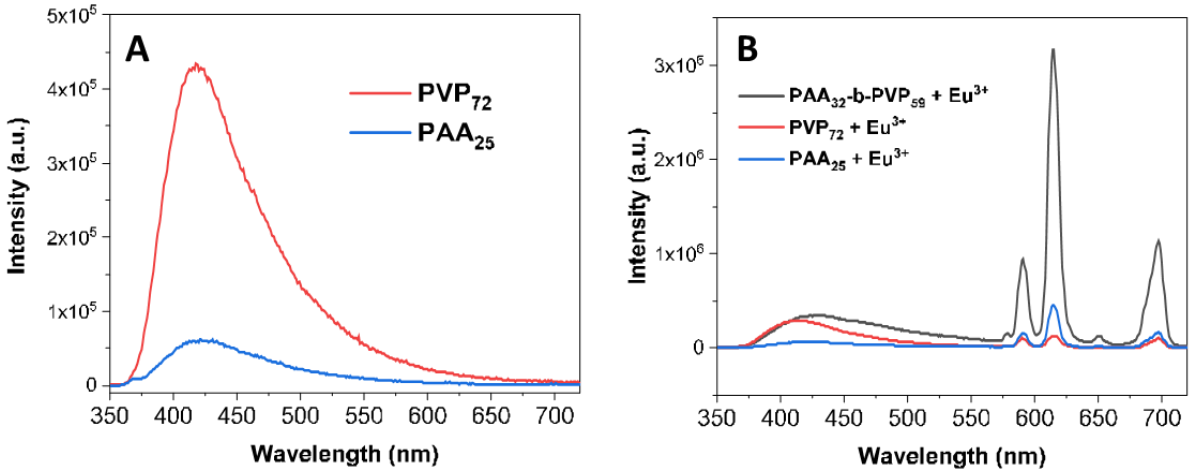

Figure 52. Emission spectra (λ_{ex} = 256 nm) of PVP_{72} homopolymer solution and PAA_{25} homopolymer solution (**A**) and comparison of emission spectra of mixtures of homopolymers or copolymer PAA_{32}-*b*-PVP_{59} with europium ions at the same concentration of lanthanide ions (**B**).

Finally, when the homopolymers are mixed with Eu^{3+} ions and compared to the Eu^{3+}/PAA_{32}-b-PVP_{59} HPICs, a more intense signal is obtained in the case of block copolymer. This might be ascribed to a more efficient dehydration/confinement of Eu^{3+} ions in presence of DHBCs.

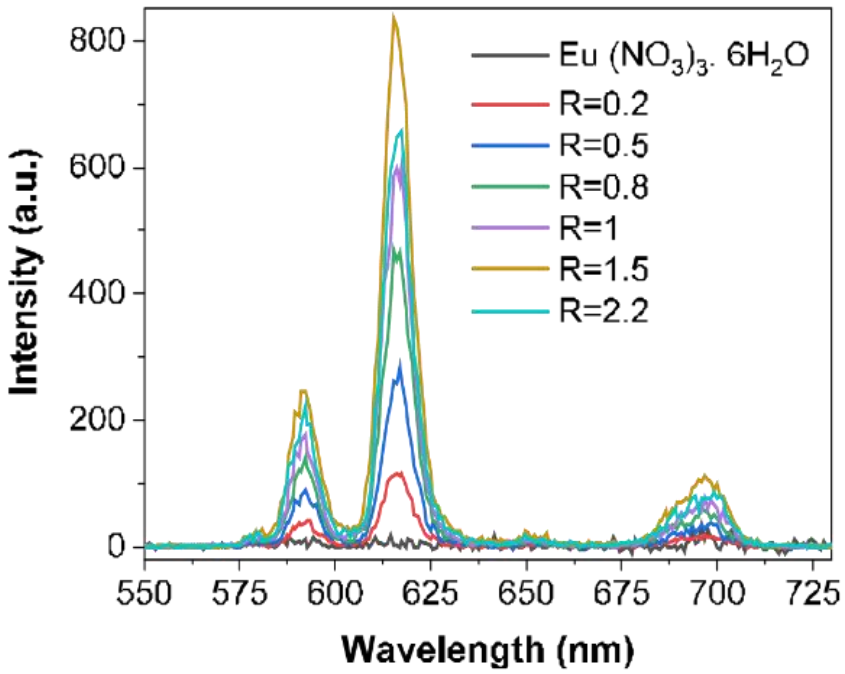

Figure 53. Emission spectra (λ_{ex}=256 nm) of Eu^{3+}/PAA_{32}-*b*-PVP_{59} HPICs at different R ratios. [PAA_{32}-*b*-PVP_{59}] = 0.1%wt in water solvent

Emission spectra as a function of R ratio are given in **Figure 53.** Strong emission was detected at 590 nm and 615 nm, corresponding respectively to the $^7D_0$ to $^7F_1$ and $^7D_0$ to $^7F_2$ transitions of Eu^{3+} [64], while no significant intensity was detected in the emission spectrum of an aqueous solution of $Eu(NO_3)_3$ with a concentration of Eu^{3+} similar to the one in HPICs with R=1.

The number of water molecules in the first coordination sphere of Eu^{3+} ions was further estimated using fluorescence lifetime measurements and the equation proposed by R.M. Supkowski et al.[66] For this purpose, lifetime measurements were made in both H_2O and D_2O solvents and the number of water molecules is estimated using the **Equation 11** and reported in **Table 5**.

Equation 11. Number of water molecules q depending on lifetimes in H_2O and D_2O solvents according to Horrocks and Supkowski's work[66]

$$q = 1.11 * (1/\tau_{H2O} - 1/\tau_{D2O} - 0.31) \quad \textbf{(Eq 4)}$$

Table 5. Lifetimes in H_2O (τ_{H2O}) and in D_2O (τ_{D2O}) for each R ratio (R=3.[Eu^{3+}]/[AA]) and the corresponding number of water molecules (q) in the first coordination sphere of europium ion calculated with Equation 11

R	τ_{H2O} (ms)	τ_{D2O} (ms)	Water molecules (q)
0.2	0.24	2.77	3.9
0.5	0.26	2.65	3.5
0.8	0.24	2.51	3.8
1.0	0.25	2.37	3.6

Whatever the value of the Ratio R is, a mean number of 3.7 ± 0.2 water molecules per Eu^{3+} is estimated. The number of water molecules is significantly lower than the 9 expected for the fully hydrated europium salt in water[67]. Coordinated water molecules are replaced by carboxylates units of the copolymer which electrostatically interact with the positively charged Eu^{3+} ions and limit the non-radiatively deactivation of the $^7D_0$ excited state by energy transfer to the OH vibrational modes of coordinated water molecules[64,68]. Above R=1, the intensity of the absorbance band at 615 nm decreases whereas the one of the absorbance band at 591 nm is not affected. Consequently, the ratio between the two absorbance bands decreases and reveals a different environment of the Eu^{3+} ions for R=2.2. Same observation can be done when the normalized intensities of the $^7D_0$ to $^7F_2$ transition at 615 nm in respect to the Eu^{3+} concentration were plotted as a function of R (**Figure 54**). A strong decrease of the normalized intensity was observed for R>1 and should correspond to the presence of free (and poorly emitting) europium ions in solution.

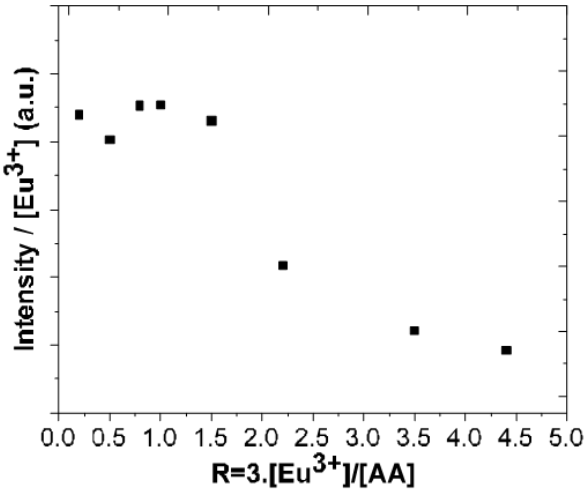

Figure 54. Normalized intensities of the $^7D_0 \rightarrow {}^7F_2$ transition at 615 nm in respect to the Eu^{3+} concentration as a function of R ratios. [PAA_{32}-*b*-PVP_{59}]=0.1%wt in water solvent

III.3.3. Comparison of fluorescence properties with Eu^{3+}/PAA_{44}-*b*-PEG_{80}

One last study consists in comparing the HPICs structures made with PAA_{32}-*b*-PVP_{59} to the HPICs previously studied in the team by using obtained PAA_{44}-*b*-PEG_{80} block copolymer. DLS measurements were already compared in the **III.1.1.** part of this chapter and show similar global size of the nanostructures. Knowing that, it is interesting to study the luminescence properties related to each of this structure to understand if the nature of the stabilizing block has any effect on the intensity. For that purpose, phosphorescence study was realized on HPICs mixtures with each block copolymer and Eu^{3+} ions, both at R=1 and pH = 7. As the number of carboxylate functions is different for the two block copolymers, latter ones were introduced in solution in a way the AA functions' concentration is the same ([AA] = 2.7 mM), but the weight percentage is then different between the two block copolymers. That way, europium ions' concentration is the same too ([Eu^{3+}] = 0.9 mM).

On **Figure 55,** the comparison of the phosphorescence spectra shows a slight decrease of the intensity of $^7D_0$ to $^7F_2$ transition at 615 nm for Eu^{3+}/PAA_{44}-*b*-PEG_{80} HPICs. The ratio F_2/F_1 is different from Eu^{3+}/PAA_{32}-*b*-PVP_{59} showing that the lanthanide has a different environment. Its interaction with the block copolymer may depend on the nature of the stabilizing block, resulting in different internal structuration of the HPICs and thus a different close environment for Eu^{3+}ion.

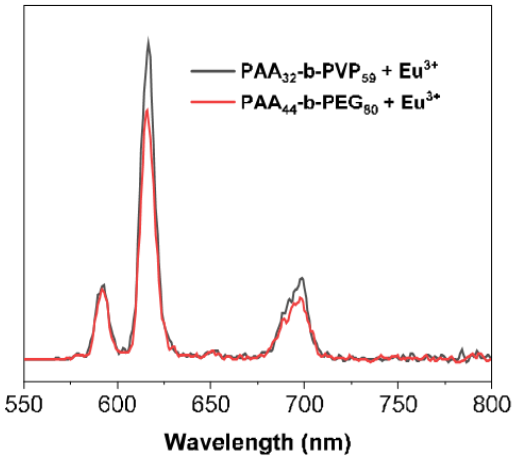

Figure 55. Phosphorescence spectra of HPICs mixture containing either PAA_{32}-*b*-PVP_{59} block copolymer (black line) or PAA_{44}-*b*-PEG_{80} block copolymer (red line) with Eu^{3+} ions at R=1 and pH = 7. [Block copolymer] = 0.1%wt in water solvent; [Eu^{3+}] = 1.3 mM.

III.4. Influence of pH onto the stability of the PAA_{32}-*b*-PVP_{59} based HPICs

As the HPICs are formed by electrostatic interactions between the negatively charged carboxylic acid groups of the PAA block and the positively charged lanthanide ions, their stability should be dependent of pH and this stability could be investigated by using the europium fluorescence and/or DLS. A HPICs solution for R=1 at pH=7 is split into 6 different solutions, on

which a HCl solution is progressively added to target a particular pH value. The samples are analyzed in DLS to know about the influence of the pH on the global size of the nanostructures. As it can be seen on **Figure 56**, until pH=5, the nanostructures' size starts to increase. Then, from pH=4 to pH=2, the destabilization of HPICs could be observed, as evidenced by the increase of the scattered light intensity and the very high size (200nm) at pH=2. As the pH decreases, carboxylate groups are progressively protonated leading probably to the destabilization of the HPICs assemblies.

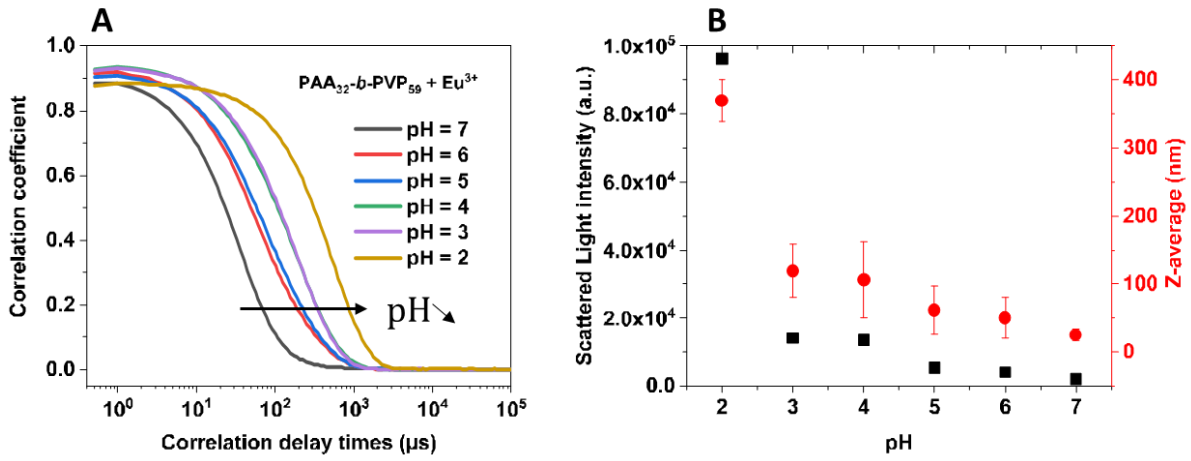

Figure 56. Correlation functions using the NNLS method (**A**) and typical evolutions of the scattered light intensity (black squares) and Z-average diameter (red squares) (**B**) obtained from the analysis of correlogram measured for Eu^{3+}/PAA_{32}-*b*-PVP_{59} HPICs at different pH values for R=1. [PAA_{32}-*b*-PVP_{59}] = 0.1%wt in water solvent; [Eu^{3+}] = 1.3 mM

To confirm this hypothesis, the pK_A value of this block copolymer was investigated by titration as illustrated in **Figure 57**. PAA polymer is a weak polyelectrolyte and its ionization process can be represented as follows:

$$HAA \rightleftharpoons H^+ + AA^-,$$

where AA^- is the conjugate base and H^+ the dissociated charge which dissolves into the solution.

Contrary to small molecules, the ionization behavior of polyelectrolytes is much more complexed, because it takes into account the progressive protonation or deprotonation of each ionizable groups which are close to each other, due to the chain connectivity. The high number of these ionization states induce associated titration curves which are smooth and deformed and do not allow to ascribe specific pK_A values to these ionization states. The titration curve of PAA_{32}-*b*-PVP_{59} block copolymer was performed by adding a solution of 0.1M HCl and the evolution of pH with the added volume of HCl is plotted in **Figure 57**.

It could be observed that the pH decreasing continuously till reaching almost a plateau around pH 3. A pK_A=3.19 was calculated for a degree of protonation of the polymer α=50%, by using the relation of Henderson-Hasselbalch. This value is lower than the value of pKa of propionic acid (4.9).

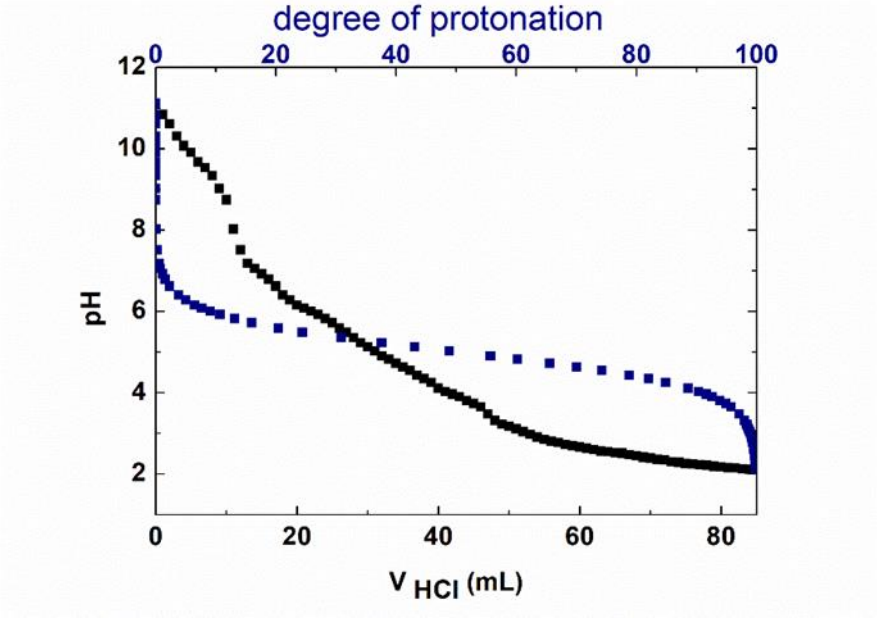

Figure 57. Titration curve of PAA_{32}-*b*-PVP_{59} copolymer (0.1%$_{wt}$) on which it was added a 0.1M HCl solution. pH values were recorded at each add of HCl (black curve) and the corresponding protonation degree curve (blue curve)

As can be observed in the **Figure 57,** for a pH>4, 90% of the polymer is still ionized, which is in agreement with the integrity of the HPICs. At a pH<4, the protonation of the polymer becomes more and more important, leading to the disintegration of the HPICs. The disassembly of HPICs for the pH<4 was also evidenced by the fluorimetry. Same samples are then excited at λ_{ex} = 256 nm and analyzed through phosphorescence mode. On **Figure 58**, the variation of pH has actually an influence on the intensity of each of the characteristic emission peaks of Eu^{3+} ions. The lower the pH, the lower the intensity. The three last pH values show very low intensity near the signal when Eu^{3+} ions are free. This confirms that under the pK_A, protonation of the carboxylate groups leads to a replacement by a water molecule in the inner sphere of Eu^{3+} ion and thus induces the decrease of the intensity and the disassembly of the HPICs.

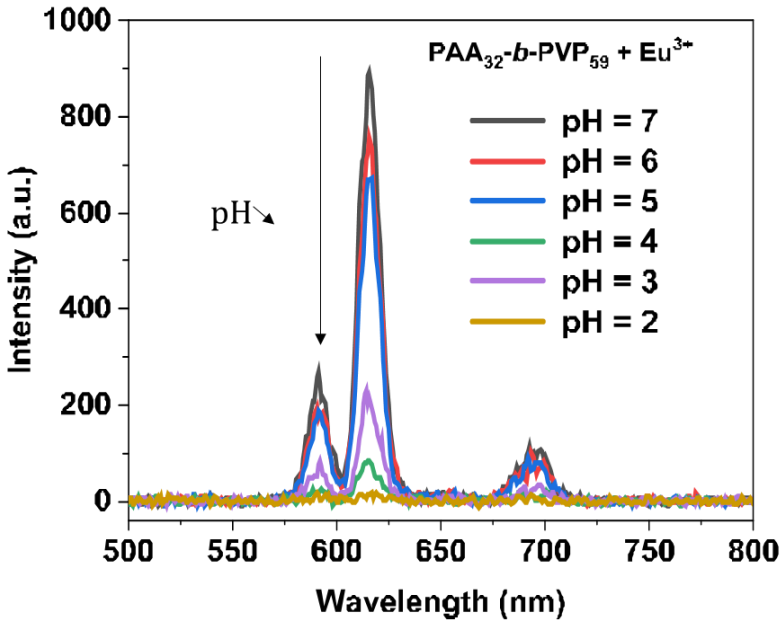

Figure 58. Emission spectra of Eu^{3+} /PAA_{32}-*b*-PVP_{59} HPICs at R =1 at different pH values. An unexplained inverse tendency is observed regarding emission spectra of HPICs solution at pH = 4 and pH = 3. [PAA_{32}-*b*-PVP_{59}] = 0.1%wt in water solvent; [Eu^{3+}] = 1.3 mM.

Another way to prove the chelation of Eu^{3+} ions is to measure the lifetime, as made in previous studies. Indeed, when Eu^{3+} ions are free, their lifetime is shorter than when they are chelated with ligands. Lifetimes measurements are made on every sample with varying pH value (**Figure 59**). The luminescence decay curves were fitted by an equation of the form $I(t) = I(0) \exp(-t/\tau)$ by using Origin curve-fitting program to obtain lifetimes values.

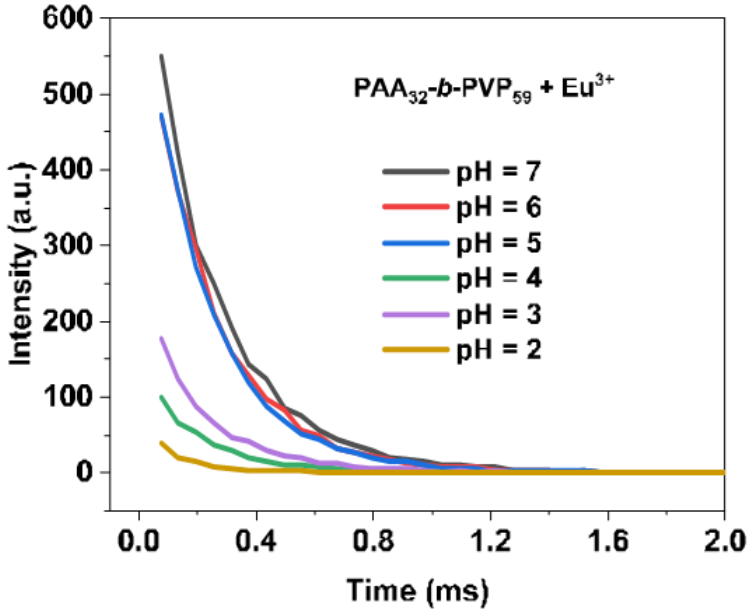

Figure 59. Lifetimes measurements in H_2O of the Eu^{3+}/PAA_{32}-*b*-PVP_{59} HPICs solution at different pH values

In **Table 6**, the lifetimes for each pH value in H_2O and in D_2O are reported with the corresponding number of water molecules *q*, calculated thanks to **Equation 11**.

Table 6. Lifetimes in H_2O (τ_{H2O}) and in D_2O (τ_{D2O}) for each pH value of the HPICs solution and the corresponding number of water molecules (q) in the first coordination sphere of europium ion calculated with Equation 11.

pH	Lifetime in H_2O (ms)	Lifetime in D_2O (ms)	Number of water molecules *q*
7	0.23	2.23	3.9
6	0.23	1.96	3.9
5	0.22	1.75	4.1
4	0.19	0.92	4.2
3	0.20	1.06	4.3
2	0.12	0.58	7.1

As expected, by decreasing the pH value of the HPICs solution, the lifetime of Eu^{3+} ions in both solvents, H_2O and D_2O, decreases from pH=4 progressively until being almost divided by 2 at pH=2, corresponding to a number of water molecules close to the one of hydrated Eu^{3+} ions (7.1 and 9 respectively). This confirms again the progressive protonation of carboxylate groups, which induces the release of the Eu^{3+} ions from their electrostatic interaction with the copolymer. The number of water molecules, *q,* supports this affirmation too, because it increases progressively and then drastically from 4 to 7 between pH=3 and pH=2.

IV Towards biological applications

Now that the assembly mechanism was studied and that numerous parameters have been varied to evaluate the impact on the implied interactions, we will now focus on the behavior of these nanostructures in the biological medium.

When introduced to complex biological media containing electrolytes, proteins, lipids, etc., the HPICs are subjected to a range of bindings which determine their behavior in this environment. The aspects of HPICs' behavior in biological systems which are important to monitor, are the stability in terms of aggregation state and of integrity, i.e. the states of "not disassembly" leading to the releasing of lanthanide ions in the medium. HPICs stability will significantly alter *in vitro* behavior (the uptake, cytotoxicity), as well as *in vivo* fate (pharmacokinetics, toxicity, biodistribution.[69] Then, the HPICs stability was further studied by DLS and by fluorimetry thanks to the Eu^{3+} ions' properties in different media: in high ionic strength conditions, as a function of pH, in biological media with and without serum proteins.

IV.1. Colloidal stability and properties of the HPICs in biological media

First of all, the colloidal behavior of HPICs (R=1) was assessed in high ionic strength conditions by addition of NaCl solutions of concentration up to 2 mol·L^{-1}. No substantial aggregation was evidenced through DLS measurements up to 1 mol·L^{-1} (**Figure 60**), slight loss of scattered light intensity is indicative of the presence of some aggregates beyond 1 mol·L^{-1} of NaCl. This observation is in good agreement with quasi null Zeta potential value indicating that the colloidal stability of these HPICs objects does not rely on electrostatic stability but rather on steric stabilization supported by hydrated PVP chains on the outer corona of the HPICs architecture.

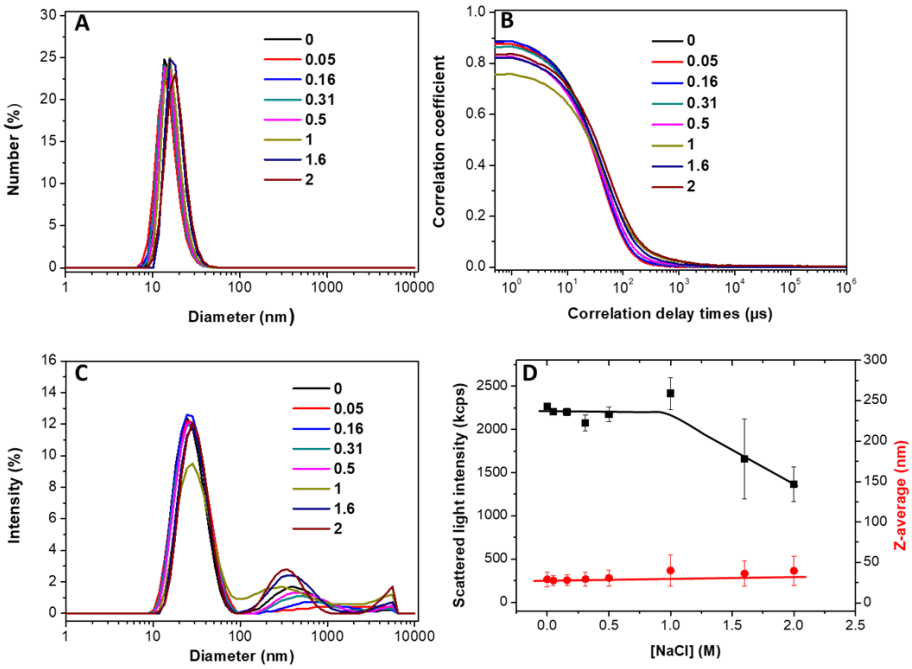

Figure 60. Colloidal stability of Gd^{3+}/PAA_{32}-*b*-PVP_{59} HPICs for R=1 as determined by mono-angle DLS measurements. Number-averaged (**A**) and intensity-averaged (**C**), size distributions of hydrodynamic diameter of HPICs obtained from the analysis of correlograms (**B**) Z-average size (diameter in nm, in red) with corresponding scattered light intensity (in black) (**D**) at different concentrations of NaCl(M).The lines are just guide for the eyes.

The integrity of nanostructures was also conserved with high dilution (up to 50 times) (**Figure 61**). Stability over this range of dilution demonstrates that the nanostructures are not in equilibrium with free copolymer and Gd^{3+} ions.

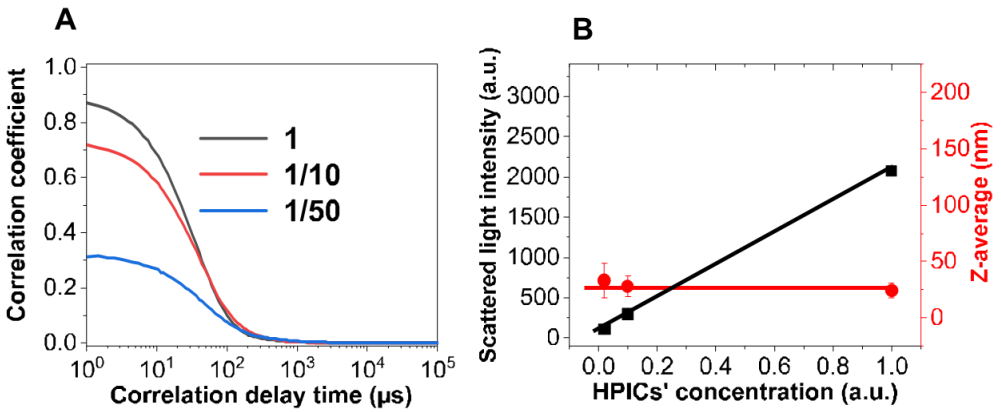

Figure 61. A. Evolution of the correlogram obtained for various dilution factor of a Gd^{3+}/PAA_{32}-*b*-PVP_{59} HPICs sample (R=1) (scattering angle: 173°, mono-angle DLS instrument). It could be observed that the correlogram is not shifted towards longer correlation delay times, indicating that no larger nanostructures were obtained by diluting the sample. The correlation coefficient decreases in intensity because of the decrease of the recorded signal. **B.** Evidence of the constant mean diameter, Z-average value with dilution and decrease of the scattered light intensity. a.u. (arbitrary unit) [PAA_{32}-*b*-PVP_{59}] = 0.1%wt in water solvent. [Gd^{3+}] = 1.3 mM

A key issue concerns the stability of HPICs in complete cell culture medium (CCM) containing 10% of fetal bovine serum (FBS). Nevertheless, attempts to evidence the presence of HPICs by tracking their light scattering failed because of the presence of fetal bovine serum rich in proteins and lipids with considerable sizes. (**Figure 62**) However, in serum-free cell culture medium (SfCM) (without proteins but rich in inorganic salts such as: carbonate, phosphate, chloride and nitrate) the integrity of the Eu^{3+}/PAA_{32}-*b*-PVP_{59} HPICs could be evidenced by DLS (**Figure 62**). In contrast, $Eu(NO_3)_3$ forms big aggregates in this medium.[70]

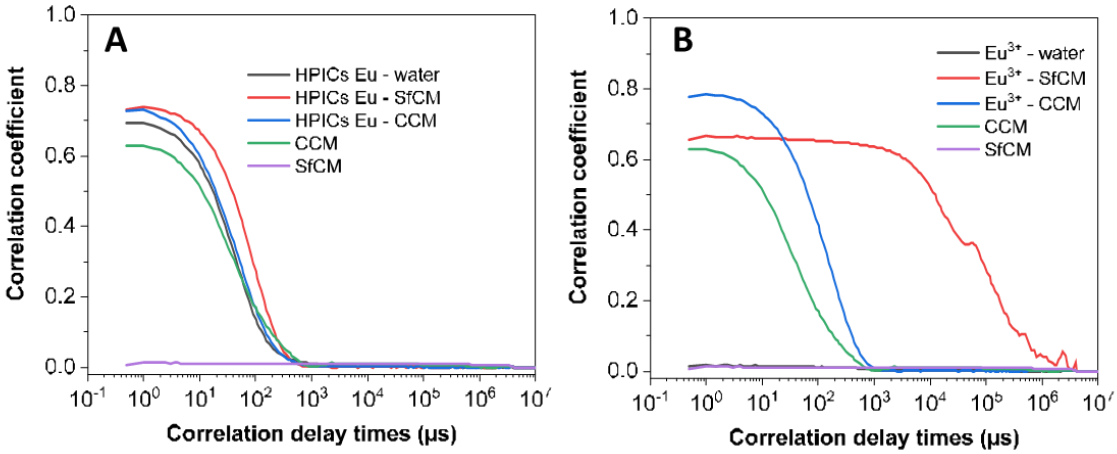

Figure 62. A. DLS measurements (correlation functions) of Eu^{3+} /PAA_{32}-*b*-PVP_{59} HPICs (R=1) in water, serum-free culture medium (SfCM) and complete cell culture medium (CCM), respectively and of the SfCM and CCM alone. **B**. DLS measurements (correlation functions) of Eu^{3+} free ions in water, SfCM and CCM. [PAA_{32}-*b*-PVP_{59}] = 0.07%wt in water solvent, or SfCM or CCM, [Eu^{3+}] = 0.9mM.

To further investigate the HPICs stability in complete cell culture medium, luminescent measurements were performed by using Eu^{3+}/PAA_{32}-*b*-PVP_{59} HPICs as a valuable luminescent probe.[61,69,71] Indeed, if the HPICs are not structured anymore, the intensity will decrease because free Eu^{3+} ions are less luminescent than the HPICs' structure, as previously seen in water. A pH-dependent color indicator, red phenol, is often introduced in the complete cell culture medium to follow any pH variation. Unfortunately, this color affects the sensitivity of the HPICs regarding luminescence properties. In order to remove the parasite fluorescence signals arising from all the fluorescence compounds present in this complete cell culture medium, phosphorescent mode experiments were performed.[72]

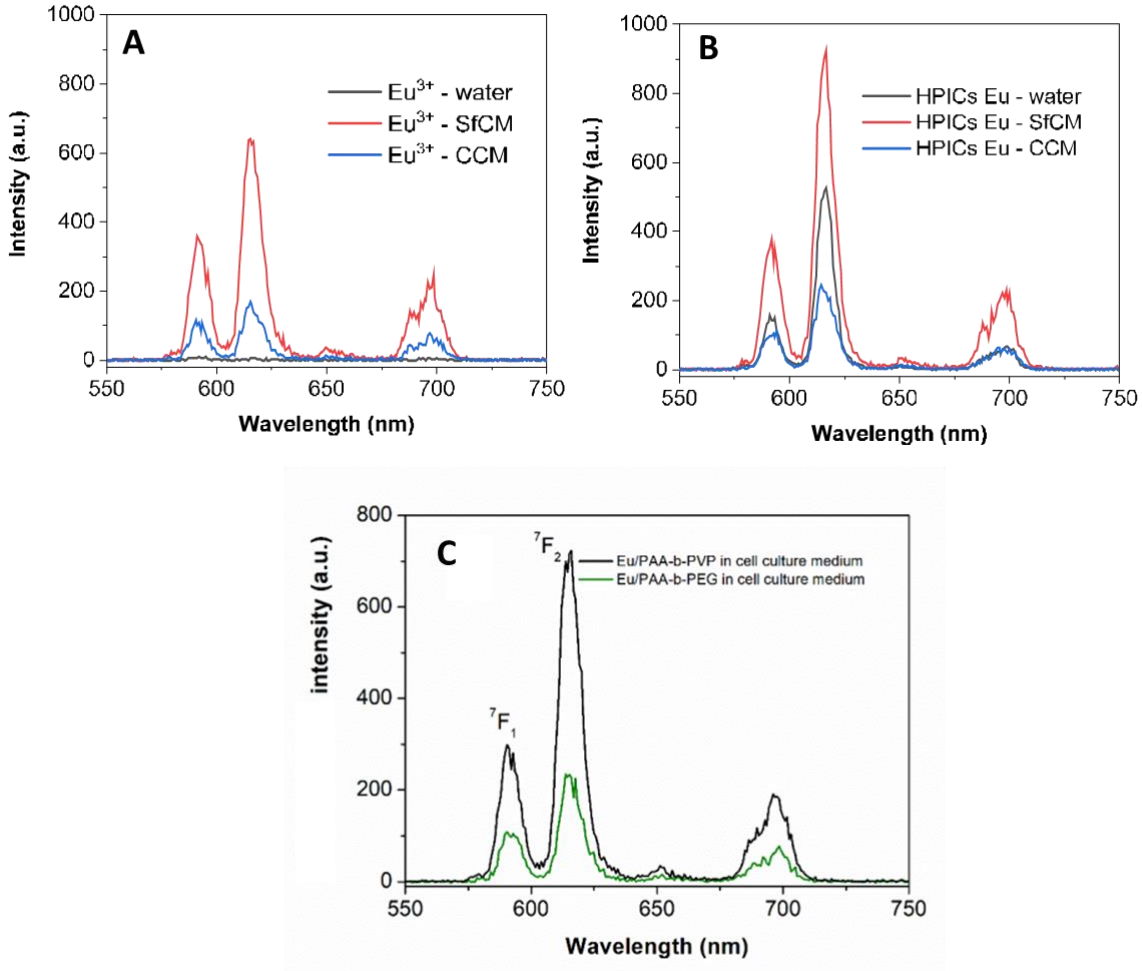

Figure 63. Comparison of time-resolved emission spectra (λ_{ex}=256 nm) of (**A**) Eu^{3+} /PAA_{32}-*b*-PVP_{59} HPICs (R=1) in water and in cell culture medium and of the $Eu(NO_3)_3$ in cell culture medium. (**B**) Eu^{3+} /PAA_{32}-*b*-PVP_{59} HPICs (R=1) and of Eu^{3+} /PAA_{44}-*b*-PEG_{80} HPICs (R=1) in cell culture medium (**C**).

As shown in **Figure 63 A**, the luminescence intensity of $Eu(NO_3)_3$ is significantly increased both in complete cell culture medium (CCM) and serum free culture medium (SfCM) compared to water, confirming the complexation of Eu^{3+} ions by the constituents present in these media.[70] The luminescence intensity of Eu^{3+}/PAA_{32}-*b*-PVP_{59} HPICs is also modified in both media (**Figure 63B**). The medium-dependent variation in intensity follows the order: serum-free culture medium (SfCM), water and complete cell culture medium (CCM). Moreover, the ratio of the luminescent intensity of the transition bands $^5D_0$ $^7F_2$ (615 nm) to $^5D_0$ $^7F_1$ (590 nm), the first one being solely dependent on the environment, decreases by 22 % from 3.2 in water to 2.5 in SfCM and by 28% in CCM.[64,69,73] Despite the nearly identical fine structure of the luminescence spectra of Eu^{3+}/PAA_{32}-*b*-PVP_{59} HPICs and $Eu(NO_3)_3$ in the different media, they do not match at all, demonstrating a different and specific chemical environment of Eu^{3+} ions in these two samples and the role of the PAA-*b*-PVP polymer in the protection of Eu^{3+} ions. In addition, the luminescence intensity of Eu^{3+}/PAA_{44}-*b*-PEG_{80} HPICs in CCM is much more affected than Eu^{3+}/PAA_{32}-*b*-PVP_{59} HPICs one (**Figure 63 C**). Based on the spectroscopic finding, it could be concluded that the HPICs are affected by the culture medium[69] but that HPICs based on PAA_{32}-*b*-PVP_{59} are more stable in such a complex environment. However, the exact description of the nature of the interaction of HPICs with the serum protein is not trivial and is the scope of a future work.[74]

IV.2. **Biological in vitro assays**

Cytotoxicity of the different elements forming the PAA_{32}-*b*-PVP_{59} HPICs was assessed *in vitro,* in complete cell culture medium, on human colorectal tumor cells HCT- 116. Cell viability was measured using PrestoBlue assay. For that purpose, cells were incubated for 48h with increasing concentrations of polymer PAA_{32}-*b*-PVP_{59}, $Eu(NO_3)_3$ or $Gd(NO_3)_3$ aqueous solutions, and Eu^{3+}/PAA_{32}-*b*-PVP_{59} HPICs or Gd^{3+}/ PAA_{32}-*b*-PVP_{59} HPICs. (**Figure 64 A**).

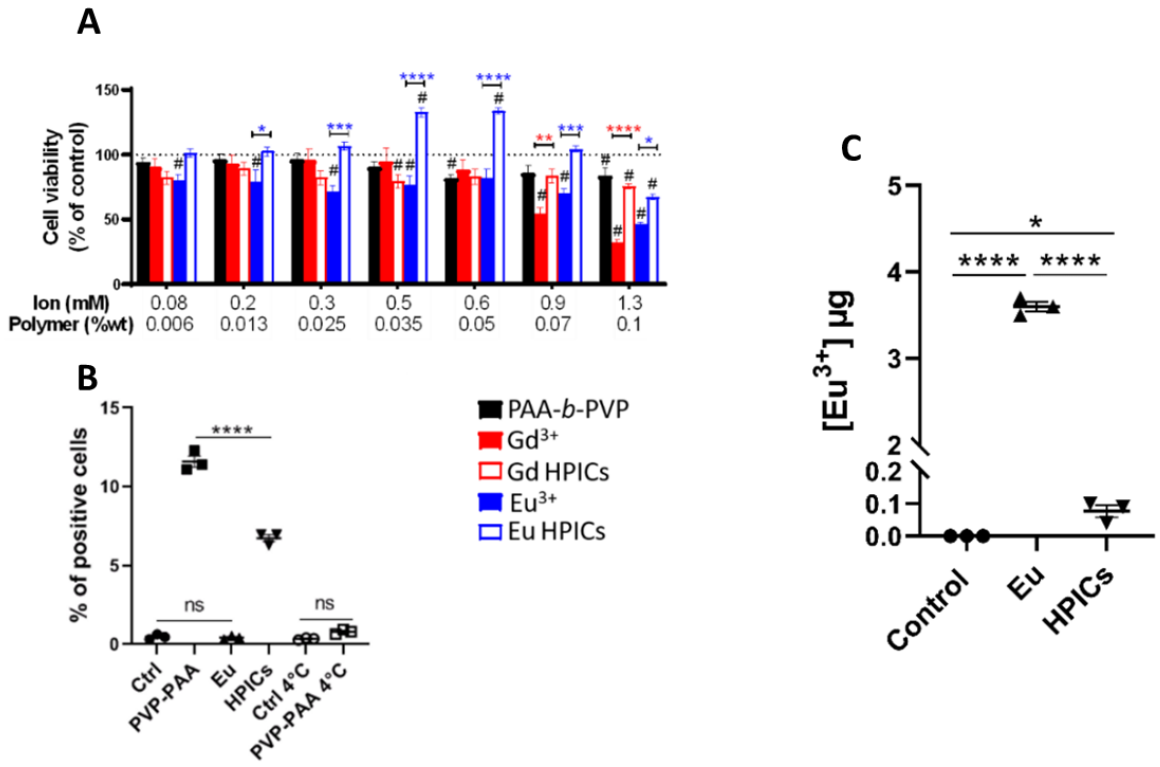

Figure 64. A. Quantification of HPICs cytotoxicity on human colorectal tumour cells HCT-116 after 48h of treatment. n=6. Data are represented as mean ± SEM. Statistical differences were analyzed either by 1-way ANONA followed by Dunnett's multiple comparisons post-test for each condition compared to the control one « no treatment » (# symbols, p<0,05) or by 2-way ANOVA to compare conditions with each other (blue or red stars, * p<0,05; ** p<0,01; *** p<0,001; **** p<0,0001). **B**. Flow cytometry analysis of PAA_{32}-*b*-PVP_{59} levels in HCT-116 cells when incubated over 6h with PAA_{32}-*b*-PVP_{59} alone, $Eu(NO_3)_3$ and Eu-HPICs and for condition of incubation at 4°C. (excitation at 405 nm, readout BV-711A filter) Statistical analysis by 1-way ANOVA followed by Tukey's multiple comparisons test. Ns=non-significant; **C**. ICP-MS analysis quantifying penetration of free Eu^{3+} and of Eu^{3+} in PAA_{32}-*b*-PVP_{59} HPICs. Statistical analysis by unpaired-t test. *=p

Results concerning the polymer PAA_{32}-*b*-PVP_{59} show a limited cytotoxicity toward HCT-116, since at the highest concentration (0.1%wt) at least 80% of cells were viable. This is considerably more than the viability (only 50%) of the HCT-116 cells observed for PAA_{44}-*b*-PEG_{80} copolymer at 0.09%wt[15]. Eu^{3+} ions, from $Eu(NO_3)_3$ salt, significantly and statistically affect cell viability, over the whole range of concentrations used. For Gd^{3+} ions from $Gd(NO_3)_3$ salt, cell viability decreases to less than 50% at 0.9 mM. In a remarkable manner, when these ions were encapsulated within the PAA_{32}-*b*-PVP_{59} HPICs structure, their cytotoxicity undoubtedly and statistically decreased. Thus, the HPICs were better tolerated than the free Gd^{3+} or Eu^{3+} ions especially at the highest concentrations. These results point to the beneficial role of the PAA_{32}-*b*-PVP_{59} polymer for decreasing toxicity of the lanthanide ions, even that their environment is affected by the complete cell culture medium as demonstrated upper. A similar decrease in cytotoxicity was observed when lanthanide were encapsulated in PAA_{44}-*b*-PEG_{80} polymer.[15] The pro-proliferative effect of Eu^{3+}/PAA_{32}-*b*-PVP_{59} HPICs at certain concentrations can be noted, a phenomenon that we are not currently able to explain in terms of the biological mechanisms

involved. In order to study the Eu^{3+}/PAA_{32}-*b*-PVP_{59} HPICs cell uptake, flow cytometry experiments were performed. For that purpose, HCT-116 cells were incubated for 6h with 0.07%wt PAA_{32}-*b*-PVP_{59}, 0.9mM $Eu(NO_3)_3$ aqueous solution and the corresponding Eu^{3+}/ PAA_{32}-*b*-PVP_{59} HPICs (**Figure 64 B**). As expected, no fluorescence coming from Eu^{3+} was detected due to technical limitations of the conventional, dedicated to biology cytometer, i.e excitation laser and simultaneous fluorescence detection was clearly not optimal for Eu^{3+} excitation.[75]

However, fluorescence signal (Excitation = 405 nm, Emission Max = 711 nm) was detected for the samples incubated with PAA_{32}-*b*-PVP_{59} polymer, due to autofluorescence of the PVP block of the polymer.[65] This represents a real advantage compared to the non autofluorescent PAA_{44}-*b*-PEG_{80} copolymer, thus avoiding the use of additional fluorescents dyes. It was found that the percentage of cell labeling is low: 12% of the cell population was labeled in the presence of PAA_{32}-*b*-PVP_{59} copolymer and twice less, approximately 7% in the presence of Eu^{3+}/PAA_{32}-*b*-PVP_{59} HPICs. Interestingly, when incubation with copolymer was performed at 4°C, no fluorescent signal was observed within the cells, meaning that endocytosis is a major actor in the process of internalization of the copolymer. Complementary, for the quantification of europium inductively coupled plasma-mass spectrometry (ICP-MS) was used. The quantity of Eu^{3+} ions, when the cells were incubated with 0.9mM of $Eu(NO_3)_3$, amounts to about 23.6 nmol Eu^{3+}/20×10^6 cells after 6h of exposure, comparable with the value reported for Eu^{3+} ions uptake into FaDu cell.[70] (**Figure 64 C**) The amount of Eu^{3+} ions decreases at 0.5 nmol Eu^{3+}/20×10^6 cells, when the cells were incubated with Eu^{3+}/PAA_{32}-*b*-PVP_{59} HPICs containing 0.9mM of Eu^{3+} ions. This is in agreement with the low percentage of labeling found by flow cytometry experiments. Furthermore, these results correlate to the cell viability data. Consequently, our results underline that HPICs organization prevents lanthanide ions and polymer's cytotoxicity and cell penetration compared to their free counterparts, mainly by increasing architecture stability of the nanocarrier.

V Properties of the structure as a potential MRI contrast agent

The HPICs nanostructures are now validated from an *in vitro* point of view in terms of cytotoxicity and could then be applied in biological applications. The aim of this final part is to evaluate the properties of Gd^{3+}/ PAA_{32}-*b*-PVP_{59} HPICs as potential contrast agent for imaging field and particularly MRI. The relaxivity notion and the factors impacting the relaxation properties of MRI contrast agents, were explained in the introduction of this chapter. This part is focused then on relaxivity measurements regarding Gd^{3+}/ PAA_{32}-*b*-PVP_{59} HPICs realized in both water and

complete cell culture medium. Besides, some *in vivo* tests are realized to evaluate the real effect of the Gd^{3+}/ PAA_{32}-*b*-PVP_{59} HPICs in a mouse organism as an MRI contrast agent.

V.I. Relaxivity measurements on HPICs nanostructures in water and cell culture medium

The relaxivity of both types of Gd^{3+} HPICs, formulated either with PAA_{32}-*b*-PVP_{59} or PAA_{44}-*b*-PEG_{80} copolymers, is determined in the absence and presence of complete cell culture medium (**Figure 65**).

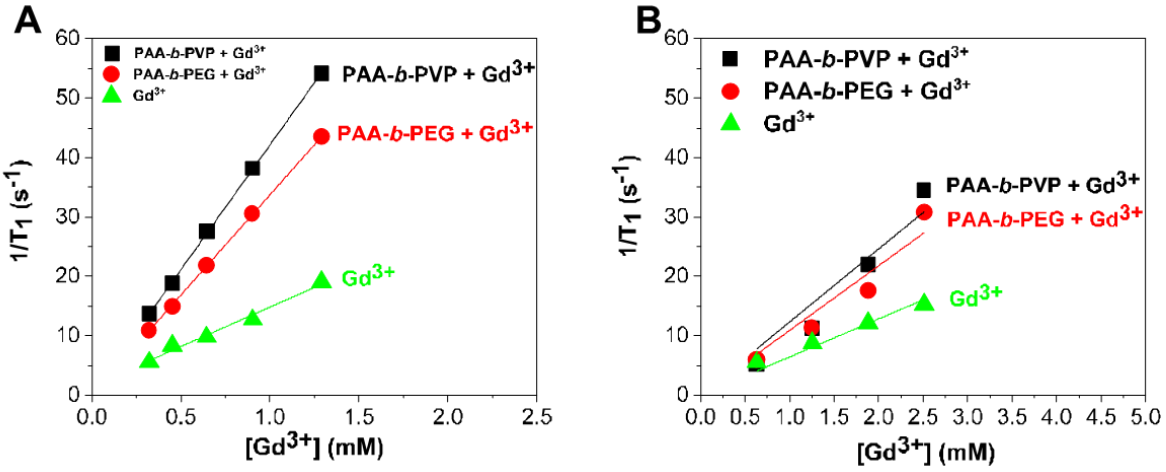

Figure 65. Change in the longitudinal relaxation time as a function of the concentration of Gd^{3+} ions in water (**A**) and complete cell culture medium (**B**).

In water the r_1 relaxivity of Gd^{3+}/PAA_{32}-*b*-PVP_{59} HPICs was measured to be $r_1 = 42 \pm 0.36$ $mM^{-1}.s^{-1}$ (25°C, 0.47T) very close to the one measured for Gd^{3+}/PAA_{44}-*b*-PEG_{80} HPICs in the same conditions i.e. $r_1 = 33 \pm 0.36$ $mM^{-1}.s^{-1}$ (whereas a value equal to $r_1 = 48 \pm 2$ $mM^{-1}.s^{-1}$ was measured at 1.4T).[14] However, when mixed with the complete cell culture medium the r_1 relaxivity falls at $r_1 = 16 \pm 1.65$ $mM^{-1}.s^{-1}$ and $r_1 = 13 \pm 2.05$ $mM^{-1}.s^{-1}$ for Gd^{3+}/PAA_{32}-*b*-PVP_{59} and Gd^{3+}/PAA_{44}-*b*-PEG_{80} HPICs, respectively (**Table 7**). This behavior is consistent with the modifications of the HPICs in complete cell culture medium as suggested by luminescence experiments. Even that, the values are larger than the values displayed by commercial molecular complexes which are lower than 6 $mM^{-1}.s^{-1}$ in human plasma at 37°C and 0.47T.[61] Additionally, *in vivo* tests performed using Gd^{3+}/PAA_{44}-*b*-PEG_{80} HPICs, have already shown very promising results in terms of magnetic relaxivity properties. Considering the low toxicity detected for these Gd^{3+}/ PAA_{32}-*b*-PVP_{59} HPICs, we are confident that these two types of HPICs could be conceived for future developments as MRI contrast agents.

Table 7. Values of the longitudinal relaxivities (r_1) for the HPICs and $Gd(NO_3)_3$ in water and complete cell culture medium.

Medium	Relaxivity r_1 ($mM^{-1}.s^{-1}$)		
	Gd^{3+}/PAA_{32}-b-PVP_{59}	Gd^{3+}/PAA_{44}-b-PEG_{80}	Gd^{3+}
Water	42 ± 0.36	33 ± 0.36	13 ± 0.96
Complete Cell culture medium	16 ± 1.65	13± 2.05	5.2 ± 0.05

V.2. *In vivo* assays

In order to pursue the idea of using these Gd^{3+}/PAA_{32}-*b*-PVP_{59} nanostructures as potential MRI CAs, *in vivo* experiments were performed. Previous in vitro tests approved the non-significant cytotoxicity of the HPICs nanostructures for concentrations suitable to perform *in vivo* experiments on mice and to obtain preliminary determinations of MR contrast efficacy, pharmacokinetic properties, and tolerance. Moreover, the relaxivity measurements confirmed high values in both water and complete cell culture medium for the HPICs nanostructures as potential T_1 CAs.

The *in vivo* MR contrast was assessed after intravenous (IV) bolus injection of Gd^{3+}/PAA_{32}-*b*-PVP_{59} HPICs and compared to the use of GdDOTA (Dotarem) with an equivalent Gd concentration. Tissue uptake and elimination properties were assessed using a T_1-weighted dynamic sequence of coronal images centered on the abdominal cavity, acquired during 30 min after IV injection of Gd^{3+} (HPICs or GdDOTA) at 15 µmol/kg equivalent Gd concentration. In **Figure 66**, regions of interest are given corresponding to the renal Cortex of both kidneys and the bladder. Comparatively to Dotarem, PAA_{32}-*b*-PVP_{59} HPICs significantly increase contrast in all the studied organs: an enhanced contrast of about +67% is measured in T_1-weighted images of the kidney intravascular space for PAA_{32}-*b*-PVP_{59} HPICs after 30 min (1% for GdDOTA, **Figure 66)** and show similar trends than the ones previously measured with PAA_{44}-*b*-PEG_{80} HPICs.[14]

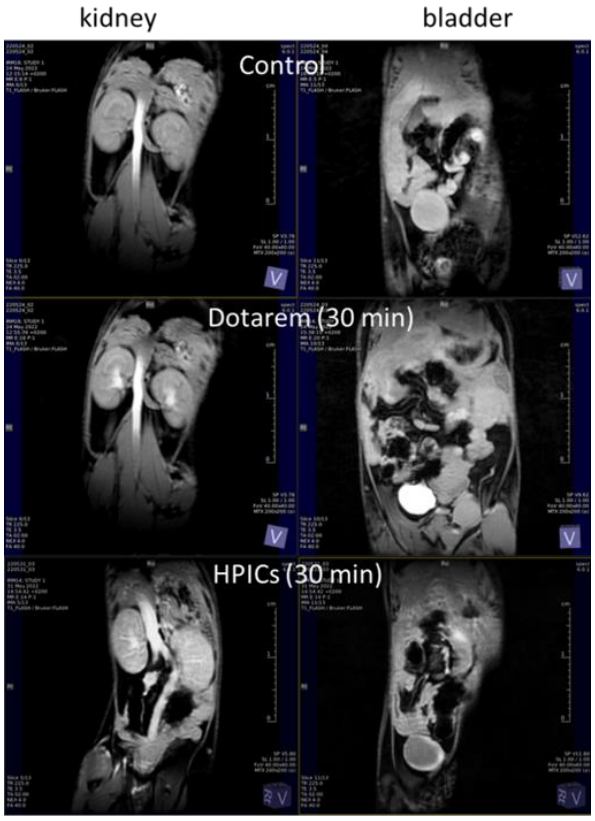

Figure 66. Coronal T_1-weighted images 30 min after injection of GdDOTA (middle), Gd^{3+}/PAA_{32}-*b*-PVP_{59} HPICs (bottom) in comparison with a control (top). The images are centered on the kidneys (left) and bladder (right).

In addition, the elimination process for the Gd^{3+}/PAA_{32}-*b*-PVP_{59} HPICs was followed by monitoring signal enhancement vs time in the bladder (**Figure 67**). Whereas GdDOTA was quickly eliminated from the blood circulation as assessed by the high signal intensity in the bladder after 30 min, Gd^{3+}/PAA_{32}-*b*-PVP_{59} HPICs residence time is relatively long through a urinary and hepatobiliary elimination processes and a persistent enhancement of the vascular signal. Moreover, direct injection in Pelvis enables to assess the *in vivo* colloidal stability of Gd^{3+}/PAA_{32}-*b*-PVP_{59} HPICs. (**Figure 68**) Indeed, contrast enhancement remains confined to the intraperitoneal cavity for the Gd^{3+}/ PAA_{32}-*b*-PVP_{59} HPICs indicating the non-penetration of the pelvic barrier by the HPICs nanostructures and no leak of the Gd^{3+} ions out of the HPICS. Quantitative biokinetic studies are still needed, but these preliminary studies of a relatively simple HPIC show surprisingly good stability and superior magnetic relaxivity properties in vitro and *in vivo*, even at high magnetic field.

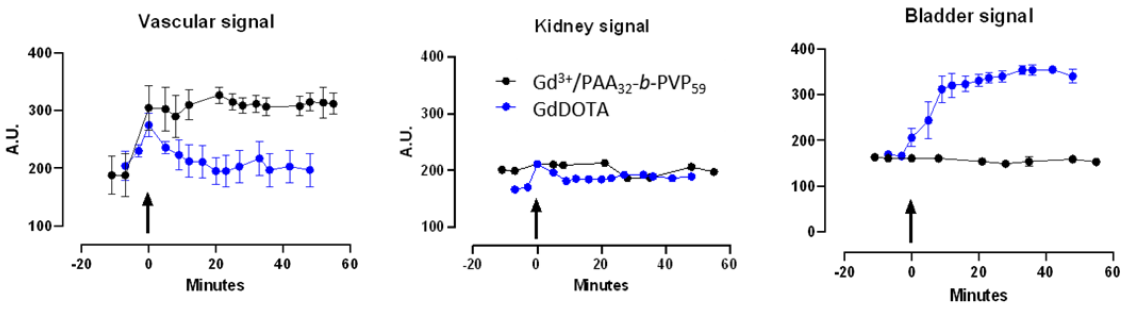

Figure 67. Typical evolution of the MRI signal following the administration (arrow) of GdDOTA (blue) or Gd^{3+}/PAA_{32}-b-PVP_{59} HPICs (black) from the vascular space (rectangular shaped ROI taken in the slice at the level of the inferior vana cava, the kidney (ellipse shaped ROI taken in a horizontal image covering all the right kidney) and in the bladder (circular shaped ROI taken in a horizontal image covering all the bladder). A.U. (arbitrary unit of the MRI signal expressed as mean value +- SD measured in ROIs).

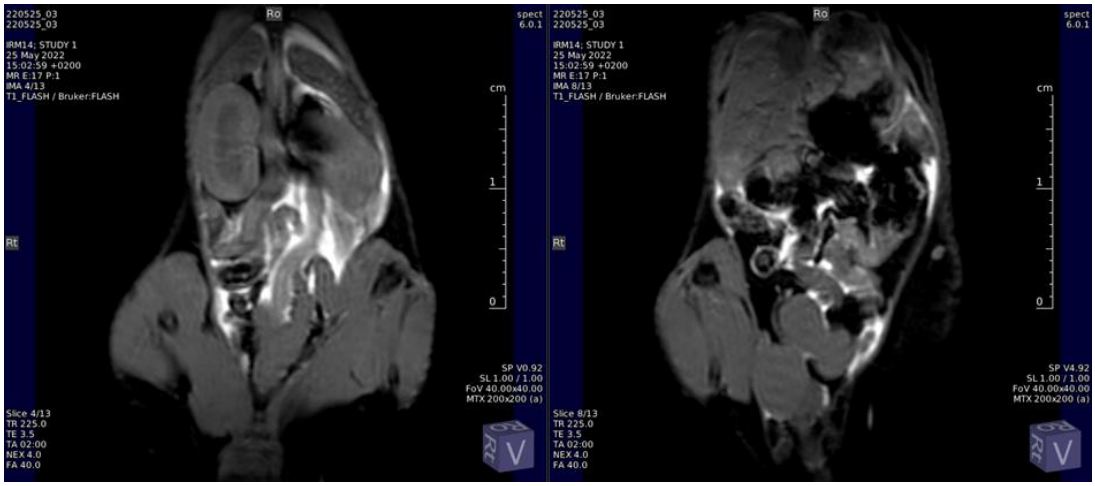

Figure 68. Horizontal slices of the abdomen acquired after 40 min following the intraperitoneal administration of Gd^{3+}/PAA_{32}-b-PVP_{59} HPICs. Cut at the kidney level on the left and at the level of the bladder on the right.

VI Additional work regarding block configuration influence

This last part of this chapter is the beginning of a study on the influence of the configuration of the block copolymer onto hybrid assemblies. Three different strategies of variation were interesting to test to evaluate the different influences on the formation of HPICs (**Scheme 9**).

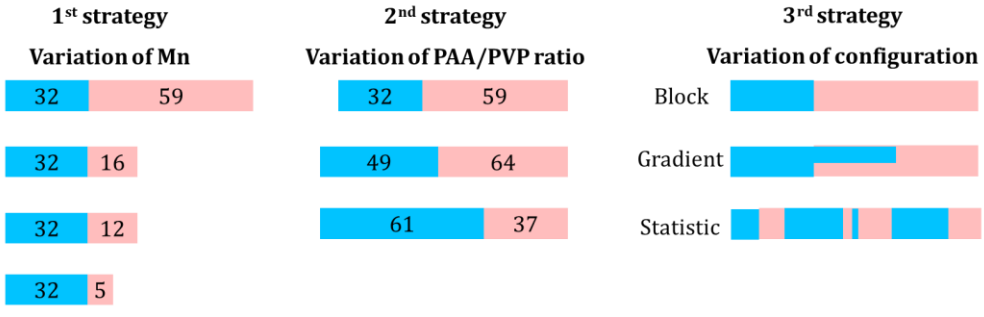

Scheme 9. Strategies for the modulation of the polymer ability to interact with the lanthanide ions.

The aim of this part was to investigate the influence of the modulation of the polymer structure on the formation of the HPICs. Only one variation was completely assessed which is the one consists in varying the PVP block length by reducing it until being shorter than the PAA block. The second strategy was based on the variation of both blocks length, while maintaining the overall molecular weight constant. Block copolymers were synthesized but physico-chemical experiments are still in progress. The third strategy illustrated in **Scheme 9**, was only partially explored regarding the statistical configuration, but is still to pursue in the project.

VI.1 Influence of the length of the PVP block on the HPICs architecture

Gd^{3+}/PAA-*b*-PVP HPICS were prepared with three different PAA-*b*-PVP copolymers, whose length of the PVP chain decreases from the initial length (PVP_{59}) (i.e. PVP_{30}, PVP_{16}, PVP_{12}, PVP_5) while the PAA chain length remains constant. The samples for R=1 and pH=7 were characterized by DLS (**Figure 69**). It could be observed that the shorter the PVP length, the more the correlograms are shifted toward higher sizes. Indeed, a monomodal size could be observed only for the sample of reference, i.e. the one previously studied, formed with the PAA_{32}-*b*-PVP_{59} polymer. (**Figure 69 A** and **B**).

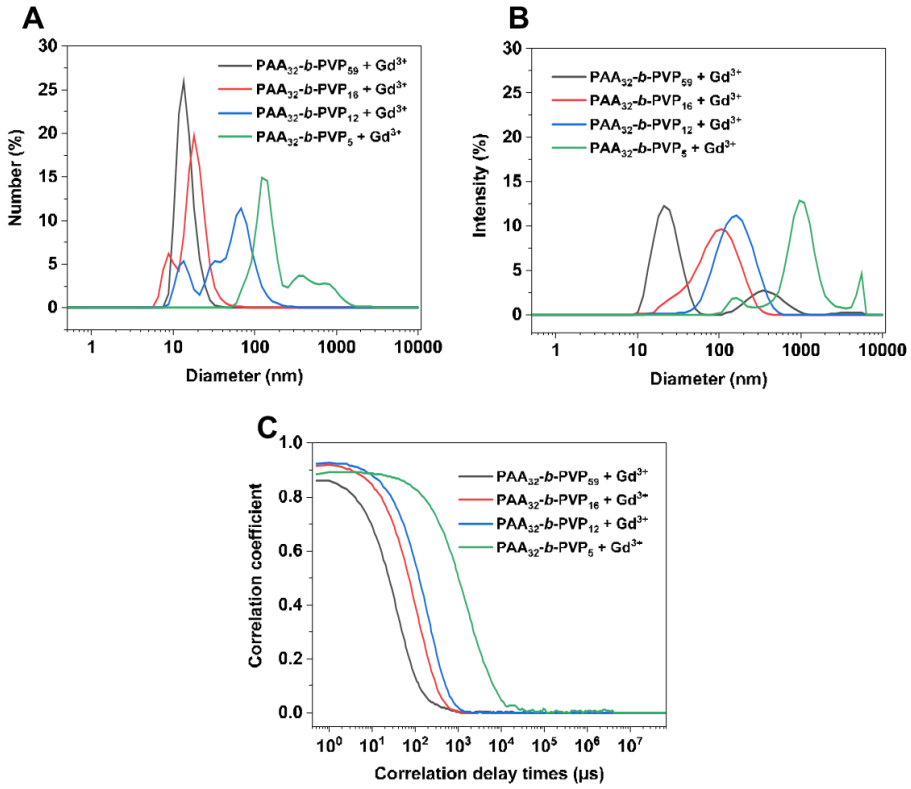

Figure 69. DLS analysis of the mixtures containing the different block copolymers PAA_n-*b*-PVP_m with varied PVP block length and Gd^{3+} ions at R=1 and pH = 7.

The variation of the lanthanide (replacing the Gd^{3+} ions by Eu^{3+} ions) was tested with every copolymer and didn't change the architecture of the HPICs, as could be observed by DLS for the HPICs formed with the PAA_{32}-*b*-PVP_{16} (**Figure 70**). Sizes' range is also in agreement with the reference sample, formed with the i.e. PAA_{32}-*b*-PVP_{59} copolymer.

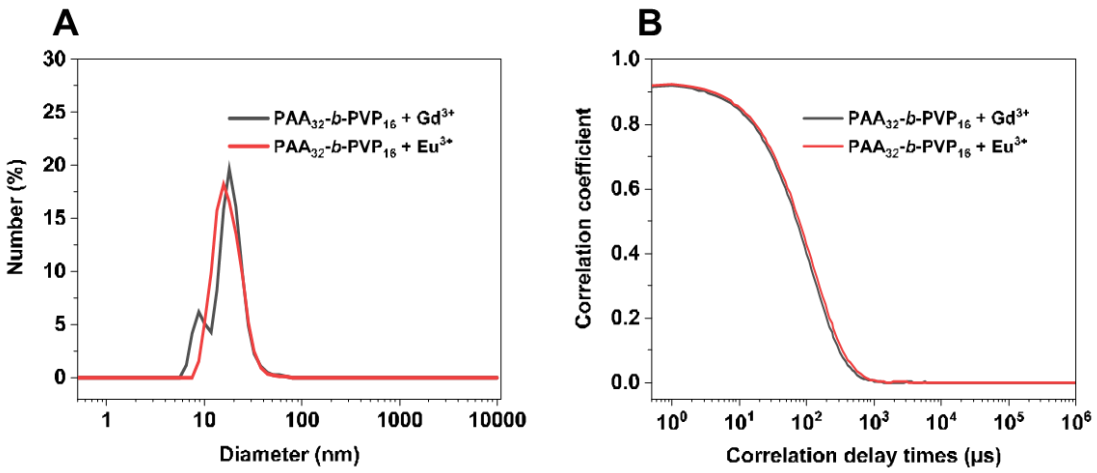

Figure 70. DLS analysis of the mixtures containing PAA_{32}-b-PVP_{30} and gadolinium ions (black lines) or europium ions (red lines) at R=1 and pH = 7.

As the size results obtained with PAA_{32}-*b*-PVP_{16} were the most similar to the ones obtained with the reference polymer PAA_{32}-*b*-PVP_{59}, fluorimetry investigation was realized onto this sample. The emission spectra measured in phosphorescent mode are given in **Figure 71** for the Eu^{3+}/ PAA_{32}-*b*-PVP_{16} in comparison with the Eu^{3+}/ PAA_{32}-*b*-PVP_{59} one, for the same concentration in Eu^{3+} ions, i.e. 1.3mM.

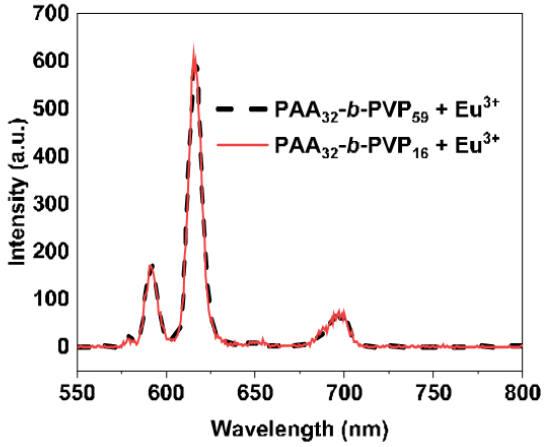

Figure 71. Phosphorescence spectra of the HPICs structures made of PAA_{32}-*b*-PVP_{59} (dot black line) or PAA_{32}-*b*-PVP_{16} (red line) and Eu^{3+}ions at R=1 and pH = 7 at the same concentration of Eu^{3+} ions.

It could be observed that the two spectra superpose perfectly, which means that the Eu^{3+} ions are in the same environment in the two samples, even if the PVP length is different.

(**Figure 69**, **Figure 71)** This confirms that the PAA block polymer is implied in interactions affecting the near environment of Eu^{3+} ions, that could influence their luminescence properties.

VI.2. Influence of the PAA/PVP ratio at a fixed Molecular Weight

Three polymers with a similar molecular weight of around 8 000 g mol^{-1} were chosen, and the length of the two blocks was varied., i.e. PAA_{32}-*b*-PVP_{59} (the reference polymer); PAA_{49}-b-PVP_{64} and PAA_{61}-*b*-PVP_{37}. Exact molecular weight and characteristics are reported into **Table 4**. The study of assembly of these block copolymers is still undergoing.

VI.3. Investigation on the configuration of the copolymer

Now that the block configuration has been widely explored, the interest is now to try other configurations of the copolymer such as random one. Because our attempts to synthesize a random copolymer with the same composition as the block one was not easy to implement, a commercially available PAA-*r*-PVP was tested to have preliminary results. However its composition is different compared with the reference one, i.e. PVP_{416}-*r*-PVP_{270}, the molecular weight being considerably higher. As can be seen on **Figure 72**, both DLS and fluorimetry analysis were performed when the polymer was mixed with Eu^{3+} ions and compared to the results obtained with the block configuration.

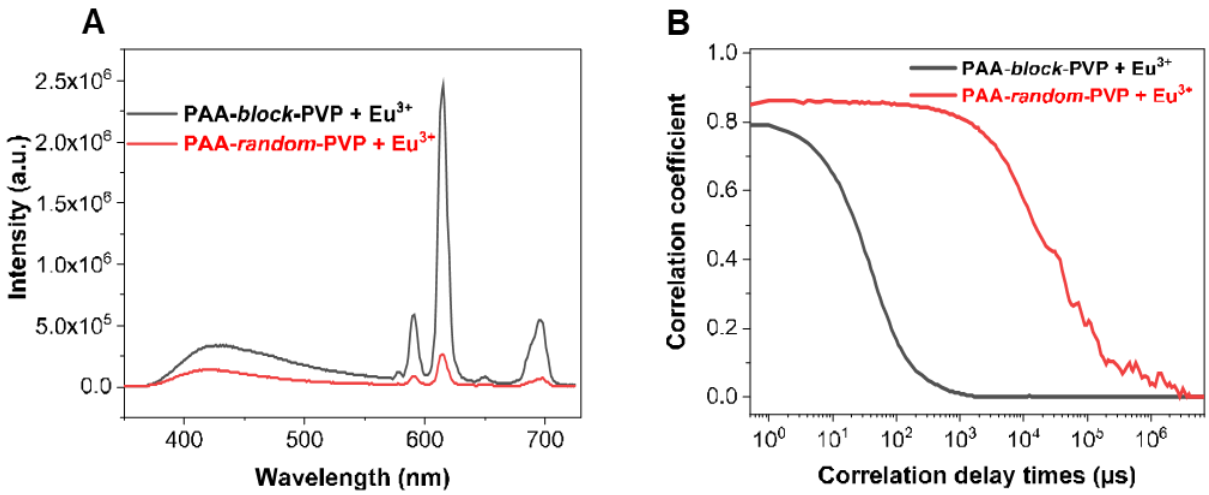

Figure 72. Commercial random PAA_{416}-*r*-PVP_{270} copolymer vs. block PAA_{32}-*b*-PVP_{59} copolymer: Comparison of emission spectra (A) (λ_{ex}=325 nm) and (B) DLS correlograms of Eu^{3+} /PAA_{32}-*b*-PVP_{59} HPICs and Eu^{3+}/PAA_{416}-*r*-PVP_{270} mixture ([polymer]=0.2% wt) for R=1

As evidenced on **Figure 72.B**, the correlogram is strongly shifted to the right, evidencing no well-defined nanostructures. The fluorescence properties are considerably affected also when the random configuration was used. This is probably due to the stronger steric effect imposed by the statistical configuration, with the carboxylate groups, no more isolated in a single block, but sprinkle throughout the polymeric chain in between the PVP groups.

Therefore, the synergistic effect of the carboxylate groups brought together on the chelation of the Eu^{3+} ions is lost, and thus they manifest more difficulties to chelate Eu^{3+} ions, even if the charges' ratio is R=1. The water molecules could then be more numerous and the intensity is consequently affected.

VI.4. Conclusion on the influence of molecular architecture

The comparison with randomly distributed and homopolymers demonstrated that block structure is the structure of choice to obtain HPICs nanoobjects with well-defined morphology. Moreover, while PAA block promotes the interaction with trivalent ions, PVP block with a sufficient length is necessary to obtain well-defined nano-objects. Complementary experiments to study the effect of polymer structure on colloidal stability and relaxation properties are actually underway to complete this first set of experiments.

VII Conclusions

In this chapter, a PAA-*b*-PVP double hydrophilic polymer with different size lengths of the two blocks was successfully synthesized by RAFT polymerization. These polymers were then mixed with trivalent ions (i.e. Eu^{3+}, Gd^{3+} and Y^{3+}) in order to form HPICs structures. The best formulation was obtained for the polymer with the PAA_{32}-*b*-PVP_{59} composition. The formation of HPICs was studied by using different techniques: DLS, fluorimetry, ATR-FTIR and ^1H NMR. It was demonstrated that these new HPICs showed similar well-defined architectures, size and size distribution as the analogues based on PAA-*b*-PEG copolymer., i.e. 25 nm. The PAA-*b*-PVP copolymer had low toxicity alone and effectively contributed to the decrease of the toxicity of the lanthanide ions when they were enclosed into the HPICs. Despite clear evidence of interaction with the serum proteins from the complete cell culture medium, which partially alters the fluorescence and relaxivity properties, the composition of the HPICs seems to be still mostly integral which is not the case of the PAA-*b*-PEG analog. This is supported *in vitro* by a low toxicity and low cell penetration of the HPICs compared to their individual constituents and in vivo by the impossibility of these HPICs to penetrate the pelvic barrier of mice, with no leak of the Gd^{3+} ions as demonstrated by monitoring the magnetic resonance contrast of the peritoneal cavity. Finally, the Gd^{3+}/ PAA_{32}-*b*-PVP_{59} HPICs showed enhanced T_1-MRI contrast compared to the GdDOTA (of about +67% measured in T_1-weighted images of the intravascular space after 30 min after intravenous injection into mice) and equivalent relaxivity efficiency compared to the PAA-*b*-PEG analogues, thus contributing as a new interesting probe to be used in MRI.

VIII References

(1) Pinkerton, N. M.; Behar, L.; Hadri, K.; Amouroux, B.; Mingotaud, C.; Talham, D. R.; Chassaing, S.; Marty, J.-D. Ionic Flash NanoPrecipitation (IFNP) for the Facile, One-Step Synthesis of Inorganic–Organic Hybrid Nanoparticles in Water. *Nanoscale* **2017**, *9* (4), 1403–1408. https://doi.org/10.1039/C6NR09364G.

(2) Shin, H.-W.; Sohn, H.; Jeong, Y.-H.; Lee, S.-M. Construction of Paramagnetic Manganese-Chelated Polymeric Nanoparticles Using Pyrene-End-Modified Double-Hydrophilic Block Copolymers for Enhanced Magnetic Resonance Relaxivity: A Comparative Study with Cisplatin Pharmacophore. *Langmuir* **2019**, *35* (19), 6421–6428. https://doi.org/10.1021/acs.langmuir.9b00406.

(3) Das, T.; Sharma, A.; Talukder, G. Effects of Lanthanum in Cellular Systems. *Biol. Trace Elem. Res.* **1988**, *18* (1), 201–228. https://doi.org/10.1007/BF02917504.

(4) Sieber, M. A.; Lengsfeld, P.; Frenzel, T.; Golfier, S.; Schmitt-Willich, H.; Siegmund, F.; Walter, J.; Weinmann, H.-J.; Pietsch, H. Preclinical Investigation to Compare Different Gadolinium-Based Contrast Agents Regarding Their Propensity to Release Gadolinium in Vivo and to Trigger Nephrogenic Systemic Fibrosis-like Lesions. *Eur. Radiol.* **2008**, *18* (10), 2164–2173. https://doi.org/10.1007/s00330-008-0977-y.

(5) Yon, M. Gadolinium-Based Contrast Agents_ From Gadolinium Complexes to Colloidal Systems. *Int. J. Pharm.* **2019**, 10.

(6) Kanda, T.; Ishii, K.; Kawaguchi, H.; Kitajima, K.; Takenaka, D. High Signal Intensity in the Dentate Nucleus and Globus Pallidus on Unenhanced T1-Weighted MR Images: Relationship with Increasing Cumulative Dose of a Gadolinium-Based Contrast Material. *Radiology* **2014**, *270* (3), 834–841. https://doi.org/10.1148/radiol.13131669.

(7) Kanda, T.; Fukusato, T.; Matsuda, M.; Toyoda, K.; Oba, H.; Kotoku, J.; Haruyama, T.; Kitajima, K.; Furui, S. Gadolinium-Based Contrast Agent Accumulates in the Brain Even in Subjects without Severe Renal Dysfunction: Evaluation of Autopsy Brain Specimens with Inductively Coupled Plasma Mass Spectroscopy. *Radiology* **2015**, *276* (1), 228–232. https://doi.org/10.1148/radiol.2015142690.

(8) Kanda, T.; Osawa, M.; Oba, H.; Toyoda, K.; Kotoku, J.; Haruyama, T.; Takeshita, K.; Furui, S. High Signal Intensity in Dentate Nucleus on Unenhanced T1-Weighted MR Images: Association with Linear versus Macrocyclic Gadolinium Chelate Administration. *Radiology* **2015**, *275* (3), 803–809. https://doi.org/10.1148/radiol.14140364.

(9) Radbruch, A.; Weberling, L. D.; Kieslich, P. J.; Eidel, O.; Burth, S.; Kickingereder, P.; Heiland, S.; Wick, W.; Schlemmer, H.-P.; Bendszus, M. Gadolinium Retention in the Dentate Nucleus and Globus Pallidus Is Dependent on the Class of Contrast Agent. *Radiology* **2015**, *275* (3), 783–791. https://doi.org/10.1148/radiol.2015150337.

(10) El Jundi, A.; Buwalda, S. J.; Bakkour, Y.; Garric, X.; Nottelet, B. Double Hydrophilic Block Copolymers Self-Assemblies in Biomedical Applications. *Adv. Colloid Interface Sci.* **2020**, *283*, 102213. https://doi.org/10.1016/j.cis.2020.102213.

(11) Harada, A.; Kataoka, K. Polyion Complex Micelle Formation from Double-Hydrophilic Block Copolymers Composed of Charged and Non-Charged Segments in Aqueous Media. *Polym. J.* **2018**, *50* (1), 95–100. https://doi.org/10.1038/pj.2017.67.

(12) Schmidt, B. V. K. J. Double Hydrophilic Block Copolymer Self-Assembly in Aqueous Solution. *Macromol. Chem. Phys.* **2018**, *219* (7), 1700494. https://doi.org/10.1002/macp.201700494.

(13) Taton, D.; Wilczewska, A.-Z.; Destarac, M. Direct Synthesis of Double Hydrophilic Statistical Di- and Triblock Copolymers Comprised of Acrylamide and Acrylic Acid Units via the MADIX Process. *Macromol. Rapid Commun.* **2001**, *22* (18), 1497–1503. https://doi.org/10.1002/1521-3927(20011201)22:18<1497::AID-MARC1497>3.0.CO;2-M.

(14) Frangville, C.; Li, Y.; Billotey, C.; Talham, D. R.; Taleb, J.; Roux, P.; Marty, J.-D.; Mingotaud, C. Assembly of Double-Hydrophilic Block Copolymers Triggered by Gadolinium Ions: New Colloidal MRI Contrast Agents. *Nano Lett.* **2016**, *16* (7), 4069–4073. https://doi.org/10.1021/acs.nanolett.6b00664.

(15) Yon, M.; Gineste, S.; Parigi, G.; Lonetti, B.; Gibot, L.; Talham, D. R.; Marty, J.-D.; Mingotaud, C. Hybrid Polymeric Nanostructures Stabilized by Zirconium and Gadolinium Ions for Use as Magnetic Resonance Imaging Contrast Agents. *ACS Appl. Nano Mater.* **2021**, *4* (5), 4974–4982. https://doi.org/10.1021/acsanm.1c00495.

(16) Jeong, Y.-H.; Shin, H.-W.; Kwon, J.-Y.; Lee, S.-M. Cisplatin-Encapsulated Polymeric Nanoparticles with Molecular Geometry-Regulated Colloidal Properties and Controlled Drug Release. *ACS Appl. Mater. Interfaces* **2018**, *10* (28), 23617–23629. https://doi.org/10.1021/acsami.8b06905.

(17) Seo, E.; Kim, J.; Hong, Y.; Kim, Y. S.; Lee, D.; Kim, B.-S. Double Hydrophilic Block Copolymer Templated Au Nanoparticles with Enhanced Catalytic Activity toward Nitroarene Reduction. *J. Phys. Chem. C* **2013**, *117* (22), 11686–11693. https://doi.org/10.1021/jp4027139.

(18) Lee, H. J.; Kim, S. E.; Kwon, I. K.; Park, C.; Kim, C.; Yang, J.; Lee, S. C. Spatially Mineralized Self-Assembled Polymeric Nanocarriers with Enhanced Robustness and Controlled Drug-Releasing Property. *Chem Commun* **2010**, *46* (3), 377–379. https://doi.org/10.1039/B913732G.

(19) Tanaka, S.; Lin, J.; Kaneti, Y. V.; Yusa, S.; Jikihara, Y.; Nakayama, T.; Zakaria, M. B.; Alshehri, A. A.; You, J.; Hossain, Md. S. A.; Yamauchi, Y. Gold Nanoparticles Supported on Mesoporous Iron Oxide for Enhanced CO Oxidation Reaction. *Nanoscale* **2018**, *10* (10), 4779–4785. https://doi.org/10.1039/C7NR08895G.

(20) Zhang, K.; Yeung, M. C.-L.; Leung, S. Y.-L.; Yam, V. W.-W. Manipulation of Nanostructures in the Co-Assembly of Platinum(II) Complexes and Block Copolymers. *Chem* **2017**, *2* (6), 825–839. https://doi.org/10.1016/j.chempr.2017.04.017.

(21) Pound, G.; Aguesse, F.; McLeary, J. B.; Lange, R. F. M.; Klumperman, B. Xanthate-Mediated Copolymerization of Vinyl Monomers for Amphiphilic and Double-Hydrophilic Block Copolymers with Poly(Ethylene Glycol). *Macromolecules* **2007**, *40* (25), 8861–8871. https://doi.org/10.1021/ma0710075.

(22) Markiewicz, K. H.; Seiler, L.; Misztalewska, I.; Winkler, K.; Harrisson, S.; Wilczewska, A. Z.; Destarac, M.; Marty, J.-D. Advantages of Poly(Vinyl Phosphonic Acid)-Based Double Hydrophilic Block Copolymers for the Stabilization of Iron Oxide Nanoparticles. *Polym. Chem.* **2016**, *7* (41), 6391–6399. https://doi.org/10.1039/C6PY01558A.

(23) Zhang, X.; Wang, K.; Liu, M.; Zhang, X.; Tao, L.; Chen, Y.; Wei, Y. Polymeric AIE-Based Nanoprobes for Biomedical Applications: Recent Advances and Perspectives. *Nanoscale* **2015**, *7* (27), 11486–11508. https://doi.org/10.1039/C5NR01444A.

(24) Luo, L.; Ranger, M.; Lessard, D. G.; Le Garrec, D.; Gori, S.; Leroux, J.-C.; Rimmer, S.; Smith, D. Novel Amphiphilic Diblock Copolymer of Low Molecular Weight Poly(*N* -Vinylpyrrolidone)- *b Lock* -Poly(D , L -Lactide): Synthesis, Characterization, and Micellization. *Macromolecules* **2004**, *37* (11), 4008–4013. https://doi.org/10.1021/ma035910q.

(25) Luo, Y.; Hong, Y.; Shen, L.; Wu, F.; Lin, X. Multifunctional Role of Polyvinylpyrrolidone in Pharmaceutical Formulations. *AAPS PharmSciTech* **2021**, *22* (1), 34. https://doi.org/10.1208/s12249-020-01909-4.

(26) Benahmed, A.; Ranger, M.; Leroux, J. [No Title Found]. *Pharm. Res.* **2001**, *18* (3), 323–328. https://doi.org/10.1023/A:1011054930439.

(27) Song, T.; Gao, F.; Guo, S.; Zhang, Y.; Li, S.; You, H.; Du, Y. A Review of the Role and Mechanism of Surfactants in the Morphology Control of Metal Nanoparticles. *Nanoscale* **2021**, *13* (7), 3895–3910. https://doi.org/10.1039/D0NR07339C.

(28) Ravin, H. A.; Seligman, A. M.; Fine, J. Polyvinyl Pyrrolidone as a Plasma Expander: Studies on Its Excretion, Distribution and Metabolism. *N. Engl. J. Med.* **1952**, *247* (24), 921–929. https://doi.org/10.1056/NEJM195212112472403.

(29) Brydson, J. A. Miscellaneous Vinyl Thermoplastics. In *Plastics Materials*; Elsevier, 1999; pp 466–477. https://doi.org/10.1016/B978-075064132-6/50058-9.

(30) Aroua, S.; Tiu, E. G. V.; Ayer, M.; Ishikawa, T.; Yamakoshi, Y. RAFT Synthesis of Poly(Vinylpyrrolidone) Amine and Preparation of a Water-Soluble C_{60} -PVP Conjugate. *Polym. Chem.* **2015**, *6* (14), 2616–2619. https://doi.org/10.1039/C4PY01333F.

(31) Farias, M. A. de; Gonçalves, M. do C. Synthesis and Applications of Polystyrene-Block-Poly(N-Vinyl-2-Pyrrolidone) Copolymers. *Polímeros* **2016**, *26* (1), 1–10. https://doi.org/10.1590/0104-1428.2066.

(32) Amis, T. M.; Renukuntla, J.; Bolla, P. K.; Clark, B. A. Selection of Cryoprotectant in Lyophilization of Progesterone-Loaded Stearic Acid Solid Lipid Nanoparticles. *Pharmaceutics* **2020**, *12* (9), 892. https://doi.org/10.3390/pharmaceutics12090892.

(33) Chun, M.-K.; Cho, C.-S.; Choi, H.-K. Characteristics of Poly(Vinyl Pyrrolidone)/Poly(Acrylic Acid) Interpolymer Complex Prepared by Template Polymerization of Acrylic Acid: Effect of Reaction Solvent and Molecular Weight of Template. *J. Appl. Polym. Sci.* **2004**, *94* (6), 2390–2394. https://doi.org/10.1002/app.21176.

(34) Chun, M.-K.; Cho, C.-S.; Choi, H.-K. Mucoadhesive Drug Carrier Based on Interpolymer Complex of Poly(Vinyl Pyrrolidone) and Poly(Acrylic Acid) Prepared by Template Polymerization. *J. Controlled Release* **2002**, *81* (3), 327–334. https://doi.org/10.1016/S0168-3659(02)00078-0.

(35) Nurkeeva, Z. S.; Khutoryanskiy, V. V.; Mun, G. A.; Bitekenova, A. B.; Kadlubowski, S.; Shilina, Y. A.; Ulanski, P.; Rosiak, J. M. Interpolymer Complexes of Poly(Acrylic Acid) Nanogels with Some Non-Ionic Polymers in Aqueous Solutions. *Colloids Surf. Physicochem. Eng. Asp.* **2004**, *236* (1–3), 141–146. https://doi.org/10.1016/j.colsurfa.2004.01.026.

(36) Swift, T.; Seaton, C. C.; Rimmer, S. Poly(Acrylic Acid) Interpolymer Complexes. *Soft Matter* **2017**, *13* (46), 8736–8744. https://doi.org/10.1039/C7SM01787A.

(37) Ghaffarlou, M.; Sütekin, S. D.; Güven, O. Preparation of Nanogels by Radiation-Induced Cross-Linking of Interpolymer Complexes of Poly (Acrylic Acid) with Poly (Vinyl Pyrrolidone) in Aqueous Medium. *Radiat. Phys. Chem.* **2018**, *142*, 130–136. https://doi.org/10.1016/j.radphyschem.2017.04.019.

(38) Shuping, J.; Liu, M.; Chen, S.; Chen, Y. Complexation between Poly(Acrylic Acid) and Poly(Vinylpyrrolidone): Influence of the Molecular Weight of Poly(Acrylic Acid) and Small Molecule Salt on the Complexation. *Eur. Polym. J.* **2005**, *41* (10), 2406–2415. https://doi.org/10.1016/j.eurpolymj.2005.05.006.

(39) Ito, T.; Otani, N.; Fujii, K.; Mori, K.; Eriguchi, M.; Koyama, Y. Bioadhesive and Biodissolvable Hydrogels Consisting of Water-swellable Poly(Acrylic Acid)/Poly(Vinylpyrrolidone) Complexes. *J. Biomed. Mater. Res. B Appl. Biomater.* **2020**, *108*. https://doi.org/10.1002/jbm.b.34407.

(40) Liang, R.; You, S.; Ma, L.; Li, C.; Tian, R.; Wei, M.; Yan, D.; Yin, M.; Yang, W.; Evans, D. G.; Duan, X. A Supramolecular Nanovehicle toward Systematic, Targeted Cancer and Tumor Therapy. *Chem Sci* **2015**, *6* (10), 5511–5518. https://doi.org/10.1039/C5SC00994D.

(41) Guinaudeau, A.; Coutelier, O.; Sandeau, A.; Mazières, S.; Nguyen Thi, H. D.; Le Drogo, V.; Wilson, D. J.; Destarac, M. Facile Access to Poly(N-Vinylpyrrolidone)-Based Double Hydrophilic Block Copolymers by Aqueous Ambient RAFT/MADIX Polymerization. *Macromolecules* **2014**, *47* (1), 41–50. https://doi.org/10.1021/ma4017899.

(42) Corpart, P.; Charmot, D.; Biadatti, T.; Zard, S.; Michelet, D.; Rhodia Chimie. Method for Block Polymer Synthesis by Controlled Radical Polymerization. WO1998058974A1.

(43) Chiefari, J.; Chong, Y. K. (Bill); Ercole, F.; Krstina, J.; Jeffery, J.; Le, T. P. T.; Mayadunne, R. T. A.; Meijs, G. F.; Moad, C. L.; Moad, G.; Rizzardo, E.; Thang, S. H. Living Free-Radical Polymerization by Reversible Addition−Fragmentation Chain Transfer: The RAFT Process. *Macromolecules* **1998**, *31* (16), 5559–5562. https://doi.org/10.1021/ma9804951.

(44) Phuong Le, T.; Moad, G.; Rizzardo, E.; Thang, S. H. Polymerization with Living Characteristics. WO1998001478A1

(45) Charmot, D.; Corpart, P.; Adam, H.; Zard, S. Z.; Biadatti, T.; Bouhadir, G. Controlled Radical Polymerization in Dispersed Media. *Macromol. Symp.* **2000**, *150* (1), 23–32. https://doi.org/10.1002/1521-3900(200002)150:1<23::AID-MASY23>3.0.CO;2-E.

(46) Keddie, D. J. A Guide to the Synthesis of Block Copolymers Using Reversible-Addition Fragmentation Chain Transfer (RAFT) Polymerization. *Chem Soc Rev* **2014**, *43* (2), 496–505. https://doi.org/10.1039/C3CS60290G.

(47) Jacquin, M.; Muller, P.; Lizarraga, G.; Bauer, C.; Cottet, H.; Théodoly, O. Characterization of Amphiphilic Diblock Copolymers Synthesized by MADIX Polymerization Process. *Macromolecules* **2007**, *40* (8), 2672–2682. https://doi.org/10.1021/ma062600+.

(48) Talu, M.; Özgün, H. B. Alkaline Hydrolysis of Poly(Ethyl Acrylate) and Styrene-Ethyl Acrylate Copolymer. *Eur. Polym. J.* **1990**, *26* (1), 5–7. https://doi.org/10.1016/0014-3057(90)90088-L.

(49) Mestivier, M.; Li, J. R.; Camy, A.; Frangville, C.; Mingotaud, C.; Benoît-Marquié, F.; Marty, J.-D. Copper-Based Hybrid Polyion Complexes for Fenton-Like Reactions. *Chem. – Eur. J.* **2020**, *26* (62), 14152–14158. https://doi.org/10.1002/chem.202002362.

(50) Gineste, S.; Lonetti, B.; Yon, M.; Giermanska, J.; Sztucki, M.; Coppel, Y.; Mingotaud, A.-F.; Chapel, J.-P.; Marty, J.-D.; Mingotaud, C. Hybrid Polymeric Micelles Stabilized by Gallium Ions: Structural Investigation. *J. Colloid Interface Sci.* **2022**, 9.

(51) Loos, J.; Sourty, E.; Lu, K.; de With, G.; v. Bavel, S. Imaging Polymer Systems with High-Angle Annular Dark Field Scanning Transmission Electron Microscopy (HAADF−STEM). *Macromolecules* **2009**, *42* (7), 2581–2586. https://doi.org/10.1021/ma8026589.

(52) Mourdikoudis, S.; Pallares, R. M.; Thanh, N. T. K. Characterization Techniques for Nanoparticles: Comparison and Complementarity upon Studying Nanoparticle Properties. *Nanoscale* **2018**, *10* (27), 12871–12934. https://doi.org/10.1039/C8NR02278J.

(53) Deacon, G. B.; Phillips, R. J. Relationships between the Carbon-Oxygen Stretching Frequencies of Carboxylato Complexes and the Type of Carboxylate Coordination. *Coord. Chem. Rev.* **1980**, *33* (3), 227–250. https://doi.org/10.1016/S0010-8545(00)80455-5.

(54) Sutton, C. C. R.; da Silva, G.; Franks, G. V. Modeling the IR Spectra of Aqueous Metal Carboxylate Complexes: Correlation between Bonding Geometry and Stretching Mode Wavenumber Shifts. *Chem. – Eur. J.* **2015**, *21* (18), 6801–6805. https://doi.org/10.1002/chem.201406516.

(55) Brittain, H. G.; Richardson, F. S.; Martin, R. B. Terbium(III) Emission as a Probe of Calcium(II) Binding Sites in Proteins. *J. Am. Chem. Soc.* **1976**, *98* (25), 8255–8260. https://doi.org/10.1021/ja00441a060.

(56) Majeed, S.; Shivashankar, S. A. Novel Spherical Hierarchical Structures of GdOOH and Eu:GdOOH: Rapid Microwave-Assisted Synthesis through Self-Assembly, Thermal Conversion to Oxides, and Optical Studies. *J Mater Chem C* **2014**, *2* (16), 2965–2974. https://doi.org/10.1039/C3TC32492C.

(57) Chen, F.; Zhang, X. H.; Hu, X. D.; Zhang, W.; Zeng, R.; Liu, P. D.; Zhang, H. Q. Synthesis and Characteristics of Nanorods of Gadolinium Hydroxide and Gadolinium Oxide. *J. Alloys Compd.* **2016**, *664*, 311–316. https://doi.org/10.1016/j.jallcom.2015.12.225.

(58) Kang, J.-G.; Min, B.; Sohn, Y. S. Synthesis and Characterization of Gd(OH)3 and Gd2O3 Nanorods. *Ceram. Int.* **2015**, *41*, 1243–1248.

(59) Jia, Y.; Luo, T.; Yu, X.-Y.; Sun, B.; Liu, J.-H.; Huang, X.-J. Synthesis of Monodispersed α-FeOOH Nanorods with a High Content of Surface Hydroxyl Groups and Enhanced Ion-Exchange Properties towards As(v). *RSC Adv* **2013**, *3* (36), 15805–15811. https://doi.org/10.1039/C3RA40980E.

(60) Cotton, S. A. Lanthanides: Aryl Compounds. In *Encyclopedia of Inorganic and Bioinorganic Chemistry*; John Wiley & Sons, Ltd, 2012.

(61) Syamchand, S. S.; Sony, G. Europium Enabled Luminescent Nanoparticles for Biomedical Applications. *J. Lumin.* **2015**, *165*, 190–215. https://doi.org/10.1016/j.jlumin.2015.04.042.

(62) Buenzli, J. C. G.; Yersin, J. R. Fluorescence Spectra and Lifetime Measurements of Aqueous Solutions of Europium Nitrate and Perchlorate. *Inorg. Chem.* **1979**, *18* (3), 605–607. https://doi.org/10.1021/ic50193a017.

(63) Heffern, M. C.; Matosziuk, L. M.; Meade, T. J. Lanthanide Probes for Bioresponsive Imaging. *Chem. Rev.* **2014**, *114* (8), 4496–4539. https://doi.org/10.1021/cr400477t.

(64) Binnemans, K. Interpretation of Europium(III) Spectra. *Coord. Chem. Rev.* **2015**, *295*, 1–45. https://doi.org/10.1016/j.ccr.2015.02.015.

(65) Song, G.; Lin, Y.; Zhu, Z.; Zheng, H.; Qiao, J.; He, C.; Wang, H. Strong Fluorescence of Poly(N-Vinylpyrrolidone) and Its Oxidized Hydrolyzate. *Macromol. Rapid Commun.* **2015**, *36* (3), 278–285. https://doi.org/10.1002/marc.201400516.

(66) Supkowski, R.; Jr, W. On the Determination of the Number of Water Molecules, q, Coordinated to Europium(III) Ions in Solution from Luminescence Decay Lifetimes. *Inorganica Chim. Acta - INORG CHIM ACTA* **2002**, *340*, 44–48. https://doi.org/10.1016/S0020-1693(02)01022-8.

(67) Cotton, S. A.; Raithby, P. R. Systematics and Surprises in Lanthanide Coordination Chemistry. *Coord. Chem. Rev.* **2017**, *340*, 220–231. https://doi.org/10.1016/j.ccr.2017.01.011.

(68) Zhang, J.; Liu, Y.; Li, Y.; Zhao, H.; Wan, X. Hybrid Assemblies of Eu-Containing Polyowometalates and Hydrophilic Block Copolymers with Enhanced Emission in Aqueous Solution. Angewandte. 2012.

(69) Yu, J.; Parker, D.; Pal, R.; Poole, R. A.; Cann, M. J. A Europium Complex That Selectively Stains Nucleoli of Cells. *J. Am. Chem. Soc.* **2006**, *128* (7), 2294–2299. https://doi.org/10.1021/ja056303g.

(70) Sachs, S.; Heller, A.; Weiss, S.; Bok, F.; Bernhard, G. Interaction of Eu(III) with Mammalian Cells: Cytotoxicity, Uptake, and Speciation as a Function of Eu(III) Concentration and Nutrient Composition. *Toxicol. In Vitro* **2015**, *29* (7), 1555–1568. https://doi.org/10.1016/j.tiv.2015.06.006.

(71) Zhang, J.; Dai, L.; Webster, A. M.; Chan, W. T. K.; Mackenzie, L. E.; Pal, R.; Cobb, S. L.; Law, G.-L. Unusual Magnetic Field Responsive Circularly Polarized Luminescence Probes with Highly Emissive Chiral Europium(III) Complexes. *Angew. Chem. Int. Ed.* **2021**, *60* (2), 1004–1010. https://doi.org/10.1002/anie.202012133.

(72) Sy, M.; Nonat, A.; Hildebrandt, N.; Charbonnière, L. J. Lanthanide-Based Luminescence Biolabelling. *Chem Commun* **2016**, *52* (29), 5080–5095. https://doi.org/10.1039/C6CC00922K.

(73) Parker, D.; Yu, J. A PH-Insensitive, Ratiometric Chemosensor for Citrate Using Europium Luminescence. *Chem Commun* **2005**, No. 25, 3141–3143. https://doi.org/10.1039/B502553B.

(74) De Rosa, C.; Melchior, A.; Sanadar, M.; Tolazzi, M.; Giorgetti, A.; Ribeiro, R. P.; Nardon, C.; Piccinelli, F. Effect of the Heteroaromatic Antenna on the Binding of Chiral Eu(III) Complexes to Bovine Serum Albumin. *Inorg. Chem.* **2020**, *59* (17), 12564–12577. https://doi.org/10.1021/acs.inorgchem.0c01663.

(75) Condrau, M. A.; Schwendener, R. A.; Zimmermann, M.; Muser, M. H.; Graf, U.; Niederer, P.; Anliker, M. Time-Resolved Flow Cytometry for the Measurement of Lanthanide Chelate Fluorescence: II.

Instrument Design and Experimental Results. *Cytometry* **1994**, *16* (3), 195–205. https://doi.org/10.1002/cyto.990160303.

Chapter III

Interactions between ligands-surface gold nanoparticles and Gadolinium ions for sensing applications

I Introduction

Depending on their composition (metals, metal oxide…,) and morphology, inorganic nanoparticles (NPs) exhibit different optical, electronic or magnetic properties. In addition, their combination with well-chosen organic compound enables to develop novel properties or amplify the already existing ones.

Hence, gold nanoparticles (AuNPs) are widely popular among other NPs because they are easily synthesized and functionalized and exhibit interesting optical properties. Experimental parameters such as reaction temperature, reaction time, precursors ratio, surfactants, etc., can be adjusted to target specific shape, size or surface chemistry. Latter characteristics influence the AuNPs resulting properties and can target specific applications. AuNPs present a characteristic Surface Plasmon Resonance (SPR) band that opens their applications to sensing[1], diagnostics and photothermal treatments[2]. Moreover, the properties of individual AuNPs may differ from the collective properties obtained for AuNPs' assemblies. These collective properties are initiated by a spatial organization of AuNPs and the variation of their interparticle distance. The SPR property of AuNPs is particularly convenient to study the assembly process of the NPs, as it depends on their environment[3]. The aggregation of AuNPs may induce a change of color which can be the base of colorimetric tests and is used in the sensing domain. By analyzing the UV-visible spectra of the solution, the interactions of the particles with other species can then be identified and quantified. Various molecular ligands like small molecules, DNA, proteins and polymers can be employed to organize this assembly of AuNPs. Some stimuli-responsive chemicals can be introduced to control the aggregation process, and potentially make the system reusable.

Regarding the detection of metal ions, gold and silver nanoparticles have largely been considered as potential sensing platforms[4]. Some gold nanoparticles are designed to detect different metal ions simultaneously.[5] Zhang et al. have functionalized gold particles with 2-mercaptosuccinic acid and have tested their probe in presence of different metal cations (**Figure 73**).

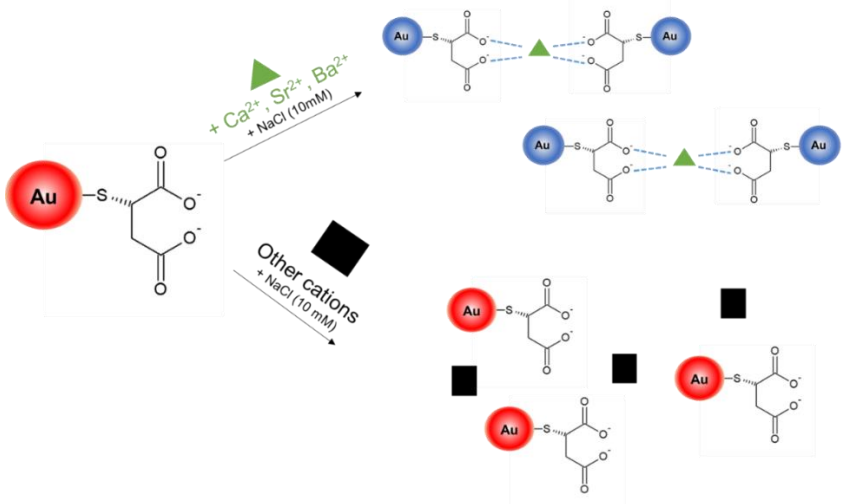

Figure 73. Scheme of the interaction between 2-mercapto succinic acid and Ca^{2+},Sr^{2+}, Ba^{2+} and other cations: Fe^{2+}, Fe^{3+},Al^{3+},Zn^{2+}, Ni^{2+}, Co^{2+}, Mg^{2+}, Cu^{2+},Pb^{2+} and Cd^{2+} [5].

The test revealed a selective detection of three cations: Ca^{2+}, Sr^{2+} and Ba^{2+}, on the thirteen cations tested. To improve the sensitivity regarding the previous three cations, a range of concentrations was applied for each of them and the degree of aggregation was then associated to precise the concentrations' values. The size of the cation seemed to influence the detection limit value, for instance barium ion is bigger and induced an aggregation process at lower concentrations than the two other cations. Gold nanoparticles can also be functionalized in a way that they interact specifically with one metal ion at a certain oxidation degree, like the chromium ion Cr (III) against the Cr (VI) specie thanks to 5,5'-dithio-bis-(2-nitrobenzoic acid)-modified gold nanoparticles[6].

Lanthanide ions have also already been titrated thanks to colorimetric methods. Hence, 1,2,3-triazole-4,5-dicarboxylic acid-functionalized gold nanoparticles (TADA@AuNPs) were used to detect selectively chromium (III) (Cr^{3+}) and europium (III) (Eu^{3+}) ions[7] among several other metal ions. These ions are interesting to titrate as Cr^{3+} acts as regulator of insulin on the control of blood sugar in human beings and Eu^{3+} are mainly used in energy field. As for previous examples, the SPR band is red-shifted when TADA@AuNPs interact with Cr^{3+} and Eu^{3+} ions and aggregate (**Figure 74**). The mechanism for binding Cr^{3+} and Eu^{3+} is explained through the interaction between the positive charges of these ions and the carboxylate groups on the surface of the TADA@AuNPS, proved by FTIR analysis and UV-visible spectra measurement. A relation between the concentration of ions and the measured shift of the SPR band can be found. These functionalized AuNPs were then considered as a colorimetric probe to detect selectively chromium and europium ions and calibration curves were available. Limits of detection were established and a final test was settled on lake water samples.

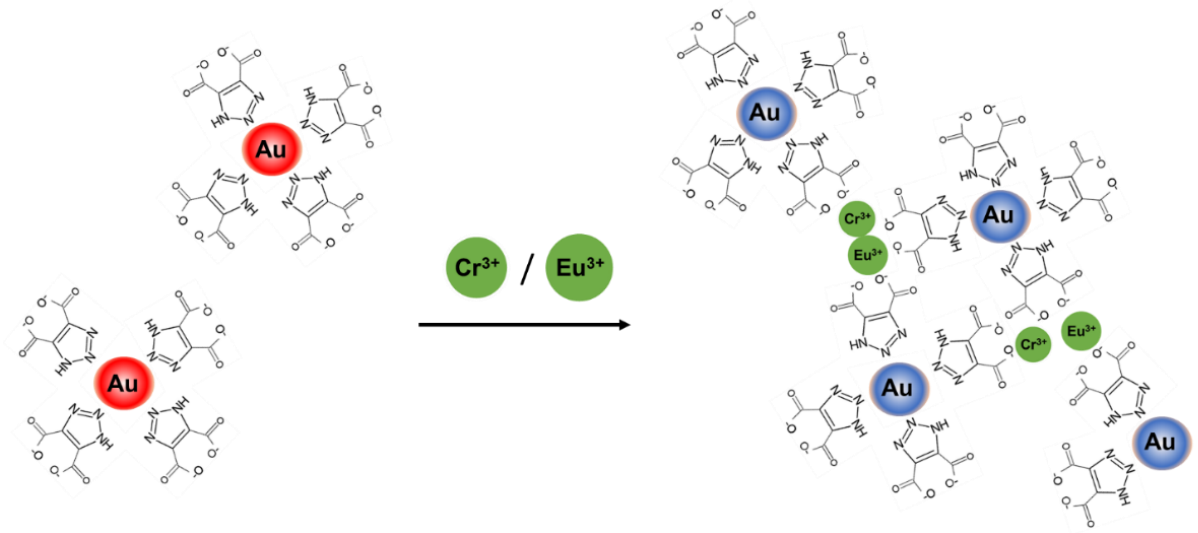

Figure 74. Scheme of the interaction between negatively charged TADA@AuNPs and Cr^{3+} and Eu^{3+} ions[7]

Among metal ions, lanthanides have seen their field of application increased in recent years, both for their catalytic, optical and magnetic properties.[8] Lanthanides have been associated to gold nanoparticles for applications in imaging field like fluorescence imaging or magnetic resonance imaging (MRI), to improve the fluorescence or the contrast of the probe system.[9] As explained in **chapter II**, most of the clinically used contrast agents (CAs) in MRI are based on the use of gadolinium molecular complexes like Dotarem®, Magnevist®… Nevertheless, developing new gadolinium-based CAs with enhanced relaxivity properties is of paramount importance. Indeed, the current CAs improve the contrast thanks to a certain quantity of gadolinium injected and the ongoing objectives are then to reduce this quantity while keeping performant contrast enhancement, because gadolinium-based CAs are accumulating in the tissues in a dangerous way.[10] Gadolinium ion (Gd^{3+}) has been proved to be toxic towards tissues, through acute toxicity, ocular irritations and intense contractibility of the muscles.[11] Besides, there is a risk of substitution of calcium ions by Gd^{3+} contributing to cellular reactions and leading then to possible diseases.[12] There is an urgent need to evaluate the potential quantity of these free gadolinium ions in contrast agents 'preparations.

Indeed, new structures of CAs are based on ionic state of gadolinium to improve its hydration level and enhance thus relaxivity performances. The **chapter II** was dealing with the design of these Hybrid Polyionic Complexes (HPICs) based on ionic interactions between Gd^{3+} and an ionizable block copolymer. Latter structures have proved their efficiency as potential MRI CAs, with two kind of block copolymers PAA-*b*-PEG [13] and PAA-*b*-PVP (**chapter II**). To ensure a non-toxicity of these structures, a titration by ICP-MS of free Gd^{3+} was realized after a filtration process of the HPICs sample, on the filtrate sample and showed non-significant quantity of Gd.

In addition, cytotoxicity assays were performed, and showed no relevant toxicity in agreement with the ICP-MS results. Various methods can be employed to detect and quantify Gd^{3+} ions[14], but latter procedures can be difficult to implement and are both time and money consuming. For this purpose, the idea of a bench test to evaluate rapidly if some gadolinium is present in the samples, arises.

This routine test should be easy to implement and gives rapidly an answer about the presence of Gd^{3+} ions. As stated above, AuNPs represent suitable sensing probes in that context. Their functionalization with proper ligands and their interactions with ions of interest might lead to an aggregation process, revealed by a color change of the solution. Its quantification via UV-visible spectroscopy should enable to know if Gd^{3+} ions are present and to estimate roughly the concentration in the studied sample. This test can be useful for CAs preparation containing Gd^{3+}, as a first estimation before launching heavier procedures of quantification.

Objectives

The main objective of the following work is to identify and to understand the interactions between the ligands located on the surface of the gold nanoparticles (AuNPs) and the gadolinium ions (Gd^{3+} ions). Once the mechanism is well understood, the control of those interactions could be applied to settle a colorimetric test for the detection of Gd^{3+} ions in systems like contrast agents' preparations.

First, a ligand prone to interact with lanthanide ions and particularly Gd^{3+} ions must be chosen and defined as the receptor specie in the sensing method. Furthermore, this ligand must be able to bind to AuNPs to ensure the colorimetric involvement, thanks to plasmonic properties. An easy synthesis protocol must then be inquired to design AuNPs functionalized with this specific ligand. Once, the synthesis process established, the functionalized AuNPs must be characterized through different techniques like UV-visible spectroscopy, Dynamic Light Scattering (DLS) for the size and the zeta potential of the particles, as well as the Transmission Electron Microscopy (TEM).

The understanding of the interaction mechanism between AuNPs and Gd^{3+} must be engaged through different techniques such as UV-visible spectroscopy to confirm a prospective interaction between the two species through absorbance changes, particularly SPR band shifts. Quartz Crystal Microbalance with Dissipation monitoring (QCM-D) technique will be used to characterize more precisely the interactions existing at gold surface.

The design of the colorimetric test should comprise a calibration step and an exploration of the limits of detection and of the error range. Finally, test phases would be investigated to evaluate its potential application regarding CAs' preparation.

II Synthesis and characterization of the functionalized gold nanoparticles

This first section is consecrated to the synthesis of citrate-stabilized gold nanoparticles using a very well-known process published by Turkevich et al.[15] and to the ligand-exchange process used to produce new functionalized gold nanoparticles.[16] Latter new functionalized gold nanoparticles are then characterized and compared to the citrate-stabilized AuNPs through different techniques such as Dynamic Light Scattering (DLS), UV-visible spectroscopy and Transmission Electron Microscopy (TEM).

II.1 Synthesis of citrate stabilized gold nanoparticles

Here in order to have access to gold nanoparticles (AuNPs) with controlled morphology and functionalization, we decided to synthesize 20 nm AuNPs according to the Turkevich and Frens method[15,17]. The synthetic protocol of these nanoparticles noted as AuNP@citrate is detailed in the experimental part section.

The obtained AuNP@citrate nanoparticles were analyzed through UV-visible spectroscopy. A surface plasmon resonance (SPR) band is clearly visible with a maximum absorbance at λ = 522 nm[3]. An estimation of the diameter of the AuNPs can be obtained from the ratio of the absorbance measured at the maximum of the peak to the one at λ = 450 nm as detailed in **Figure 75**[18]. From the measured ratio value of A_{522nm}/A_{450nm} equal to 1.68, an average diameter of 17 nm can be estimated[18]. A similar size was found by Transmission Electron Microscopy (TEM) shown in **Figure 76**.

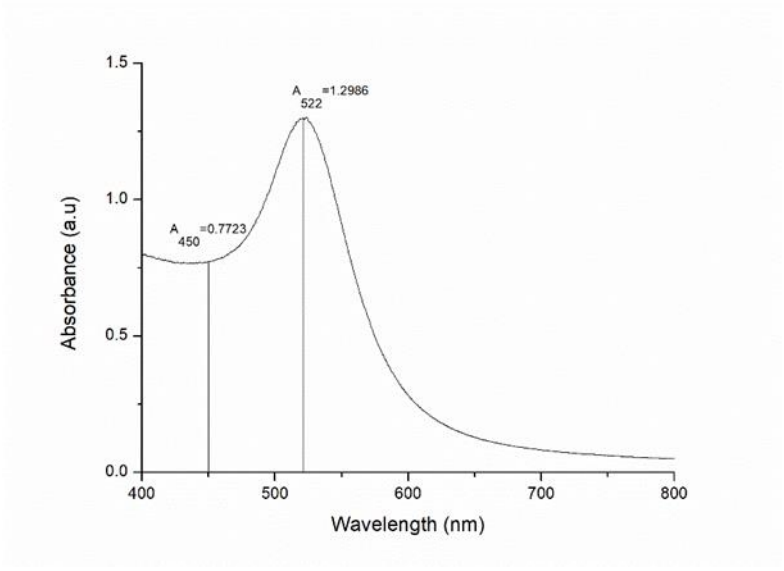

Figure 75. UV-visible Spectra of AuNP@citrate ([Au]=0.28mM)

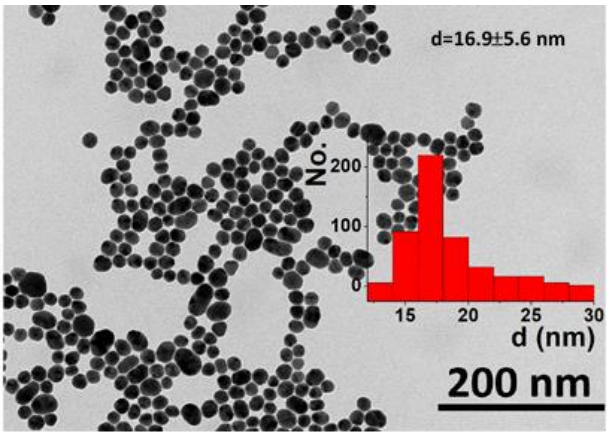

Figure 76. TEM micrograph of AuNP@citrate nanoparticles and corresponding size (inset)

AuNP@citrate nanoparticles were analyzed by Dynamic Light Scattering (DLS) technique and an intensity-averaged hydrodynamic diameter equal to D_H=31±11 nm was obtained. Latter value is higher than TEM obtained diameter value, which is consistent with the fact that DLS technique measures hydrated particle diameter, contrary to UV-visible or TEM techniques that measure naked particle diameter. A zeta potential equal to ξ=-35±3 mV was found evidencing as expected a negative surface charge of the NPs.

II.2 Synthesis of Bis(p-sulfonatophenyl)phenylphosphine functionalized gold nanoparticles (AuNP@BSPP)

Albeit the convenience and reproducibility of the citrate-stabilized nanoparticles synthesis, the resulted colloidal solution displays poor stability due to the weak binding of the citrate ions to the gold surface. This weak interaction between ligands and gold surface has thus led to ligand replacement in presence of lanthanide salts[19]. This is of paramount importance to find a ligand able to be bound in a stronger way with gold surface and to bear negative charge to interact with lanthanides ions and particularly gadolinium ions.

The Bis(p-sulfonatophenyl)phenylphosphine (BSPP) ligand is commercially available and bears two sulfonate anionic groups of low basicity, the nanoparticles are consequently strongly negatively charged (**Figure 77**).

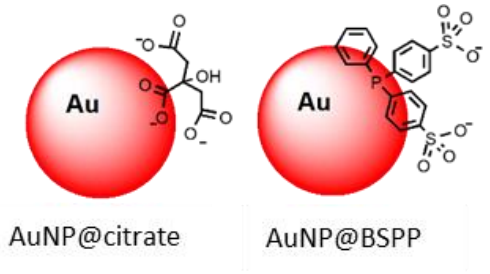

Figure 77. Schematic representation of AuNP@citrate (left) and AuNP@BSPP (right)

In addition, the interaction with the surface of the gold nanoparticles is ensured by the phosphine group whose interaction strength is higher than the electrostatic interaction between AuNPs and citrate. AuNP@BSPP were thus exploited by C. J. Loweth to establish efficient functionalization of AuNPs with ssDNA[20]. AuNP@BSPP remain stable even for high nanoparticles concentrations and keep their red wine color. Another advantage of using BSPP as capping agent is the ability to easily redisperse AuNP@BSPP precipitated by the addition of salt or by centrifugation[21]. Despite the large use of AuNP@BSPP, there is no study concerning their behavior in the presence of lanthanide ions, so far.

With a view to compare to AuNP@citrate nanoparticles and to confirm the ligand exchange at the gold nanoparticles' surface, UV-visible spectroscopy, DLS and TEM analysis are engaged. A slight increase of the maximum absorbance of the SPR band peak from λ = 522 to 523 nm is observed upon addition of the phosphine ligand due to changes of the dielectric environment around nanoparticles (**Figure 78.A)**[3,22]. An average diameter of 17.2 ± 4.0 nm is measured from TEM images (**Figure 78.B**) in good agreement with pristine AuNP@citrate.

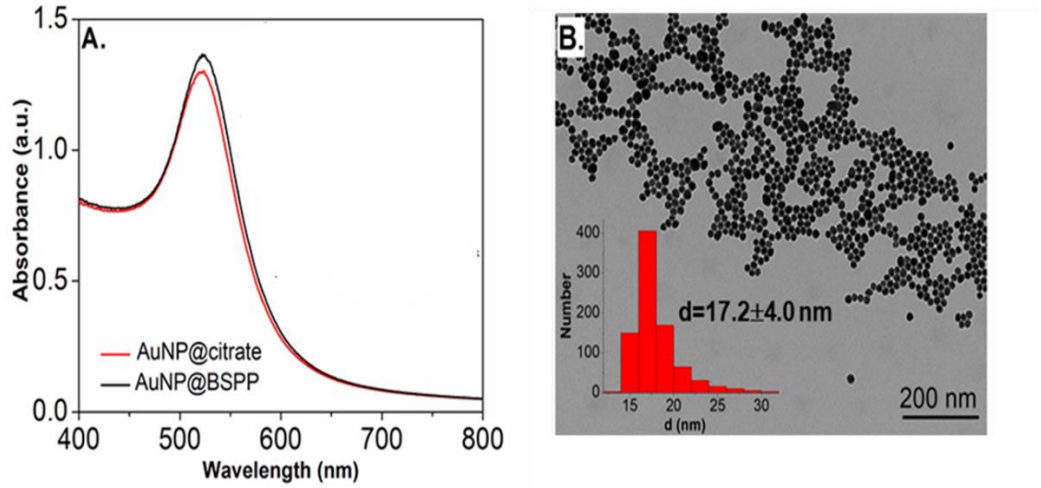

Figure 78. (**A**) UV-visible of AuNP@citrate (red curve) and AuNP@BSPP (black curve). ((Au]=0.28mM) (**B**) Transmission electron microscopy image of AuNP@BSPP and the respective size distribution histogram (inset).

In addition, the efficiency of ligand exchange is assessed from DLS and by sedimentation field-flow fractionation (SdFFF) measurements (see **Figure 79** and **Figure 80**). A small peak is observed in DLS at sizes lower than 5 nm due to rotational diffusion of particles[23]. AuNP@BSPP are now fully characterized and compared to pristine AuNP@citrate nanoparticles. Ligand exchange process has been effectively realized according to zeta potential measurements, UV-visible spectra and SdFFF analysis.

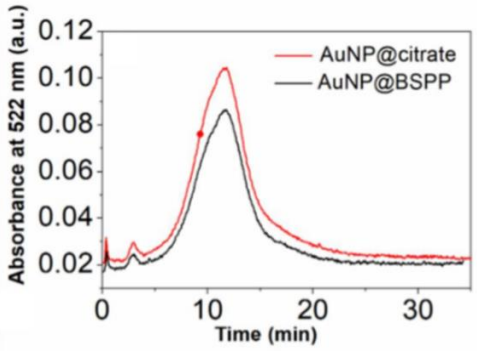

Figure 79. SdFFF chromatogram of AuNP@citrate and AuNP@BSPP, respectively

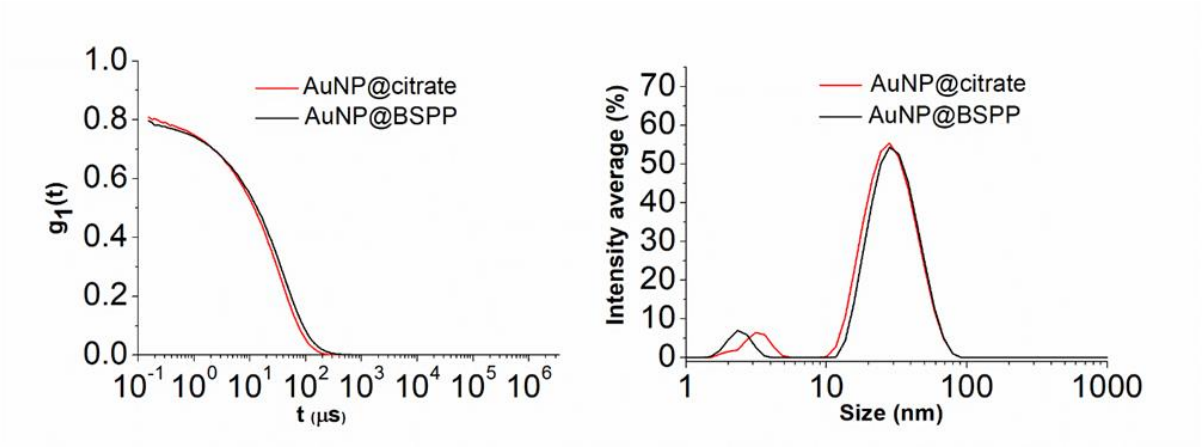

Figure 80. Correlogram functions (left) and intensity-averaged hydrodynamic diameter distribution (right) estimated from dynamic light scattering measurements of AuNP@citrate (red curve) and AuNP@BSPP (black curve) for a gold concentration of ca. 0.28 mM estimated in gold ions.

To further evidence the negative charge of AuNP@BSPP nanoparticles, zeta potential measurements were made and compared to AuNP@citrate one. (**Figure 81**). Zeta potential of AuNP@citrate and AuNP@BSPP solutions are ξ=-35±3 mV and ξ=-40±5mV respectively.

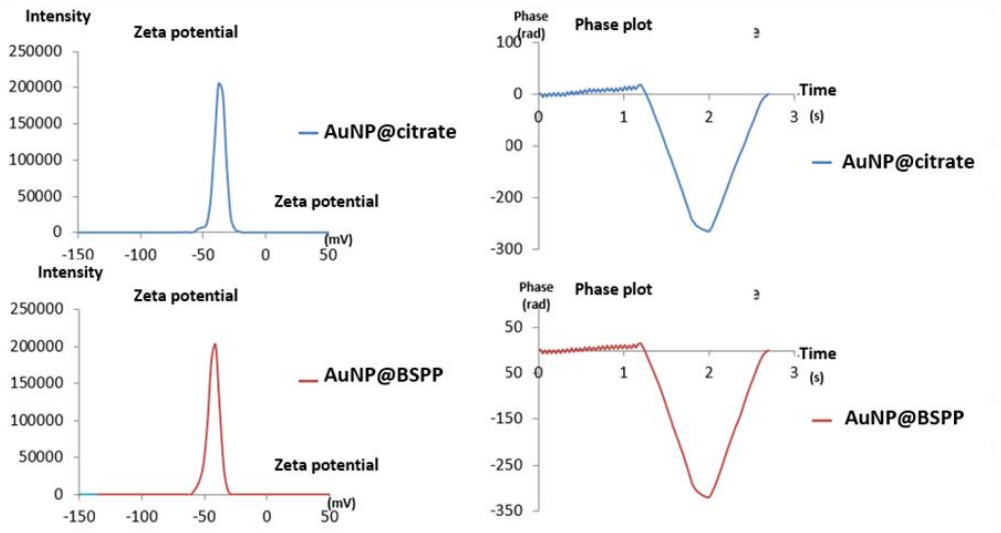

Figure 81. Zeta potential and corresponding phase plot for AuNP@citrate and AuNP@BSPP ([Au]=0.28mM)

III Colorimetric observations and kinetic investigation upon the aggregation process of AuNPs interacting with ions

Following part is devoted to the study of the behavior of the previously synthesized functionalized AuNPs in presence of Gd^{3+} ions. As detailed in the first part of this chapter, colorimetric observations should indicate whether an environmental change of the AuNPs happens or not. A first phase of observation is investigated upon the addition of Gd^{3+} ions on AuNP@BSPP nanoparticles and AuNP@citrate as well, for comparison. On a second time, it will be necessary to characterize those observations from a kinetic and mechanistic point of view.

III.1 Colorimetric assay and qualitative evaluation of Gd^{3+} ions concentration

In order to assess the possibility for AuNP@BSPP to interact with Gd^{3+} ions, increasing concentrations of Gd^{3+} are added onto AuNP@BSPP solutions. As depicted in **Figure 82**, latter addition of Gd^{3+}, from 2 to 60 µM, to AuNP@BSPP induce a progressively color change from red to blue. However, no color change is observed when the same range of Gd^{3+} concentrations is added to AuNP@citrate. The solution color change is directly linked to the aggregation state of the AuNPs. As explained at the beginning of this chapter, colorimetric tests are based on this visual indication to know about the dispersion of the AuNPs in solution. The bigger the resulting assembly of AuNPs is, the more shifted the SPR band is towards infra-red wavelength domain, revealed by a blue color of the solution. On the contrary, AuNP@citrate nanoparticles seem to save their aggregation state, represented only with a red color, characteristic of well-dispersed gold nanoparticles.

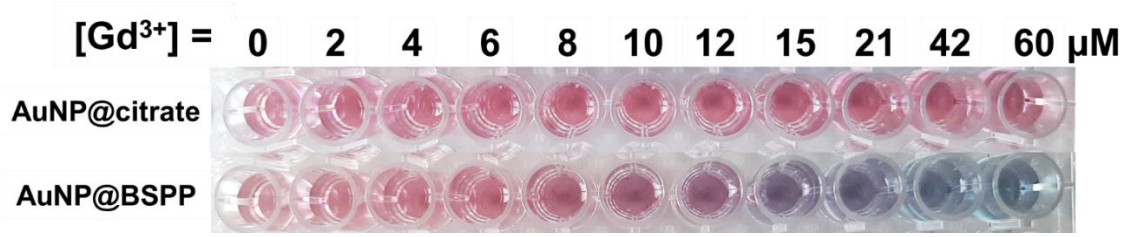

Figure 82. Photographs showing the color response of AuNP@citrate (first line) and of AuNP@BSPP (second line) solutions after incubation with increasing concentrations of Gd^{3+}. Both AuNPs solutions were used at the same concentration of 0.14 mM gold ions or circa 1 nM AuNPs of 17 nm in size.

In order to understand the behavior of AuNP@citrate nanoparticles, it was decided to pursue this test by introducing higher gadolinium ions concentration on those nanoparticles, i.e. until 300 µM. (**Figure 83**)

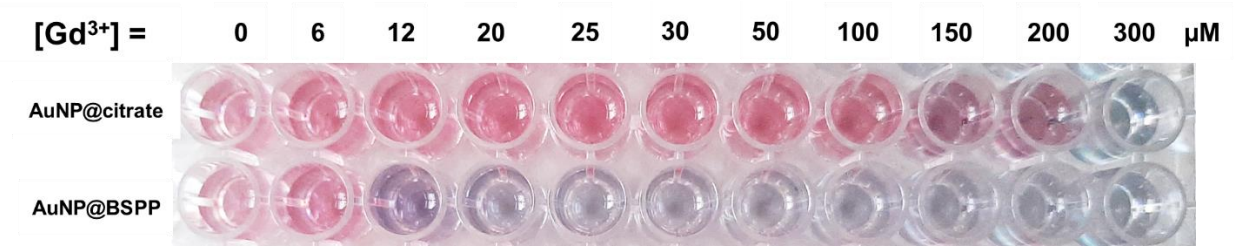

Figure 83. Photographs showing the color response of AuNP@citrate and AuNP@BSPP after incubation with increasing concentration of Gd^{3+}. Both AuNPs solutions were used at the same concentration of 0.14 mM gold ions or circa 1 nM AuNPs of 17 nm in size.

On this new range of concentrations, AuNP@citrate seem to be sensitive to Gd^{3+} ions from 100 µM, according to the color of the solution. Therefore, AuNP@BSPP has a sensing limit for Gd^{3+} ions significantly lower than AuNP@citrate. It questions then about the mechanism involved in this interaction between Gd^{3+} ions and AuNPs. For that purpose, the study of the evolution in time of the absorbance spectra was carried out at those same concentrations of Gd^{3+}. In agreement with the visual observation, the wavelength corresponding to the maximum of the peak is progressively red-shifted from 523 nm up to 636 nm for concentration of Gd^{3+} increasing from 0 to 60 µM (**Figure 84**), whereas concerning the AuNP@citrate no significate wavelength shift is observed even after 4 hours of incubation. Indeed, the study of the evolution of the absorbance spectra was conducted during 4 hours revealing a temporal change related to a kinetic of aggregation for each concentration. The kinetic for AuNP@BSPP is presented in **Figure 85.** Brut absorbance spectra of every concentration of Gd^{3+} ions introduced are shown for 4 hours (**Figure 85.A**) and normalized absorbance spectra as well (**Figure 85.B**).

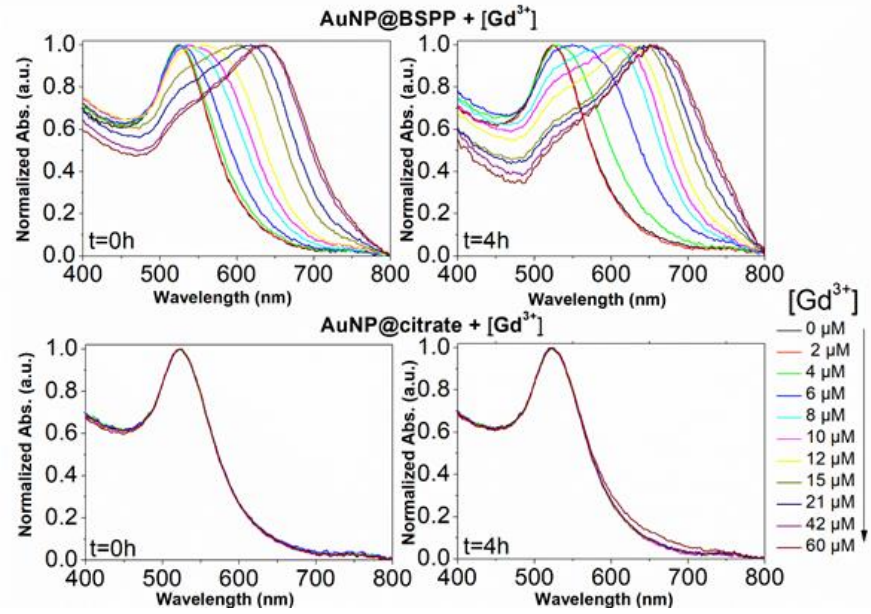

Figure 84. The evolution of UV-Visible spectra of AuNPs with the addition of increasing concentrations of Gd^{3+} at initial time and after 4h. On the top spectra of AuNP@BSPP and on the bottom for Au@citrate for a concentration of AuNPs of ca. 0.14 mM estimated in gold ions.

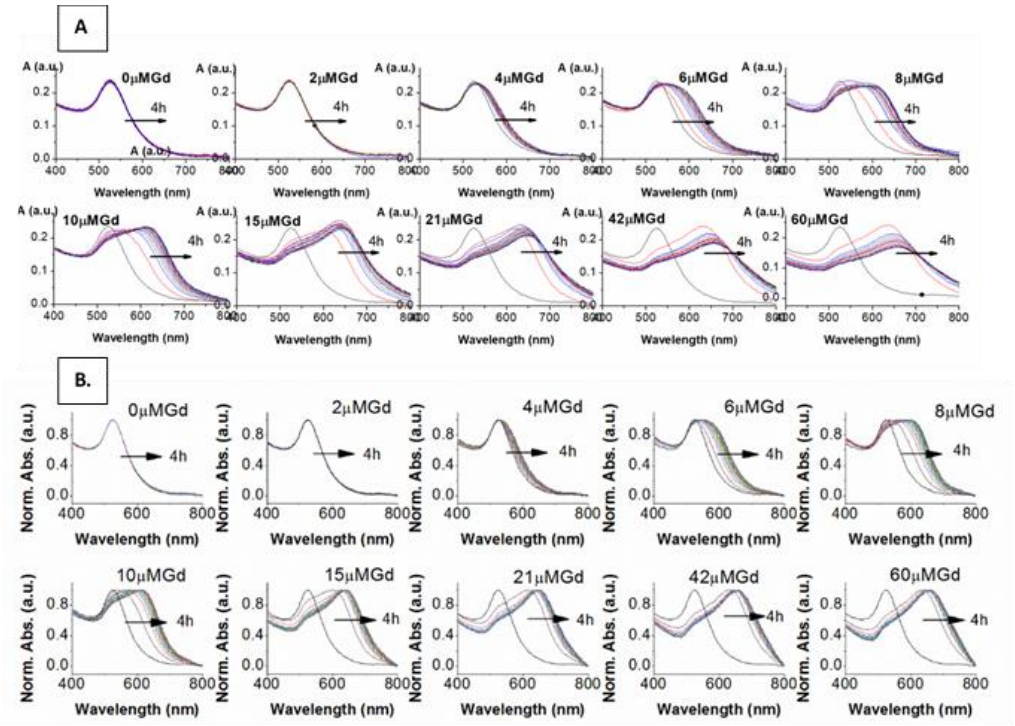

Figure 85. Evolution of the UV-vis spectra as a function of time for AuNP@BSPP upon addition of increasing concentration of Gd^{3+} (measurement time interval 15 minutes for a period of 4h). Gold concentration of ca. 0.14 mM estimated in gold ions. (**A**) Brut absorbance spectra and (**B**) Normalized absorbance spectra.

This first qualitative approach enables to understand the difference of behaviors of the two kind of AuNPs regarding Gd^{3+} ions. AuNP@BSPP represent a probe able to detect very low quantity of Gd^{3+} ions, i.e. µM order of concentration. Both synthesis and use of AuNP@BSPP are easy to investigate and lead to a simple method to evaluate Gd^{3+} ions concentration in a sample. The color represents a good indicator for the range of concentrations concerned, but does not give precise value. Latter method was until now only qualitative, and needed to be further performed to become a quantitative sensing process.

III.2 Quantitative estimation of gadolinium ions concentration by calculations of aggregation parameters

In order to analyze quantitatively these results, we further used the semiempirical spectroscopic flocculation parameter (FP) as described by Maya et al.[24]. The flocculation parameter is defined as follow. First, the UV-visible spectra of the AuNPs and those registered at different concentrations of Gd^{3+} and different times of incubation were normalized to the intensity of the surface plasmon resonance (SPR) wavelength. Then, the integrated absorption between wavelength limits 600 and 800 nm of original spectra of AuNPs was subtracted from those calculated for the spectra of interest (**Figure 86**).

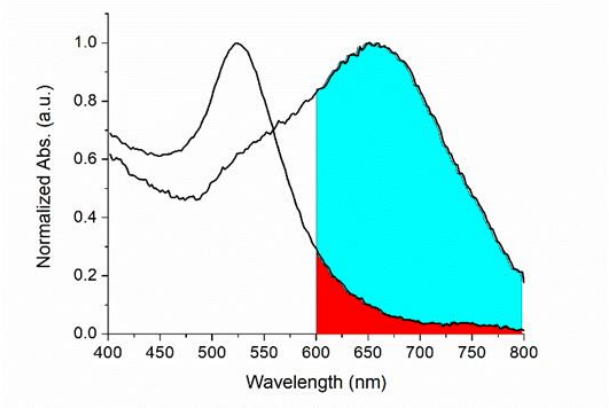

Figure 86. Normalized UV-visible spectra of AuNP@BSPP after and before the incubation with 60 μM of Gd^{3+} and the representation of the corresponding integrated areas for the subsequent calculation of the flocculation parameter. The blue part corresponds to the flocculation parameter.

FP value represents the degree of aggregation of the AuNPs induced by a certain concentration of Gd^{3+} ions at a certain time after the addition of the ions. The higher the value of FP, the more aggregated the AuNPS are in solution, which is represented by a larger red-shift of the SPR band and a blue tendency color. Calibration curves are then step by step built up with these FP values. **Figure 87** illustrates the time dependence of the FP value of AuNP@BSPP at different concentrations in Gd^{3+} ions. AuNP@BSPP aggregation increase with time to reach a plateau and at increasing rates with the Gd^{3+} concentration. The experimental kinetic data were analyzed by fitting the flocculation parameter by a monoexponential equation (1)

$$FP = FP_{max}\ (1 - \exp(-t/\tau_F\ )) \quad (1)$$

where FP_{max} represents the plateau value and τ_F is a characteristic time describing the aggregation kinetic[25].

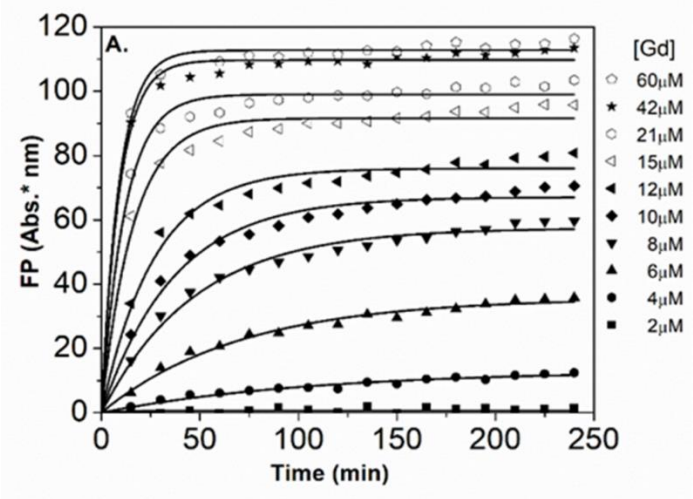

Figure 87. Time dependence of the FP of AuNP@BSPP plotted for increasing concentrations in Gd^{3+} together with the best fit to eq. 1

The evolution in time of the FP values clearly indicates a two-step mechanism. First FP values are increasing rapidly according to the Gd^{3+} ions concentration present in the solution. The second step starts when the FP value becomes constant with time, exposing a no more evolving aggregation state from a kinetic point of view. This plateau is attained faster and faster when the concentration of Gd^{3+} ions increases. To have access to this rate of aggregation, the data extracted from the fit with **Eq. (1)** are used as follow.

$$\text{Aggregation Rate (Abs.*nm*min}^{-1}) = -FP_{max}/\tau_F$$

Aggregation rates, i.e. maximum slopes, are thus reported for every concentration of Gd^{3+} ions and are shown in **Figure 88** (blue dots)[26]. A second parameter is also retained to describe the aggregation mechanism according to the concentration of Gd^{3+} ions, this is the flocculation parameter value calculated after 4 hours of incubation. As a time-dependence is identified regarding FP value, a correct quantification of Gd^{3+} ions concentration must be done by referring to a permanent state of aggregation, i.e. when the plateau is attained by FP values. Hence, calibration curve to find precise gadolinium ions value is established on FP values at 4 hours (**Figure 88** black dots).

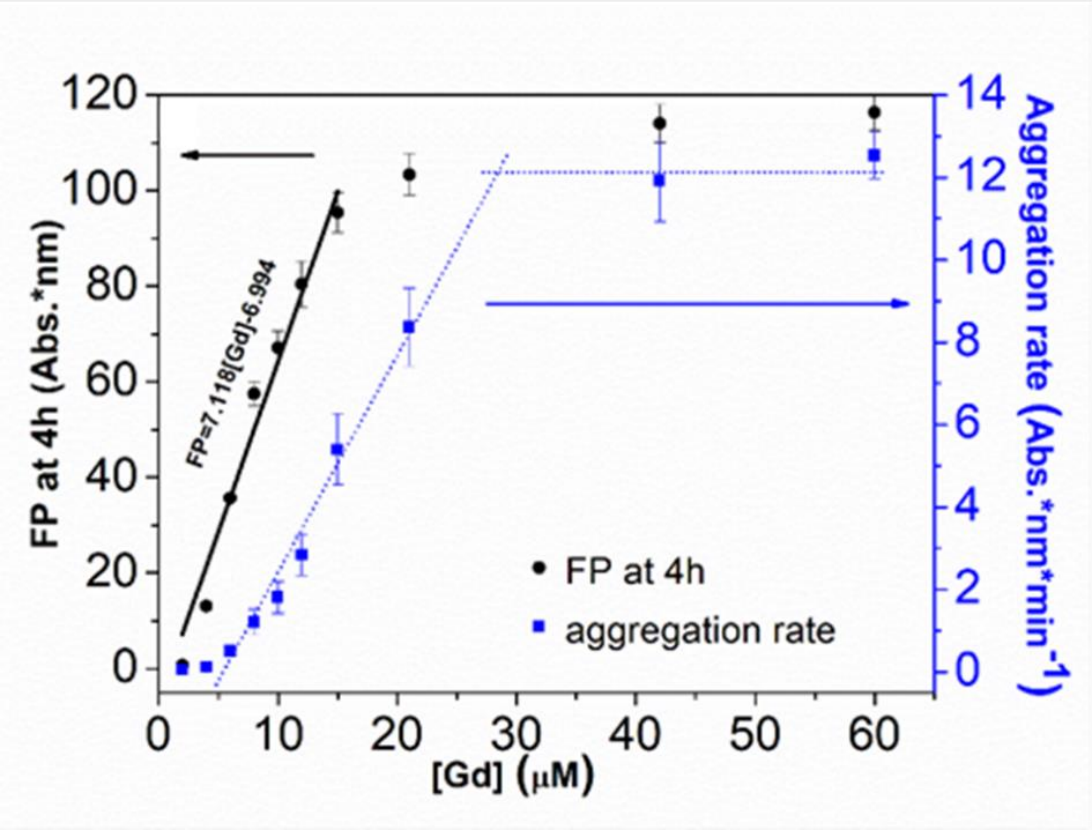

Figure 88. Corresponding FP at 4h (black dots) and aggregation rate (blue dots) plotted vs. concentrations of Gd^{3+} ions.

Regarding the black dots (**Figure 88**), a continuous increase is observed when the concentration of Gd^{3+} is varied from 2 to 18 µM. These results evidence the high detection capacity of AuNP@BSPP for considerably low Gd^{3+} ions' concentrations and could be easily exploited to develop a colorimetric test. The validation of this approach to determine gadolinium content was carried out following the recommendations of standard ISO 5725 and 17025. The equation of the calibration curve is given by:

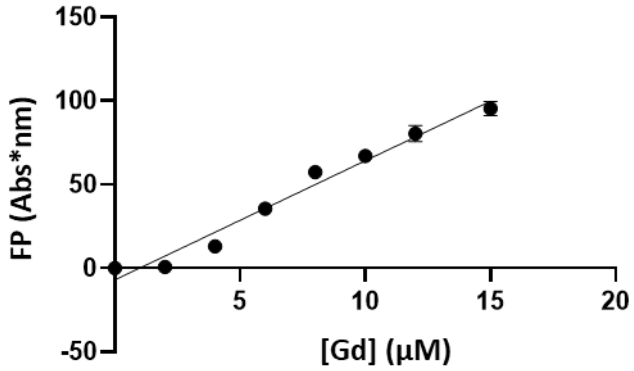

$FP = a + b \times [Gd]$

with a linear correlation coefficient r^2 equal to = 0.974

$a = -6.994$ and $s_a = 4.096$

$b = 7.118$ and $s_b = 0.478$

This calibration line will be used in the last part of this article. The limits of detection and of quantification were calculated from these values as:

$[Gd]_{LD} = (a + 3 \times s_a)/b = 0.74$ µM and $[Gd]_{LQ} = (a + 10 \times s_a)/b = 4.76$ µM

$FP_{LD} = a + 3 \times s_a = 5.27$ nm and $FP_{LQ} = a + 10 \times s_a = 33.90$ nm

The repeatability of the method is estimated from a series of nine independent measurements. The coefficient of variation (CV) of repeatability was calculated from those nine measurements that lead to the determination of the respective FP values: 22.77, 21.22, 21.89, 22.80, 20.78, 22.11, 24.83, 18.14 and 19.99 with a mean of 21.62 nm and a corresponding standard deviation equal to 1.90. CV= 1.90/21.62*100=8.8%. The standard deviation on gadolinium concentration values obtained from calibration curve for a sample with unknown concentration of gadolinium was evaluated by using the following equation:

$$s_c = \frac{s_r}{b}\sqrt{\frac{1}{M} + \frac{1}{n} + \frac{(\overline{y_c} - \overline{y})^2}{b^2 . \Sigma (x - \overline{x})^2}}$$

with M the number of repetitions for the unknown sample, n the number of points used to establish the calibration curve (here n=9), y and x represent the coordinates of the point in the calibration line, $s_r^2 = s_b^2 * (\sum (x - \langle x \rangle)^2$, y_C is equal to the value of FP estimated on the sample with unknown concentration of gadolinium.

The blue dots (**Figure 88**) confirm the observations made on **Figure 87** about an increase of the aggregation rate value with increasing concentrations of Gd^{3+}. This tendency is stopping over a concentration of 28 µM. Beyond this concentration, the aggregation rate reaches a plateau and becomes constant. The observed aggregation of AuNP@BSPP may reflect the well-known process of coagulation induced by the addition of electrolytes. This process described by the DLVO theory predicts, as observed here, a slow and fast aggregation regime. The threshold salt concentration needed to induce rapid aggregation (here 28 µM) is referred as the critical coagulation concentration (CCC)[27]. Schulze–Hardy rule demonstrates a relationship between CCC of colloids and the valence of extra counter ionic electrolytes (z)[28]. Accordingly, divalent and trivalent ions are much more capable of causing precipitation of colloids from their suspensions than the monovalent ones.

III.3 Evaluation of the interactions of gold nanoparticles with other metal cations

As stated previously, the valence of the extra counter ionic electrolytes has been proved to influence the critical coagulation concentration (CCC) value. In order to find out such behaviors and to have more insights into the aggregation process of AuNP@BSPP, the influence of the valence of cations onto the relative aggregation rate was further studied. In addition to Gd^{3+} ions the influences of Ca^{2+} divalent and Na^{+} monovalent ions were investigated.

As for the Gd^{3+} ions, increasing concentrations of cations were added on AuNP@BSPP and AuNP@citrate nanoparticles. Range of concentrations necessary to induce the aggregation were found to be higher than for the trivalent ions, as expected according to Schulze-Hardy rule. It was essential to find the range of concentrations revealing a progressive color change for AuNP@BSPP solutions, to further investigate the study of aggregation rate and flocculation parameter. (**Figure 89**)

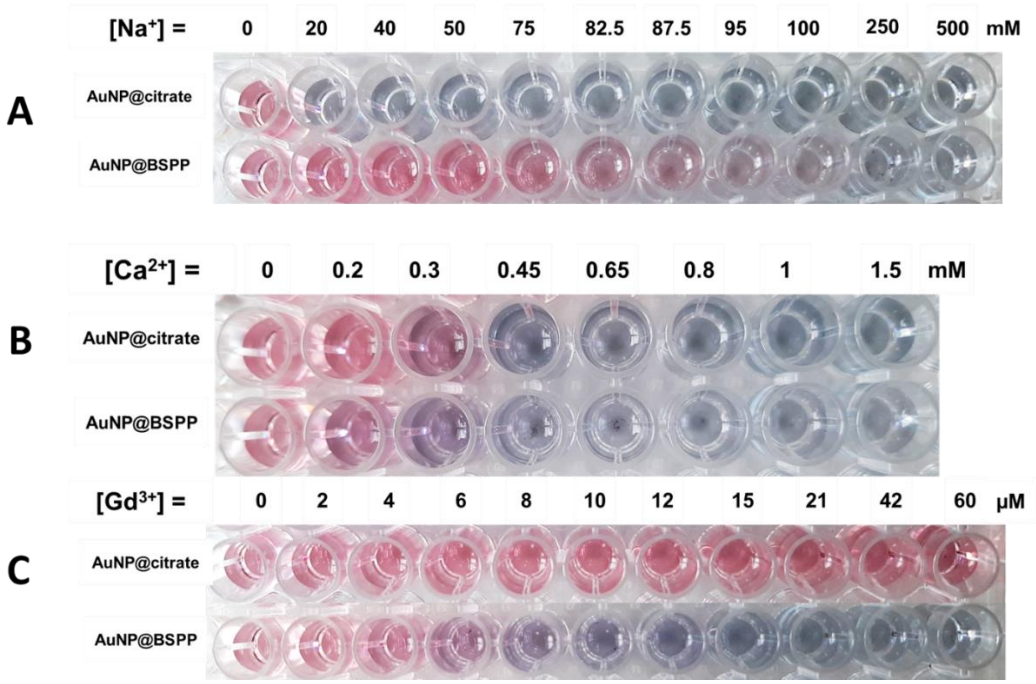

Figure 89. Photographs showing the color response of AuNP@citrate and AuNP@BSPP after incubation with increasing concentration of Na^+ (A), Ca^{2+} (B) and Gd^{3+} (C), respectively.

Absorbance study was then applied onto both of Na^+ and Ca^{2+} ions during 4 hours with a spectrum recorded every 15 minutes. Latter data were used in the same way as for Gd^{3+} ions through the calculation of flocculation parameter with time-dependence and for every concentration tested. The effect of the concentration of these different cations on the relative aggregation rate is depicted in **Figure 90**.

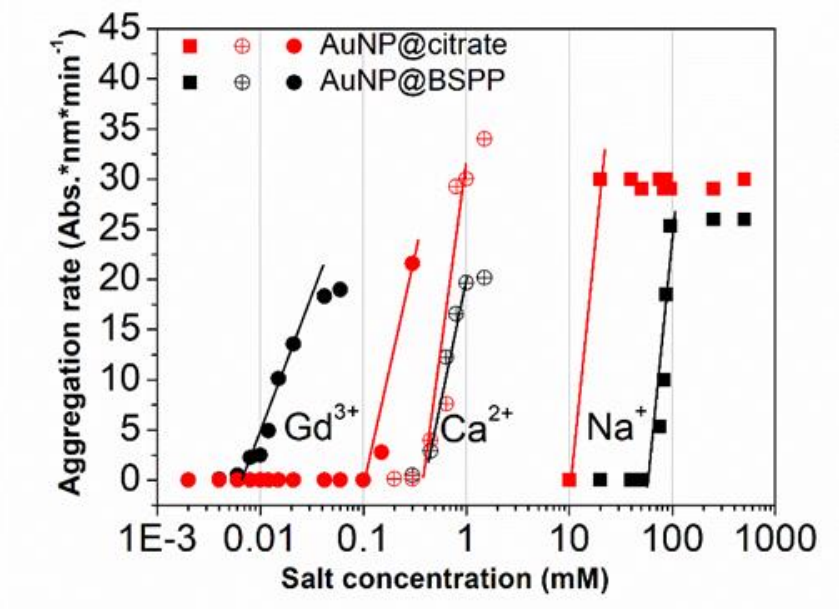

Figure 90. Comparison of aggregation behavior of AuNP@BSPP (black plot) with the one of AuNP@citrate (red plots) in the presence of mono, di and trivalent cations (Na^+, Ca^{2+} and Gd^{3+} respectively).

This aggregation process is compared to the one of AuNP@citrate. For the three ions and for both types of NPs the characteristic slow and fast aggregation regimes were evidenced. Moreover, the values of CCCs lies between 10 and 100 mM for Na^+ ions, around 1 mM for Ca^{2+} ions and between 0.01 and 0.1 mM for Gd^{3+} ions. The CCCs which separate the two regimes decrease in order of monovalent, divalent and trivalent ions which is in agreement with the Schulze–Hardy rule[27].

For the monovalent Na^+ ions, the CCC for AuNP@BSPP is higher than the value for AuNP@citrate: 100 mM and 50 mM respectively. This difference reflects the higher negative charge of AuNP@BSPP (zeta potential ξ=-40±5mV) compared with the one of AuNP@citrate (zeta potential ξ=-35±3mV). This is in agreement with an aggregation mainly induced by the compression of the electrical double layer of the NPs. For the divalent ions the same CCCs were observed for the two kind of NPs, indicating a stronger adsorption of divalent ions to the surface[27]. Noteworthy, this tendency is reversed for Gd^{3+} ions. The CCC of AuNP@BSPP of 0.03 mM is one order of magnitude lower than for the AuNP@citrate (0.3 mM). This reversed trend could be attributed to a specifically and more effective interaction of the Gd^{3+} ions with the negatively sulfo-groups stabilizing the AuNP@BSPP than with the citrate groups stabilizing the AuNP@citrate[29].

AuNP@BSPP nanoparticles are able to interact with other cations than Gd^{3+} and could then be used as sensing probe towards those species. Moreover, the observed behaviors confirmed rules like the Schulze-Hardy one. This colorimetric method was proved to be reproducible and showed both low limits of detection and quantification of Gd^{3+} ions. In order to understand the difference observed between AuNP@BSPP and AuNPcitrate regarding Gd^{3+} ions, additional characterizations were performed, to have more insights on the interactions existing between Gd^{3+} ions and AuNPs.

IV Study of the interactions between gadolinium ions and AuNP@BSPP

There is an interaction between gadolinium (Gd^{3+}) ions and AuNP@BSPP nanoparticles, inducing a progressive aggregation process by increasing the concentration in lanthanide ions. As demonstrated before, the range of sensitivity of AuNP@BSPP is one order of magnitude lower than the AuNP@citrate one (CCC=0.03 mM and 0.3 mM respectively), revealing a different mechanism of interaction. Both the large size of AuNPs leading to low molecular tumbling of the ligands together with the paramagnetic character of Gd^{3+} ions do not allow an easy study of these systems by NMR[30]. In order to have more details on the interaction phenomenon between AuNPs and Gd^{3+} ions, complementary studies using quartz crystal microbalance with dissipation monitoring (QCM-D) technique were performed.

IV.1 Quartz crystal microbalance (QCM) measurements

QCM-D is a powerful analytical strategy for characterizing the adsorption of molecules on 2D surfaces[31] and it was already successfully used to study colloidal nanoparticles solutions[32,33]. With a possibility to detect mass changes as low as 1 ng.cm^{-2}, QCM-D was especially used to probe the interaction with macromolecules, such as proteins, nucleic acids, lipid bilayers, bacteria, polymers[32–37]. Scarcely are the studies with low molecular weight molecules often caused by either a low grafting density, limited binding affinity, or a combination of these factors[38]. However, the adsorption of fluorescein-5-Isothiocyanate onto gold surfaces passivated either with citrate or with BSPP[38] and the detection of Cu^{2+} ions[39] were recently studied through QCM-D sensing experiments.

Despite the similarity of the functionalized nanoparticles in terms of size, negative charge and absorbance ability, the two ligands, citrate and BSPP, may differ in their behavior approaching the gold surface. In the view of clarifying those interactions, first QCM-D experiments were focused on the interaction of citrate and BSPP with bare gold surface. Solutions of citrate (24 mM in water, pH 5.5) and BSPP (24 mM in water, pH 6.5) were deposited at a flow rate of 40 µL·min^{-1}. A decrease in frequency is observed suggesting the attachment of both molecules on the gold surface (**Figure 91**).

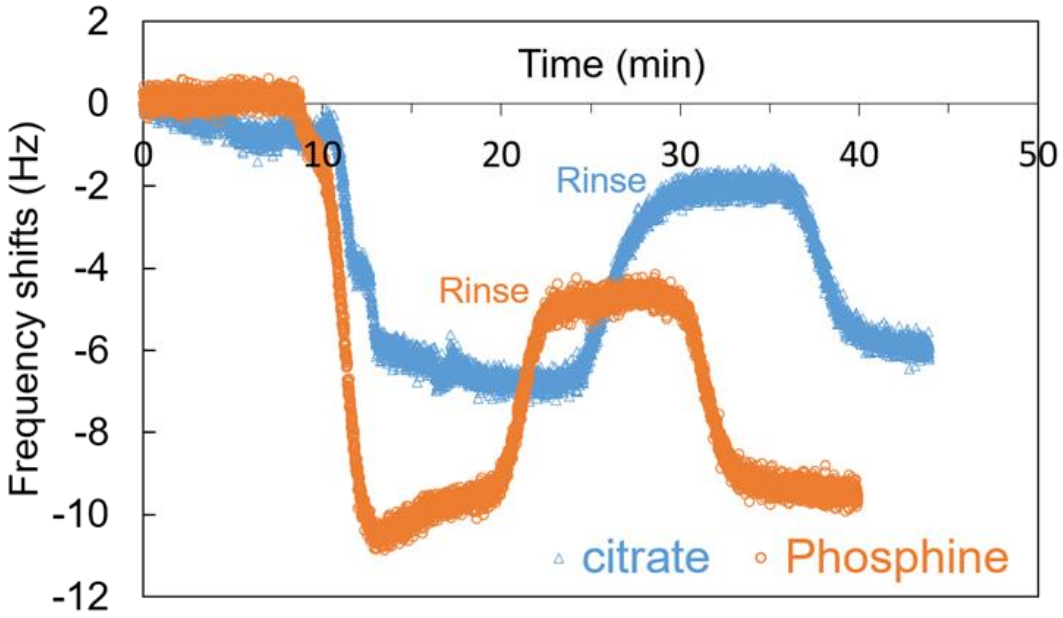

Figure 91. QCM-D measurements showing the shift in frequency with time for the deposition on a gold surface of the citrate (24mM) (blue curve) and the phosphine BSPP (24mM) (orange curve). After the steady-state was reached, the substrate was rinsed with water in order to wash out the reversible attached molecules.

A surface coverage of 0.3 molecules per nm^2 is calculated using the Sauerbrey[40] equation (**Eq.2**) for both citrate and BSPP.

$$\Delta m = -\frac{\Delta f . C}{n} \quad \textbf{(Eq.2)}$$

where Δm is the adsorbed mass per unit surface, Δf the variation of frequency observed at overtone n and C=17.7 $ng.cm^{-2}$ a constant characteristic of instrument. By reporting to respective molecular weights, the surface coverage can be estimated. Even if this model only applies to uniform and rigid thin film deposits, it allows a simple quantitative study and a direct comparison of experiences.

However, during the rinsing step almost all the adsorbed citrate is washed out, causing the frequency increasing progressively until almost reaching its initial value. This is consistent with a weak interaction of citrate with the gold surface via Au-COO^- electrostatic interactions estimated to be 2 $kcal.mol^{-1}$ [41,42]. In contrast, after the washing step half of the BSPP molecules remains on gold surface leading to an apparent surface coverage of retained phosphine equal to Γ=0.14 molecules per nm^2. This difference with citrate is expected according to the strong Au-P interaction which is about 15-20 $kcal{\cdot}mol^{-1}$ [43]. Additionally, BSPP bearing two Ph-SO_3^- functions (pKa of -2.8), suggests cooperative or competitive participation of Au-SO_3^- electrostatic interactions during the adsorption process. This could induce steric hindrances on the surface that could be responsible of low adsorption behavior and partial desorption of BSPP as reported for QCM-D studies [32,33].

Following experiments consist in the study of the interactions existing between Gd^{3+} ions and pre-coated gold surfaces. The preparation of the gold substrates for the subsequent Gd^{3+} ions deposition consisted first in their overnight incubation with citrate and BSPP solutions (24 mM in water). Concerning the further adsorption of Gd^{3+} ions, in order to avoid desorption of citrate ions, injection of Gd^{3+} ions was performed by keeping constant the concentration of citrate (24 mM) throughout the experiment[32]. In order to evaluate the intensity of interaction between Gd^{3+} ions and the pre-coated surfaces, increasing concentrations of Gd^{3+} ions were injected successively and each step was quantified by a corresponding frequency shift (ΔF). In the case of BSPP, the substrate was rinsed, equilibrated before the adsorption of Gd^{3+} ions and eluted with water, to keep only the stabilized ligand layer on the gold surface. **Figure 92** shows the evolution of ΔF_7 as a function of time when the measurements are carried out as sequential depositions of solutions of $Gd(NO_3)_3$ of increasing concentrations on the two pre-coated gold surfaces.

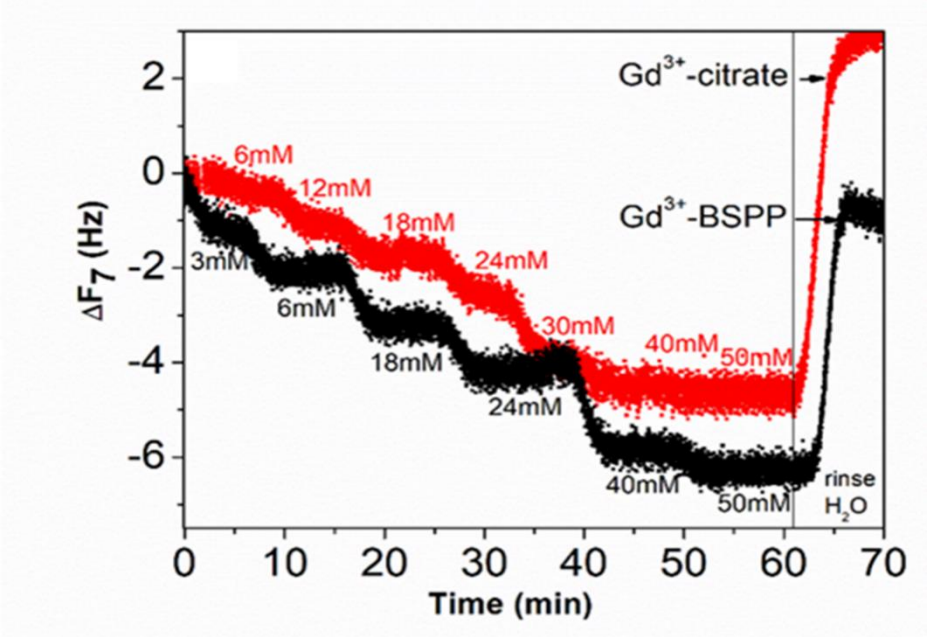

Figure 92. Frequency shift with time (ΔF_7 7th overtone) for Gd^{3+} ions adsorption. The measurements were carried out as sequential deposition of increasing concentration of Gd^{3+} ions.

On the two type of ligands covered surfaces, the successive Gd^{3+} ions depositions lead to a higher frequency shift value increasing with the concentration in lanthanide ions. This tendency is finally attenuated at highest concentrations, likely attaining a plateau value, revealing like a saturation effect. Then the rinsing step shows again a difference of affinity between the ligands and the gold surface. Indeed, the water flow applied on the BSPP-covered gold surface rinses the entire quantity of Gd^{3+} ions deposited but not the ligand layer, as the frequency shift comes back to almost zero value, which corresponds to the value associated to a stabilized BSPP layer.

On the contrary, water flow induces a higher loose of deposited mass, i.e. frequency shift (Sauerbrey equation eq.2) regarding the citrate covered gold surface. This is explained by the first experiment where the interaction between citrate and gold surface was proved to be weaker than the BSPP one. This is the reason why Gd^{3+} ions solutions for citrate coated surfaces were prepared in citrate solution (24 mM) to avoid the remove of the ligand. The difference of interactions is also clearly seen on **Figure 93** where the same gadolinium ions (3 mM) solution in water is applied on both citrate and BSPP coated surfaces. The deposition is actually made on BSPP covered surface, symbolized by a decrease of the frequency shift, whereas the remove of the citrate ligand is observed through the increase of the frequency shift, associated to a loose of deposited mass.

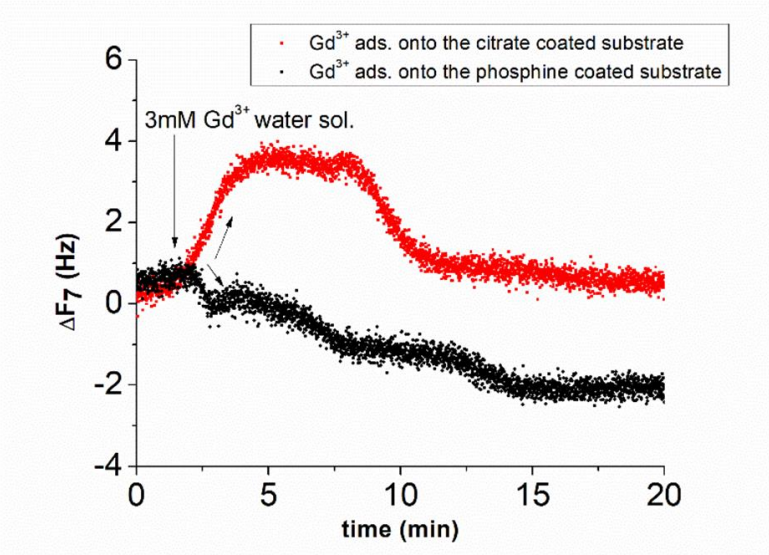

Figure 93. QCM-D measurements showing the shift in frequency with time for the adsorption of 3mM aqueous solution of Gd^{3+} ions onto a citrate (red curve) and onto a BSPP pre-coated gold QCM-D surface, respectively.

To better quantify those depositions steps as for previous ligands ones, calculations of the surface coverage were made by using the Sauerbrey equation. (eq.2). Resulting data were subsequently fitted by two types of isotherm models: Langmuir and Langmuir-Freundlich. describing the interaction of the adsorbing molecule, i.e. Gd^{3+} ion, with the adsorption surface sites.[44,45] The Langmuir model is described by **Eq 3**:

$$\Gamma = \frac{\Gamma_{max}\, K_L [Gd^{3+}]}{1 + K_L [Gd^{3+}]} \qquad \textbf{(Eq 3)}$$

where: **Γmax** is the maximum surface coverage of gadolinium ions (nmol/cm²)

[Gd^{3+}] is the gadolinium ions concentration (mM)

K_L is the binding Langmuir constant that corresponds to the inverse of the Gd^{3+} concentration that is required to obtain one-half of Γmax (mM^{-1})

Langmuir-Freundlich equation

$$\Gamma = \frac{\Gamma_{\max} * (K_{LF} [Gd^{3+}])^n}{1 + (K_{LF} [Gd^{3+}])^n} \qquad \textbf{(Eq 4)}$$

where: **Γmax** is the maximum surface coverage of gadolinium ions (nmol/cm²)

[Gd^{3+}] is the gadolinium ions concentration (mM)

K_{LF} is the binding Langmuir-Freundlich constant that corresponds to the inverse of the Gd^{3+} concentration that is required to obtain one-half of Γmax (mM^{-1})

n Langmuir-Freundlich coefficient, and represents the degree of non-linearity

When n = 1, eq. 4 converts to the Langmuir model. For n > 1, eq. (4) may be identified as describing a cooperative reaction between the sorption site and n sorbate molecules.

Both of the isotherm models were applied to citrate covered and BSPP covered surfaces, to determine which one is better describing the adsorption phenomenon occurring during gadolinium ions depositions (**Figure 94**). Fitting data resulting are reported in the **Table 8**.

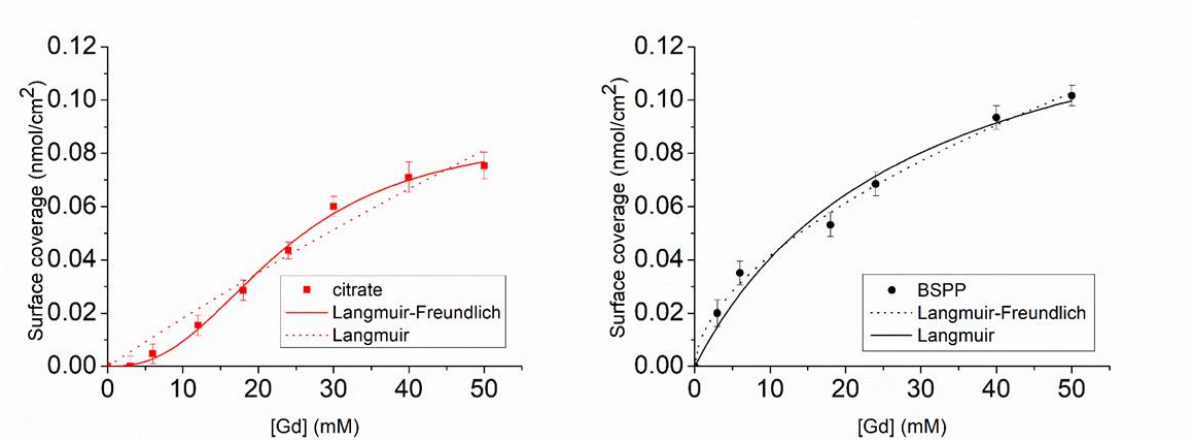

Figure 94. Plot of the surface coverage versus concentration of Gd^{3+} ions, fitted using both Langmuir and Langmuir-Freundlich model. On the left for the citrate pre-coated surface and on the right for the BSPP pre-coated substrate.

Table 8. Fit parameters for the adsorption of Gd^{3+} ions obtained from the fit to a Langmuir and Langmuir-Freundlich type adsorption isotherm.

Isotherm model	**Parameters** Gd^{3+} **absorbate**	**Coated QCM-substrate**	
		citrate	**phosphine**
Langmuir	$\Gamma_{max(L)}$ $(nmol/cm^2)$	-	0.15±0.02
	K_L (mM^{-1})	-	0.034±0.010
	R^2	-	0.97
Langmuir-Freundlich	$\Gamma_{max(LF)}$ $(nmol/cm^2)$	0.088±0.005	40.70±7387.65
	$K_{LF}(mM^{-1})$	0.042±0.002	5.10^{-7}±1.64(E-4)
	n	2.5±0.2	0.56
	R^2	0.99	0.99

For the adsorption onto the BSPP coated substrate, the experimental data are best fitted by the Langmuir isotherm model (R^2= 0.93) that assumes gradual saturation of sorption sites, without lateral interactions between adsorbed molecules, producing monolayer adsorption on a homogenous adsorbent surface. This suggests a strong specific interaction of Gd^{3+} ions with the phosphine coated substrate. Rinsing with pure water increases the frequency to the level registered for the phosphine-coated substrate (see **Figure 92**) thus confirming that the phosphine is not washed out during the experiment.

Additionally, the observed differences in the results of experiments conducted on the adsorption of the Gd^{3+} on a bare gold substrate (see **Figure 95**) excludes the displacement of the phosphine passivating layer during the Gd^{3+} adsorption.

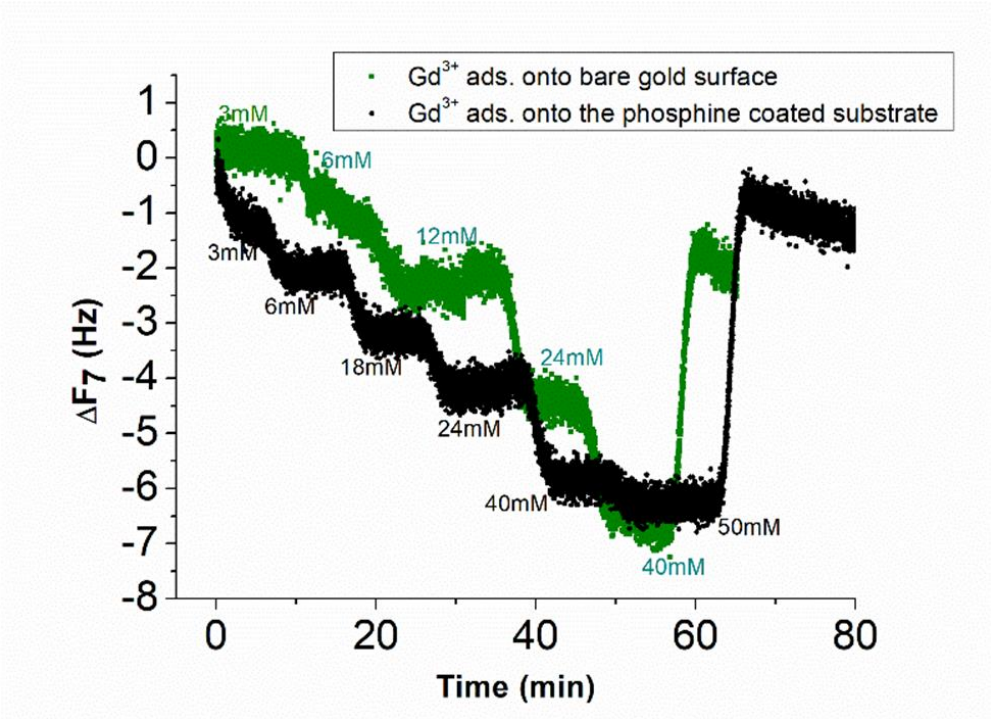

Figure 95. QCM-D measurements showing the shift in frequency with time for the adsorption of Gd^{3+} ions onto a bare gold surface (green curve) and onto a BSPP pre-coated surface (black curve), respectively. The measurements were carried out as sequential deposition of increasing concentration of Gd^{3+} ions.

In the case of the interaction of Gd^{3+} ions with citrate coated substrate, the adsorption of the Gd^{3+} ions onto the citrate coated substrate did not obey a Langmuir type isotherm model. The fitting parameter n=2.4 of the Langmuir-Freundlich isotherm (R^2 of 0.998, see **Table 8**) may be identified as describing a cooperative interaction.[46] This probably accounts for a mechanism of adsorption via the complexation between the Gd^{3+} ions and the carboxylic groups of the citrate ligand.[47]

This result stresses out that the adsorption mechanisms onto the two surfaces are significantly different and comforts the observations on the NPs. Different adsorption scenarios onto the two different surfaces are also confirmed by the plots of the measured energy dissipation per unit of mass (ΔD) vs. frequency (ΔF)[48,49] (**Figure 96**).

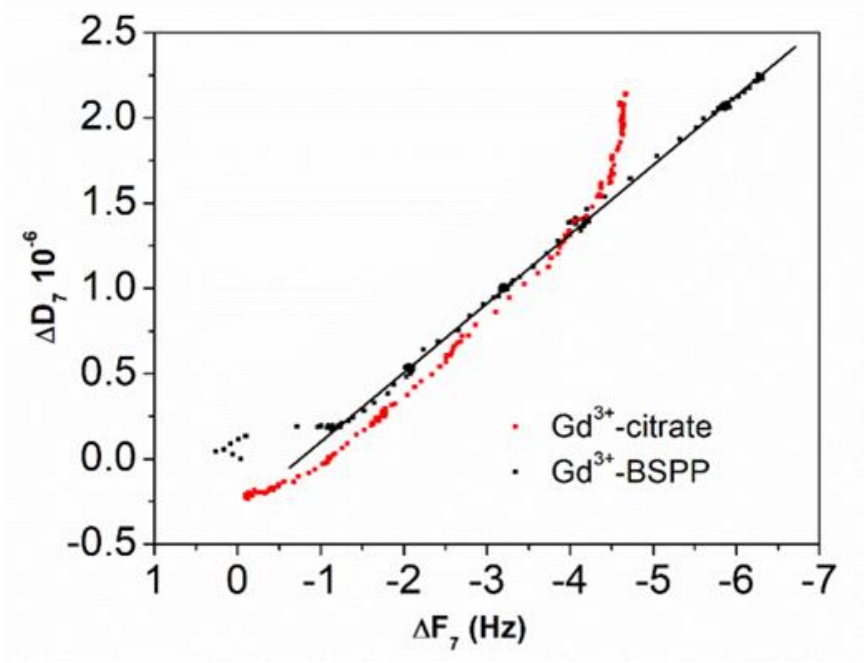

Figure 96. ΔD versus ΔF plot for the Gd^{3+} ions adsorbed onto the citrate (red dots) and onto the BSPP coated gold surface (black dots), respectively.

Concerning BSPP coated surface, ΔD/ΔF ratio remains constant suggesting an interaction of Gd^{3+} ions as a single layer *via* specific interactions.[49] On the contrary, for citrate coated surfaces, the nonlinear variation of the ΔD with the ΔF can be related to the formation of loosely bound conformations between citrate or/and its complexes with the Gd^{3+} ions and the gold substrate.[49] These weak interactions with the gold substrate induce a full desorption of citrate and Gd^{3+} ions after rinsing surface with pure water (see **Figure 92**).

As a consequence of the specific interaction between Gd^{3+} ions and the phosphine coated substrate, measurements as sequential depositions of increasing concentrations Gd^{3+} with a washing step in between each deposition step show full reversibility, short response and recovery times (**Figure 97**). Furthermore, the frequency response versus Gd^{3+} ions concentration shows a satisfactory linear behavior in-between the experimented concentration range (**Figure 97** inset). This QCM-D experiment accounts for the sensing performance of the Gd^{3+}-Au-BSPP 2D-system and demonstrates the relevance to address an easier way to implement bench test, based on Gd^{3+}-AuNP@BSPP 3D system.

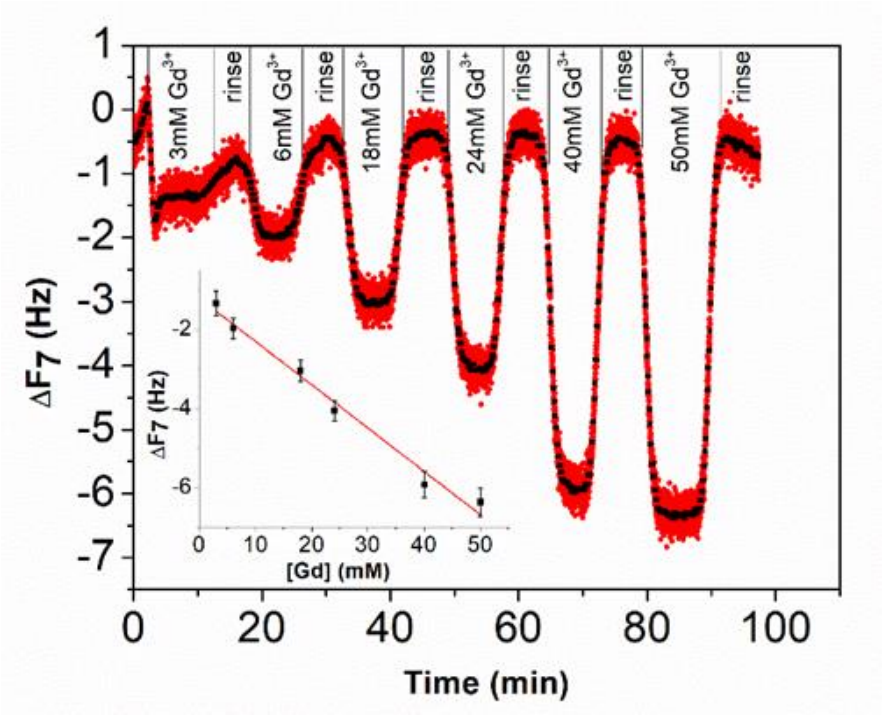

Figure 97. Response of the QCM-D gold sensor pre-coated with the BSPP molecules, to the increasing concentration of Gd^{3+} ions. A washing step with water between each Gd^{3+} ions deposition step was performed.

QCM-D measurements have identified the difference between the two ligands from an interaction point of view, with the gold surface on one hand, through the rinsing step. On the other hand, by adding the same concentrations of Gd^{3+} ions, deposited masses are different according to the kind of layer present on the gold surface. Latter observation tends to consider different interactions between Gd^{3+} ions and the two ligands covering the AuNPs. To better understand the nature of this difference, further investigations are made on AuNP@BSPP and AuNP@citrate in presence of Gd^{3+} ions.

IV.2 Interactions between AuNPs and Gd^{3+} ions

One of the criteria for the choice of the ligand to functionalize AuNPs was the ability to interact with positive ions like Gd^{3+}, that is to say to possess negatively charged chemical groups. Zeta potential measurements were investigated to characterize the functionalized AuNPs. Results obtained are similar for AuNP@citrate and AuNP@BSPP, -35±3 mV and -40±5mV respectively. To have more insights on the nature of interactions of Gd^{3+} ions with those negatively charged surface, zeta potential measurements weremade on AuNP@BSPP and AuNP@citrate solutions in presence of Gd^{3+} ions. After addition of 25 µM of Gd^{3+} ions, zeta potential of Gd^{3+}-AuNP@BSPP decreases up to -8± 6mV. As only a small decrease of pH is measured (from 7 to 6.4), this reduction could be mainly explained by the NPs surface charge screened by Gd^{3+} ions.[50] This ζ potential

change might be responsible for their aggregation and color change. Regarding the AuNP@citrate system, no change on the value of ζ-potential and of pH (i.e 5.7), and thus on the colloidal stability is evidenced after the addition of 25 µM of Gd^{3+} ions.

As evidenced through the colorimetric test assay, AuNP@BSPP interact with Gd^{3+} ions with a higher sensitivity than AuNP@citrate and range of concentrations are higher for the detection of Ca^{2+} and Na^{+} ions. The hard nature of the sulfonate group favors the interaction with the hard rare-earth Gd^{3+} ion, although sulfonate groups are regarded as weak ligands. However, the weak coordination nature of sulfonate groups makes its coordination mode very sensitive to chemical environment.[51,52] The aggregation of the AuNP@BSPP is made possible by creating interaction with the sulfonate groups through cooperative electrostatic interactions and hydrogen bondings. These interactions, have been described in literature as labile interactions, that do not require replacement of the ligands like water or hydroxy groups (from the partial hydrolysis of water at pH>5.7) present in the first coordination sphere of the Gd^{3+} ion.[53] Numerous examples of this behavior are found in the crystal structures of lanthanide ion complexes of sulfonatocalixarenes, leading to the identification of multiple coordination spheres around the metal ions.[52,53] The interaction between Gd^{3+} and an increased number of styrene sulfonate groups accounted for the strong polystyrenesulfone-Gd^{3+} binding.[54] Here, hydrogen bonds are formed with the ligands presents in this first coordination sphere. These interactions can thus be easily broken by changing chemical environment as demonstrated by QCM-D experiments during rinsing step (*vide supra*).

These labile interactions were confirmed through TEM images of mixtures of AuNP@BSPP and different concentrations of Gd^{3+} ions: 6 µM (for the slow aggregation regime) and 60 µM (for the fast one) shown in **Figure 98** and compared to images of AuNP@BSPP alone and of the same mixtures with AuNP@citrate. A grey shell connecting the NPs is observed for AuNP@BSPP samples with 6 and 60 µM of gadolinium ions. This shell connects the NPs and is also found in their immediate surroundings. As investigated by Schubert et al., this shell could be attributed to the presence of the Gd hydroxides and could be considered as an argument for the aggregation of the nanoparticles via interactions of sulfonate groups with the Gd^{3+} ions without replacement of the ligands from the first coordination sphere of the Gd.[50] Regarding the AuNP@citrate system, no grey shell is detected.

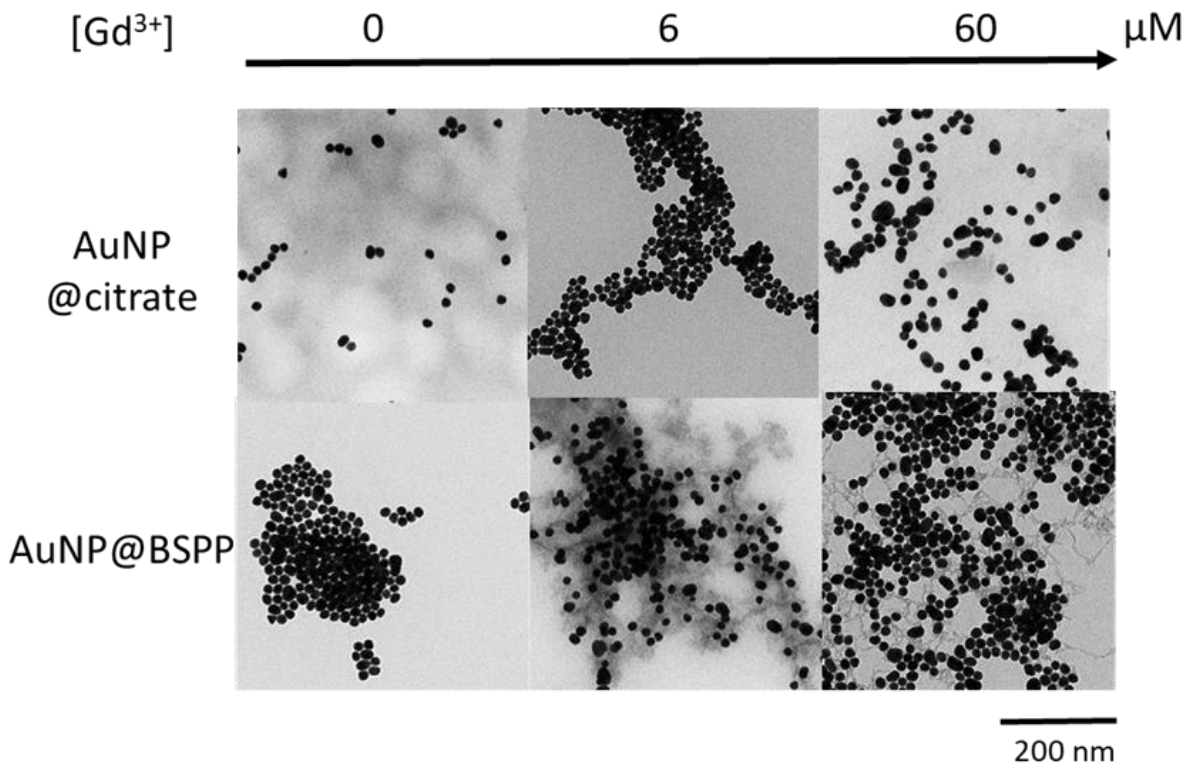

Figure 98. TEM images of AuNP@citrate (top) and AuNP@BSPP (bottom) before and after incubation with 6 and 60 µM of $Gd(NO_3)_3$, respectively

According to the literature[47], a complex based on the interaction between Gd^{3+} and the free carboxylic groups from citrate ligand, is mainly described as a 1:1 complex through a direct binding in the first coordination sphere of the ion by replacing the water and/or hydroxy groups. Hence, as the concentration of Gd^{3+} ions used in the experiments depicted in **Figure 85** is low comparatively to the concentration of citrate present in solution (about 30 times lower), the formation of 1:1 complexes with either the citrate in interaction with the surface of AuNPs or with the citrate free in solution is favored.[55] Au surfaces retain their negative net charge as shown by ζ-potential measurements. This further prevents the aggregation process of AuNP@citrate solution in presence of Gd^{3+} for such concentration and makes the system unsuitable for the developing of a colorimetric sensing test.

As previously enounced, only labile interactions, grouping both electrostatic and hydrogen bondings, exist between sulfonate groups of AuNP@BSPP and Gd^{3+} ions. It has been proved that by adding ethylenediamine tetra(methylene phosphonic acid) (EDTMP) to a solution of aggregated AuNP@BSPP redispersed the functionalized gold nanoparticles, characterized by a blue-shift of the absorbance and a color change from blue to purple or red (**Figure 99**).

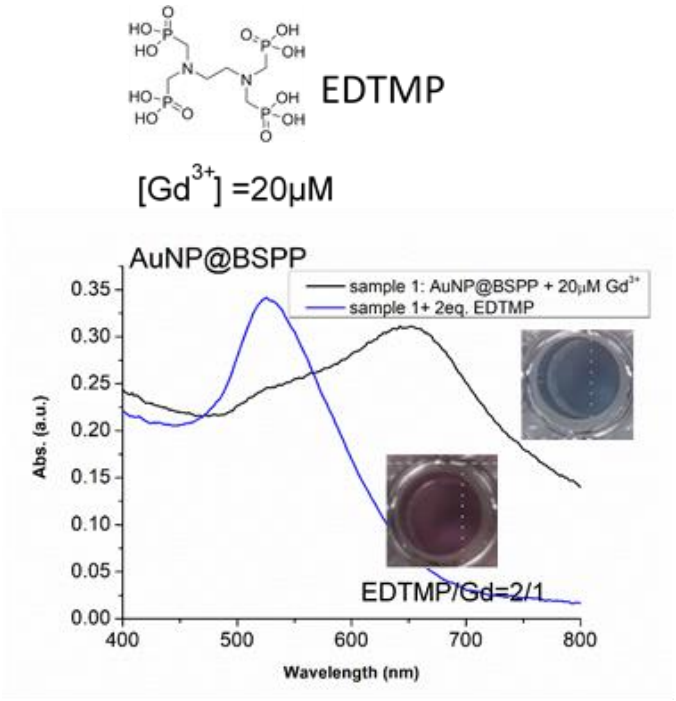

Figure 99. UV-visible spectra of AuNP@BSPP containing 20µM of Gd^{3+} (black curve) and of the same sample after addition of 2 equivalents of EDTMP compared to Gd^{3+} (blue curve)

Adding another competitive coordinating ligand for the Gd^{3+} ions induces this disaggregation process and allows the system to be used again for another test. The interactions between the sulfonate groups and the Gd^{3+} ions make the AuNP@BSPP system extremely sensitive and suitable for the developing of a cost-effective, fast and easy bench colorimetric assay (see **Figure 100**).

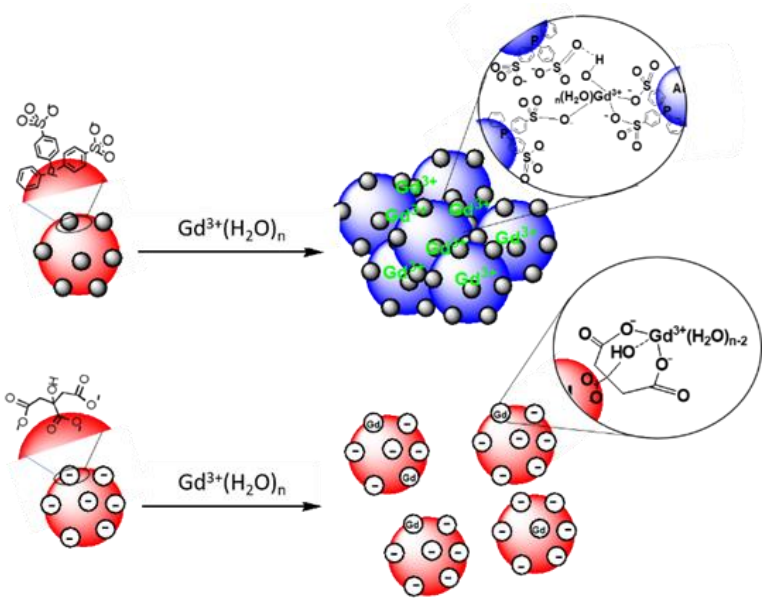

Figure 100. Schematic representation of the interaction of Gd^{3+} ions with the surface of AuNP@BSPP and AuNP@citrate, respectively.

V AuNP@BSPP as colorimetric sensing probe

In view of the described results the system is suitable to sense Gd^{3+} ions in prepared samples. In order to get information about the feasibility of the test the results were compared with more precise techniques like ICP-MS. To evaluate the colorimetric test using AuNP@BSPP, we decided to probe preparations of contrast agents for MRI application.

As detailed in the first two chapters of this work, new kind of nanostructures raised among the contrast agents for MRI. They are based on ionic interactions between double hydrophilic block copolymer (DHBC) and metal ions, and are named Hybrid Polyionic Complexes (HPICs). On Figure 29, the formation mechanism is illustrated when mixing a certain concentration of gadolinium ions and the DHBC, here PAA-*b*-PEG. We remind here the definition of the charges' ratio R calculated with the carboxylate functions concentration and the ions concentration:

$$R = 3 . \frac{[Ln^{3+}]}{[AA]}$$

Over the neutral ratio R=1, as illustrated on Fig. 29, free gadolinium ions are present in the preparation of the contrast agents. The use of the colorimetric test would here be useful to quantify this excess of free Gd^{3+} ions, in order to prevent toxicity issues.[10]

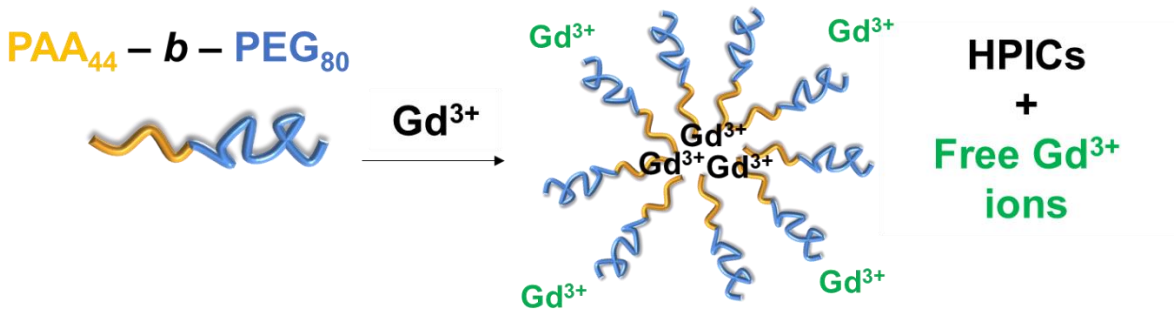

Figure 101. Representation of the mechanism of formation of Hybrid Polyion Complexes (HPICs) with excess of gadolinium ions.

First investigations were made on HPICs structures made with previous block copolymer PAA-b-PEG. C. Frangville et al. did quantify this excess of free Gd^{3+} by using the ICP-MS technique, so the comparison would be relevant.[13] Based on the presented results in **Figure 87**, AuNP@BSPP would allow the quantification of free Gd^{3+} ions present in solution. Five different HPICs with five different charge ratios (Gd^{3+} /PAA): 0.9, 1.1, 1.5, 2 and 2.5 were prepared. The obtained colloids have a mean hydrodynamic diameter around 20 nm as determined by dynamic light scattering (DLS).

As illustrated in **Figure 102**., solutions of HPICs were placed into a centrifugal tube Amicon Ultra 30k to be centrifugated during 90 minutes at 3,000xg and 21°C. Filtrates were kept and measured for pH values. All of them were at pH around 6. The colorimetric test was then applied on those 5 filtrates (**Figure 103**).

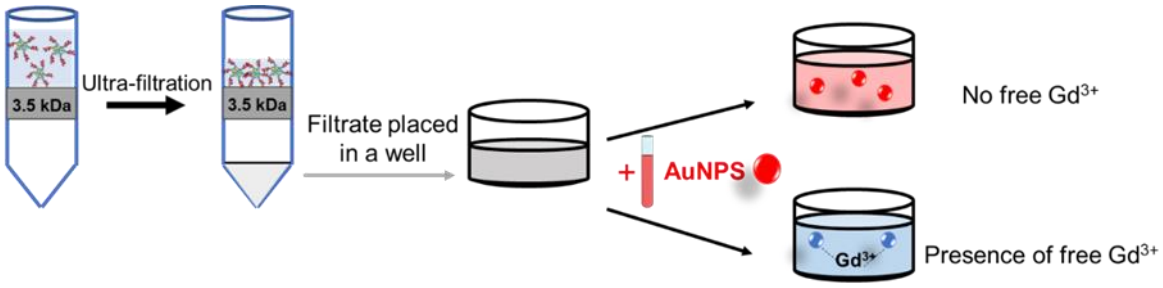

Figure 102. Scheme of titration method based on AuNPs.

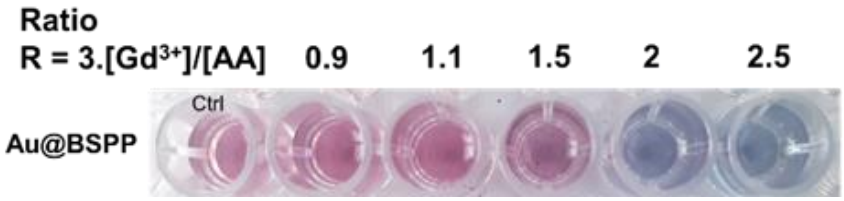

Figure 103. Photographs showing the color response of AuNP@BSPP to increasing ratios R of positive charges over negative charges.

As expected, for the lower ratio 0.9 no color change is observed, ratio higher than 1.1 lead to a change of observed color suggesting the presence of free Gd^{3+} ions. This color change is illustrated onto absorbance spectra recorded during 4 hours every 15 minutes, spectra at t_0 and at 4 hours are shown in **Figure 104.**

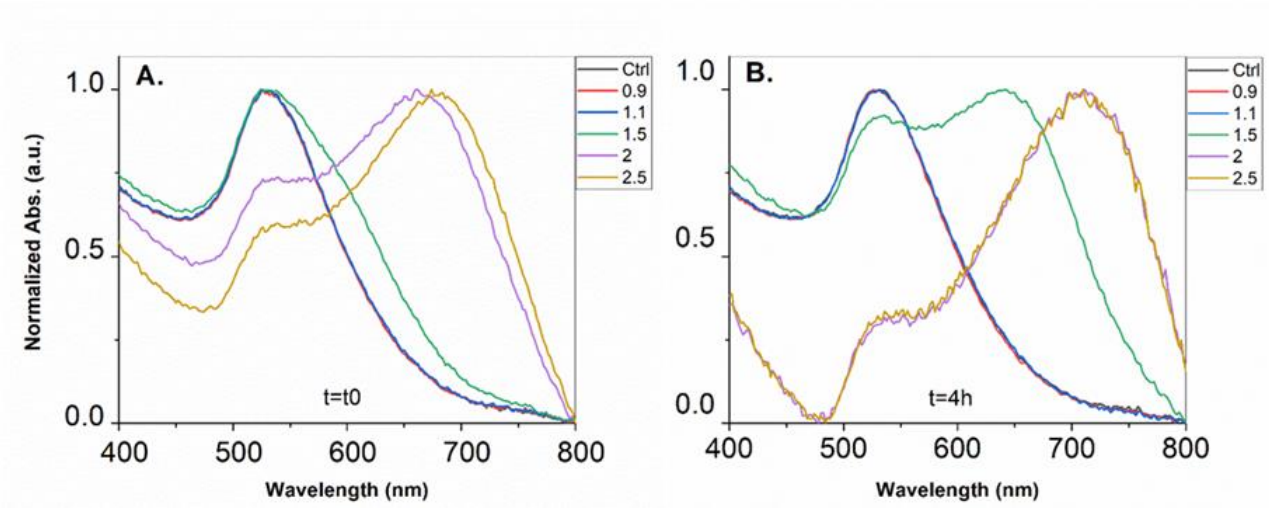

Figure 104. UV-visible spectra of AuNP@BSPP in the presence of the filtrate resulted from the purification of HPICs of different ratios R (positive charges over negative charges) registered at t0=15min (A) and at t=4h (B).

The two lowest ratios correspond to very low concentrations of free Gd^{3+} ions and as expected no shift of the SPR band is shown, even after 4 hours of kinetic. Regarding the ratio 1.5, there is at the beginning a slight shift of the SPR band, which evolves during 4 hours, like for concentrations belonging to linear range of the test. Finally, the two highest ratios are the most shifted and evolve with time too, to be at the end very near from each other.

Beyond this qualitative evaluation, quantitative measurements based on UV-visible spectroscopy and on the calibration curve presented in **Figure 88** were further used. The same calculations based on the UV-visible spectra at each time for each ratio as for the **Figure 88** elaboration, were used. Particularly FP values were positioned onto the calibration curve and associated to a corresponding Gd^{3+} ions' concentrations. The first two filtrates, at ratio 0.9 and 1.1 do not contain any quantifiable amount of Gd^{3+}. For the charge ratio 1.5, an estimation of free Gd^{3+} ions content of 13.2 ± 0.8 µM is measured, in good agreement with the 12 µM expected value. Evaluation of the Gd^{3+} content for the two highest charge ratios is not relevant as the obtained values are not in the linearity range determined previously.

The determination of free Gd^{3+} through the calculation of the ratio of absorbance measured at two different wavelengths at 524 and 640 nm as proposed in the literature (**Figure 105**)[7,56] represents another way. By taking the values at 4 hours, it is possible to obtain a linear range of this absorbance ratio versus the concentration in Gd^{3+} ions (**Figure 106**). The resulting linear relation leads to the concentrations of gadolinium ions sum up in **Table 9**.

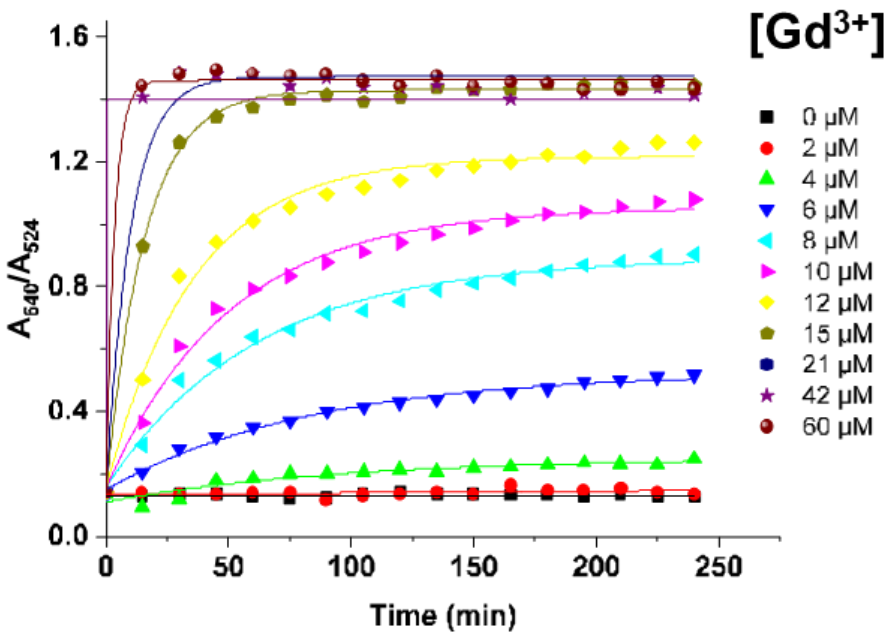

Figure 105. Time dependence of the absorbance ratio A_{640}/A_{524}

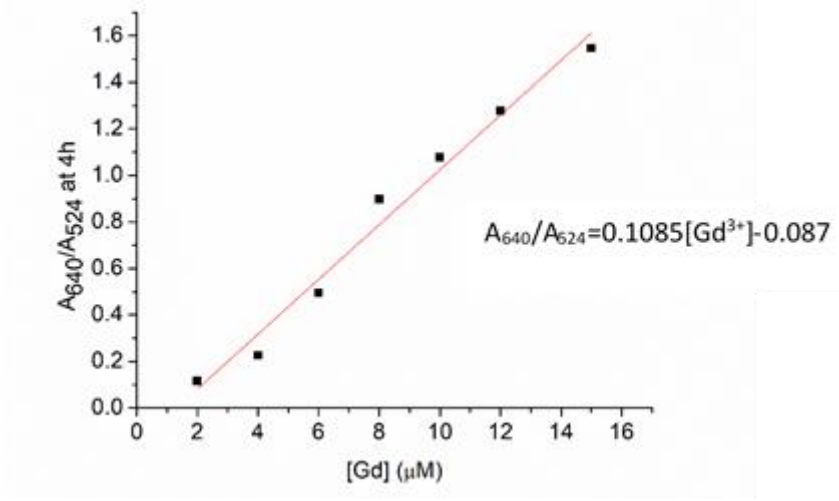

Figure 106. Linear range of the absorbance ratio (A_{640}/A_{524}) at 4h plotted vs. concentration of $Gd(NO_3)_3$.

Table 9. Estimation of the concentration of free Gd^{3+} ions with the equation $A_{640}/A_{524}=0.1085[Gd^{3+}]-0.087$.

R = 3.[Gd3+]/[AA]	**Estimated concentration of free Gd3+ ions with the equation (µM)**
0.9	5
1.1	5.7
1.5	10.6
2	10.9
2.5	11

Latter method leads to concentrations of Gd^{3+} ions which are not in agreement with the expected values, because the difference the ratios 1.5, 2 and 2.5, seems to low. This can be explained by the fact that this method is based on the intensity of the absorbance of the AuNPs, which is affected by their precipitation after 4 hours in presence of sufficient Gd^{3+} concentrations. On the contrary, the method based on the FP value evaluation, is built up with normalized areas, giving then a more precise quantification of the concentration of Gd^{3+} ions. The estimated value from FP value determination compares very favorably with the one estimated from ICP measurements 9.8±0.5 µM obtained with a higher accuracy. Hence, the application of the colorimetric test and the aggregation index method has proved to give good estimations of the concentrations of free Gd^{3+} ions.

Similar study was realized on the HPICs nanostructures elaborated in Chapter II, based on the mixtures of the PAA-*b*-PVP block copolymer and Gd^{3+} ions. This time, R values are higher to broaden the range of free Gd^{3+} ions.

The method of isolation of the samples, through ultra-filtration, and of quantification of the free Gd^{3+} ions with AuNP@BSPP are the same as for the previous PAA-*b*-PEG based HPICs nanostructure. Four ratios R are tested: 0.95, 2.2, 5.4 and 8.8. UV-vis spectroscopy technique was used again to quantify the SPR shift at t_0 (**Figure 107.A**) and after 4 hours (**Figure 107.B**), by using the calibration of the colorimetric test. Resulting obtained values for the free Gd^{3+} ions concentration are reported on the **Figure 107.C** and directly compared to expected concentration from theoretical calculations and effective concentrations measured by ICP-MS.

The ratio near neutral value R=0.95 shows as expected non-significant concentration of free Gd^{3+} ions according to the three estimations. Then, when R value increases theoretical and ICP-MS data are near from each other. This confirms the coordination chemistry established between three carboxylate groups for one gadolinium ion (III), which supposes that over the neutral ratio, the excess of Gd^{3+} ions cannot be coordinated anymore. The value resulting from the colorimetric test is not so far from the two others for R=2.2, but tends to underestimate the real gadolinium ions concentration when R value increases. This colorimetric test can then be used as a rapid routine test to know if free Gd^{3+} ions are present, but is not enough based on precise data to give correct estimations when the concentrations are out of the linearity range established during the calibration phase.

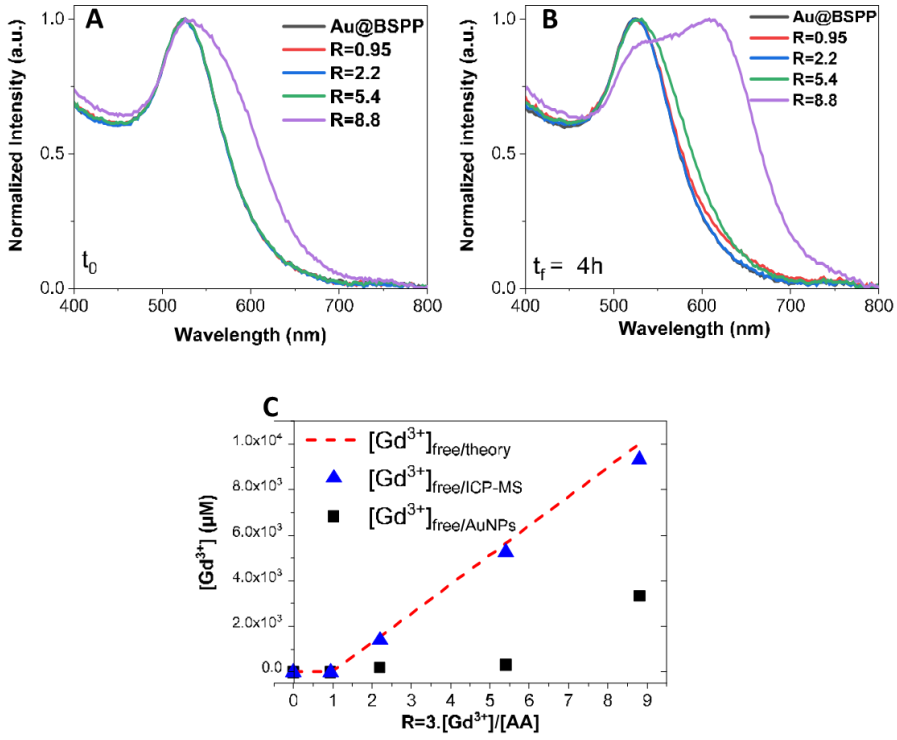

Figure 107. UV spectra of the mixtures of gold nanoparticles noted as Au@P on the plot and the diluted filtrated samples of HPICs containing PAA_{32}-b-PVP_{59} and Gadolinium ions for different R ratio (0.95, 2.2, 5.4 and 8.8) at initial time t_0 (A) and after 4 hours (B) Approximative value of free Gd^{3+} ions found in the filtrated

It is now interesting to compare this new method of determination of Gd^{3+} ions quantity to the current techniques, from a quantitative point of view. Most of the mainly used apparatus to sense Gd^{3+} ions are expensive and difficult to implement, but still give high-precision results, which are taken as reference in the elaboration of such new methods of sensing. Some of those analysis techniques are enounced in **Table 3** with their characteristics in terms of quantification like the linear range of detection and the lower limits of detection and of quantification. The limits and ranges of detection of AuNP@BSPP are comparable with the one obtained by conventional method like chromatographic techniques coupled either with a spectroscopic or with ICP techniques (see **Table 10**).

Table 10. Limits and range of detection of Gadolinium of the presented method using AuNP@BSPP and of the conventional methods found in the literature.

ANALYSIS TECHNIQUES	GADOLINIUM SPECIE	LINEAR OR FITTING RANGE OF CONCENTRATIONS	LIMITS OF DETECTION	LIMITS OF QUANTIFICATION	REF.
UV-VIS	Gd^{3+}	0 – 18 µM	0.74 µM	4.76 µM	This paper
MEKC[1]/ UV-VIS	Gd-based contrasting agents	5-200 µM or 100-5000 µM according to Gd CAs	0.40 – 20 µM	N.P.[2]	57
HPLC[3] / UV-VIS	GdDTPA-BMA	2-800 µM (serum) 10-2000 µM (urine)	0.3 µM (serum) 1.1 µM (urine)	2 µM (serum) 10 µM (urine)	58
HPLC[3] / ICP-AES[4]	Gadodiamide	0-590 µM (ICP-AES of serum)	1.9 µM (ICP-AES of serum)	6.5 µM (ICP-AES of serum)	59
ESI-MS[5] / ICP-OES[6]	Gd-based contrasting agents	5 – 100 µM	0.1 - 1 µM	0.5 – 5 µM	60
HPLC[3] / ICP-OES[6]	Gd-based contrasting agents	2.5 – 500 µM	0.05 – 0.2 µM	0.16 – 0.73 µM	61

Despite their simplicity, high sensitivity and convenience, few are the colorimetric tests based on AuNPs designed for the detection of lanthanide ions, thus justifying the importance to develop a colorimetric test based on AuNP@BSPP. Moreover, limits of detection and quantification are of similar range than the ones found for detection of other metal ions through colorimetric techniques.[5,7]

VI Conclusions and project objectives

The main objective of this work was the study of the interactions between gold nanoparticles functionalized with specific ligands and gadolinium ions. The nanoparticles are functionalized with phosphine-sulfonate ligand, commercially available, whose interaction with gold surface is stronger than citrate common ligand, according to QCM-D measurements. Those BSPP-covered gold nanoparticles have proved a high sensitivity towards Gd^{3+} ions with a limit of detection of 0.74 µM. The question about the mechanism of interaction between BSPP ligands and gadolinium ions was considered and the observations pointed out the double character of those interactions. There are both electrostatic and hydrogen bonding phenomenon, stressing the labile nature of the interactions between ligands and Gd^{3+} ions, still shown through QCM-D measurements. The weakness behavior has again been proved through a reversible aggregation process. Indeed, by adding an amine compound, the gold nanoparticles are dispersed and stabilized again in solution.

BSPP ligands were also prone to interact with other cations such as Na^{+} or Ca^{2+} with higher concentration ranges. The comparison of behaviors with citrate-stabilized gold nanoparticles showed the difference in the nature of the involved interactions with different strength.

The investigations on the kinetic of aggregation of the AuNP@BSPP in presence of certain concentrations of Gd^{3+} ions led to the design of calibration curve based on flocculation parameter values. This one shows a linearity range from 0 to 18 µM, used further to quantify Gd^{3+} ions quantity in samples such as MRI contrast agents' preparations. Those results were found to be near from ICP-MS values[13] when values belong to this linearity range. For higher concentration values, the test does not allow a correct estimation of this concentration of free ions, but only warn their presence in the solution through the aggregation of the AuNPs.

We are now familiar with interactions occurring between ligands on the surface of gold nanoparticles and metal ions, particularly gadolinium ions. Future perspectives deal with a study about interactions occurring between polymers and gold surface, in a view of a functionalization process. Latter polymeric gold surfaces would then be investigated in interactions with metal ions to form structured multifunctional assemblies for biomedical applications.

VII References

(1) Saha, K.; Agasti, S. S.; Kim, C.; Li, X.; Rotello, V. M. Gold Nanoparticles in Chemical and Biological Sensing. *Chem. Rev.* **2012**, *112* (5), 2739–2779. https://doi.org/10.1021/cr2001178.

(2) Elahi, N.; Kamali, M.; Baghersad, M. H. Recent Biomedical Applications of Gold Nanoparticles: A Review. *Talanta* **2018**, *184*, 537–556. https://doi.org/10.1016/j.talanta.2018.02.088.

(3) Amendola, V.; Pilot, R.; Frasconi, M.; Maragò, O. M.; Iatì, M. A. Surface Plasmon Resonance in Gold Nanoparticles: A Review. *J. Phys. Condens. Matter* **2017**, *29* (20), 203002. https://doi.org/10.1088/1361-648X/aa60f3.

(4) Oliveira, E.; Núñez, C.; Santos, H. M.; Fernández-Lodeiro, J.; Fernández-Lodeiro, A.; Capelo, J. L.; Lodeiro, C. Revisiting the Use of Gold and Silver Functionalised Nanoparticles as Colorimetric and Fluorometric Chemosensors for Metal Ions. *Sens. Actuators B Chem.* **2015**, *212*, 297–328. https://doi.org/10.1016/j.snb.2015.02.026.

(5) Zhang, J.; Wang, Y.; Xu, X.; Yang, X. Specifically Colorimetric Recognition of Calcium, Strontium, and Barium Ions Using 2-Mercaptosuccinic Acid-Functionalized Gold Nanoparticles and Its Use in Reliable Detection of Calcium Ion in Water. *The Analyst* **2011**, *136* (19), 3865. https://doi.org/10.1039/c1an15175d.

(6) Hughes, S. I.; Dasary, S. S. R.; Singh, A. K.; Glenn, Z.; Jamison, H.; Ray, P. C.; Yu, H. Sensitive and Selective Detection of Trivalent Chromium Using Hyper Rayleigh Scattering with 5,5′-Dithio-Bis-(2-Nitrobenzoic Acid)-Modified Gold Nanoparticles. *Sens. Actuators B Chem.* **2013**, *178*, 514–519. https://doi.org/10.1016/j.snb.2012.12.003.

(7) Mondal, P.; Yarger, J. L. Colorimetric Dual Sensors of Metal Ions Based on 1,2,3-Triazole-4,5-Dicarboxylic Acid-Functionalized Gold Nanoparticles. *J. Phys. Chem. C* **2019**, *123* (33), 20459–20467. https://doi.org/10.1021/acs.jpcc.9b03721.

(8) Bünzli, J.-C. G. Benefiting from the Unique Properties of Lanthanide Ions. *Acc. Chem. Res.* **2006**, *39* (1), 53–61. https://doi.org/10.1021/ar0400894.

(9) Lewis, D. J.; Pikramenou, Z. Lanthanide-Coated Gold Nanoparticles for Biomedical Applications. *Coord. Chem. Rev.* **2014**, *273–274*, 213–225. https://doi.org/10.1016/j.ccr.2014.03.019.

(10) Rogosnitzky, M.; Branch, S. Gadolinium-Based Contrast Agent Toxicity: A Review of Known and Proposed Mechanisms. *BioMetals* **2016**, *29* (3), 365–376. https://doi.org/10.1007/s10534-016-9931-7.

(11) Haley, T. J.; Raymond, K.; Komesu, N.; Upham, H. C. TOXICOLOGICAL AND PHARMACOLOGICAL EFFECTS OF GADOLINIUM AND SAMARIUM CHLORIDES. 7.

(12) Das, T.; Sharma, A.; Talukder, G. Effects of Lanthanum in Cellular Systems. *Biol. Trace Elem. Res.* **1988**, *18* (1), 201–228. https://doi.org/10.1007/BF02917504.

(13) Frangville, C.; Li, Y.; Billotey, C.; Talham, D. R.; Taleb, J.; Roux, P.; Marty, J.-D.; Mingotaud, C. Assembly of Double-Hydrophilic Block Copolymers Triggered by Gadolinium Ions: New Colloidal MRI Contrast Agents. *Nano Lett* **2016**, 5.

(14) Telgmann, L.; Sperling, M.; Karst, U. Determination of Gadolinium-Based MRI Contrast Agents in Biological and Environmental Samples: A Review. *Anal. Chim. Acta* **2013**, *764*, 1–16. https://doi.org/10.1016/j.aca.2012.12.007.

(15) Turkevich, J.; Stevenson, P. C.; Hillier, J. A Study of the Nucleation and Growth Processes in the Synthesis of Colloidal Gold. *Discuss. Faraday Soc.* **1951**, *11*, 55. https://doi.org/10.1039/df9511100055.

(16) Schmid, G.; Lehnert, A. The Complexation of Gold Colloids. *Angew. Chem. Int. Ed. Engl.* **1989**, *28* (6), 780–781. https://doi.org/10.1002/anie.198907801.

(17) Frens, G. Controlled Nucleation for the Regulation of the Particle Size in Monodisperse Gold Suspensions. *Nat. Phys. Sci.* **1973**, *241* (105), 20–22. https://doi.org/10.1038/physci241020a0.

(18) Haiss, W.; Thanh, N. T. K.; Aveyard, J.; Fernig, D. G. Determination of Size and Concentration of Gold Nanoparticles from UV−Vis Spectra. *Anal. Chem.* **2007**, *79* (11), 4215–4221. https://doi.org/10.1021/ac0702084.
(19) Vanegas, J. P.; Scaiano, J. C.; Lanterna, A. E. Thiol-Stabilized Gold Nanoparticles: New Ways To Displace Thiol Layers Using Yttrium or Lanthanide Chlorides. *Langmuir* **2017**, *33* (43), 12149–12154. https://doi.org/10.1021/acs.langmuir.7b01898.
(20) Loweth, C. J. DNA-Based Assembly of Gold Nanocrystals.
(21) Heuer-Jungemann, A.; Feliu, N.; Bakaimi, I.; Hamaly, M.; Alkilany, A.; Chakraborty, I.; Masood, A.; Casula, M. F.; Kostopoulou, A.; Oh, E.; Susumu, K.; Stewart, M. H.; Medintz, I. L.; Stratakis, E.; Parak, W. J.; Kanaras, A. G. The Role of Ligands in the Chemical Synthesis and Applications of Inorganic Nanoparticles. *Chem. Rev.* **2019**, *119* (8), 4819–4880. https://doi.org/10.1021/acs.chemrev.8b00733.
(22) Liz-Marzán, L. M. Tailoring Surface Plasmons through the Morphology and Assembly of Metal Nanoparticles. *Langmuir* **2006**, *22* (1), 32–41. https://doi.org/10.1021/la0513353.
(23) Bhattacharjee, S. DLS and Zeta Potential – What They Are and What They Are Not? *J. Controlled Release* **2016**, *235*, 337–351. https://doi.org/10.1016/j.jconrel.2016.06.017.
(24) Mayya, K. S.; Patil, V.; Sastry, M. On the Stability of Carboxylic Acid Derivatized Gold Colloidal Particles: The Role of Colloidal Solution PH Studied by Optical Absorption Spectroscopy. *Langmuir* **1997**, *13* (15), 3944–3947. https://doi.org/10.1021/la962140l.
(25) Rahme, K.; Vicendo, P.; Ayela, C.; Gaillard, C.; Payré, B.; Mingotaud, C.; Gauffre, F. A Simple Protocol to Stabilize Gold Nanoparticles Using Amphiphilic Block Copolymers: Stability Studies and Viable Cellular Uptake. *Chem. - Eur. J.* **2009**, *15* (42), 11151–11159. https://doi.org/10.1002/chem.200901564.
(26) Volkert, A. A.; Subramaniam, V.; Haes, A. J. Implications of Citrate Concentration during the Seeded Growth Synthesis of Gold Nanoparticles. *Chem Commun* **2011**, *47* (1), 478–480. https://doi.org/10.1039/C0CC02075C.
(27) Oncsik, T.; Trefalt, G.; Borkovec, M.; Szilagyi, I. Specific Ion Effects on Particle Aggregation Induced by Monovalent Salts within the Hofmeister Series. *Langmuir* **2015**, *31* (13), 3799–3807. https://doi.org/10.1021/acs.langmuir.5b00225.
(28) Chu, Y.; Chen, J.; Haso, F.; Gao, Y.; Szymanowski, J. E. S.; Burns, P. C.; Liu, T. Expanding the Schulze–Hardy Rule and the Hofmeister Series to Nanometer-Scaled Hydrophilic Macroions. *Chem. – Eur. J.* **2018**, *24* (21), 5479–5483. https://doi.org/10.1002/chem.201706101.
(29) Kissa, E. *Dispersions - Characterization, Testing and Measurement*; Surfactant Science series; 1999; Vol. 84.
(30) Marbella, L. E.; Millstone, J. E. NMR Techniques for Noble Metal Nanoparticles. *Chem. Mater.* **2015**, *27* (8), 2721–2739. https://doi.org/10.1021/cm504809c.
(31) Tonda-Turo, C.; Carmagnola, I.; Ciardelli, G. Quartz Crystal Microbalance With Dissipation Monitoring: A Powerful Method to Predict the in Vivo Behavior of Bioengineered Surfaces. *Front. Bioeng. Biotechnol.* **2018**, *6*, 158. https://doi.org/10.3389/fbioe.2018.00158.
(32) Brewer, S. H.; Glomm, W. R.; Johnson, M. C.; Knag, M. K.; Franzen, S. Probing BSA Binding to Citrate-Coated Gold Nanoparticles and Surfaces. *Langmuir* **2005**, *21* (20), 9303–9307. https://doi.org/10.1021/la050588t.
(33) Glaria, A.; Beija, M.; Bordes, R.; Destarac, M.; Marty, J.-D. Understanding the Role of ω-End Groups and Molecular Weight in the Interaction of PNIPAM with Gold Surfaces. *Chem. Mater.* **2013**, *25* (9), 1868–1876. https://doi.org/10.1021/cm400480p.
(34) Tajik-Ahmadabad, B.; Mechler, A.; Muir, B. W.; McLean, K.; Hinton, T. M.; Separovic, F.; Polyzos, A. A QCM-D and SAXS Study of the Interaction of Functionalised Lyotropic Liquid Crystalline Lipid Nanoparticles with SiRNA. *ChemBioChem* **2017**, *18* (10), 921–930. https://doi.org/10.1002/cbic.201600613.
(35) Bailey, C. M.; Kamaloo, E.; Waterman, K. L.; Wang, K. F.; Nagarajan, R.; Camesano, T. A. Size Dependence of Gold Nanoparticle Interactions with a Supported Lipid Bilayer: A

QCM-D Study. *Biophys. Chem.* **2015**, *203–204*, 51–61. https://doi.org/10.1016/j.bpc.2015.05.006.

(36) Van Lehn, R. C.; Ricci, M.; Silva, P. H. J.; Andreozzi, P.; Reguera, J.; Voïtchovsky, K.; Stellacci, F.; Alexander-Katz, A. Lipid Tail Protrusions Mediate the Insertion of Nanoparticles into Model Cell Membranes. *Nat. Commun.* **2014**, *5* (1), 4482. https://doi.org/10.1038/ncomms5482.

(37) Marsh, Z. M.; Lantz, K. A.; Stefik, M. QCM Detection of Molecule–Nanoparticle Interactions for Ligand Shells of Varying Morphology. *Nanoscale* **2018**, *10* (40), 19107–19116. https://doi.org/10.1039/C8NR05605F.

(38) Glomm, W. R.; Bidegain, B. F.; Volden, S.; Sjöblom, J. A Quartz Crystal Microbalance Study of the Adsorption of Fluorescein-5-Isothiocyanate onto Gold Surfaces. *J. Dispers. Sci. Technol.* **2006**, *27* (5), 651–656. https://doi.org/10.1080/01932690600662745.

(39) Beduoğlu, A.; Sevim, A. M.; Koca, A.; Altındal, A.; Altuntaş Bayır, Z. Thiazole-Substituted Non-Symmetrical Metallophthalocyanines: Synthesis, Characterization, Electrochemical and Heavy Metal Ion Sensing Properties. *New J. Chem.* **2020**, *44* (14), 5201–5210. https://doi.org/10.1039/D0NJ00466A.

(40) Sauerbrey, G. Verwendung von Schwingquarzen zur W�gung d�nner Schichten und zur Mikrow�gung. *Z. F�r Phys.* **1959**, *155* (2), 206–222. https://doi.org/10.1007/BF01337937.

(41) Chen, F.; Li, X.; Hihath, J.; Huang, Z.; Tao, N. Effect of Anchoring Groups on Single-Molecule Conductance: Comparative Study of Thiol-, Amine-, and Carboxylic-Acid-Terminated Molecules. *J. Am. Chem. Soc.* **2006**, *128* (49), 15874–15881. https://doi.org/10.1021/ja065864k.

(42) Park, J.-W.; Shumaker-Parry, J. S. Structural Study of Citrate Layers on Gold Nanoparticles: Role of Intermolecular Interactions in Stabilizing Nanoparticles. *J. Am. Chem. Soc.* **2014**, *136* (5), 1907–1921. https://doi.org/10.1021/ja4097384.

(43) Cortie, M. B.; McDonagh, A. *Gold Chemistry*; Weinheim, Germany, 2009.

(44) Sips, R. On the Structure of a Catalyst Surface. *J. Chem. Phys.* **1948**, *16* (5), 490–495. https://doi.org/10.1063/1.1746922.

(45) Langmuir, I. THE ADSORPTION OF GASES ON PLANE SURFACES OF GLASS, MICA AND PLATINUM. *J. Am. Chem. Soc.* **1918**, *40* (9), 1361–1403. https://doi.org/10.1021/ja02242a004.

(46) Keren, Y.; Borisover, M.; Bukhanovsky, N. Sorption Interactions of Organic Compounds with Soils Affected by Agricultural Olive Mill Wastewater. *Chemosphere* **2015**, *138*, 462–468. https://doi.org/10.1016/j.chemosphere.2015.06.085.

(47) Jackson, G. E.; du Toit, J. Gadolinium(III)in Vivo Speciation. Part 1. A Potentiometric and Spectroscopic Study of Gadolinium(III) Citrate Complexes. *J. Chem. Soc. Dalton Trans.* **1991**, No. 6, 1463. https://doi.org/10.1039/dt9910001463.

(48) Huang, R.; Yi, P.; Tang, Y. Probing the Interactions of Organic Molecules, Nanomaterials, and Microbes with Solid Surfaces Using Quartz Crystal Microbalances: Methodology, Advantages, and Limitations. *Environ. Sci. Process. Impacts* **2017**, *19* (6), 793–811. https://doi.org/10.1039/C6EM00628K.

(49) Kwon, K. D.; Green, H.; Bjöörn, P.; Kubicki, J. D. Model Bacterial Extracellular Polysaccharide Adsorption onto Silica and Alumina: Quartz Crystal Microbalance with Dissipation Monitoring of Dextran Adsorption. *Environ. Sci. Technol.* **2006**, *40* (24), 7739–7744. https://doi.org/10.1021/es061715q.

(50) Schubert, J.; Radeke, C.; Fery, A.; Chanana, M. The Role of PH, Metal Ions and Their Hydroxides in Charge Reversal of Protein-Coated Nanoparticles. *Phys. Chem. Chem. Phys.* **2019**, *21* (21), 11011–11018. https://doi.org/10.1039/C8CP05946B.

(51) Cai, J. Structural Chemistry and Properties of Metal Arenesulfonates. *Coord. Chem. Rev.* **2004**, *248* (11–12), 1061–1083. https://doi.org/10.1016/j.ccr.2004.06.014.

(52) Ling, I.; Raston, C. L. Primary and Secondary Directing Interactions of Aquated Lanthanide(III) Ions with p-Sulfonated Calix[n]Arene. *Coord. Chem. Rev.* **2018**, *375*, 80–105. https://doi.org/10.1016/j.ccr.2017.11.004.

(53) Zand, R.; Agrawal, B.; Goldstein, I. PH-Dependent Conformational Changes of Concanavalin A. *Proc. Natl. Acad. Sci. U. S. A.* **1971**, *68* (9), 2173—2176. https://doi.org/10.1073/pnas.68.9.2173.

(54) Amirov, R. R.; Burilova, E. A.; McMillan, Z. T.; Amirova, L. R.; Ziyatdinova, A. B.; Shayimova, J. R.; Bukharov, M. S.; Dimiev, A. M.; Zakharov, A. V. An NMR Relaxivity and ESR Study of the Interaction of the Paramagnetic Manganese(II) and Gadolinium(III) Ions with Anionic, Cationic and Neutral Water-Soluble Polymers and Their Mixtures. *J. Mol. Liq.* **2017**, *238*, 184–192. https://doi.org/10.1016/j.molliq.2017.04.131.

(55) Frost, M. S.; Dempsey, M. J.; Whitehead, D. E. The Response of Citrate Functionalised Gold and Silver Nanoparticles to the Addition of Heavy Metal Ions. *Colloids Surf. Physicochem. Eng. Asp.* **2017**, *518*, 15–24. https://doi.org/10.1016/j.colsurfa.2016.12.036.

(56) Maiolo, D.; Paolini, L.; Di Noto, G.; Zendrini, A.; Berti, D.; Bergese, P.; Ricotta, D. Colorimetric Nanoplasmonic Assay To Determine Purity and Titrate Extracellular Vesicles. *Anal. Chem.* **2015**, *87* (8), 4168–4176. https://doi.org/10.1021/ac504861d.

(57) Andrási, M.; Gáspár, A.; Kovács, O.; Baranyai, Z.; Klekner, Á.; Brücher, E. Determination of Gadolinium-Based Magnetic Resonance Imaging Contrast Agents by Micellar Electrokinetic Capillary Chromatography. *ELECTROPHORESIS* **2011**, *32* (16), 2223–2228. https://doi.org/10.1002/elps.201100185.

(58) Hvattum, E.; Normann, P. T.; Jamieson, G. C.; Lai, J.-J.; Skotland, T. Detection and Quantitation of Gadolinium Chelates in Human Serum and Urine by High-Performance Liquid Chromatography and Post-Column Derivatization of Gadolinium with Arsenazo III. *J. Pharm. Biomed. Anal.* **1995**, *13* (7), 927–932. https://doi.org/10.1016/0731-7085(95)01311-8.

(59) Normann, P. T.; Joffe, P.; Martinsen, I.; Thomsen, H. S. Quantification of Gadodiamide as Gd in Serum, Peritoneal Dialysate and Faeces by Inductively Coupled Plasma Atomic Emission Spectroscopy and Comparative Analysis by High-Performance Liquid Chromatography. *J. Pharm. Biomed. Anal.* **2000**, *22* (6), 939–947. https://doi.org/10.1016/S0731-7085(00)00255-7.

(60) Künnemeyer, J.; Terborg, L.; Nowak, S.; Scheffer, A.; Telgmann, L.; Tokmak, F.; Günsel, A.; Wiesmüller, G.; Reichelt, S.; Karst, U. Speciation Analysis of Gadolinium-Based MRI Contrast Agents in Blood Plasma by Hydrophilic Interaction Chromatography/Electrospray Mass Spectrometry. *Anal. Chem.* **2008**, *80* (21), 8163–8170. https://doi.org/10.1021/ac801264j.

(61) Kahakachchi, C. L.; Moore, D. A. Speciation of Gadolinium in Gadolinium-Based Magnetic Resonance Imaging Agents by High Performance Liquid Chromatography Inductively Coupled Plasma Optical Emission Spectrometry. *J. Anal. At. Spectrom.* **2009**, *24* (10), 1389. https://doi.org/10.1039/b907044c.

Chapter IV

Block copolymer self-assembly and interactions with gold nanoparticles

I Introduction

This last chapter will focus on assemblies of gold nanoparticles (AuNPs) and PAA-*b*-PVP copolymers promoted by a change of pH.

In **chapter III**, the assembly process of AuNPs was promoted by the interactions of metal ions with citrate or Bis(p-sulfonatophenyl)phenylphosphine) (BSPP) ligands present at their surface. According to the nature of the ligand capping the AuNPs, different interaction mechanisms with the metallic ions were evidenced. The interaction with Gd^{3+} ions resulted in the aggregation of AuNP@BSPP and a color change even at very low concentrations of Gd^{3+} ions (i.e. mM range). Even if the formed aggregates are poorly defined, these ones are well adapted for sensing applications.

However, when biomedical applications like imaging, drug delivery or cancer therapy are considered, assemblies with a controlled size and specific compositions are required. As discussed in **chapter I**, the use of polymers has proved its efficiency for such a purpose. Indeed, polymers act as efficient stabilizing agents of AuNPs and avoid their irreversible aggregation. Moreover, they can induce a controlled assembly of AuNPs, through polymer self-assembly or stimuli application.

As discussed in **chapter II**, PAA_{32}-*b*-PVP_{59} block copolymer thanks to PAA block, is pH-responsive. Moreover, it might interact with AuNPs and promote their colloidal stability in aqueous solutions. Therefore, PAA_{32}-*b*-PVP_{59} is a perfect candidate to trigger the assembly of AuNPS in solution.

Objectives

The following work deals with the effect of pH on the assembly process of PAA-*b*-PVP block copolymer and of preformed AuNPs stabilized by this polymer. The first objectives lie in the characterization of these nanostructures and in the understanding of the involved mechanisms. Then several experimental parameters (polymer or AuNPs concentration, polymer structures and composition…) are varied to trigger the characteristic of obtained assemblies. Finally, the addition of ions on these structures or the in situ formation of AuNPs will be studied.

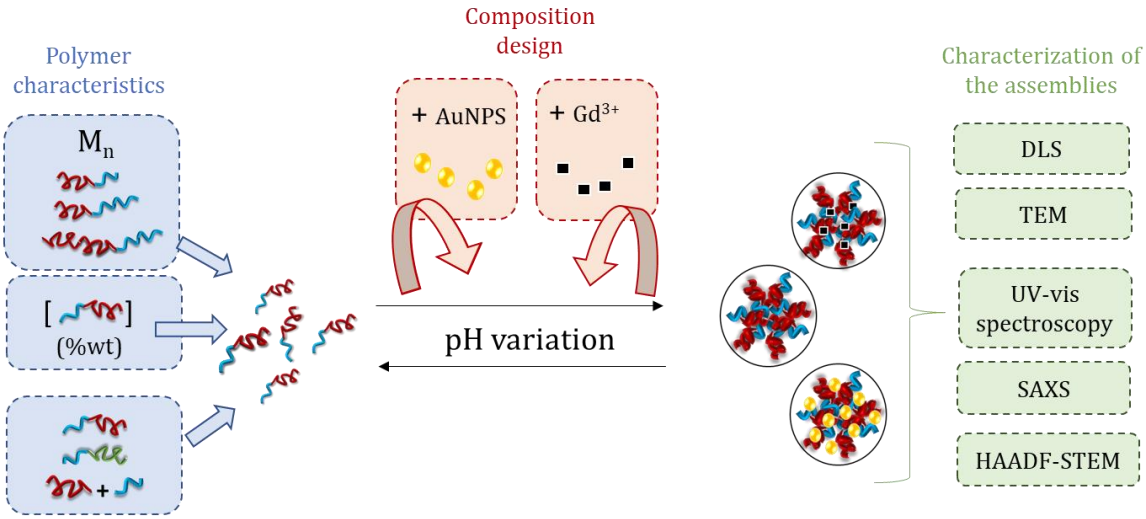

Scheme 10. Objectives of the chapter regarding the study of the influence of the polymer characteristics (molecular weight, concentration, configuration) and the incorporation of inorganic species such as gold nanoparticles (AuNPs) or gadolinium ions (Gd^{3+}) onto the final assemblies obtained after the self-assembly of the polymer or the interactions between inorganic and organic matter, under pH variation.

II Formation and characterization of the nanostructures

II.1 PAA_{32}-*b*-PVP_{59} self- assembly

Stimuli-responsive block copolymers have been extensively used to induce the formation of aggregates[1–3]. For example, pH-responsive BCPs can assemble under pH variation and thus be used as cargo for anti-cancer drugs like doxorucibin (DOX)[4]. The block copolymer PAA_{32}-*b*-PVP_{59} containing pH-sensitive acrylate functions (AA) shows morphological changes under pH variation. When the pH of a solution of PAA_{32}-*b*-PVP_{59} (pH=9) was decreased, the solution became cloudy, due to the decreasing of the solubility of the polymer with the progressively protonation of the acrylic acid moeities (**Figure 108**).

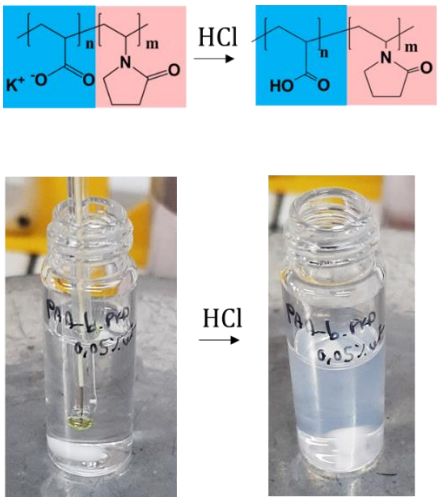

Figure 108. Schematic representation of the acidification of PAA_{32}-*b*-PVP_{59} block copolymer. Photo of the visual observation during the acidification.

Nevertheless, event at pH=2.5 no precipitation could be observed. To have more insights into the behavior of the BCP in solution, Dynamic Light Scattering (DLS) and Transmission Electron Microscopy (TEM) techniques were used to characterize the solution at different pH values. DLS measurements are presented in **Figure 109**. For pH > 4, correlation functions are characteristics of colloids with non-pure Brownian motion. The low scattered intensity supports the formation of non-organized structure present in few numbers in solution. At pH < 4, scattered light intensity increases in agreement with the presence of objects in the solution. Also, the error onto Z-average value is largely decreasing, associated to a correlation function typical from well-defined structures. Hydrodynamic diameter equal to 118± 24 nm, to 137±13 nm and to 262±8 nm are found at pH=4, pH=3 and pH=2.5 respectively.

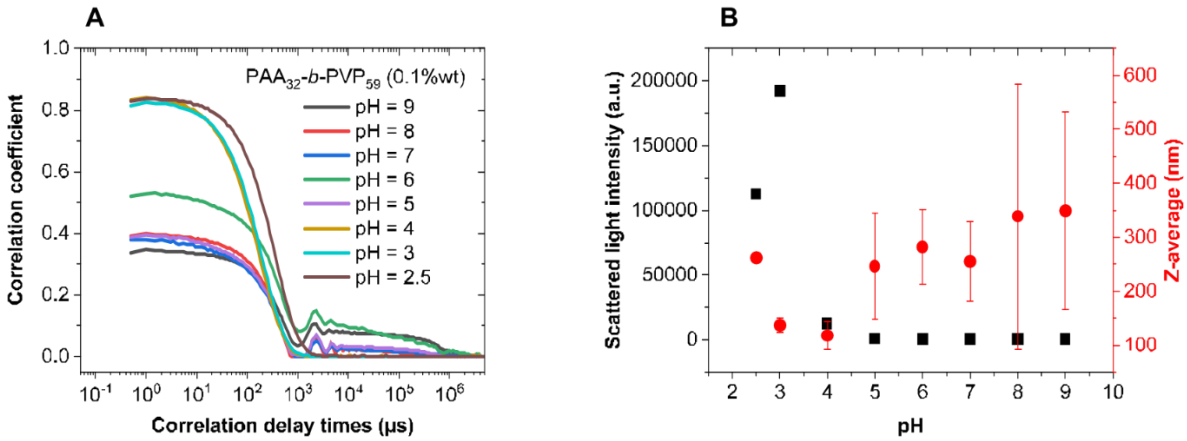

Figure 109. (**A**) Correlation functions and (**B**) typical evolutions of the scattered light intensity (black squares) and Z-average diameter (red dots) measured by a mono-angle DLS instrument for a PAA_{32}-*b*-PVP_{59} solutions at 0.1 %wt at different pH values.

TEM is in agreement with the observations onto the DLS pictures (**Figure 110**). The PAA_{32}-*b*-PVP_{59} block copolymer adopts no particular shape until attaining pH=4, where nanoassemblies are forming. Their shape is nearly spherical and their size seems to increase with decreasing pH until pH=2.5, at which the measured average diameter is equal to 484 ± 125 nm (**Figure 111**).

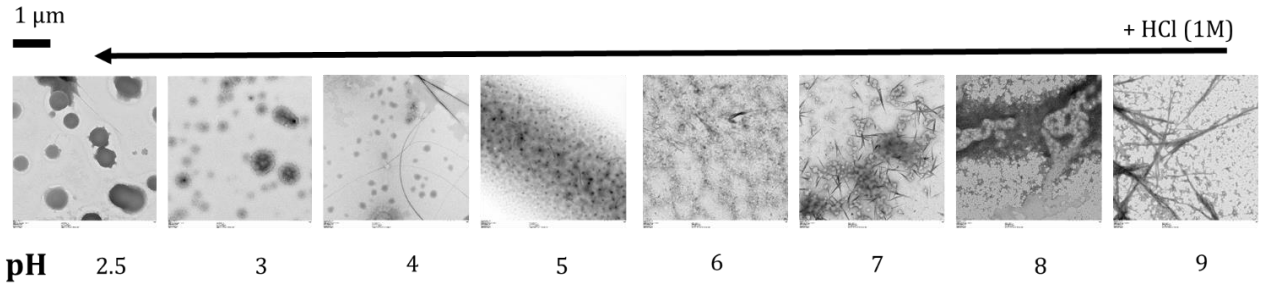

Figure 110. TEM pictures of PAA_{32}-*b*-PVP_{59} solution (0.1%wt) at different pH steps during progressive HCl solution (1M) adding. Uranyl acetate was used to stain the sample.

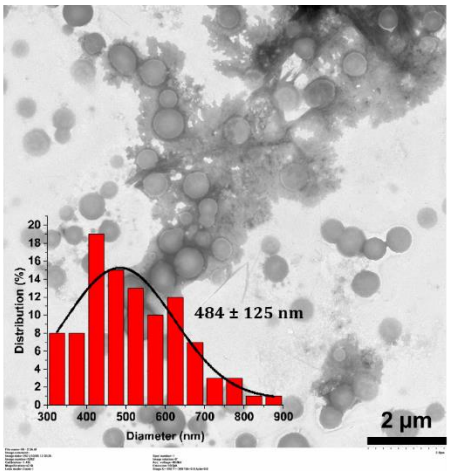

Figure 111.TEM pictures of nanoassemblies formed at pH=2.5 in the PAA_{32}-*b*-PVP_{59} solution (0.1%wt) after adding HCl solution (1 M) and associated distribution analysis about the size of the structures (200 counts).

The behavior of the PAA_{32}-*b*-PVP_{59} block copolymer changed then radically around pH 4, to self-assemble into nanostructures with increasing size when pH is decreased. As explained at the beginning, PAA is a ionizable polymer, which AA functions are progressively protonated when pH is decreased. The determination of the pK_A value of this block copolymer has been studied in **chapter II.** The self-assembly process observed here could be then due to the protonation of the PAA, which concerns more and more acrylate functions by decreasing the pH (ionization level equal to 5, 43 and 62 % at pH=2.5, pH=3 and pH=4 respectively). As widely reported in the literature, PAA and PVP homopolymers have been generally mixed together at low pH to form gels or interpolymer complexes through hydrogen bonds.[5–11] Hydrogen bond and Van der Waals interactions could be here responsible of this self-assembly process. Zeta potential measurements were realized onto the samples (**Figure 112**). As expected, the global charge of the PAA_{32}-*b*-PVP_{59} solution is negative, due to acrylate functions. As these AA functions are progressively protonated, the global charge increases more and more until attaining $\xi = -3 \pm 0.8$ mV for pH=2.5, which is near from neutral charge.

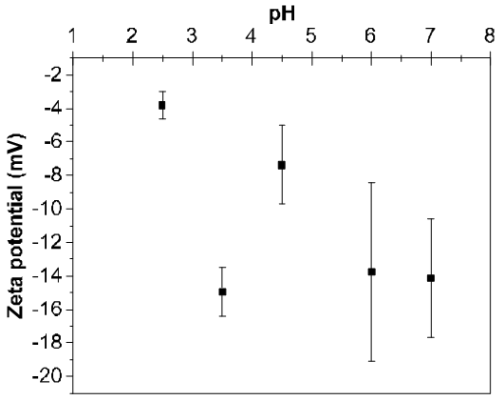

Figure 112. Zeta potential measurements onto PAA_{32}-*b*-PVP_{59} block copolymer solution (0.1%wt) at different pH values after adding HCl solution (1M)

An additional pH variation was realized on a PAA_{32}-*b*-PVP_{59} block copolymer solution at 0.05%wt (dilution by two). The pH of the initial solution at 9 is directly decreased until pH=2.5 (**Figure 113**).

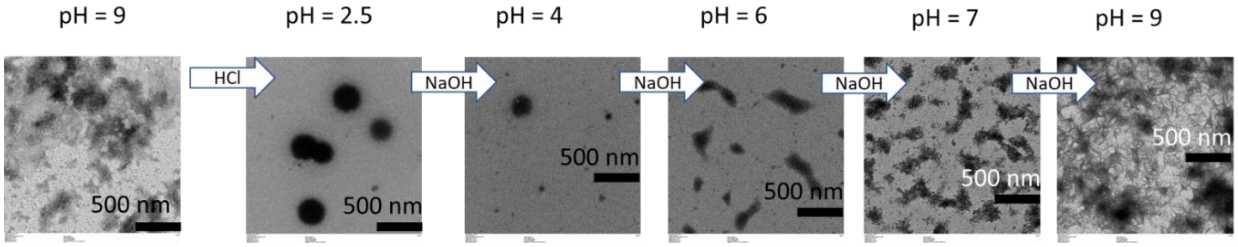

Figure 113. TEM pictures of the PAA_{32}-*b*-PVP_{59} block copolymer solution (0.05%wt) at different pH values after one adding of HCl solution (1M) and several progressive adding of NaOH solution (1M). Uranyl acetate was used to stain the sample.

The obtained nanostructures at pH = 2.5 are smaller with an average diameter of 315 ± 83 nm and this is probably due to copolymer concentration, but needs to be confirmed with supplementary tests. To the solution at pH=2.5, sodium hydroxide (NaOH) was progressively added to come back to the initial pH around 9. PAA_{32}-*b*-PVP_{59} block copolymer returns progressively to similar organization as at the initial state, with the exception that salts are much present.

The reversible behavior of the observed assembly mechanism is again confirmed through Small Angle X-ray Scattering (SAXS) measurements onto initial solution of PAA_{32}-*b*-PVP_{59} block copolymer at pH =9, at pH=2.5 and again at pH=9 after adding HCl and NaOH (**Figure 114**). Indeed, when assembled system are present in solution (at pH=2.5), SAXS signal radically changes and then comes back to initial signal when the pH is increased to 9. By performing Static Light Scattering (SLS) analysis, the q range can be broadened and a final plateau is obtained to allow a fit of the curve and thus an estimation of the gyration radius. A fitting model was investigated by B. Lonetti in our team through the use of SASVIEW software. This fitting model was applied onto the curve resulting from the combination of the SLS and SAXS data (**Figure 114B**). As detailed in the experimental part of this work, this model takes into account spatial inhomogeneities in the spherical structures like in hydrogels[12] allowing different correlation lengths describing both global and internal organization at nanoscale.

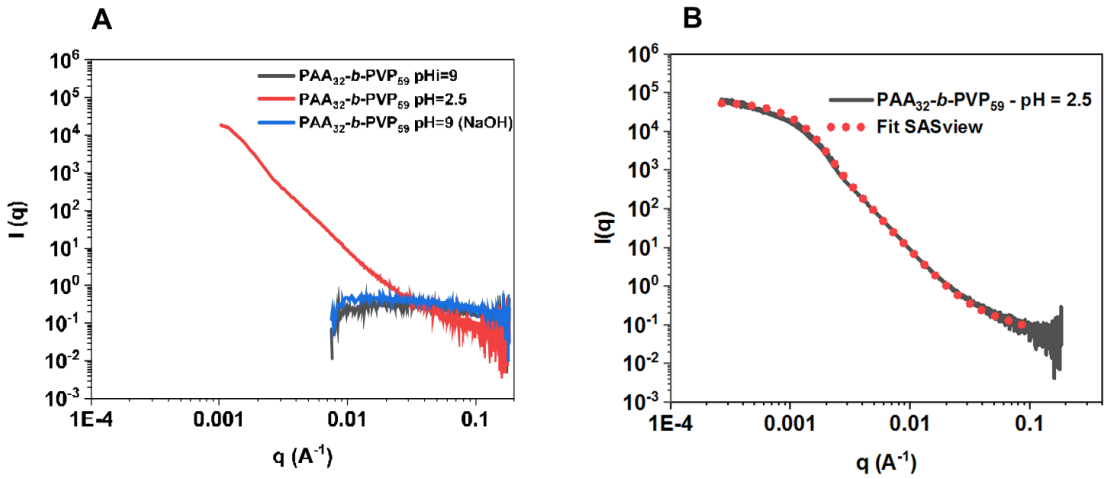

Figure 114. SAXS analysis of PAA_{32}-*b*-PVP_{59} block copolymer solution (0.05%wt) at different pH values; pHi=9 (black), pH = 2.5 after adding HCl (1M) solution (red) and pH=9 after adding HCl (1M) and then NaOH (1M) solutions (blue) (**A**) SAXS and SLS analysis combined onto one graph for PAA_{32}-*b*-PVP_{59} block copolymer solution (0.05%wt) at pH = 2.5 and fit of the curve (red dots) (**B**)

As explained in **chapter I**, supplementary microscopy techniques can be used to enable a 3D visualization of the nanostructures. We further characterized the system by TEM and MEB microscopy (**Figure 115**). On both pictures, we can differentiate two kind of structures: white ones with cubic shape which must be salt crystals due to pH adjustment, and some drops of contrasted matter deposited on the grid, which are the nanoassemblies of PAA_{32}-*b*-PVP_{59}. The 3D representation of these nanoassemblies seem to confirm the near-spherical shape estimated with 2D pictures and calculations from scattering techniques.

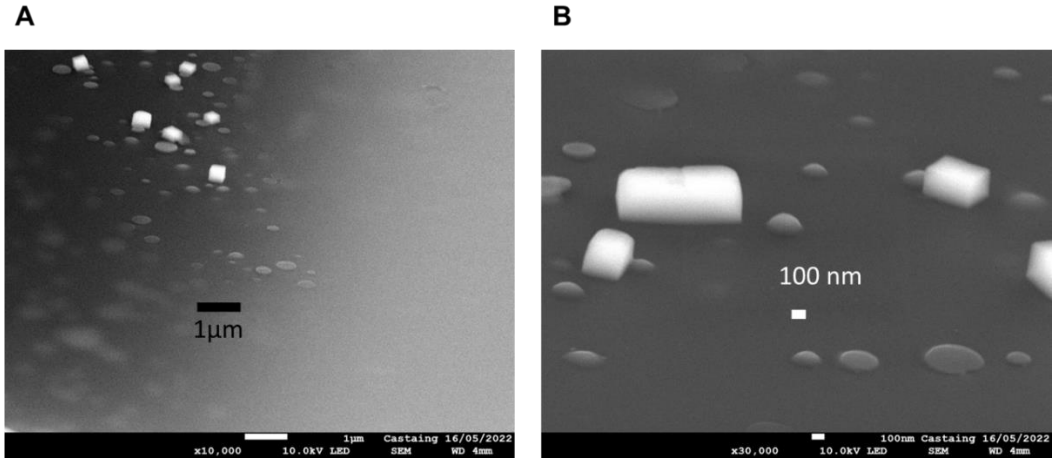

Figure 115. MEB pictures of PAA_{32}-*b*-PVP_{59} block copolymer solution (0.05%wt) at pH=2.5 deposited on a TEM grid tilted

Now that the pH-responsiveness of the PAA_{32}-*b*-PVP_{59} block copolymer has been studied and investigated into the design of assemblies, the interest is now lying into the incorporation of gold nanoparticles into these polymer-based assemblies.

II.2 Hybrid assemblies based on interactions between PAA_{32}-*b*-PVP_{59} and gold nanoparticles

As detailed in **chapter I**, several strategies are employed to functionalize AuNPs with block copolymers. The one chosen here consists in a ligand exchange starting from AuNPs synthesized thanks to the Turkevich method.[13] The affinity of PVP for gold has been widely investigated in the literature, particularly the role of PVP into the nanoparticle synthesis (in situ method).[14–17] Capping of AuNPs with PVP have been commonly described and have found interesting applications into biological fields[18–20] thanks to PVP biocompatibility.

Preformed Au@citrate NPs were centrifuged to remove citrate ligands' excess and the resulting AuNPs solution was mixed to PAA_{32}-*b*-PVP_{59} block copolymer solution to obtain a sample with 0.05%wt of PAA_{32}-*b*-PVP_{59} and a fixed concentration of gold of [Au]=500 µM. The value of final pH was equal to 8.8. A simple stirring during few minutes was performed. UV-vis spectra and DLS analysis were performed on the Au@citrate NPs and on the sample containing the Au@citrate NPs mixed with the PAA_{32}-*b*-PVP_{59} after stirring (**Figure 116**). A slight increase in the size is detected in DLS analysis, accompanied by a higher correlation signal and a less polydisperse population in terms of size. UV-vis spectra do not show significant changes in absorbance with a limpid red solution.

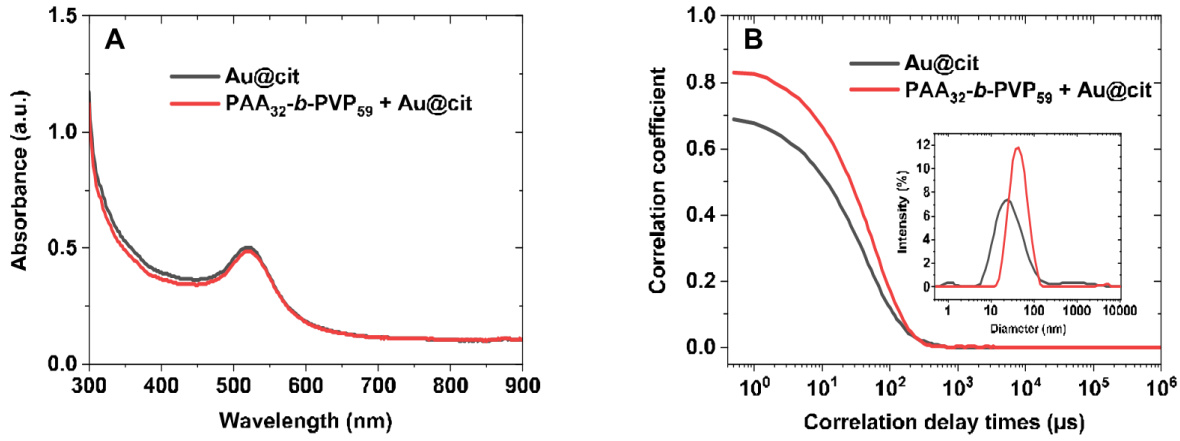

Figure 116. (**A**) UV-visible spectra and (**B**) DLS analysis of Au@citrate NPs and the sample mixing Au@citrate NPs and PAA_{32}-*b*-PVP_{59} block copolymer after stirring few minutes. [PAA_{32}-*b*-PVP_{59}] = 0.05%wt, [Au] = 500 µM, pH = 8.8 for the sample. Inset of (B) corresponds to distribution average size in intensity.

When the pH of the solution is decreased to pH=2.5, using HCl solution (1M), the solution becomes more purple and more turbid. The visual observation is confirmed with UV-vis spectroscopy: the plasmonic band of the sample is shifted (slight color change) and its intensity is increased because of the diffusion caused by the turbidity of the sample (**Figure 117**).

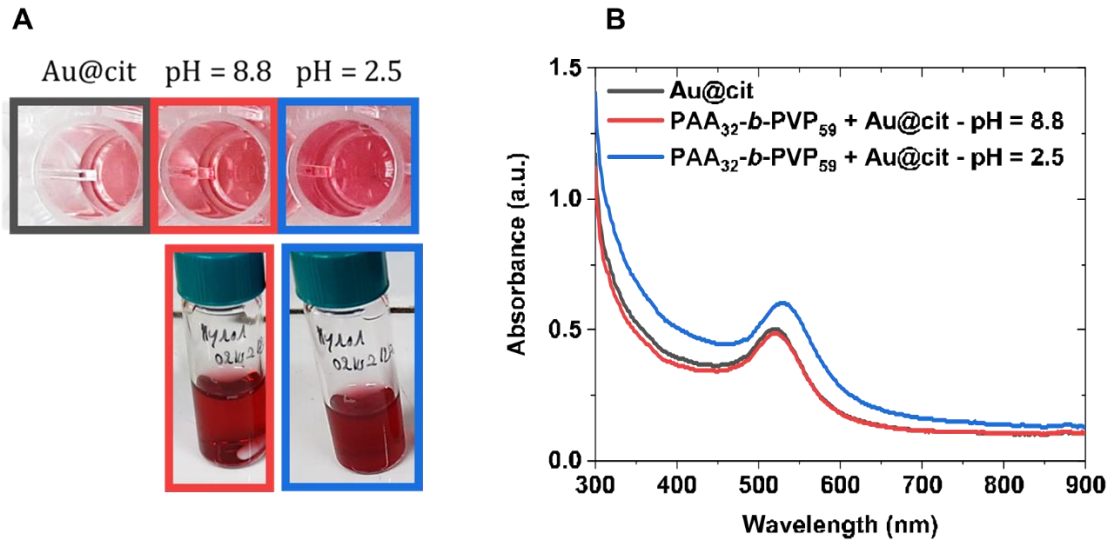

Figure 117. (**A**) Pictures of samples analyzed in UV-vis spectroscopy: Au@cit NPs (grey con toured), Au@cit NPs + PAA_{32}-*b*-PVP_{59} at pH=8.8 (red contoured) and Au@cit NPs + PAA_{32}-*b*-PVP_{59} at pH=2.5 (blue contoured). (**B**) UV-vis spectra of the samples. [PAA_{32}-*b*-PVP_{59}] = 0.05%wt, [Au] = 500 µM.

DLS measurements were performed at pH=8.8 and pH=2.5 (**Figure 118A**). Whereas at pH=8.8, a hydrodynamic diameter, D_H, equal to 29 ± 6 nm is measured, a D_H value of 164 ± 10 nm is measured at pH=2.5. This increase might be responsible for the observed turbidity of the solution. TEM pictures were realized onto the two samples at pH=8.8 (**Figure 118B)** and pH=2.5 (**Figure 118C)**, Whereas at pH=8.8 isolated AuNPs are observed, large spherical objects comprising several AuNPS with an average diameter equal to 275 ± 70 nm are visible on the TEM grid. Zeta potential of the obtained nanostructures is about ξ = -6.7±0.5 mV which is slightly more negative than polymeric nanostructures. The AuNPs seem then well functionalized by PAA_{32}-*b*-PVP_{59} as they are brought into the polymeric assembly under pH variation.

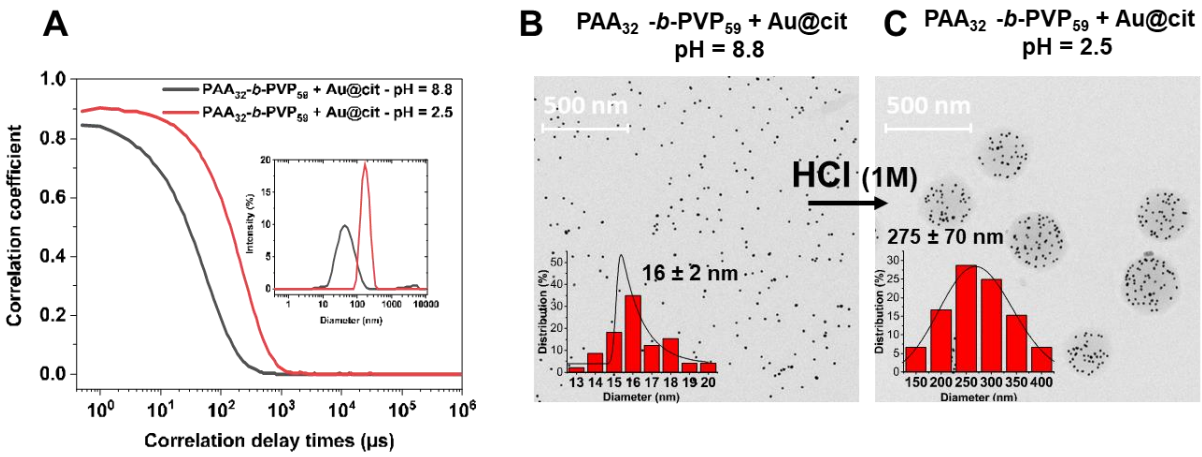

Figure 118. (**A**) Correlation functions using the NNLS method and distribution average size in intensity (inset) for the sample PAA_{32}-*b*-PVP_{59} + Au@cit at pH=8.8 and pH=2.5 (**B**) TEM picture with size distribution analysis of PAA_{32}-*b*-PVP_{59} + Au@cit at pH=8.8 and (**C**) at pH=2.5. [PAA_{32}-*b*-PVP_{59}]=0.05%wt; [Au]=500 µM.

By observing these TEM pictures, one question raises about the localization of gold nanoparticles into the assembly, whether they are on the surface, or inside the polymer structure based on hydrogen bonds. To answer this question, analysis able to inform about morphology such as SAXS, STEM and MEB were applied. As for the block copolymer self-assembly study, the question of the reversibility has been investigated and SAXS analysis proved that the assembly mechanism was fully reversible as the initial and the final signals superposed each other (**Figure 119A**). As detailed in **chapter I**, several domains are illustrated on the SAXS curves associated to different analysis of the nanostructure. Indeed, Guinier region located for small q (0.001 – 0.001 A^{-1}) inform about the global nanostructure size and morphology, whereas near q= 0.1 A^{-1}, the analysis will provide information about the single gold nanoparticle. The same fitting investigation was realized by B. Lonetti and the resulting fitting curve is represented onto the **Figure 119B.** As explained precisely in the experimental part, the model takes this time into account the presence of the gold nanoparticles and considers them as hard spheres.

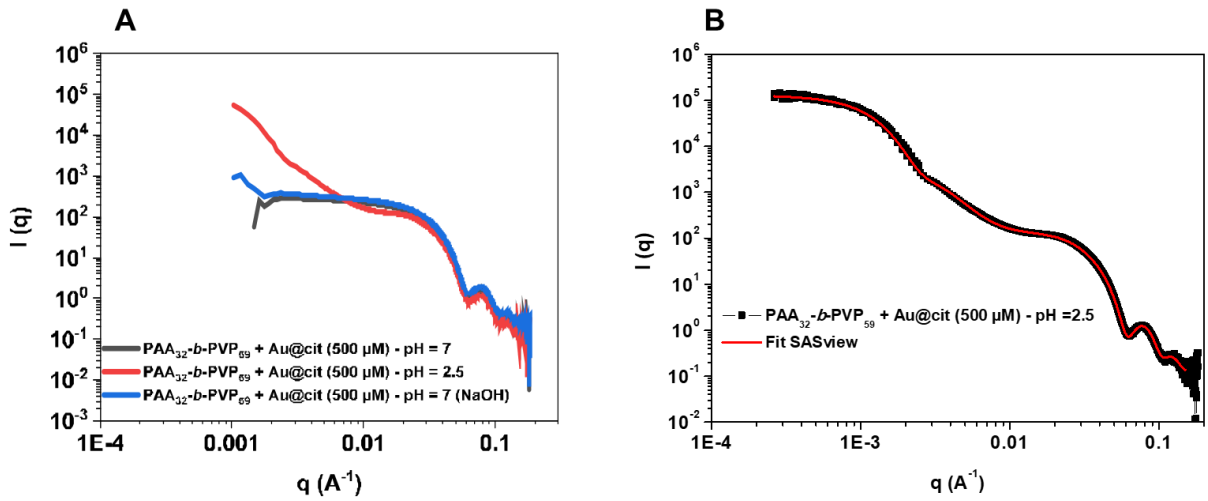

Figure 119. SAXS analysis of the sample containing PAA_{32}-*b*-PVP_{59} block copolymer (0.05%wt) and Au@citrate ([Au]=500µM) at different pH values; pHi=8.8 (black), pH = 2.5 after adding HCl (1M) solution (red) and pH=9 after adding HCl (1M) and then NaOH (1M) solutions (blue) (**A**) SAXS and SLS analysis combined onto one graph for the sample PAA_{32}-*b*-PVP_{59} + Au@citrate at pH = 2.5 and fit of the curve (red dots) (**B**)

To visualize the 3D morphologies adopted by the block copolymer and the AuNPs and to answer to the question about the localization of AuNPs, MEB microscopy and HAADF-STEM techniques were used. HAADF-STEM was first realized on the classic TEM grid (**Figure 120**) and MEB (**Figure 121**) onto the tilted TEM grid where the sample containing PAA_{32}-*b*-PVP_{59} and Au@citrate at pH=2.5 was deposited.

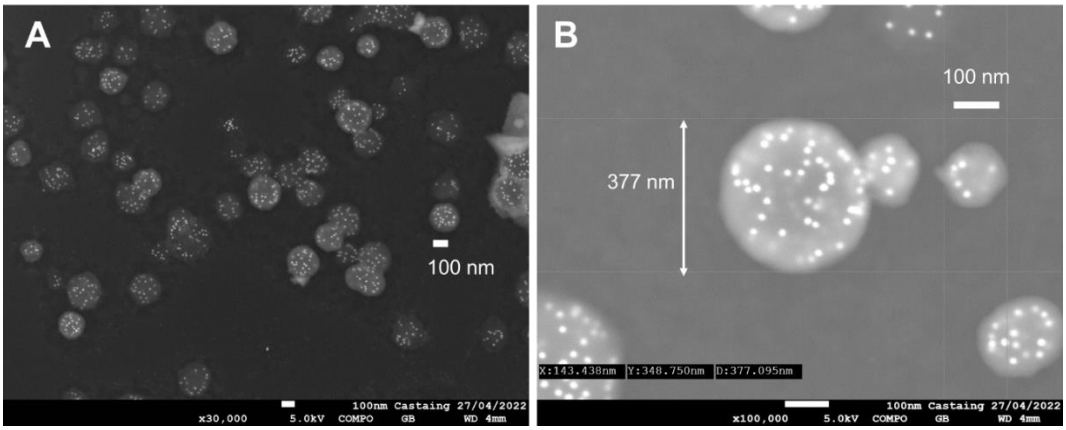

Figure 120. HAADF-STEM pictures of PAA_{32}-b-PVP_{59} (0.05%wt) + Au@citrate ([Au]=500 µM) sample at pH=2.5 at two different scales x30.000 (**A**) and x100,000 (**B**)

HAADF-STEM technique is based on the density and thickness differentiation, the brighter the denser and the deeper the darker. Thanks to this technique, the nanoassemblies reveal several layers which are more or less bright. Some white dots, corresponding to AuNPs which are very dense material, are very bright compared to other ones which are poorly visible and seem to belong to a deeper layer as they shine less. According to apparatus parameters, the sample would be too thick to allow a correct visualization of the background layer of the deposit. This means that the AuNPs which are deeply localized, are actually inside the polymer structure and not on the other side of the surface of the nanostructure.

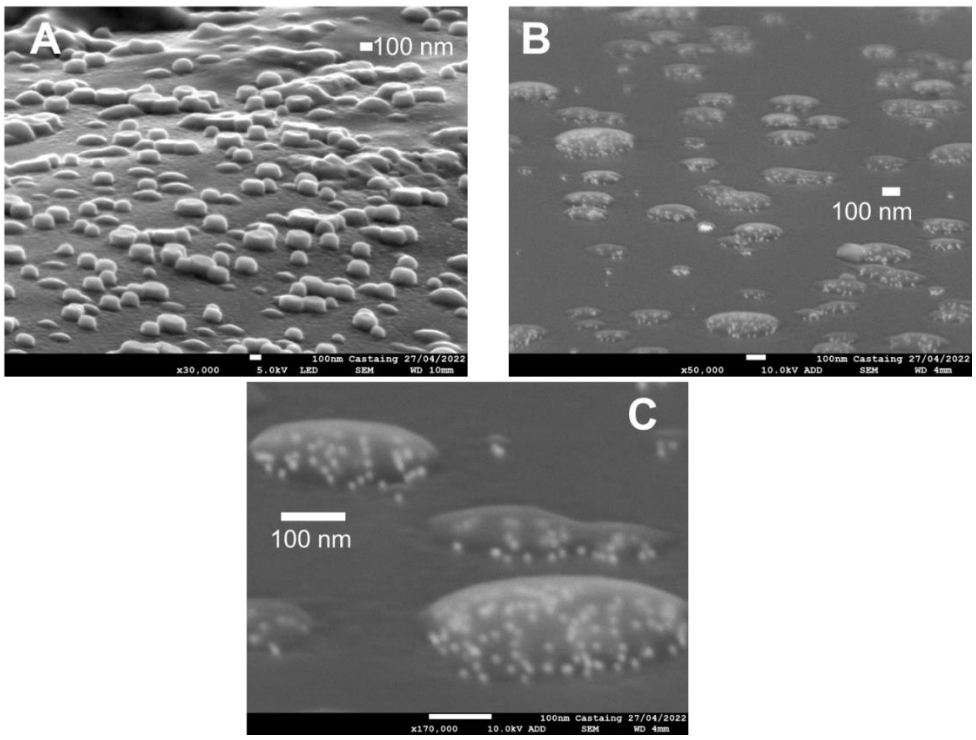

Figure 121.MEB pictures of tilted TEM grid of PAA_{32}-*b*-PVP_{59} (0.05%wt) + Au@citrate ([Au]=500µM) sample at pH=2.5 at different scales x30,000 (**A**), x50,000 (**B**) and x170,000 (**C**)

MEB pictures inform about the morphology adopted on the grid by visualizing it from another angle (**Figure 121**). The surface tension seems to be different from the one of the block copolymer self-assembly structures. Indeed, the structures containing AuNPs seem to have a higher contact angle in general cases but some of them lie flat on the grid. A quick observation would suppose that this contact angle depends on the density of AuNPs contained in the polymer structure, but this hypothesis still need to be confirmed with further studies.

A final elemental map was realized onto this grid to know about the internal organization of the block copolymer and the Au@citrate NPs (**Figure 122**). Only PVP contains nitrogen, so the nitrogen map indicates the localization of this polymer, regarding oxygen map, it indicates both PAA and PVP localization. It seems that no organized structuration is adopted by the block copolymer in the nanoassembly.

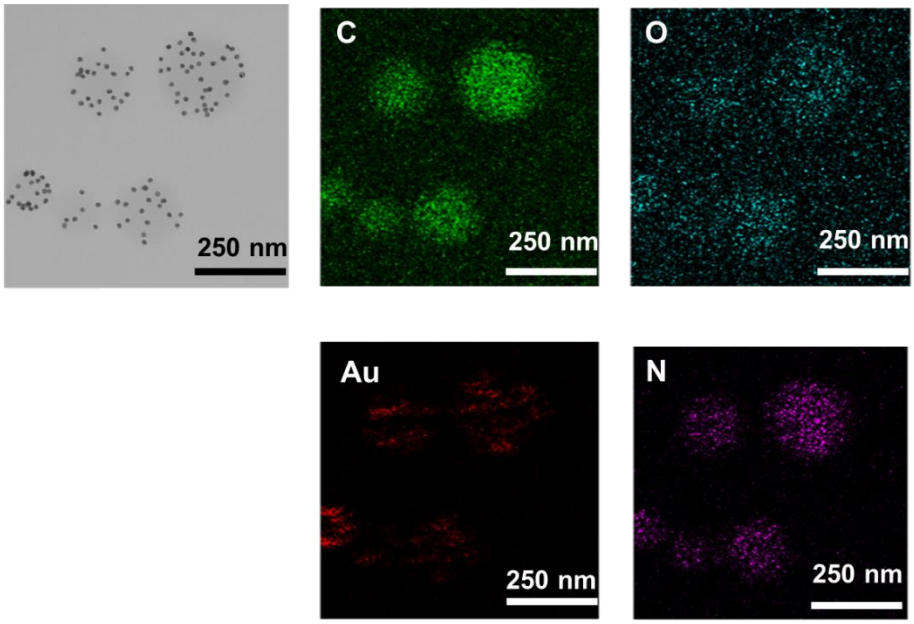

Figure 122. TEM picture and elemental maps of the sample containing PAA_{32}-*b*-PVP_{59} (0.05%wt) and Au@citrate NPs ([Au]=500 µm) for the following elements: carbon, oxygen, gold and nitrogen.

II.3 Effect of the addition of salt

The stability of the observed structures was first studied by adding different quantity of a solution of NaCl (1M) to preformed nanoassemblies at pH=2.5 ([PAA_{32}-*b*-PVP_{59}]=0.05%wt and [Au]=500 µM). DLS analysis shows that a slight change in terms of size and scattered light intensity after the first addition of NaCl, but further increased of NaCl concentration does not change significantly measured size (**Figure 123**). Apart from the dilution effect, UV-vis spectrum remains constant demonstrating the good colloidal stability upon addition of salt.

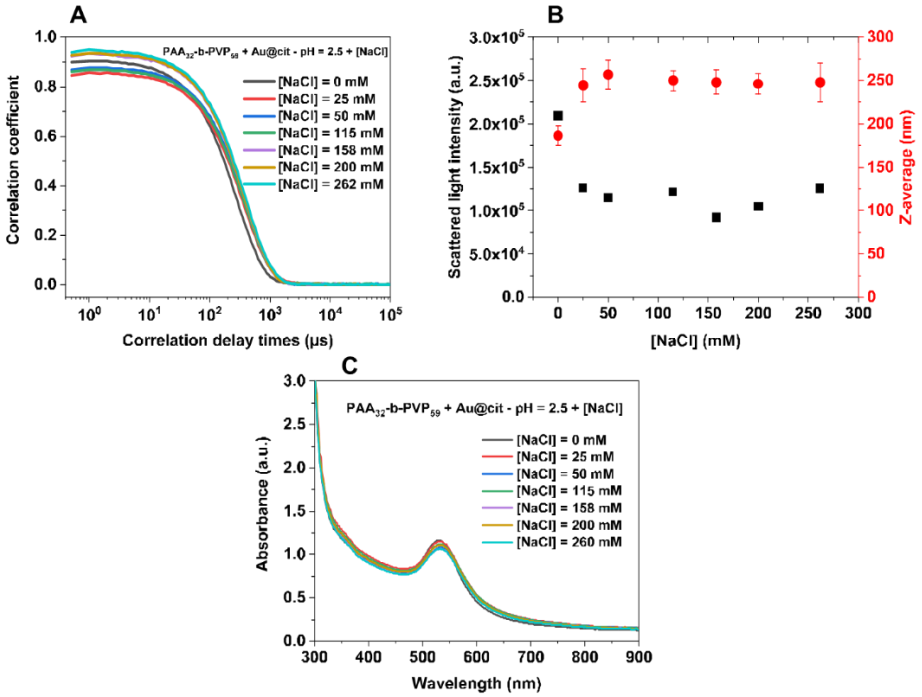

Figure 123. (**A**) Correlation functions using the NNLS method, (**B**) typical evolutions of the scattered light intensity (black squares) and Z-average diameter (red dots) and (**C**) UV-vis spectra of the sample containing PAA_{32}-*b*-PVP_{59} (0.05%wt) and Au@citrate NPs ([Au]=500 µM) with increasing concentration of NaCl ([NaCl]= 0-0.26 M)

TEM pictures were then realized on four concentrations of NaCl: 0; 50; 115 and 262 mM. On **Figure 124,** when NaCl is added, the presence of salt crystals is observed and the initial hybrid nanostructures which are localized between the crystal salts seem to remain intact.

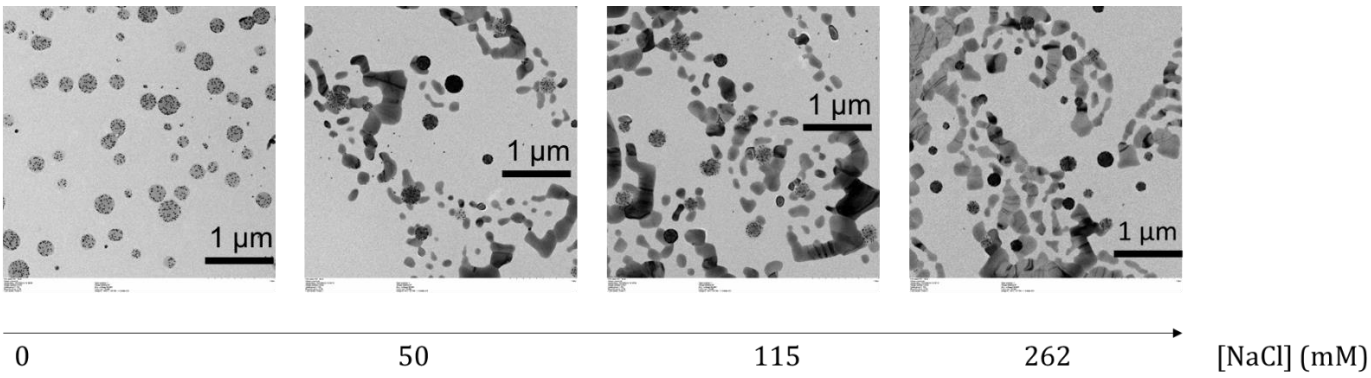

Figure 124. TEM pictures of the sample containing PAA_{32}-*b*-PVP_{59} (0.05%wt) and Au@citrate NPs ([Au]=500 µM) with increasing concentration of NaCl ([NaCl]= 0-0.26 M)

A second experiment was then performed by performing the addition of NaCl at pH=8.8 before lowering it to pH=2.5. Only one concentration was tested [NaCl] = 115 mM, the one that is currently used into biological media. DLS measurements were realized and compared to the reference solution before and after pH decrease, and to the previous results obtained by adding NaCl (115 mM) after assembly (**Figure 125**).

Adding NaCl salt before decreasing pH, seems to have no critical influence on the assembly mechanism, as nanostructures are still formed after the decrease of pH. Measured hydrodynamic diameter 248 ± 23 nm is similar to the one measured when the salt was added after the formation of nano-assemblies (250 ± 12 nm). However, both sizes remain higher than the one measured without the addition of salt (164 ± 10 nm). TEM pictures shows the presence of nano-assemblies among salt crystals (**Figure 126**).

A

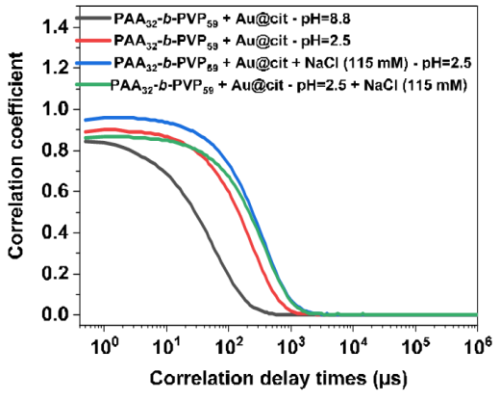

B

Samples	PAA_{32}-*b*-PVP_{59} (0.05%wt) + Au@citrate ([Au]=500µM) pH = 8.8	PAA_{32}-*b*-PVP_{59} (0.05%wt) + Au@citrate ([Au]=500µM) pH = 2.5	PAA_{32}-*b*-PVP_{59} (0.05%wt) + Au@citrate ([Au]=500µM) + NaCl (115mM) then pH =2.5	PAA_{32}-*b*-PVP_{59} (0.05%wt) + Au@citrate ([Au]=500µM) pH = 2.5 then NaCl (115 mM)
Scattered light intensity (a.u)	$1.\ 10^4$	$23.\ 10^4$	$8.\ 10^4$	$12.\ 10^4$
Z-average (nm)	36 ± 14	164 ± 10	248 ± 23	250 ± 12

Figure 125. (**A**) Correlation functions using the NNLS method, (**B**) Scattered light intensity and Z-average diameter data measured by a mono-angle DLS instrument for samples containing PAA_{32}-*b*-PVP_{59} (0.05%wt) and Au@citrate NPs ([Au]=500 µM), at initial pH=8.8, pH=2.5 and with adding NaCl salt ([NaCl]=115 mM) before and after assembly process.

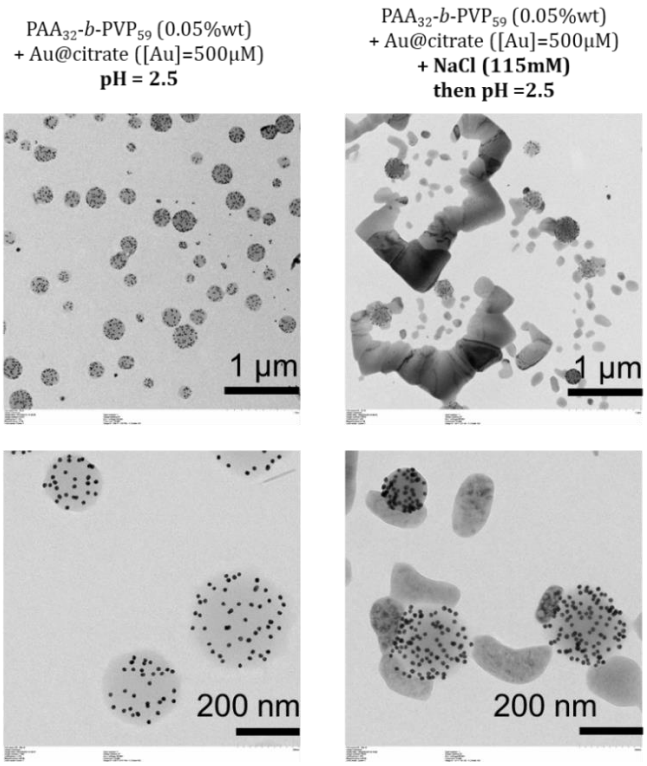

Figure 126. TEM pictures of samples containing PAA_{32}-*b*-PVP_{59} (0.05%wt) and Au@citrate NPs ([Au]=500 µM) at pH=2.5 and withtout (left) or with (right) adding NaCl salt ([NaCl]=115 mM).

Conclusion

Figure 127 enables to compare the assemblies based either on the solely PAA_{32}-*b*-PVP_{59} and on the hybrid assemblies comprising AuNPs (concentration of block copolymer equal to 0.05%wt). Moreover **Table 11** presents the estimation of size of the assembly formed at pH=2.5 for different systems issued from DLS and TEM measurements. The presence of AuNPs seems to lower significantly the final size of the obtained nano-assemblies.

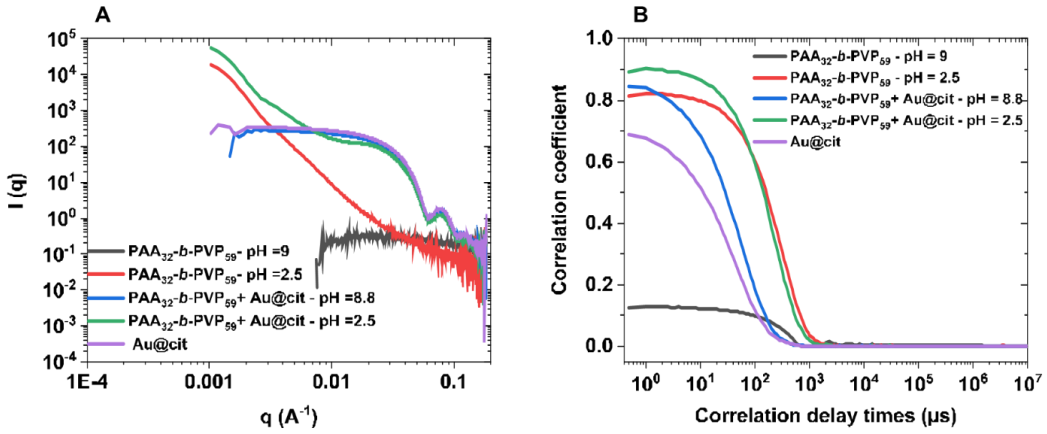

Figure 127. (A) SAXS analysis and (B) Correlation functions using NNLS method of the samples: PAA_{32}-*b*-PVP_{59} block copolymer alone or mixed with Au@citrate NPS, both at pH = 9 and pH=2.5 and the Au@citrate NPs alone. [PAA_{32}-*b*-PVP_{59}] =0.05%wt; [Au] = 500 µM.

Table 11. Size characterizations of the samples PAA_{32}-*b*-PVP_{59} block copolymer assemblies at pH=2.5 at two concentrations 0.1%wt and 0.05%wt and the hybrid assembly mixing PAA_{32}-*b*-PVP_{59} and Au@citrate NPs at pH=2.5, through two different techniques: DLS and TEM.

Sample	DLS analysis	TEM distribution analysis
PAA-b-PVP (0.1%wt)	D_H = 262 ± 8 nm R_H ~ 131 nm	D = 484 ± 125 nm R ~ 242 nm
PAA-b-PVP (0.05%wt)	D_H = 213 ± 6 nm R_H ~ 106.5 nm	D = 315 ± 83 nm R ~ 157.5 nm
PAA-b-PVP (0.05%wt) + Au@cit (500 µM)	D_H = 164 ± 10 nm R_H ~ 82 nm	D = 275 ± 70 nm R ~ 137.5 nm

Therefore, the formation of well-controlled spherical hybrid colloids is induced by a change of pH. Starting from well dispersed individual AuNPs at pH=8.8 stabilized by PAA_{32}-*b*-PVP_{59} block copolymer, the lowering until pH=2.5, induces the protonation of PAA block and the formation of hydrogen bonding network that induces the formation of observed nanostructures. These structures present good colloidal stability and disappeared quickly with an increase of pH in a reversible manner. In order to have more insights onto the formation mechanism of these assemblies, in the next section some investigations are made regarding gold surface interactions through QCM-D measurements and the influence of some parameters onto the assembly process and the final obtained morphology.

III Insights on the mechanism of formation of nano-assemblies

The following part essentially concerns the understanding of the formation mechanism of the studied self-assembly of PAA_{32}-*b*-PVP_{59} block copolymer and the hybrid assembly with AuNPs. This will further allow to design more precisely the final assembled nanostructures.

III.1 QCM-D Measurements

The first investigations regarding assembly mechanism of PAA_{32}-*b*-PVP_{59} block copolymer and AuNPs were made using QCM-D technique. Latter technique has been detailed into the **chapter III**, when the interactions of gold surface with citrate and BSPP ligands were examined. To remind, the QCM-D technique consists in measuring frequency variations of an oscillating quartz crystal, generally due to molecules' accumulation onto the surface. In our experiments, bare gold disks are used and solutions containing polymers or other small molecules are flowing in the chamber containing the disk. Some incubation periods can be realized to optimize the accumulation.

The objective is here to evaluate the affinity of the block copolymer towards the gold surface. As a pH stimulus is engaged into this assembly process, the solution of block copolymer is tested at different pH values to evaluate the influence onto the interactions with gold surface. In order to highlight the effect of block structure, the behavior of the two commercial homopolymers PAA_{25} and PVP_{72} with molecular weights as near as possible from the ones used in the block version was also studied. Frequency variations (ΔF) are recorded for the seventh overtone and as well as the associated energy dissipation (ΔD) (**Figure 128**). Weight variations (Δm) and surface coverage values were calculated for every tested system to have a comparison. (**Figure 129**).

Before rinsing, block copolymer solution at pH=2.5 seems to have the highest affinity with gold surface, as the number of grafted molecules (0.100 molecules/nm^2) is higher than all the other tested systems. However, after rinsing, this is the PAA polymer which adsorbs with a higher affinity, 0.050 molecules/nm^2 at pH=3.3 against 0.023 molecules/nm^2 for the block copolymer at pH=2.5. On the contrary, PVP polymer adsorbs much less (0.016 molecules/nm^2 at pH=2.5) than PAA or the block copolymer, even if the frequency shift is as high as for PAA: indeed, reporting weight shifts to molecular weight to obtain surface coverage, evidences that there are less PVP molecules grafted onto the gold surface than PAA ones. As only low pH values allow high adsorption, these results might be ascribed to hydrogen intramolecular bonds between polymer chains.

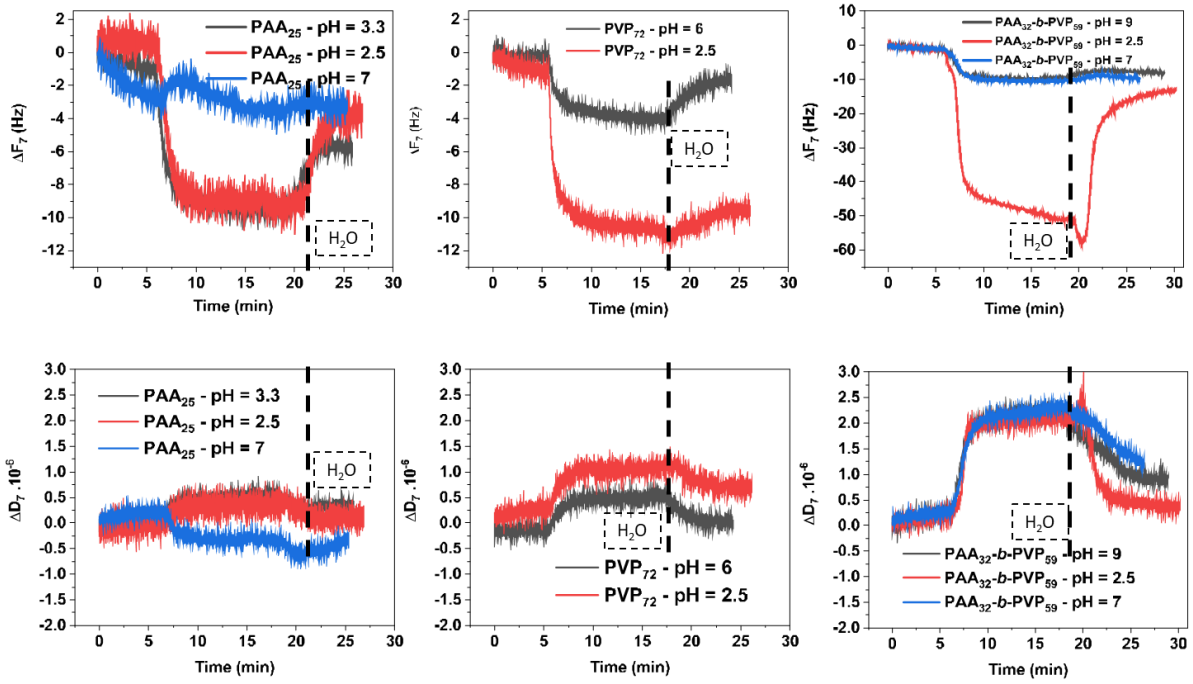

Figure 128. Frequency shift and energy dissipation shift with time (ΔF_7, ΔD 7th overtone) for different polymer solutions; PAA_{25}, PVP_{72} and PAA_{32}-*b*-PVP_{59} at different pH values. The start of rinsing step is here represented by a black dot line and the text H_2O, meaning that a water solution is introduced in the chamber.

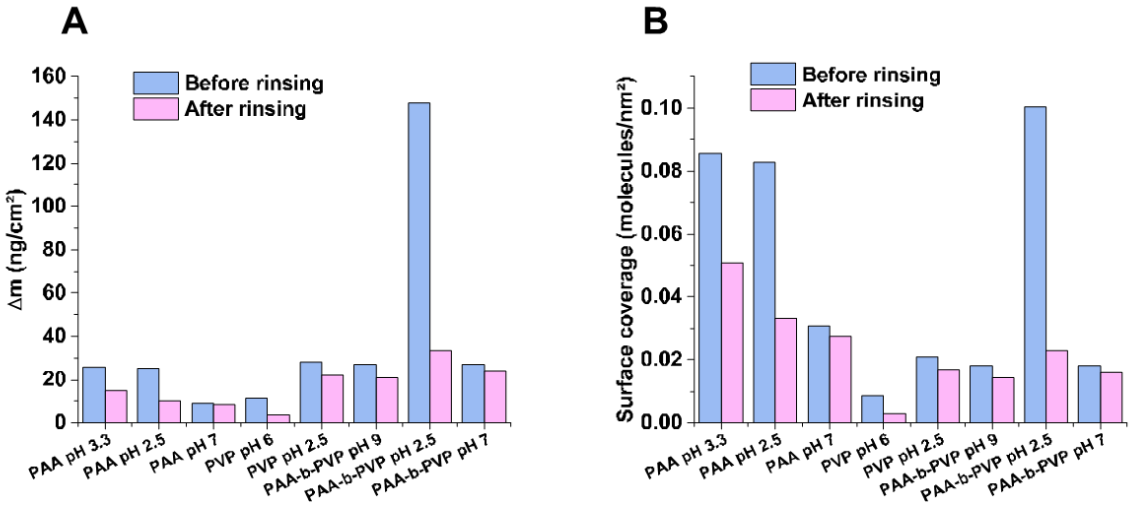

Figure 129. Adsorbed mass per surface unit Δm (ng/cm^2) (**A**) and surface coverage (molecules/nm^2) (**B**) calculated values for each polymer system with associated pH, before and after rinsing step in the QCM-D experiments.

The frequency shift values, after rinsing step with water, increase for the systems involving low pH and PAA polymer, meaning that a weight loss is detected on the gold surface. This can confirm the weak behavior of the interactions existing between PAA_{25}, or PAA_{32}-*b*-PVP_{59} and the gold surface, supporting then the hypothesis of hydrogen bondings. On the contrary, the rinsing step does not lead to significant molecules removing (δ = 0.004 molecules/nm^2) regarding PVP_{72} deposited at low pH (2.5).

An additional interaction is then suspected to exist between PVP polymer and gold and could then explain as well why the frequency shifts of the block copolymer does not come back to initial values like this is the case for PAA_{25} after rinsing step. To have more deep insights into the role of hydrogen bondings, additional experiments are realized by inducing pH decrease directly into the QCM chamber. The BCP is introduced at pH=9 into the chamber and then HCl (1M) solution is introduced to induce a local pH decrease and hopefully creation of hydrogen bondings (**Figure 130**).

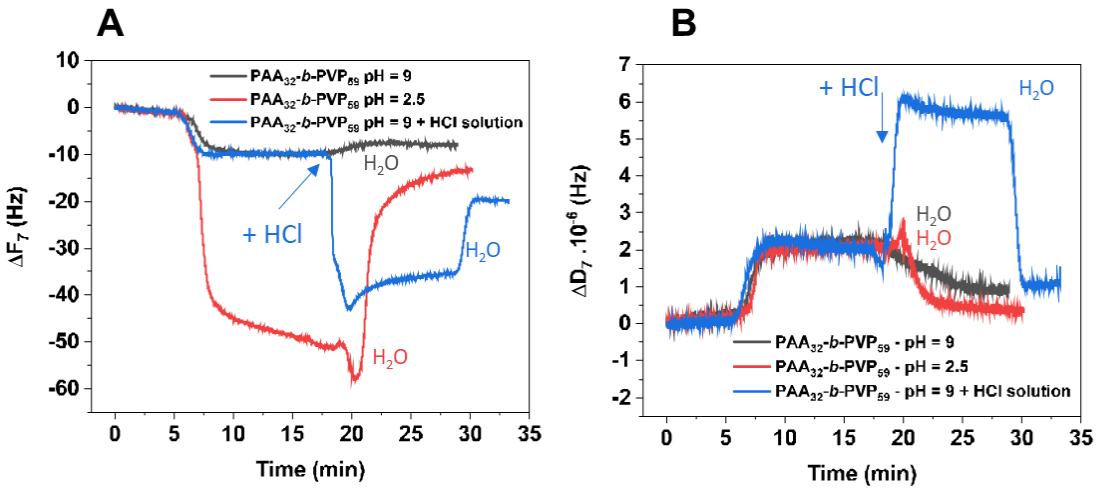

Figure 130. Frequency shift (**A**) and energy dissipation shift (**B**) with time (ΔF_7, ΔD 7th overtone) for solutions of PAA-b-PVP BCP at two pH values: pH=9 (black curve), pH=2.5 (red curve) and a successive addition of PAA-b-PVP BCP solution at pH=9 and then HCl solution (1M) (blue curve). H_2O symbolizes the start of the rinsing step with water solution and HCl with HCl solution respectively.

As expected, the frequency shifts of PAA_{32}-*b*-PVP_{59} copolymer at pH=9 are the same at the beginning and then after adding HCl solution, ΔF_7 decreases (accumulated weight increases), but does not attain the value of the PAA-*b*-PVP solution initially at pH=2.5, probably because the pH is not decreased enough. What was already remarked in **Figure 128** is that the energy dissipation shift was the same whatever the pH of the polymer solution. However, on **Figure 130B,** ΔD shifts increases when HCl solution is added. This experiment confirms that adding HCl solution, induces a higher adsorption onto the gold surface and an increase of the energy dissipation.

In a complementary experiment, PAA_{25} and PVP_{72} homopolymers are mixed together at a chosen pH before injection (**Figure 131**), or successively introduced into the chamber with injection order variation, PAA or PVP first, at two possible pH: 2.5 or 7 (**Figure 132**).

In **Figure 131**, tendencies observed about the adsorption of 'PAA + PVP' solution are similar to the block copolymer, with a higher adsorption at low pH values (0.248 molecules/nm^2). However, energy dissipation shift ΔD is higher for pH=2.5 than for the two other pH values. A slight decrease of ΔF, and slight increase of ΔD, are observed after starting the rinsing step, before adopting the inverse tendency.

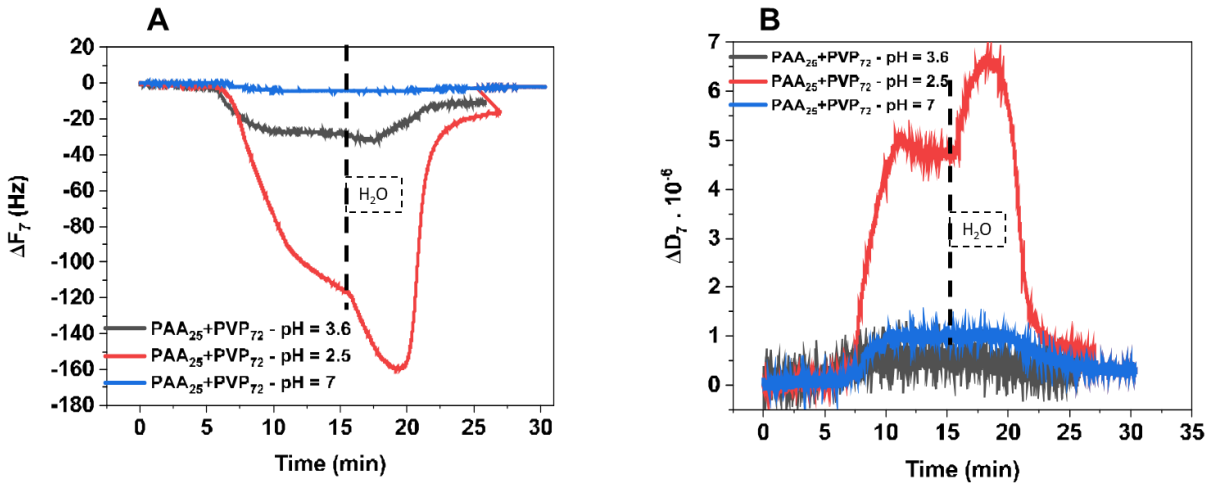

Figure 131. Frequency shift (**A**) and energy dissipation shift (**B**) with time (ΔF_7, ΔD 7th overtone) for solutions of PAA_{25} and PVP_{72} homopolymers mix at three pH values: pH=3.6 (black curve), pH=2.5 (red curve) and pH=7 (blue curve). The start of rinsing step is here represented by a black dot line and the text H_2O, meaning that a water solution is introduced in the chamber.

As seen on **Figure 132**, the solutions at pH=2.5 show once again higher adsorption than the ones at pH=7. Regarding pH=7, whatever the first polymer, the adsorption is similar in the two cases, whereas there is a slight difference regarding solutions at pH =2.5. No significant difference between the systems regarding energy dissipation.

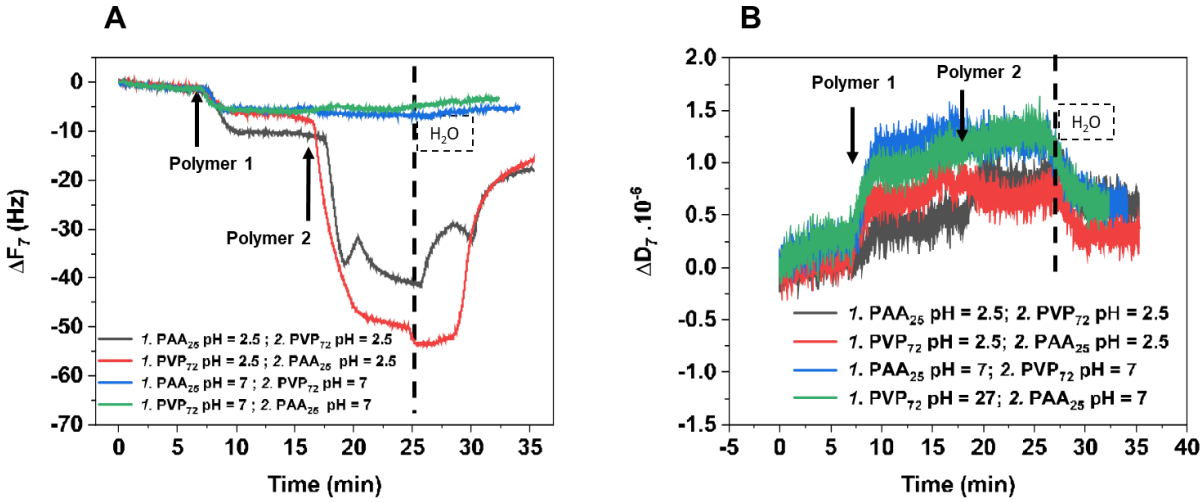

Figure 132. Frequency shift (**A**) and energy dissipation shift (**B**) with time (ΔF_7, ΔD 7th overtone) for solutions of PAA_{25} and PVP_{72} homopolymers mix at three pH values: pH=3.6 (black curve), pH=2.5 (red curve) and pH=7 (blue curve).

As in **chapter II**, the comparison of PAA_{32}-*b*-PVP_{59} with PAA_{44}-*b*-PEG_{80} block copolymer can inform about the role of the PVP into the studied mechanisms. For this reason, the interaction of PAA_{44}-*b*-PEG_{80} with gold surface is also evaluated (**Figure 133**).

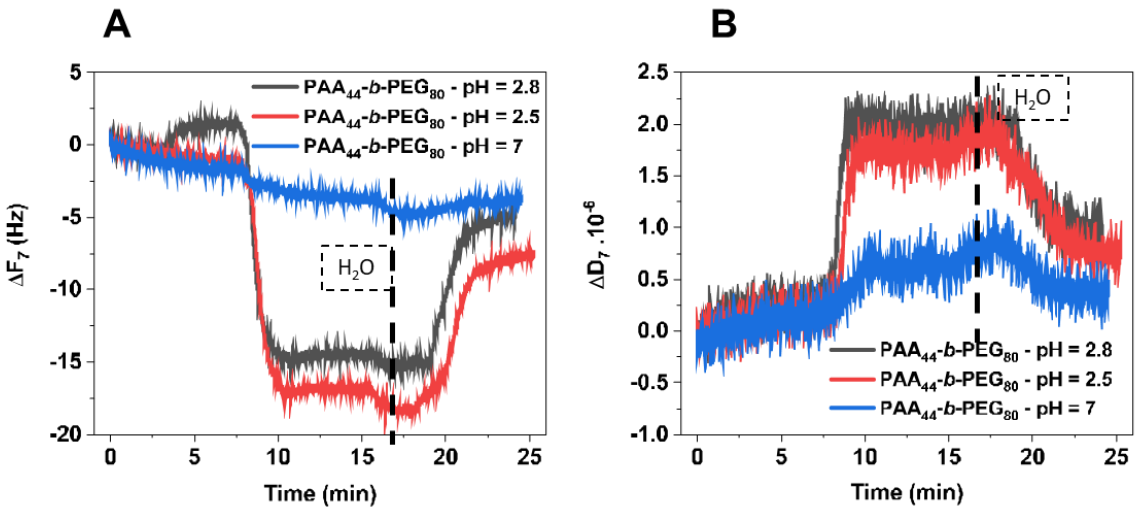

Figure 133. Frequency shift (**A**) and energy dissipation shift (**B**) with time (ΔF_7, ΔD 7th overtone) for solutions of PAA_{44}-*b*-PEG_{80} three pH values: pH=2.8 (black curve), pH=2.5 (red curve) and pH=7 (blue curve). The start of rinsing step is here represented by a black dot line and the text H_2O, meaning that a water solution is introduced in the chamber.

The low pH values allow higher adsorption onto the gold surface. As initial pH of 2.8 of PAA_{44}-*b*-PEG_{80} solution is near from the pH=2.5, no big difference is observed between the two curves (0.002 molecules/nm^2). Before rinsing, weight adsorbed (Δm) and number of molecules grafted (Γ) are calculated for these experiments and were found significantly lower (0.029 molecules/nm^2 at pH=2.5 and 0.009 molecules/nm^2 at pH=7) than the values obtained for PAA_{32}-*b*-PVP_{59} at pH=2.5 (0.100 molecules/nm^2 at pH=2.5 and 0.018 molecules/nm^2 at pH=7 (**Figure 134**).

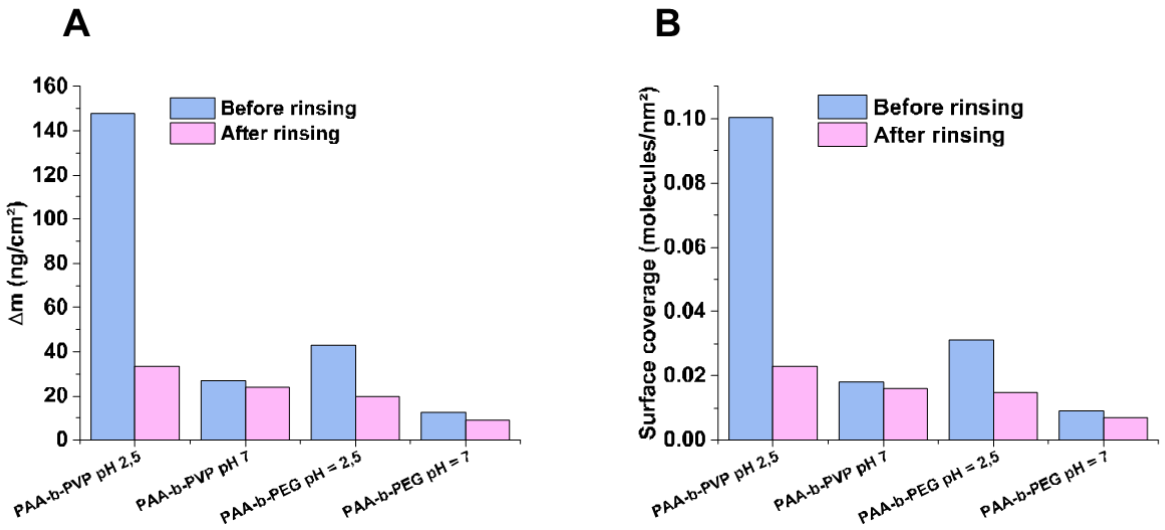

Figure 134. Adsorbed mass per surface unit Δm (ng/cm^2) (**A**) and surface coverage (molecules/nm^2)(**B**) calculated values for each polymer system with associated pH, before and after rinsing step in the QCM-D experiments.

III.2 Influence of the concentration of block copolymer

The previous experiments highlight a high affinity between PAA_{32}-*b*-PVP_{59} and gold surface. A low pH value promotes the formation of a hydrogen bond network that is suspected to induce a higher adsorption onto the gold surface. This mechanism might also explain the assembly process observed in solution: block copolymers adsorbed onto preformed AuNPs are prone to interact at low pH with other polymer chains present either on the surface of AuNPs or present as free chains in solution and to form nanoassemblies of AuNPs. To confirm this hypothesis, for a fixed concentration of AuNPs, increasing amount of block copolymer were added from 10^{-5} to 10^{-1} %wt and the pH further adjusted at pH=2.5.

As clearly seen in **Figure 135**, the concentration of PAA_{32}-*b*-PVP_{59} influences strongly the stability of AuNPs in solution. Between 10^{-5} and 10^{-3} %wt, the solution is blue or purple and aggregates of AuNPs are evidenced on TEM grids. The quantity of block copolymer is not sufficient to stabilize AuNPs and to induce the formation of nanoassemblies.

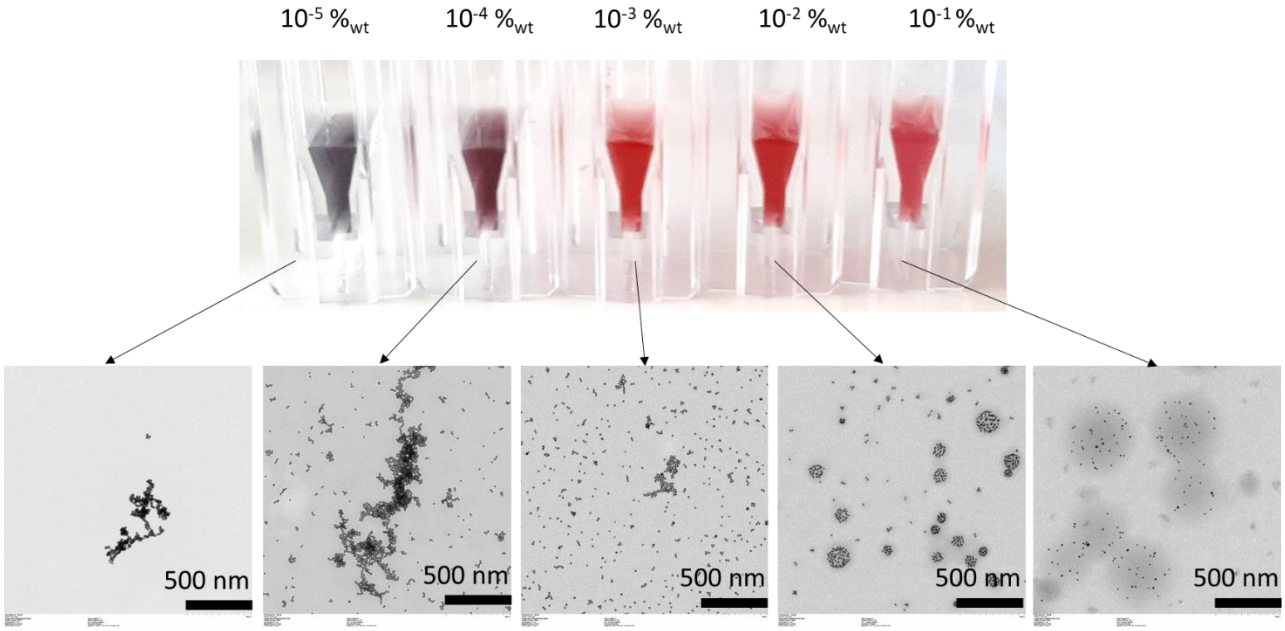

Figure 135. Photos of solutions containing varying PAA_{32}-*b*-PVP_{59} block copolymer concentration ([PAA_{32}-*b*-PVP_{59}]=10^{-5}-10^{-1}%wt) and fixed [Au] = 500µM at pH=2.5, associated to the TEM pictures of the five samples

By increasing the block copolymer concentration ([PAA_{32}-*b*-PVP_{59}]>10^{-3} %wt), the solution adopts red and then pink colors and become turbid. This is confirmed by UV-vis spectra (**Figure 136C**) and by TEM pictures (**Figure 135**), where we can observe the nanoassemblies of Au@citrate NPs and PAA_{32}-*b*-PVP_{59}. Therefore, a minimal polymer concentration is required to induce the formation of well-defined hybrid assemblies and this concentration seems to be around 10^{-2} %wt, which corresponds to a surface coverage of 0.35 molecules/nm^2 of polymer onto the gold nanoparticles.

This value is in the same range as the values found in the QCM-D analysis, but still higher (0.10 molecules/nm^2 of PAA-*b*-PVP at pH=2.5 before rinsing and 0.022 molecules/nm^2 after rinsing). Interestingly, by increasing again the BCP concentration, the nanoassemblies are still present, but their size has greatly increased and this is confirmed by DLS measurements (**Figure 136.B,C**) and TEM distribution analysis (**Figure 138**).

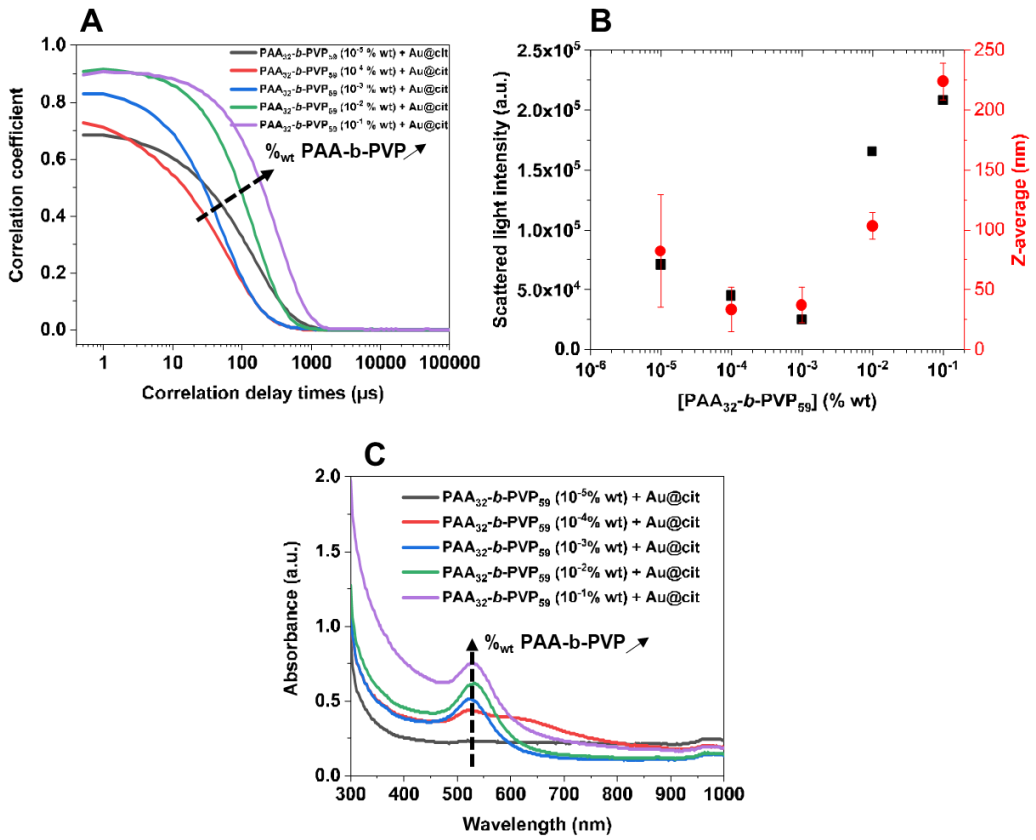

Figure 136. (**A**) Correlation functions using NNLS method, (**B**) typical evolutions of the scattered light intensity (black squares) and Z-average diameter (red dots) and (**C**) UV-vis spectra of the samples containing varying [PAA$_{32}$-*b*-PVP$_{59}$] concentrations between 10^{-5} and 10^{-1}%wt and fixed [Au]=500µM, adjusted at pH=2.5 with HCl solution (1M). Arrows are indicating the progressive increase of the block copolymer concentration.

These results confirm that the assembly mechanism is actually based onto the network of block copolymer built through hydrogen bondings in acidic conditions. As the block copolymer is in interaction with Au@citrate NPs, it brings them together, leading to these hybrid assemblies, which size seems to depend on the polymer concentration. To have more insight onto this influence, a restricted concentration range is tested between 10^{-2} and 10^{-1} %wt (**Figure 137**, **Figure 139**). A critical concentration is evidenced between 0.01 and 0.02%wt as confirmed from both TEM (**Figure 137**) and DLS measurements (**Figure 139**). The size of the nanoassemblies then slightly increases with BCP concentration. For the highest concentration, as seen in the previous experiment (**Figure 135**), some nanoassemblies only made from block copolymer, because no AuNPs inside, are observed, which confirms a large excess of polymer.

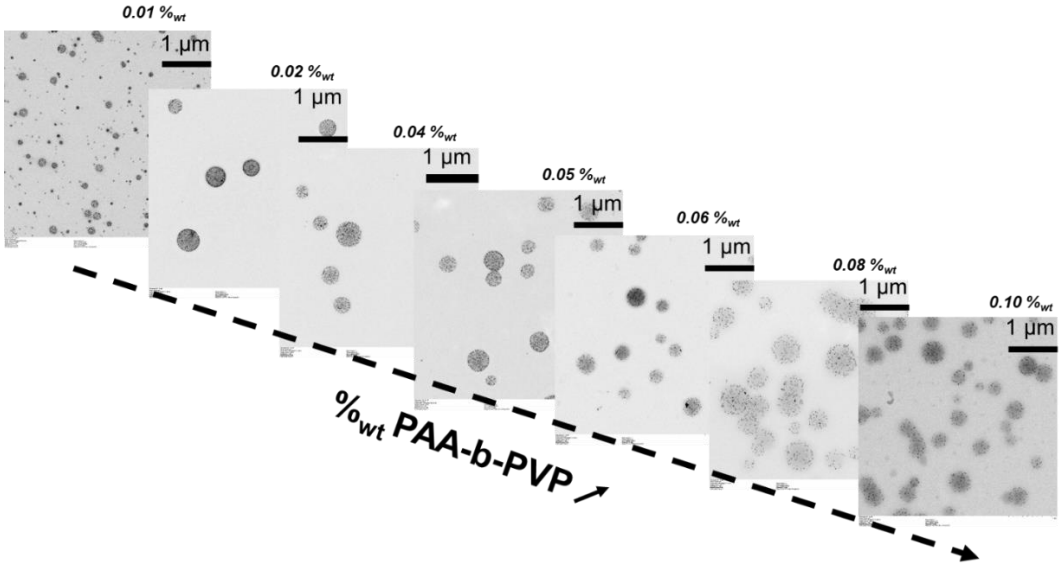

Figure 137. TEM pictures of samples with varying PAA_{32}-*b*-PVP_{59} concentrations from 0.01 to 0.1 %wt and a fixed [Au]=500 µM at pH = 2.5 after adding HCl (1M)

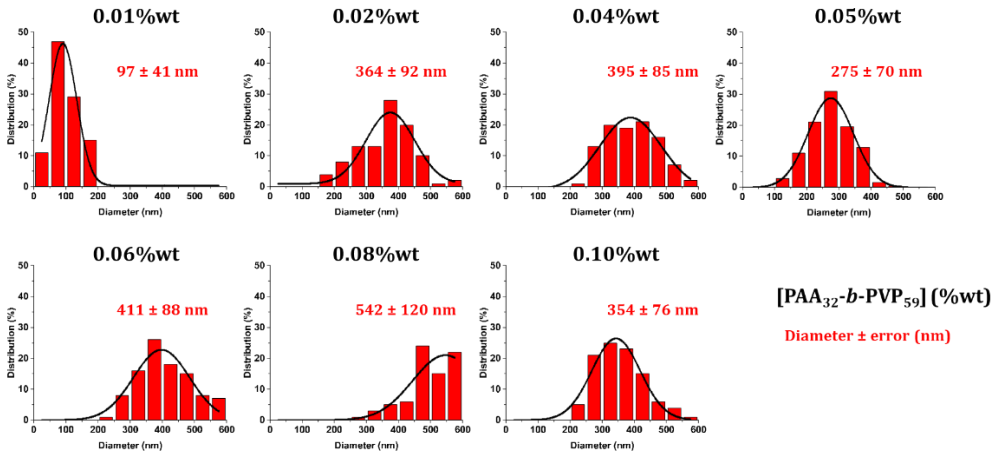

Figure 138. Size distribution diagrams associated to the TEM pictures of the samples with varying PAA_{32}-*b*-PVP_{59} concentrations from 0.01 to 0.1 %wt and a fixed [Au]=500 µM at pH=2.5 after adding HCl (1M)

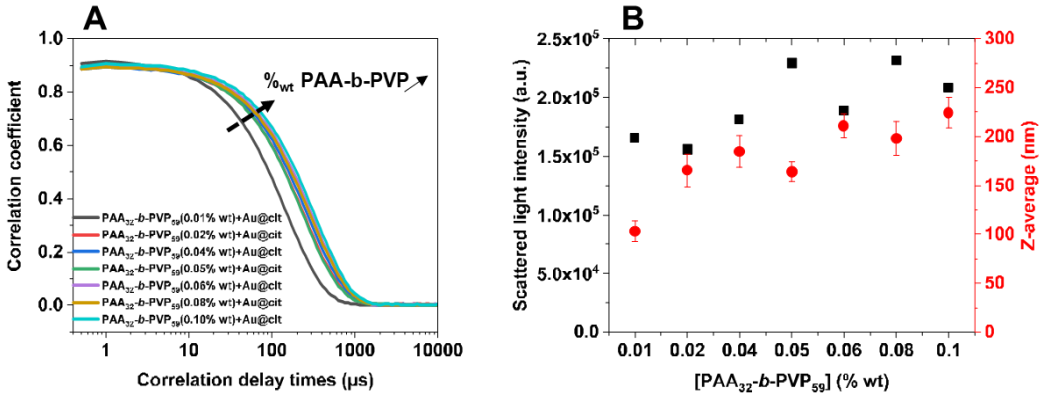

Figure 139. Correlation functions using the NNLS method (**A**) and typical evolutions of the scattered light intensity (black squares) and Z-average diameter (red dots) (**B**), measured by a mono-angle DLS instrument for samples containing varying PAA_{32}-*b*-PVP_{59} concentration (0.01 – 0.1%wt) at pH=2.5 after adding HCl (1M)

III.3 Kinetics of aggregation

To evaluate the kinetic associated to this assembly process, UV-vis spectroscopy was performed onto samples containing PAA_{32}-*b*-PVP_{59} with and without preformed AuNPs. To minimize the formation of salt relative to the addition of HCl or NaOH, we decided to reduce the concentration of PAA_{32}-*b*-PVP_{59} (0.014%wt) and keep the same ratio with gold than in previous experiment ([Au] = 144 µM).

In the case of the copolymer alone, the UV-vis spectra of the assembly mechanism show progressive increase of the global absorbance, in agreement with the turbid aspect of the solution (**Figure 140A**). The disassembly process is followed on **Figure 140B.** The evolution of absorbance at λ=350 nm as a function of time is shown in **Figure 140C.** It evidenced that the disassembly process occurred more rapidly than the assembly one.

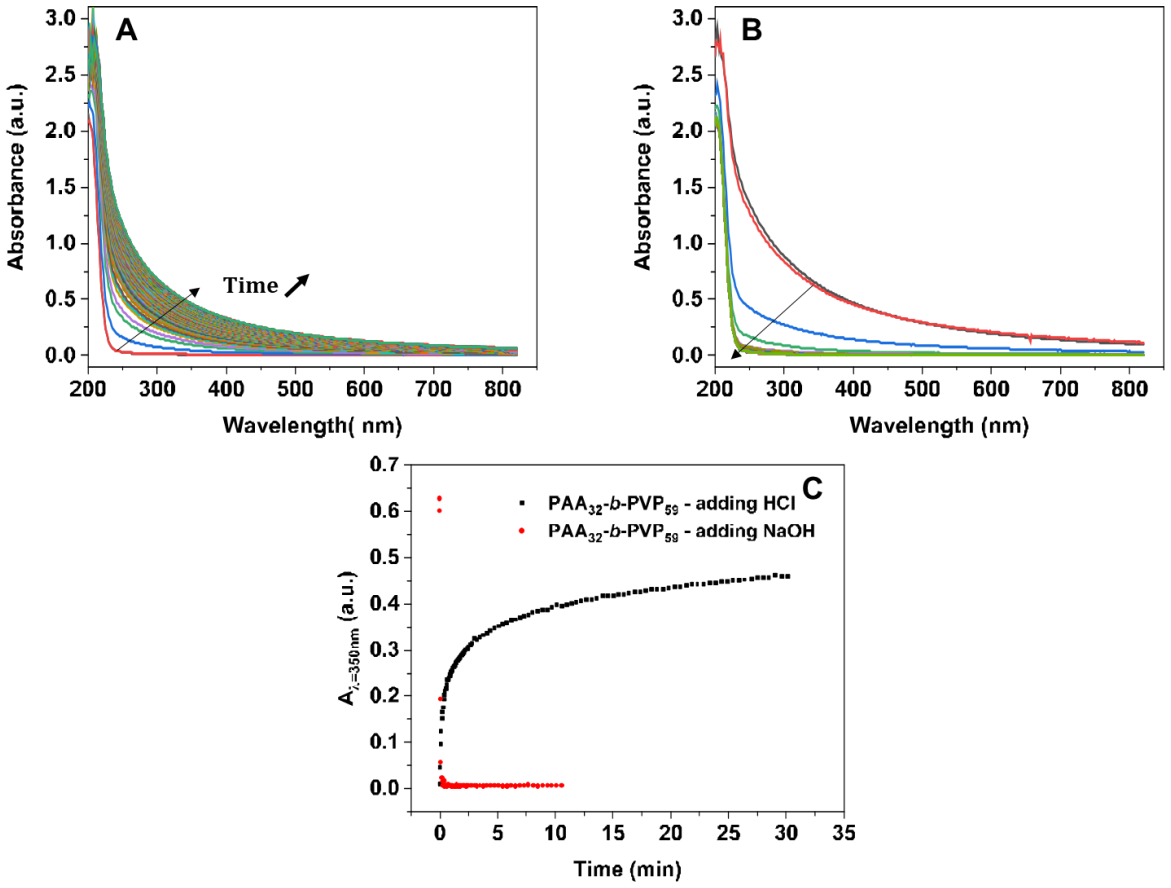

Figure 140. UV-vis spectra (100 scans) of PAA_{32}-*b*-PVP_{59}solution under pH variation after adding 10 µL of HCl solution (1M) (**A**) 10 µL of NaOH (1M) (**B**) Time evolution of the absorbance measured at λ=350 nm for both assembly and disassembly mechanisms (**C**)

A similar study was realized in the presence of AuNPs. As seen on **Figure 141**, the assembly mechanism is again slower than the disassembly one. The chosen absorbance is this time λ=750nm, but the intensity is very low.

The short formation/disassembly time (a few seconds) also suggests a high level of hydration of the system in its different states allowing a rapid diffusion of protons and a fast conformation change of the PAA chains. Reversible behavior was further investigated with several cycles (**Figure 142**).

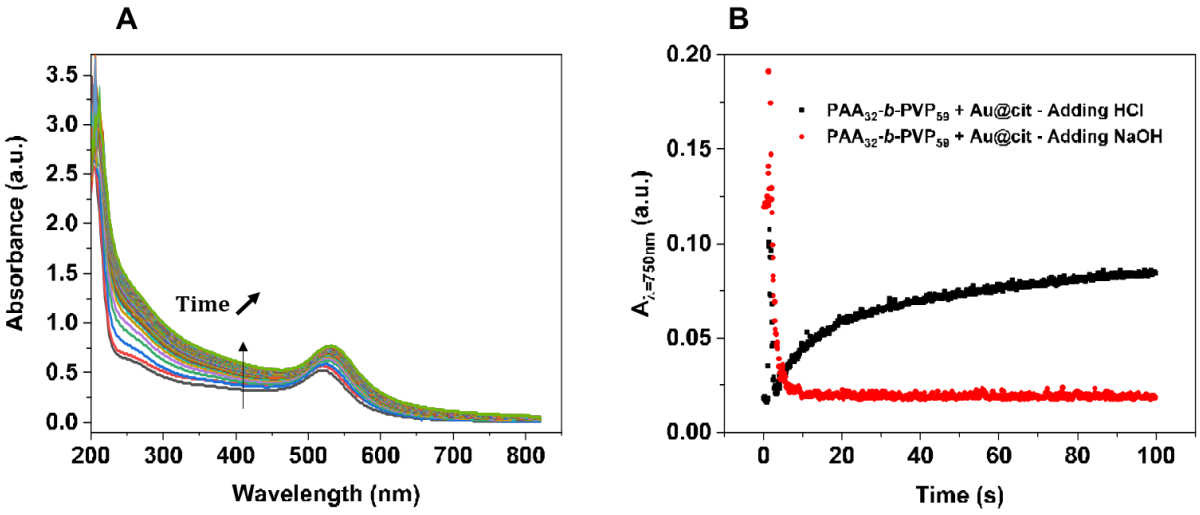

Figure 141. UV-vis spectra (100 scans) of PAA_{32}-*b*-PVP_{59} + Au@citrate solution under pH variation after adding 10 µL of HCl solution (1M) (**A**) Time evolution of the absorbance measured at λ=750 nm for both assembly and disassembly mechanisms (**B**)

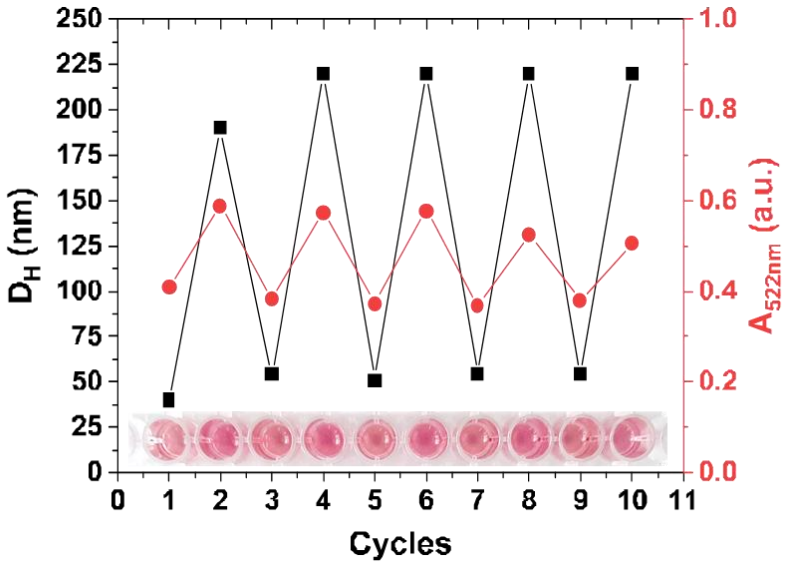

Figure 142. Reversibility study based on D_H measurements from DLS (black square) and absorbance values at λ=522 nm from UV-vis spectroscopy analysis (red circles) realized during 5 cycles of assembly and disassembly of PAA_{32}-*b*-PVP_{59} + Au@citrate sample at pH=9 and pH=2.5. [PAA_{32}-*b*-PVP_{59}] = 0.05%wt; [Au] = 500 µM.

The cycle study was made with reference concentrations [PAA_{32}-*b*-PVP_{59}] = 0.05%wt and [Au] = 500µM, to evaluate if the observed reversible behavior for previous lower concentrations ([PAA_{32}-*b*-PVP_{59}]=0.014%wt and [Au]=144 µM) was valuable here too. As observed on **Figure 142**, the assembly mechanism is actually reversible as similar diameters are measured before and

after assembly, as well as the SPR band intensity characteristic of the environment of the AuNPs in solution. The accumulation of salts may explain the slight increase of the diameter (observed in **II.3**) after two complete cycles (cycle 4), and the slight decrease of absorbance from cycle 8.

III.4 Effect of pH on the formation of nanoassemblies

In the previous experiments the formation of nanoassemblies was induced by a direct transition to pH=2.5. In this new set of experiments, the effect of the targeted final pH on the assembly process is evaluated. For this purpose, a HCl solution (1M) was added progressively onto PAA_{32}-*b*-PVP_{59} (0.05%wt) + Au@cit. The evolution of size as a function of pH was followed thanks to DLS measurements (**Figure 143 A,B**), UV-vis spectroscopy (**Figure 143C**) and TEM technique (**Figure 143**). A first evolution in both size and morphology is observed from pH=4, where Au@citrate NPs start to be involved in polymer self-assembly process, but no homogeneous well-defined structures are present yet. This pH value of 4 correlates with the pK_A value measured onto the copolymer solution in **chapter II,** indicating a protonation degree of 90%. A second clear evolution occurs when pH goes from pH=3 to pH=2.5, where the size is highly increased and the TEM pictures show well-defined nanoassemblies containing most of the Au@citrate NPs.

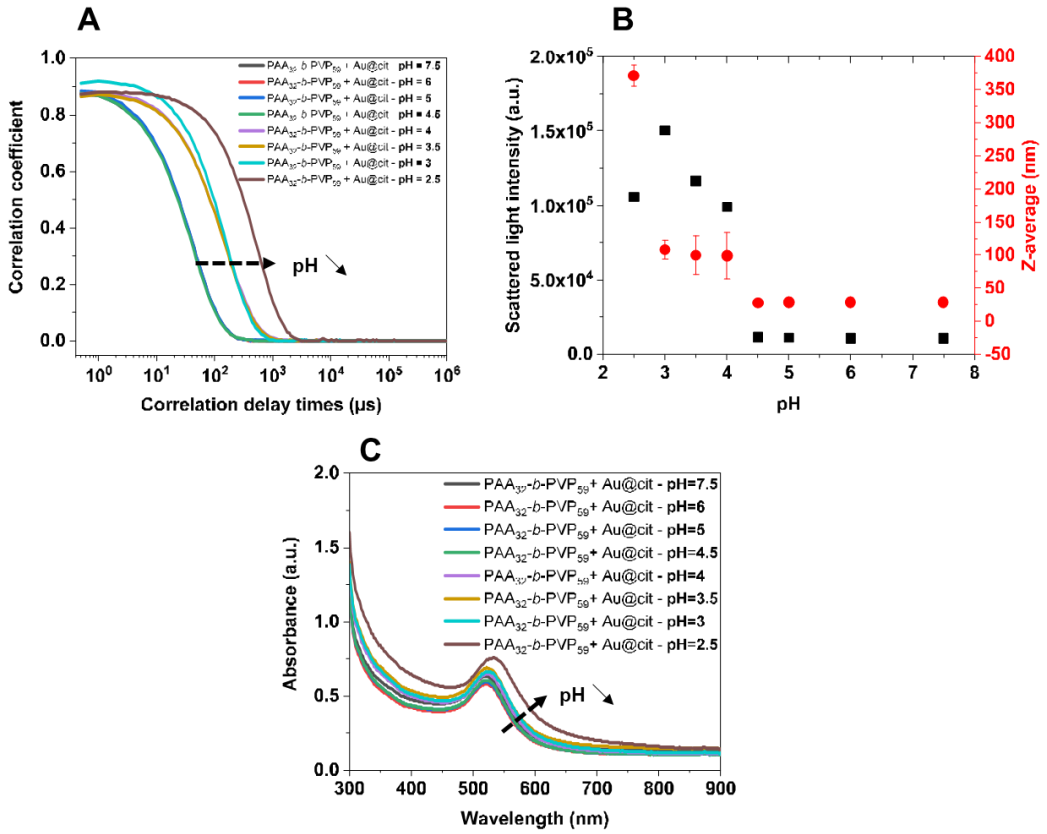

Figure 143. (**A**) Correlation functions using NNLS method, (**B**) typical evolutions of the scattered light intensity (black squares) and Z-average diameter (red dots) and (**C**) UV-vis spectra of the samples containing PAA_{32}-*b*-PVP_{59} (0.05%wt) and Au@citrate ([Au]=500µM), adjusted at varying pH values with HCl solution (1M). Arrows are indicating the progressive decrease of the pH value.

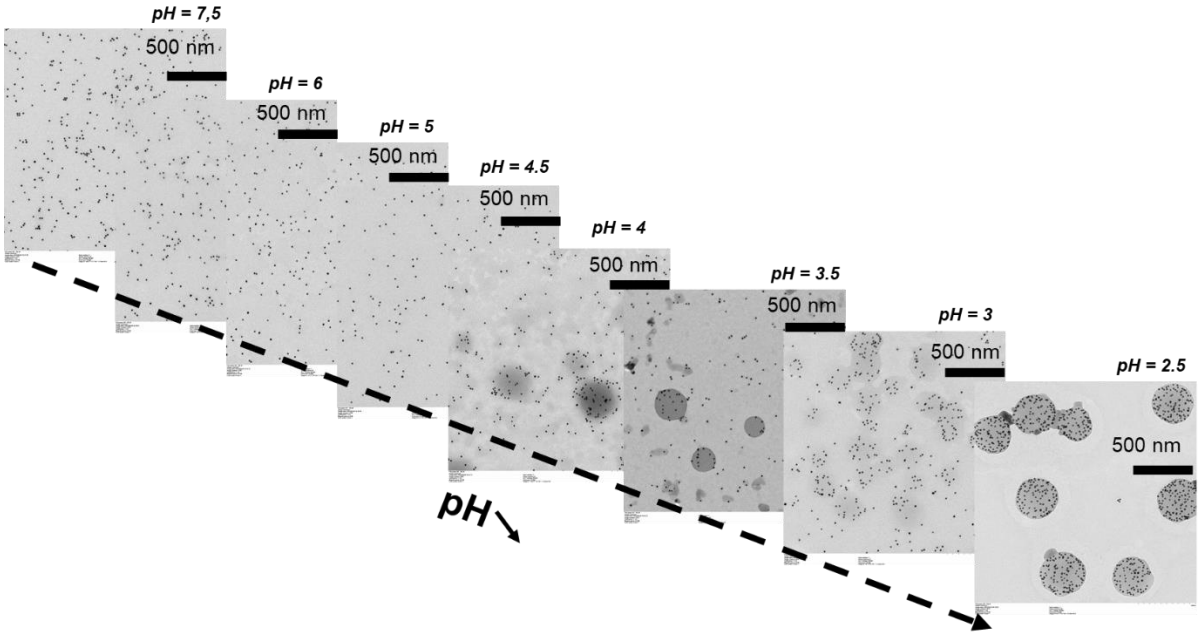

Figure 144. TEM pictures of samples containing PAA_{32}-*b*-PVP_{59} (0.05%wt) and Au@citrate ([Au]=500 µM) at varying pH after adding progressively HCl solution (1M).

There is thus this need to lower the pH under pH=3 to obtain the final nanoassemblies structures. The Au@citrate are progressively assembled through self-assembly of the PAA_{32}-*b*-PVP_{59} block copolymer under pH variation toward acidic conditions.

III.5 Influence of preparation protocol

It has to be noted that, in the same conditions ([polymer]=0.05 %wt, [Au]=500 µM), the final size measured here at pH=2.5, is higher than the one obtained by lowering the pH directly to pH=2.5 (see section **III.2**, **Figure 139**) : 371 ± 15 nm and 207 ± 25 nm . This suggests that the formation of theses assemblies follows a kinetic way. This point will be discussed in the next section. A complementary experiment was made to confirm that there was no significant effect of HCl addition pathway on the final size of nano-assembly, as can be seen on **Figure 145**.

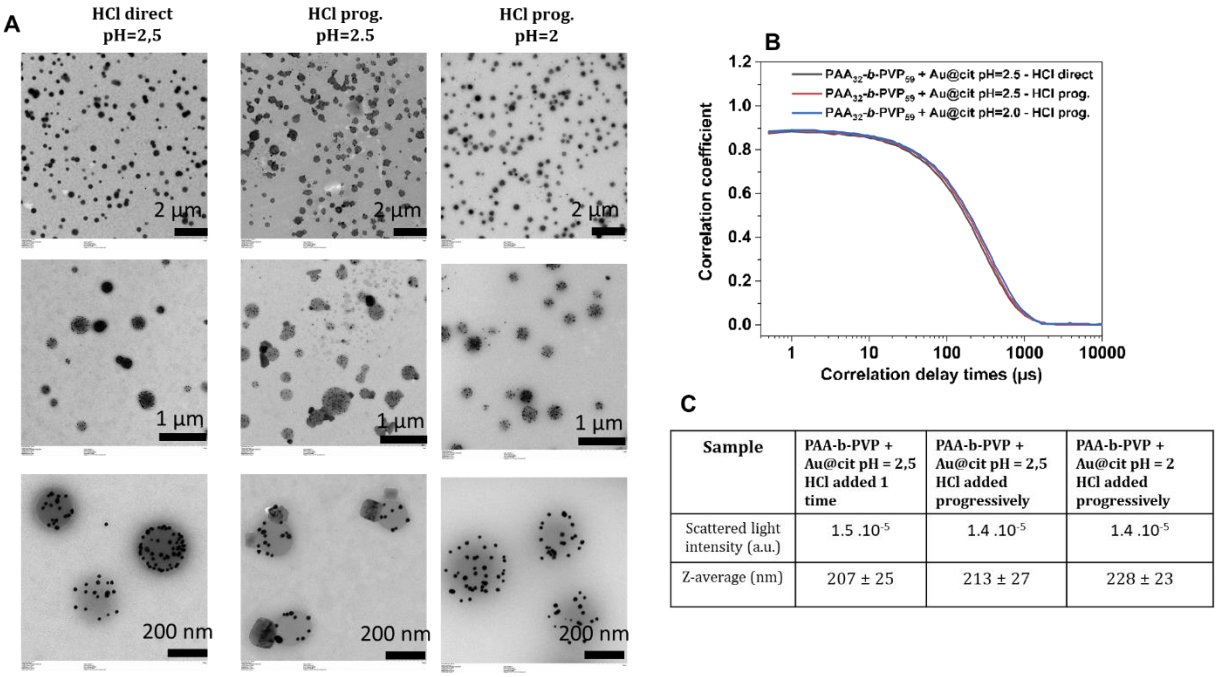

Sample	PAA-b-PVP + Au@cit pH = 2,5 HCl added 1 time	PAA-b-PVP + Au@cit pH = 2,5 HCl added progressively	PAA-b-PVP + Au@cit pH = 2 HCl added progressively
Scattered light intensity (a.u.)	$1.5 .10^{-5}$	$1.4 .10^{-5}$	$1.4 .10^{-5}$
Z-average (nm)	207 ± 25	213 ± 27	228 ± 23

Figure 145. (**A**) TEM pictures of the samples containing PAA_{32}-*b*-PVP_{59} (0.05%wt) and Au@citrate ([Au]=500 µM) adjusted at pH=2.5 by adding HCl solution (1M) through 2 ways: only one direct add ("HCl direct") or several add ("HCl prog.") and this second way is used to decrease until pH=2 (**B**) Corresponding correlation functions using NNLS method and (**C**) Table showing the data from DLS measurements: Scattered light intensity and Z-average size.

To confirm this, last experiments were made regarding the effect of the initial pH and of the dilution onto the final obtained structures for samples containing PAA_{32}-*b*-PVP_{59} without (pathway 1 et 2) or with (pathway 3 et 4) Au@citrate. To answer these questions, four different preparations protocol (**Scheme 11**) were realized by keeping the final polymer and Au@citrate concentrations fixed to 0.014%wt and 144 µM respectively.

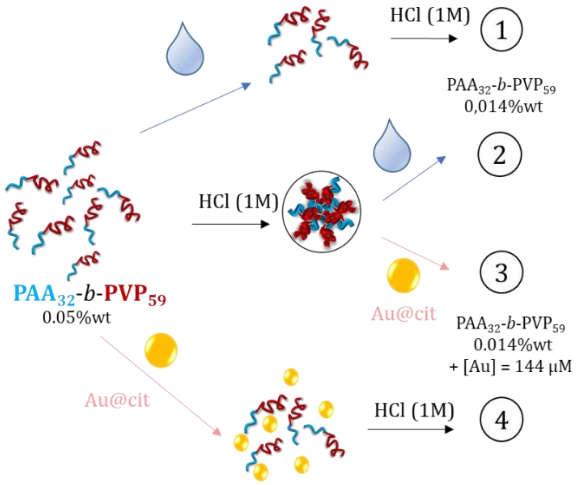

Scheme 11. Sample preparation protocols to obtain nanoassemblies composed of PAA_{32}-*b*-PVP_{59} (0.014%wt) with or without Au@citrate ([Au]=144 µM): (1) Dilution then lowering pH onto PAA_{32}-*b*-PVP_{59} solution; (2)Lowering pH then dilution onto PAA_{32}-*b*-PVP_{59} solution; (3) Lowering pH onto PAA_{32}-*b*-PVP_{59} then introducing Au@citrate; (4) Introducing Au@citrate into PAA_{32}-*b*-PVP_{59} solution at high pH value then lowering pH.

First, the nanoassemblies obtained from protocols 1 and 2, block copolymer only, were examined through TEM and DLS analyses. (**Figure 146**). DLS results seem to indicate that the dilution onto polymer solution after lowering the pH, seems to have no effect onto the obtained nanoassemblies. TEM pictures show similar morphologies obtained for the two protocols. However, the contrasting agent (uranyl acetate) seems to interact differently when the sample from protocol 2 is deposited on the grid.

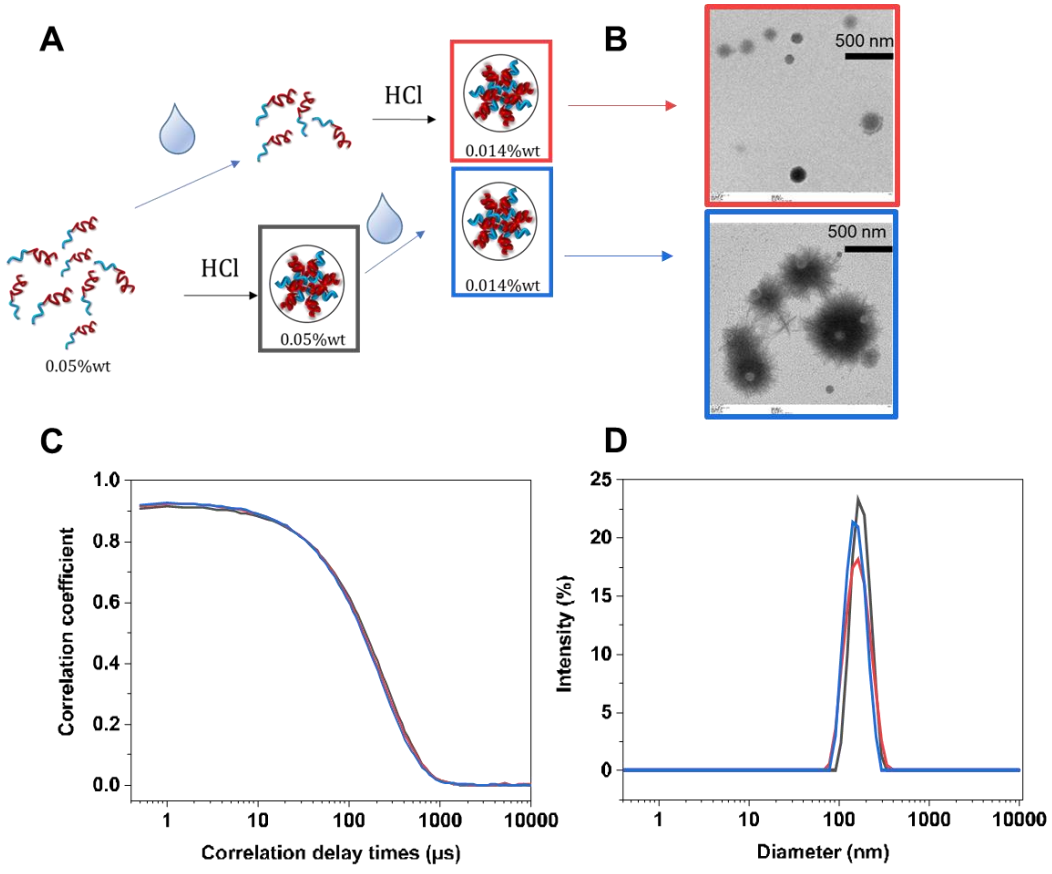

Figure 146. (**A**) Sample preparation protocols 1 and 2 to obtain nano-assemblies composed of PAA_{32}-*b*-PVP_{59} (0.014%wt) (**B**) TEM pictures of the samples issued from protocols 1 (red) and 2 (blue) and the associated schematic representation. [PAA_{32}-*b*-PVP_{59}] = 0.014%wt. (**C**) Correlation functions using the NNLS method and (**D**) distribution average size in intensity for the samples issued from different steps of the protocols.

Regarding hybrid assemblies (protocols n°3 and 4), the time when the Au@citrate are incorporated into the polymer solution is critical, as it can influence the composition of the final nanoassemblies (**Figure 147**). If the Au@citrate are added before lowering the pH, they will be incorporated into the final polymer assembly. Otherwise, when the polymer is already self-assembled, Au@citrate NPs remains apart from the nanoassemblies. UV-vis spectroscopy analysis was performed on the different samples containing AuNPs (**Figure 148**) and shows that the sample of protocol n°3 leads to a higher absorbance, because of BCP self-assembly which contribute to diffusion. In that case no shift of the SPR band is observed, contrary to the sample from protocol n°4, which confirms an assembly comprising the Au@citrate NPs.

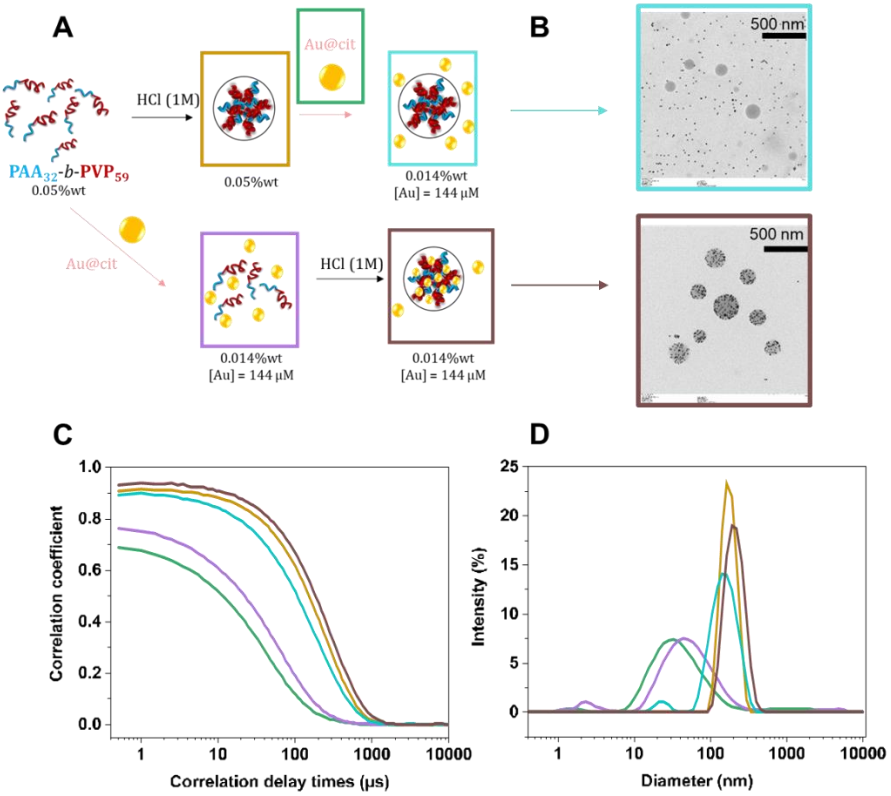

Figure 147. (**A**) Sample preparation protocols 1 and 2 to obtain nano-assemblies composed of PAA_{32}-*b*-PVP_{59} (0.014%wt) (**B**) TEM pictures of the samples issued from protocols 1 (red) and 2 (blue) and the associated schematic representation. [PAA_{32}-*b*-PVP_{59}] = 0.014%wt; [Au]=144µM. (**C**) Correlation functions using the NNLS method and (**D**) distribution average size in intensity for the samples issued from different steps of the protocols. Colors of the square circling the systems are the same that on the DLS curves.

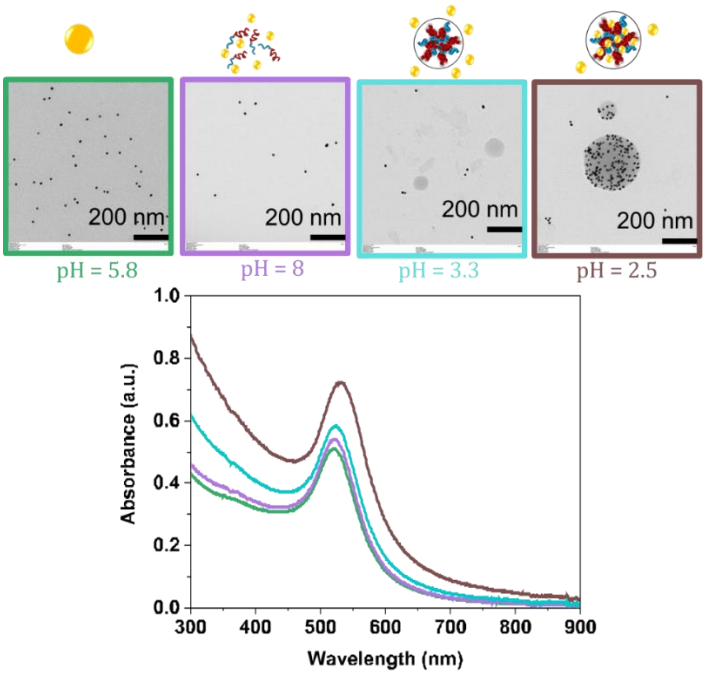

Figure 148. UV-vis spectra of the samples containing Au@citrate: Au@citrate alone, mixed with PAA_{32}-*b*-PVP_{59} at pH=8, mixed with self-assembled PAA_{32}-*b*-PVP_{59} at pH=3.3 and mixed with PAA_{32}-*b*-PVP_{59} at pH=2.5 with associated TEM pictures and schematic representation of the systems.

The sample issued from protocol n°3 leads to nanostructures which hydrodynamic diameter is significantly lower from the one of the sample issued from protocol n°4 (**Table 12**).

Table 12. Data from DLS measurements: Scattered light intensity and Z-average size for different systems in the protocols.

N° protocol	**1**	**2 & 3**	**2**	**3**	**4**	**4**
[PAA_{32}-*b*-PVP_{59}](%wt)	0.014	0.05	0.014	0.014	0.014	0.014
[Au] (µM)	0	0	0	144	144	144
pH	2.5	2.5	3	3.3	8.2	2.5
Scattered light intensity (a.u.) (*10^4)	6	20	6	6	0.5	10
Z-average (nm)	154 ± 11	170 ± 4	147 ± 7	117 ± 31	36 ± 16	196 ± 14

As can be seen on **Figure 149**, for the system issued from protocol n°3, no evolution was observed after 1 week and no further adsorption on polymer assemblies can be observed. This implies that in protocol n°4, Au@citrate NPs are not simply adsorbed on polymer structures but are positioned inside the nanoassemblies, which support the results from HAADF-STEM (**II.2**).

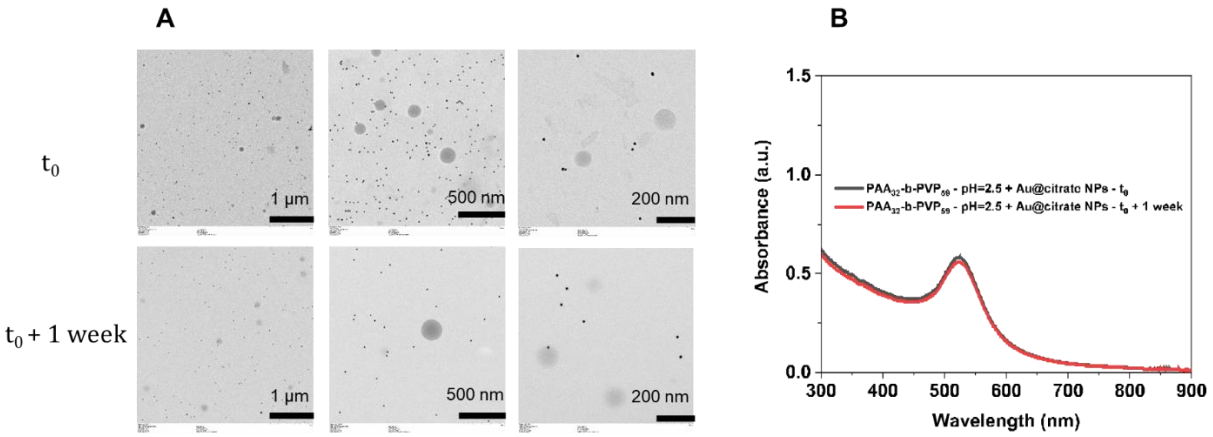

Figure 149. (**A**) TEM pictures and (**B**) UV-vis spectra of the sample issued from the protocol n°3 with P PAA_{32}-*b*-PVP_{59} at pH=2.5 (0.014%wt) and Au@citrate NPs([Au] = 144µM) incorporated after pH lowering at t_0 and after 1 week.

IV Effect of polymer structure and composition

The previous experiments suggest that in solution preformed particles are covered with polymer and in acidic medium the excess polymer binds the particles together by a hydrogen bonding network to form the observed nanospheres. The next section will discuss on the effect of polymer structure (block PAA_{32}-b-PVP_{59} vs homopolymers PAA_{25} and PVP_{72}) and composition (PAA_{32}-*b*-PVP_{59} vs PAA_{44}-*b*-PEG_{80}).

IV.1 Comparison with PAA-b-PEG

PVP polymer was largely used for the stabilization of AuNPs as detailed in **II.2**. Another double hydrophilic block copolymer (DHBC) with a different stabilizing block polymer, PEG, is here evaluated towards its ability to induce self-assembly process and hybrid assemblies with Au@citrate NPs.

Concerning the polymer PAA_{44}-*b*-PEG_{80} alone, DLS measurements show that a structuration occurs at pH=2.5 with an increase of the correlation coefficient and of the scattered light intensity (**Figure 150.B**), but the correlation function seems to reveal the presence of heterogeneous structures in solution. TEM pictures of the sample at pH=2.5 are shown onto **Figure 153** (first line) where nanostructures can be observed and are similar to the ones observed with PAA_{32}-*b*-PVP_{59}. Acidic conditions seem to be suitable for PAA_{44}-*b*-PEG_{80} to self-assemble, probably based as well onto hydrogen bondings initiated by PAA protonated block.

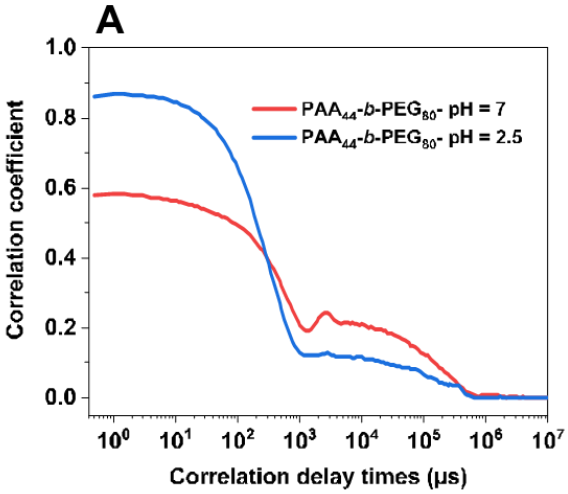

B

PAA_{44}-b-PEG_{80} (0.05%wt)	pH = 7	pH = 2.5
Scattered light intensity (a.u)	462	1 877
Z-average (nm)	560 ± 282	239 ± 41

Figure 150. Correlation functions using the NNLS method (**A**) and Scattered light intensity and Z-average size (**B**) of the samples containing PAA_{44}-*b*-PEG_{80} (0.05%wt) at different pH values: 7; 2.5

Then, as for PAA_{32}-*b*-PVP_{59}, the block copolymer PAA_{44}-*b*-PEG_{80} was mixed with Au@citrate NPs and the pH adjusted at a value of 7 before decreasing it until 2.5. At pH=7, DLS measurements reveal low global sizes corresponding to Au@citrate NPs dispersed into the polymer solution

without any aggregation as also proved by UV-vis spectroscopy (**Figure 152**). By lowering the pH to pH=2.5, an increase in the global size is detected in DLS and the visual observation of the sample indicates that the environment of Au@citrate NPs has dramatically evolved, as the solution color changes from red to blue.

A

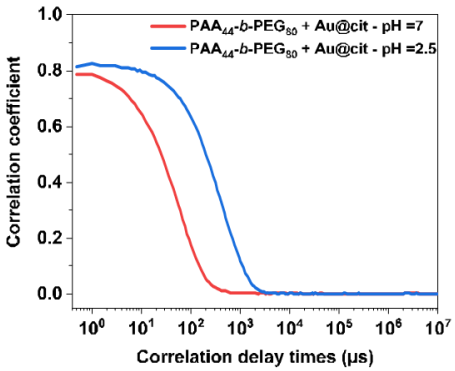

B

PAA_{44}-b-PEG_{80} (0.05%wt) + Au@citrate NPs ([Au]=500 µM)	pH = 7	pH = 2.5
Scattered light intensity (a.u)	7 978	41 022
Z-average (nm)	35 ± 12	332 ± 98

Figure 151. Correlation functions using the NNLS method (A) and Scattered light intensity and Z-average size (**B**) of the samples containing PAA_{44}-*b*-PEG_{80} (0.0.5%wt) + Au@citrate ([Au] = 500µM) at two pH values: pH=7 and pH=2.5.

The behavior of the sample containing PAA_{44}-*b*-PEG_{80} and Au@citrate NPs is therefore very different from the one containing PAA_{32}-*b*-PVP_{59} block copolymer, at pH=2.5 that remains pink colored. This suggest for PAA_{44}-*b*-PEG_{80} an irreversible aggregation process. This hypothesis is confirmed from the analysis of TEM pictures (**Figure 153**). Even if the DLS correlation function indicates a homogeneous population, which could resemble to nanostructures obtained with PAA_{32}-*b*-PVP_{59}, TEM reveals the presence of clusters of AuNPs in solution which precipitates in the flask.

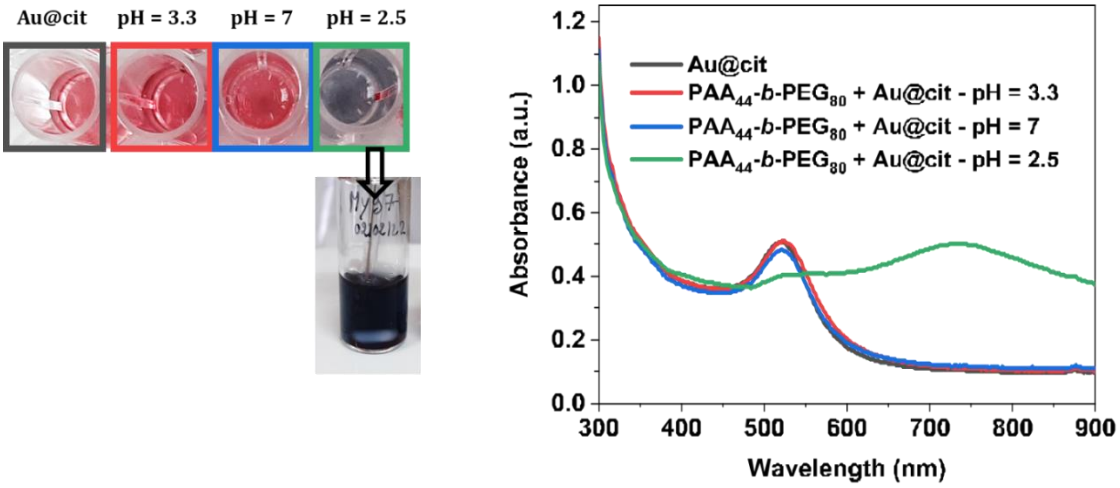

Figure 152. Photos of the wells containing different samples: Au@citrate NPs alone (as a reference) and PAA_{44}-*b*-PEG_{80} (0.05%wt) + Au@citrate NPs ([Au]=500 µM) at different pH values: 3.3; 7; 2.5 and corresponding UV-vis spectra.

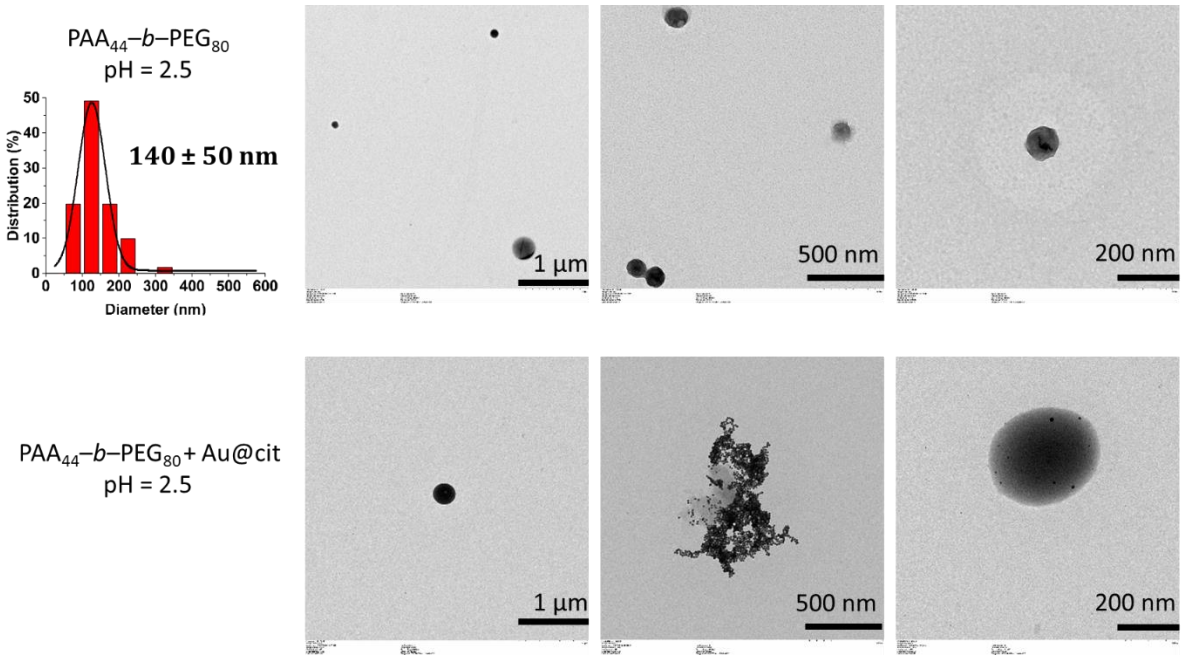

Figure 153. TEM pictures of the samples containing PAA_{44}-*b*-PEG_{80} (0.05%wt) without (first line) and with Au@citrate NPs (second line) ([Au]=500 µM). Distribution size analysis for the sample PAA_{44}-*b*-PEG_{80} (0.05%wt).

This comparison between PVP and PEG polymers show that PEG did not stabilize Au@citrate in acidic conditions, and thus no hybrid assembly can be obtained with this method using the PAA_{44}-*b*-PEG_{80} as block copolymer. The PVP polymer presents then this stabilizer role of Au@citrate NPs at low pH values and through its self-assembly enables the controlled aggregation of AuNPs into one hybrid assembly.

IV.2 Comparison with PAA and PVP homopolymers

In the present work, the obtained nano-assemblies are based on hydrogen bonds between the PAA_{25} and the PVP_{72} block polymers. The questions lie then onto the interest in having a block structure. The following study consists in comparing the previous experiments using PAA_{32}-*b*-PVP_{59} block copolymer to samples containing a mixture of the two corresponding homopolymers PAA_{25} and PVP_{72}.

First section is about lowering the pH of a solution containing PAA_{25} and PVP_{72} homopolymers with a total weight concentration equal to the one used for PAA_{32}-*b*-PVP_{59} BCP, i.e. 0.05%wt. DLS measurements show that at initial pH of 3.6, some well-defined structures are present in solution and their size is enlarged when pH is decreased until pH=2.5. The associated lower scattered light intensity supposes that there might be a beginning of precipitation. Then increasing the pH until 7 leads to bigger structures but associated to a low correlation coefficient and large error on the Z-average diameters corresponding to big aggregates of polymers. Complementary SAXS analysis were performed onto the pH of 7 and 2.5, but the intensities recorded were too low to enable any reliable treatment. Further new analysis will be organized.

A

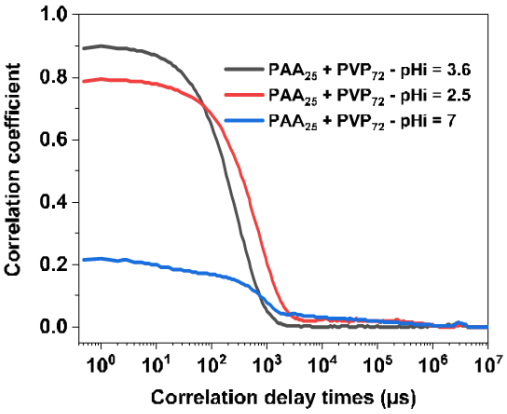

B

PAA_{25} + PVP_{72} (0.05%wt)	pH = 3.6	pH = 2.5	pH = 7
Scattered light intensity (a.u)	6 630	1 153	430
Z-average (nm)	200 ± 37	448 ± 69	556 ± 247

Figure 154. Correlation functions using the NNLS method (A) and Scattered light intensity and Z-average size (**B**) of the samples containing PAA_{25}+PVP_{72} (0.05%wt) at three pH values: 3.6; 2.5; 7.

TEM pictures were made onto the sample at the three pH values and show actually the nanostructures initially present in solution, with a size augmentation at pH=2.5 and the presence of final aggregates at pH=7 (**Figure 155**). Hence, mixing PAA_{25} and PVP_{72} homopolymers did lead to well-defined polymer-based nano-assemblies by lowering the pH until 2.5 as for PAA_{32}-*b*-PVP_{59} block copolymer. Size distribution analysis was made onto these TEM pictures for the sample at pH=2.5 and the size of the nanostructures was found as D = 560 ± 112 nm, which is larger than the size obtained for the block (315 ± 8 nm) The final obtained sizes are larger, but the mechanism seems to be similar and based on the formation of hydrogen bonds between PAA_{25} and PVP_{72}.

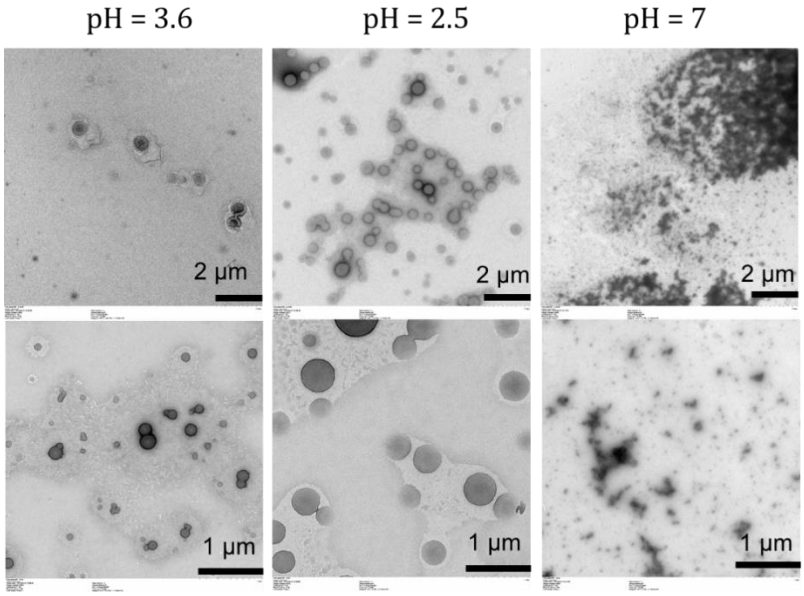

Figure 155. TEM pictures of the sample containing PAA_{25}+PVP_{72} (0.05%wt) at three pH values: 3.6; 2.5; 7.

What happens now in the presence of preformed AuNPs? The interactions between the two homopolymers at various pH and the gold surface have been already studied through QCM-D analysis (**III.1**). These measurements proved that the affinity with gold surface did exist and is higher at low pH. The behavior in solution was further studied: a progressive addition of HCl (1M) onto the sample containing PAA_{25}, PVP_{72} and Au@citrate was realized. DLS measurements show a progressive increase of the global size in solution with decreasing pH value and a large size gap between pH=2.5 and pH=2, which is remarked as well on TEM pictures (**Figure 157**). Size distribution analysis was made onto these TEM pictures for the sample at pH=2.5 and the size of the nanostructures was found as D = 166 ± 101 nm. SAXS measurements were realized at pH=2.5 and pH=7 but are still under study. The internal organization of the two homopolymers has been studied through HAADF-STEM pictures and associated EDX analysis focused on carbon (C), oxygen (O) and nitrogen (N) elements. (**Figure 158**).

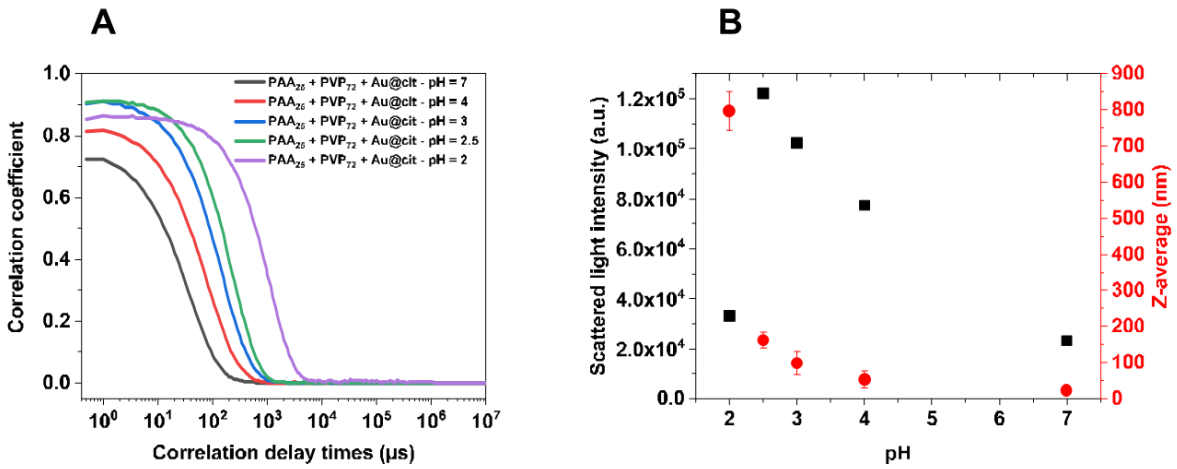

Figure 156. Correlation functions using the NNLS method (**A**) and typical evolutions of the scattered light intensity (black squares) and Z-average diameter (red dots) (**B**), measured by a mono-angle DLS instrument for samples containing PAA_{25}+PVP_{72} (0.05%wt) + Au@citrate NPs ([Au]=500 µM]) at varying pH values after adding progressively HCl (1M).

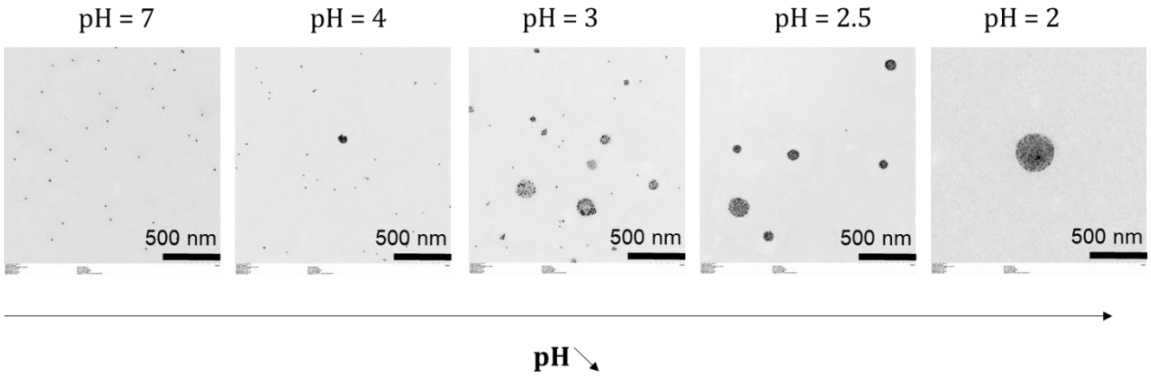

Figure 157. TEM pictures of the sample containing PAA_{25}+PVP_{72} (0.5%wt) + Au@citrate NPs ([Au]=500 µM]) at varying pH values after adding progressively HCl (1M)

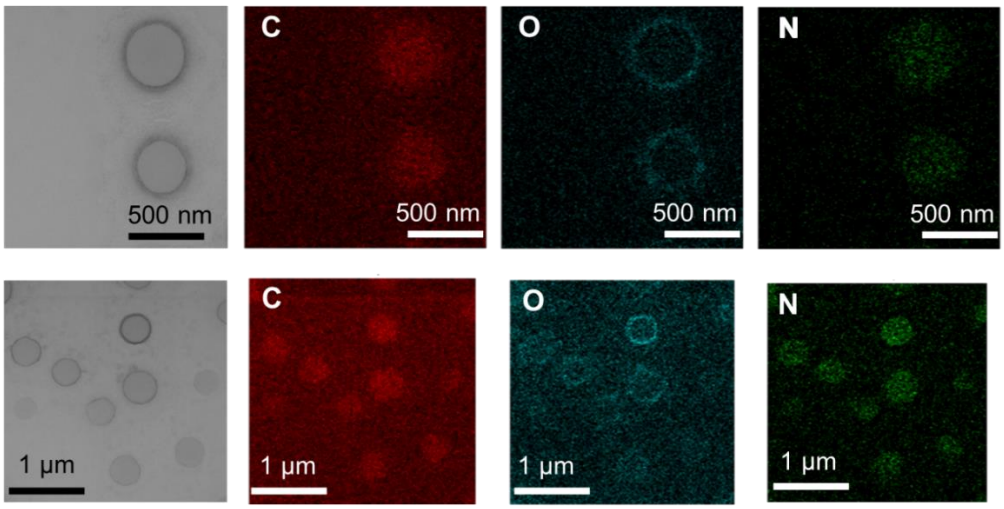

Figure 158. TEM pictures and elemental maps of the sample containing PAA_{25}+PVP_{72} (0.05%wt) and) for the following elements: carbon, oxygen, and nitrogen, at two observation scales

As observed onto the elemental maps realized onto PAA_{25} + PVP_{72} homopolymers solution, a corona rich in oxygen element is present into the nanostructures. As PAA polymer contains more oxygen element (44%wt compared to 14%wt for PVP), it appears that the protonated PAA forms this corona into the assembly. This analysis revealed also that nitrogen rich PVP seems to be in the core of the nanoassembly. These results suggest a core-shell organization of the nanoassemblies made of PAA_{25} and PVP_{72}. An elemental mapping realized onto hybrid assemblies containing PAA, PVP and Au@citrate NPs is given in **Figure 159**. Contrary to previous pictures, no core-shell representation is clearly seen, the polymers seem to be mixed into the nano-assembly around the Au@citrate NPs without any organized structuration, like for PAA_{32}-*b*-PVP_{59} block copolymer (**Figure 122**).

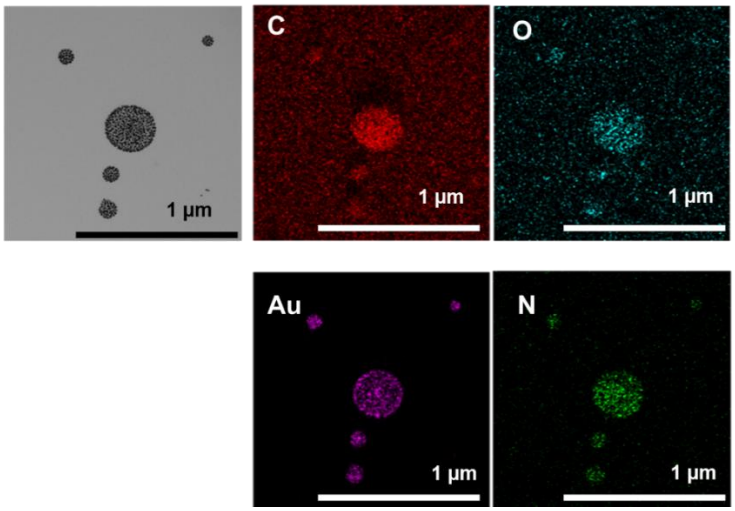

Figure 159. TEM pictures and elemental maps of the sample containing PAA_{25}+PVP_{72} (0.05%wt) and Au@citrate NPs ([Au]=500 µm) for the following elements: carbon, oxygen, gold and nitrogen, at two observation scales

At 0.05 %wt, the assembly mechanism seems then to be in both cases, block copolymer or mixture of homopolymers, based on the formation of hydrogen bonds induced by a decrease of pH. To see if any difference exists between the two systems, an experiment is realized at higher polymer concentration (1%wt) in solution for samples containing only polymers and the ones containing both polymers and Au@citrate NPs.

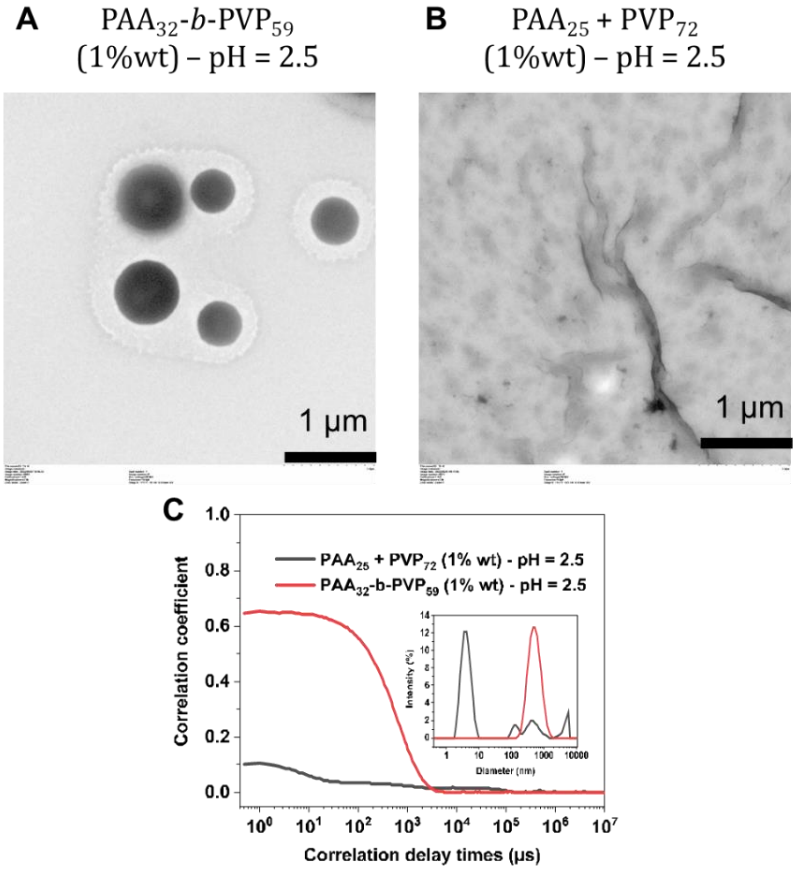

Figure 160. TEM pictures of the samples containing PAA_{32}-*b*-PVP_{59} (1%wt) (A) and PAA_{25}+PVP_{72} (1%wt) (B) and corresponding correlation functions using the NNLS method and (inset) distribution average size in intensity.

At a polymer concentration of 1 %wt, whereas the block copolymer structure enables the formation of nanostructures (with a Z-average value around 450 nm), the mixture of homopolymers does not lead to well-defined nanostructures. Only the block structure is suitable for the structuration of nanoassemblies in solution at this concentration. This result is further confirmed in presence of Au@citrate NPs. Visually, after 2 days only the block configuration leads to nanoassemblies with good colloidal stability (**Figure 160**). In addition, TEM pictures revealed that PAA_{25} + PVP_{72} + Au@citrate system led to poorly defined nanoassemblies. Therefore, in the case of homopolymers only a restricted concentration range allows structuration and good stabilization of AuNPs at low pH.

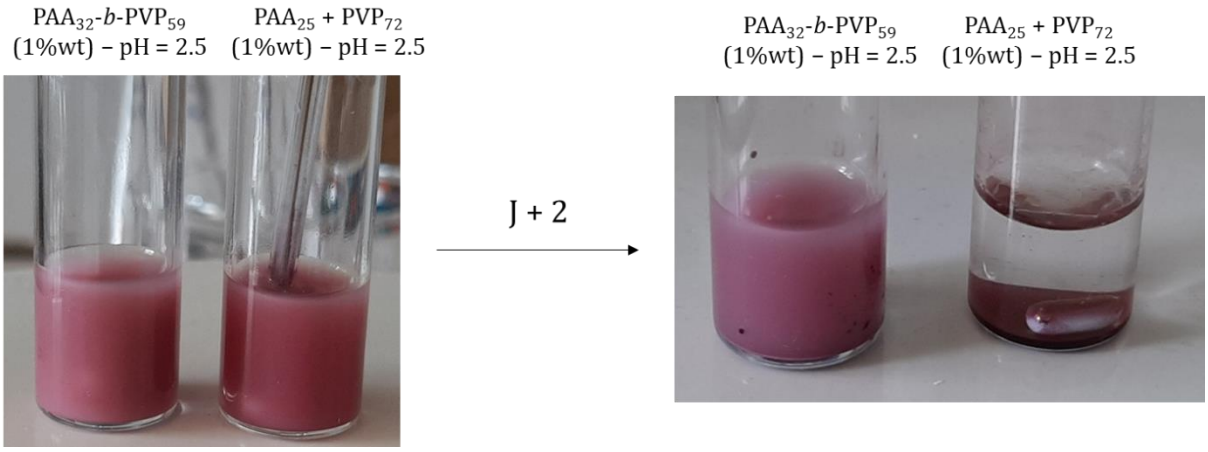

Figure 161. Photos of the solutions containing PAA_{32}-b-PVP_{59} (1%wt) or PAA_{25}+PVP_{72} (1%wt) and Au@citrate NPs ([Au]=500µM) at pH=2.5 after adding HCl solution (1M)

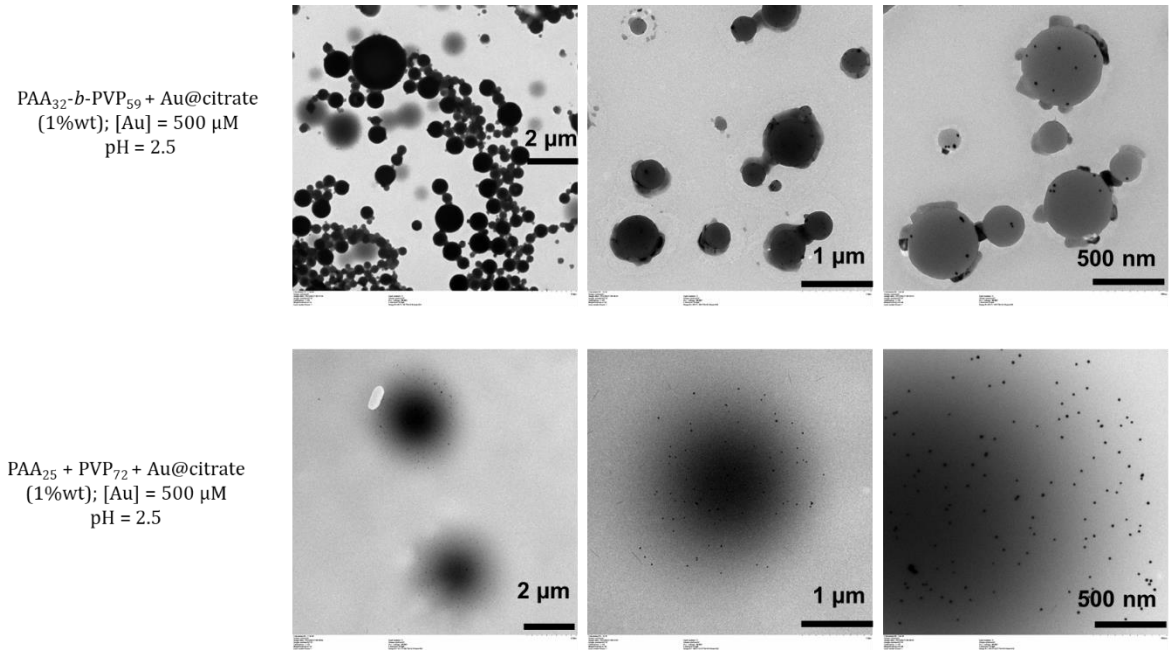

Figure 162. TEM pictures of the samples containing PAA_{32}-*b*-PVP_{59} (1%wt) (A) or PAA_{25}+PVP_{72} (1%wt) (B) and Au@citrate NPs ([Au]=500µM) at pH=2.5 after adding HCl solution (1M)

V Controlling the morphology of nanoassemblies

Nanoassemblies are thus obtained at low pH. Now, it is now critical to see to what extent it is possible to control the structure of the obtained nanoobjects (size, density of particles). As explored in **chapter I**, the design of the polymer used in assembly process, can influence the final size, morphology or stability of the obtained assembled system. Similarly, the weight ratio of AuNPs to polymer, might be of paramount importance to design the final assembly. These different parameters will be studied in the next sections.

V.1 Effect of the AuNPs concentration

For a fixed polymer concentration equal to 0.05%wt, the concentration of AuNPs was now varied. For each concentration of gold, pH was decreased until pH=2.5 to observe the final hybrid nanoassemblies. DLS analysis was realized onto 5 different samples containing varying [Au]: 135, 272, 500, 820, 1510 µM (**Figure 163**).

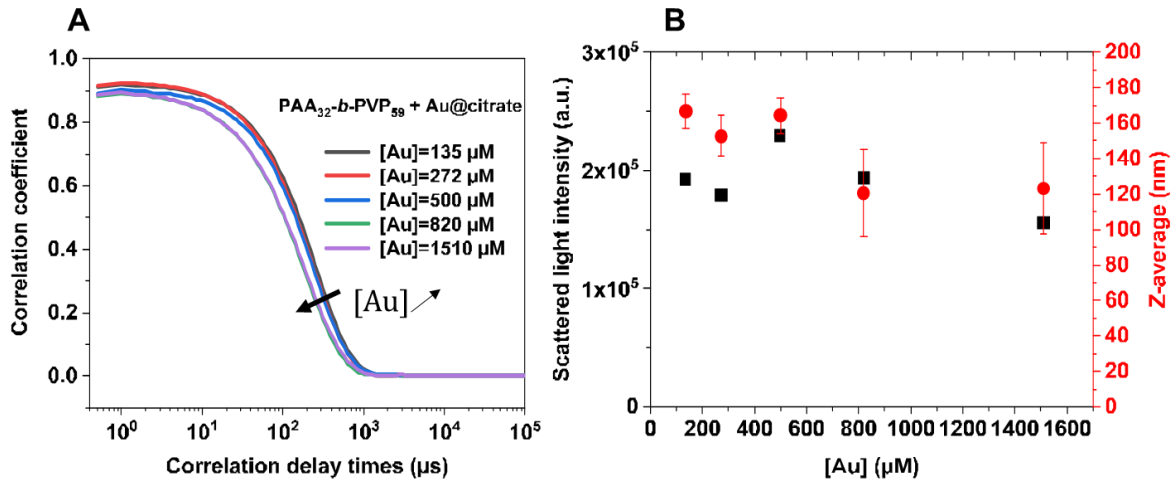

Figure 163. Correlation functions using the NNLS method (**A**) and typical evolutions of the scattered light intensity (black squares) and Z-average diameter (red dots) (**B**), measured by a mono-angle DLS instrument for samples containing PAA_{32}-*b*-PVP_{59} (0.05%wt) + Au@citrate NPs with varying concentration: [Au] = 135; 272; 500; 820; 1510 µM at pH=2.5 after adding HCl (1M).

By increasing the gold concentration ([Au]), the global size of the obtained nanoassemblies at pH=2.5, slightly decreases but is associated with a large standard deviation from 166 ± 10 nm to 123 ± 26 nm. No significant change regarding the scattered light intensity and the correlation function is measured. This seems to indicate that the nanostructures seem to be similar whatever the gold concentration. TEM pictures confirm this hypothesis, by showing that the nanostructures have similar morphology and approximatively same size. Nevertheless, these structures appear to differ from the apparent density of AuNPs (**Figure 164**). The relation between Au@citrate NPs' density and nanostructure size is still under study.

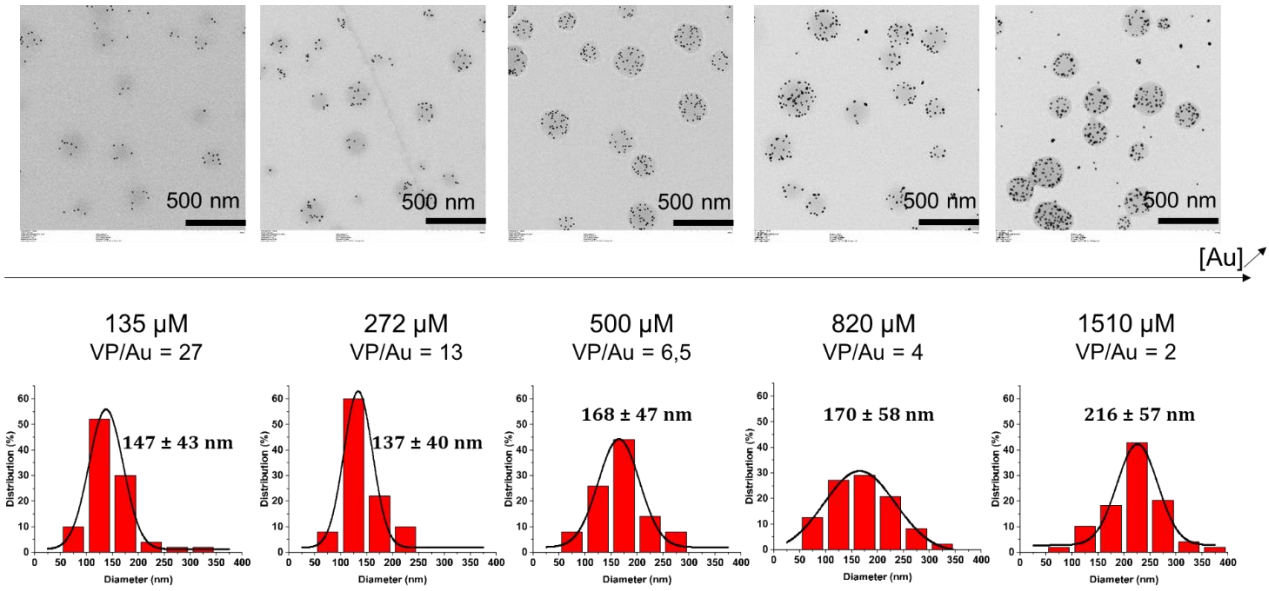

Figure 164. TEM pictures and associated distribution size analysis of samples containing PAA_{32}-*b*-PVP_{59} (0.05%wt) and varying concentrations of Au@citrate NPs: 135; 272; 500; 820; 1510 µM at pH=2.5 after adding HCl solution (1M).

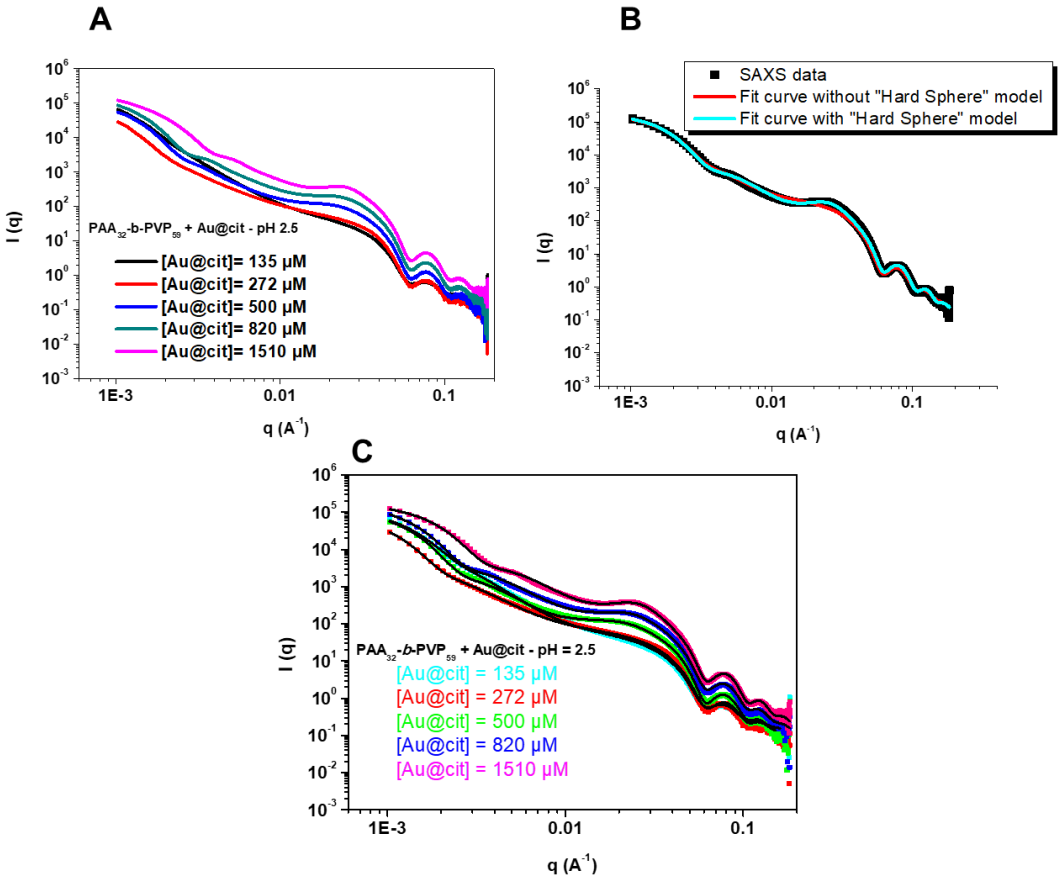

Figure 165.(**A**) SAXS curves for the samples containing PAA_{32}-b-PVP_{59} (0.05%wt) and varying Au@citrate NPs concentration: 135, 272, 500, 820, 1510 µM at pH=2.5 (**B**) SAXS data (black squares) and fit curves applied according to two models considering hard sphere model (cyan curve) or not (red curve) (C) SAXS curves for the samples containing PAA_{32}-b-PVP_{59} (0.05%wt) and varying Au@citrate NPs concentration: 135, 272, 500, 820, 1510 µM at pH=2.5 with associated fitting curves applied according to the best adapted model.

Finally, SAXS analysis was performed to evaluate the morphological evolution of the nanostructures containing more or less Au@citrate NPs (**Figure 165**). The intensity is increasing with the concentration of AuNPs but in the Guinier region, the tendencies seem to differ a little. This observation is confirmed with the fitting because at higher concentrations, 500, 820 and 1510 µM, of Au@cit NPs, the fitting model needed to be improved by considering the AuNPs as interacting hard spheres. As seen on **Figure 165B,** when the hard sphere model is taken into account for the q range corresponding to AuNPs, the fit is better. Thus the organization and the interaction between the AuNPs in the nanopolymeric structure vary according to their density. These experiments also confirm that AuNPs are well inside the polymeric nanostructure and not on the surface.

V.2 Effect of the polymer composition

As seen in **chapter I**, the molecular weight of the polymers can influence both assembly mechanism and final morphology of the obtained nanostructure. As the PVP polymer interacts particularly with gold surface, polymers with different molecular weight comprising a fixed PAA block and PVP block with increased length. Block copolymers PAA_{32}-*b*-PVP_{59}, PAA_{32}-*b*-PVP_{12} and PAA_{32}-*b*-PVP_6 synthesized in **chapter II** were studied here for their ability to induce the formation of nanoassemblies with and without Au@citrate NPs. DLS measurements of obtained nanostructures for polymer alone are presented in **Figure 166A**. The global size of the obtained nanostructures decreases with decreasing Mn_{PVP}.

Experiment with Au@citrate NPs were then performed by keeping a VP/Au ratio constant. As the concentration of polymer is kept constant this induces that [Au] is in relation with the change of [PVP]. Results from DLS and TEM experiments are given in **Figure 166** and **Figure 167** respectively. A significant decrease of nanoassemblies' size is observed between PAA_{32}-*b*-PVP_{59} and PAA_{32}-*b*-PVP_{12} or PAA_{32}-*b*-PVP_5 (around 100 nm and 85 nm, respectively). However, the hybrid assemblies formed with PAA_{32}-*b*-PVP_5 are bigger and more well-defined than the ones formed with PAA_{32}-*b*-PVP_{12}. By taking in account the error ranges onto Z-average, the two nanostructures can be considered as similar, which is in agreement with the near DP values. These results confirms that playing on the molecular weight of the BCP can actually influence the final size of the nanoassembly, as remarked about the copolymer concentration (**III.2**). It is noteworthy that an experiment was made by keeping [Au]=500 µM and showed the same size evolution as the present study, with the exception that the density of AuNPs was higher (as seen previously in the variation of [Au] into a fixed copolymer concentration: **V.1**).

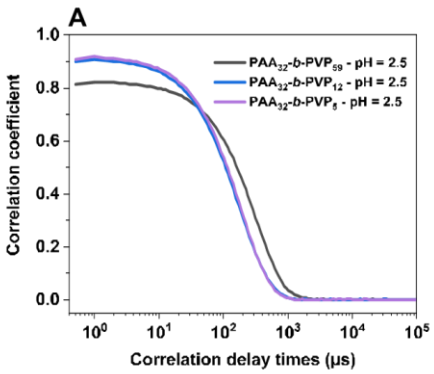

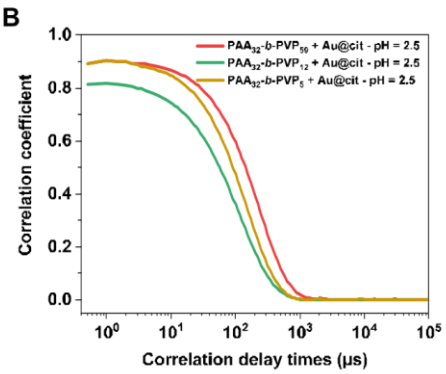

Sample at pH = 2.5	PAA_{32}-*b*-PVP_{59} (0.05%wt)	PAA_{32}-*b*-PVP_{12} (0.05%wt)	PAA_{32}-*b*-PVP_5 (0.05%wt)
Scattered light intensity (a.u)	19.10^4	8.10^4	8.10^4
Z-average (nm)	213 ± 6	116 ± 21	129 ± 11

Sample at pH = 2.5 and VP/Au = 6.5	PAA_{32}-*b*-PVP_{59} (0.05%wt) + Au@cit ([Au] = 500µM)	PAA_{32}-*b*-PVP_{12} (0.05%wt) + Au@cit ([Au] = 400µM)	PAA_{32}-*b*-PVP_5 (0.05%wt) + Au@cit ([Au] =300µM)
Scattered light intensity (a.u)	23.10^4	14.10^4	14.10^4
Z-average (nm)	164 ± 10	75 ± 20	100 ± 12

Figure 166. Correlation functions using the NNLS method and associated scattered light intensity measured by a mono-angle DLS instrument for samples containing PAA_{32}-*b*-PVP_m (0.05%wt) without (**A**) or with (**B**) Au@citrate NPs at a fixed VP/Au=6.5, with m corresponding to the DP of PVP, all samples are at pH=2.5 after adding HCl (1M).

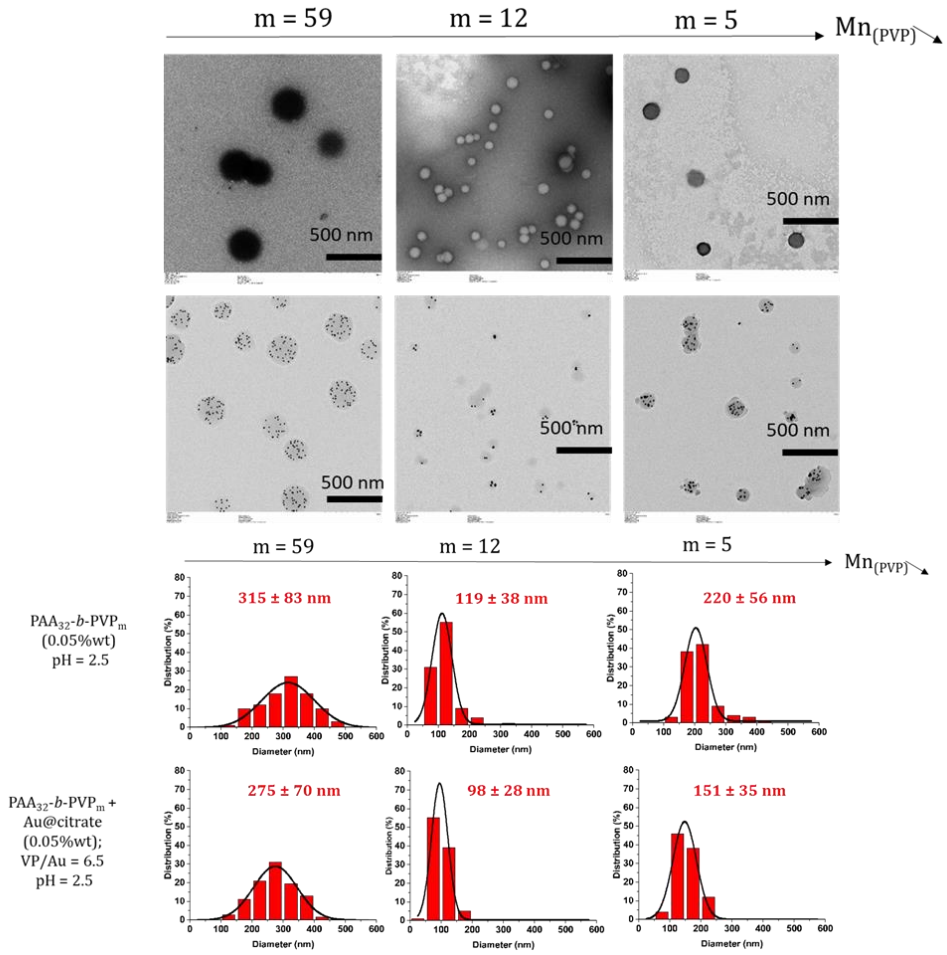

Figure 167. TEM pictures and associated size distribution diagrams of samples containing PAA_{32}-*b*-PVP_m (0.05%wt) without (first line) or with (second line) Au@citrate NPs at a fixed VP/Au=6.5, with m corresponding to the DP of PVP, all samples are at pH=2.5 after adding HCl (1M).

V.3 Effect of the addition of polymers to the initial system

Regarding polymers' parameters, the concentration, the molecular weight, the stabilizing block nature and the configuration (block or homopolymer) were until now studied. A last study consists in varying the polymer composition in the sample, by adding homopolymers or other block copolymers to the present PAA_{32}-*b*-PVP_{59} . The influence onto the size and morphology of obtained nanostructures was studied at low pH as well as the colloidal behavior at higher pH. For that purpose, PAA_{25}, PVP_{72} and PAA_{44}-*b*-PEG_{80} were added to PAA_{32}-*b*-PVP_{59}, by keeping a total polymer concentration of 0.05%wt and a percentage of AA functions and VP or EG functions fixed. The systems were studied with or without the addition of Au@citrate. The ratio of VP functions from PAA_{32}-*b*-PVP_{59} (VP_{block}) to [Au] was fixed to 6.5 for all the samples.

DLS measurements were realized after lowering the pH until pH=2.5. In the absence of AuNPs, as seen on **Figure 168A**, whereas the addition of PAA_{25} increases the final size, no evolution can be evidenced with PVP. The addition of PAA_{44}-*b*-PEG_{80} leads to smaller sizes. Similar tendencies are observed for hybrid assemblies. To have more insights onto the real impact of adding these polymers, scattered light intensity and Z-average values are reported in **Table 13**.

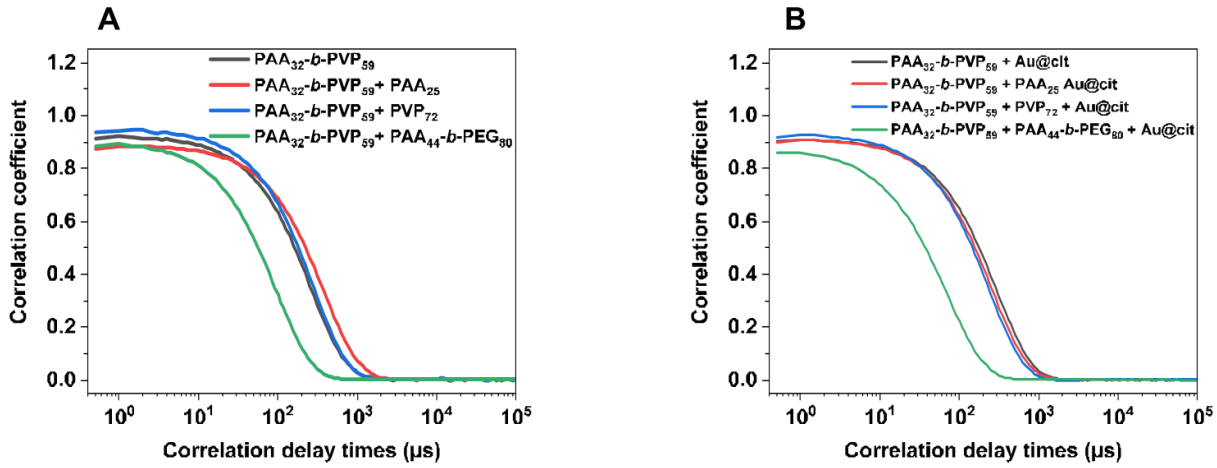

Figure 168. Correlation functions using the NNLS method of the samples containing PAA_{32}-*b*-PVP_{59} alone, with PAA_{25}, with PVP_{72}, with PAA_{44}-*b*-PEG_{80}, without (**A**) or with (**B**) Au@citrate NPs. [polymer]=0.05%wt. VP_{block}/Au=6.5. [Au] = 500 µM for the PAA_{32}-*b*-PVP_{59} sample and [Au]=250 µM for the other samples. All samples are adjusted at pH=2.5 after adding HCl solution (1M).

Table 13. Scattered light intensity and Z-average values measured by a mono-angle DLS instrument for samples of the samples containing PAA_{32}-*b*-PVP_{59} alone, with PAA_{25}, with PVP_{72}, with PAA_{44}-*b*-PEG_{80}, without (**A**) or with (**B**) Au@citrate NPs. [polymer]=0.05%wt. VP/Au=6.5. [Au] = 500 µM for the PAA_{32}-*b*-PVP_{59} sample and [Au]=250 µM for the other samples. All samples are adjusted at pH=2.5 after adding HCl solution (1M).

A

Sample at pH = 2.5	**PAA_{32}-*b*-PVP_{59} (0.05%wt)**	**PAA_{32}-*b*-PVP_{59} + PAA_{25} (0.05%wt)**	**PAA_{32}-*b*-PVP_{59} + PVP_{72} (0.05%wt)**	**PAA_{32}-*b*-PVP_{59} + PAA_{44}-*b*-PEG_{80} (0.05%wt)**
Scattered light intensity (a.u)	17.10^4	11.10^4	10.10^4	7.10^4
Z-average (nm)	177 ± 9	257 ± 25	187 ± 3	62 ± 7

B

Sample at pH = 2.5 and VP_{block} /Au = 6.5	**PAA_{32}-*b*-PVP_{59} (0.05%wt) + Au@citrate ([Au]=500µM)**	**PAA_{32}-*b*-PVP_{59} + PAA_{25} (0.05%wt) + Au@citrate ([Au]=250µM)**	**PAA_{32}-*b*-PVP_{59} + PVP_{72} (0.05%wt) + Au@citrate ([Au]=250µM)**	**PAA_{32}-*b*-PVP_{59} + PAA_{44}-*b*-PEG_{80} (0.05%wt) + Au@citrate ([Au]=250µM)**
Scattered light intensity (a.u)	22.10^4	20.10^4	15.10^4	2.10^4
Z-average (nm)	187 ± 11	172 ± 10	151 ± 9	44 ± 9

TEM pictures were realized to visualize the obtained nanoassemblies at pH=2.5 using the different polymer compositions (**Figure 169**). As remarked in DLS, the nanostructures formed in presence of the homopolymers PAA_{25} and PVP_{72} present some difference of sizes.

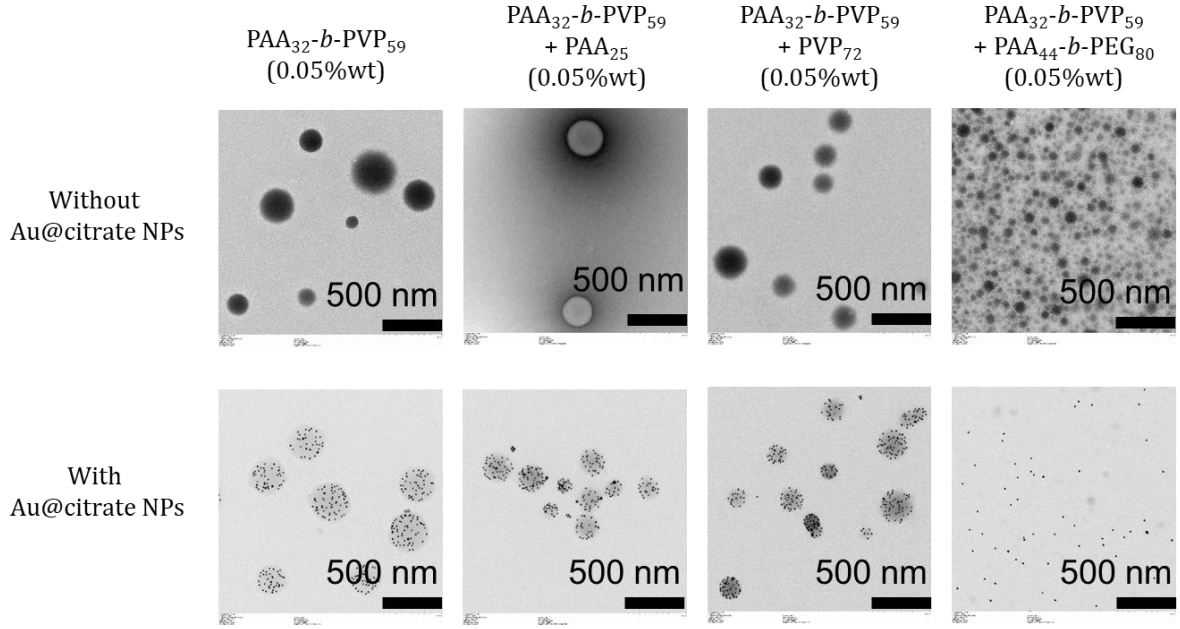

Figure 169. TEM pictures of the samples containing PAA_{32}-*b*-PVP_{59} alone, with PAA_{25}, with PVP_{72}, with PAA_{44}-*b*-PEG_{80}, without (first line) or with (second line) Au@citrate NPs. [polymer]=0.05%wt. VP/Au=6.5. [Au] = 500 µM for the PAA-b-PVP sample and [Au]=250 µM for the other samples. All samples are adjusted at pH=2.5 after adding HCl solution (1M).

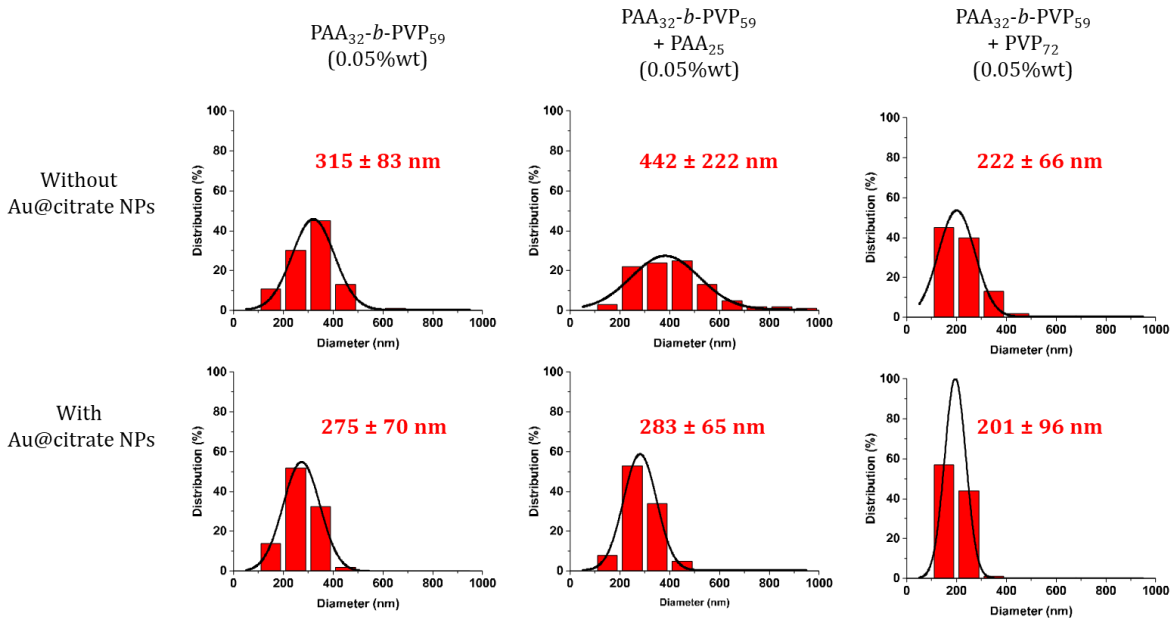

Figure 170. Size distribution diagrams associated to TEM pictures of **Figure 169**

Regarding PAA_{44}-*b*-PEG_{80}, it is interesting to see that in presence of this second polymer, the assembly process seems to be significantly affected. Indeed, for the solely polymers system, observed nanostructures are similar to the ones obtained without PAA_{44}-*b*-PEG_{80} in terms of morphology, but with smaller size. On the TEM picture, it seems like a huge network of the two DHBCs is created and some interactions lead to nanostructures formation. When PAA_{44}-*b*-PEG_{80} is mixed with PAA_{32}-*b*-PVP_{59} in presence of Au@citrate NPs, TEM picture clearly shows that no hybrid assembly is formed at pH=2.5. Some nanoassemblies of very small size are observed on the TEM picture and seem to be only composed of polymers. The interaction between the PAA_{44}-*b*-PEG_{80} and the Au@citrate NPs has been already studied in this work (**IV.1**) and showed that this DHBC was not able in these concentration and pH ranges to stabilize the Au@citrate NPs in solution. In presence of PAA_{44}-*b*-PEG_{80} Au@citrate NPs cannot precipitate or assemble.

VI Composition tunability and stability issues

The assembly mechanism of the PAA_{32}-*b*-PVP_{59} block copolymer was studied in presence or in absence of Au@citrate NPs and then many parameters were varied to better understand their influence on the final obtained nanoassemblies. This final part is then dedicated to studies showing that the system can be diversified in terms of composition. The first alternative concerns the gold nanoparticles, which were until now preformed Au@citrate NPs incorporated into polymer solution after being washed from excess of citrate ligand. In the next paragraph, *in situ* formation of the AuNPs in presence of the PAA_{32}-*b*-PVP_{59} is investigated and the resulting hybrid samples are compared to the previous ones with preformed Au@citrate NPs. Finally, the self-assembly of the PAA_{32}-*b*-PVP_{59} in presence of lanthanide ions, like gadolinium, is studied. Some first experiments are about mixing the block copolymer with both gadolinium ions and gold nanoparticles.

VI.1 AuNPs formation in situ

In the following section, the gold nanoparticles are synthesized through another method, which was quickly explained in **chapter I** and named as *in situ* or "direct synthesis" method. This protocol consists in reducing gold salt in solution to perform gold nanoparticles' synthesis. The **chapter I** was focused on the use of polymers as reductants of gold salts with or without the help of small molecules such as citrate or borohydride ($NaBH_4$). Here, the PVP polymer is the ligand which will be particularly implied into the synthesis and the functionalization of the final AuNPs.

The *in situ* method is generally used to have a control over the morphology and the size of the obtained AuNPs. A specific protocol named "seeded growth synthesis" is particularly employed to broaden the size range and access to uniformity of the final AuNPs. This protocol is divided into 2 steps: nucleation (seeds formation) and growth. Nucleation step consists in the pure reduction of the gold salt Au(III) into metallic gold state Au(0) through the use of reductants. Then, gold salt is added during the growth step, accompanied by a reductant, to modify the size of the AuNPs. The reductants become then the temporary stabilizers of the resulting AuNPs. However, incorporation of additional ligands during the synthesis, like polymers, can have a great impact onto the morphology, the size and the final functionalization of the AuNPs.[21,22] One of the main advantage of the ligands' incorporation is their ability to stabilize gold precursors and avoid the self-nucleation process, which happens at high precursors' concentrations and lead to heterogeneous sizes of final AuNPs. By being complexed to gold precursors, the ligands induce a decrease of the concentration of the equilibrium Au(0) monomers to a value much lower than the nucleation threshold, which allows a uniform growth of the AuNPs, as schematized by C. Gao et al.[23] (**Figure 171**) regarding PVP functionalization of AuNPs.

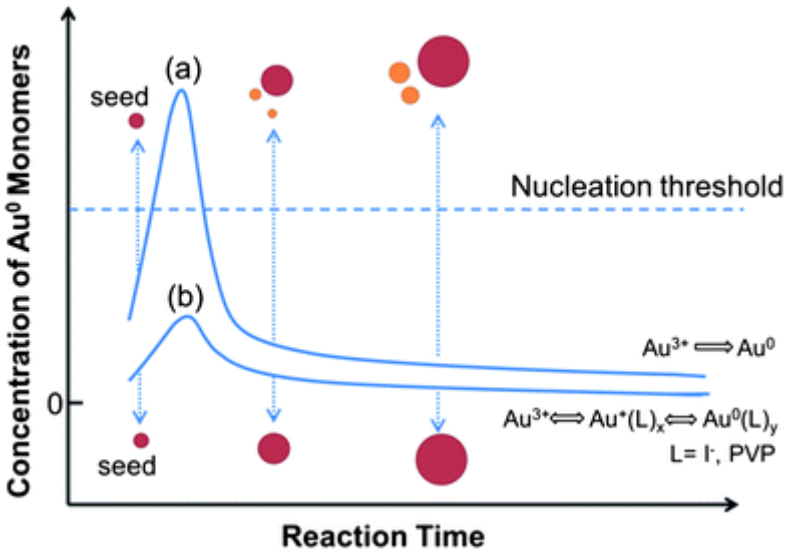

Figure 171. Schematic diagram depicting the stages of the growth of Au nanoparticles in a seeded synthesis without (**a**) and with (**b**) self-nucleation being suppressed by additional coordinating ligands. Seeded growth at high precursor concentrations without self-nucleation can be achieved by stabilizing precursors through complexation with strong ligands, which greatly decreases the concentration of the equilibrium Au^0 "monomers" in the reaction to a value much lower than the nucleation threshold. The initial coordinating ligand to Au^{3+}, Cl^-, a much weaker ligand than I^-, is not shown in this scheme for simplicity. [23]

Indeed, PVP was widely used in nanoparticles' synthesis[14,17] as it was proved to influence the size[24] and the morphology[25] of the obtained NPs and its role as a stabilizer[26] and electron donor[27,28]. PVP is then often introduced at initial step with the gold salt and when reductant is added, the seeded growth process starts. In the present work, the PVP polymer is comprised into the PAA_{32}-*b*-PVP_{59} block copolymer, which will be the chosen ligand for the functionalization of the resulting AuNPs. One protocol was taken from the literature to realize this in situ synthesis of AuNPs in presence of PAA_{32}-*b*-PVP_{59} [29]. This initial protocol was made to form sub-100 nm colloidosomes by first mixing PVP polymer, gold salt and $NaBH_4$ to obtain gold seeds and then organize emulsion by adding amine to induce the Au@PVP seeds assembly. Finally, growth step was performed by adding gold salt and ascorbic acid, and a final template removal allowed the obtention of colloidosomes. Only the nucleation and growth conditions are reused here, no emulsion or template removal is performed, as the objective is to prove that these resulting AuNPs can be assembled through pH variation as for the Au@citrate NPs. The two steps are schematized onto **Scheme 12**. A strong reductant, $NaBH_4$, was first chosen to perform the nucleation step and obtain gold seeds (Au seeds) in interaction with PAA_{32}-*b*-PVP_{59} block copolymer. Then, ascorbic acid was the second reductant for the growth step of the seeds to obtain AuNPs. The two steps were realized at room temperature under stirring.

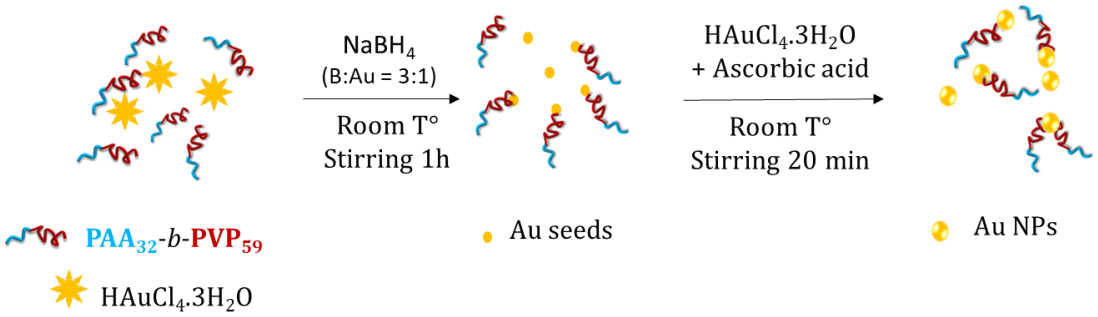

Scheme 12. Schematization of nucleation step and growth step onto a system comprising PAA_{32}-*b*-PVP_{59} block copolymer and $HAuCl_4.3H_2O$ salt. Reductants used are sodium borohydride ($NaBH_4$) for the nucleation step at a ratio of 3:1 to the gold concentration and ascorbic acid for the growth step. Room T°=20°C.

A first test was performed by introducing 0.1%wt of PAA_{32}-*b*-PVP_{59} block copolymer with [Au]=121 µM and B:Au ratio equal to 3.3 : 1, to have a slight excess of $NaBH_4$ compared to gold and to have polymer concentration range near from the ones studied in previous experiments. The solution's color was initially pale yellow and darkened after incorporation of $NaBH_4$. After 1 hour of stirring, no color change was observed and the resulting seeds solution was diluted by two before the growth step. Gold salt was added and final [Au]=500µM to have the same gold concentration as for Au@citrate NPs. Ascorbic acid was added at a ratio ascorbic: Au = 3.4 : 1 and the solution color became red after few seconds (**Figure 172**). UV-vis spectra clearly show the apparition of the SPR band after growth step, proving the formation of the AuNPs.

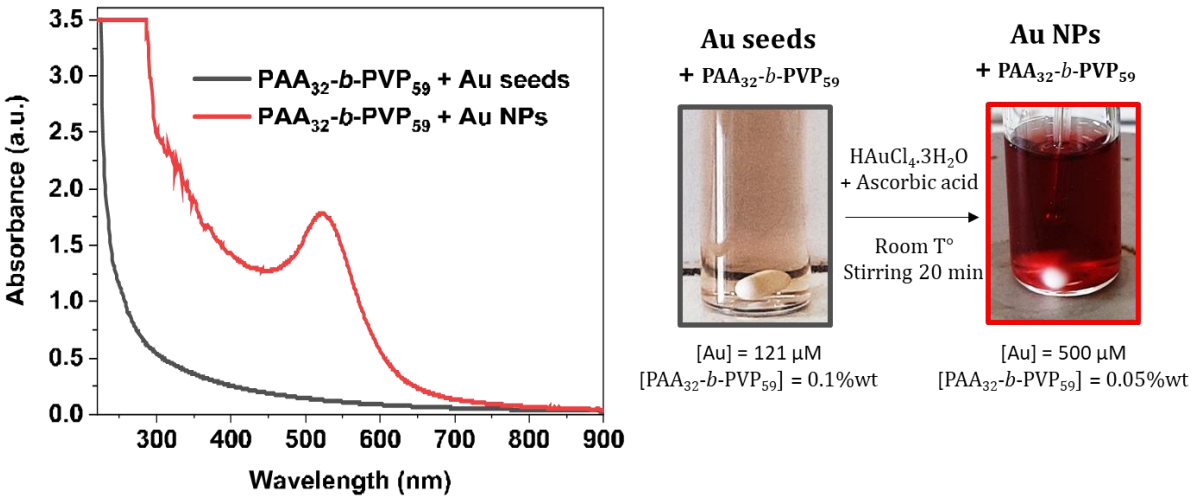

Figure 172. UV-vis spectra of the sample containing PAA_{32}-*b*-PVP_{59} (0.1%wt) and Au seeds ([Au]=121 µM) (grey) which is the sample issued from nucleation step and the sample containing PAA_{32}-*b*-PVP_{59} (0.05%wt) and AuNPs ([Au]=500 µM) issued from growth step (red) and associated photos of the solutions.

DLS measurements were performed on the two samples to see if size evolution could be evaluated. On **Figure 173**, correlation function is increasing when seeds become nanoparticles, as well as the scattered light intensity, meaning that more well-defined nano-objects are obtained after

growth step. Regarding the size, the global size value for Au seeds sample is bigger than the one for AuNPs, but according to previous observations, this would be only due to polymer aggregates in interaction with the Au seeds.

A

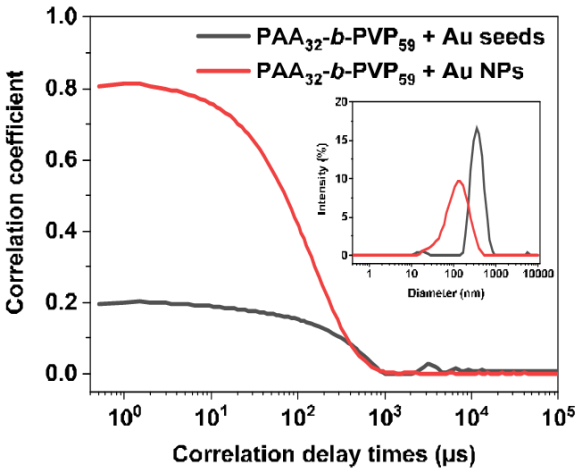

B

Samples	PAA_{32}-*b*-PVP_{59} + Au seeds (0.1%wt) [Au]=121 µM	PAA_{32}-*b*-PVP_{59} + Au NPs (0.05%wt) [Au]=500 µM
Scattered light intensity (a.u)	$1.2.10^3$	73.10^3
Z-average (nm)	295 ± 69	97 ± 27

Figure 173. Correlation functions using the NNLS method (A) and scattered light intensity and Z-average values measured by a mono-angle DLS instrument (B) for the samples PAA_{32}-*b*-PVP_{59} (0.1%wt) and Au seeds ([Au]=121 µM) (grey) which is the sample issued from nucleation step and the sample containing PAA_{32}-*b*-PVP_{59} (0.05%wt) and AuNPs ([Au]=500 µM) issued from growth step (red)

To know about the structures formed in solution, TEM pictures were made and are shown in **Figure 174**. As observed onto these pictures, the seeds seem dispersed in the polymer and their small size confirms the associated UV-vis spectra (**Figure 172**). When growth step is performed, the resulting AuNPs have different sizes, proving that the growth process was not equal for each seed. What is remarked as well, is that these heterogeneous AuNPs are grouped, like if they were assembled. The pH measurements indicate the Au seeds solution is at pH=8.7 and after growth step, the AuNPs soluion is at pH=2.4. This final pH value is precisely in the range where the block copolymer is self-assembling into nanostructures based on hydrogen bondings. Thanks to the previous studies made with Au@citrate NPs, the nanostructures formation observed here is well understood. Indeed, adding chloroauric and ascorbic acids, make decrease the pH enough to attain this value of 2.4 at which BCP self-assembles and brings AuNPs together as it functionalizes them. To know about the behavior of these obtained nanostructures, pH variation was performed by adding sodium hydroxide (NaOH).

DLS and UV-vis spectroscopy analysis are shown on **Figure 175** and the pH variation indicates a global size decrease from pH=3, which is globally maintained at higher pH values. Regarding UV-vis spectra, a slight SPR band shift is observed toward lower wavelengths with increasing pH, supposing that the AuNPs are more dispersed in solution, which could support the size decrease. The assembly mechanism would then be again based only on hydrogen bondings, which are thus broken when pH is increased.

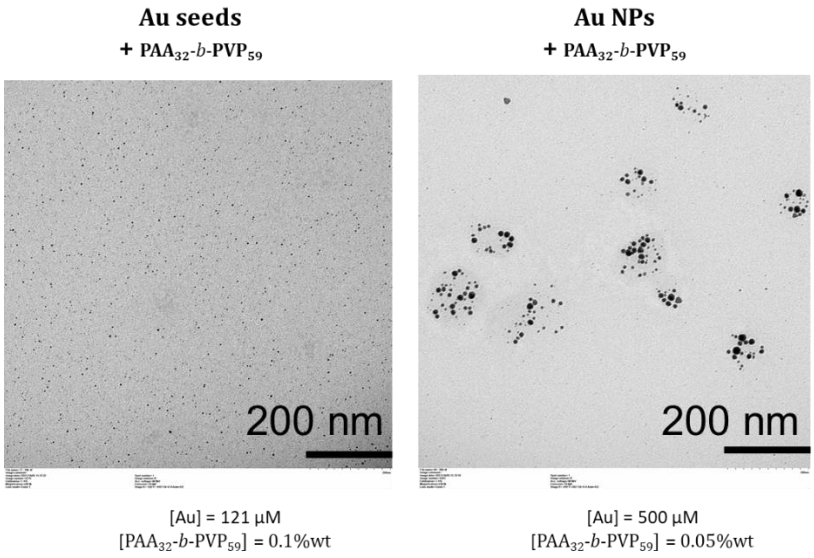

Figure 174. TEM pictures of the samples PAA_{32}-*b*-PVP_{59} (0.1%wt) and Au seeds ([Au]=121 µM) (left) which is the sample issued from nucleation step and the sample containing PAA_{32}-*b*-PVP_{59} (0.05%wt) and AuNPs ([Au]=500 µM) issued from growth step (right).

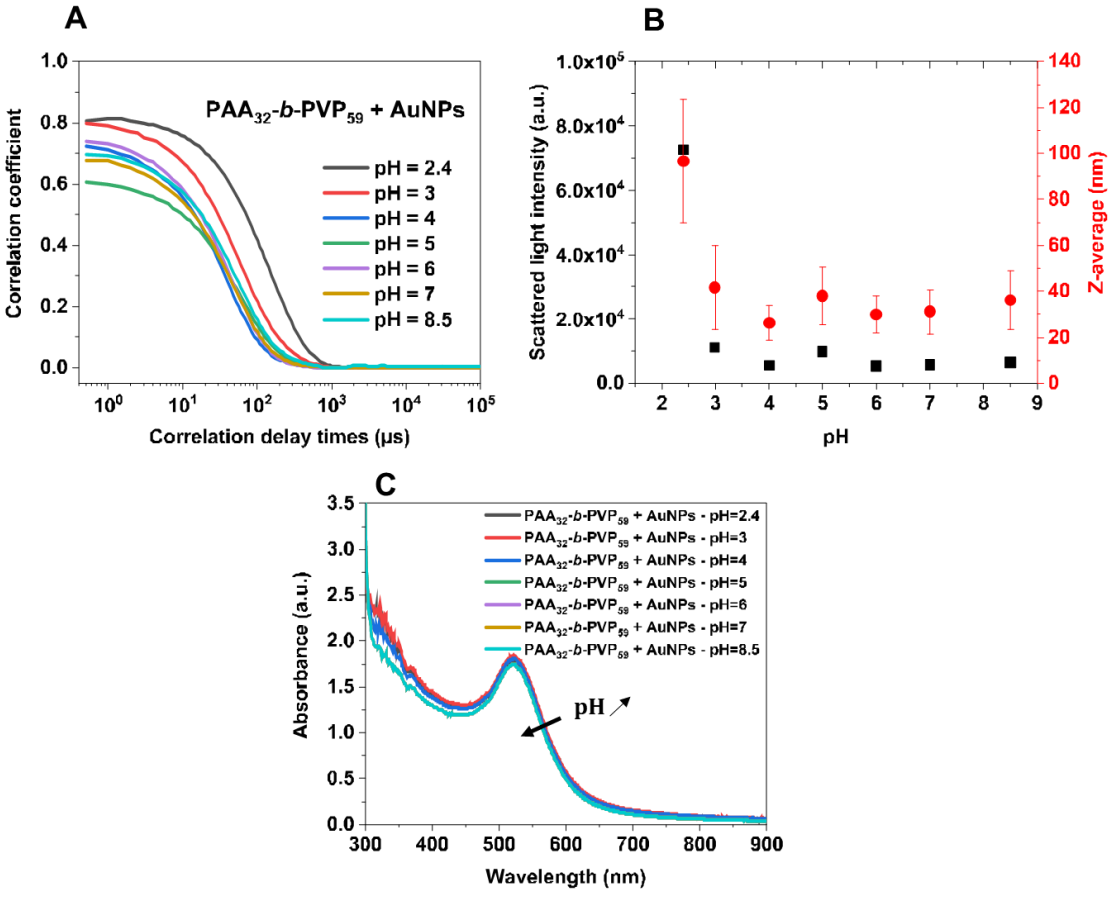

Figure 175. Correlation functions using the NNLS method (**A**), typical evolutions of the scattered light intensity (black squares) and Z-average diameter (red dots) (**B**) and UV-vis spectra (C) of the sample containing PAA_{32}-*b*-PVP_{59} (0.05%wt) and AuNPs ([Au]=500 µM) issued from growth step at varying pH after adding NaOH solution (1M).

TEM pictures confirm the destructuration of the nanoassemblies observed initially at pH=2.4 just after growth process, when pH is increased (**Figure 176**). However, some polymers assemblies are present on TEM pictures at high pH without particularly grouping AuNPs, probably formed because of ascorbate species.

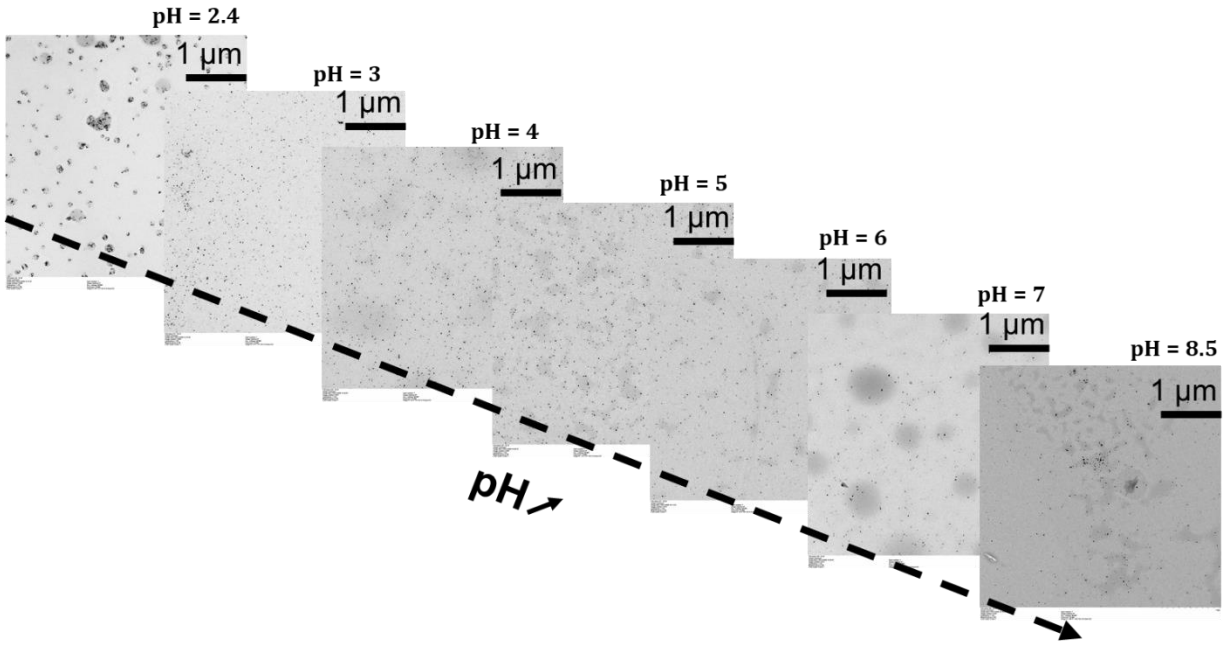

Figure 176. TEM pictures of the sample containing PAA_{32}-*b*-PVP_{59} (0.05%wt) and AuNPs ([Au]=500 µM) issued from growth step at varying pH after adding NaOH solution (1M).

Numerous supplementary studies were performed onto this system based on in situ synthesized AuNPs, but will not figure in this manuscript. Nevertheless, their purpose and some results are exposed here. Some studies focused on the wish to have more controlled size of the AuNPs; because the growth was considered as not completed. For that purpose, temperature influence was investigated and leads to precipitation of the AuNPs, as well as sonication. The nucleation was as well deeply studied, with variation of the ratio between $NaBH_4$ and gold salt, but the results did not show significative difference with reference samples. The pH was as well varied in this nucleation step to evaluate its impact and proved that assemblies of the Au seeds were obtained and conserved if the growth step was further applied. Similar experiments as for Au@citrate NPs were as well performed like changing the VP/Au ratio, pH reversibility and PAA_{44}-*b*-PEG_{80} comparison. The variation of VP/Au ratio leads to similar nanoassemblies but the variation of AuNPs density is not as obvious as for the Au@citrate NPs. The nanoassemblies formed at pH=2.4, are destructured by increasing pH and formed again by decreasing pH until pH=2.5, proving then the reversibility behavior. Finally, PAA_{44}-*b*-PEG_{80} does not stabilize AuNPs formed in situ neither.

VI.2 Adding lanthanides to bring properties

A final different way to design the composition of these hybrid assemblies, is to add ions, which would be able to interact with the PAA polymer of the PAA-*b*-PVP block copolymer. As in **chapter II**, the choice of these ions was turned onto lanthanides, because of their interesting properties like magnetism for gadolinium or luminescence for europium. In this final part of this work, the objectives were to study the previous pH-responsive assembly mechanism of the PAA_{32}-*b*-PVP_{59} BCP in presence of gadolinium ions and pursue these first investigations until a system mixing the BCP, the ions and the gold nanoparticles. The purpose is to evaluate the interactions existing between the ions and the BCP under pH variation, and the resulting influence onto the nanostructures based onto polymer self-assembly. The same work will be performed onto the system comprising additional gold nanoparticles.

VI.2.1 pH variation onto the system comprising PAA_{32}-*b*-PVP_{59} and gadolinium ions

A first pH variation study was realized in this work in **chapter II** (**Chapter II – III.4.1**), onto the HPICs sample containing PAA_{32}-*b*-PVP_{59} (0.1%wt) and europium ions ($[Eu^{3+}]$=1.3mM). The results showed that the size was progressively increasing and a huge size gap was observed between pH=3 and pH=2. Supplementary luminescence studies did confirm the decomplexation of the lanthanide by the block copolymer, visible through the decrease of the phosphorescence intensity, which was supposed to be due to the PAA protonation and then to the inability of PAA to chelate ionic species. However, as the study was focused on the HPICs nanostructures and their stability under pH variation, no TEM was performed at low pH values. Nevertheless, later in the project, the self-assembly of the block copolymer was studied (present chapter IV) and the resulting DLS analysis did meet the ones realized in **chapter II**, with increasing sizes at low pH values.

The objective is now to study again these HPICs samples under pH variation, by taking care about the nanostructures potentially formed at low pH. To compare this study to the ones realized onto BCP self-assembly and hybrid assemblies with gold nanoparticles, the first chosen polymer concentration was 0.05%wt. The first lanthanide tested was gadolinium, which is the more prone to be used in further biological applications. The ratio between PAA and Gd^{3+} ions was fixed to R=1, corresponding to neutral charge. A classic HPICs sample was then prepared by mixing PAA_{32}-*b*-PVP_{59}, water and Gd^{3+} ions, but this time, contrary to **chapter II**, the pH was not adjusted to pH=7, but maintained at initial pH=5.2. Then pH variation was applied by adding HCl solution (1M) until attaining pH=2.5. To evaluate the behavior at higher pH, NaOH solution (1M) was then added.

DLS analysis was realized onto initial pH=5.2, at pH=2.5 and then at two higher pH values: pH=5.8 and pH=9 (**Figure 177**). As for the BCP self-assembly results, after decreasing the pH until pH=2.5, the size is increased from classic HPICs nanostructures' size (26 nm) to imposing nanostructures of 270 nm. The presence of Gd^{3+} ions do not influence the assembly process, which confirms the results obtained with Eu^{3+} ions in **chapter II**. However, when pH is then increased, the results obtained regarding size evolution are different from the ones of the PAA_{32}-*b*-PVP_{59} BCP alone. When Gd^{3+} ions are present in the sample, the assembly process seems to be not anymore pH-reversible. The obtained size at pH=2.5 is conserved after increase of the pH, nevertheless the intensity size distribution and the scattered light intensity both indicate a signal decrease, which could support a morphological change.

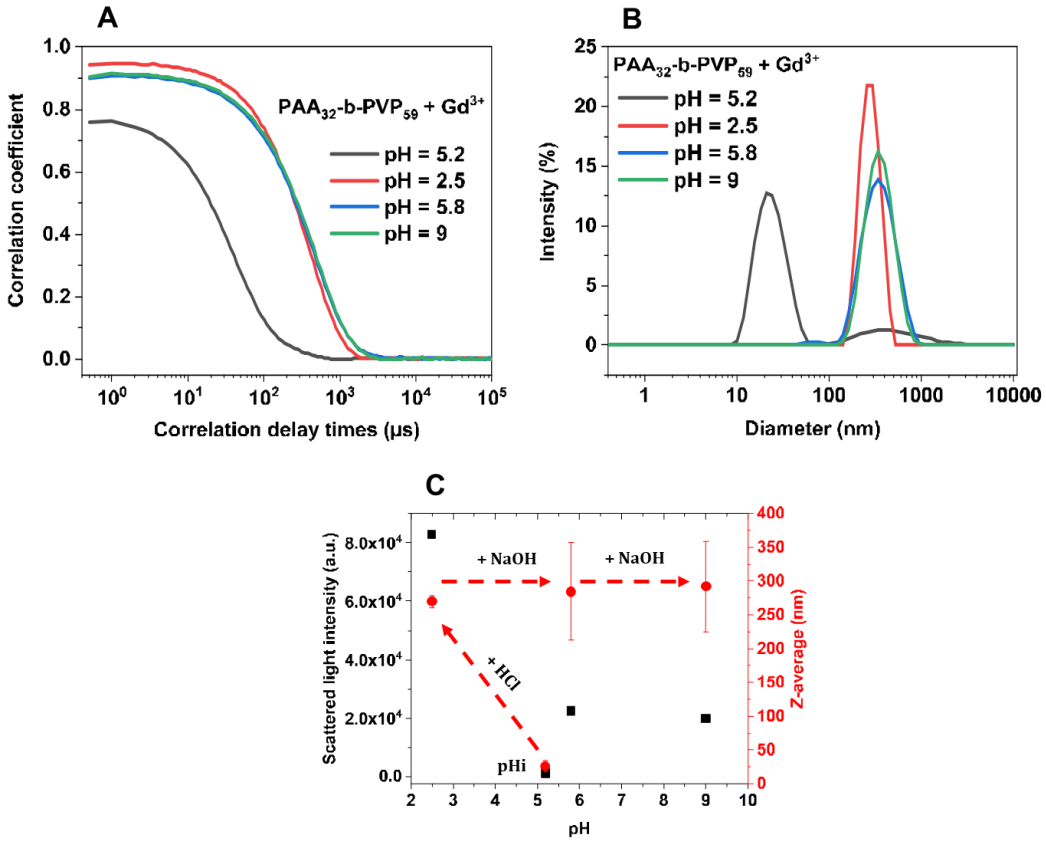

Figure 177. (**A**) Correlation functions using the NNLS method, (**B**) Distribution average size in intensity and (**C**) Typical evolutions of the scattered light intensity (black squares) and Z-average diameter (red dots) for the sample containing PAA_{32}-*b*-PVP_{59} (0.05%wt) and Gd^{3+} ions (0.7mM) at varying pH after adding first HCl solution (1M) and then NaOH solution (1M).

To have deeper insight into the structures contained into the sample at higher pH, both visual observations (**Figure 178**) and TEM pictures (**Figure 179**) were made. The solution was limpid at initial step and became turbid at pH=2.5, which was the case for PAA_{32}-*b*-PVP_{59} alone too. But, after increasing the pH, the solution did not come back to initial aspect, a slight turbid appearance was still observed. Despite this turbid aspect, no precipitation was observed. As the

solution still diffused at higher pH values, the presence of imposing nanostructures could be a cause and this was already supported by DLS data.

Samples were deposited on TEM grids, without any contrasting agent, as the gadolinium naturally brings contrast under X-ray. As observed on **Figure 179**, the nanostructures at pH=2.5 are similar to the ones observed for the PAA_{32}-*b*-PVP_{59} alone system, but with bigger sizes. Size distribution analysis was performed onto the TEM picture of the sample at pH=2.5 and the diameter found was D=422 ± 118 nm. On TEM pictures at higher pH, the previous nanostructures are still present but their aspect seem to have a little bit changed, like if the corona was more "soft" or "flexible". This could explain the lower scattered light intensity and the less turbid aspect in solution. What is certain is that the nanostructures are maintained at higher pH after being formed at pH=2.5. Gadolinium ions seem then to help the nanostructures to be maintained, despite the hydrogen bondings hypothetic break.

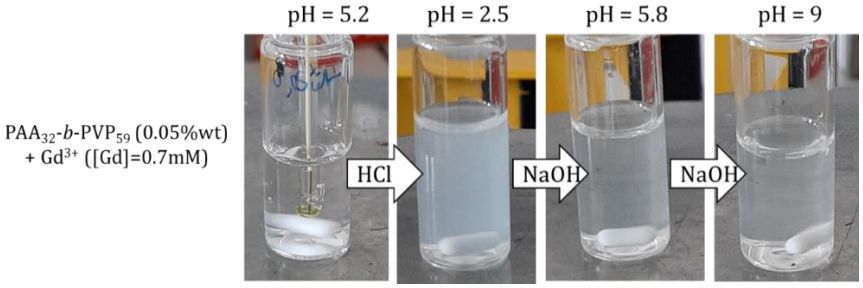

Figure 178. Photos of the sample containing PAA_{32}-*b*-PVP_{59} (0.05%wt) and Gd^{3+} ions (0.7mM) at varying pH after adding first HCl solution (1M) and then NaOH solution (1M).

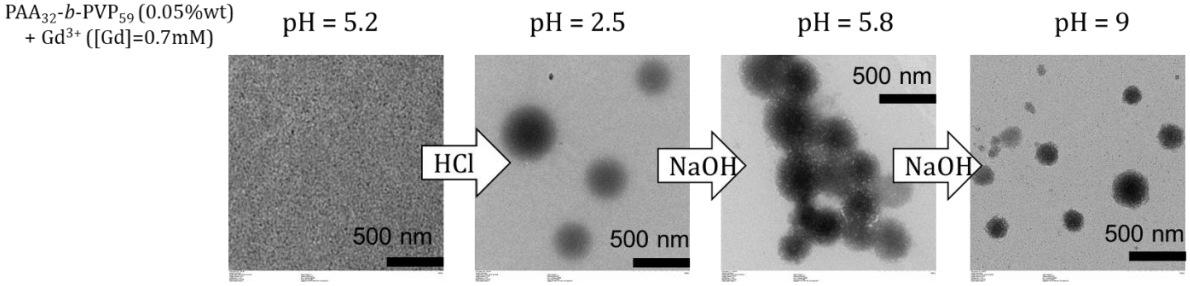

Figure 179. TEM pictures of the sample containing PAA_{32}-*b*-PVP_{59} (0.05%wt) and Gd^{3+} ions (0.7mM) at varying pH after adding first HCl solution (1M) and then NaOH solution (1M).

Additional experiments were realized at higher polymer concentration (0.1%wt), to be in the same conditions as the HPICs study in **chapter II**. DLS analysis results lead to similar tendency under pH variation (**Figure 180**). A first increase in size by decreasing pH until pH=2.5, and then a slight increase when pH is increased until pH=9. The measured sizes are bigger than the ones for 0.05%wt, which confirms again the influence of the polymer concentration onto the final assemblies' size. The aspect of the obtained nanostructures changes from acidic to basic conditions according to photos of the solution and TEM pictures (**Figure 181**), and this is again

supported with a decrease of the scattered light intensity. Size distribution analysis was performed onto the TEM picture of the sample at pH=2.5 and the diameter found was D=440 ± 121 nm.

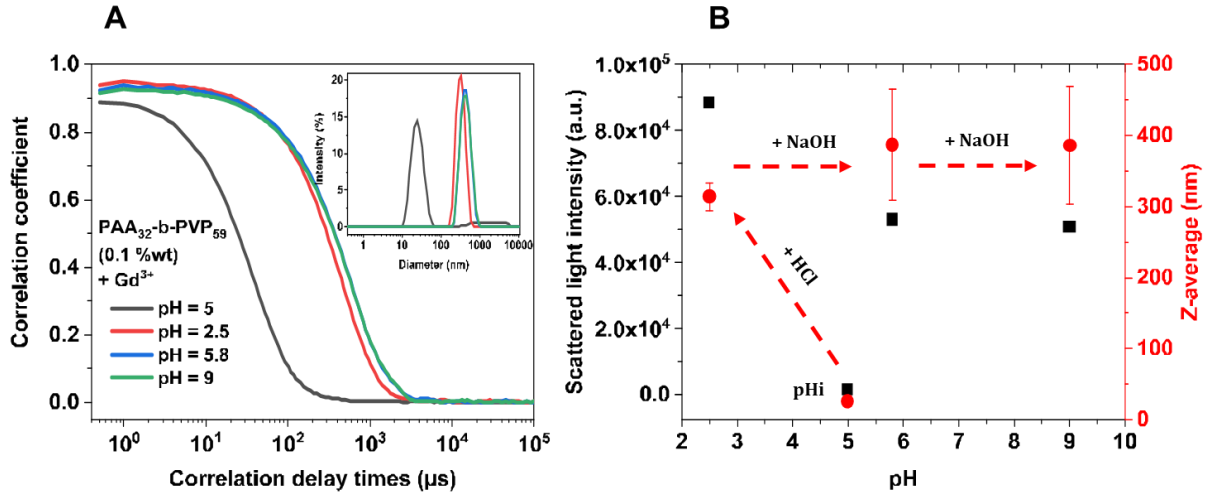

Figure 180. (**A**) Correlation functions using the NNLS method, (**inset**) Distribution average size in intensity and (**B**) Typical evolutions of the scattered light intensity (black squares) and Z-average diameter (red dots) for the sample containing PAA_{32}-*b*-PVP_{59} (0.1%wt) and Gd^{3+} ions (1.4 mM) at varying pH after adding first HCl solution (1M) and then NaOH solution (1M).

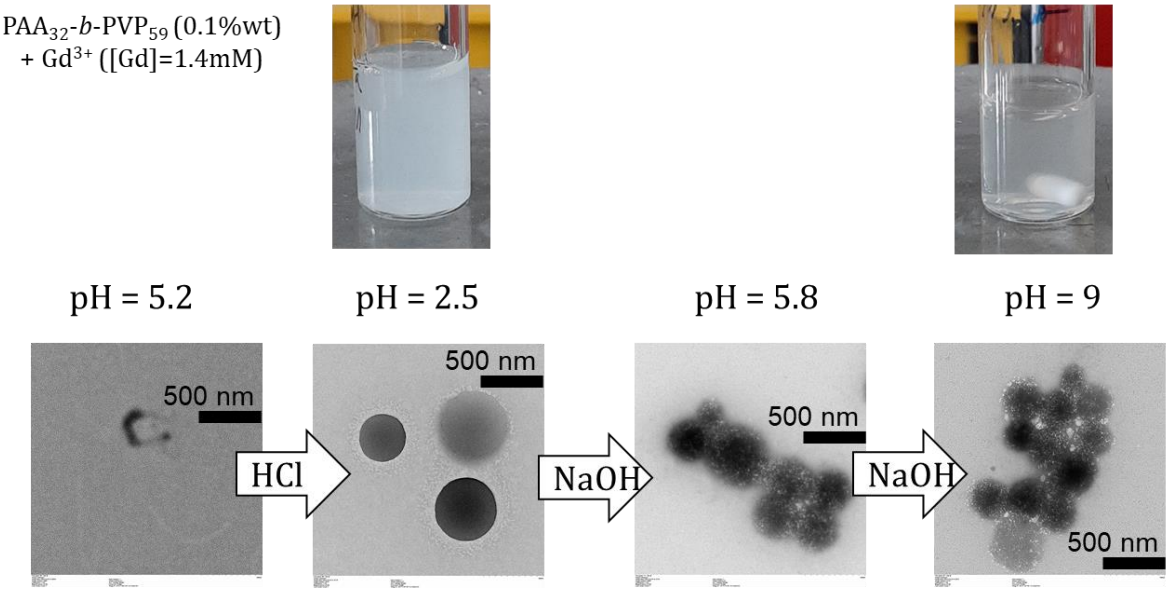

Figure 181. TEM pictures of the sample containing PAA-b-PVP (0.1%wt) and Gd^{3+} ions (1.4 mM) at varying pH after adding first HCl solution (1M) and then NaOH solution (1M) and photos of the sample at pH=2.5 and pH=9.

Some studies were started to try to understand what is the role of Gd^{3+} ions into this assembly mechanism and this maintain of the structures at high pH values, which was not possible when the BCP was alone, or with gold nanoparticles. As performed in **III.3**, the kinetic of the mechanisms involved during pH variation was investigated through UV-vis spectroscopy, thank to the diffusion of the solution when pH is decreased (**Figure 182**). The assembly process seems

fast and then progressively evolve with time. When NaOH is added to the solution, a large decrease of $A_{\lambda=350nm}$ is observed but the final value is not exactly the initial absorbance value, which could support the previous observations, with the non-reversible behavior.

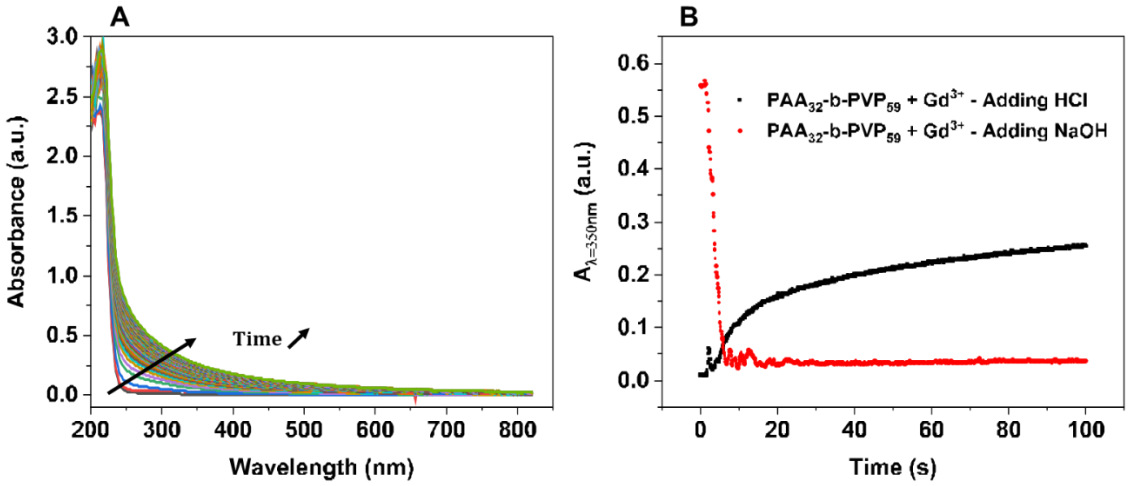

Figure 182. UV-vis spectra (100 scans) of PAA_{32}-*b*-PVP_{59} (0.014%wt) + Gd^{3+} ions ([Gd] = 0.2mM) solution under pH variation after adding 8 µL of HCl solution (1M) (**A**) Time evolution of the absorbance measured at λ=350 nm for both assembly and disassembly mechanisms (**B**)

Zeta potential measurements were performed onto the nanostructures at pH=2.5 and at pH=9, the results were respectively ξ=-5.1 ± 2 mV and ξ=-4.1 ± 0.3 mV. As gadolinium ions are able to form hydroxides around pH=7, as studied in **chapter II** through ATR-FTIR spectroscopy (**Chapter II – III.2.1**), their presence may appear when the pH is increased once the nanostructures are formed at low pH. As the initial pH of the samples are under pH=7, some experiments were realized by increasing the initial pH over pH=7 and then decrease it until pH=2.5, to finally increase the pH again and observe if some differences were observed.

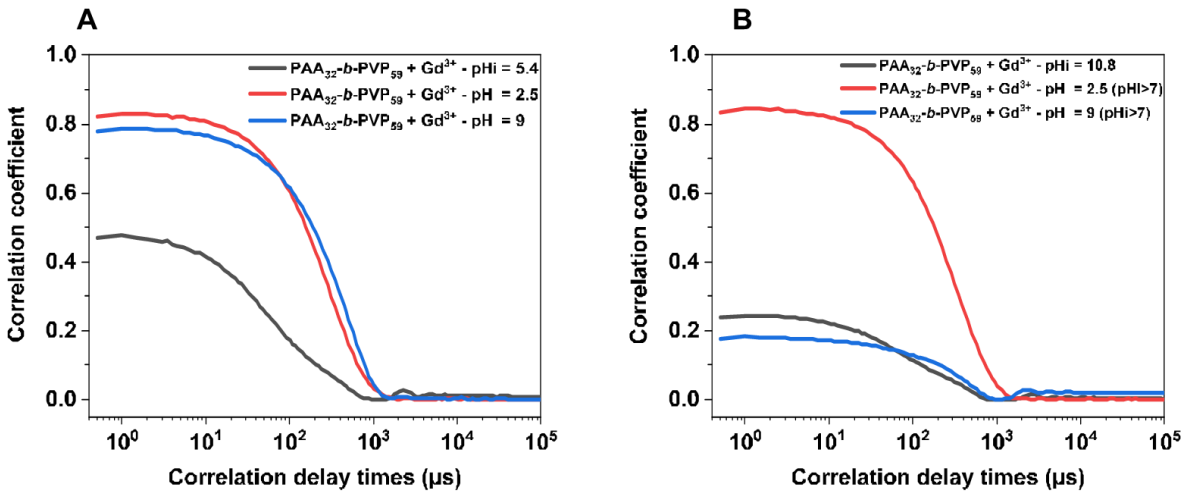

Figure 183. Correlation functions using the NNLS method for the sample containing PAA_{32}-*b*-PVP_{59} (0.014%wt) + Gd^{3+} ions ([Gd] = 0.2mM) with initial pH of 5.4 (**A**) 10.8 (**B**) at varying pH values after adding HCl solution (1M) and then NaOH solution (1M).

Table 14. Scattered light intensity and Z-average values measured by a mono-angle DLS instrument for the sample containing PAA_{32}-*b*-PVP_{59} (0.014%wt) + Gd^{3+} ions ([Gd] = 0.2mM) with initial pH of 5.4 or 10.8 at varying pH values after adding HCl solution (1M) and then NaOH solution (1M).

Samples	**PAA_{32}-*b*-PVP_{59}** (0.014%wt) + Gd^{3+} ([Gd]=0.2mM) **pHi = 5.4**	**PAA_{32}-*b*-PVP_{59}** (0.014%wt) + Gd^{3+} ([Gd]=0.2mM) **pHi = 2.5**	**PAA_{32}-*b*-PVP_{59}** (0.014%wt) + Gd^{3+} ([Gd]=0.2mM) **pH = 9**	**PAA_{32}-*b*-PVP_{59}** (0.014%wt) + Gd^{3+} ([Gd]=0.2mM) **pHi = 10.8**	**PAA_{32}-*b*-PVP_{59}** (0.014%wt) + Gd^{3+} ([Gd]=0.2mM) **pH = 2.5 (pHi>7)**	**PAA_{32}-*b*-PVP_{59}** (0.014%wt) + Gd^{3+} ([Gd]=0.2mM) **pH = 9 (pHi>7)**
Scattered light intensity (a.u)	$9.5 .10^2$	$545 .10^2$	$17 .10^2$	$7.7 .10^2$	$392 .10^2$	$9.0 .10^2$
Z-average (nm)	49 ± 35	220 ± 4	284 ± 94	66 ± 58	245 ± 9	182 ± 23

DLS measurements indicate that increasing the initial pH before inducing assembly process through pH decrease, has an impact on the initial solution, but do not avoid the assembly of the BCP at pH=2.5. However, when pH is finally increased, the nanostructures' size decreases, which is the contrary of the sample where initial pH was not modified. The presence of hydroxides before the assembly process could then have a little impact on the final nanostructures at high pH. The hydroxides might be the chemical species responsible for the maintain of the nanostructures, and their concentration could may be directly impact the final size of the nanostructures. TEM pictures illustrate this impact (**Figure 184**).

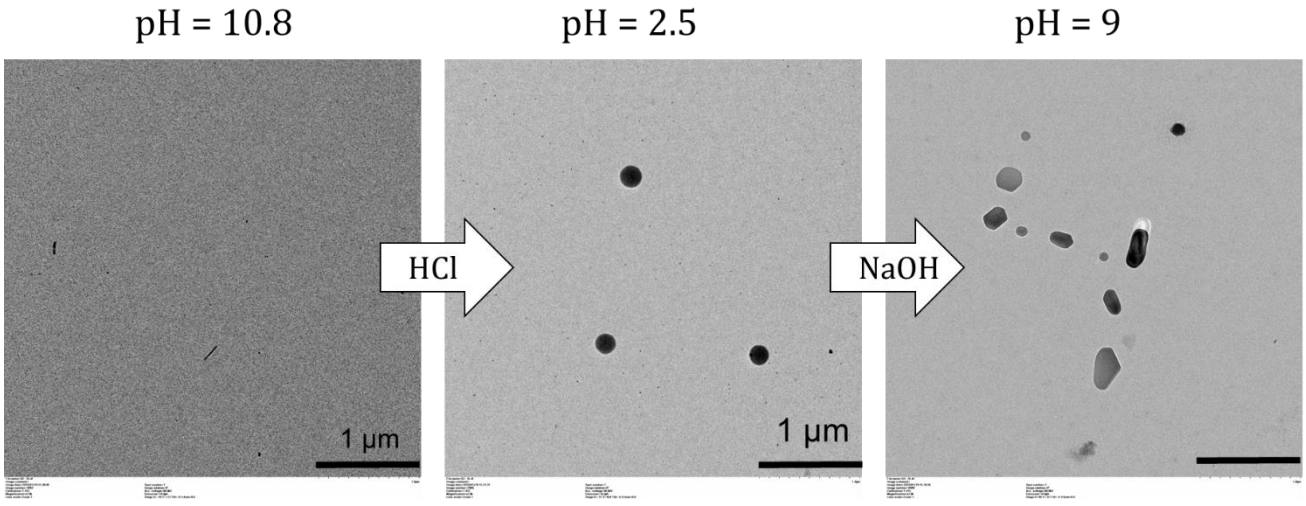

Figure 184. TEM pictures of the sample containing PAA_{32}-*b*-PVP_{59} (0.014%wt) + Gd^{3+} ions ([Gd] = 0.2mM) with initial pH of 10.8 at varying pH values after adding HCl solution (1M) and then NaOH solution (1M).

The role of Gd^{3+} ions into the PAA_{32}-*b*-PVP_{59} block copolymer assembly is still not obvious and needs to be pursued through future work. The thing to retain is that adding Gd^{3+} ions seems to maintain the nanostructures at higher pH, which could be advantageous if the systems are vowed to be applied in biological fields.

VI.2.2 pH variation onto the system comprising PAA_{32}-*b*-PVP_{59}, gadolinium ions and gold nanoparticles

This last section deals with the pH variation of a system comprising PAA_{32}-*b*-PVP_{59} block copolymer, Gd^{3+} ions and gold nanoparticles. As in the previous paragraph, the aim is to understand if the Gd^{3+} ions presence has an influence onto the assembly process of gold nanoparticles through polymer self-assembly, and onto the final sizes and morphologies of the potential nanostructures.

A first experiment was made by only mixing the BCP, the Gd^{3+} ions and the Au@citrate NPs and performing a pH variation to study the assembly process by decreasing the pH and the behavior at higher pH then.

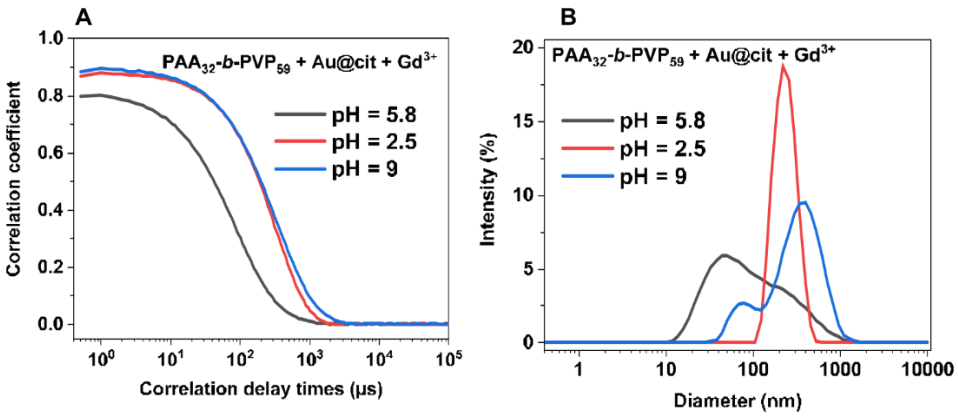

Figure 185. (A) Correlation functions using the NNLS method, (B) Distribution average size in intensity for the sample containing PAA_{32}-*b*-PVP_{59} (0.05%wt) + Gd^{3+} ions ([Gd] = 0.7mM) + Au@citrate NPs ([Au]=500µM) at varying pH values after adding HCl solution (1M) and then NaOH solution (1M).

DLS analysis shows actually a first size increase from initial pH to pH=2.5, which confirms the assembly process (**Figure 185**). Then when pH is increased, as for the previous experiments where the BCP was mixed with Gd^{3+} ions, the process is proved to be not reversible, as the size analysis is not the same as initially (**Figure 185** and **Table 15**). The nanostructures formed at pH=2.5, seem to be maintained at higher pH too.

Table 15. Scattered light intensity and Z-average values measured by a mono-angle DLS instrument for the sample containing PAA_{32}-*b*-PVP_{59} (0.05%wt) + Gd^{3+} ions ([Gd] = 0.7mM) + Au@citrate NPs ([Au]=500 µM) at varying pH values after adding HCl solution (1M) and then NaOH solution (1M).

Samples	**PAA_{32}-*b*-PVP_{59}** (0.05%wt) **+ Gd^{3+}** ([Gd]=0.7mM) + **Au@citrate** ([Au]=500 µM) **pHi = 5.8**	**PAA_{32}-*b*-PVP_{59}** (0.05%wt) **+ Gd^{3+}** ([Gd]=0.7mM) + **Au@citrate** ([Au]=500 µM) **pH = 2.5**	**PAA_{32}-*b*-PVP_{59}** (0.05%wt) **+ Gd^{3+}** ([Gd]=0.7mM) + **Au@citrate** ([Au]=500 µM) **pH = 9**
Scattered light intensity (a.u)	7.10^3	106.10^3	15.10^3
Z-average (nm)	58 ± 27	222 ± 13	226 ± 88

To visualize the evolution of this system mixing the block copolymer, Gd^{3+} ions and Au@citrate NPs, TEM pictures were made at the different pH values (**Figure 186**). Size distribution analysis was performed onto the TEM picture of the sample at pH=2.5 and the diameter found was D=282 ± 89 nm. As observed on these pictures, the nanostructures are mostly conserved after pH increase, but some gold nanoparticles embedded in polymer are detached from the main nanoassemblies which size is near from 200 nm according to DLS data. This explains the double peak recorded in intensity distribution size (**Figure 185.B**). Gadolinium ions seem then to influence as well the behavior of the hybrid assemblies containing PAA_{32}-*b*-PVP_{59} BCP and Au@citrate NPs, in basic conditions. Zeta potential measurements were realized onto the sample at pH=2.5 and pH=9, and were respectively ξ=-5.3 ± 0.4 mV and ξ=-2.8 ± 0.7 mV.

Latter values are in the same range as all the formed nanostructures based on PAA_{32}-*b*-PVP_{59} BCP and additional compounds such as Gd^{3+} ions and AuNPs.

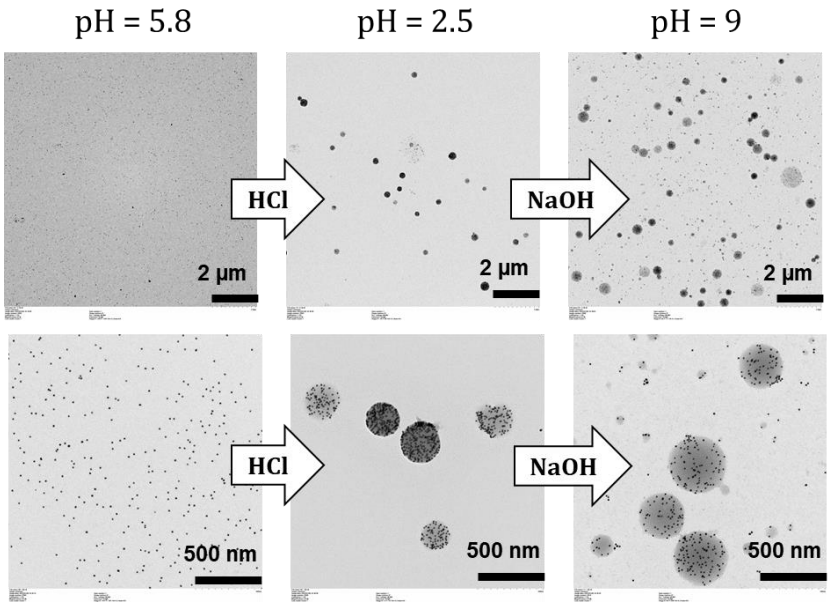

Figure 186. TEM pictures of the sample containing PAA_{32}-*b*-PVP_{59} (0.05%wt) + Gd^{3+} ions ([Gd] = 0.7mM) + Au@citrate NPs ([Au]=500 µM) at varying pH values after adding HCl solution (1M) and then NaOH solution (1M).

As in situ preparation method was tested in previous experiments, it was once again investigated in presence of Gd^{3+} ions. The same protocol as the one detailed previously (**VI.1**) was realized in presence of Gd^{3+} ions from the starting nucleation step, with a fixed charges ratio R=3.[Gd^{3+}]/[AA]=1. As the final pH obtained after the growth was pH=2.5, a pH variation was realized by adding NaOH solution (1M) to observe the behavior at higher pH. Photo of the sample at varying pH is shown in **Figure 187**. The color of the sample is purple at the beginning, at low pH values, and became more and more red and translucid with increasing pH. This would be in agreement with a progressive release of AuNPs, as previously observed with Au@citrate NPs.

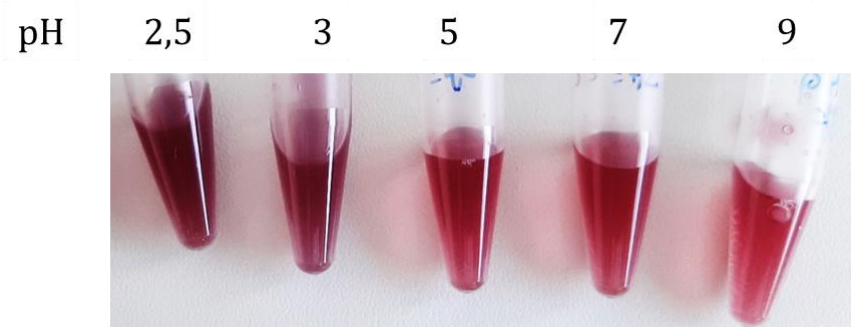

Figure 187. Photo of the sample containing PAA_{32}-*b*-PVP_{59} (0.05%wt) + Gd^{3+} ions ([Gd] = 0.7mM) + "in situ" Au NPs ([Au]=500 µM) at varying pH values after adding NaOH solution (1M).

DLS measurements were performed onto each pH value and show that the size is globally maintained when the pH is increased, but the error onto the size value increases too and the scattered light intensity decreases, which supports the hypothesis of a morphological change despite the size maintain (**Figure 188**). This is confirmed with TEM pictures (**Figure 189**), where the nanostructures become less structured and some AuNPs are released, which explains the red color.

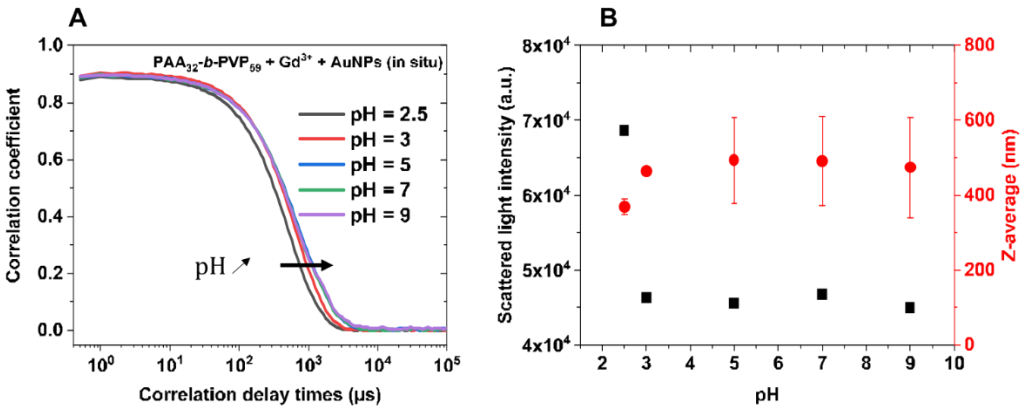

Figure 188. (**A**) Correlation functions using the NNLS method, (**inset**) Distribution average size in intensity and (**B**) Typical evolutions of the scattered light intensity (black squares) and Z-average diameter (red dots) for the sample containing PAA_{32}-*b*-PVP_{59} (0.05%wt), Gd^{3+} ions (0.7 mM) and in situ AuNPs ([Au]=500 µM) at varying pH after adding NaOH solution (1M).

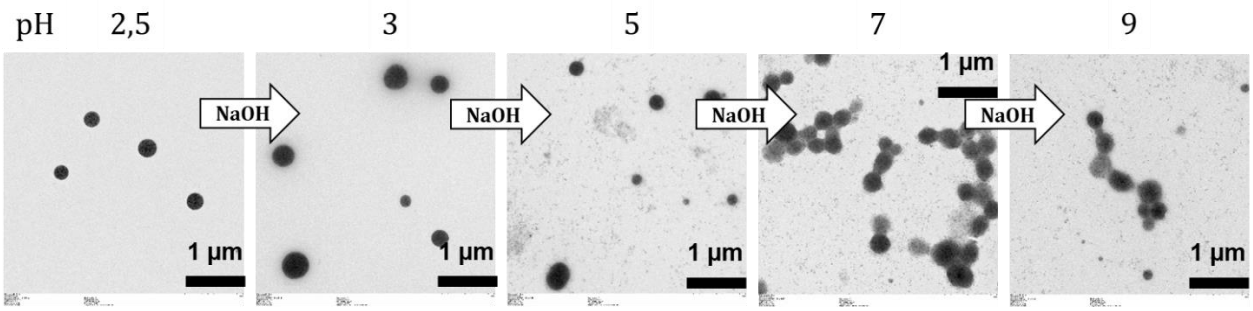

Figure 189. TEM pictures of the sample containing PAA_{32}-*b*-PVP_{59} (0.05%wt), Gd^{3+} ions (0.7 mM) and in situ AuNPs ([Au]=500 µM) at varying pH after adding NaOH solution (1M).

As UV-vis spectra for the previous concentrations demonstrate saturation, the kinetic study was realized with the same range as for other systems, i.e. PAA_{32}-*b*-PVP_{59} (0.014%wt), [Gd]=0.2mM and [Au]=144 µM. On **Figure 190**, the time evolution of the absorbance confirms that when pH is increasing, the initial absorbance is not equal to the final one, and the comparison with the previous system, comprising only PAA_{32}-*b*-PVP_{59} and Au@citrate NPs, evidences the role of the Gd^{3+} ions regarding the behavior at high pH values.

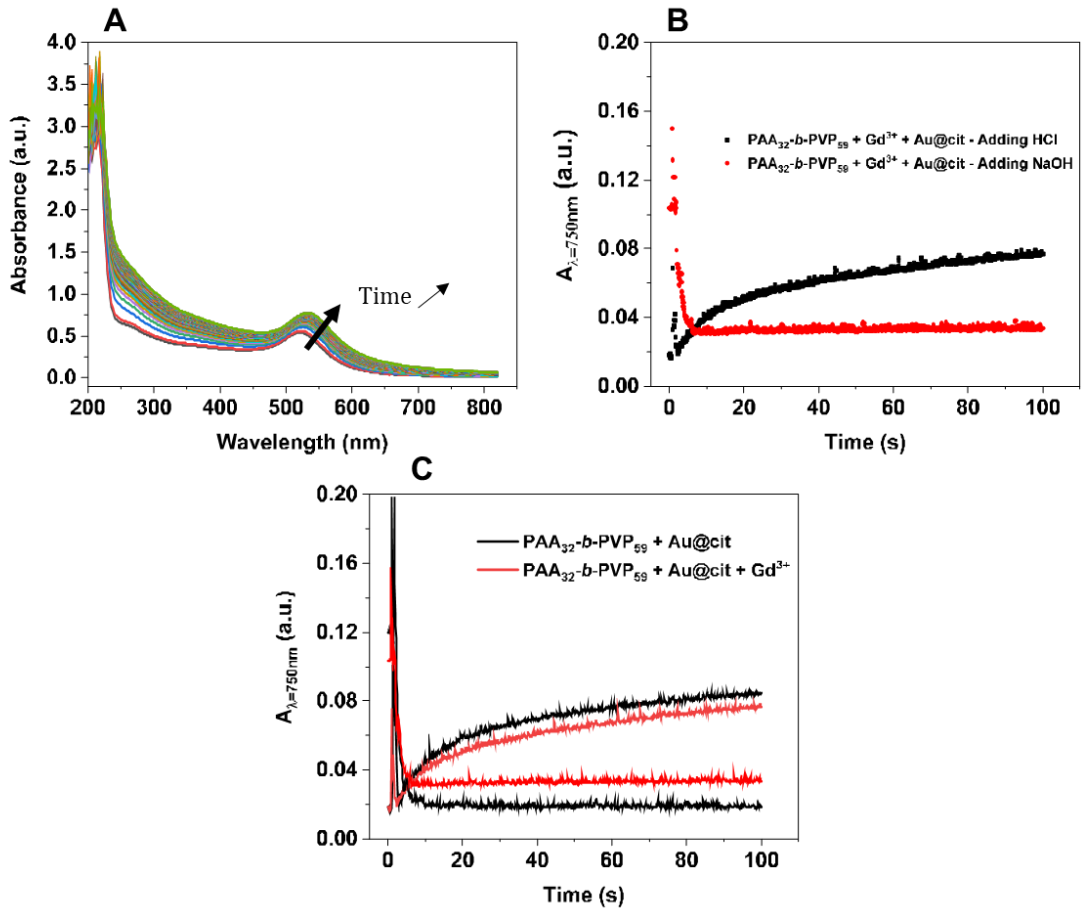

Figure 190. UV-vis spectra (100 scans) of PAA_{32}-*b*-PVP_{59} (0.014%wt) + Gd^{3+} ions ([Gd] = 0.2mM) + Au@citrate NPs ([Au]=144µM) solution under pH variation after adding 8 µL of HCl solution (1M) (**A**) Time evolution of the absorbance measured at λ=750 nm for both assembly and disassembly mechanisms (**B**) Comparison with the system PAA_{32}-*b*-PVP_{59}+ Au@citrate NPs (**C**)

In order to pursue this comparison with the system comprising PAA_{32}-*b*-PVP_{59} and Au@citrate NPs, the same variation of the concentration of gold nanoparticles with fixed BCP concentration was performed (**Figure 191**). Same results are obtained, global similar size of the nanostructures is observed whatever the gold concentration, with a slight increase for the highest concentrations. For these last concentrations (820 and 1510 µM), the scattered light intensity is decreasing and is due to the slight precipitation occurring in solution. Indeed, the sizes are so huge that a start of precipitation was observed in the flasks containing the samples.

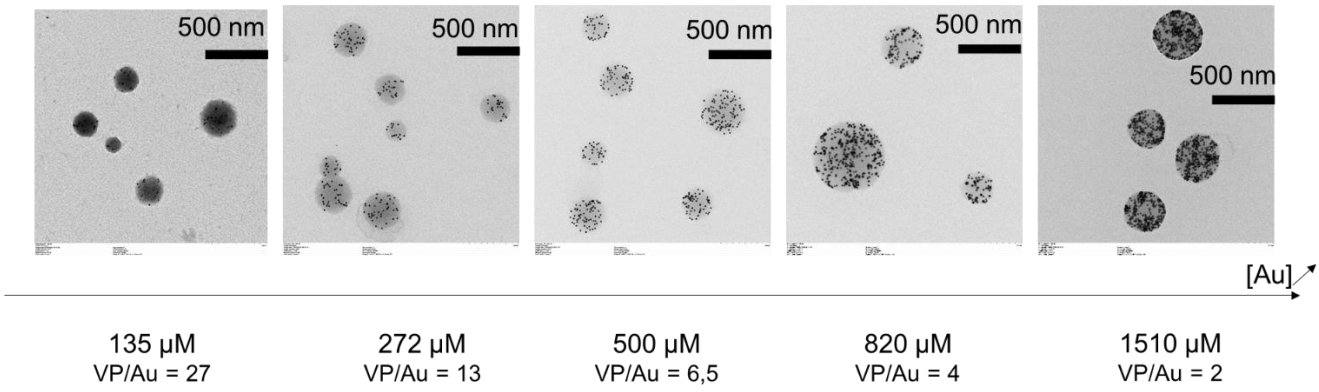

Figure 191. TEM pictures samples containing PAA_{32}-b-PVP_{59} (0.05%wt) + Gd^{3+} ions and varying concentrations of Au@citrate NPs: 135; 272; 500; 820; 1510 µM at pH=2.5 after adding HCl solution (1M).

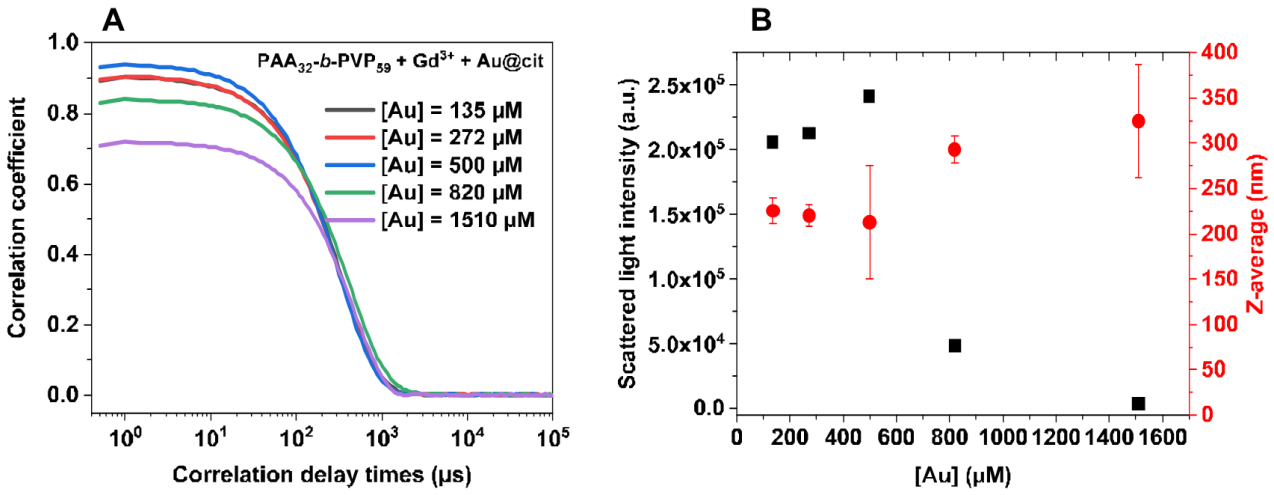

Figure 192. (**A**) Correlation functions using the NNLS method, (**inset**) Distribution average size in intensity and (**B**) Typical evolutions of the scattered light intensity (black squares) and Z-average diameter (red dots) for the sample containing PAA_{32}-b-PVP_{59} (0.05%wt) + Gd^{3+} ions and varying concentrations of Au@citrate NPs: 135; 272; 500; 820; 1510 µM at pH=2.5 after adding HCl solution (1M).

Finally, to understand the interactions existing between the Gd^{3+} ions and the block copolymer or the gold nanoparticles, some filtration processes were realized onto the different kind of studied nanostructures' systems (**Scheme 13**). Indeed, the samples were prepared as usual by mixing the block copolymer and the gadolinium ions, and then adding or not gold nanoparticles. Then, the pH was decreased until pH=2.5 to form the nanostructures. The samples were then divided into two parts, one maintained at pH=2.5 and the other into which the pH was increased until pH=7. The two sample parts at each pH, were then filtrated onto centrifugation tubes with Mw=3 500 g/mol as cut-off. The resulting filtrate solutions were analyzed by ICP-MS to quantify the gadolinium content and diluted versions were as well titrated using the colorimetric test elaborated in **chapter III**.

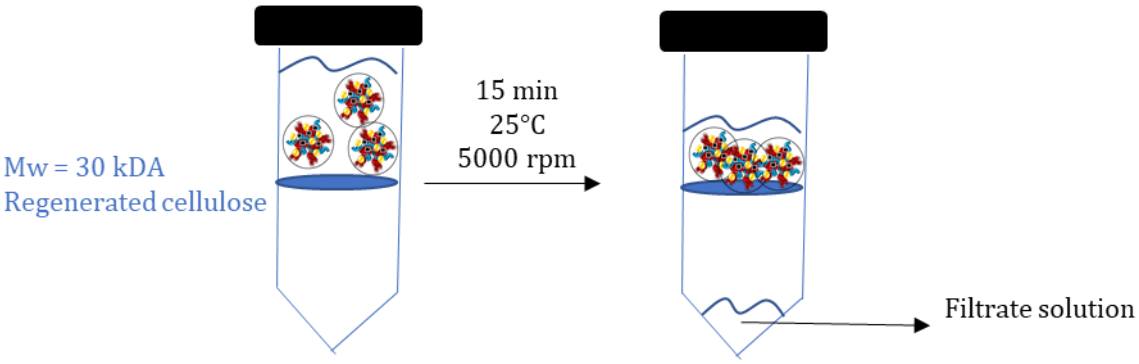

Scheme 13. Filtration process representation onto a sample containing nanostructures

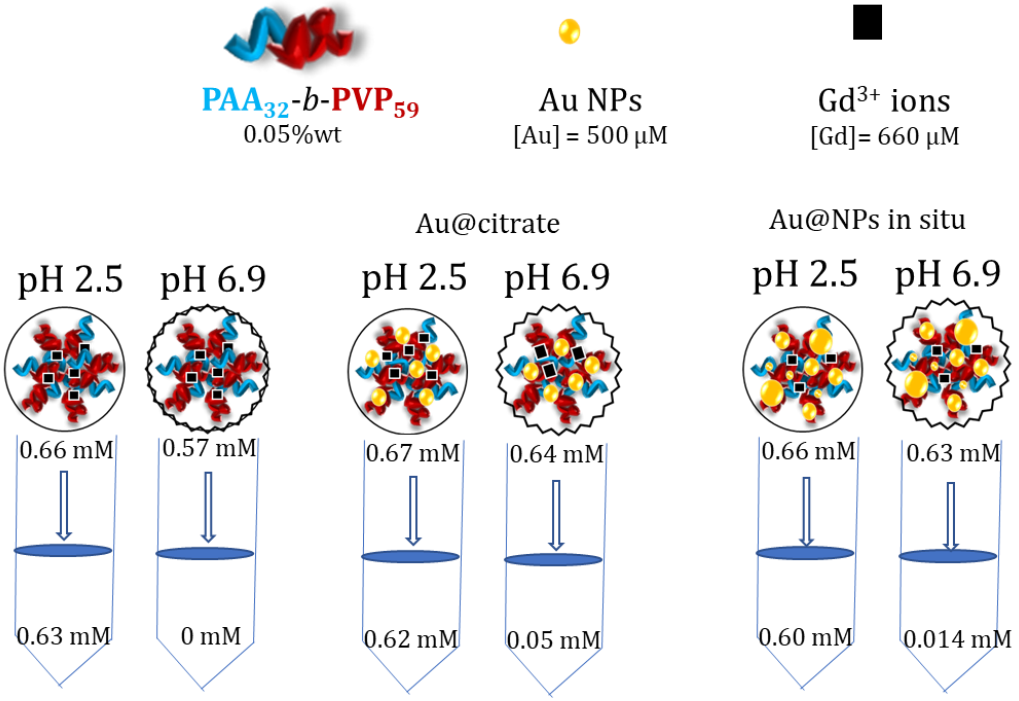

Scheme 14. ICP-MS results introduced in the schematization of the filtration processes for the 6 tested systems comprising PAA_{32}-*b*-PVP_{59} (0.05%wt) and Gd^{3+} ions ([Gd] = 0.7 mM) without or with gold nanoparticles which are either performed Au@citrate NPs or AuNPs formed in situ ([Au]=500 µM) at varying pH, either pH=2.5 or pH=6.9.

The results of ICP-MS are shown on **Scheme 14** and evidence the weak gadolinium quantity titrated into filtrate solutions resulting from samples adjusted at pH=7, compared to the quasi total initial concentration value of gadolinium titrated in the filtrates resulting from samples at pH=2.5. The colorimetric test results confirm visually the presence of gadolinium ions into filtrates resulting from samples at pH=2.5, which color is more pink meaning that a slight aggregation process is going on between the Au@BSPP NPs used here as reference. These last results suggest that the gadolinium ions are not in interaction with the nanostructures at low pH, but should be in ionic interaction with PAA at higher pH, and these interactions may help in maintaining the nanostructure, despite the hydrogen bondings theoretical break.

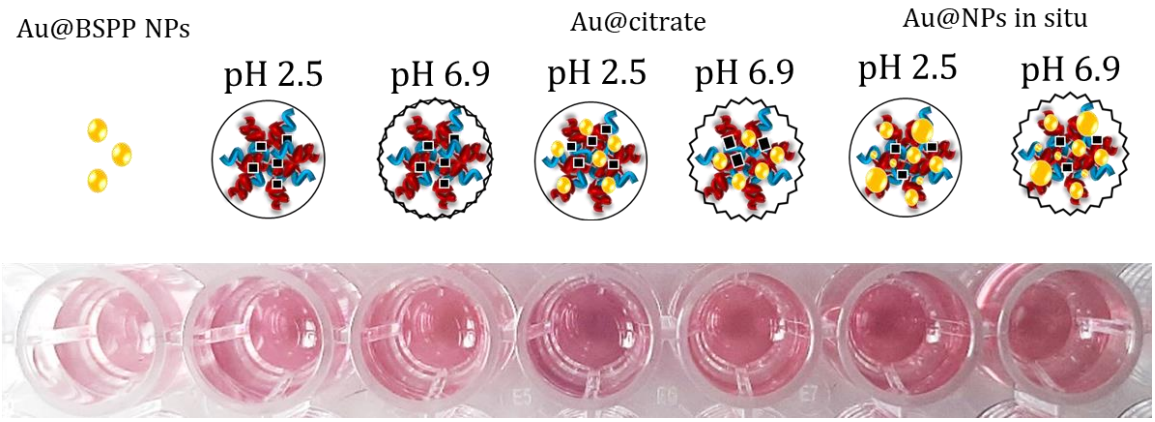

Figure 193. Photos of the wells containing the different resulting filtrate solutions after centrifuging the samples containing nanostructures, which composition is schematized over the corresponding well, and Au@BSPP NPs used for the colorimetric test based on aggregation of Au@BSPP NPs under gadolinium ions presence.

All these tests represent the beginning of a larger study which must be made upon the real role of the gadolinium ions into these pH-responsive systems. The maintain of these nanostructures at higher pH could represent great opportunities for biological applications such as imaging field or cancer therapy.

VII Conclusions and Perspectives

In this chapter, the study of the pH-responsiveness of the synthesized PAA-*b*-PVP block copolymer was investigated through the use of many characterization techniques such as DLS, SAXS, TEM, EDX analysis. Lowering the pH of a solution containing the PAA-*b*-PVP leads to the obtention of nanostructures based on hydrogen bondings which size can vary according to molecular weight and concentration of the BCP. The assembly mechanism is pH-sensitive, the resulting nanostructures are then only present in acidic conditions. Interactions of the PAA-*b*-PVP BCP with gold nanoparticles enable the obtention of hybrid assemblies which sizes are near from the polymer self-assemblies, in same polymer concentration conditions. By playing on the ratio between the BCP and the AuNPs, the AuNPs' density into the nanostructures can be varied. Both block configuration and PVP as stabilizing block are necessary criteria to obtain these nanostructures, and their composition can be easily tuned by introducing AuNPs formed in situ. Finally, the introduction of ions, such as gadolinium, impacts the behavior of the nanostructures at high pH, and needs to be studied in deep to control the maintain of these hybrid assemblies and hopefully going towards interesting biological applications such as imaging or theranostic.

VIII References

(1) Yin, J.; Chen, Y.; Zhang, Z.-H.; Han, X. Stimuli-Responsive Block Copolymer-Based Assemblies for Cargo Delivery and Theranostic Applications. *Polymers* **2016**, *8* (7). https://doi.org/10.3390/polym8070268.

(2) Kelley, E. G.; Albert, J. N. L.; Sullivan, M. O.; Epps, III, T. H. Stimuli-Responsive Copolymer Solution and Surface Assemblies for Biomedical Applications. *Chem Soc Rev* **2013**, *42* (17), 7057–7071. https://doi.org/10.1039/C3CS35512H.

(3) Liu, Y.; Sun, Y.; Zhang, W. Synthesis of Stimuli-Responsive Block Copolymers and Block Copolymer Nano-Assemblies. *Chin. J. Chem.* **2022**, *40* (8), 965–972. https://doi.org/10.1002/cjoc.202100821.

(4) Tang, H.; Zhao, W.; Yu, J.; Li, Y.; Zhao, C. Recent Development of PH-Responsive Polymers for Cancer Nanomedicine. *Molecules* **2019**, *24* (1). https://doi.org/10.3390/molecules24010004.

(5) Chun, M.-K.; Cho, C.-S.; Choi, H.-K. Characteristics of Poly(Vinyl Pyrrolidone)/Poly(Acrylic Acid) Interpolymer Complex Prepared by Template Polymerization of Acrylic Acid: Effect of Reaction Solvent and Molecular Weight of Template. *J. Appl. Polym. Sci.* **2004**, *94* (6), 2390–2394. https://doi.org/10.1002/app.21176.

(6) Chun, M.-K.; Cho, C.-S.; Choi, H.-K. Mucoadhesive Drug Carrier Based on Interpolymer Complex of Poly(Vinyl Pyrrolidone) and Poly(Acrylic Acid) Prepared by Template Polymerization. *J. Controlled Release* **2002**, *81* (3), 327–334. https://doi.org/10.1016/S0168-3659(02)00078-0.

(7) Nurkeeva, Z. S.; Khutoryanskiy, V. V.; Mun, G. A.; Bitekenova, A. B.; Kadlubowski, S.; Shilina, Y. A.; Ulanski, P.; Rosiak, J. M. Interpolymer Complexes of Poly(Acrylic Acid) Nanogels with Some Non-Ionic Polymers in Aqueous Solutions. *Colloids Surf. Physicochem. Eng. Asp.* **2004**, *236* (1–3), 141–146. https://doi.org/10.1016/j.colsurfa.2004.01.026.

(8) Swift, T.; Seaton, C. C.; Rimmer, S. Poly(Acrylic Acid) Interpolymer Complexes. *Soft Matter* **2017**, *13* (46), 8736–8744. https://doi.org/10.1039/C7SM01787A.

(9) Ghaffarlou, M.; Sütekin, S. D.; Güven, O. Preparation of Nanogels by Radiation-Induced Cross-Linking of Interpolymer Complexes of Poly (Acrylic Acid) with Poly (Vinyl Pyrrolidone) in Aqueous Medium. *Radiat. Phys. Chem.* **2018**, *142*, 130–136. https://doi.org/10.1016/j.radphyschem.2017.04.019.

(10) Shuping, J.; Liu, M.; Chen, S.; Chen, Y. Complexation between Poly(Acrylic Acid) and Poly(Vinylpyrrolidone): Influence of the Molecular Weight of Poly(Acrylic Acid) and Small Molecule Salt on the Complexation. *Eur. Polym. J.* **2005**, *41* (10), 2406–2415. https://doi.org/10.1016/j.eurpolymj.2005.05.006.

(11) Ito, T.; Otani, N.; Fujii, K.; Mori, K.; Eriguchi, M.; Koyama, Y. Bioadhesive and Biodissolvable Hydrogels Consisting of Water-swellable Poly(Acrylic Acid)/Poly(Vinylpyrrolidone) Complexes. *J. Biomed. Mater. Res. B Appl. Biomater.* **2020**, *108*. https://doi.org/10.1002/jbm.b.34407.

(12) Falcao, A. N.; Skov Pedersen, J.; Mortensen, K. Structure of Randomly Crosslinked Poly (Dimethylsiloxane) Networks Produced by Electron Irradiation. *Macromolecules 26*, 5350–5364.

(13) Turkevich, J.; Stevenson, P. C.; Hillier, J. A Study of the Nucleation and Growth Processes in the Synthesis of Colloidal Gold. *Discuss Faraday Soc* **1951**, *11* (0), 55–75. https://doi.org/10.1039/DF9511100055.

(14) Koczkur, K. M.; Mourdikoudis, S.; Polavarapu, L.; Skrabalak, S. E. Polyvinylpyrrolidone (PVP) in Nanoparticle Synthesis. *Dalton Trans.* **2015**, *44* (41), 17883–17905. https://doi.org/10.1039/C5DT02964C.

(15) Das, T.; Kolli, V.; Karmakar, S.; Sarkar, N. Functionalisation of Polyvinylpyrrolidone on Gold Nanoparticles Enhances Its Anti-Amyloidogenic Propensity towards Hen Egg White Lysozyme. *Biomedicines* **2017**, *5* (2). https://doi.org/10.3390/biomedicines5020019.

(16) Seoudi, R.; Fouda, A. A.; Elmenshawy, D. A. Synthesis, Characterization and Vibrational Spectroscopic Studies of Different Particle Size of Gold Nanoparticle Capped with

Polyvinylpyrrolidone. *Phys. B Condens. Matter* **2010**, *405* (3), 906–911. https://doi.org/10.1016/j.physb.2009.10.012.

(17) Hoppe, C. E.; Lazzari, M.; Pardiñas-Blanco, I.; López-Quintela, M. A. One-Step Synthesis of Gold and Silver Hydrosols Using Poly(N-Vinyl-2-Pyrrolidone) as a Reducing Agent. *Langmuir* **2006**, *22* (16), 7027–7034. https://doi.org/10.1021/la060885d.

(18) Alijagic, A.; Barbero, F.; Gaglio, D.; Napodano, E.; Benada, O.; Kofroňová, O.; Puntes, V. F.; Bastús, N. G.; Pinsino, A. Gold Nanoparticles Coated with Polyvinylpyrrolidone and Sea Urchin Extracellular Molecules Induce Transient Immune Activation. *J. Hazard. Mater.* **2021**, *402*, 123793. https://doi.org/10.1016/j.jhazmat.2020.123793.

(19) Mohamed, T.; Matou-Nasri, S.; Farooq, A.; Whitehead, D.; Azzawi, M. Polyvinylpyrrolidone-Coated Gold Nanoparticles Inhibit Endothelial Cell Viability, Proliferation, and ERK1/2 Phosphorylation and Reduce the Magnitude of Endothelial-Independent Dilator Responses in Isolated Aortic Vessels. *Int. J. Nanomedicine* **2017**, *Volume 12*, 8813–8830. https://doi.org/10.2147/IJN.S133093.

(20) Ramalingam, V.; Varunkumar, K.; Ravikumar, V.; Rajaram, R. Target Delivery of Doxorubicin Tethered with PVP Stabilized Gold Nanoparticles for Effective Treatment of Lung Cancer. *Sci. Rep.* **2018**, *8* (1), 3815. https://doi.org/10.1038/s41598-018-22172-5.

(21) Ling, D.; Hackett, M. J.; Hyeon, T. Surface Ligands in Synthesis, Modification, Assembly and Biomedical Applications of Nanoparticles. *Nano Today* **2014**, *9* (4), 457–477. https://doi.org/10.1016/j.nantod.2014.06.005.

(22) Mozaffari, S.; Li, W.; Dixit, M.; Seifert, S.; Lee, B.; Kovarik, L.; Mpourmpakis, G.; Karim, A. M. The Role of Nanoparticle Size and Ligand Coverage in Size Focusing of Colloidal Metal Nanoparticles. *Nanoscale Adv* **2019**, *1* (10), 4052–4066. https://doi.org/10.1039/C9NA00348G.

(23) Gao, C.; Vuong, J.; Zhang, Q.; Liu, Y.; Yin, Y. One-Step Seeded Growth of Au Nanoparticles with Widely Tunable Sizes. *Nanoscale* **2012**, *4* (9), 2875–2878. https://doi.org/10.1039/C2NR30300K.

(24) Barbosa, S.; Agrawal, A.; Rodríguez-Lorenzo, L.; Pastoriza-Santos, I.; Alvarez-Puebla, R. A.; Kornowski, A.; Weller, H.; Liz-Marzán, L. M. Tuning Size and Sensing Properties in Colloidal Gold Nanostars. *Langmuir* **2010**, *26* (18), 14943–14950. https://doi.org/10.1021/la102559e.

(25) Kedia, A.; Kumar, P. S. Solvent-Adaptable Poly(Vinylpyrrolidone) Binding Induced Anisotropic Shape Control of Gold Nanostructures. *J. Phys. Chem. C* **2012**, *116* (44), 23721–23728. https://doi.org/10.1021/jp306952d.

(26) Haesuwannakij, S.; Kimura, T.; Furutani, Y.; Okumura, K.; Kokubo, K.; Sakata, T.; Yasuda, H.; Yakiyama, Y.; Sakurai, H. The Impact of the Polymer Chain Length on the Catalytic Activity of Poly(N-Vinyl-2-Pyrrolidone)-Supported Gold Nanoclusters. *Sci. Rep.* **2017**, *7* (1), 9579. https://doi.org/10.1038/s41598-017-10165-9.

(27) Boekfa, B.; Pahl, E.; Gaston, N.; Sakurai, H.; Limtrakul, J.; Ehara, M. C–Cl Bond Activation on Au/Pd Bimetallic Nanocatalysts Studied by Density Functional Theory and Genetic Algorithm Calculations. *J. Phys. Chem. C* **2014**, *118* (38), 22188–22196. https://doi.org/10.1021/jp5074472.

(28) Gupta, A.; Boekfa, B.; Sakurai, H.; Ehara, M.; Priyakumar, U. D. Structure, Interaction, and Dynamics of Au/Pd Bimetallic Nanoalloys Dispersed in Aqueous Ethylpyrrolidone, a Monomeric Moiety of Polyvinylpyrrolidone. *J. Phys. Chem. C* **2016**, *120* (31), 17454–17464. https://doi.org/10.1021/acs.jpcc.6b05097.

(29) Zhang, L.; Fan, Q.; Sha, X.; Zhong, P.; Zhang, J.; Yin, Y.; Gao, C. Self-Assembly of Noble Metal Nanoparticles into Sub-100 Nm Colloidosomes with Collective Optical and Catalytic Properties. *Chem Sci* **2017**, *8* (9), 6103–6110. https://doi.org/10.1039/C7SC01841J.

General conclusions

As introduced in the opening of this manuscript, the understanding of assembly processes occurring in nature and the wish to mimic them has gained in interest in the recent scientific research. The reproduction of these assemblies at nanoscale level by using synthetic building blocks aims at understanding the role of each compound into the assembly mechanism and the influence of the numerous parameters involved in it. The work reported in this manuscript brings its contribution into these scientific investigations, by presenting a complete study about assemblies obtained from a block copolymer, metal ions and gold nanoparticles. The main objectives of this project were 1) to understand the role of each compound incorporated in solution into the assembly mechanism, 2) to understand the influence of each parameter likely related to the assembly process, and 3) to characterize the final assemblies and evaluate their potential applications.

The main compound studied in this work was the block copolymer PAA-*b*-PVP. This polymer was synthesized via RAFT polymerization process in dioxane and fully characterized by ^{1}HNMR, ATR-FTIR and SEC analysis, which confirms high conversion rates (C=98%), leading to well-controlled molecular weight. The process was realized several times to obtain different polymer lengths, for further studies about the influence of the molecular weight onto assembly mechanism. The PAA-b-PVP did represent the main template of the studied assemblies and investigations were made onto several kind of assemblies: its self-assembly, the hybrid assemblies with either ions, or gold nanoparticles, or even both. For each of these assemblies, the three objectives were studied.

Regarding the self-assembly, the pH-responsiveness of the PAA-*b*-PVP was studied through pH variation between pH=9 and pH=2.5 and did lead to the formation of self-assembled systems based onto hydrogen bondings interactions in acidic conditions between protonated PAA and carbonyl function of the PVP. Due to the pH-dependence of those interactions, the process was actually reversible when pH was increased towards basic range and associated kinetics were described as fast processes of some seconds. The obtained nanostructures were characterized by DLS and TEM and present a global size of around 200 nm at 0.05%wt. The concentration of the polymer in solution did influence this final global size with increasing concentration leading to increasing sizes, and same effect was detected with an increasing PVP length. The comparison with a sample containing the two homopolymers did confirm the advantage of the block configuration, which shows higher stability over a larger concentration range.

Two polymer states became then attractive for further hybrid assemblies; one ionic state at high pH value, enabling potential interactions with ions and further applications in biological media at physiological pH; and one protonated state which can help in collecting inorganic compounds into one nanostructure.

The first studied hybrid assemblies comprised the PAA-*b*-PVP and metal ions: Gd^{3+}, Eu^{3+} and Y^{3+}. The obtained nanostructures were named HPICs and were based onto ionic interactions between the ions and carboxylate functions of the BCP. By varying the charges ratio (R=3.[Ions]/[Acrylate functions]) and the pH value, structures with optimized size and stability were obtained for R=1, neutral charge, and pH=7. In these last conditions, attractive luminescence properties with Eu^{3+} ions and relaxation properties with Gd^{3+} ions were observed and did permit further assays in biological media. In vitro cytotoxicity did confirm the low cytotoxicity of the HPICs in contact with cells and drove the study towards in vivo assays in mice to evaluate the T_1 MRI signal. Last investigations approved engaging results regarding the use of the Gd^{3+}/PAA-b-PVP HPICs as potential CAs in MRI. Indeed, the positive contrast was increased by +67% compared to the currently used Gd-DOTA agent, with no release of free gadolinium ions, thus avoiding side effects in the body.

The second hybrid assembly is based on the interactions between AuNPs and the PAA-b-PVP BCP, which are formed under pH variation in acidic conditions. The assembly mechanism is similar to the self-assembly of the BCP and based on hydrogen bondings, making it as well reversible. Whatever the gold nanoparticles preparation, in situ or preformed, the interaction with the PAA-b-PVP is sufficient to induce their assembly into the polymeric structure under pH=3. Microscopy investigations helped into the understanding of the localization of the AuNPs, confirming that they were actually inside the polymeric nanostructure. Gold concentration was varied and showed that the internal density of AuNPs was depending on this concentration without drastically affecting the global size of the polymeric nanostructures. This density variation is of great interest for further potential applications like X-ray based imaging field or radiotherapy, as the collective effect provided by the assembly process enhance the properties of the AuNPs. The same variations regarding the BCP's characteristics, length, concentration and configuration, were as well realized in presence of the AuNPs. As the polymer stabilized AuNPs, when the concentration or the configuration was not adapted, the precipitation occurred, reinforcing then the role of the polymer into these hybrid assemblies.

Finally, one non-controlled assembly was as well studied and permitted to set a colorimetric test able to detect the presence of gadolinium ions in a fast and easy way, with detection and quantitatification limits of 0.74 µM and 4.76 µM respectively. This assembly process was based on the interactions between Au@BSPP NPs and Gd^{3+} ions, which were observed through the optical properties' change in solution of the AuNPs. The colorimetric following could then rapidly give an idea of a quantity of free Gd^{3+} ions in the sample and this test was actually used in the preparation of the HPICs assemblies and as well onto the pH-responsive nanoassemblies, after filtration process.

The perspectives of this project at short term will focus on the variation of the polymer configuration and its influence onto the resulting assemblies obtained under pH variation. A large synthesis work must be engaged to have access to gradient, statistical configurations or different compositions into block copolymers, as already started in this work by varying the PVP block length. Some starting assays were realized to obtain the statistical configuration, but the process revealed many difficulties, demanding time to be solved.

Interesting perspectives concern the design of the composition of the hybrid assembly by tuning on the nature of the ions or the nanoparticles. First ideas were emitted regarding the use of platinum complexes, which would be integrated to the polymeric assembly, or the use of silver nanoparticles, to bring different properties.

Perspectives with longer term will essentially focus on the last investigations conducted onto the pH-responsive nanoassemblies based on the interactions between PAA-b-PVP, AuNPs and Gd^{3+} ions. These last studies dealt with the incorporation of Gd^{3+} ions into the self-assembly of the BCP and into the hybrid assembly comprising both gold nanoparticles and the BCP. When Gd^{3+} ions were present, the pH variation revealed that these ions have a particular role into the assembly process. Indeed, in their presence, the nanostructures formed in acidic conditions, seem to be a little maintained when pH is increased again until basic conditions. However, both shape and size of these nanostructures at higher pH values are not similar to the ones obtained at pH=2.5. Nevertheless, the Gd^{3+} ions clearly have an influence onto the existing interactions into the hybrid assembly. The aim of the future work is to clearly decrypt the nature of the interactions existing between the ions, the nanoparticles and the block copolymer, to understand what is maintaining these nanoassemblies despite the increase of pH and thus the break of hydrogen bondings.

Once the precise role of Gd^{3+} ions fully understood, the variation of the critical parameters must be engaged following the same study strategy as for the other assemblies. Finally, when the control of the nanostructures is achieved, the evaluation of their properties would allow to turn into biological applications, as this hybrid assembly would contain both ions and nanoparticles. One precise idea concerns the use in theranostic field, which combines imaging with radiotherapy. The obtained hybrid assembly would contain paramagnetic specie (Gd) enhancing thus the contrast for MRI and X-ray receptors (AuNPs) able to transform the received energy into electrons and then create radicals to attack cancerous cells.

Experimental section

I Materials

Solvents

Water was purified through a filter and ion exchange resin using a Purite device (resistivity 18.2 MΩcm). 1,4-Dioxane (≥99.0%) (VWR) was filtrated on alumina prior to use. Diethyl ether and absolute ethanol (VWR), N,N-dimethylformamide anhydrous (99.8%) (Sigma Aldrich) were used as received. Chlorhydric acid (HCl) (37%) was purchased from Fischer Chemical. $CDCl_3$ and D_2O (99.9%D) solvents were purchased from Eurisotop and used as received for ^{1}HNMR experiments and D_2O for some fluorimetry analysis.

Monomers

Methyl Acrylate (MA) (99%, contains ≤100 ppm monomethyl ether hydroquinone as inhibitor) (Sigma Aldrich) was filtrated on alumina. 1-vinyl-2-pyrrolidone (N-VP) (purum, ≥97.0% (GC)) (Sigma Aldrich) was distilled prior to use and filtrated on alumina.

Initiators

2,2'-azobis(2-methylpropionitrile) (98%) (AIBN) (Sigma Aldrich) was recrystallized from methanol and dried at room temperature under vacuum. (2,2'-Azobis(4-methoxy-2,4-dimethylvaleronitrile) (V-70) (Wako Chemicals) was used as received.

RAFT agent

The methyl 2((ethoxycarbonothioyl)thio)-propanoate RAFT agent (XA_1) was synthesized according to to a previously published procedure (X. Liu et al., ACS Macro Lett., 2015, 4, 1, 89-93).

Other organic molecules

1,3,5-trioxane (≥99%) (Sigma Aldrich) was used as received

Polymers

All the polymers were used as received: PAA_{44}-b-PEG_{80} (Polymer SourceTM); the statistical PAA_{416}-*r*-PVP_{270} copolymer (Polymer Source); PAA_{25} (Sigma Aldrich); (PVP_{72}) (Alfa Aesar).

Inorganic salts and molecules

All the inorganic compounds were used as received: $Gd(NO_3)_3.6H_2O$ (99.99% trace metals basis) (Sigma Aldrich), $Eu(NO_3)_3.5H_2O$, (99.9% trace metals basis) (Sigma Aldrich), $Y(NO_3)_3.6H_2O$ (99.8% trace metals basis) (Sigma Aldrich), Sodium Chloride NaCl (>99%) (Alfa Aesar). $Ca(NO_3)_2.4H_2O$ (>99%) Sodium hydroxide NaOH (>85%, KOH basis) (Sigma Aldrich). Potassium hydroxide (KOH) (Sigma Aldrich). $HAuCl_4.3H_2O$ (≥99.9%) (Alfa Aesar). Tri-sodium citrate dihydrate (>99%) (Sigma Aldrich). Bis-(p-sulfonatophenyl)phenylphosphine (BSPP) dehydrate dipotassium salt (97%) (Sigma Aldrich). Sodium Borohydride $NaBH_4$ (>98%) (Sigma Aldrich). Ascorbic acid (>99%) (Sigma Aldrich).

II General Procedures

II.1 Mono-angle dynamic light scattering (DLS)

Mono-angle dynamic light scattering measurements were realized using a Zetasizer Nano-ZS (Malvern Instruments, Ltd, UK) with integrated 4 mW He-Ne laser, λ = 633 nm. Light scattering intensity (at 173°) was measured using the same recording parameters for all the samples. In order to obtain Z-average sizes of the colloidal structures, the correlation functions were analyzed *via* cumulant method. For each sample, 5 series of 10 recorded signals of 10 seconds were realized for size data records at a controlled temperature of 25°C.

II.2 Zeta potential measurement

Zeta potential measurements were realized using a Zetasizer Nano-ZS (Malvern Instruments, Ltd, UK) with integrated 4 mW He-Ne laser, λ = 633 nm. Light scattering intensity (at 173°) was measured using the same recording parameters for all the samples. 3 series of 10 recorded signals of 10 seconds were realized for size data records at a controlled temperature of 25°C.

II.3 Multi-angle dynamic light scattering

Multi-angle dynamic light scattering was used to characterise hydrodynamic. Wave scattering vector is described as a function of the angle θ by the equation Eq. (1),

$$q = \frac{4\pi n}{\lambda} sin(\theta/2)$$

where n is the refractive index of the solvent, λ is the wavelength of the incident light. Measurements give access to the autocorrelation function of the scattered light intensity. A mathematical treatment leads to the decay rate Γ, which is related to the diffusion coefficient D_0 ($\Gamma = D_0.q^2$). Hydrodynamic radius is obtained from the Stockes-Einstein relation (Eq. 2),

$$R_h = \frac{kT}{6\pi\eta D_0}$$

where k is the Boltzmann constant, T the temperature, η the viscosity of the solvent.

Light scattering experiments were performed using a commercial goniometer (3D LS Spectrometer, LS Instruments AG, Switzerland) equipped with a Cobolt laser (λ = 660 nm, 100 mW), a two channel multiple tau correlator (auto and cross correlation, 1088 real time channels). The sample cell was held in a decalin-filled quartz vat. The temperature was controlled using a Julabo CF31 cryo-compact circulator. Static and dynamic light scattering experiments were carried out from 12° to 150° (corresponding to scattering wave vectors from $2{,}7.10^{-4}$ $Å^{-1}$ to $2{,}4.10^{-3}$ $Å^{-1}$). A 3D setup was used to analyze concentrated samples, which splits the beam into two

beams, focused in the same spot. Datas from scattered light are collected at a specific scattering vector with two independent photon detectors. This configuration makes it possible to eliminate the influence of multiple scattered photons.

Autocorrelation functions were recorded as a function of the scattering angle. The curves were then analyzed with the home-made MULTI-STORMS program developed by Dr C. Mingotaud, written and compiled with MATLAB ®. This software is designed for the analysis of data and offers the choice in the methods used to extract information from the correlograms, and then to evaluate the size distributions. Mathematical adjustments of the correlograms are realized based on different models based on the shape and the scattering properties of the particles to be described.

II.4 Static Light Scattering (SLS)

In MASLS, the excess of scattered intensity by a sample with respect to the solvent is converted into absolute intensity (Rayleigh ratio R_θ, in cm^{-1}) using toluene as a reference, for which the excess Rayleigh ratio is known ($R_{\theta toluene}$= 8.56×10^{-6} cm^{-1} at 660 nm).

$$R_{\theta,sample} = \frac{I_{sample} - I_{solvent}}{I_{toluene}} \cdot \left(\frac{n_{solvent}}{n_{toluene}}\right)^2 \cdot R_{\theta,toluene}$$

Where I_{sample}, $I_{solvent}$ and $I_{toluene}$ are the scattering intensities of the sample solution, the solvent, and the toluene respectively, and where $n_{solvent}$ and $n_{toluene}$ are the refractive indexes of the solvent and the toluene at 660 nm, respectively n_{water} = 1.33 and $n_{toluene}$ = 1.49 at 25 °C).

For small particles,

$$\frac{Kc}{R_\theta} \cong \frac{1}{M_w} \cdot \left(1 + \frac{R_g^2}{3} q^2\right) \cdot (1 + A_2 c)$$

Where **c** is the concentration, M_w the molecular weight of the scatterers, R_g their radius of gyration, A_2 the second virial coefficient and K a scattering constant defined as:

$$K = \frac{4\pi^2 n_{solvent}^2}{N_a \lambda^4} \cdot \left(\frac{dn}{dc}\right)^2$$

where N_a is the Avogadro number and (dn/dc) the refractive index increment of the solute.

II.5 Transmission Electron Microscopy (TEM)

Samples were prepared by deposition of one drop of sample solution on a carbon coated copper grids (CF200-Cu 200 mesh from Tel Pella Inc.) For some samples, an additional negative stained procedure was applied using uranyl acetate (2 wt.%). Low resolution transmission electron

microscopy (TEM) measurements were performed on a Hitachi HT7700 device operating at 70kV in collaboration with the platform CMEAB from Toulouse.

II.6 High-angle annular dark-field scanning transmission electron microscopy (HAADF-STEM)

STEM-HAADF analysis were performed on a Field Emission Electron Jeol 2100F Microscope (200kV), with an electron probe of 1nm in size, available to Raimond Castaing center of microscopy, Toulouse. A bright field was used for the samples containing both polymers and gold nanoparticles to distinguish better the dispersion of the nanoparticles into the polymeric structure.

II.7 UV-visible Spectroscopy

UV-visible spectra were measured with a SPECTROstar Nano® – BMG Labtech absorbance plate reader. Multi-well plates with 96 well- cell culture plates sterile F-bottom type from Cellstar ® - Greiner bio-one were used. For the measurements the wells were loaded with a total volume of 200 µL.

II.8 pH measurements

pH measurements were realized onto HANNA instruments microprocessor pH 210 pH meter. Calibration procedure was applied before each measurements' series, by measuring first a buffer solution at pH=7 and then another buffer solution either at pH=4 for acidic range measurements and pH=10 for basic range measurements.

II.9 Citrate-capped Gold Nanoparticles Synthesis

All glassware and magnetic stir bars used for gold nanoparticles synthesis were carefully washed with aqua regia (HCl/HNO_3 3:1, v/v) and abundantly rinsed in distilled water. Since the $HAuCl_4$ is corrosive, a glass spatula was used in order to avoid the contact with metal. Gold nanoparticles with a diameter of 16 nm were prepared following the procedure of Turkevich[6]. 10 mL of a solution of sodium citrate tribasic trihydrate ($17mmol.L^{-1}$) was added to 180ml of a boiling aqueous solution of $HAuCl_4$ ($0.3mmol.L^{-1}$). The reaction mixture was maintained to 100°C for 30 minutes under magnetic stirring before allowing to cool it down to room temperature. A color change from pale yellow to blue and dark red in the end of the reaction was observed.

II.10 Quartz Crystal Microbalance – Dissipation monitoring (QCM-D)

QCM-D measurements were performed on a QCM-D QSense Explorer device with one sensor at AIME platform from INSA Toulouse. AT-cut gold-coated quartz crystals with a fundamental resonance frequency of 10 MHz were purchased from QSense Biolin Scientific. All experiments

were conducted at 20°C and a flow rate of 40 µl min^{-1}. The frequency shifts (ΔF) and the dissipation coefficient (ΔD) were recorded as a function of time at different overtones (1, 3, 5, 7, 9, 11, 13). Sensor chamber was incubated with citrate or BSPP solutions overnight (~16 hours). The data was collected and analyzed with QSoft and QTool softwares.

In a QCM-D experiment, the adsorption of molecules on the gold surfaces is assessed by monitoring the frequency shift (ΔF) and dissipation shift (ΔD) (the frictional and viscoelastic energy losses in the system) as a function of time. The changes in frequency are proportional to the changes in the wet-mass deposited on the gold surface according to the Sauerbrey equation[51]: (eq 1)

$$\Delta m = -\frac{\Delta f . C}{n} \quad \text{(eq.1)}$$

where Δm is the adsorbed mass, Δf the variation of frequency observed at overtone n and C=17,7 ng cm^{-2} a constant characteristic of instrument. Even if this model only applies to uniform and rigid thin film deposits, it allows a simple quantitative study and a direct comparison of experiences.

II.11 Nuclear Magnetic Resonance (NMR)

^1H NMR experiments were performed on a 300 MHz Bruker spectrometer using $CDCl_3$ and D_2O as solvent at room temperature. Chemical shifts were reported in ppm.

II.12 Attenuated Total Reflectance- Fourier Transformed Infra-Red Spectroscopy (ATR-FTIR)

All IR measurements were recorded, in a powder form after lyophilization of the HPICs solutions, using a Nicolet 6700 FT-IR spectrometer from Thermo Fischer Scientific in ATR mode on a diamond crystal.

II.13 Small Angle X-ray Scattering (SAXS)

Small-Angle X-ray Scattering (SAXS) measurements were performed at the SWING beamline of the Soleil Synchrotron (Saint Aubin, France). The 2D SAXS patterns were collected using a EigerX4M detector. A sample-to-detector distance of 6.2 m at 12keV was employed in order to cover a q-range, from 1×10^{-3} to 0.18 $Å^{-1}$ where q is the scattering wave vector defined as $q = (4\pi/\lambda) \sin \vartheta/2$, λ being the wavelength. Measurements were performed in borosilicate capillaries of 1.5 mm. The measured two-dimensional SAXS patterns were corrected for detector artefacts, normalized to absolute intensity scale and azimuthally averaged to obtain the intensity profile $I(q)$ as a function of q using standard procedures using Foxtrot software. The background

scattering was measured in a separate capillary and subtracted from each averaged sample intensity profile.

The scattering curves of the copolymer at low pH present a Guinier region at low scattering vectors followed by two distinct regions characterized by different power law exponents in a similar way as swollen polymeric microgels. The scattering intensity of a microgel is usually described as the sum of different contributions describing the overall particle shape and size and the internal fluctuations.

In our case, at high q the curve is characterized by a power law decrease I(q) α $q^{-5/3}$, expected for a self-avoiding polymer chain in good solvent. In the intermediate q-range, the power law exponent is higher and indicates the presence of larger scale heterogeneities with fractal dimension 3.2. The overall curve could be well described using a Guinier term and two Lorentzian terms often used in the case of semi dilute polymer solutions plus an incoherent background:

$$I_{poly}(q) = I(0)_G \exp\left(-q^2 \frac{R_g^2}{3}\right) + \frac{I(L_1)}{1 + (q\xi_1)^n} + \frac{I(L_2)}{1 + (q\xi_2)^n} + Bckg \quad (1)$$

The Guinier term gives the overall size of the nano-objects and the two Lorentzian terms inform on the two internal characteristic length scales. The system could be sketched as a semi dilute polymer solution characterized by density inhomogeneities at length scales larger than those of the characteristic blobs. The smaller correlation length corresponds to blob size, below which the behaviour is the one of self-avoiding chains. The longer size corresponds to the correlation length of the density fluctuations inside the nano-objects probably due to inhomogeneous distribution of the two blocks of the copolymer.

This description is still valid in the presence of gold nanoparticles, but in this case a term accounting for the presence of gold nanoparticles has to be considered. First trial fits have been performed using the following expression which seems to quite well describe the experimental data:

$$I(q) = I_{poly}(q) + I_{Au}(q) \cdot S(q) \quad (2)$$

where

$$I_{Au}(q) = scale \cdot \left[\frac{\sin(qr) - qr\cos(qr)}{(qr)^3}\right]^2 \quad (3)$$

And S(q) is the hard sphere structure factor considering and interaction potential of the form

$$U(r) = \begin{cases} \infty & r < 2R \\ 0 & r \geq 2R \end{cases} \quad (4)$$

II.14 HPICs preparation

0.5% wt. solution of PAA_{32}-b-PVP_{59} were prepared by dissolution of the necessary quantity of the copolymer in Milli-Q water (18.2mΩ). Gd^{3+}, Eu^{3+} and Y^{3+} stock solutions (65mM) were prepared by dissolution of $Gd(NO_3)_3 \cdot 6H_2O$, $Eu(NO_3)_3.5H_2O$ and $Y(NO_3)_3.6H_2O$, respectively in Milli-Q water. HPICs were formed by mixing solutions of PAA_{32}-b-PVP_{59} (0.5 % wt) with solutions of Gd^{3+}, Eu^{3+} and Y^{3+}, respectively. Lanthanide ions' concentrations were adjusted in order to vary the molar fraction R=3.[Ln^{3+}]/[AA] between the positive charges of lanthanide ions and the negative ones of the polymers between 0.2 and 2.2 within the HPICs. After mixing, the pH of the solutions was adjusted to 6.8–7.

II.15 COOH titration – pKA

The samples were prepared in a glass flask of 4 mL and put under stirring. pH measurements were then continuously made into the solution. pH was step by step increased by adding HCl solution (0.1M) and the pH value was noted.

II.16 Relaxivity measurement

Longitudinal relaxation times T_1 (ms) were measured at 0.47T using a minispec mq20 relaxometer from Bruker at a constant temperature of 25°C.

II.17 ICP-MS titration

Inductively coupled plasma - atomic emission spectroscopy (ICP-MS) analysis were performed by Antellis company (http://www.antellis.com).

III Chapter II

III.1 Synthesis of the PAA_{32}-b-PVP_{59} block copolymer

Step 1: Synthesis of a poly(methyl acrylate)-xanthate macro RAFT agent (PMA-XA_1): XA_1 (0.77 g, 3.7 x 10^{-3} mol), methyl acrylate MA (10 g, 12 x 10^{-2} mol), 1,4-dioxane (5 g, 5.7 x 10^{-2} mol), AIBN (61 mg, 3.7 x 10^{-4} mol) and 1,3,5-trioxane (0.1 g, 1.1 x 10^{-3} mol) were introduced at room temperature in a Schlenk flask. The reaction mixture was degassed by purging with argon for 30 min, heated and stirred at 70°C for 6 hours. The polymerization mixture was then cooled down at room temperature, a sample withdrawn and analyzed by ^{1}H NMR to access the monomer conversion (98%) and the solvent was evaporated using a rotary vacuum evaporator. The obtained polymer was characterized without further purification by ^{1}H NMR (**Chapter II- II-2- Figure 3**) (300MHz

in $CDCl_3$) δ ppm: 1.3-1.6 (2H, -C**H**$_2$-CH(CO_2CH_3)-S(C=S)-OEt), 1.3-1.6 (3H, C**H**$_3$-CH_2-O- end-group), 1.6-1.8 (2(n-1)H, -C**H**$_2$-CH(CO_2CH_3)-), 2.25-2.5 (1(n-1)H, -CH_2-C**H**(CO_2CH_3)-, 3.7 (3(n+1)H, -CO_2C**H**$_3$), 4.4 (1H, -CH_2-C**H**(CO_2CH_3)-S(C=S)-OEt), 4.7 (2H, CH_3-C**H**$_2$-O- end-group). The degree of polymerization (DP_n) was calculated by as presented in **Chapter II – II-2- Equation 1**. $M_{n,th}$ = 2750 g/mol. $M_{n,NMR}$ = 2750 g/mol.; ATR-FTIR spectroscopy: ν(C=O) ester group=1736 cm^{-1}.

Step 2: Block Copolymerization of 1-vinyl-2-pyrrolidone (NVP) in 1,4-dioxane. The macro-RAFT agent (PMA-XA_1) from step 1 (2g, 7 x 10^{-3} mol), NVP (3.8 g, 3.4 x 10^{-2} mol), 1,4-dioxane (3.5 g, 4 x 10^{-2} mol), V-70 (46 mg, 1.5 x 10^{-4} mol) and 1,3,5-trioxane (0.1 g, 1.1 x 10^{-3} mol) were introduced at room temperature in a Schlenk flask. The reaction mixture was degassed by purging with argon for 30 min, heated and stirred at 35°C for 12 hours. The reaction mixture was then cooled down at room temperature and a sample was withdrawn to measure NVP conversion (97%) and calculate the DP_n of the PVP block by ^{1}H NMR analysis (**Chapter II - II-3 – Figure 4**): (300MHz in $CDCl_3$) δ ppm: 1.20 (3H, C**H**$_3$-CH_2-O- end-group), 1.30-1.5 (2mH, -N-CH_2-C**H**$_2$-CH_2-CO(N)), 1.6-1.8 (2nH, -C**H**$_2$-CH(CO_2CH_3)-), 2.0-2.18 (2mH, -C**H**$_2$-CH($NCH_2CH_2CH_2CO(N)$)-), 2.18-2.25 (1nH, -CH_2-C**H**(CO_2CH_3)), 2.25-2.5 (2mH, -N-CH_2-CH_2-C**H**$_2$-CO(N)), 3-3.5 (2mH, -N-C**H**$_2$-CH_2-CH_2-CO(N)), 3.7 (3(n+1)H, -CO_2C**H**$_3$), 3.8-4.0 (1mH, -CH_2-C**H**($NCH_2CH_2CH_2CO(N)$)-), 4.6 (2H, CH_3-C**H**$_2$-O- end-group) ($M_{n,th}$ = 8300 g/mol. $M_{n,NMR}$ = 9300 g/mol. The final composition was established as PMA_{32}-*b*-PVP_{59}. ATR -FTIR spectroscopy: ν(C=O) ester group=1736 cm^{-1} and ν(C=O) PVP ring=1674 cm^{-1}. For the purification, the reaction crude was precipitated in diethyl ether, filtrated and dried in a vacuum oven over night to remove solvent traces.

Step 3: Hydrolysis of PMA-b-PVP to form PAA-b-PVP. The PMA-*b*-PVP copolymer obtained in step 2 (4.5 g, 5.4 x 10^{-4} mol), ethanol (15.8 g, 0.34 mol) and potassium hydroxide (KOH) (9.5 g, 0.17 mol) were introduced at room temperature in a 50 ml round-bottom flask. The reaction mixture was refluxed (60°C) for 12 hours, cooled down at room temperature and concentrated under vacuum. The residue was introduced in a dialysis membrane with a Molecular Weight Cut-Off (MWCO) of 3.5 kDa and dialyzed in pure MiliQ water in a 2L beaker for 2 days. Finally, the aqueous PAA-*b*-PVP solution was lyophilized to obtain PAA-*b*-PVP as a powder. This final product was characterized by ^{1}H NMR (300MHz in D_2O) δ ppm (**Chapter II – II-4 – Figure 8**): range 1.4-1.53 (2nH,-C**H**$_2$-CH(COOH)-), 1.6-1.75 (2mH, -N-CH_2-C**H**$_2$-CH_2-CO(N)), 1.82-2.05 (2mH, -C**H**$_2$-CH($NCH_2CH_2CH_2CO(N)$)-), 2.07-2.19 (1nH, -CH_2-C**H**(COOH)-), 2.2-2.5 (2mH, -N-CH_2-CH_2-C**H**$_2$-CO(N)), 3.0-3.35 (2mH, -N-C**H**$_2$-CH_2-CH_2-CO(N)), 3.4-3.8 (1mH, -CH_2-C**H**($NCH_2CH_2CH_2CO(N)$)-) and by ATR- FTIR spectroscopy: ν(C=O) PVP ring=1674 cm^{-1} and ν_{as}(OCO)=1564 cm^{-1} and ν_{sym}(OCO)=1402 cm^{-1} (**Chapter II – II-4 – Figure 7**).

III.2 ^{1}H NMR experiments-Y^{3+}-titration

^{1}H NMR experiments-Y^{3+}-titration were performed on a Bruker Avance 600 MHz spectrometer equipped with a 5 mm triple resonance inverse Z-gradient probe (TBI 1H, 31P, BB). The sample were prepared in a mixture of 10% vol. D_2O and 90% vol. H_2O and the pH was adjusted to 7. The temperature was set to 25 °C.

^{1}H spin-lattice relaxation times (T_1) were measured using the excitation sculpting inversion-recovery pulse sequence t1iresgp. The relaxation delay was 6 s and the acquisition time was 1s. For each measurement, the recovery times were from 50 ms to 6 s and 8 points were collected.

III.3 Size Exclusion Chromatography (SEC) experiments

Size exclusion chromatography (SEC) measurements were performed with a system composed of an Agilent technologies guard column (PLGel20 µm, 50 × 7.5 mm) and a set of three columns (TSKgel Alpha-2500, Alpha-3000, Alpha-3500 TOSOH BIOSCIENCE). Detections were realized using a Varian Prostar UV detector (dual wavelength analysis at 290 and 254 nm), a MiniDawn TREOS multi-angle light scattering detector (Wyatt Technology Corporation) and a Wyatt Optilab® rEX refractive index detector. DMF LiBr (10mM) was used as eluent at 50°C (flow rate, 1 mL/min). Prior to injections, the samples were prepared at a concentration of 10 mg/mL and filtrated through a 0.45 µm PTFE filter. Recorded data were treated using the Wyatt Astra 7.1 software.

III.4 dn/dc measurements

dn/dc measurements were realized onto a DNDC-2010 apparatus from Polymer Standard Service (PSS). Calibration procedure was realized by measuring the dn/dc values for KCl water solutions with 6 various concentrations (0.5-8 mg/mL). dn/dc measurements for samples were realized on 6 solutions of dissolved polymer in DMF-LiBr with various concentrations (0.5-8 mg/mL). The plot of the 6 measures was treated with a linear regression which must cross the origin and align each point. The slope of this linear regression corresponds to the dn/dc value.

III.5 Fluorescence Spectroscopy

Emission spectra and luminescence decays at room temperature of the Eu HPICs were measured using a Cary Eclipse spectrofluorimeter equipped with a xenon flash lamp source (60-75 kW, flash period 2 to 3 µs) and a Hamamatsu R928 photomultiplier.

Lifetimes τ (uncertainty ≤5%) were determined by monitoring the decay at 615 nm, following pulsed excitation. The luminescence decay curves were fitted by an equation of the form $I(t) = I(0) \exp(-t/\tau)$ by using Origin curve-fitting program.

III.6 In vitro cytotoxicity assays

III.6.1 Cell culture.

Human HCT-116 colorectal cancer cells (CCL-247) were recently purchased from ATCC and grown in DMEM high 4.5 $g.l^{-1}$ glucose, GLUTAMax (Fisher scientific, Waltham, MA, USA) and supplemented with 10% of heat-inactivated fetal bovine serum and 100 U/ml penicillin, and 100 $\mu g.ml^{-1}$ streptomycin. Cells were maintained at 37°C in a humidified atmosphere containing 5 % CO_2 and used under passage 12. All along the experiments, cells were tested negative for mycoplasma (MycoAlert mycoplasma detection kit, Lonza).

III.6.2 Cytotoxicity experiment.

The day before the experiments, 10,000 HCT-116 were seeded in 96-well plates. The day of experiment, cells were incubated for 48h at 37°C with increasing concentration of Gd and Eu HPICs and its individual components, respectively, PAA-*b*-PVP polymer and $Gd(NO_3)_3$ or $Eu(NO_3)_3$ aqueous solutions, at similar concentrations as the ones tested for HPICs. Cell viability was quantified using PrestoBlue reagent (Fisher scientific) according to the manufacturer's instructions. Briefly, after 48h of incubation, cell culture medium was removed and cells were incubated for 30 min at 37°C with 100 µl of 1X PrestoBlue reagent diluted in PBS, before reading absorbance on a plate reader at 570 nm and 600 nm Synergy H1 (Biotek, Winooski, VT, USA). Six biological replicates were produced and analyzed for each condition. Data analysis was performed using GraphPad Prism 8 program (GraphPad Software, Inc., La Jolla, CA, USA) and data were expressed as mean ± SEM. Statistical comparisons were performed using one-way analysis of variance (ANOVA) followed by Dunnett's post-test in comparison to the control condition. *$p < 0.05$, **$p < 0.01$, ***$p < 0.001$ and ****$p < 0.0001$.

III.6.3 Intracellular HPICs quantification by flow cytometry.

The day before the experiments, 80,000 HCT-116 were seeded in 12-well plates. Cells were incubated for 6 hours with cell culture medium containing each component of the HPICs, respectively PAA-*b*-PVP polymer alone (0.07%wt), or $Eu(NO_3)_3$ aqueous solution (0.9mM) or corresponding Eu-HPICs. An additional set of experiments was performed at 4°C instead or 37°C for PAA-*b*-PVP polymer alone (0.07%wt) condition. After incubation, cells were washed once with PBS and then cells were trypsinized and transferred on ice within a U-bottom 96-well plate. Cells were analyzed with a BD LSR Fortessa flow cytometer equipped with an HTS module for plate reading, using the 405 nm laser for excitation and fluorescence emission was collected using the BV 711A filter, which allowed the detection of the maximum of signal. At least 20,000 events were acquired in each well. Data were analyzed with FlowJo v10 (FlowJo). Three biological replicates were produced and analyzed for each condition. Statistical comparisons were performed using

one-way analysis of variance (ANOVA) followed by Tukey's multiple comparison post-test. *p < 0.05, **p < 0.01, ***p < 0.001 and ****p < 0.0001.

III.6.4 Intracellular Eu^{3+} quantification by ICP-MS.

Inductively coupled plasma-mass spectrometry (ICP-MS) was used to quantify europium penetration in cells. For that purpose, 20 million of HCT-116 cells grown in $75cm^2$ flask were incubated for 6h at 37°C with 0.9mM $Eu(NO_3)_3$ aqueous solution or the Eu^{3+}/PAA_{32}-b-PVP_{59} HPICs. After incubation cells were washed twice with 10 ml of PBS, trypsinized and cell pellets were sent to GLINCS (Villeurbanne, France) for ICP-MS analysis on Nexion 2000 (Perkin Elmer).

III.7 In vivo assays

III.7.1 Mice

6 BALB/cOlaHsd mice (Envigo) aged 10-12 wk were used for MRI experiments.

All *in vivo* experimental procedures were approved by our institutional animal care and use committee CEEA122 (APAFIS 5192-2016041911336422 and 34703-2022011811542488) and conducted in compliance with the Ethics Committee pursuant to European legislation translated into French Law as Decret 2013-118 dated 1st of February 2013.

III.7.2 Small animal MRI

Animals were anesthetized with isoflurane (induction 3%-4%, maintenance 1.5% (isoflurane/O2) to insert a catheter in the tail vein. Then, the mice is placed in a specific MRI imaging cell (Minerve, Esternay, France) to preserve the health status (SPF), ensure the temperature regulation and the breathing monitoring. Animals received a dose of 15µmole/Kg of Gd equivalent (100µl) (Dotarem®, Guerbet, France) or HPICs followed by a 200 µl flush of saline.

MR image acquisitions were performed on a Biospec 7 T dedicated to small animals (Bruker, Wissenbourg, France). Acquisitions of the abdominal images were carried out with a 40 mm transmit-receive volume coil and triggered on breathing to reduce motion artifacts. T1 weighted images were acquired using Flash sequence with the following parameters: TR=220ms; TE= 3.5ms; flip angle: 40° ; number of average : 4 ; FOV : 40x40 mm ; resolution 200x200 µm ; 13 slices of 1 mm thickness ; fat suppression ; acquisition time : 2 min.

IV Chapter III

IV.1 Phosphine-capped gold nanoparticles synthesis

AuNP@citrate were further functionalized with dipotassium bis(p-sulfonatophenyl)phenylphosphine dihydrate following a literature procedure (C.J. Loweth, Angewandte, 1999, 38, 12, 1808-1812). For a typical reaction, 100mL of AuNP@citrate solution

was stirred with sulfonated phenylphosphine ligand (30mg, 0.06mmol) for one night. The AuNP@P were isolated by adding solid NaCl until the color changed from dark red to blue, followed by centrifugation (2000 rpm for 5 minutes at 20°C). The isolated particles were then redispersed in a solution of sulfonated phenylphosphine (0.5 $mmol.L^{-1}$). A new cycle of precipitation was performed by adding methanol (about 6 mL), followed by their redispersion in the sulfonated phenylphosphine solution. In this way the AuNP@P particles were cleaned from the citrate ligand and can be concentrated to give any desired concentration.

IV.2 Multi-well preparation

Each well of the plate destinated to be measured was filled with a maximum volume of 200 µL. For a givenline, first well was associated to the blank (water) and the second to a standard corresponding either to the AuNP@citrate or to the AuNP@BSPP at the same concentration (0.14 mM in gold atoms). For next wells, mixtures of 2 or 3 components were made, in the following way of addition 1) water; 2) metallic salt solution (except for standard well); 3) AuNPs solution. Concentrations of the AuNPs were checked through UV-visible spectroscopy of the solution before micro-plates elaboration, by evaluating the optical density for the maximum absorbance value. Metallic salt solutions were added in order to obtain increasing concentration from one well to another. UV-vis spectroscopy analysis was conducted at 15 min after addition of the AuNPs in the wells and recorded every 15 minutes for 4 hours.

V Chapter IV

V.1 Ex situ gold nanoparticles functionalization by polymer

A polymer solution was placed into a flask and under stirring, the preformed gold nanoparticles (Au@citrate NPs) solution was added. After 5 minutes, the pH was measured and decreased until pH=2.5 to observe the assembly of the AuNPs through polymer self-assembly. The functionalization can be confirmed if the AuNPs were comprised into the polymer assemblies, which can be observed through the various characterization techniques such as DLS, TEM, UV-visible spectroscopy or SAXS. According to the polymer type, AuNPs can either be stabilized or precipitated, but in the two cases, the interaction is confirmed.

V.2 In situ gold nanoparticles synthesis

A polymer solution was placed into a flask and under stirring, the gold salt solution was introduced and then the mixture was stirred for 5 minutes. Borohydride sodium ($NaBH_4$) solution was prepared as follow: the salt was introduced into a dried flask and then a certain water volume was quickly introduced to solubilize the salt and obtain a concentration of [$NaBH_4$] = 55 mM. Very rapidly, the solution is placed into a flask filled with ice to slow down the hydrolysis reaction:

$$NaBH_4 + 2\,H_2O \rightarrow NaBO_2 + 4H_2$$

After cooling the salt solution for 5 minutes, the adequate volume is introduced into the previous mixture under stirring. The resulting mixture, named “Au seeds” was stirred for 1 hour. The “Au seeds” solution was then characterized by DLS, UV-vis and TEM techniques. The “Au seeds” solution was diluted by two and gold salt was added under stirring. Then, ascorbic acid solution (63 mM) was added in adequate volume to the mixture to obtain the “AuNPs” solution. According to the concentrations and the possible supplementary compounds (ions), the color change from brown to red was more or less fast. pH measurements were made onto the final solution once the color of the sample did not change any more. Usual characterization techniques were then investigated to characterize the obtained AuNPs formed in situ.

V.3 Elemental maps – Energy Dispersive X-ray (EDX)

The EDX analysis was performed onto the TEM grids observed with the Field Emission Electron Jeol 2100F Microscope (200kV). The maps were realized under scanning mode. The detector window collected the X-ray signals, which were associated to the corresponding elements.

V.4 MEB

The pictures of the tilted TEM grids to obtain 3D visualization were obtained thanks to MEB Jeol JSM7800F apparatus. The backscattering pictures, obtained with COMPO detector, aim at distinguish the gold nanoparticles, containing a heavier element (Au) than the polymer. Tilting the grids enabled to evidence that the gold nanoparticles were inside the polymer structure and not on the surface.

V.5 Kinetics measurements on UV-visible

The samples were placed into precision cells made of Quartz SUPRASIL® and analyzed onto a diode array spectrophotometer HP8452A (Hewlett…)….

Samples were introduced at initial pH. The record of the UV-vis spectra was started and after 2 recorded spectra every 0.1s, and under stirring, either HCl solution (1M) or NaOH solution (1M) were injected in one time. 100 spectra were recorded for a wavelength range: 250-850 nm and 1000 spectra for specific range to follow $A_{\lambda=350nm}$ or $A_{\lambda=750nm}$.

I Introduction

La recherche scientifique s'est toujours inspirée de la nature, afin d'en imiter les phénomènes observés et les mettre à profit d'applications dans divers domaines tels que l'énergie, l'environnement ou encore la médecine. L'étude d'assemblages moléculaires connaît aujourd'hui une avancée scientifique portée par les nanotechnologies qui permettent une meilleure compréhension des mécanismes impliqués dans ces assemblages. En effet, le concept de l'assemblage peut répondre à diverses problématiques telles que l'encapsulation d'une molécule, l'amélioration de propriétés à travers un effet collectif, ou encore une méthode détection de certaines interactions moléculaires. Il est critique de pouvoir avoir une marge de manœuvre sur les composés impliqués dans ces assemblages afin de confectionner des structures finales adaptées à l'application visée. Pour répondre à ce besoin, l'utilisation de copolymères à blocs s'avère particulièrement adaptée, puisque les avancées en termes de synthèse de polymères permettent aujourd'hui d'avoir à la fois un contrôle sur la configuration, la masse moléculaire et la fonctionnalité du produit final.

Les copolymères à blocs sont fortement utilisés au sein d'assemblages basés sur leur autoassemblage en solution, mais également au sein de structures qualifiées d'hybrides, mélangeant ces polymères à des espèces inorganiques, telles que des ions ou des nanoparticules. Ce caractère hybride présente l'avantage de combiner stabilité et performances, qui sont des critères essentiels dans de nombreux domaines d'applications. Le travail réalisé dans le cadre de ce projet de thèse traite de l'étude de ces assemblages hybrides, notamment de leur mécanisme de formation, afin de pouvoir contrôler à la fois leur structure finale et les propriétés associées pour d'éventuelles applications en biologie, et particulièrement en imagerie biomédicale.

Les travaux reportés dans ce manuscrit ont été effectués sur trois composés principaux : un copolymère à blocs (PAA-*b*-PVP), des ions métalliques (Gd^{3+},Eu^{3+}, Y^{3+}) et des nanoparticules d'or. Une première partie est consacrée à l'étude bibliographique des assemblages hybrides en solution. Puis les chapitres II, III et IV portent sur un travail expérimental réalisé sur des assemblages basés sur des interactions moléculaires entre les trois composés précédemment énoncés. La compréhension du mécanisme de formation de ces assemblages et leur caractérisation en termes de propriétés sont le cœur de ce travail de thèse.

II Chapitre I – Etude bibliographique

Dans cette première partie, une approche théorique et une synthèse des dernières avancées scientifiques concernant les assemblages moléculaires en solution à base de copolymères à blocs sont réalisées. L'autoassemblage des copolymères à blocs est premièrement abordé à travers une explication de l'influence des caractéristiques propres du polymère sur le mécanisme de formation et la morphologie de la structure obtenue. Les différentes stratégies d'assemblage basées sur l'utilisation d'un stimulus externe sont également énoncées. Dans un second temps, la littérature concernant les assemblages hybrides est engagée à travers des exemples portant sur des assemblages à base de copolymères à blocs et d'ions, ou de nanoparticules d'or. Enfin, les techniques de caractérisation les plus utilisées dans l'étude d'assemblages en solution sont détaillées, ainsi que les potentiels domaines d'applications de ces structures assemblées.

II.1 Les copolymères à blocs : synthèse et autoassemblage

Les copolymères à blocs sont définis comme des polymères comportant 2 monomères ou plus, qui peuvent être répartis de différentes façons le long de la chaîne polymérique. La diversité des techniques de polymérisation d'aujourd'hui permet d'avoir accès à des polymères bien précis, dont la masse moléculaire, la configuration et l'architecture sont parfaitement contrôlées. Cette diversité est illustrée en **Figure I-1** où deux catégories d'architectures principales sont érigées : les copolymères linéaires et les copolymères branchés. Notre travail sera focalisé davantage sur les copolymères linéaires qui sont plus faciles à synthétiser et plus communément utilisées dans la littérature. Une certaine marge de manœuvre est néanmoins conservée, puisque 3 configurations différentes existent pour les copolymères linéaires : bloc, gradient, et statistique.

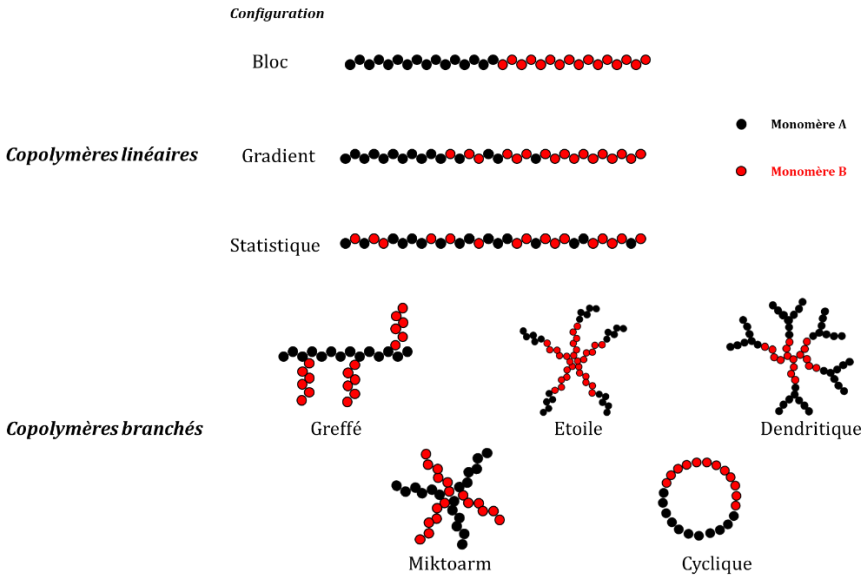

Figure II-1 - Configurations des copolymères linéaires (bloc, gradient, statistique) et architectures des copolymers branchés (greffé, étoile, dendritique, miktoarm and cyclique)

Afin de contrôler au mieux la composition de ces copolymères linéaires, les techniques de polymérisation les plus adaptées sont la polymérisation radicalaire par transfert d'atomes (ATRP) et la polymérisation radicalaire contrôlée par transfert de chaîne réversible par addition-fragmentation (RAFT). Ainsi, il est possible d'avoir accès à des copolymères très précis, qui seront destinés à des applications spécifiques à travers leur utilisation en tant que chaîne singulière ou à travers l'assemblage de plusieurs chaînes en solution. Ce travail portera essentiellement sur la configuration bloc des copolymères linéaires : en différenciant les copolymères amphiphiles, possédant un seul bloc soluble dans l'eau, des doubles hydrophiles, en possédant deux, et sur leur assemblage en solution aqueuse.

Comme énoncé précédemment, deux causes peuvent entraîner l'autoassemblage du copolymère à blocs (CPB) : ses caractéristiques propres ou sa réponse à un stimulus externe. L'autoassemblage des CPB amphiphiles repose sur des principes thermodynamiques visant à réduire l'interface entre les blocs insolubles dans l'eau et l'eau, afin de minimiser l'énergie d'interface libre. Les interactions entre les deux blocs , et entre chaque bloc et le solvant, sont dirigées par certaines caractéristiques propres du polymère : la fraction volumique relative (f), la solvophobicité, et le degré de polymérisation de chaque bloc. Ces trois paramètres sont intimement reliés à un seul, nommé paramètre d'empilement critique (packing parameter), ρ, défini de la manière suivante :

$$\rho = (v/a_0.l_c)$$

Où v est le volume de la chaîne hydrophobe, a_0 est l'aire optimale du groupe hydrophilie de tête, et l_c est la longueur de la queue hydrophobe. La valeur de ce paramètre est très utilisée dans la littérature pour prédire la morphologie adoptée suite à l'autoassemblage du copolymère à blocs, qui dépendra de la courbure de la chaîne polymère (Figure I-2).

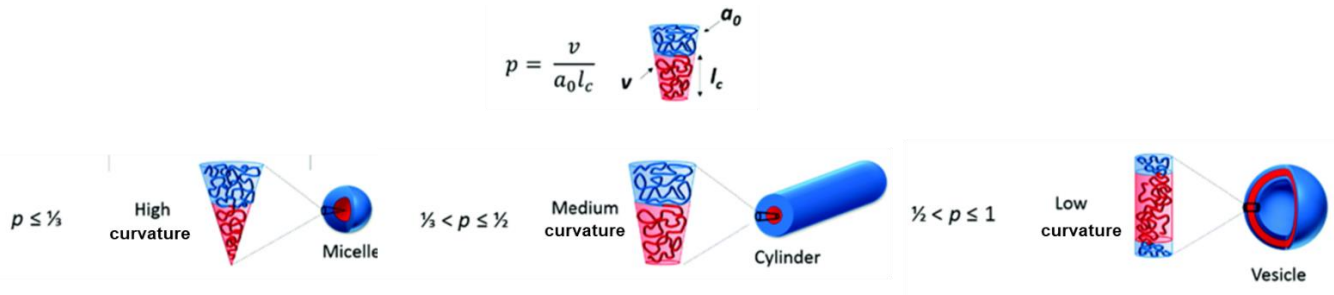

Figure II-2. Les diverses morphologies obtenues selon les différentes valeurs du paramètre d'empilement critique et la courbure du polymère

Contrairement aux tensioactifs classiques, les CPB sont capables d'adopter des morphologies qui ne sont pas toujours en équilibre thermodynamique, grâce à leur bloc hydrophobe plus imposant. Cet accès à l'équilibre thermodynamique, par exemple pour la

morphologie de type micelle, dépend de trois contributions énergétiques : le degré d'étirement du cœur de la micelle, la tension interfaciale entre le cœur de la micelle et le solvant, et les interactions répulsives existantes entre les chaînes présentes dans la couronne de la micelle. De nombreux facteurs ont prouvé leur influence sur ces contributions énergétiques, comme la composition du copolymère, sa concentration en solution, sa fonctionnalité en bout de chaîne, sa masse moléculaire, son indice de polydispersité, ainsi que l'ajout d'autres polymères ou molécules tensioactives.

L'autoassemblage des copolymères à blocs était jusque là contrôlé à travers les caractéristiques propres au polymère, modulables à travers la synthèse de celui-ci, ou à travers sa quantité en solution. Néanmoins, il est possible de provoquer l'autoassemblage du polymère en appliquant un stimulus externe, ayant une influence sur le polymère même ou sur son environnement en solution, le conduisant à s'autoassembler. Les stimuli physiques les plus utilisés sont la température et la lumière. Les polymères thermosensibles deviennent insolubles dans un certain domaine de température et sont classés en deux catégories. Certains sont caractérisés par une température critique basse (LCST) et d'autres par une température critique haute (UCST). L'autoassemblage a lieu quand la température est au-dessus de la LCST ou en-dessous de la UCST. Ces températures caractéristiques dépendent grandement de la structure du polymère, tout comme la sensibilité à la lumière, qui constitue un deuxième stimulus physique. Un exemple illustre l'utilisation d'une lumière UV pour induire l'autoassemblage d'un polymère tribloc. L'accès à différentes morphologies dépend du temps d'irradiation et la réversibilité du processus est possible en appliquant de la lumière visible (**Figure I-3**).

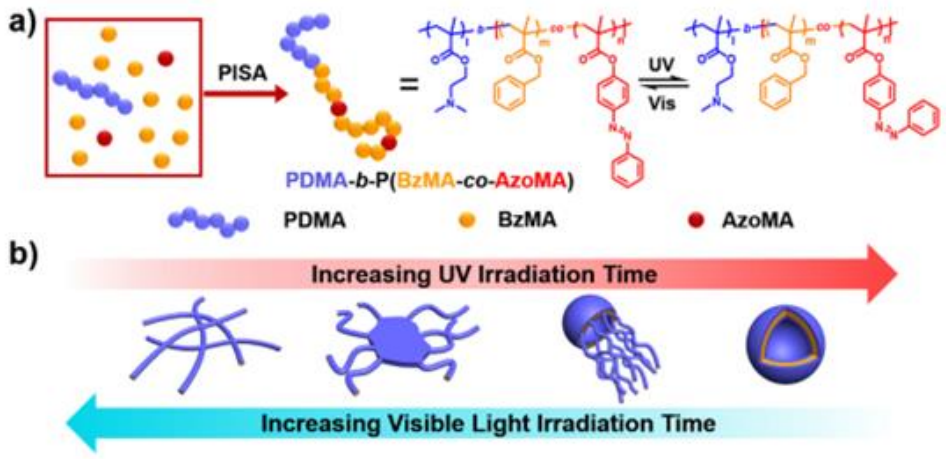

Figure II-3. (a) Préparation et isomérisation de copolymères sensible à la lumière et (b) Aperçu mécanistique des morphologies obtenues, des bâtonnets jusqu'aux vésicules, de manière photo-réversible. Le polymère à blocs a été obtenu à travers une polymérisation PISA, c'est-à-dire un processus d'autoassemblage induit par polymérisation des monomères.

Les stimuli chimiques reposent sur une variation de la composition de la solution, en variant le pH ou en ajoutant d'autres composés comme des ions ou des gaz. Le pH constitue le stimulus principal de ce travail et également de la plupart des études dans la littérature. Une valeur critique de pH, le pK_A, sépare les zones de solubilité et d'insolubilité du copolymère, qui s'autoassemble lorsque son caractère hydrophobe est trop important. La variation du pH conduit généralement à la protonation ou la déprotonation d'une fonction ionisable présente dans la chaîne polymère, ce qui peut soit favoriser des interactions ioniques avec d'autres espèces en solution, ou bien la formation de liaisons hydrogène. Les applications les plus communes des polymères sensibles au pH concernent la délivrance contrôlée de médicaments, en jouant sur les différentes valeurs de pH au sein du corps et également, la formation de gels dont la structure peut être modulée en variant la valeur du pH. Les autres stimuli chimiques consistent à ajouter des ions ou des gaz comme le CO_2, qui peuvent conduite à l'autoassemblage du copolymère ou à un changement de morphologie lorsque celui-ci est déjà auto-assemblé. La combinaison des stimuli physique et des stimuli chimiques est très largement privilégiée puisqu'elle multiplie les possibilités en termes de morphologies et donne accès à des systèmes sensibles à différentes variations de paramètres.

Les exemples précédents traitaient essentiellement des copolymères amphiphiles et une section est à présent consacrée aux copolymères double hydrophiles qui ont gagné en réputation ces dernières années, notamment grâce à leur solubilité complète dans l'eau leur permettant un usage plus aisé pour les applications en biologie. Leur composition se résume généralement à un bloc ionisable, pouvant interagir avec d'autres espèces ioniques ou être sensible au pH, et un bloc stabilisant, qui assurera une stabilité colloïdale en solution, comme le PAA-b-PEG (**Figure I-4**).

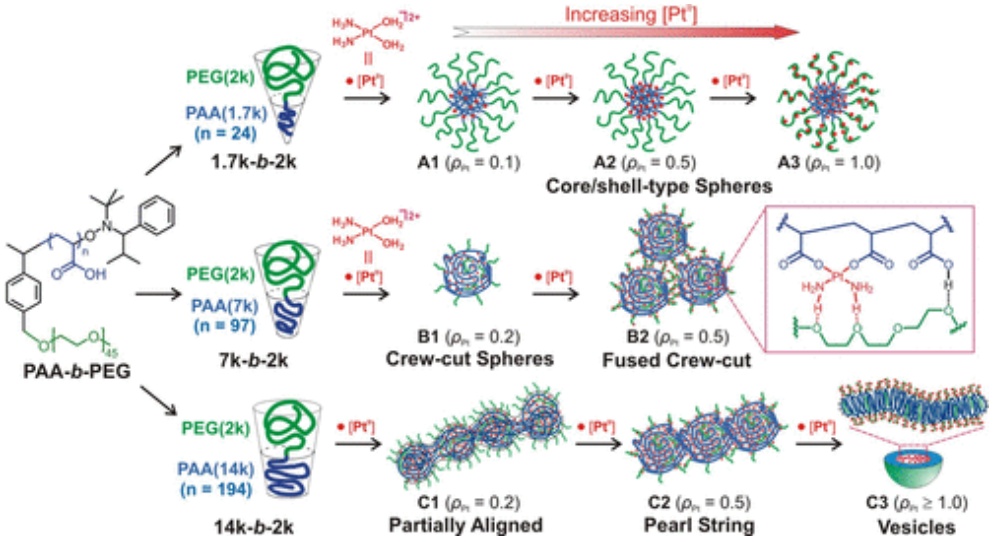

Figure II-4. Schéma des transitions entre les morphologies adoptées par les nanostructures contenant le complexe de platine Pt^{II} , dépendantes à la fois de la longueur bloc chélateur PAA et de la concentration en complexe de Pt^{II}

L'exemple ci-dessus illustre l'assemblage basé sur l'interaction d'un copolymère double hydrophile, PAA-b-PEG, et d'un complexe de platine, et dont la morphologie dépend à la fois la longueur du PAA et de la concentration en complexe de platine (**Figure I-4**).

II.2 Assemblages hybrides à base de copolymères à blocs

II.2.1 Assemblages composés d'ions et de copolymères à blocs

La formation d'assemblages hybrides est initiée par l'ajout de matière inorganique. Comme déjà évoqué, le caractère ionisable de certains polymères favorise leurs interactions en solution avec des ions, qui dans certains cas conduisent à l'assemblage du copolymère à travers la complexation de l'ion métallique, comme illustré en **Figure I-5.**

Les copolymères amphiphiles possédant un polymère ionisable peuvent être ici utilisées pour former des assemblages hybrides en présence d'ions, et permettent notamment d'obtenir un matériau final comme un film ou une membrane suite à l'évaporation du solvant organique dans lequel ils étaient solubilisés. Certains travaux ont ainsi pu obtenir des films à base de PS-b-PAA et d'ions Eu^{3+}, dont les propriétés de photoluminescence étaient remarquables, ou encore des membranes antibactériennes constituées de ce même copolymère et d'ions Ag^{+}, Zn^{2+} et Cu^{2+}.

Concernant l'utilisation des copolymères double hydrophile, les premiers travaux portaient sur des assemblages appelés HPICs, formés suite à l'ajout d'ions métalliques sur une solution de copolymère à blocs. Le groupe de N. Sanson a pu établir un mécanisme de structuration qui conduit à la formation d'un cœur constitué d'un complexe à caractère insoluble résultant de l'interaction entre le bloc ionisant et les ions, et d'une couronne favorisant la solubilisation de l'assemblage dans l'eau.

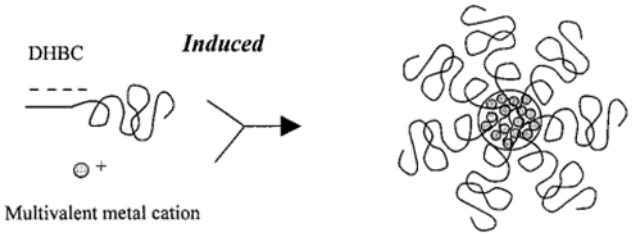

Figure II-5. Représentation schématique des HPICs sous forme de micelles

La variation de la nature des blocs du copolymère double hydrophile et du type d'ions a conduit à de nombreuses études semblables, dont la finalité dépend essentiellement des propriétés apportées par les ions. Par exemple, les ions gadolinium et manganèse apportent leurs propriétés magnétiques, qui sont amplifiées lorsque ces ions sont incorporés au sein des complexes ioniques. Les assemblages hybrides contenant ces ions, peuvent ainsi être utilisés en tant qu'agents de contraste pour l'imagerie par résonance magnétique (IRM). Sur le même principe, l'incorporation

des ions europium pour la luminescence et des ions cuivre pour de la catalyse de type réaction de Fenton, conduit également à des assemblages hybrides fonctionnels.

Lorsque le polymère est sensible à un autre stimulus que le pH, comme la température, son interaction avec les ions peut affecter ses propriétés thermosensibles et ainsi modifier les domaines de solubilité. En jouant à la fois sur la température et le pH, il devient alors possible d'obtenir plusieurs types de morphologies. Enfin, dans certains cas, les assemblages hybrides polymère-ion peuvent interagir de nouveau avec des ions, et ces interactions conduisent à des réactions chimiques formant des nanoparticules ou des hydroxides,

II.2.2 Assemblages de nanoparticules inorganiques et de copolymères à blocs

L'assemblage de nanoparticules inorganiques permet l'acquisition de propriétés collectives dont la performance surpasse celle des nanoparticules individuelles. Parmi les nanoparticules les plus utilisées, celles à base d'or constituent une majorité des études, puisqu'elles sont synthétisées à l'aide procédés simples et reproductibles. La modulation de leur taille, leur forme et leur fonctionnalisation est également aisée et très reportée dans la littérature, ce qui ouvre un éventail de possibilités concernant leur incorporation au sein de systèmes plus complexes. Afin d'obtenir des assemblages hybrides à base de nanoparticules d'or (AuNPs) et de polymères, il est nécessaire d'explorer dans un premier temps les trois possibilités de fonctionnalisation des AuNPs par les polymères, illustrées ci-dessous.

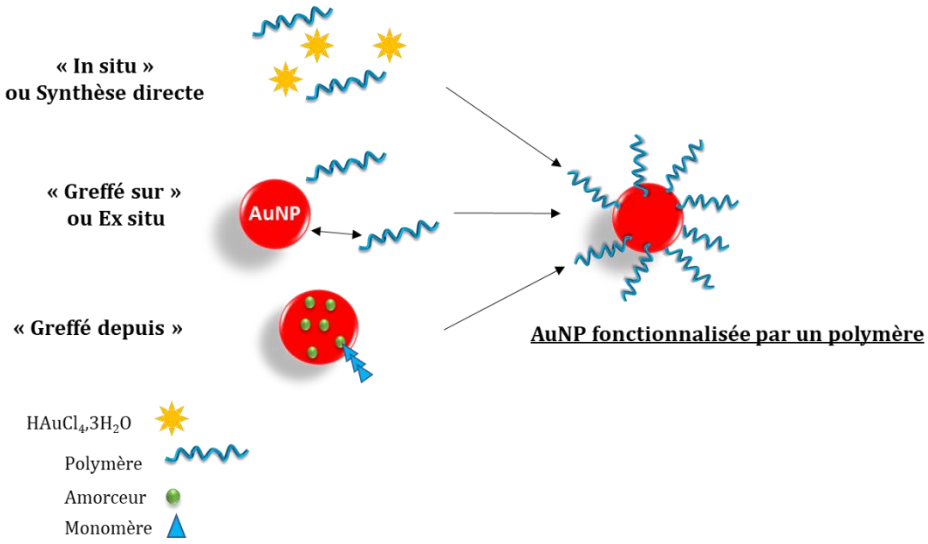

Figure II-6. Méthodes communes de fonctionnalisation des nanoparticules d'or (AuNPs) par des polymères

La méthode « in situ » se base sur l'interaction du sel inorganique d'or avec des espèces réductrices, telles que du borohydrate de sodium ($NaBH_4$) ou des fonctions amines pouvant être présentes au sein de polymères. Ainsi, les AuNPs sont formées en présence du polymère, qui va ainsi les fonctionnaliser. L'utilisation de la poly(vinylpyrrolidone) (PVP) est très reportée dans ce

cas-là, car il a été prouvé à de nombreuses reprises, que la PVP interagissait fortement avec l'or et l'argent lors de la nucléation et de la croissance des NPs. En effet, la PVP est souvent utilisée pour orienter la croissance de certaines facettes de la NP et ainsi favoriser une certaine forme ou taille finale. La PVP assure également une stabilisation des NPs, évitant leur aggrégration en solution.

La méthode ex situ nécessite des AuNPs déjà formées et fonctionnalisées avec un ligand dont l'interaction avec la surface d'or est suffisamment faible pour permettre un remplacement aisé par un polymère. Certaines fonctions chimiques, comme celles contenant du soufre, vont interagir davantage avec la surface d'or et permettre une fonctionnalisation plus forte. Enfin il est possible de fonctionnaliser la surface d'or avec des molécules capables d'initier la polymérisation d'un monomère entrant en interaction avec elles, afin de faire croître une chaîne polymère directement sur la particule d'or.

Ainsi ces différentes méthodes d'interaction dessinent deux schémas d'assemblages possibles : un portant sur l'assemblage d'AuNPs fonctionnalisées par les polymères et l'autre basé sur l'ajout d'AuNPs sur un système assemblé de polymères, illustrés ci-dessous.

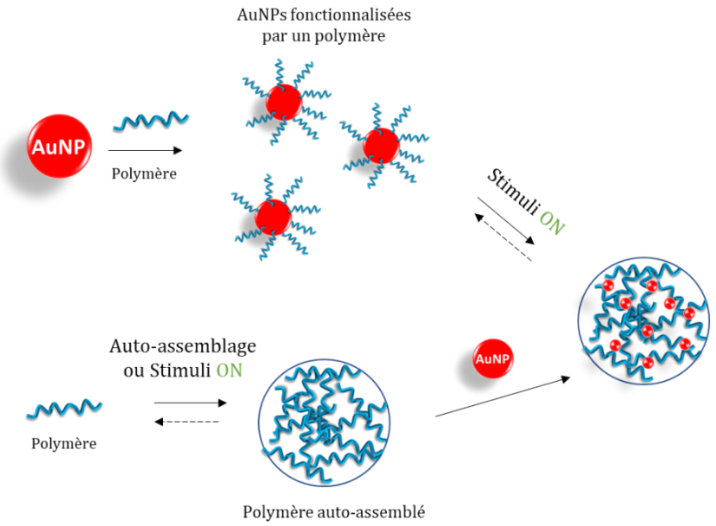

Figure II-7. Stratégies d'assemblages de polymères et de nanoparticules d'or (AuNPs) conduisant à des assemblages hybrides.

Comme précédemment, il est possible de jouer sur les caractéristiques propres au polymère pour indure son auto-assemblage ou l'assemblage des AuNPs qu'il fonctionnalise. Il est également très commun d'utiliser des polymères sensibles à certains stimuli physiques ou chimiques, pour provoquer ces types d'assemblages. Certains travaux se sont également portés sur l'utilisation des polymères ou de molécules telles que l'ADN pour contrôler précisément la localisation des AuNPs au sein des structures hybrides finales. Cette organisation contrôlée des nanoparticules inorganiques permet pour certaines applications d'acquérir des propriétés ciblées et pouvant être modérées.

II.3 Techniques de caractérisation des assemblages hybrides

Deux grandes catégories de techniques sont ici détaillées concernant la caractérisation des assemblages à base de polymères, d'ions et de nanoparticules inorganiques : les techniques de diffusion de rayons et les techniques de microscopie. Pour avoir une caractérisation complète de ces types de structures, il faut combiner ces deux catégories qui apportent chacune des informations relatives à la taille, la morphologie et la dispersion des structures en solution.

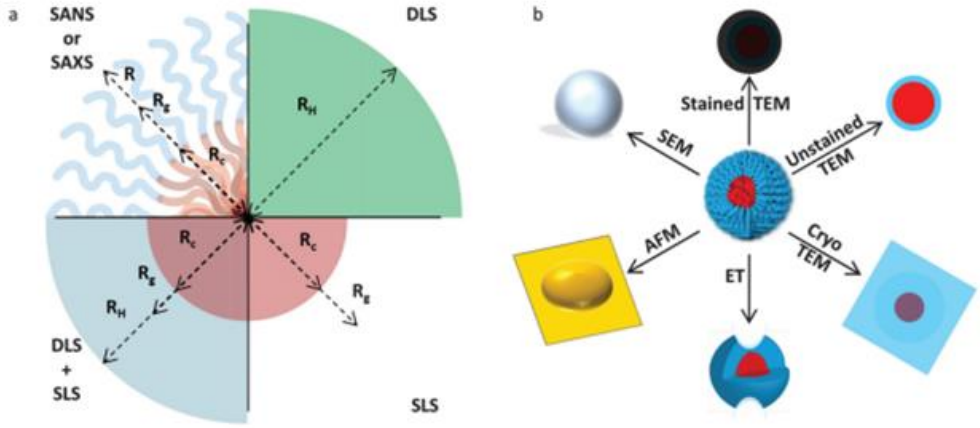

Figure II-8. Schéma représentant les différentes informations récoltées suite aux analyses de diffusion de rayons (A) et aux observations en microscopie (B) dans le cas d'une micelle sphérique.

Les techniques de diffusion les plus utilisées sont celle de la diffusion dynamique de la lumière (DLS), diffusion statique de la lumière (SLS), diffusion des rayons X (SAXS) et diffusion des neutrons (SANS). Elles sont toutes basées sur l'analyse du rayonnement diffusé par les structures en solution à un certain angle de détection. Elles donnent des informations sur la taille, la forme et les interactions intrinsèques des structures détectées en solution. Les analyses DLS et SLS informent sur le rayon hydrodynamique (R_H), taille en solution aqueuse, et le rayon de gyration (R_g), taille stricte. Les analyses SAXS et SANS sont effectuées à plus petite échelle et permettent ainsi une description de l'organisation interne des nanostructures. Les résultats issus de ces analyses sont généralement rapportés à des modèles mathématiques décrivant des morphologies bien spécifiques, qui ne correspondent pas toujours aux structures réellement observées. C'est pour cette raison, que les techniques basées sur la microscopie sont utilisées en complément, afin d'apporter une information visuelle concernant les structures en solution. Elles sont divisées en 3 catégories : optiques, électroniques et à balayage. Certaines d'entre elles se basent sur l'absorption d'électron et de rayons X, il est donc plus aisé de voir par les éléments inorganiques avec un Z élevé que les composés organiques comme les polymères, sur lesquels sont généralement ajoutés des agents contrastants. La TEM permet une visualisation en 2D de l'échantillon déposé et séché sur une grille. Une version cryogénisée (Cryo-TEM) de cette technique permet de s'exempter des déformations structurales dues au dépôt ou au séchage.

Enfin, il est possible de « tilter » ces grilles à différents angles afin de reconstituer une image en 3D de l'échantillon, il s'agit de la tomographie électronique (ET). Cette dernière technique étant particulièrement coûteuse, d'autres techniques de microscopie plus courants, la MEB et l'AFM, sont utilisées pour obtenir une visualisation en 3D des structures en solution.

III Chapitre II : Assemblages à base de PAA-b-PVP et d'ions métalliques : Gd^{3+}, Eu^{3+}, Y^{3+}.

Cette deuxième partie porte sur l'étude d'assemblages hybrides constitués d'un copolymère à blocs PAA-b-PVP et d'ions métalliques comme Gd^{3+}, Eu^{3+} et Y^{3+}. Notre intérêt s'est particulièrement porté sur l'ion gadolinium (Gd^{3+}), qui est généralement complexé par des structures organiques afin d'améliorer ses propriétés magnétiques, tout en assurant un agent non toxique dans l'organisme. Dans ce cadre, le PAA-b-PEG, un polymère double hydrophile, a été utilisé pour interagir à travers les fonctions carboxylate avec Gd^{3+} et former les structures introduites précédemment appelées HPICs. Les propriétés remarquables de relaxivité de ces structures ont conduit à des tests in vivo, qui ont confirmé une potentielle application en tant qu'agents de contraste pour l'IRM. Nous proposons dans ce travail une alternative au bloc stabilisant PEG afin de diversifier la préparation des HPICs en ayant notamment plus de manœuvre sur la synthèse du copolymère PAA-b-PVP. Les avantages du polymère PVP résident principalement dans sa facilité de synthèse, sa solubilité dans l'eau, sa biocompatibilité, et son utilisation très reportée en tant que stabilisant au sein de préparations destinées aux applications en biologie, telles que la bétadine. Les objectifs cette partie consistent à synthétiser ce copolymère à blocs PAA-b-PVP et étudier les interactions établies entre lui et les ions métalliques testés, afin de comprendre le mécanisme de formation des potentielles structures HPICs et évaluer leurs propriétés en tant qu'agents de contraste pour l'IRM. Ce cadre d'étude se base sur une comparaison avec les travaux réalisés sur les HPICs à base de PAA-b-PEG.

III.1 Synthèse du copolymère à blocs PAA-b-PVP

Grâce à la collaboration établie entre notre équipe de physico-chimistes et l'équipe spécialisée en synthèse de polymères (P3R), un protocole de synthèse du copolymère PAA-b-PVP a pu être établi en utilisant la technologie RAFT. Cette méthode de polymérisation repose sur l'utilisation d'un agent de transfert grâce auquel les réactions prématurées de terminaison seront fortement limitées et la polymérisation davantage contrôlée. Des synthèses de ce copolymère ont été réalisées par l'équipe P3R dans l'eau, mais elles conduisaient à la forme protonée du PAA qui conduisait à de nombreuses réactions de terminaison et réactions secondaires. Le protocole de synthèse choisi est détaillé ci-dessous en 3 étapes principales.

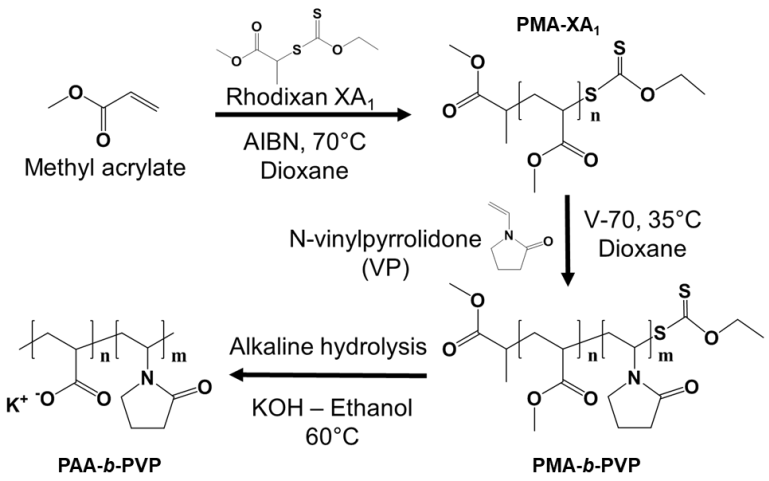

Figure III-1. Schématisation du protocole de synthèse du copolymère PAA-b-PVP en 3 étapes : 1) polymérisation RAFT du polymère Poly(méthyl acrylate) (PMA-XA_1), 2) polymérisation RAFT du polymère Poly(vinylpyrrolidone) (PVP) pour obtenir le copolymère à blocs PMA-b-PVP, 3) Hydrolyse en milieu basique de PMA-b-PVP pour obtenir PAA-b-PVP.

Comme le PMA-XA_1 constitue un agent RAFT plus efficace que son équivalent avec le PVP, le PMA est choisi comme le premier polymère à synthétiser pour optimiser le rendement final en copolymère PMA-b-PVP. Le PVP supportant plus difficilement les plus hautes températures, il a été décidé que celle-ci soit diminuée et qu'un autre amorceur, le V-70, un dérivé de l'AIBN soit utilisé en adéquation avec T=35°C. Enfin, une hydrolyse en milieu basique est réalisée afin d'obtenir un copolymère soluble dans l'eau, pour les perspectives d'étude du projet. Différentes masses molaires de copolymère ont pu être obtenues grâce à ce protocole de synthèse, qui mène à de très hautes conversions, et les caractéristiques précises des copolymères obtenus ont été définies suite à des analyses en ^{1}HNMR, ATR-FTIR et en chromatographie d'exclusion stérique (SEC). La composition qui sera la plus étudiée est la suivante : PAA_{32}-b-PVP_{59}.

III.2 Formation et caractérisation des HPICs à base de PAA-*b*-PVP

Parfaitement soluble dans l'eau, le copolymère PAA_{32}-b-PVP_{59} est ainsi étudié en présence des ions métalliques Gd^{3+}, Eu^{3+} et Y^{3+}. Les études se basent sur la variation du ratio de charges entre les fonctions carboxylate du polymère et les cations, défini comme $R=3.[M^{3+}]/[AA]$, avec M : cation métallique et AA : fonctions acide acrylique. Les échantillons sont analysés en DLS, technique présentée précédemment, pour obtenir une estimation de la taille des structures formées en solution aqueuse. La nature de l'ion métallique n'influence pas significativement la taille de la structure qui correspond en moyenne à un diamètre de 25 nm, ce qui est proche des 22 nm trouvés pour les structures à base de PAA-b-PEG. Cette taille est atteinte à partir d'un ratio de charges proche de l'unité, correspondant à une charge globale neutre, qui est effectivement confirmée par une mesure du potentiel zeta proche de 0 mV. Des images en HAADF-STEM ont permis de mesurer la taille du corps composé des ions Gd^{3+}, de 6.4±0.8 nm, qui est plus petite que

celle des nanostructures observées en TEM avec un diamètre d'environ 12 nm, confirmant ainsi l'encapsulation des ions au sein du polymère.

Afin d'identifier la nature des interactions existantes entre les fonctions carboxylate du bloc PAA et les cations, des analyses ATR-FTIR ont été réalisées sur les formes lyophilisées des échantillons à différents ratios de charges entre l'ion gadolinium et les fonctions AA (**Figure III- 2**. *Spectre ATR-FTIR du copolymère PAA32-b-PVP59 (courbe bleue) et des échantillons HPICs Gd3+/PAA32-b-PVP59 à différents ratios R.*.

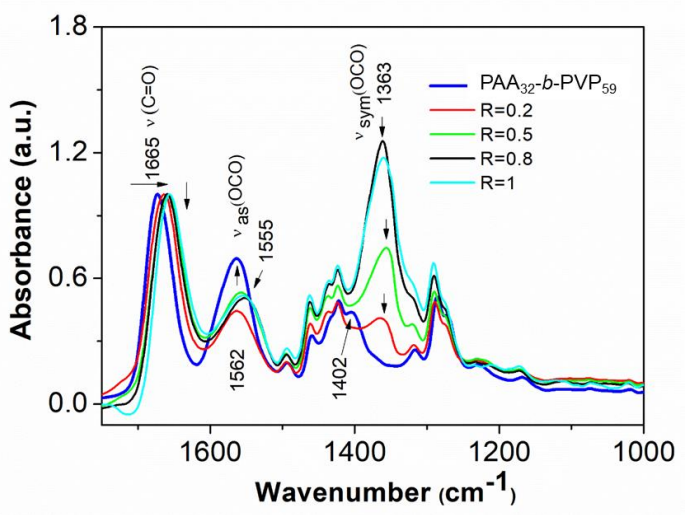

Figure III- 2. Spectre ATR-FTIR du copolymère PAA_{32}-b-PVP_{59} (courbe bleue) et des échantillons HPICs Gd^{3+}/PAA_{32}-b-PVP_{59} à différents ratios R.

Les bandes d'absorbance symétriques (1363 cm^{-1}) et asymétriques (1555 cm^{-1}) des fonctions carboxylate évoluent en fonction de la valeur du ratio R. La valeur de l'écart entre ces 2 bandes et son évolution ont permis de qualifier la complexation du gadolinium est de type monodentate, ce qui est en accord avec le caractère acide de l'ion, qui prône les interactions électrostatiques au sein de la première sphère de coordination du gadolinium. Pour des valeurs de R>1, les bandes carboxylate n'évoluent plus et seules les bandes caractéristiques des hydroxides de gadolinium apparaissent. Des analyses complémentaires en spectroscopie ^{1}HNMR ont de plus confirmé que les ions interagissaient davantage avec le bloc PAA, suggérant une structure core-shell organisée avec un « core » formé du PAA et des ions et une couronne de PVP. Ces résultats sont également confirmés après des analyses réalisées en RMN en utilisant l'ion Yttrium.

Des études en fluorimétrie ont été réalisées sur les structures HPICs à base de PAA-b-PVP et d'ions Eu^{3+}, qui sont des lanthanides à propriétés luminescentes. L'autofluorescence du PVP conduit à réaliser l'étude en mode phosphorescence pour uniquement observer la réponse radiative de l'ion europium complexé ou non. Ainsi, en faisant varier le ratio de charges R, les spectres d'émission

associés sont enregistrés en mode phosphorescence, c'est-à-dire en imposant un temps de délai entre l'excitation de l'échantillon et l'observation du spectre d'émission.

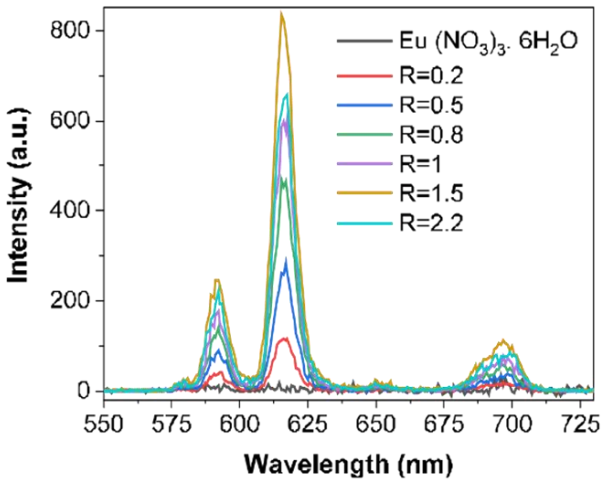

Figure III- 3. Spectres d'émission (λ_{ex}=256 nm) des échantillons HPICs Eu^{3+}/ PAA-*b*-PVP à différents ratios R

Les 3 bandes caractéristiques de l'ion europium figurent sur ces spectres ($^5D_0$ – $^7F_1$ à 591 nm, $^5D_0$ – $^7F_2$ à 615 nm et $^5D_0$ – $^7F_4$ à 697 nm). L'intensité des deux premières bandes augmente avec l'augmentation du ratio R, puis pour le dernier ratio (2.2) elle redescend. Il est également remarqué que l'intensité de l'ion seul est très inférieure à celle des spectres des HPICs. En effet, l'ion europium seul ne luminesce pas intensément car il y a un transfert non radiatif transmis aux groupements OH présents au sein des molécules d'eau dans la sphère de coordination de l'ion. Il est possible de calculer le nombre de molécules d'eau dans cette sphère en mesurant le temps de vie de l'ion à la fois dans H_2O et D_2O et en utilisant l'équation d'Horrocks et Supkowski (ci-dessous) :

$$q = 1.11 * (1/\tau_{H2O} - 1/\tau_{D2O} - 0.31)$$

Ces mesures sont réalisées sur l'ensemble des ratios et indiquent qu'en moyenne 3,7 molécules d'eau entourent l'ion jusqu'à un ratio R=1. Au-dessus de R=1, l'intensité de la bande à 615 nm rapportée à la concentration en ion Eu^{3+} est constante jusqu'à R=1 puis diminue pour R>1, indiquant un changement d'environnement de l'ion Eu^{3+}. La fluorimétrie est également utilisée dans le cadre d'une variation du pH de l'échantillon HPICs et a démontré une décomplexation progressive de l'ion europium par le bloc PAA, qui se protone au fur et à mesure de la diminution du pH, et qui est donc remplacé par des molécules d'eau qui diminuent les temps de vie et les intensités d'émission de l'ion europium. La mesure du pK_A du copolymère seul, pK_A ~3.2, confirme un changement de la taille des structures et de leurs propriétés luminescentes autour du pH = 4.

III.3 Tests en milieu biologique

L'intérêt se porte à présent sur le comportement de ces structures HPICs en milieux biologiques, ainsi que sur les propriétés dans ces milieux qui pourraient conduire à des applications en imagerie. Les HPICs à base de PAA-*b*-PVP et des ions Gd^{3+} ou Eu^{3+} sont préparés dans un milieu avec une forte concentration en NaCl (2M), le milieu de culture cellulaire sans sérum et celui avec sérum. D'après les analyses en fluorimétrie, la stabilité des HPICs est assurée en présence de NaCl. Cependant, la stabilité en milieu de culture cellulaire doit être étudiée plus précisément, car les analyses en fluorimétrie et en DLS ne permettent pas de conclure. Néanmoins une comparaison avec le PAA-b-PEG permet d'indiquer que les HPICs à base de PAA-b-PVP semblent néanmoins moins affectés par le milieu biologique en termes de propriétés luminescentes.

Des tests *in vitro* ont été réalisés sur des cellules humaines colorectales HCT 116, les systèmes testés sont les suivants : PAA-b-PVP seul, HPICs-Gd, HPICs-Eu, Gd^{3+} et Eu^{3+}. Différentes concentrations sont mises au contact des cellules pendant 48h puis la viabilité des cellules est mesurée par absorbance à l'aide d'un additif (PrestoBlue). Les résultats ont démontré que la cytotoxicité du copolymère était très limitée même à la plus haute concentration (0.1%wt). En revanche, comme attendu, les ions sont toxiques lorsqu'ils sont seuls au contact des cellules. Cette cytotoxicité est drastiquement réduite lorsque les ions sont encapsulés au sein des structures HPICs. Ainsi, les résultats démontrent que les HPICs peuvent être utilisés en milieu cellulaire à des concentrations en polymère et en ions autour de 0.07%wt et 0.9 mM, respectivement.

Des mesures de relaxivité ont été réalisées sur les HPICs-Gd dans l'eau et dans le milieu de culture cellulaire avec sérum et ont démontré un très bon potentiel de ces structures pour être utilisées en tant qu'agents de contraste pour l'IRM. Les valeurs enregistrées sont plus élevées que l'ion Gd^{3+} seul et les HPICs à base de PAA-b-PEG. Des tests in vivo ont alors été engagés sur des souris pour évaluer le comportement des HPICs dans l'organisme et quantifier le contraste apporté.

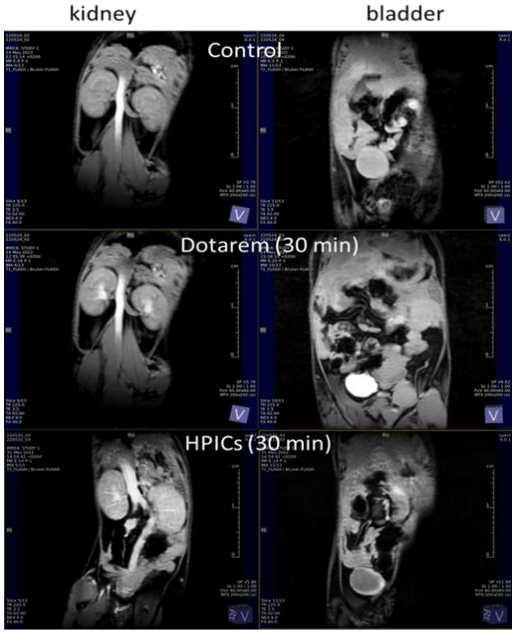

Figure III- 4. Images coronaires basées sur le signal T_1 30 min après injection du Gd-DOTA (milieu) et des HPICs-Gd (bas) comparés au contrôle (haut). Les images sont centrées sur les reins (gauche) et la vessie (droite).

Les résultats de ces tests in vivo ont prouvé que le temps de clairance des structures HPICs était plus important que le Gd-DOTA qui est rapidement retrouvé dans la vessie. De plus l'apport de contraste des structures HPICs a été évalué à +67% par rapport au Gd-DOTA, ce qui constitue un bon point de départ pour une série d'essais in vivo avec un suivi de la distribution de l'agent dans l'organisme et de sa quantification.

IV Chapitre III – Interactions entre des nanoparticules d'or fonctionnalisées et des ions métalliques

Comme expliqué précédemment, la préparation d'agents de contraste à base de gadolinium pour l'IRM, nécessite une précaution particulière quant à la présence d'ions Gd^{3+} libres, qui sont toxiques pour l'organisme. Bien que les techniques de titration comme l'ICP-MS soient précises, elles sont également coûteuses et longues à réaliser. L'objectif de ce chapitre était alors d'élaborer un test rapide de quantification des ions Gd^{3+}, entre autres ion, qui serait basé sur l'aggrégation des nanoparticules d'or (AuNPs), comme beaucoup de tests reportés dans la littérature. En effet, les propriétés plasmoniques des AuNPs permettent de savoir visuellement si celles-ci sont agrégées en solution ou non, à travers une potentielle interaction avec des ions.

Dans ce contexte, des AuNPs stabilisées par des ligands citrate (AuNP@citrate), synthétisées par la classique méthode Turkevich, sont modifiées en surface à travers un échange de ligand avec la bis(p-sulfonatophenyl)phenylphosphine (BSPP). Ce ligand interagit fortement avec la surface d'or à travers son atome de phosphore et est capable d'interagir avec des ions par voie électrostatique.

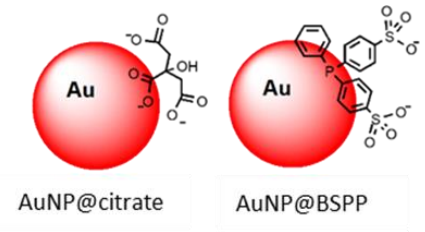

Figure IV-1. Représentation schématique des AuNP@citre (gauche) et des AuNP@BSPP (droite)

Des concentrations croissantes en ions Gd^{3+} sont ajoutées aux AuNP@citrate et AuNP@BSSP et un suivi cinétique en spectroscopie UV-visible est réalisé. Seules les AuNP@BSPP s'aggrègent au contact des ions, le suivi UV-vis permet ainsi de quantifier cette aggrégation à travers l'utilisation d'un paramètre de flocculation (FP) défini comme étant l'aire d'absorbance supplémentaire acquise lors de l'aggrégation. Ainsi, il est possible de savoir pour chaque concentration en ion Gd^{3+}, à quelle vitesse l'aggrégation (aggregration rate) des AuNP@BSPP se déroule et quel est le paramètre de flocculation final maximal (FPmax) acquis. Une relation linéaire est établie entre FPmax et la concentration en Gd^{3+}, ce qui permettra de connaître la concentration des ions au sein d'une solution inconnue, après mélange de celle-ci avec les AuNP@BSPP.

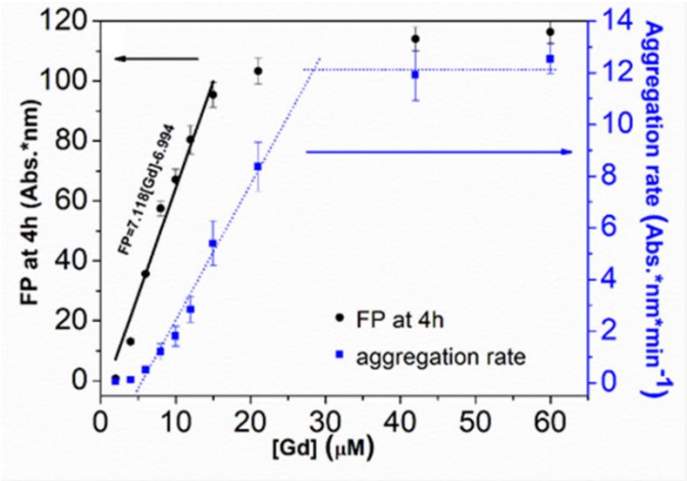

Figure IV-2. FP à 4h (noir) and Vitesse d'aggrégation (bleu) en fonction de la concentration en Gd^{3+}

Afin de comprendre la nature des interactions entre les AuNP@BSPP et les ions, et de comprendre la différence avec les AuNP@citrate, des essais sur une microbalance à quartz sont réalisés. Les solutions de ligands sont mises au contact de la surface d'or des quartz et la mesure de la fréquence des vibrations de ces disques, directement reliées à la masse déposée sur le disque, permet de quantifier l'interaction de ces ligands avec la surface d'or. L'ajout des ions par-dessus ces couches de ligands à la surface d'or, permet également, à travers l'application de modèles, d'identifier la nature des interactions existantes entre les ligands et les ions Gd^{3+}. Il est alors révélé que l'ion Gd^{3+} forme un complexe 1 :1 avec le citrate et comme le citrate est en large excès en solution, l'interaction avec cet ion ne permet pas la formation d'un réseau entre les AuNP@citrate,

contrairement aux AuNP@BSPP, qui interagissent elles à la fois à travers des liaisons hydrogène et des liaisons electrostratiques avec l'ion Gd^{3+}.

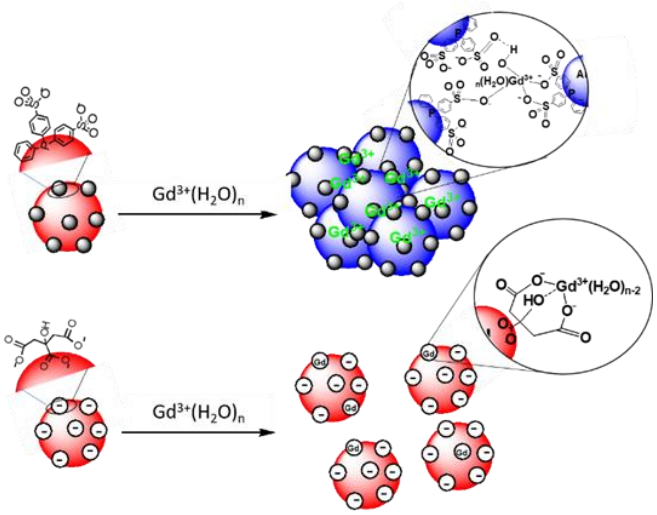

Figure IV- 3. Schéma des interactions entre les AuNP@citrate, les AuNP@BSPP et les ions Gd^{3+}

Le test a été appliqué à des préparations de HPICs à base de PAA-b-PEG ou PAA-b-PVP et d'ions Gd^{3+} à différents ratios. Ces échantillons étaient filtrés pour récupérer les ions Gd^{3+} potentiellement libres en solution et les AuNP@BSPP ont été ajoutées à ces filtrats. Les titrations ont été complétées avec une quantification ICP-MS. Les résultats démontrent que le test permet de déterminer aisément et rapidement la présence de ces ions Gd^{3+} en solution avec une relation linéaire établie entre 0 et 18 µM. Les limites de quantification et de détection de ce test sont 4.76 µM et 0.74 µM, respectivement. Les valeurs des concentrations en Gd^{3+} issues du test sont précises pour les faibles concentrations en solution, pour des valeurs plus élevées il est préférable d'utiliser l'ICP-MS.

V Chapitre IV – Etude de l'autoassemblage du PAA-b-PVP et des assemblages avec des nanoparticules d'or et des ions répondant à la variation de pH

Cette dernière partie du travail de thèse porte sur l'étude de la sensibilité au pH du copolymère synthétisé précédemment, le PAA-b-PVP, qui amène à l'autoassemblage du copolymère et à des assemblages hybrides constitués de nanoparticules d'or et/ou d'ions.

V.1 Formation et caractérisation des assemblages répondant au pH

Comme expliqué au cours du chapitre bibliographique, l'utilisation du stimulus du pH permet d'induire l'autoassemblage de copolymères à blocs constitués d'un groupe chimique ionisable. En diminuant le pH, le PAA est protoné progressivement et l'apparition de liaisons hydrogène avec le PVP, reportée abondamment dans la littérature entre les homopolymères PAA et PVP, conduit

à la formation de nanoassemblages en solution. La faiblesse de ces liaisons permet d'avoir un processus d'autoassemblage réversible. L'interaction privilégiée du polymère PVP avec l'or reportée dans la littérature dirige notre étude vers l'étude des interactions entre le PAA-b-PVP et des AuNPs en solution. La stabilisation des AuNPs est effectivement assurée par le PAA-b-PVP et confirmée lorsque la variation de pH est appliquée, puisque les nanoassemblages observés précédemment avec le polymère seul, sont ici formés et semblent incorporer les AuNPs. Des observations en HAADF-STEM confirment que les AuNPs sont bien à l'intérieur des nanostructures à travers une nuance du contraste en profondeur.

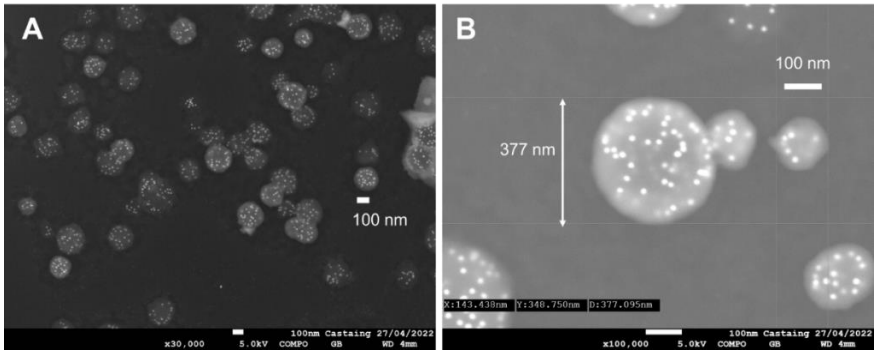

Figure V- 1. Images HAADF-STEM de l'échantillon contenant le PAA_{32}-b-PVP_{59} (0.05%wt) et les Au@citrate ([Au]=500 µM) à pH=2.5 à deux échelles x30.000 (**A**) and x100,000 (**B**)

V.2 Compréhension du mécanisme de formation des assemblages

La compréhension du mécanisme de formation de ces nanoassemblages s'est construite à travers des essais sur microbalance à quartz, des suivis UV-visible de la cinétique de l'assemblage et des variations de paramètres tels que la concentration en copolymère. Il est ressorti des ces études que 1) le copolymère a une affinité supérieure à celle des homopolymères avec les surfaces d'or, particulièrement en milieu acide ; 2) les cinétiques de formation et de « destruction » des assemblages sont très rapides, supposant un échange rapide des ions et donc des structures très hydratées ; 3) la concentration en polymère est un paramètre critique pour la stabilisation des AuNPs et la taille finale du nanoassemblage obtenu après diminution du pH.

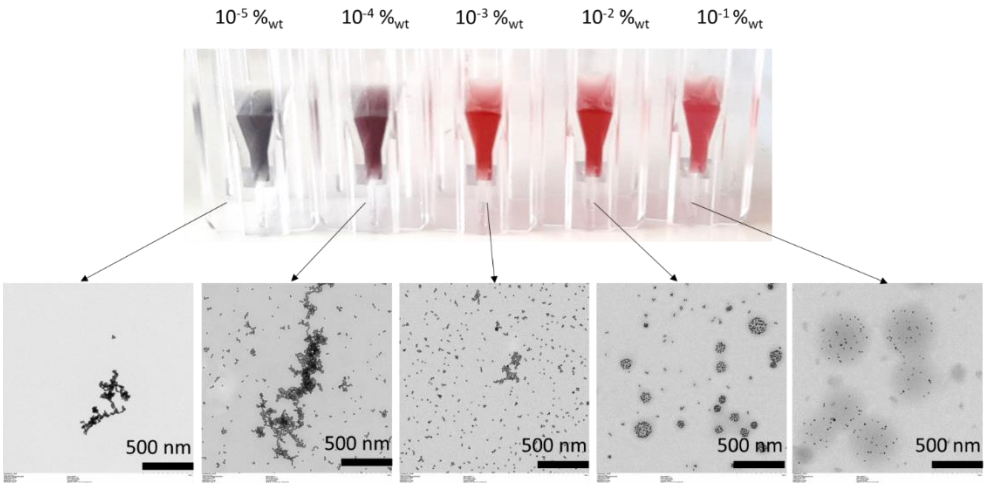

Figure V- 2. Photos des solutions contenant des concentrations variables en copolymère PAA_{32}-*b*-PVP_{59} ([PAA_{32}-*b*-PVP_{59}]=10^{-5}-10^{-1}%wt) et une concentration fixe en nanoparticules d'or [Au] = 500µM à pH=2.5, associées aux images TEM des 5 échantillons

La variation de la préparation des ces assemblages est également effectuée : l'ajout de NaCl avant ou après la diminution du pH, n'influence pas la formation des structures ; par contre, lorsque les AuNPs sont ajoutées une fois que le polymère est auto-assemblé à pH 2.5, elles ne sont pas incorporées dans les structures, même une semaine après, ce qui prouve que l'interaction du PVP avec l'or doit être effectuée avant que celui-ci forme des liaisons hydrogène avec l'autre bloc PAA.

V.3 Variation des paramètres impliqués dans l'assemblage

Afin de valoriser l'utilisation du copolymère à blocs et du PVP comme bloc stabilisant, des comparaisons sont effectuées avec le copolymère PAA-b-PEG et le mélange des homopolymères PAA et PVP. Le PAA-*b*-PEG seul forme lui aussi des nanoassemblages en conditions acides, dont la formation se base sur des liaisons hydrogène également. Seulement, le PAA-b-PEG ne stabilise pas les AuNPs en solution, la variation du pH conduit alors à des précipitations, ce qui confirme que le PVP est davantage adapté pour la stabilisation d'AuNPs et la formation d'assemblages hybrides.

Le mélange des deux homopolymères a également été testé seul et en présence de AuNPs. La diminution du pH de 'PAA+PVP' conduit à la formation de nanoassemblages dont la taille est supérieure à celle des structures obtenues avec le copolymère à blocs (environ 200 nm de différence en DLS et en TEM). Les interactions à l'origine de l'assemblage sont également des liaisons hydrogènes. Néanmoins, certaines différences sont décelées à travers l'analyse élémentaire et la variation de la concentration en polymère.

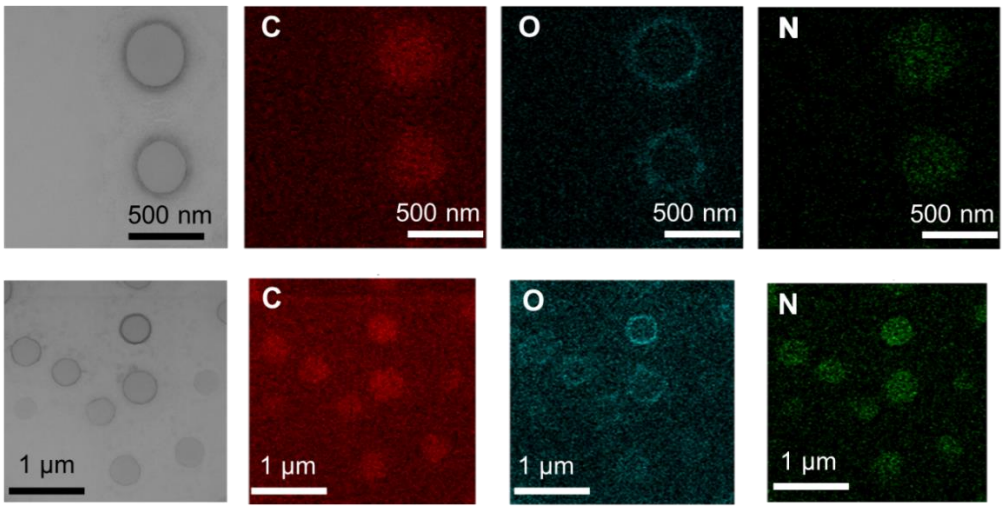

Figure V-3. Images TEM et analyses élémentaires de l'échantillon contenant le mélange PAA_{25} + PVP_{72} (0.05%wt) pour les éléments suivants : carbone, oxygène, azote à deux échelles d'observation.

Comme observé sur les images ci-dessus, l'élément oxygène semble être préférentiellement localisé en bordure des nanoassemblages. L'azote semble réparti dans la nanostructure, mais des images complémentaires sur des échantillons avec les AuNPs, confirment une localisation au centre des nanoassemblages, ce qui supposerait une configuration core-shell, mais qui nécessite des analyses complémentaires. Des tests à des concentrations de 1%wt en polymère ont été réalisés en présence des AuNPs et le mélange des homopolymères finit par précipiter en solution, contrairement à l'échantillon contenant le copolymère à blocs. Ces comparaisons justifient la nécessité d'une configuration bloc et du polymère PVP pour assurer la stabilité des AuNPs.

La variation en concentration des AuNPs en conservant la concentration en copolymère, a été réalisée et montre que cela agit sur la densité en AuNPs à l'intérieur des nanoassemblages sans affecter significativement la taille des nanoassemblages. A la concentration la plus élevée (1510 µM) il semble même que les AuNPs ne soient pas toutes incorporées dans les nanoassemblages, révélant une limitation vis-à-vis de la fonctionnalisation du polymère. Des analyses en SAXS révèlent l'apparition d'une interaction supplémentaire entre les AuNPs pour les plus hautes concentrations en AuNPs, suggérant une proximité évidente entre celles-ci au sein des structures polymériques.

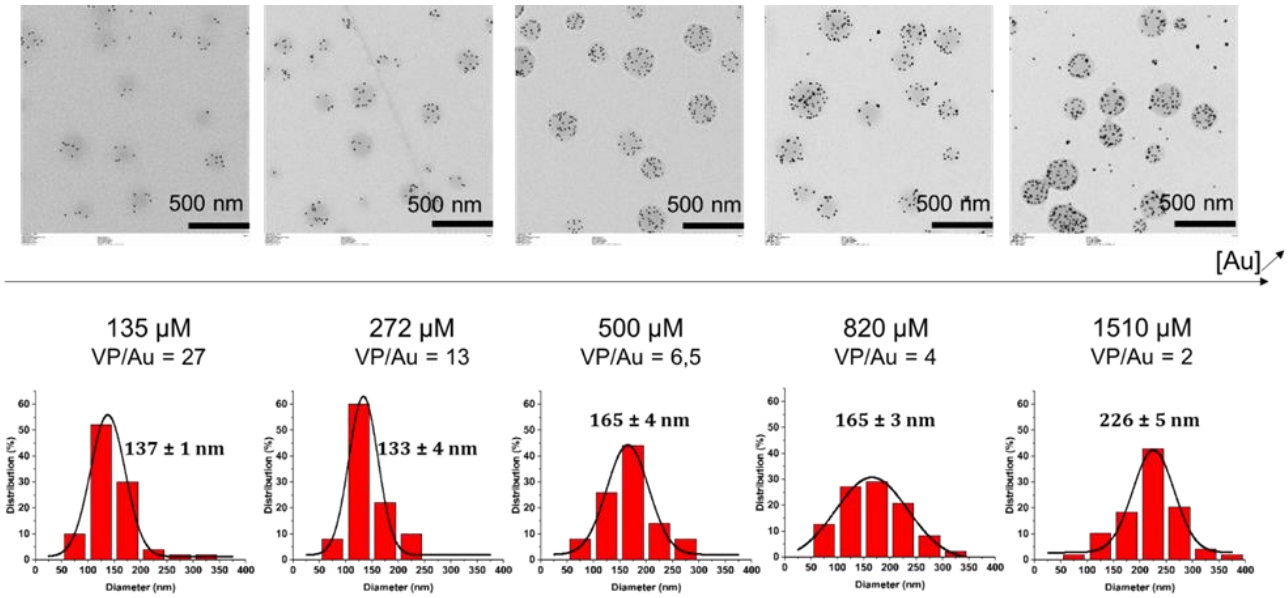

Figure V- 4. Images TEM et distributions de taille des échantillons contenant une concentration fixe en copolymère PAA-b-PVP (0.05%wt) et des concentrations variables en AuNPs: 135, 272, 500, 820, 1510 µM, à pH = 2.5.

Afin d'évaluer les limites de la formation des ces assemblages, les différentes versions du copolymère à blocs, comprenant différentes longueurs du bloc PVP, sont testées seules et en présence des AuNPs. Réduire la longueur totale du copolymère en changeant la longueur du PVP conduit à une diminution de la taille des nanoassemblages formés. L'ajout de polymères supplémentaires, PAA, PVP ou PAA-b-PEG, au sein de l'échantillon est également engagé et certaines variations de taille sont observées pour l'ajout du PAA ou du PVP, mais restent très faibles. Par contre, l'ajout de PAA-b-PEG empêche la formation de nanoassemblages incorporant les AuNPs sans pour autant mener à la précipitation. Un réseau de liaisons hydrogène semble se former entre les deux copolymères et mène à des nanoassemblages polymériques en l'absence d'AuNPs, ou à un réseau en solution maintenant les AuNPs dispersées.

Plusieurs paramètres reliés au polymère et aux concentrations en solution, ont été jusqu'ici étudiés, et pour cette dernière partie, la variation de la composition inorganique est engagée. Les nanoparticules d'or testées étaient jusqu'ici des nanoparticules préformées et fonctionnalisées par des ligands citrate, puis par échange de ligand, par le copolymère à blocs. Des essais sont réalisés en utilisant la voie de fonctionnalisation « in situ » c'est-à-dire en synthétisant les AuNPs en présence du polymère. Une étape de nucléation est réalisée dans un premier temps en introduisant le copolymère à blocs, le sel d'or et l'agent réducteur, ici le $NaBH_4$. Des germes d'or sont ainsi obtenus, puis l'ajout de sel d'or supplémentaire et d'un second agent réducteur, l'acide ascorbique, la croissance des germes mène à l'obtention de nanoparticules d'or. Pour s'assurer de la fonctionnalisation de ces AuNPs, la variation de pH de l'échantillon final est réalisée pour former les nanoassemblages. Effectivement, les nanostructures obtenues contiennent les AuNPs formées

in situ, mais ne présentent pas des formes aussi sphériques qu'avec les AuNP@citrate. De plus, la taille et la forme des AuNPs in situ sont très variées, significatives d'une croissance inégale, nécessitant une optimisation certaine du processus.

Enfin les derniers travaux sont très exploratoires et l'interprétation des résultats reste à approfondir. La variation de pH est appliquée sur les systèmes HPICs étudiés précédemment, pour évaluer le comportement du copolymère en présence des ions gadolinium. Il semble que les ions Gd^{3+} n'empêchent pas la formation des nanoassemblages en conditions acides. Cependant, le processus n'est plus complètement réversible, car en réaugmentant la valeur du pH, les nanoassemblages ne semblent pas complètement déstructurés. Le même phénomène est observé en présence de nanoparticules d'or (préformées ou non) et les études cinétiques effectuées en UV-visible confirment la non-réversibilité à travers la différence d'absorbance avant augmentation et après diminution du pH. En conditions basiques, il semble néanmoins que les AuNPs soient peu à peu libérées des nanoassemblages. Les ions gadolinium ont ainsi une influence sur le maintien des nanoassemblages en conditions basiques mais ne permettent pas une conservation totale.

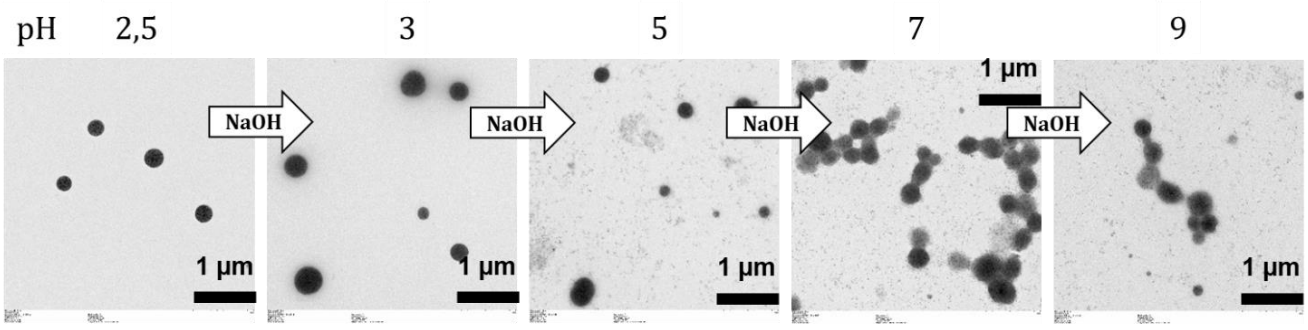

Figure V-5. Images TEM de l'échantillon contenant PAA_{32}-*b*-PVP_{59} (0.05%wt), ions Gd^{3+} (0.7 mM) et les AuNPs formées in situ ([Au]=500 µM) à différentes valeurs de pH suite à l'ajout d'une solution NaOH (1M)

Des procédés de filtration sont réalisés sur les systèmes contenant les ions gadolinium à pH=2.5 et à pH=7 et la titration des ions a été effectuée sur les filtrats, par ICP-MS et grâce au test colorimétrique mis en place précédemment. Il en a été conclu que les filtrats des systèmes à pH=2.5 contiennent la totalité des ions introduits, alors qu'à pH=7, très peu d'ions sont retrouvés dans le filtrat. Cela confirme que les ions ne sont pas contenus dans les nanoassemblages, mais interagissent en conditions basiques par liaisons électrostatiques avec le bloc PAA. La compréhension du rôle précis des ions gadolinium dans ces systèmes est à poursuivre et à affiner.

VI Conclusions

L'étude d'assemblages moléculaires à l'échelle nanométrique est très engagée dans la recherche scientifique avec pour but de mimer les phénomènes issus de la nature, et de comprendre les mécanismes de formation de ces assemblages et les paramètres clés qui y sont reliés. Le travail de

ce projet de thèse s'inscrit donc dans cette thématique, présentant une étude complète sur des assemblages en solution de copolymères à blocs, d'ions métalliques et de nanoparticules d'or. Les objectifs principaux étaient de comprendre le rôle de chacun des composés, l'influence de chaque paramètre relié au mécanisme d'assemblage et de caractériser les assemblages obtenus.

Le composé principalement utilisé dans cette étude est le copolymère à blocs PAA-b-PVP. Il a été synthétisé par voie RAFT dans le dioxane et caractérisé par les analyses ^{1}HNMR, ATR-FTIR et SEC, qui ont confirmé une haute conversion et une masse moléculaire contrôlée. Ce copolymère représente le composé de base des assemblages étudiés. Il s'autoassemble de façon réversible en conditions acides, formant des nanoassemblages à base de liaisons hydrogène dont la taille est aux alentours de 200 nm pour une concentration à 0.05%wt. Cette taille est modulable à travers la concentration, la masse moléculaire du copolymère et également l'ajout des homopolymères associés PAA et PVP.

Le copolymère à blocs peut interagir en milieu basique avec des ions métalliques à travers le groupement ionisable PAA. Des structures HPICs de 25 nm de diamètre sont obtenues avec plusieurs types d'ions : Gd^{3+}, Eu^{3+}, Y^{3+}. Le mécanisme de formation est étudié grâce aux techniques spectroscopiques, qui confirment une interaction le bloc PAA formant un cœur légèrement hydrophobe entouré du PVP formant la couronne hydrophile. Les propriétés de fluorescence et de relaxivité de ces structures donnent de bons espoirs quant à l'utilisation des structures pour l'imagerie médicale, et les tests positifs in vitro et in vivo constituent un bon point de départ.

Dans un souci de vérification de l'absence d'ions Gd^{3+} dans la préparation d'agents de contraste pour l'IRM, un test colorimétrique basé sur l'aggrégation des AuNPs en solution a été élaboré pour titrer ces ions. A travers l'utilisation d'un paramètre reflétant l'aggrégation des AuNPs nommé paramètre de flocculation, une courbe d'étalonnage a pu être établie et permet de relier le décalage de la bande SPR à la concentration en ions Gd^{3+} en solution. Le test n'est pas spécifique et n'est pas précis pour de trop hautes concentrations en ions, mais permet malgré tout de rapidement savoir si les ions sont présents ou non, ce qui évite l'utilisation de techniques coûteuses.

Enfin, les assemblages hybrides regroupant PAA-b-PVP et les AuNPs, préformées ou formées in situ, sont étudiés du point de vue mécanistique. Le bloc PVP et la configuration bloc se révèlent indispensables pour stabiliser les AuNPs à toute valeur de pH. Les AuNPs sont bien incorporées à l'intérieur des structures polymériques et leur densité varie avec leur concentration. Pour finir, l'ajout d'ions gadolinium semble influencer ces mécanismes d'assemblage, à travers un maintien des structures en conditions basiques. Cependant, ces essais nécessitent une étude approfondie.

Résumé de thèse

L'étude des assemblages à l'échelle moléculaire connaît aujourd'hui un essor grandissant. Les mécanismes impliqués dans la formation de ces assemblages, grandement inspirés de phénomènes issus de la nature, ont permis d'ouvrir les portes de nombreuses applications en biologie telle que l'imagerie médicale, la délivrance de principes actifs ou encore le traitement du cancer. Pour ces applications, ces assemblages doivent à la fois présenter une grande stabilité en milieu biologique et des propriétés compatibles avec le domaine visé. Ce travail porte ainsi sur l'étude de différents assemblages mettant en jeu des copolymères à blocs, des ions trivalents (Y^{3+}, $Gd^{3+,}$ Eu^{3+}) et des nanoparticules d'or.

Nous avons tout d'abord montré que le poly(acide acrylique)-*bloc*-poly(N-vinyl-2-pyrrolidone) (PAA-*b*-PVP) synthétisé par un procédé RAFT forme en présence d'ions trivalents tel que Y^{3+}, $Gd^{3+,}$ Eu^{3+}, des structures nanométriques. Ces assemblages possèdent une bonne stabilité colloïdale en solution aqueuse et une faible toxicité cellulaire *in vitro*. Les colloïdes à base de gadolinium ont en outre démontré de très bonnes performances en tant qu'agent de contraste pour l'imagerie IRM. Nous avons enfin montré que le PVP est un substitut du PEG à considérer pour la création d'assemblages à visée biologique.

Dans un second temps, l'étude d'assemblages à base de nanoparticules d'or et d'ions a été engagée. Les interactions générées modifient les propriétés optiques des particules d'or, ce qui a conduit à la mise en œuvre facile et rapide d'un test colorimétrique. Ce test a permis la détection et quantification d'ions Gd^{3+} jusqu'à des concentrations de l'ordre du mM. Un contrôle systématique des échantillons dédiés à l'imagerie par IRM a pu ainsi être réalisée sans avoir recours à des techniques chronophages et très coûteuses.

Enfin, les derniers travaux portent sur des assemblages supracolloïdaux dont la formation provient du caractère pH-sensible du PAA-*b*-PVP en solution. L'abaissement du pH d'une solution aqueuse de ce copolymère conduit à la formation d'objets sphériques par la mise en place de liaisons hydrogène entre les groupements « acide acrylique » (AA) et « vinyle pyrrolidone » (VP). La taille de ces objets dépend à la fois des caractéristiques propres au polymère (configuration, masse moléculaire) et de sa concentration en solution. En dépit de sa simplicité, ce type d'assemblage réversible présente la particularité de pouvoir piéger en son sein, là aussi de façon réversible, des NPs d'or initialement mises en présence du polymère. L'interaction forte entre la surface des NPs d'or et les fonctions VP du polymère sont ici la force motrice, induisant l'intégration des NPs d'or au sein des assemblages. Des tests préliminaires portant sur différents assemblages hybrides à base de copolymère PAA-*b*-PVP, d'ions de Gd^{3+} et de NPs d'or ont été initiés ouvrant ainsi des perspectives vers la construction des matériaux à propriétés originales.

Scientific research about assemblies at molecular scale knows now an expanding development. Indeed, the mechanisms involved into the formation of these assemblies are highly inspired from natural phenomenon. Therefore, the mimic of these assembly strategies at nanometer scale permit the access of many biological application fields such as imaging field, drug delivery or cancer treatment. For that purpose, assemblies targeting these applications, must at least present both obvious stability in biological medium and suitable properties for the chosen field. This present work is about the study of assemblies involving block copolymers, trivalent ions (Y^{3+}, Gd^{3+}, Eu^{3+}) and gold nanoparticles.

First, we showed that the poly(acrylic acid)-block-poly(N-vinyl-2-pyrrolidone) (PAA-b-PVP) polymer synthesized via a RAFT polymerization process, formed in presence of trivalent ions such as (Y^{3+}, Gd^{3+}, Eu^{3+}) nanostructures. Latter assemblies displayed good colloidal stability in water and a low cytotoxicity in vitro. Besides, the gadolinium-based colloids revealed high performance as contrast agents for MRI imaging field. We demonstrated at the end that PVP offers a great opportunity to replace PEG into the design of assemblies for biological applications.

Secondly, the study of assemblies involving gold nanoparticles and ions was explored. The resulting interactions modified the gold nanoparticles' optical properties, which lead to an easy and simple set up of a colorimetric test. This test allows the detection and quantification of Gd^{3+} ions in the range of mM concentrations. A systematic control of the samples prepared for MRI imaging was then realized without using time-consuming and expensive techniques.

Finally, the investigations regarding supracolloidal assemblies based on the pH-responsiveness behavior of the PAA-b-PVP in solution were conducted. Lowering the pH of water solution of this copolymer induced the formation of spherical objects based on hydrogen bonds' creation between the acrylic acid (AA) and vinyl pyrrolidone (VP) functions. The final size of these objects depends on both polymer's initial characteristics (configuration, molecular weight) and on its concentration in solution. Despite its simplicity, this assembly process was proved to be reversible and showed the particularity to enable the reversible trap of gold NPs initially introduced in the polymer solution. Indeed, the strong interaction between gold NPS and VP functions represent here the driving force leading to the entrapment of the gold NPs into the assemblies. Preliminary tests were conducted onto hybrid assemblies of PAA-b-PVP, Gd^{3+} ions and gold NPs, opening then perspectives toward design of materials with original properties.